ADVANCED PROCESSES FOR WASTEWATER TREATMENT AND WATER REUSE

EDITED BY: Rui C. Martins, Rosa M. Quinta-Ferreira, Maria Graca Rasteiro,
Renato Falcão Dantas and Marta Gmurek
PUBLISHED IN: Frontiers in Environmental Science and Frontiers in Chemistry

frontiers Research Topics

ISSN 1664-8714
ISBN 978-2-88966-344-6
DOI 10.3389/978-2-88966-344-6

About Frontiers

Frontiers is more than just an open-access publisher of scholarly articles: it is a pioneering approach to the world of academia, radically improving the way scholarly research is managed. The grand vision of Frontiers is a world where all people have an equal opportunity to seek, share and generate knowledge. Frontiers provides immediate and permanent online open access to all its publications, but this alone is not enough to realize our grand goals.

Frontiers Journal Series

The Frontiers Journal Series is a multi-tier and interdisciplinary set of open-access, online journals, promising a paradigm shift from the current review, selection and dissemination processes in academic publishing. All Frontiers journals are driven by researchers for researchers; therefore, they constitute a service to the scholarly community. At the same time, the Frontiers Journal Series operates on a revolutionary invention, the tiered publishing system, initially addressing specific communities of scholars, and gradually climbing up to broader public understanding, thus serving the interests of the lay society, too.

Dedication to Quality

Each Frontiers article is a landmark of the highest quality, thanks to genuinely collaborative interactions between authors and review editors, who include some of the world's best academicians. Research must be certified by peers before entering a stream of knowledge that may eventually reach the public - and shape society; therefore, Frontiers only applies the most rigorous and unbiased reviews.
Frontiers revolutionizes research publishing by freely delivering the most outstanding research, evaluated with no bias from both the academic and social point of view. By applying the most advanced information technologies, Frontiers is catapulting scholarly publishing into a new generation.

What are Frontiers Research Topics?

Frontiers Research Topics are very popular trademarks of the Frontiers Journals Series: they are collections of at least ten articles, all centered on a particular subject. With their unique mix of varied contributions from Original Research to Review Articles, Frontiers Research Topics unify the most influential researchers, the latest key findings and historical advances in a hot research area! Find out more on how to host your own Frontiers Research Topic or contribute to one as an author by contacting the Frontiers Editorial Office: researchtopics@frontiersin.org

ADVANCED PROCESSES FOR WASTEWATER TREATMENT AND WATER REUSE

Topic Editors:
Rui C. Martins, University of Coimbra, Portugal
Rosa M. Quinta-Ferreira, University of Coimbra, Portugal
Maria Graca Rasteiro, University of Coimbra, Portugal
Renato Falcão Dantas, Campinas State University, Brazil
Marta Gmurek, Lodz University of Technology, Poland

Citation: Martins, R. C., Quinta-Ferreira, R. M., Rasteiro, M. G., Dantas, R. F., Gmurek, M., eds. (2021). Advanced Processes for Wastewater Treatment and Water Reuse. Lausanne: Frontiers Media SA. doi: 10.3389/978-2-88966-344-6

Table of Contents

frontiers
in Environmental Science

EDITORIAL
published: 17 November 2020
doi: 10.3389/fenvs.2020.611159

Editorial: Advanced Processes for Wastewater Treatment and Water Reuse

Rui C. Martins[1]*, Rosa M. Quinta-Ferreira[1], Maria Graça Rasteiro[1], Renato Dantas[2] and Marta Gmurek[3]

[1] Department of Chemical Engineering, CIEPQPF – Centro de Investigação em Engenharia dos Processos Químicos e dos Produtos da Floresta, University of Coimbra, Coimbra, Portugal, [2] Faculdade de Tecnologia, Universidade Estadual de Campinas Paschoal Marmo, Limeira, Brazil, [3] Department of Molecular Engineering, Faculty of Process and Environmental Engineering, Lodz University of Technology, Lodz, Poland

Keywords: advanced oxidation processes, treatment processes integration, water reuse, environmental impact assessment, materials functionalization

Editorial on the Research Topic

Advanced Processes for Wastewater Treatment and Water Reuse

Water scarcity is one of the major challenges faced by mankind (Loeb, 2016). There is a real need to develop ways of using wastewater as a source of reusable water. These streams constitute indirect potable water sources that are often discharged into natural resources (Lee and von Gunten, 2010). The treated effluents must thus be safe for both ecosystems and human health. Even if current wastewater treatment processes can fulfill the required discharge thresholds, trace compounds (both organic and inorganic) in the treated streams present a dangerous potential threat. These compounds show refractory characteristics and are often not fully removed by conventional treatment technologies. Although found in trace levels, their real impact on human health is yet unknown. Moreover, due to their accumulation capacity and biorefractory features, these compounds are starting to be found in drinking water. Bearing these concerns in mind, the European Commission has listed several chemical contaminants whose concentration in natural water resources must be followed by member states.

In wastewater treatment plants (WWTPs), the release of micropollutants is an emerging concern as it is currently not regulated anywhere in the world. Therefore, it is expected that new quality standards for measuring how these harmful contaminants enter the environment, including subsidies such as pharmaceuticals, antibiotic-resistant bacteria, endocrine disrupters, will be included in the revised "Urban Waste Water Treatment Directive." Even though the sustainable use of recycled water to supplement the potable water supply is possible; current wastewater treatment systems are not efficient in removing toxic contaminants and other pollutants may have a strong environmental impact.

McLain and Gachomo evaluated the influence of chemicals that are of emerging concern (pharmaceuticals) due to the fact that they are often not fully removed by traditional wastewater treatment facilities on microbial growth. The authors concluded that even the low concentrations of these compounds found in reclaimed water can lead to a biological response from both microorganisms and plants, which is a serious threat to ecosystems. Although the effect on public health is not fully known, such substances must be efficiently removed from water for human applications since some compounds have already been connected with tumors (Molins-Delgado et al., 2016) and reproductive problems (Esplugas et al., 2007). The shortening of the water supply is pushing us toward strategies of wastewater reclamation and reuse (Gomes et al., 2017). Extracting

OPEN ACCESS

Edited and reviewed by:
Björn Vinnerås,
Swedish University of Agricultural Sciences, Sweden

***Correspondence:**
Rui C. Martins
martins@eq.uc.pt

Specialty section:
This article was submitted to Water and Wastewater Management, a section of the journal Frontiers in Environmental Science

Received: 28 September 2020
Accepted: 02 October 2020
Published: 17 November 2020

Citation:
Martins RC, Quinta-Ferreira RM, Rasteiro MG, Dantas R and Gmurek M (2020) Editorial: Advanced Processes for Wastewater Treatment and Water Reuse. Front. Environ. Sci. 8:611159. doi: 10.3389/fenvs.2020.611159

safe reusable water from treated wastewater requires the development of advanced technologies. Among them, oxidation systems such as ozonation, Fenton's process, and persulfate oxidation may be interesting approaches.

Ozone is a powerful oxidant able to react with compounds with high electronic density sites. However, total mineralization is usually not achieved, and the by-products formed may have a higher toxic character than parent compounds. The development of suitable solid catalysts to enhance ozone action over pollutants is an important research area. The use of a catalyst may reduce the costs of this operation and a more efficient ozone usage may be possible. Hu et al. described the production of (Mn)-based Y zeolites in the catalytic ozonation process and showed the potential of such materials for the degradation of refractory contaminants such as nitrobenzene, which is listed as a potential carcinogen.

Fenton's process is another industrially interesting technology as classic Fenton's peroxidation does not require sophisticated equipment and needs only hydrogen peroxide and iron salts. However, one of its main drawbacks is related to the use of a homogeneous catalyst (iron) that must be removed from the treated water after the oxidation process. The development of a suitable solid catalyst can overcome such shortcomings, also allowing the catalyst to recover and be reused. Zhu et al. concluded that CuO/CeO_2 is a suitable solid material to enhance diclofenac removal from water trough Fenton's like reactions. An alternative to Fenton's peroxidation is explored by Xian et al. who tested the persulfate oxidation of organic compounds (acid orange 7 and diclofenac) using Spinel Ferrite MFe_2O_4 as a heterogeneous catalytic material.

Separation technologies are also interesting processes that can be applied as single treatments or integrated with other types of methodologies. Miranda et al. evaluated the efficiency of aluminum coagulants in dissolved air flotation for the treatment of paper mill wastewater. The development of flocculants from natural sources such as wood wastes was successfully applied in the treatment of effluents from the textile industry by Grenda et al.

The removal and recovery of heavy metals from water is also a recurring theme in this Research Topic. The development of adsorbents from green, renewable, and sustainable sources is a step forward toward a circular economy. Zulu et al. functionalized sawdust cellulose with interesting results regarding Vanadium removal from water. Wang, Zhu, Xu et al. used eco-friendly Pickering-MIPEs as an alternative method to produce multi-porous materials in the removal of metals from water. In one paper, Wang, Zhu, Wang et al. were studied, while in a second Wang, Zhu, Xu et al. were addressed. As(III) and As(V) were removed by a hybrid adsorbent that was produced by intercalation of inorganic and organic surfactants onto kaolin clay. Mudzielwana et al. concluded that it is suitable to remove such material from groundwater. Wastewater effluent from E-waste is an emerging concern, as it can contain considerable amounts of valuable metals. Zhang et al. describe how the introduction of a hyperbranched dendrimer-like polymer onto silica gel, leads to a suitable adsorbent that can recover Au.

We hope that this Research Topic can make important contributions, shedding light on the paths that will enable us to reach suitable treatment strategies and obtain safe reusable water from wastewater.

AUTHOR CONTRIBUTIONS

All authors listed have made a substantial, direct and intellectual contribution to the work, and approved it for publication.

REFERENCES

Esplugas, S., Bila, D., Krause, L., and Dezotti, M. (2007). Ozonation and advanced oxidation technologies to remove endocrine disrupting chemicals (EDCs) and pharmaceuticals and personal care products (PPCPs) in water effluents. *J. Hazardous Mater.* 149, 631–642. doi: 10.1016/j.jhazmat.2007.07.073

Gomes, J., Costa, R., Quinta-Ferreira, R. M., and Martins, R. C. (2017). Application of ozonation for pharmaceuticals and personal care products removal from water. *Sci. Total Environ.* 586, 265–283. doi: 10.1016/j.scitotenv.2017.01.216

Lee, Y., and von Gunten, U. (2010). Oxidative transformation of micropollutants during municipal wastewater treatment: comparison of kinetic aspects of selective (chlorine, chlorine dioxide, ferrate IV, and ozone) and non-selective oxidants (hydroxyl radicals). *Water Res.* 44, 555–566. doi: 10.1016/j.watres.2009.11.045

Loeb, B. (2016). Water-energy-food. *Ozone Sci. Eng.* 38, 173–174. doi: 10.1080/01919512.2016.1166029

Molins-Delgado, D., Díaz-Cruz, M.S., and Barceló, D. (2016). Ecological risk assessment associated to the removal of endocrine-disrupting parabens and benzophenone-4 in wastewater treatment. *J. Hazardous Mater.* 310, 143–151. doi: 10.1016/j.jhazmat.2016.02.030

Conflict of Interest: The authors declare that the research was conducted in the absence of any commercial or financial relationships that could be construed as a potential conflict of interest.

frontiers in Chemistry

ORIGINAL RESEARCH
published: 14 August 2019
doi: 10.3389/fchem.2019.00577

Fabrication of Triethylenetetramine Terminal Hyperbranched Dendrimer-Like Polymer Modified Silica Gel and Its Prominent Recovery Toward Au (III)

Ying Zhang, Rongjun Qu, Ting Xu, Yu Zhang, Changmei Sun, Chunnuan Ji and Ying Wang*

School of Chemistry and Materials Science, Ludong University, Yantai, China

To further increase the quantity and density of functional groups on adsorbent, terminal triethylenetetramine hyperbranched dendrimer-like polymer modified silica-gel (SG-TETA and SG-TETA2) was synthesized. The hyperbranched dendrimer-like polymer was successfully introduced onto silica gel and new cavities were formed, which was demonstrated by FTIR, SEM, and BET. The highest adsorption capacities of SG-TETA and SG-TETA2 obtained from Langmuir model toward Au(III) were 2.11, and 2.27 mmol g^{-1}, respectively, indicating that SG-TETA2 possessing more functional groups had a better adsorption ability. Moreover, the adsorbents combined with Au(III) ion through chelation and electrostatic attraction mechanism, after which reduction reactions for Au(III) ion loaded on adsorbents proceeded. SG-TETA2 had better adsorption selectivity than SG-TETA in removing Au(III) in Au-existed ion solution systems. SG-TETA2 had higher overall adsorption capacities compared to silica-gel-based hyperbranched polymers functionalized by diethylenetriamine. Therefore, the effective recovery makes SG-TETA2 a practical adsorbent in removing Au(III) ion from e-wastes and industrial effluents with much prospect.

Keywords: silica-gel, triethylenetetramine, dendrimer-like highly branched polymer, Au(III), adsorption

Edited by:
Marta Gmurek,
Lodz University of Technology, Poland

Reviewed by:
Maria Helena Gil,
University of Coimbra, Portugal
Shixing Wang,
Kunming University, China

***Correspondence:**
Rongjun Qu
rongjunqu@sohu.com

Specialty section:
This article was submitted to Chemical and Process Engineering, a section of the journal Frontiers in Chemistry

Received: *31 May 2019*
Accepted: *30 July 2019*
Published: *14 August 2019*

Citation:
Zhang Y, Qu R, Xu T, Zhang Y, Sun C, Ji C and Wang Y (2019) Fabrication of Triethylenetetramine Terminal Hyperbranched Dendrimer-Like Polymer Modified Silica Gel and Its Prominent Recovery Toward Au (III). Front. Chem. 7:577. doi: 10.3389/fchem.2019.00577

INTRODUCTION

Gold (Au) is an indispensable and important precious metals that performs many functions, as it is one of the raw materials commonly found in electronics, catalysts, anti-corrosion materials (Das, 2010; Chen et al., 2015; Vojoudi et al., 2017). The extraction and recovery of Au(III) are not easy because the golden content in environmental, geological, and electronic materials is very low. With the industrial demand and its value rising steeply in recent years, the economic incentive to increase recycling or recovery of Au(III) from waste solutions has risen as well (Zhang et al., 2017). A variety of techniques such as chemical precipitation (Soylak and Tuzen, 2008; Boudesocque et al., 2014), membrane separation (Kargari et al., 2006; Wang et al., 2017), solvent extraction (Vidhate et al., 2015), and adsorption (Zhen et al., 2016; Tofan et al., 2017; Yu and Fein, 2017) have been introduced into enrich, and recover gold from waste water. Among these methods, the adsorption method has been evaluated as the most effective way, with attractive features such as easy operation, low-cost, and is particularly suitable for recovering the low level of gold which exists in industry wastewater.

Stable performance of matrix and effective chelating groups are the basic conditions of promising adsorbents. Nitrogen-containing adsorbents are commonly used as one of the most effective adsorbents for recovering Au(III). Plenty of designed adsorbents with high nitrogen content have been applied to selectively adsorb Au(III) from aqueous solution (Ahamed et al., 2013; Ebrahimzadeh et al., 2013; Tofan et al., 2017). Theory and empirical study indicate that nitrogen-containing adsorbents possess not only high adsorption capacities but excellent selectivity for binding Au(III).

The poly(amidoamine) (PAMAM) dendrimers exhibit excellent adsorption performance, relying on its unique three-dimensional steric configuration, and nanoscale shape, and topography exactly matching high density nitrogen-containing sites. The hyper-branched structures, lots of cavities and the presence of multiple functional groups between the branches can be useful in trapping other molecules (Vunain et al., 2016; Sajid et al., 2018). PAMAM dendrimers contain a high density of nitrogen ligands belonging to nitrogen functional groups such as amines and amides, and have strong chelating affinity with metal ions (Zarghami et al., 2016; Hayati et al., 2017; Ma et al., 2017). The PAMAM dendrimers are typically fabricated via repeated two-step process including Michael addition reaction and amidation with methyl acrylate (MA) and ethylene diamine (EDA). Notably, ethylene diamine is the most common choice for the repeating reaction to increase the nitrogen-containing functional groups. However, there are some other polyethylene polyamines, including diethylenetriamine (DETA), triethylenetetramine (TETA), tetraethylenepentamine (TEPA), besides EDA which might be a better option, which have more nitrogen active sites. Our group (Zhang et al., 2015) has been trying to prepare a PAMAM dendrimer-like polymer adsorbent using DETA as a reaction unit by combination of homogeneous and heterogeneous methods, and found the synthetic adsorbents had great adsorption for Au(III) influences. It's also important to note that it was difficult to obtain prospective nitrogen content on dendrimers through a completely "heterogeneous method" because steric hindrance generated from the grafted dendrimers (Qu et al., 2006). Although the completely "homogeneous method" was improved a lot, the purification progress is hard to operate (Qu et al., 2014). Meanwhile, no one had published about using long-chain TETA as a reaction unit for the synthesis of highly branched PAMAM polymer adsorption materials.

In this work, triethylenetetramine terminal hyperbranched dendrimer-like polymer modified silica gel adsorbents were synthesized based the prepared method of PAMAM, still with the combination of homogeneous method, and heterogeneous method. The objectives of this work were to probe the influences of long-chain TETA on the adsorption properties of the sort of adsorbents. More importantly, the selective adsorption performance, and adsorption mechanic for Au(III) were given.

MATERIALS AND METHODS

Materials

Spherical silica-gel (particle size: 60–100 mesh) was obtained from Aladdin and activated as reported (Zhang et al., 2009). γ-Chloropropyltrimethoxysilane (CPTS) was bought from Qufu wanda chemical co. and used as received. MA and TETA were analytical reagent grade. $HAuCl_4 \cdot 4H_2O$ was purchased from Sinopharm Chemical Reagent Co.

Instruments and Apparatus

The morphology was taken using a SU8010 (Hitachi, Japan). FTIR spectra were reported using a FTIR spectrophotometer Nicolet iS50 (Nicolet, American). Elemental analysis was obtained from the Elementar VarioEL III instrument, Elementar Co., Germany. The nitrogen adsorption–desorption isotherms were performed using ASAP Micromeritics (2020, USA). X-ray photoelectron spectroscopy were performed on ESCALAB Xi^+ (Thermo Fisher Scientific, American). The concentrations of metal ions were supplied on the atomic absorption spectrometer (VARIAN AA240, American).

Preparation of SG-TETA, and SG-TETA2

The synthetic process of silica-gel-based dendrimer-like polymers are illustrated in **Scheme 1**. CPTS-TETA were obtained by according to our previous work (Zhang et al., 2009). CPTS (15 mL, 82.0 mmol) was refluxed with TETA (25 mL, 167.0 mmol) in methanol of 150 mL under protection of nitrogen about 12 h. Then CPTS-TETA was obtained through evaporation of solvent methanol. Next, CPTS-TETA was mixed with 15.0 g of activated silica gel in 150 mL of toluene under mechanical stirring and a nitrogen atmosphere. After continuous shaking under a reflux condition for 12 h, the target product first generation dendrimer adsorbent SG-TETA was extracted in turn with toluene and ethanol, and dried at 50°C for 72 h. The SG-TETA (6.6 g) and MA (16 ml, 176 mmol) were further dispersed in 50 mL methanol for 72 h at 50°C. Then the SG-TETA-MA was produced via filtering and extracting by methanol over 24 h. Next, the SG-TETA-MA (3.0 g) was treated with 60 ml (402 mmol) of TETA in 100 mL of methanol at 50°C for 5 days in water bath. Finally, the second generation dendrimer adsorbent SG-TETA2 was obtained after filtrating, washing and drying.

Adsorption Study

The adsorption data was evaluated by the atomic absorption spectrometer. Each adsorption was repeated 3 times and the adsorption data averaged. The adsorbed Au(III) at equilibrium were obtained by calculating as follows:

$$q_e = \frac{(C_0 - C_e)V}{m} \tag{1}$$

Here q_e (mmol g^{-1}), C_0 (mmol L^{-1}), and C_e (mmol L^{-1}) are adsorption amount, initial and equilibrium, m (g) is the amount of adsorbent, and V (L) is the volume of the Au (III) solution.

After adsorption, the adsorbents loaded with Au(III) were immersed into 0.1 mol L^{-1} HCl solution with a mass concentration of 4% thiourea. Then the regenerated adsorbent was washed 3 times with distilled water, and be served as the next adsorption/desorption cycle.

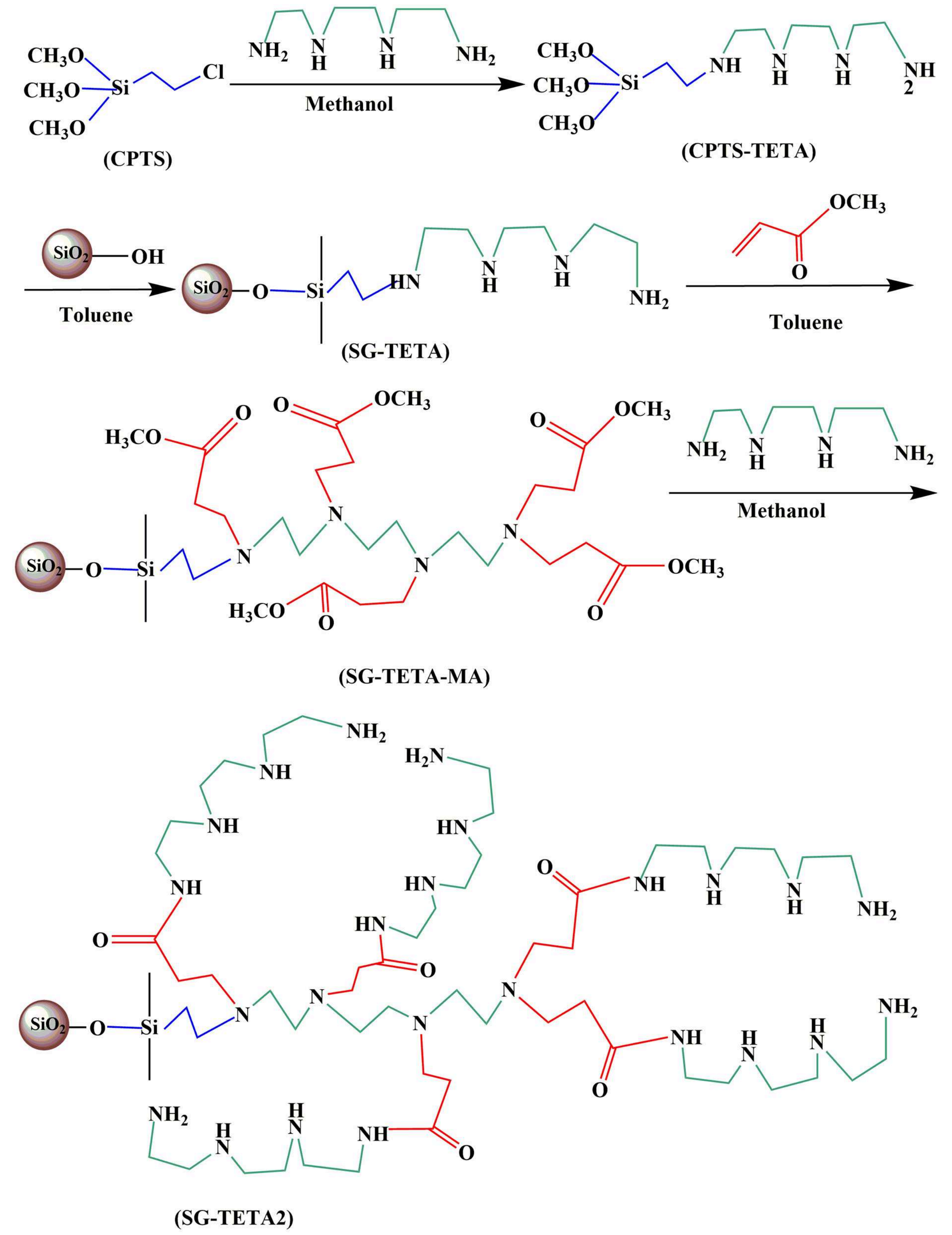

SCHEME 1 | The synthesis schematic of SG-TETA and SG-TETA2.

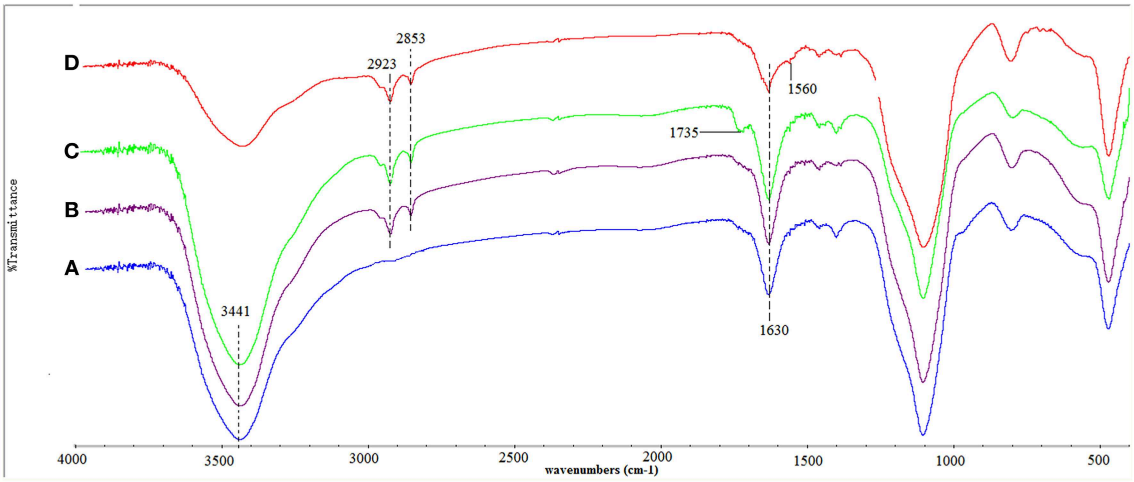

FIGURE 1 | Infrared spectra of silica-gel **(A)**, SG-TETA **(B)**, SG-TETA-MA **(C)**, and SG-TETA2 **(D)**.

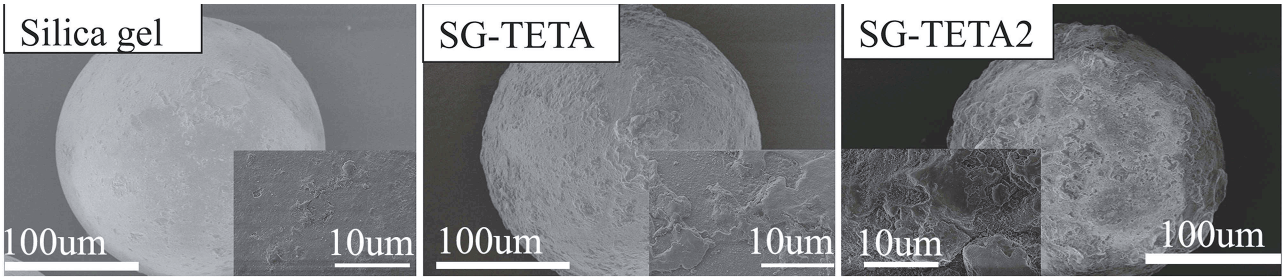

FIGURE 2 | SEM images of silica-gel, SG-TETA, and SG-TETA2.

RESULTS AND DISCUSSION

Characterization of Adsorbents

The FT-IR spectra of silica-gel, SG-TETA, SG-TETA-MA, and SG-TETA2 were showed on **Figure 1**. Silica-gel (**Figure 1A**) shows some characteristic bands at 3,441 cm^{-1} (stretching vibrations of Si-OH), 1,102 $\text{cm}^{-1}$of stretching vibration of Si-O-Si (Tian et al., 2010; Niu et al., 2014). In the spectrum of SG-TETA (**Figure 1B**), the new peaks appeared at 2,853 and 2,923 cm^{-1} were assigned to the symmetric and asymmetric CH_2 bands, which indicated the successful attach of carbon chain of CPTS-TETA on the surface of silica-gel. In ester-terminated grafting samples SG-TETA-MA (**Figure 1C**), the absorption at about 1,735 cm^{-1} indicated the existence of ester bonds ($–COOCH_3$) (Mahmoudalilou et al., 2018). The absorption peaks 1,735 cm^{-1} of ester bonds in TETA-terminated SG-TETA2 disappeared (**Figure 1D**) but the peaks at about 1,560 cm^{-1} (N-H bending/C-N stretching, amide II) and 1,654 cm^{-1} (C = O, amide I) appeared, which suggested that the form of amides (Hayati et al., 2017). Hence, it was concluded that silica-gel supported TETA-terminated hyperbranched dendrimer-like polymer were successfully prepared by the step by step progress.

Figure 2 presents SEM images of Silica-gel, SG-TETA, and SG-TETA2, respectively. Obviously, the surface of silica-gel was relatively smooth. However, the surface of SG-TETA and SG-TETA2 became rougher after a series of reactions, which further suggested that the adsorbent was synthesized (Liu et al., 2013).

The contents of N in the SG-TETA, SG-TETA-MA, and SG-TETA2 demonstrated on **Table 1**, and the experimental content of amine groups be calculated. Compared to experimental content, the theoretical contents were many times greater than those. That might be due to intra-, inter- crosslinkings as well as steric hindrance, similar results were also found in our previous work (Qu et al., 2006; Zhang et al., 2015). After the Michael addition reaction between SG-TETA and MA, the functional groups content obviously decreased, and then increased after the amidation reaction. This is notably different from the results of series of silica-gel based DETA-terminated hyperbranched dendrimer-like polymer (Zhang et al., 2015). As one might expect, the long-chain of TETA with better stretch and flexibility had a positive effect on increasing the functional groups content of SG-TETA2. Moreover, compared to the porous structure parameters of SG-DETA2 in **Table 1**, SG-TETA2 not only retain

TABLE 1 | Elemental analysis results and porous structure parameters of Silica-gel, SG-TETA, SG-TETA-MA, SG-TETA2.

Materials	*N* (%)	*N* (mmol g^{-1})	Amine groups content (mmol g^{-1})		BET surface area (m^2 g^{-1})	BJH desorption cumulative volume of pores (cm^3 g^{-1})[a]	BJH desorption average pore diameter (nm)
			Theoretical	Experimental			
Silica-gel	-	-	-	-	429.92	0.97	7.80
SG-TETA	3.68	2.62	3.28	0.66	260.90	0.58	6.51
SG-TETA-MA	2.60	1.86	1.98	0.46	238.89	0.48	5.90
SG-TETA2	3.78	2.70	4.64	0.68	260.32	0.53	6.09

[a] *The BJH Desorption cumulative volume v of pores between 1.7 and 300 nm diameter.*

existing pores and also increase new pores relying on nice stretch and flexibility of long-chain polyamine TETA.

Effect of pH on Adsorption of Au(III)

According to the surface properties of adsorbents and gold attribute, the experimental range of pH was chosen from 1.0 to 4.0. The desired pH was adjusted with HCl and NaOH solutions. **Figure 3** displayed the effect of pH on the adsorption of SG-TETA and SG-TETA2 for Au(III). With the increasing of pH, the adsorbed quantity increased first and attained the maximum at pH 2.5. The $[AuCl_4]^-$ complex ion are stabilized in highly acidic conditions, and nitrogen atoms of the functional group were positively charged through protonation at the same time (Ogata and Nakano, 2005). Hence, the electrostatic attraction would dominate under selected conditions. The lower adsorption at pH 1.0 was because of competition from Cl^- and $[AuCl_4]^-$. But the OH^- substituted some Cl^- in the $[AuCl_4]^-$ to form the $[AuCl_{4-n}(OH)_n]^-$ complex ions ($0 \leq n \leq 4.0$) under weak acidic environment (Ando et al., 2018). Thus, with pH from 2.5 to 4.0 increasing, chloride-hydroxide complexes of Au(III) formed because of the reduction of protonated amines and hydroxide substitution reaction proceeds and the adsorption decreased gradually (Zhen et al., 2016). On the other hand, Au(III) ions are more likely to coordinate with lone pairs of electron of nitrogen on primary and secondary amines (Ahamed et al., 2013). The adsorption capacities of SG-TETA2 (2.15 mmol g^{-1}) for Au(III) were slightly above SG-TETA's adsorption capacities (1.98 mmol g^{-1}), which sufficient to explain a bit, the increase of generation was beneficial to adsorption. Compared to the DETA chain (the adsorption amounts of SG-DETA and SG-DETA2 were 1.95 and 1.98 mmol g^{-1}) (Zhang et al., 2015), the long-chain TETA demonstrates an advantage on adsorption capacities.

Adsorption Kinetics

Figures 4A,B shows the adsorption kinetic curves for Au(III) ions on silica-gel based dendrimer-like polymers adsorbents from 5 to 35°C. The adsorption process of SG-TETA for Au(III) proceeded rapidly first at all four temperatures, and reached the adsorption equilibrium at 180 min. And for SG-TETA2, the adsorption for Au(III) still proceeded rapidly at first but final equilibrium was reached after 90 min. By comparing them, the adsorption rate of SG-TETA2 for Au(III) is more rapidly, which may depend on the more amine groups and cavities in the second generation dendrimer-like functional groups with long-chain TETA. Rapid adsorption will beneficial to ensure economy efficiency of important practical significance. For the temperature effects, adsorption amounts of SG-TETA was affected slightly by temperature, while the adsorption amounts of SG-TETA2 had clear increase as the temperature went up under the experimental conditions. That is, the first generation SG-TETA seemed less susceptible to the temperature because the less crosslinking and little steric hindrance. However, more hydrogen bonds, the crosslinkings of amino, and blockages of the pores formed by introducing of more functional groups on the second generation adsorbents SG-TETA2 caused obstructions for Au(III) diffusion into the interior of holes at lower temperature. With the increasing of temperature, the stretch of long chains, the channels of molecular enlarges, and the combination for ions increases.

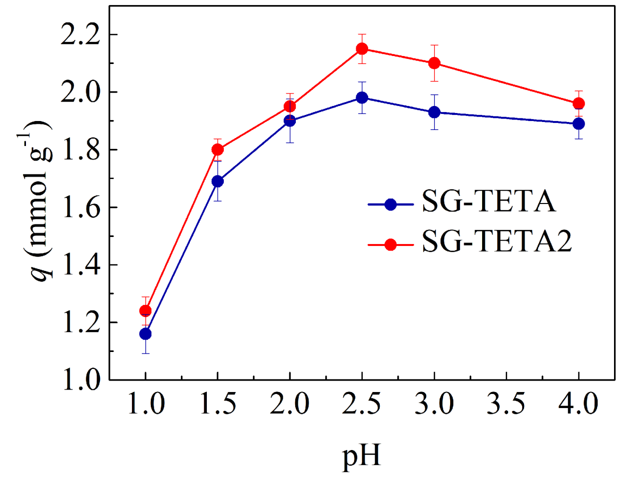

FIGURE 3 | Effect of pH on the adsorption of Au(III) on SG-TETA and SG-TETA2 (initial concentration of Au(III) solution: 2.428 mmol L^{-1}; 25°C).

The kinetic data for Au(III) were analyzed by pseudo-first-order model (Konggidinata et al., 2017) and pseudo-second-order model (Nourmoradi et al., 2012) expressed as,

$$\ln\frac{(q_e - q_t)}{q_1} = -k_1 t \tag{2}$$

$$\frac{t}{q_t} = \frac{1}{k_2 q_2^2} + \frac{t}{q_2} \tag{3}$$

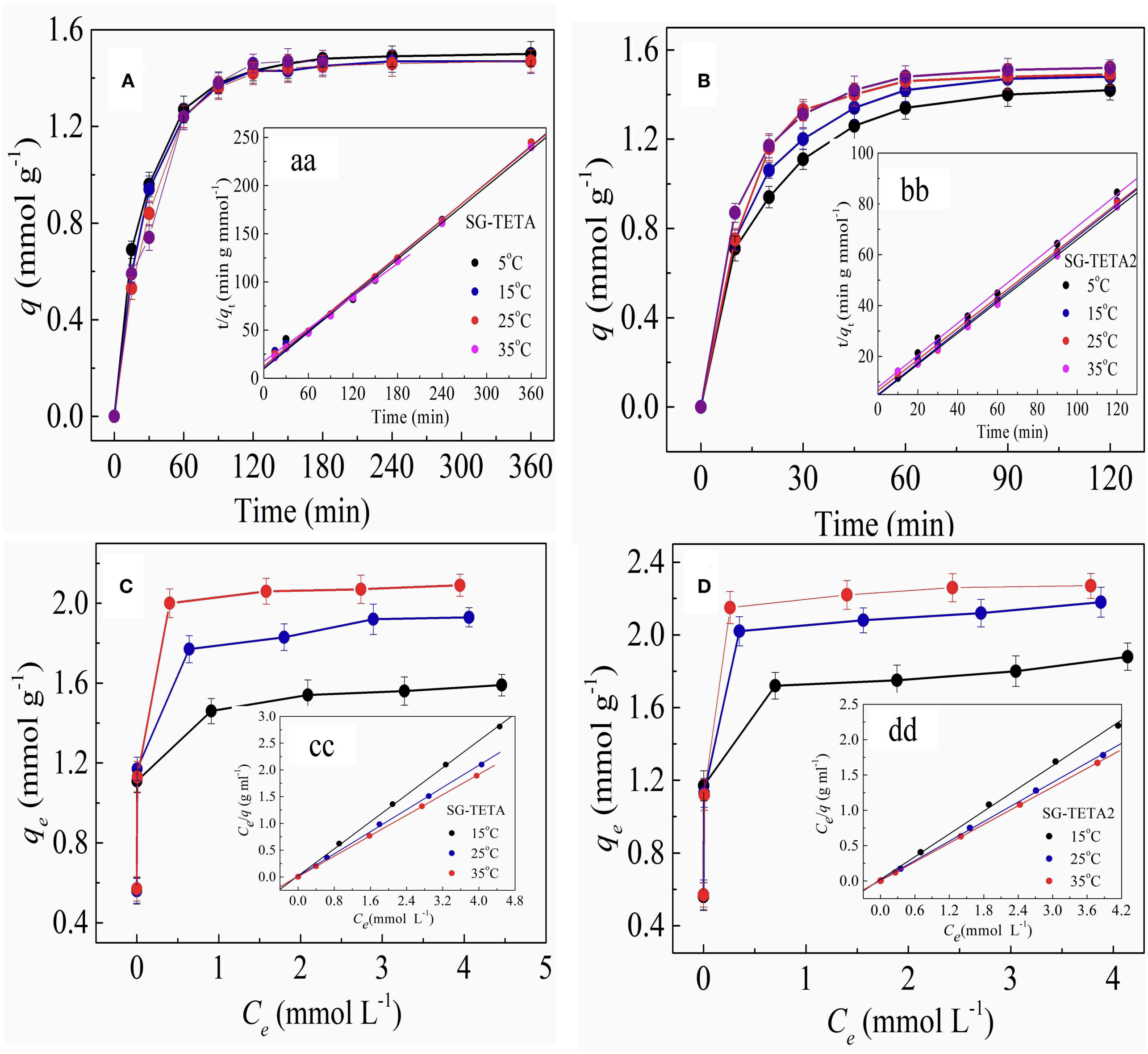

FIGURE 4 | Adsorption kinetics for Au(III) on SG-TETA **(A)** and SG-TETA2 **(B)** (initial concentration of Au(III) solution: 2.428 mmol L^{-1}; pH 2.5), pseudo-second-order kinetic plots for the adsorption of Au(III) onto on SG-TETA **(aa)** and SG-TETA2 **(bb)**; Isotherm for the adsorption of Au(III) on SG-TETA **(C)** and SG-TETA2 **(D)**, Langmuir isotherms for the adsorption of Au(III) on SG-TETA **(cc)** and SG-TETA2 **(dd)**.

Where, q_e (mmol g^{-1}) and q_t (mmol g^{-1}) are the amounts of Au(III) adsorbed at equilibrium and at time t, k_1 (min^{-1}) and k_2 (g $mmol^{-1}$ min^{-1}) are the first order rate constant.

The kinetic parameters determined by the rate equations were summarized in **Table 2**. The fitting curves of pseudo-second-order (**Figures 4aa,bb**) were better than those of pseudo-first-order model, and the R^2 values were more than 0.996 for Au(III) on SG-TETA and SG-TETA2, which means the Au(III) adsorbed rate determining step on SG-TETA and SG-TETA2 may be dominant by chemisorption but not mass transfer in solution (Nourmoradi et al., 2012; Monier and Abdel-Latif, 2013; Xiong et al., 2014; Qu et al., 2018). Also, the uptake capacities (q_e) calculated from pseudo-second-order model were close to the experimental values, which demonstrated the availability of pseudo-second-order model for the adsorption. Furthermore, the initial adsorption rate (h, mmol g^{-1} h^{-1}) and half-adsorption time $t_{1/2}$ were obtained from k_2 and q_e values using the Equations (4) and (5) (Wu et al., 2005), reflecting the speed of adsorption equilibrium were listed on **Table 2**.

$$h = k_2 q_e^2 \tag{4}$$

$$t_{1/2} = \frac{1}{k_2 q_e} \tag{5}$$

TABLE 2 | Kinetic parameters for the adsorption of Au(III) onto SG-TETA and SG-TETA2 adsorbents at various temperatures.

Adsorbents	T (°C)	$q_{e,exp}$ (mmol g^{-1})	Pseudo-first-order model			Pseudo-second-order model				
			$q_{e,cal}$ (mmol g^{-1})	k_1 (min^{-1})	R^2	$q_{e,cal}$ (mmol g^{-1})	k_2 (g $mmol^{-1}$ min^{-1})	H (mmol g^{-1} min^{-1})	$t_{1/2}$ (min)	R^2
SG-TETA	5	1.47	2.30	0.042	0.9541	1.57	0.018	0.044	1252.15	0.9895
	15	1.47	1.27	0.026	0.9911	1.58	0.032	0.080	391.18	0.9968
	25	1.47	0.98	0.023	0.9651	1.56	0.039	0.095	270.16	0.9982
	35	1.50	0.86	0.020	0.9834	1.58	0.041	0.10	238.29	0.9992
SG-TETA2	5	1.42	1.20	0.049	0.9965	1.56	0.055	0.13	135.84	0.9986
	15	1.48	1.32	0.053	0.9956	1.62	0.059	0.15	109.46	0.9991
	25	1.49	0.97	0.053	0.9809	1.61	0.078	0.20	63.41	0.9976
	35	1.52	1.02	0.052	0.9980	1.63	0.082	0.22	55.97	0.9994

TABLE 3 | Langmuir and Freundich isotherm adsorption constants for Au(III) on SG-TETA and SG-TETA2.

Adsorbents	T (°C)	Langmuir				Freundlich			D-R			
		q_e (mmol g^{-1})	q (mmol g^{-1})	K_L (mL $mmol^{-1}$)	R^2_L	n	K_F (mmol g^{-1})	R^2_F	q_m (mg g^{-1})	B (mol^2 J^{-2})	E (kJ mol^{-1})	R^2
SG-TETA	15	1.59	1.58	32.00	0.9996	1.45	11.02	0.8559	1.64	4.55×10^{-9}	10.48	0.8489
	25	1.93	1.95	32.35	0.9994	1.75	8.62	0.9093	2.02	5.59×10^{-9}	9.46	0.9176
	35	2.11	2.10.	90.34	0.9999	1.93	7.51	0.9431	2.23	2.40×10^{-9}	14.43	0.9566
SG-TETA2	15	1.88	1.86	25.98	0.9986	1.68	9.16	0.8900	1.93	5.45×10^{-9}	9.57	0.8941
	25	2.18	2.17	43.52	0.9995	1.99	7.32	0.9481	2.33	6.59×10^{-9}	8.71	0.9753
	35	2.27	2.27	81.50	0.9999	2.12	6.78	0.9485	2.50	6.87×10^{-9}	8.53	0.9804

As can be seen from **Table 2**, the increased temperature can elevate the values of initial adsorption rate h due to the faster diffusion of Au(III) at high temperatures. Furthermore, k_2 values increased and $t_{1/2}$ decreased with the increase of temperature for both adsorbents, which suggested that higher temperature benefited to adsorption, that was, the adsorption needed shorter time to achieve equilibrium at higher temperature. The k_2 values and h of SG-TETA2 had an obvious change when the temperature is $>25°C$, but little change observed was for SG-TETA. Also, less time was required for SG-TETA2 than for SG-TETA to achieve adsorption equilibrium under all treatment temperature. Thus, longer chain of functional group might make for enhancing the adsorption rate.

Adsorption Isotherms

Adsorption isotherms can critically optimize the application to be established an adsorption process. The adsorption isotherms at experimental temperatures are presented in **Figures 4C,D**. As noted in **Figures 4C,D**, that the adsorption capacity increased with the initial Au(III) concentrations increase. The increase of adsorption capacity of SG-TETA and SG-TETA2 concerned with Au(III) concentrations can be considered a greater driving force formed by a higher concentration gradient pressure.

The isotherm adsorption data were modeled by Langmuir and Freundlich Equations (6) and (7), respectively, (Gurung et al., 2011).

$$\frac{C_e}{q_e} = \frac{1}{q_{\max}K_L} + \frac{C_e}{q_{\max}} \tag{6}$$

$$\ln q_e = \ln k_F + \frac{1}{n}\ln C_e \tag{7}$$

where q_e and C_e are the equilibrium metal ion concentration on the adsorbent (mmol g^{-1}) and in the solution (mmol L^{-1}), $q_{\max}$ is the monolayer adsorption capacity of the adsorbent (mmol g^{-1}), K_L and k_F are the Langmuir adsorption constant (L^3 mg^{-1}) and the Frendlich constant, and $1/n$ related to the adsorption driving force.

The correlation coefficient ($R^2 \approx 0.99$) for the Langmuir model (Langmuir curves see **Figures 4cc,dd** showed higher values than the Freundlich model tested (**Table 3**). Meanwhile, the data of the $q_{\max}$ of SG-TETA and SG-TETA2 for Au(III) calculated by this function were 2.10 and 2.27 mmol g^{-1} at 35°C, respectively, very close to the value experimentally obtained. While, low correlation coefficient values ($R^2 < 0.95$) of Freundlich isotherm deviated the application to the adsorption process. It was assumed that uniform adsorption energies with every Au(III) made equal affinity to the site and formed a monolayer adsorbate.

The isotherm data were also analyzed by Dubinin-Radushkevich (D-R) isotherm which was usually used to decide the physical or chemical adsorption. The linear form of the D–R isotherm Equation is 8 (Niu et al., 2014):

$$\ln q_e = \ln q_{\max} - \beta\varepsilon^2 \tag{8}$$

where β is the activity coefficient ($mol^2\ J^{-2}$) and ε is the Polanyi potential [$\varepsilon = RT\ln(1 + 1/C_e)$]. E (kJ mol^{-1}) is mean free energy. The values of mean free energy (E, kJ mol^{-1}) were calculated by using β values according to Equation (9):

$$E = \frac{1}{\sqrt{2\beta}} \tag{9}$$

The adsorption is chemical adsorption in the range of 8 and 16 kJ mol^{-1} of E value while a physical adsorption the E value bellowing 8 kJ mol^{-1} (Dubinin, 1960). The results based on D-R were shown in **Table 3**, the E value of adsorption of SG TETA and SG TETA2 for Au(III) was >8.0 kJ mol, which indicated it was a chemical adsorption. But the E values are only slightly higher than 8 kJ mol^{-1}, the author therefore believed that chemical chelating reactions play the main roles in the process of absorbing Au(III), and secondly by physical adsorption due to unique surface structure. Meanwhile, the bond energies of reversible chemical complexation <10 kJ mol^{-1} are beneficial for the separation (Yen et al., 2017). Thus, the desorption of Au(III) with SG-TETA and SG-TETA2 is supposed to readily proceed in our study.

Hence, the data simulated by Langmuir, Freundlich, and D-R demonstrated that the adsorption of SG-TETA and SG-TETA2 for Au(III) fitted well by Langmuir. That is, the adsorption was favorably monolayer adsorption and chemical adsorption played a major role at different temperatures.

The adsorption capacities of this study compared to other adsorbents are listed in **Table 4**. The adsorption capacity of SG-TETA and SG-TETA2 is clearly higher than most of the reported adsorbents. The ideal dendritic structure in SG-TETA and SG-TETA2 containing high density nitrogen and oxygen ligands could result in a desired adsorption capacity for Au(III). Compared with SG-DETA and SG-DETA2, the adsorption capacities of SG-TETA, and SG-TETA2 have a certain increase because the long-chain and less crosslinkings. Besides, the adsorption rate of SG-TETA and SG-TETA2 was faster than that of SG-DETA and SG-DETA2. For SG-TETA (Wang et al., 2013) prepared by heterogeneous, the adsorption was obvious lower than SG-TETA fabricated by homogeneous in this study. For

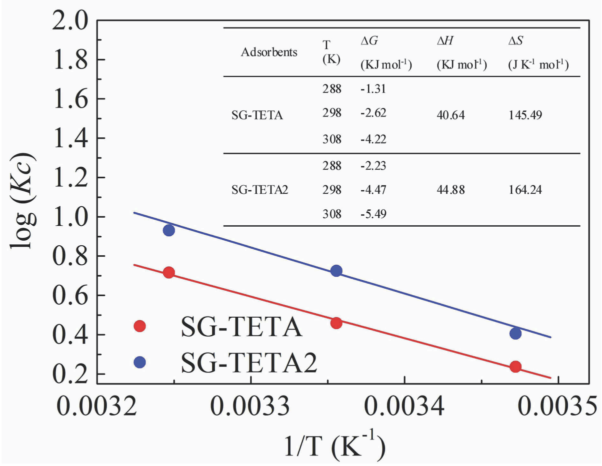

Adsorbents	T (K)	ΔG (KJ mol^{-1})	ΔH (KJ mol^{-1})	ΔS (J K^{-1} mol^{-1})
SG-TETA	288	-1.31	40.64	145.49
	298	-2.62		
	308	-4.22		
SG-TETA2	288	-2.23	44.88	164.24
	298	-4.47		
	308	-5.49		

FIGURE 5 | logK_C vs. 1/T plots and thermodynamic parameters for Au(III) adsorption on SG-TETA and SG-TETA2.

TABLE 4 | Comparison of maximum adsorption capacities (q_{max}) of some adsorbents for Au(III) from aqueous solution.

Adsorbents	pH	Adsorption time	Au(III) adsorption capacity (mmol g^{-1})	References
Silica-gel				This study
SG-TETA	2.5	4 h	2.10	
SG-TETA2	2.5	2 h	2.27	
Silica-gel				Zhang et al., 2015
SG-DETA	2.0	4 h	2.09	
SG-DETA2	2.0	4 h	2.12	
Silica-gel supported amino-terminated dendrimer-like polyamidoamine polymer				Qu et al., 2014
G1.0	3.0	24 h	1.48	
G2.0	3.0	24 h	2.45	
Silica gels functionalized with triethylenetetramine (SG-TETA)	3.29	1.5 h	1.43	Wang et al., 2013
Thioctic acid functionalized silica coated magnetite nanoparticles	5.0	4 h	1.45	Fadzilah et al., 2018
D301 resin functionalized with ethylenediamine	2.0	5 h	1.51	An et al., 2017
D301 resin functionalized with ethylenediaminethiourea	2.0	5 h	1.65	
Thiosemicarbazide functionalized corn bract	6.0	24 h	7.46	Lin et al., 2018
Thiourea modified alginate	1.0	48 h	8.47	Gao et al., 2017
Multiwalled carbon nanotubes	–	24 h	0.47	Pang and Yung, 2014
Oxidized multi-walled carbon nanotubes	2.0	1 h	0.32	Shaheen et al., 2015

much higher adsorption, the functional group mostly contain S atom, which can make adsorbed Au(III) more difficult to dilute (Pang and Yung, 2014; Gao et al., 2017). SG-TETA and SG-TETA2 had the higher adsorption amount and rate, and could be employed as a significant potential candidate for Au(III) uptake.

Thermodynamic Parameters

Figure 5 illustrated the thermodynamic parameters including Gibbs free energy changes (ΔG°), enthalpy change (ΔH°), and entropy change (ΔS°), which were based the following equations,

$$K_c = \frac{C_{Ae}}{C_e} \tag{10}$$

$$\log K_c = \frac{\Delta S}{2.303R} - \frac{\Delta H}{2.303RT} \tag{11}$$

$$\Delta G^{\circ} = -RT \ln K_c \tag{12}$$

where C_{Ae} and C_e (mg L^{-1}) are the equilibrium concentrations of Au(III) ion on adsorbent and in solution, respectively, K_c is the thermodynamic equilibrium constant, R (KJ mol^{-1}) is gas constant, T (K) is the absolute temperature, and ΔG° is the standard free energy change.

From **Figure 5**, the negative values of ΔG° indicated the adsorption was spontaneous and thermodynamically favored. The positive enthalpy (ΔH°) showed the adsorption was an endothermic process and as a result the adsorption capacity increased with an increase in temperature. The positive entropy (ΔS°) reflected an increase in the randomness at the interface of solid-liquid interface during the adsorption.

Adsorption Mechanism

High utilization of functional groups on silica-gel-based dendrimer-like polymers containing long-chain triethylenetetramine could ensure a quick and efficient adsorption capability. **Table 1** presented that the N contents of SG-TETA and SG-TETA2 were determined to be 2.62 and 2.70 (mmol g^{-1}). Thus, N of adsorbents might form complex with Au (III) by 1.24:1 (SG-TETA) and 1.19:1 (SG-TETA2). Note that the utilization of N of the second-generation SG-TETA2 was better than that of SG-TETA because of long and flexible triethylenetetramine chains. Furthermore, the crosslinkings was believed to be not obvious that the $[AuCl_4]^-$ could enter

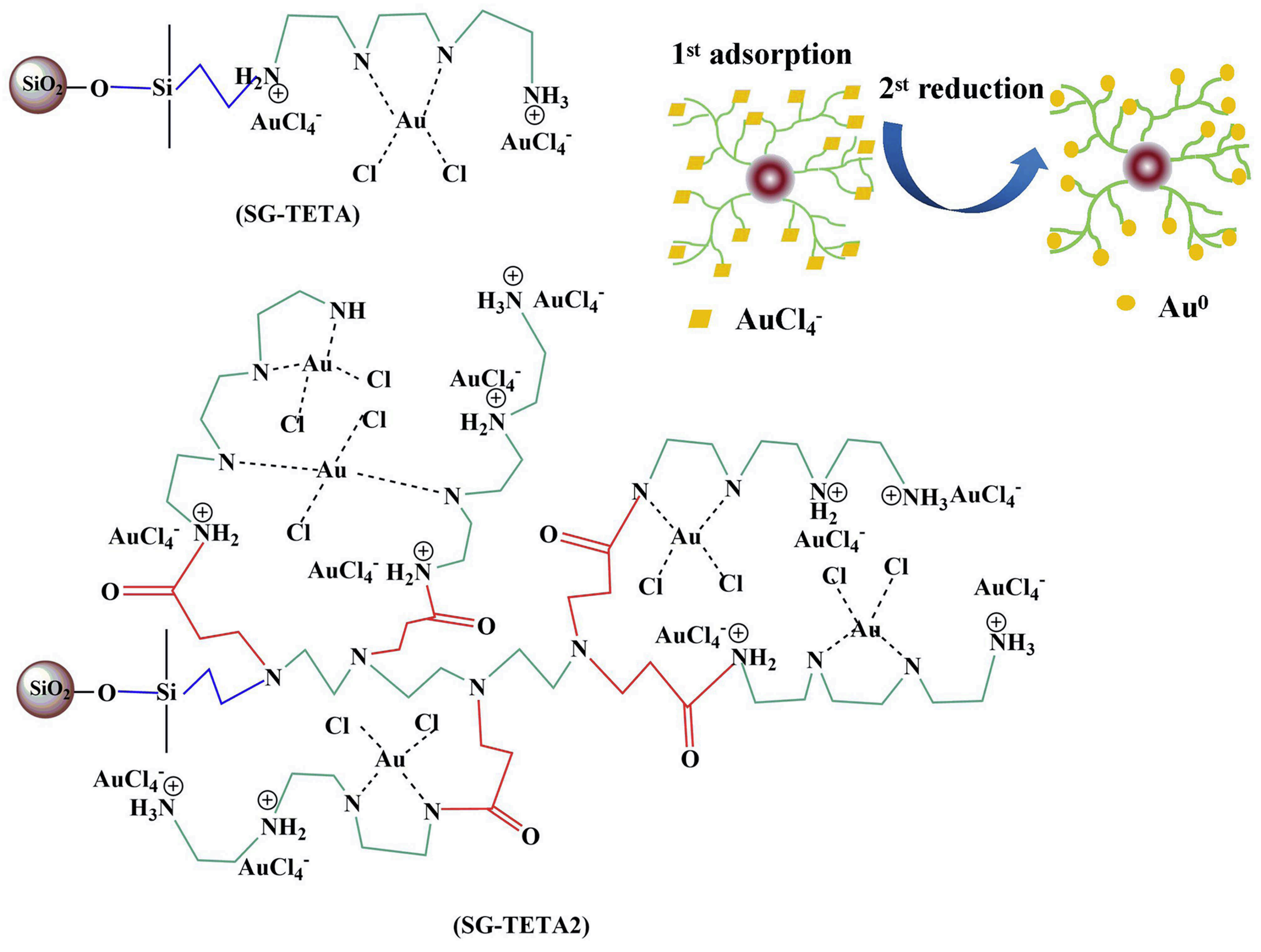

SCHEME 2 | A suggested bonding mode of SG-TETA and SG-TETA2 of silica gel surface with favorable binding of Au(III) to amino group.

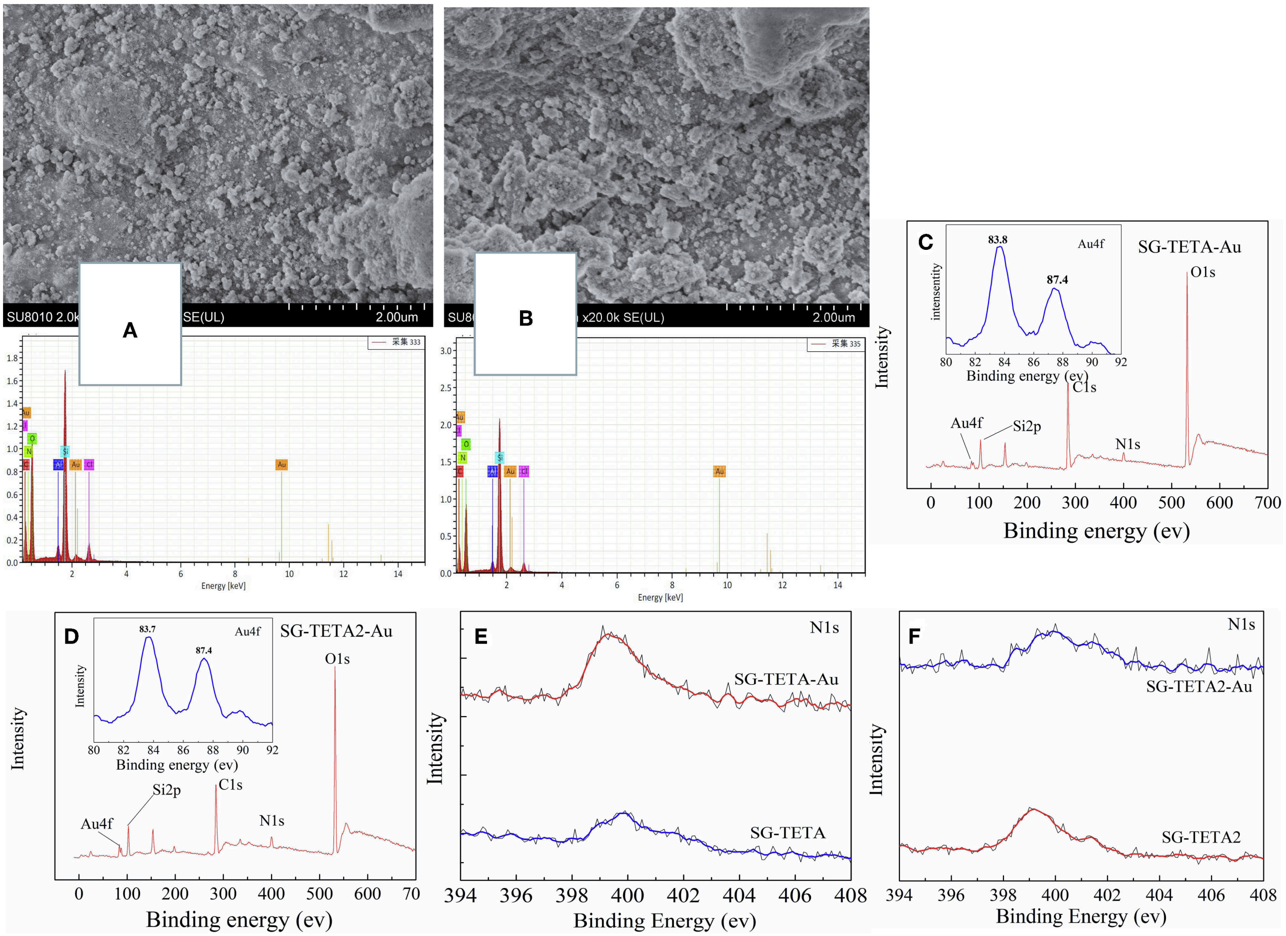

FIGURE 6 | SEM and EDX images and of SG-TETA **(A)** and SG-TETA2 **(B)** before and after adsorption of Au(III); XPS spectra of SG-TETA **(C)** and SG-TETA2 **(D)** before and after adsorption; Au 4f spectra of SG-TETA **(E)** and SG-TETA2 **(F)** before adsorption (red) and after adsorption (blue).

into inside of the functional groups and adsorb on the surface. This result also indicated that steric hindrance is one of the main causes of low functional groups contents. It was the steric hindrance of TETA2 that give the optimal channel and capture metal ions. Three possible mechanisms: electrostatic interaction, chelation and physical adsorption, were proposed to govern the adsorption for Au(III) by the adsorbents containing nitrogen and oxygen ligands from HCl media (Adhikari et al., 2013). According to the above facts, we proposed an Au(III) ion may chelate with two nitrogen atoms or electrostatic adsorption with one nitrogen atom of PAMAM dendrimer including not only external but also internal ones. A proposed complexion of amino group on SG-TETA and SG-TETA2 for Au(III) was presented in **Scheme 2**.

To gain further insight into the mechanism, **Figures 6A,B** showed the SEM and EDX images of SG-TETA and SG-TETA2 after adsorption. Obviously, there were plenty of grains distributed on the surface of the adsorbents, which might be because Au(III) ion were reduced to Au(0) after adsorption. The EDX lines at 2.2 keV indicated existence of the gold nanoparticles. Peaks were also noted around 8.2 keV which indicates the presence of gold atoms (Shah et al., 2017). X-ray photoelectron spectroscopy was further used to study the surface chemical compositions of the as-prepared and Au(III) ions adsorbed silica gel based dendrimer-like polymer. **Figures 6C,D** shows the two survey spectra manifesting surface chemical compositions of the adsorbents before and after adsorption of Au(III) ions. After adsorption, the appearance of Au on the surface of SG-TETA and SG-TETA2 was obviously observed. The peaks at 87.4 eV (Au 4f 5/2) and 83.7 eV (Au 4f 7/2) are related to Au(0), which indicated that Au(III) was reduced to Au(0) by the SG-TETA and SG-TETA2. Also the slight peaks around at 90.0 eV (Au 4f 5/2) and 82.0 eV (Au 4f 7/2) were assigned to Au(III), which demonstrated the formation of [NH_2-Au(III)] (Li et al., 2013). Therefore, the adsorbed Au(III) ions might exist in two forms: oxidation state zero and positive three, indicating that NH_2 in the functional groups could not only coordinate with Au(III) can also reduce Au(III) (Wang et al., 2010). Bonding energy peaks at 399.2 eV in **Figures 6E,F** related to free amino (-NH_2), but the peak shift to higher binding

TABLE 5 | The adsorption selectivity of adsorbents for Au(III) (Au(III) concentration: 2.428 mmol L^{-1}; concentration of coexisting metal ions: 2.5 mol L^{-1}; pH = 2.5; T = 25°C.

Adsorbents	System	Metal ions	Adsorbents capacity (mmol g^{-1})	Selective coefficient ^{a}
SG-TETA	Au(III)-Cu(II)	Au(III)	1.16	$\alpha_{Au(III)/Cu(II)} = \infty$
		Cu(II)	0	
	Au(III)-Ni(II)	Au(III)	1.29	$\alpha_{Au(III)/Ni(II)} = \infty$
		Ni(II)	0	
	Au(III)-Pb(II)	Au(III)	1.20	$\alpha_{Au(III)/Pb(II)} = \infty$
		Pb(II)	0	
SG-TETA2	Au(III)-Cu(II)	Au(III)	1.41	$\alpha_{Au(III)/Cu(II)} = \infty$
		Cu(II)	0	
	Au(III)-Ni(II)	Au(III)	1.52	$\alpha_{Au(III)/Ni(II)} = \infty$
		Ni(II)	0	
	Au(III)-Pb(II)	Au(III)	1.48	$\alpha_{Au(III)/Pb(II)} = \infty$
		Pb(II)	0	

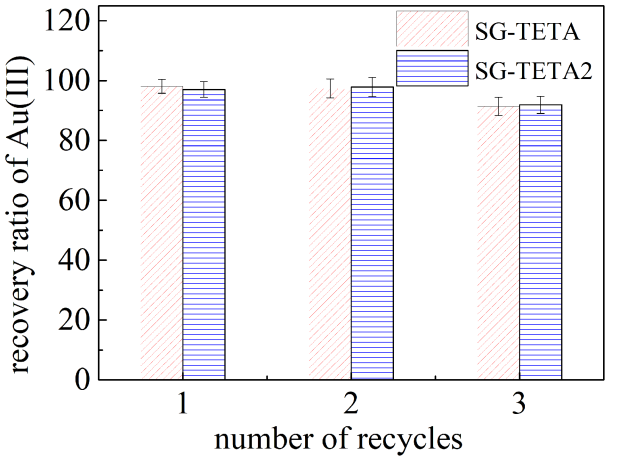

FIGURE 7 | Repetitive adsorption and desorption of Au(III) SG-TETA and SG-TETA2.

energy after adsorption of Au(III), which illustrated the -NH_2 group can attract $[AuCl_4]^-$ effectively (Gao et al., 2017). All the results above showed that the adsorption for gold on the surface of SG-TETA and SG-TETA2 was considered the adsorptive-reduct process.

Adsorption Selectivity

A series of binary ions coexistent systems, Au(III)-Cu(II), Au(III)-Pb(II), and Au(III)-Ni(II), were investigated to evaluate the adsorption selectivity of SG-TETA and SG-TETA2 for Au(III) and the results were listed in **Table 5**. From **Table 5**, Au(III) selected adsorption preferentially by SG-TETA and SG-TETA2 from the binary systems, and selective coefficients both are infinite, indicating that SG-TETA, and SG-TETA2 for adsorption Au(III) showed excellent selectivity.

Desorption and Regeneration Performance

The strong complexing agent, thiourea [$(NH_2)_2CS$)] with lower toxicity offered S and N ligands, which can leach gold by forming a complex in acidic media based the reaction (Dwivedi et al., 2014):

$$Au^0 + 2SC(NH_2)_2 \rightarrow Au[CS(NH_2)_2]_2^+ + e^- \qquad (13)$$

In this study, the adsorption-desorption recycles of SG-TETA and SG-TETA2 were repeated for 3 times by using 4% thiourea/0.1 mol L^{-1} HCl solution (**Figure 7**). The recovery of Au(III) remained above 91% in 3 cycles indicated the good adsorption of reused SG-TETA and SG-TETA2 which can remain relatively stable. The repeated adsorption-desorption results demonstrate that the adsorption sites on the surface of the SG-TETA and SG-TETA2 are reversible. Thus, these triethylenetetramine terminal hyperbranched dendrimer-like polymer adsorbents possess the most potential as a gold recovery material due to the good adsorption amount, high selectivity, and stable regeneration.

CONCLUSIONS

The adsorption properties of silica-gel-based dendrimer-like polymers functionalized by long-chain triethylenetetramine in water were investigated. The utilization of functional long-chain TETA was remarkable and therefore could remove Au(III) much effectively. The adsorption of the SG-TETA2 rapidly reached equilibrium within 90 min, while for the SG-TETA equilibrium was reached after 120 min. The fast establishment of the equilibrium for Au(III) in a short time showed the effectiveness of the adsorbent for recovery. The adsorption mechanism of SG-TETA and SG-TETA2 for Au(III) is composed by adsorption and reduction. SG-TETA and SG-TETA2 also showed excellent selectivity for the adsorption for Au(III) in a co-existed metal ion system. The long-chain TETA was beneficial for adsorption due to more sites and its flexibility.

DATA AVAILABILITY

The datasets generated for this study are available on request to the corresponding author.

AUTHOR CONTRIBUTIONS

YiZ carried out experiments and wrote the manuscript. RQ designed experiments and analyzed results. TX and YuZ carried out adorption experiments. CS, CJ, and WY characterized and analyzed experimental results.

FUNDING

The authors are grateful for the financial support by the National Natural Science Foundation of China (Grant No. 51673089, 51373074, 51073075, 51302127, and 51143006).

REFERENCES

Adhikari, B. B., Gurung, M., Alam, S., Tolnai, B., and Inoue, K. (2013). Kraft mill lignin-A potential source of bio-adsorbents for gold recovery from acidic chloride solution. *Chem. Eng. J.* 231, 190–197. doi: 10.1016/j.cej.2013.07.016

Ahamed, M. E. H., Mbianda, X. Y., Mulaba-Bafubiandi, A. F., and Marjanovic, L. (2013). Selective extraction of gold(III) from metal chloride mixtures using ethylenediamine N-(2-(1-imidazolyl)ethyl) chitosan ion-imprinted polymer. *Hydrometallurgy* 140, 1–13. doi: 10.1016/j.hydromet.2013.08.004

An, F. Q., Li, M., Wu, R. Y., Hu, T. P., Gao, J. F., and Yuan, Z. G. (2017). Effective recovery of $AuCl_4^-$ using D301 resin functionalized with ethylenediamine and thiourea. *Hydrometallurgy* 169, 356–361. doi: 10.1016/j.hydromet.2017.02.022

Ando, H., Kawamoto, D., Ohashi, H., Honma, T., Ishida, T., Okaue, Y., et al. (2018). Adsorption behavior of Au(III) complex ion on nickel carbonate and nickel hydroxide. *Colloid. Surface A* 537, 383–389. doi: 10.1016/j.colsurfa.2017.10.028

Boudesocque, S., Mohamadou, A., and Dupont, L. (2014). Efficient extraction of gold from water by liquid-liquid extraction or precipitation using hydrophobic ionic liquids. *Green Chem.* 38, 5573–5581. doi: 10.1039/C4NJ01115E

Chen, D., Cui, P., Cao, H., and Yang, J. (2015). A 1-dodecanethiol-based phase transfer protocol for the highly efficient extraction of noble metal ions from aqueous phase. *J. Environ. Sci.* 29, 146–150. doi: 10.1016/j.jes.2014.07.028

Das, N. (2010). Recovery of precious metals through biosorption-a review. *Hydrometallurgy* 103, 180–189. doi: 10.1016/j.hydromet.2010.03.016

Dubinin, M. M. (1960). The potential theory of adsorption of gases and vapors for adsorbents with energetically non-uniform surface. *Chem. Rev.* 60, 235–266. doi: 10.1021/cr60204a006

Dwivedi, A. D., Dubey, S. P., Hokkanen, S., Fallah, R. N., and Sillanpä M. (2014). Recovery of gold from aqueous solutions by taurine modified cellulose: an adsorptive-reduction pathway. *Chem. Eng. J.* 255, 97–106. doi: 10.1016/j.cej.2014.06.017

Ebrahimzadeh, H., Moazzen, E., Amini, M. M., and Sadeghi, O. (2013). Novel ion imprinted polymer coated multiwalled carbon nanotubes as a high selective sorbent for determination of gold ions in environmental samples. *Chem. Eng. J.* 215–216, 315–321. doi: 10.1016/j.cej.2012.11.031

Fadzilah, N., Razak, A., Shamsuddin, M., and Lee, S. L. (2018). Adsorption kinetics and thermodynamics studies of gold(III) ions using thioctic acid functionalized silica coated magnetite nanoparticles. *Chem. Eng. Res. Des.* 130, 18–28. doi: 10.1016/j.cherd.2017.12.004

Gao, X., Zhang, Y., and Zhao, Y. (2017). Biosorption and reduction of Au (III) to gold nanoparticles by thiourea modified alginate. *Carbohyd. Polym.* 159, 108–115. doi: 10.1016/j.carbpol.2016.11.095

Gurung, M. J., Dhikari, B. B., Kawakita, H., Ohto, K., Inoue, K., and Alamb, S. (2011). Recovery of Au(III) by using low cost adsorbent prepared from persimmon tannin extract. *Chem. Eng. J.* 174, 556–563. doi: 10.1016/j.cej.2011.09.039

Hayati, B., Maleki, A., Najafi, F., Daraei, H., Gharibi, F., and McKay, G. (2017). Super high removal capacities of heavy metals (Pb^{2+} and Cu^{2+}) using CNT dendrimer. *J. Hazard. Mater.* 336, 146–157. doi: 10.1016/j.jhazmat.2017.02.059

Kargari, A., Kaghazchi, T., Mardangahi, B., and Soleimani, M. (2006). Experimental and modeling of selective separation of gold(III) ions from aqueous solutions by emulsion liquid membrane system. *J. Membr. Sci.* 279, 389–393. doi: 10.1016/j.memsci.2005.12.027

Konggidinata, M. I., Chao, B., Lian, Q., Subramaniam, R., Zappi, M., and Gang, D. D. (2017). Equilibrium, kinetic and thermodynamic studies for adsorption of BTEX onto ordered mesoporous carbon (OMC). *J. Hazard. Mater.* 336, 249–259. doi: 10.1016/j.jhazmat.2017.04.073

Li, X., Zhan, C. C., Zhao, R., Lu, X. F., Xu, X. R., Jia, X. T., et al. (2013). Efficient adsorption of gold ions from aqueous systems with thioamide-group chelating nanofiber membranes. *Chem. Eng. J.* 229, 420–428. doi: 10.1016/j.cej.2013.06.022

Lin, G., Wang, S. X., Zhang, L. B., Hu, T., Peng, J. H., Cheng, S., et al. (2018). Synthesis and evaluation of thiosemicarbazide functionalized corn bract for selective and efficient adsorption of Au(III) from aqueous solutions. *J. Mol. Liq.* 258, 235–243. doi: 10.1016/j.molliq.2018.03.030

Liu, W., Yin, P., Liu, X. G., Dong, X. Q., Zhang, J., and Xu, Q. (2013). Thermodynamics, kinetics, and isotherms studies for gold(III) adsorption using silica functionalized by diethylenetriaminemethylenephosphonic acid. *Chem. Eng. Res. Des.* 91, 2748–2758. doi: 10.1016/j.cherd.2013.05.003

Ma, Y. X., Xing, D., Shao, W. J., Du, X. Y., and La, P. Q. (2017). Preparation of polyamidoamine dendrimers functionalized magnetic graphene oxide for the adsorption of Hg(II) in aqueous solution. *J. Colloid Interf. Sci.* 505, 352–363. doi: 10.1016/j.jcis.2017.05.104

Mahmoudalilou, M. G., Mamaqani, H. R., Azimi, R., and Abdollah, A. (2018). Preparation of hyperbranched poly (amidoamine)-grafted graphene nanolayers as a composite and curing agent for epoxy resin. *Appl. Surf. Sci.* 428 1061–1069. doi: 10.1016/j.apsusc.2017.09.237

Monier, M., and Abdel-Latif, D. A. (2013). Modification and characterization of PET fibers for fast removal of Hg(II), Cu(II) and Co(II) metal ions from aqueous solutions. *J. Hazard. Mater.* 250–251, 122–130. doi: 10.1016/j.jhazmat.2013.01.056

Niu, Y. Z., Qu, R. J., Chen, H., Mu, L., Liu, X. G., Wang, T., et al. (2014). Synthesis of silica gel supported salicylaldehyde modified PAMAM dendrimers for the effective removal of Hg(II) from aqueous solution. *J. Hazard. Mater.* 278, 267–278. doi: 10.1016/j.jhazmat.2014.06.012

Nourmoradi, H., Nikaeen, M., and Khiadani, H. H. (2012). Removal of benzene, toluene, ethylbenzene and xylene (BTEX) from aqueous solutions by montmorillonite modified with nonionic surfactant: equilibrium, kinetic and thermodynamic study. *Chem. Eng. J.* 191, 341–348. doi: 10.1016/j.cej.2012.03.029

Ogata, T., and Nakano, Y. (2005). Mechanisms of gold recovery from aqueous solutions using a novel tannin gel adsorbent synthesized from natural condensed tannin. *Water Res.* 39, 4281–4286. doi: 10.1016/j.watres.2005.06.036

Pang, S. K., and Yung, K. C. (2014). Prerequisites for achieving gold adsorption by in gold recovery. *Chem. Eng. Sci.* 107, 58–65. doi: 10.1016/j.ces.2013.11.026

Qu, R. J., Ma, X. L., Wang, M. H., Sun, C. M., Sun, X. M., Sun, S. Y., et al. (2014). Homogeneous preparation of polyamidoamine grafted silica gels and their adsorption properties as Au^{3+} adsorbents. *J. Ind. Eng. Chem.* 20, 4382–4392. doi: 10.1016/j.jiec.2014.02.005

Qu, R. J., Niu, Y. Z., Sun, C. M., Ji, C. N., Wang, C. H., and Cheng, G. X. (2006). Syntheses, characterization, and adsorption properties for metal ions of silica-gel functionalized by ester- and amino-terminated dendrimer-like polyamidoamine polymer. *Microp. Mesop. Mater.* 97, 58–65. doi: 10.1016/j.micromeso.2006.08.007

Qu, R. J., Sun, C. M., Ma, F., Zhang, Y., Ji, C. N., and Yin, P. (2018). Removal of Fe(III) from ethanol solution by silica-gel supported dendrimer-like polyamidoamine polymers. *Fuel* 219, 205–213. doi: 10.1016/j.fuel.2018.01.131

Sajid, M., Nazal, M. K., Ihsanullah, B. N., and Osman, A. M. (2018). Removal of heavy metals and organic pollutants from water using dendritic polymers based adsorbents: a critical review. *Sep. Purif. Technol.* 191, 400–423. doi: 10.1016/j.seppur.2017.09.011

Shah, K. R., Duggirala, S. M., Tipre, D. R., and Dave, S. R. (2017). Mechanistic aspects of Au(III) sorption by *Aspergillus terreus* SRD49. *J. Taiwan Inst. Chem. E.* 80, 46–51. doi: 10.1016/j.jtice.2017.08.001

Shaheen, H. A., Marwani, H. M., and Soliman, E. M. (2015). Selective adsorption of gold ions from complex system using oxidized multi-walled carbon nanotubes. *J. Mol. Liq.* 212, 480–486. doi: 10.1016/j.molliq.2015.09.040

Soylak, M., and Tuzen, M. (2008). Coprecipitation of gold(III), palladium(II) and lead(II) for their flame atomic spectrometric determinations. *J. Hazard. Mater.* 152, 656–661. doi: 10.1016/j.jhazmat.2007.07.027

Tian, Y., Yin, P., Qu, R. J., Wang, C. H., Zheng, H. G., and Yu, Z. X. (2010). Removal of transition metal ions from aqueous solutions by adsorption using a novel hybrid material silica gel chemically modified by triethylenetetraminomethylenephosphonic acid. *Chem. Eng. J.* 162, 573–579. doi: 10.1016/j.cej.2010.05.065

Tofan, L., Bunia, I., Paduraru, C., and Teodosiu, C. (2017). Synthesis, characterization and experimental assessment of a novel functionalized macroporous acrylic copolymer for gold separation from wastewater. *Process Saf. Environ.* 106, 150–162. doi: 10.1016/j.psep.2017.01.002

Vidhate, K. N., Shaikh, U. P. K., Arbad, B. R., and Lande, M. K. (2015). Extraction and separation of gold(III) with 4-(4-methoxybenzylideneimino)-5-methyl-4H-1,2,4-triazole-3-thiol in hydrochloric acid medium. *J. Saudi Chem. Soc.* 19, 54–58. doi: 10.1016/j.jscs.2011.12.018

Vojoudi, H., Badiei, A., Banaei, A., Bahar, S., Karimi, S., Ziarani, G. M., et al. (2017). Extraction of gold, palladium and silver ions using organically modified silica-coated magnetic nanoparticles and silica gel as a sorbent. *Microchim. Acta* 184, 3859–3866. doi: 10.1007/s00604-017-2414-x

Vunain, E., Mishra, A. K., and Mamba, B. B. (2016). Dendrimers, mesoporous silicas and chitosan-based nanosorbents for the removal of heavy-metal ions: a review. *Int. J. Biol. Macromol*. 86, 570–586. doi: 10.1016/j.ijbiomac.2016.02.005

Wang, F., Lai, Y., Zhao, B., Hu, B., Zhang, D., and Hu, K. (2010). Tunable growth of nanodendritic silver by galvanic-cell mechanism on formed activated carbon. *Chem. Commun*. 46, 3782–3784. doi: 10.1039/c001517b

Wang, M. H., Qu, R. J., Sun, C. M., Yin, P., and Chen, H. (2013). Dynamic adsorption behavior and mechanism of transition metal ions on silica gels functionalized with hydroxyl- or amino-terminated polyamines. *Chem. Eng. J*. 221, 264–274. doi: 10.1016/j.cej.2013.02.036

Wang, X. M., Xu, J. B., Li, L., Li, H. G., and Yang, C. F. (2017). Thiourea grafted PVDF affinity membrane with narrow pore size distribution for Au (III) adsorption: preparation, characterization, performance investigation and modeling. *Chem. Eng. J*. 314, 700–713. doi: 10.1016/j.cej.2016.12.035

Wu, Z. J., Joo, H., and Lee, K. (2005). Kinetics and thermodynamics of the organic dye adsorption on the mesoporous hybrid xerogel. *Chem. Eng. J.* 112, 227–236. doi: 10.1016/j.cej.2005.07.011

Xiong, C. H., Zhou, S. G., Liu, X. Z., Jia, Q., Ma, C. A., and Zheng, X. M. (2014). 2-Aminothiazole functionalized polystyrene for selective removal of Au(III) in aqueous solutions. *Ind. Eng. Chem. Res*. 53, 2441–2448. doi: 10.1021/ie403502r

Yen, C. H., Lien, H. L., Chung, J. S., and Yeh, H. D. (2017). Adsorption of precious metals in water by dendrimer modified magnetic nanoparticles. *J. Hazard. Mater*. 322, 215–222. doi: 10.1016/j.jhazmat.2016.02.029

Yu, Q., and Fein, J. B. (2017). Enhanced removal of dissolved Hg(II), Cd(II), and Au(III) from water by bacillus subtilis bacterial biomass containing an elevated concentration of sulfhydryl sites. *Environ. Sci. Technol*. 51, 14360–14367. doi: 10.1021/acs.est.7b04784

Zarghami, Z., Akbari, A., Latifi, A. M., and Amani, M. A. (2016). Design of a new integrated chitosan-PAMAM dendrimer biosorbent for heavy metals removing and study of its adsorption kinetics and thermodynamics. *Bioresource Technol*. 205, 230–238. doi: 10.1016/j.biortech.2016.01.052

Zhang, G. W., Zhou, Y., Ding, Z., Fu, L. K., and Wang, S. X. (2017). Nanosilica-supported thiosemicarbazide-glutaraldehyde polymer for selective Au(III) removal from aqueous solution. *RSC Adv*. 7, 55215–55223. doi: 10.1039/C7RA10199F

Zhang, Y., Qu, R., Sun, C., Chen, H., Wang, C., Ji, C., et al. (2009). Comparison of synthesis of chelating resin silica-gel-supported diethylenetriamine and its removal properties for transition metal ions. *J. Hazard. Mater*. 163, 127–135. doi: 10.1016/j.jhazmat.2008.06.070

Zhang, Y., Qu, R. J., Sun, C. M., Ji, C. N., Chen, H., and Yin, P. (2015). Improved synthesis of silica-gel-based dendrimer-like highly branched polymer as the Au(III) adsorbents. *Chem. Eng. J*. 270, 110–121. doi: 10.1016/j.cej.2015.02.006

Zhen, D., Liu, J. Z., Yuan, W. J., Yi, Y. P., and Zhao, L. (2016). Recovery of Au(III) by radiation synthesized aminomethyl pyridine functionalized adsorbents based on cellulose. *Chem. Eng. J*. 283, 504–513. doi: 10.1016/j.cej.2015.07.011

Conflict of Interest Statement: The authors declare that the research was conducted in the absence of any commercial or financial relationships that could be construed as a potential conflict of interest.

frontiers in Chemistry

ORIGINAL RESEARCH
published: 10 September 2019
doi: 10.3389/fchem.2019.00603

Preparation of Carboxymethyl Cellulose-Based Macroporous Adsorbent by Eco-Friendly Pickering-MIPEs Template for Fast Removal of Pb^{2+} and Cd^{2+}

Feng Wang [1,2]***, Yongfeng Zhu*** [1]***, Hui Xu*** [3] ***and Aiqin Wang*** [1]*

[1] Key Laboratory of Clay Mineral Applied Research of Gansu Province, Center of Eco-Material and Green Chemistry, Lanzhou Institute of Chemical Physics, Chinese Academy of Sciences, Lanzhou, China, [2] College of Petroleum and Chemical Engineering, Beibu Gulf University, Qinzhou, China, [3] Department of Chemical Engineering, College of Petrochemical Engineering, Lanzhou University of Technology, Lanzhou, China

Recently, Pickering high internal phase emulsions (Pickering HIPEs) have been widely used to fabricate macroporous materials. However, the high usage of poisonous organic solvent in HIPEs not only greatly increases the cost but also is harmful to human health and environment, which leads to limited large-scale applications. In this study, we prepared a novel monolithic macroporous material of carboxymethyl cellulose-*g*-poly(acrylamide)/montmorillonite (CMC-*g*-PAM/MMT) by the free radical polymerization *via* oil-in-water Pickering medium internal phase emulsions (Pickering MIPEs), which used the non-toxic and eco-friendly flaxseed oil as continuous phase, MMT, and Tween-20 (T-20) as stabilizer. The pore structure of the resulting macroporous materials could be tuned easily by adjusting the content of MMT, co-surfactant T-20, and the oil phase volume fraction. The maximal adsorption capacities of the prepared macroporous material for Pb^{2+} and Cd^{2+} were 456.05 and 278.11 mg/g, respectively, and the adsorption equilibrium can be reached within 30 min. Otherwise, the macroporous monolith exhibited excellent reusability through five adsorption–desorption cycles. Thus, the eco-friendly Pickering-MIPEs is a potential alternative method to be used to fabricate multi-porous adsorption materials for environmental applications.

Keywords: macroporous materials, Pickering emulsions, montmorillonite, adsorption, heavy metal

Edited by:
Maria Graca Rasteiro,
University of Coimbra, Portugal

Reviewed by:
Tianyi Ma,
University of Newcastle, Australia
Federica Valentini,
University of Rome Tor Vergata, Italy

***Correspondence:**
Aiqin Wang
aqwang@licp.cas.cn

Specialty section:
This article was submitted to
Green and Sustainable Chemistry,
a section of the journal
Frontiers in Chemistry

Received: *30 May 2019*
Accepted: *16 August 2019*
Published: *10 September 2019*

Citation:
Wang F, Zhu Y, Xu H and Wang A (2019) Preparation of Carboxymethyl Cellulose-Based Macroporous Adsorbent by Eco-Friendly Pickering-MIPEs Template for Fast Removal of Pb^{2+} and Cd^{2+}. Front. Chem. 7:603. doi: 10.3389/fchem.2019.00603

INTRODUCTION

Recently, macroporous materials with high porosity and good interconnectivity have attracted much attention in many fields, such as catalysts (Pierre et al., 2006; Zhang et al., 2008; Chan-Thaw et al., 2010; Pulko et al., 2010; Kovačič et al., 2014; Wang et al., 2014), tissue engineering scaffolds (Busby et al., 2001; Zhang et al., 2005; Hu et al., 2014; Viswanathan et al., 2015), ion exchange columns (Zhao et al., 2007; Alexandratos, 2008), electrode materials for energy storage (Liu et al., 2008; Kou et al., 2011), and water purification (Yu et al., 2015; Zhu et al., 2016c; Wu et al., 2017). Thus, many methods have been used to prepare macroporous materials. Among these technologies, the emulsion template may be the most effective method to prepare the macroporous

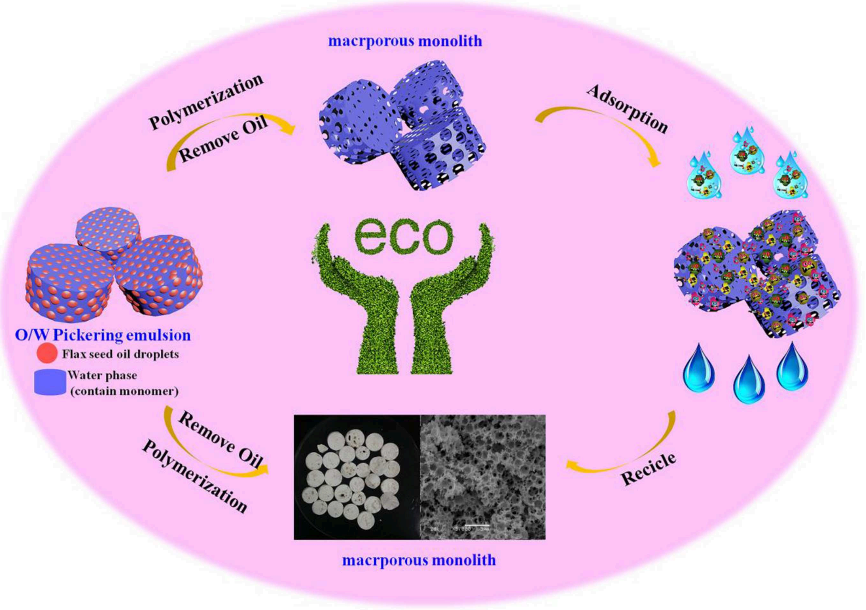

Graphical Abstract | Preparation of macroporous adsorbent from Pickering MIPEs for removal of heavy metal.

polymer with extraordinary advantages, including a well-defined pore structure, a controllable pore size, as well as inherent high porosity (Xu et al., 2015). The most well-known emulsion template technology is the high internal phase emulsions (HIPEs), which, with an internal phase volume of >74% and the prepared macroporous polymers, are also termed poly-HIPEs.

Conventional HIPEs are commonly stabilized with a large amount of surfactants (5–50 vol % with respect to the continuous phase) (Zheng et al., 2014). Inevitably, the heavy use of these surfactants significantly increases the high cost of materials (Wu et al., 2012). Thus, more and more studies involving HIPEs have focused on the Pickering HIPEs, which employ a small amount of solid particles substituting surfactants partially or totally to stabilize emulsions (Binks and Lumsdon, 1999). In addition, the macroporous poly-HIPEs created from Pickering HIPEs often have improved mechanical strength (Silverstein, 2014), additional features, and functions, due to the introduction of solid particles, such as magnetic property, photocatalytic performance, and so on (Vílchez et al., 2011).

Despite the fact that macroporous poly-HIPEs prepared from Pickering HIPEs have these excellent properties, some problems still need to be solved. Firstly, the macroporous poly-HIPEs prepared from Pickering-HIPEs, which are only stabilized by solid particles, often have closed-cell voids and super porous structures with void sizes of 200–700 μm (Ikem et al., 2010a,b, 2011). The weak permeability and the low surface area limit the application of the macroporous materials in many fields, especially in water treatment. Secondly, it also should be noted that oil/water (O/W) HIPEs often require more than 74% of organic solvent (such as toluene, *n*-hexane, *p*-xylene, liquid paraffin, and so on) in disperse phase. The wide use of these organic solvents greatly increases the cost as well as the threat to human health and environment. Thus, discovery of a new strategy, which can reduce the oil phase volume and replace the poisonous organic solvent with eco-friendly natural oil for preparation of the macroporous materials with interconnected pore structure *via* emulsion template is very meaningful.

Compared with HIPEs, medium internal phase emulsions (MIPEs, $V < 74\%$) require less organic solvents and decrease the diameter of the emulsion droplet, which is beneficial in increasing material surface area. Ikem et al. (2010b, 2011) have reported that introducing a small amount of surfactant (∼5% of the continuous phase volume) to stabilize Pickering HIPEs cooperatively with particles before polymerization will reduce the void sizes of the poly-Pickering HIPEs and results in materials with large pore throats and permeability. Otherwise, the permeability and connectivity of the poly-MIPEs can be adjusted by changing the content of nanoparticles or introducing an appropriate amount of surfactant (Wang et al., 2017a,b). According to the preceding discussion, in this study, we reported a new strategy for fabrication of macroporous material from Pickering-MIPEs, which is stabilized by montmorillonite (MMT) together with nonionic surfactant, and non-toxic low-cost flaxseed oil was used as emulsion in disperse phase. MMT, being a natural silicate clay mineral with abundant -OH groups and negatively charged, is highly hydrophilic; thus, MMT silicate clay can be used to stabilize O/W emulsion without any further modification to regulate its wettability (Shen et al., 2006; Dong et al., 2014). To the best of our knowledge, most of the present research on clay mineral-stabilized emulsion focus on the stability of emulsion or on the preparation of microspheres with Pickering emulsion polymerization. Studies involving preparation of highly macroporous polymer monoliths *via* clay mineral-stabilized Pickering emulsion template are rare. T-20 used in this study was a co-stabilizer emulsion and contributes to formation materials with connected pores. In this research, the pore structure of the prepared macroporous monolith was studied by tuning of MMT and Tween-20 (T-20) concentration and O/W ratio. The potential practical application of the macroporous polymer monoliths in the removal of heavy metal ions (Pb^{2+} and Cd^{2+}) from aqueous solution was also explored (**Graphical Abstract**).

EXPERIMENTAL SECTION

Materials

Sodium carboxymethylcellulose (CMC, chemical pure, with a viscosity of 300–800 mPa·s), ammonium persulfate (APS, analytical pure), and Tween-20 (T-20, analytical pure) were purchased from BASF Corporation. Na-MMT clay mineral with a cation exchange capacity (CEC) of 90 mEq/100 g was purchased from Southern Clay Products Inc. Flaxseed oil (FO, food grade) was purchased from the Lanzhou Yong Fan Shang Mao company (Lanzhou, China). Acrylamide (AM, chemical pure) was purchased from Shanpu Chemical Factory (Shanghai, China) and used without further treatment. *N*, *N′*-methylenebisacrylamide (MBA, chemical pure) was received from Yuan fan additives plant (Shanghai, China). Other reagents were all analytical pure and all solutions were prepared with distilled water.

Preparation of Pickering Emulsion

In order to guarantee that MMT dispersed completely in water, the MMT was initially prepared as a suspension with a certain concentration. Briefly, 10 or 15 g of MMT was added into 100 mL of deionized water and sonicated with BILON-650Y Sonifier for 30 min. In the preparation process of the Pickering emulsion, 10 mL of water containing a certain amount of MMT and an appropriate amount of T-20 was stirred at 300 rpm for 2 h in the boiling flask-3-neck in the continuous phase. Then, a determined volume of flaxseed oil was added into the continuous phase and emulsified with a GJD-B12K homogenizer at 11,000 rpm for 5 min.

Preparation of the Macroporous Monolith

The macroporous monolith was prepared *via* the free radical polymerization in the Pickering emulsion template. Firstly, a Pickering emulsion containing 0.05 g of CMC and 0.23 g of MBA was prepared according to the section *Preparation of Pickering Emulsion*. Subsequently, 2.13 g (30 mmol) of AM and 138 mg of APS were added into the as-prepared emulsion and rapidly stirred (11,000 rpm) for 1 min. Later, the emulsion was transferred into 10-mL centrifuge tubes and immersed in a 65°C water bath for 24 h to polymerize. After that, the obtained polymerization product was sectioned and washed with acetone by Soxhlet extraction for 12 h and then immersed into 0.5 mol/L NaOH aqueous alcohol solution ($V_{water}/V_{alcohol} = 3/7$) for 24 h to transfer the amide group to carboxyl. The redundant NaOH was washed with alcohol–water solution repetitively. Finally, the macroporous polymer was dried at 60°C for 4 h and named CMC-*g*-PAM/MMT. The feed compositions and the corresponding pore parameters of all the macroporous monoliths are listed in **Table 1**.

Characterization

The droplet diameters were estimated by counting 200 droplets by using Image Pro Plus as a software tool. The morphologies of the samples were characterized by a field emission scanning electron microscope (SEM, JSM-6701F, JEOL) after coating the samples with gold film. Photographs of Pickering-MIPEs were recorded by iPhone. The infrared (IR) spectra were recorded on a Nicolet NEXUS FTIR spectrometer in the range of 4,000–400 cm^{-1} using KBr pellets.

Batch Adsorption Studies

The adsorption experiments were performed by immersing 20-mg macroporous monolith into 25 mL Pb^{2+} or Cd^{2+} solutions and shocking in a thermostatic shaker (THZ-98A) at 120 rpm at 30°C for a given time to reach adsorption equilibrium. After the adsorption, the concentrations of Pb^{2+} and Cd^{2+} solutions were analyzed by a UV–visible spectrophotometer (UV-3010, HITACHI). The adsorption capacity q_e (mg/g) of the macroporous monolithic adsorbents was calculated according to the following equation:

$$q_e = (C_0 - C_e)V/m \tag{1}$$

where C_0 and C_e are the initial and the final concentration of the Pb^{2+} and Cd^{2+}, V is the volume of the Pb^{2+} and Cd^{2+} solution, and m is the adsorbent dosage.

The required pH of solution was adjusted by 0.1 mol/L HCl or NaOH solutions. The adsorption isotherms were conducted by adding adsorbents (Sample 6) into Pb^{2+} and Cd^{2+} solutions for 2 h with concentration in the 100–600 mg/L range, and the control factors of the adsorption process were evaluated with the Langmuir and the Freundlich isotherm model. The adsorption kinetics were determined with 400 mg/L Pb^{2+} and Cd^{2+} solutions by varying the adsorption time from 5 to 120 min, and the pseudo-first-order equation and pseudo-second-order equation were carried out to describe the adsorption process. All adsorption experiments were repeated thrice to guarantee the accuracy of the obtained data.

The desorption studies were performed to evaluate the recyclability of the macroporous adsorbent. After the adsorption process, the adsorbents were separated and immersed into 30 mL of HCl solution (0.5 mol/L) for 2 h to desorb and then activated with 0.5 mol/L NaOH solution for 2 h. After that, the adsorbents were washed with distilled water till neutral pH and used in the next adsorption process. The adsorption–desorption cycle was performed five times.

RESULTS AND DISCUSSION

Preparation and Structure Characteristics of CMC-G-PAM/MMT

Formation of Pickering Emulsion and the CMC-G-PAM/MMT

As shown in **Figure 1a**, the paste-like concentrated Pickering emulsion (**Figure 1a**) was prepared by adding dropwise flaxseed

TABLE 1 | Feed composition of the macroporous monolith and their corresponding average pore size (D) and surface area (A).

Codes	T-20 (%)	MMT (%)	Oil (%)	$D_{m(macro)}$ (μm)	$D_{m(pore\ throat)}$ (μm)	$A_{(macro)}$ (μm^2)	$A_{(pore\ throat)}$ (μm^2)
Sample 1	2	3	50	1.52	0.44	307.52	62.47
Sample 2	2	5	50	3.37	–	379.71	–
Sample 3	2	7	50	2.75	–	394.44	–
Sample 4	2	9	50	1.89	–	439.04	–
Sample 5	3	5	50	1.43	0.52	418.88	112.49
Sample 6	4	5	50	1.38	0.40	409.48	125.29
Sample 7	5	5	50	1.25	0.37	325.24	207.91
Sample 8	6	5	50	1.26	0.37	431.70	230.26
Sample 9	4	5	40	1.57	0.47	396.51	255.01
Sample 10	4	5	30	1.71	0.41	293.71	140.29
Sample 11	4	5	20	2.13	0.53	248.77	33.64

oil into the aqueous phase, with MMT and T-20 as the stabilizer. Firstly, the MMT interacted with Tween-20 and formed the surfactant-coated MMT, and then the coated MMT clay particle combined with each other in the water phase to create a 3D network called the "cards house" aggregation model. Because the flaxseed oil is yellow, the Pickering MIPEs were canary yellow. The emulsions can stay in the reversed glass tube without any flow, suggesting that the formed emulsion is a typical gel emulsion and the oil drop is closely packed, which is verified by its optical micrograph as shown in **Figure 1c**. It can also be observed that the size of oil drops varies from around hundreds of nanometers to several micrometers. The type of emulsion was detected by the pendant-drop method; as presented in **Figure 1b**, the emulsion droplet dispersed into the distilled water but remained round in toluene, indicating that the emulsion is an O/W emulsion.

The porous monoliths of CMC-*g*-PAM/MMT were synthesized by free radical polymerization with APS as the initiator. The sulfate anion radicals formed from the decomposition of APS under 65°C, and the -OH groups of CMC were activated and formed the macro-radicals. Then, the macro-radicals triggered the double bonds of AM and *in situ* initiated the grafting reaction of the vinyl monomers onto the CMC in the presence of the cross-linker MBA. Once the polymerization reaction ended, the prepared wet monoliths were cut into pieces (**Figure 1d**) and Soxhlet extracted by acetone to remove off the oil phase, and the end product of white monoliths were finally obtained after drying (**Figure 1e**). The macroporous polymer monoliths will finally be used as adsorbent to remove heavy metal ions from water; thus, the amide group of the monoliths must be hydrolyzed with NaOH solution to generate -COO-, based on the fact that -COO- groups are easier to combine with heavy metal ions than the acylamino. Because of the hydrogen-bond interaction between polar groups (Zhu et al., 2016a), the prepared monoliths can swell rapidly in the water and shrink during the drying process. In order to avoid pore collapse, hydrolysis was conducted in a NaOH alcohol water mixture ($V_{ethanol}/V_{water} = 7/3$) (Zhu et al., 2016c). Then, the obtained CMC-*g*-PAM/MMT was dehydrated by Soxhlet extraction with acetone again and dried in an oven at 40°C. A photograph of the final resulting CMC-*g*-PAM/MMT was shown in **Figure 1e**. **Figure 1f** showed the CMC-*g*-PAM/MMT with a well-interconnected macroporous texture. It could be observed that both the macropores and highly interconnected small pores coexisted in the resulting material. The large cell pores were generated by removal of the oil droplets, and the pore throat derives from the thinnest points of the two neighboring oil drops attributed to the shrinkage during polymerization (Zhu et al., 2016c). The introduction of MMT not only stabilized the emulsion but also participated in polymerization to dramatically improve the performance and mechanical stability of the polymer-based composite (Schexnailder and Schmidt, 2009; Shibayama, 2012).

Effect of MMT Concentration on the Macroporous Structure

We prepared a series of macroporous monoliths from Pickering emulsion, which stabilized with different amounts of MMT particles from 3 to 9% according to the volume of disperse phase. As shown in **Figure 2**, the enrichment of macrospores can be observed in the matrix of the monoliths. Besides, the surface morphologies of the monolithic materials changed obviously with increasing MMT content from 3 to 9%. The average pore sizes of the prepared monoliths were 1.52, 3.37, 2.75, and 1.89 μm, respectively, corresponding to MMT content that varied from 3, 5, 7, and 9% (**Table 1**). In the case of 3% MMT, T-20 may play a dominant role for stabilizing the emulsion. When the content of MMT increased to 5%, most of the MMT may be coated with T-20 and then fixed at the O/W interface (Ye et al., 2018). The large size of the coated MMT can only stabilize the droplet larger than T-20; thus, the pore size of macroporous monoliths increased obviously. It was worthy to note that the pore throats existed obviously when 3% MMT was used, but disappeared while increasing the amount of MMT to 5%. This phenomenon has also been found in Pickering emulsions stabilized by other solid particles (Yi et al., 2016), indicating that the pore throats can only form at a moderate ratio of MMT and Tween-20. With an MMT

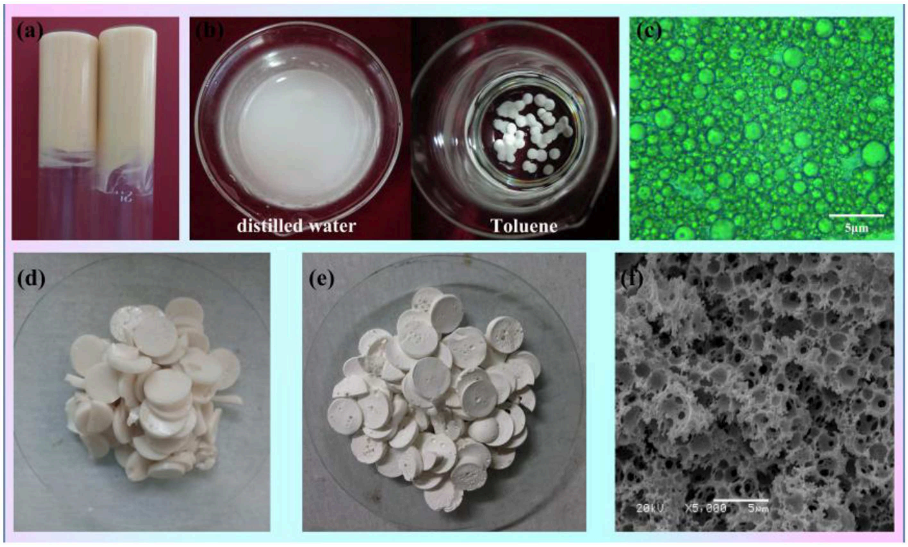

FIGURE 1 | (a) Digital photographs of the prepared Pickering MIPEs (MMT, 5%;T-20, 4%; internal phase volume, 50%). **(b)** Testing the type of emulsion by dropwise adding the emulsion droplet into the distilled water (DI) or toluene. **(c)** Optical images of the Pickering MIPEs. **(d)** Digital photographs of CMC-*g*-PAM/MMT before Soxhlet extraction. **(e)** Digital photographs and **(f)** SEM of porous CMC-*g*-PAM/MMT.

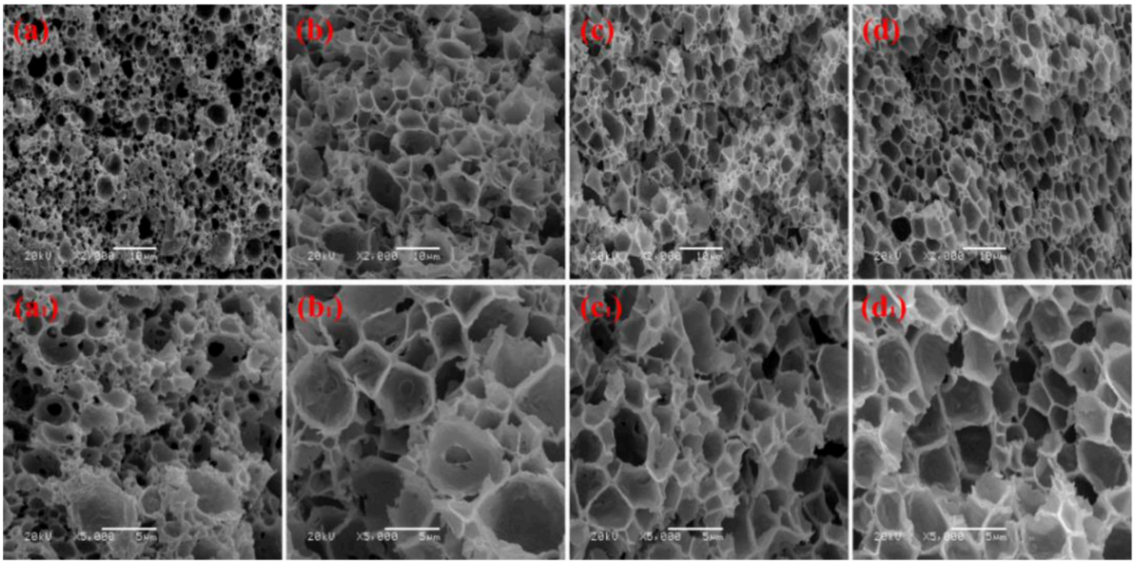

FIGURE 2 | SEM of macroporous CMC-*g*-PAM/MMT with different MMT. Three percentage (**a, a_1**, Sample 1); 5% (**b, b_1**, Sample 2); 7% (**c, c_1**, Sample 3); 9% (**d, d_1**, Sample 4).

content beyond 5%, the larger interfacial area of emulsion will be stabilized and thus the droplet size decreased. The macropore and pore throat void size distribution of the macroporous monolith with different MMT concentrations was shown in **Figure S1**.

In general, the increase in particle content will result in smaller droplet size and close packing of droplets, thus leading to more open pores during polymerization. However, as shown in **Figure 2**, the porous monoliths had a closed pore structure when the amount of the MMT increased from 5 to 9% (Samples 2, 3, and 4). The corresponding possible mechanism was presented in **Figure 3**. Once the content of MMT increased, the MMT particles packed on the O/W interface around the emulsions closely to form a solid barrier and prevent coalescence (Horozov, 2008). The increase in MMT will lead the aggregation of solid particles at the O/W interface to form a thicker particle layer, which results in a difficult fracture of polymerized film between two adjacent droplets. Thus, it is difficult to obtain monoliths with a desired interconnected structure when a high concentration of the stabilizer is used. These similar results have also been reported by Pickering emulsions stabilized by other solid particles (Wong et al., 2011; Zou et al., 2013b).

Effect of Surfactant Concentration on the Macroporous Structure

Co-surfactant concentration is also an important parameter for tuning the porosity and interconnectivity of macroporous materials prepared from Pickering emulsion template (Zhang et al., 2009, 2011; Zhu et al., 2010). The increase in co-surfactant concentration will decrease the interfacial tension and contribute to form the interconnected pore's structure simultaneously (Viswanathan et al., 2014). We therefore explored the effect of T-20 content on the microstructure of the macroporous monolith with internal phase volumes at 50% for all the starting emulsions; the SEM images were shown in **Figure 4**. When T-20 increased from 2% (Sample 2) to 3% (Sample 5), the average diameter of the macropore decreased dramatically from 3.37 to 1.43 μm (**Table 1**). Further increasing T-20 content from 3% (Sample 5) to 6% (Sample 8), it could be observed that the size of the macropore decreased, the number of pore throats per pore structure increased, and the wall thickness of the polymer layer got thin. Moreover, the surface areas of macropores and the pore throats were all increased as the T-20 content increases (**Table 1**). When T-20 content increased to 6%, a thin-wall macroporous material with perfect porosity was obtained. It is because more surfactant micelles remained at the O/W interface as T-20 content increases, which contributed to reducing the droplet size of Pickering MIPEs and resulted in forming the interconnected pores (Zou et al., 2013a). The corresponding possible mechanism was shown in **Figure 3**. The macropore size and the pore throat void size distribution of the macroporous monolith with various T-20 contentions were presented in **Figure S1**.

Effect of Volume Fraction of Disperse Phase on the Macroporous Structure

The pore size and interconnectivity of the macroporous materials are influenced significantly by the internal phase fraction. The macroporous materials prepared from different oil phase fractions of 50, 40, 30, and 20 vol % are presented in **Figure 5**. With the oil phase volume fraction decreasing, the macropore size increased and the number of pore throat decreased. When the internal phase volume fraction was 20%, the number of macro- and interconnected pores decreased significantly, while the interconnected pore still existed. This phenomenon indicated that the closely packed pore was not the only reason for forming the interconnected pore. Actually, MMT particles and the surfactant will both absorb onto the O/W interface, and the interconnected pore can also be formed at the interface stabilized by the surfactant (Zhu et al., 2016b). The macropore size and pore throat void size distribution of the prepared macroporous monoliths with variation of oil phase volume fraction were shown in **Figure S1**.

FTIR Analysis

The macroporous monoliths were synthesized by free radical polymerization with APS as the initiator. The sulfate anion radicals formed from the decomposition of APS under 65°C, and the –OH groups of CMC was activated and formed the macro-radicals. Later, the macro-radicals triggered the double bonds of AM and *in situ* initiated the grafting reaction of the vinyl monomers onto the CMC in the presence of cross-linker MBA. **Figure 6** showed the FTIR spectra of (a) AM, (b) CMC, and CMC-*g*-PAM/MMT (c) before and after hydrolysis reaction (d). As can be seen, the band at 3,433 cm^{-1} in **Figures 6C, D** was attributed to the characteristic absorption peak of O–H and intermolecular hydrogen bonds of the polysaccharide. The narrow band of $C = C$ stretching vibration at 1,612 cm^{-1} in the AM spectrum disappeared after polymerization (**Figure 6C**). Besides, the band at 1,673 cm^{-1} in the AM spectrum that was ascribed to the vibration of $C = O$ of amide was merged with the strong band (1,603 cm^{-1}) of carboxylate asymmetric vibration in the CMC spectrum and formed a strong and broad absorption band at 1,666 cm^{-1} in **Figure 6C**. After the hydrolysis of macroporous monoliths in the alkaline solution (**Figure 6D**), the absorption peak at 1,666 cm^{-1} weakened, and the asymmetric stretching vibration (1,562 cm^{-1}) and symmetrical stretching (1,407 cm^{-1}) vibration of $-COO^{-}$ strengthened. All of these proved that AM had been grafted onto CMC and a majority of acid amide groups were transformed into carboxylate groups after the hydrolysis (Ghorai et al., 2014).

Evaluation of Adsorption Properties

Effect of pH on Adsorption for Pb^{2+} and Cd^{2+}

The adsorption property of adsorbents for metal ions depends on the charge of binding sites and the metal species present in the solution. Therefore, the pH values of the metal ion solution and isoelectric point (pH of zero point charge, pH_{IEP}) of the prepared porous adsorbent (Sample 6) were determined to better understand the adsorption process. The pH_{IEP}, which represents the net external charge on the surface of the adsorbent in solution (Chingombe et al., 2005), was found to be about 4.0 for Sample 6 (**Figure 8A**). The adsorption property of the macroporous monolithic adsorbent for the heavy metal ions was investigated in different pH solutions ranging from 1 to 6. As shown in **Figure 7**, it can be found that the adsorption of Pb^{2+} and Cd^{2+} increased quickly at pH 1–4 and then remained constant. **Figure 8** showed that the surface of Sample 6 was positively charged at pH lower than pH_{IEP}, while at $pH > pH_{IEP}$, the surface of Sample 6 was negatively charged. Under acidic conditions, the adsorbents are usually protonized. When $pH < 4.0$, the protonation of the functional groups resulted in the adsorbent being positively charged and thus rejecting adsorption of Pb^{2+} and Cd^{2+}, leading to lower adsorption capacity. As the pH increases, the protonation of the functional groups decreases, thus increasing the adsorption capacity. At $pH > 4.0$, the negatively charged adsorbent attracts the metal cations to increase adsorption capacity until all the active sites were occupied, and then the saturation adsorption was reached.

Here, it also should be noted that after the adsorption, the equilibrium pH values of the Pb^{2+} and Cd^{2+} solution

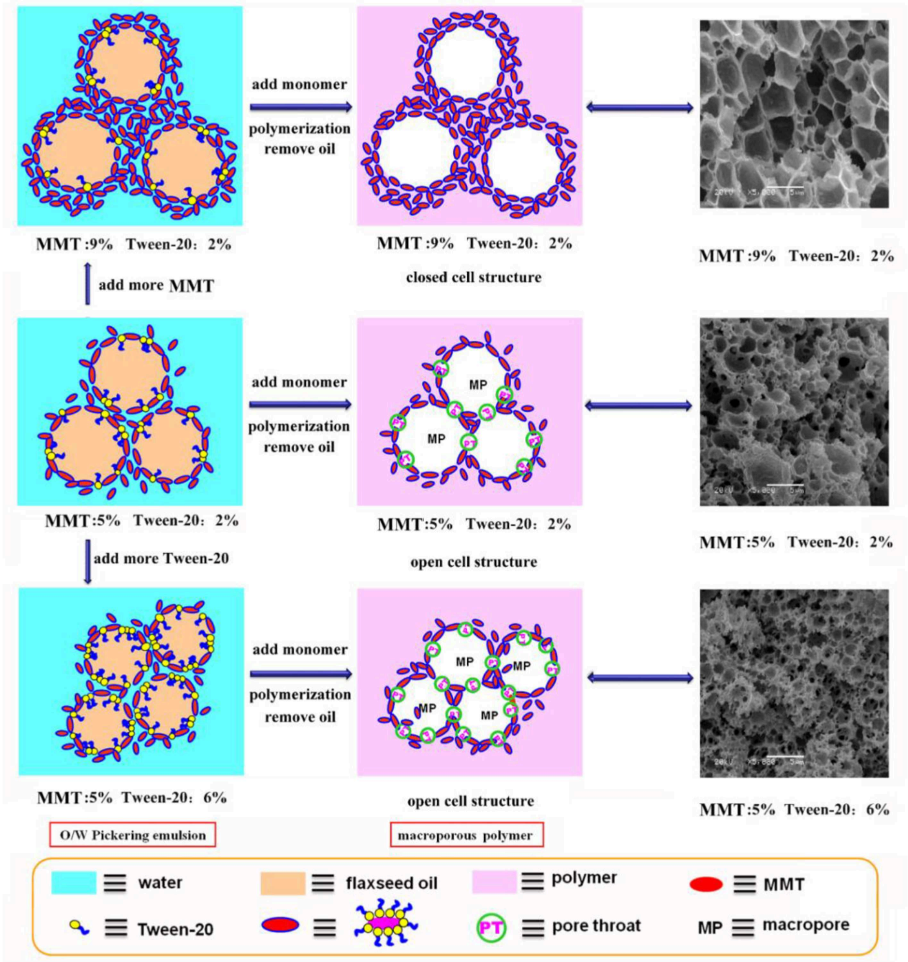

FIGURE 3 | Mechanism for the formation of CMC-*g*-PAM/MMT with closed-cell structure or open-cell structure by adding the MMT and T-20.

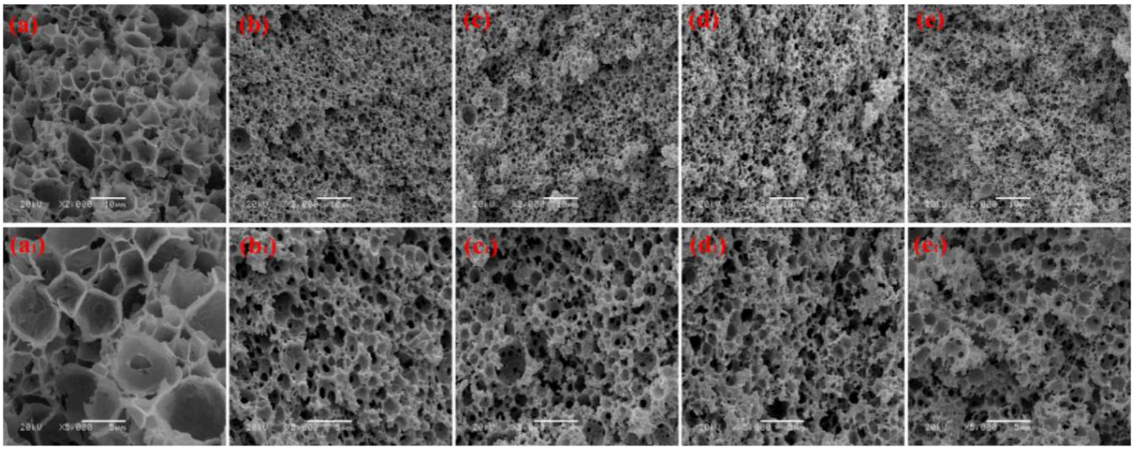

FIGURE 4 | SEM of the macroporous CMC-*g*-PAM/MMT monolith with different Tween-20. **(a, a_1)** 2% (Sample 2); **(b, b_1)** 3% (Sample 5); **(c, c_1)** 4% (Sample 6); **(d, d_1)** 5% (Sample 7); **(e, e_1)** 6% (Sample 8).

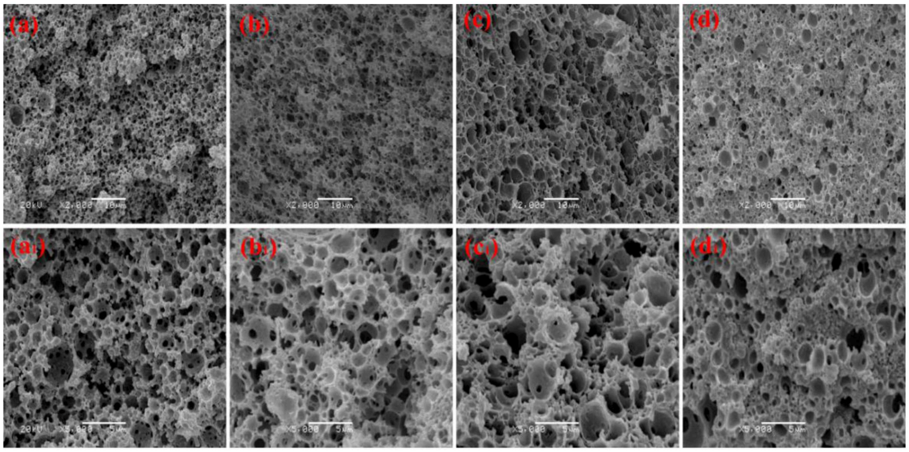

FIGURE 5 | Effect of oil phase volume fraction for the CMC-*g*-PAM/MMT **(a, a_1)** 50% (Sample 6); **(b, b_1)** 40% (Sample 9); **(c, c_1)** 30% (Sample 10); **(d, d_1)** 20% (Sample 11). All of the prepared samples prepared with 5% of MMT and 4% of T-20.

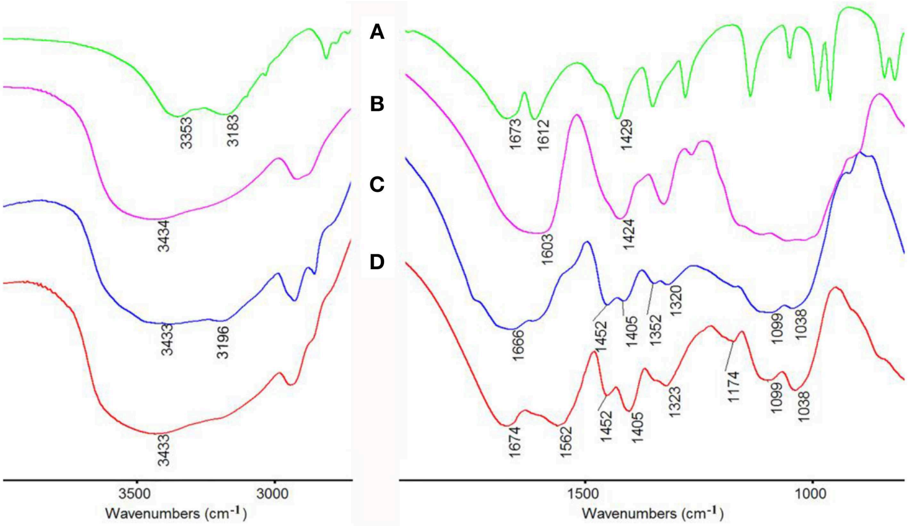

FIGURE 6 | FTIR spectra of **(A)** AM, **(B)** CMC, CMC-*g*-PAM/MMT **(C)** before and **(D)** after hydrolysis reaction.

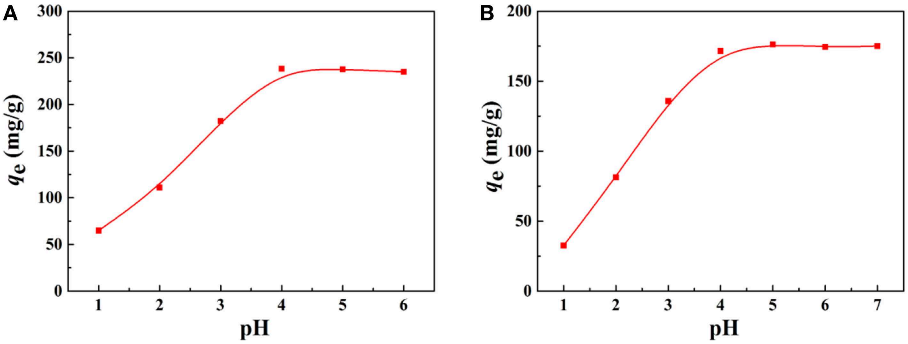

FIGURE 7 | Effect of pH on the adsorption capacity of the macroporous monolith (Sample 6) for **(A)** Pb^{2+} and **(B)** Cd^{2+}, respectively. Adsorption conditions: C_0, 200 mg/L; dosage of adsorbent, 20 mg/25 mL.

were all higher than the initial pH (**Figure 8B**). Under acidic conditions, along with the adsorption process, the -COO$^-$ and -CONH$_2$ groups were protonated and converted to -COOH and -CONH$_3^+$, which consumes H$^+$ of the solution, thus increasing the pH. The above discussion indicated that the electrostatic and complexation interactions mainly contribute to the adsorption process (Sitko et al., 2016). Taking into account that the adsorbent had high adsorption capacity for metal ions at high pH, but metal ions will precipitate at excessive high pH, the next adsorption experiments were performed at natural pH.

Effect of Initial Concentration on Adsorption for Pb^{2+} and Cd^{2+}

The saturation adsorption capacities of the macroporous monoliths for Pb^{2+} and Cd^{2+} were evaluated, and the results were shown in **Figure 9**. The increase in initial metal ions

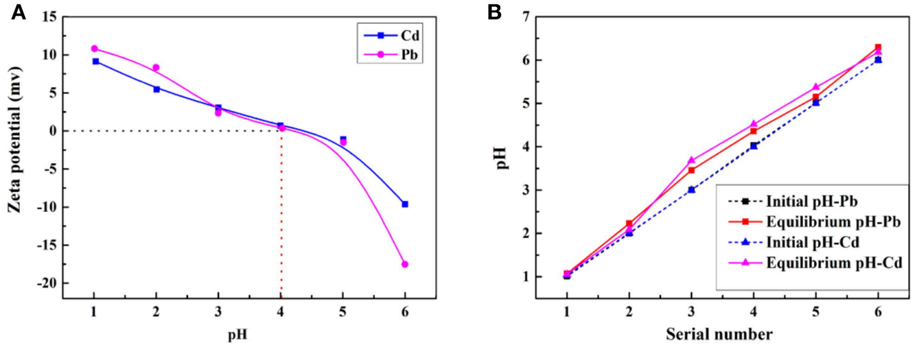

FIGURE 8 | (A) Zeta potential of CMC-*g*-PAM/MMT at different pH values. Adsorption experiments: C_0, 200 mg/L; t, 1 h; dosage of adsorbent, 50 mg/20 mL. **(B)** Initial and equilibrium pH of the solutions. Adsorption experiments: C_0, 200 mg/L; t, 1 h; dosage of adsorbent, 20 mg/25 mL.

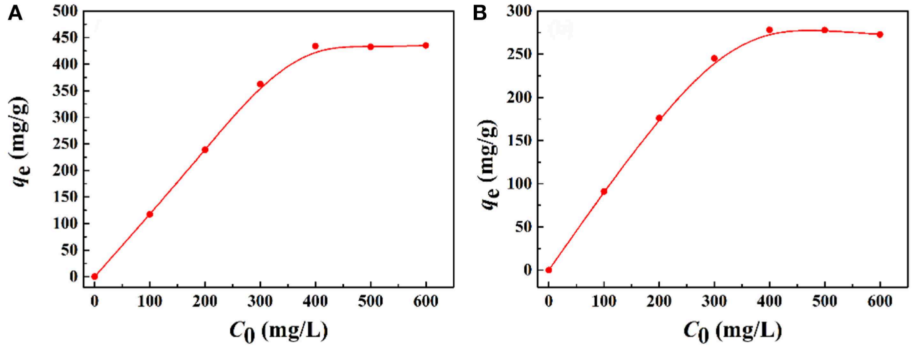

FIGURE 9 | Effect of the initial **(A)** Pb^{2+} and **(B)** Cd^{2+} concentration on the adsorption capacity of macroporous monolith (Sample 6). Adsorption conditions: dosage of adsorbent, 20 mg/25 mL; pH, natural.

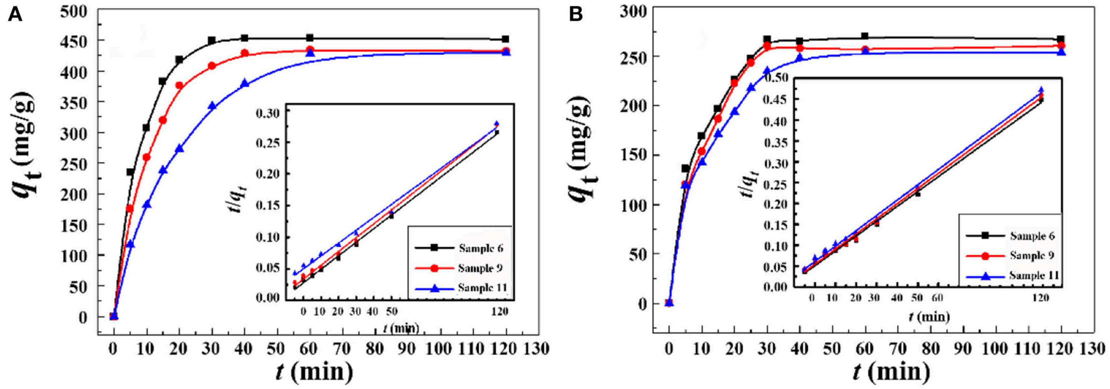

FIGURE 10 | Adsorption kinetic curves of the macroporous monolith with various oil phase volume fraction for **(A)** Pb^{2+} and **(B)** Cd^{2+}. Adsorption conditions: C_0, 400 mg/L; dosage of adsorbent, 20 mg/25 mL; pH, natural.

concentrations led to a sharp increase in adsorption capacities, and then the increasing trend became flat until adsorption saturation was reached. The reason was that the driving force at the solid–liquid interface improved with an increase in the initial metal ion concentration, which accelerated the diffusion of metal ions in the matrix and adsorbents. The maximum adsorption capacities of the macroporous monoliths were 456.05 mg/g for Pb^{2+} and 278.11 mg/g for Cd^{2+}.

The adsorption process was analyzed by the Langmuir (Equation 2) and Freundlich isotherm models (Equation 3) (Gan et al., 2018), and the equations are shown as follows:

$$C_e/\, q_e = 1/(q_m \times b) + C_e/q_m \tag{2}$$

$$Log\ q_e = logK + (1/n)log\ C_e \tag{3}$$

where C_e (mg/L) represents the equilibrium concentration of metal ions, and q_m and q_e are the amounts of metal ions adsorbed per unit mass of adsorbent at equilibrium state at any time (mg/g), respectively. b (L/mg) is the Langmuir constant related to the affinity of binding sites, K is the Freundlich constant related to adsorption capacity, and n represents the index of adsorption intensity or surface heterogeneity.

The isotherm parameters and linear correlation coefficients (R^2) for the two models were calculated and summarized in **Table S1**. The adsorption capacities calculated by the Langmuir model for Pb^{2+} and Cd^{2+} were 464.91 and 315.82 mg/g, respectively. The calculated results were closer to the experiment value. Otherwise, all the adsorption isotherm data were better fitted to the Langmuir isotherm model ($R^2 > 0.99$) than the Freundlich model. Thus, the Langmuir model was suitable to describe the adsorption process, which means that the binding sites distributed over the adsorbent surface was homogeneous and these binding sites had the same affinity for adsorption of a single molecular layer (Wen et al., 2012; Wang et al., 2013).

Effect of Contact Time on Adsorption for Pb^{2+} and Cd^{2+}

The adsorption rate is a key parameter for practical applications. Thus, the effect of contact time on the adsorption behavior was investigated. **Figure 10** showed the kinetic adsorption curves of the macroporous monoliths with different oil phase volume fraction for Pb^{2+} and Cd^{2+}. The adsorption rate of the macroporous monoliths for the metal ions increased remarkably in the first 30 min for Pb^{2+} and Cd^{2+}. In particular, Sample 6 and Sample 9 with well-interconnected pore structure showed fast adsorption rate. This was because the interconnected pores reduced the mass transfer resistance efficiently and exposed more carboxyl groups (as the binding sites for metal ions), which facilitate the accessibility of metal ions to the adsorbent. However, a large decrease in the adsorption rate was observed when the adsorbent with a relatively small number of macro- and interconnected pores and Sample 11 (prepared with 20% of internal phase volume) reached the equilibrium more than 1 h. The above facts proven that the structure of the adsorbents dramatically affected the adsorption kinetics of the macroporous monoliths for the metal ions. The high porosity and permeability of the adsorbent can improve the adsorption rate.

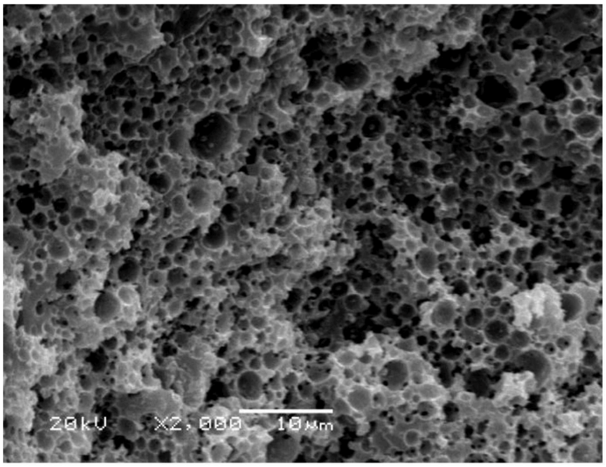

FIGURE 12 | SEM of the macroporous CMC-*g*-PAM/MMT monolith after metal-adsorption (Sample 1).

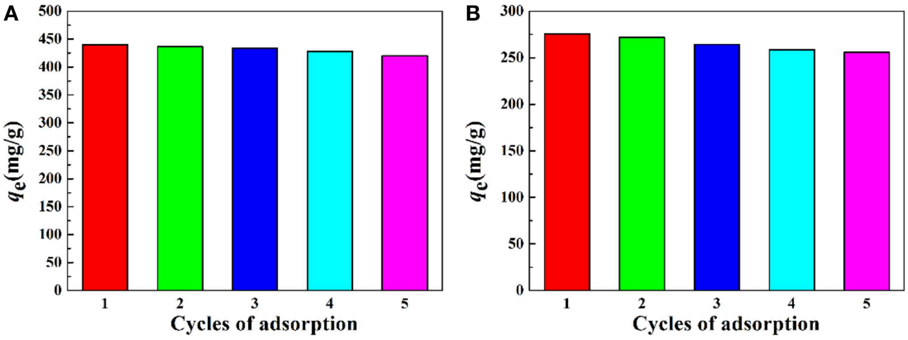

FIGURE 11 | Adsorption capacity of the macroporous monolith (Sample 6) for **(A)** Pb^{2+} and **(B)** Cd^{2+} after regenerated five times. Adsorption conditions: C_0, 400 mg/L; adsorbent dosage: 20 mg/25 mL; pH, natural.

In order to examine the dynamic adsorption process, the adsorption data were fitted by pseudo-first-order (Equation 4) and pseudo-second-order (Equation 5) (Wu et al., 2018) kinetic models. The kinetic models' equations are expressed as follows:

$$Log(q_e - q_t) = logq_e - (k_1/2.303)t \tag{4}$$

$$t/q_{t=}1/(k_2 \times q_e^2) + t/q_e \tag{5}$$

Here, q_t is the amount adsorbed for Pb^{2+} and Cd^{2+} at time t and q_e is the amount of metal ions by unit mass of adsorbents at equilibrium state. k_1 (min^{-1}) and k_2 [g/(mg min)] are the adsorption rate constants of the pseudo-first-order and pseudo-second-order models, respectively. The corresponding adsorption kinetic parameters are listed in **Tables S2, S3**. As shown in **Tables S2, S3**, the linear correlation coefficients (R^2) for the pseudo-second-order kinetic model were much higher than those for the pseudo-first-order kinetic model. Otherwise, the adsorption capacities calculated with the pseudo-second-order kinetic model ($q_{e,cal}$) were much closer to the experiment values ($q_{e,exp}$). Thus, the pseudo-second-order kinetic model fit the dynamic adsorption process well and it was controlled mainly by a chemical adsorption process (Zhou et al., 2014).

Regeneration and Reusability

The reusability of the as-prepared macroporous monolith was tested by repeating the adsorption–desorption cycle using 0.5 mol/L HCl as the desorbing agent and 0.5 mol/L NaOH as regeneration solution. As shown in **Figure 11**, the adsorption capacity had no obvious decrease with increasing the adsorption–desorption cycle. The regenerated monolith still showed high adsorption capabilities for Pb^{2+} and Cd^{2+} after being reused five times. Moreover, it should be noted that, after metal adsorption, the adsorbent still maintained a well-porous structure (**Figure 12**), and it also can be seen from **Table 2**

TABLE 2 | Comparison of adsorption capacities (q_m, mg/g) of various adsorbents for Pb^{2+} and Cd^{2+}.

Adsorbent	Cd^{2+} (mg/g)	Pb^{2+} (mg/g)	References
Tourmaline		108	Wang et al., 2011
Lignosulfonate–graphene oxide–polyaniline ternary nanocomposite		216	Yang et al., 2014
EDTA–graphene oxide		479	Madadrang et al., 2012
Fe_3O_4@DAPF core–shell ferromagnetic nanorods (CSFMNRs)		83	Venkateswarlu and Yoon, 2015
Thiocarbohydrazide cross-linked oxidized chitosan and poly(vinyl alcohol)		48	Ahmad et al., 2017
Magnetic cellulose nanocrystal/metal–organic framework composite (MCNC@Zn-BTC)		559	Wang et al., 2017a,b
Thermophilic *Geobacillus galactosidasius* sp. nov. loaded γ-Fe_2O_3 magnetic nanoparticle	37		Özdemir et al., 2016
Zr-based MOF-808 supported on polyacrylonitrile (PAN) nanofiber	225		Efome et al., 2018
TP–PS biocomposite hydrogels	194		Maity and Ray, 2017
Polyvinyl alcohol/polyacrylic acid double network gel	116	195	Chu et al., 2015
Polyampholyte	182	202	Copello et al., 2012
Thiosemicarbazide modified chitosan manlin	257	325	Li et al., 2016
Magnetic chelating resin (MIDA)	247	745	El-Bahy, 2018
MnO_2 modification of biochar (BR)	14	128	Liang et al., 2017
CMC-*g*-PAM/MMT	278	456	This study

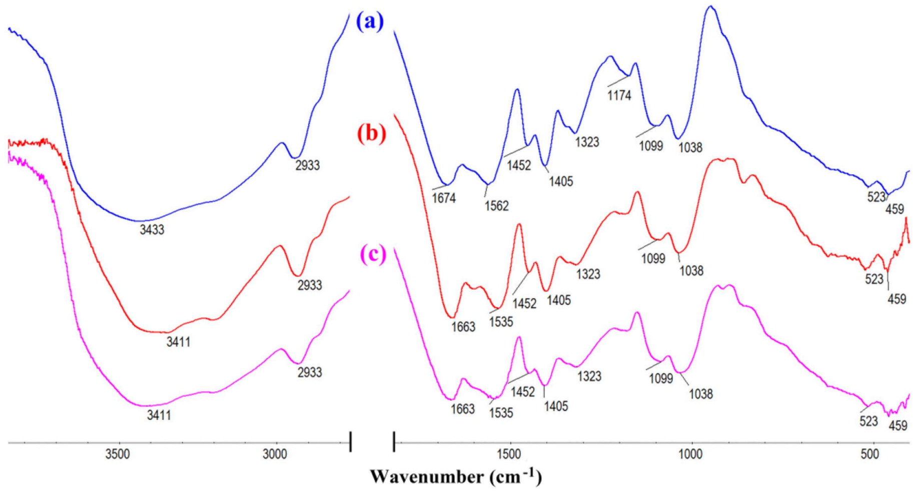

FIGURE 13 | The FTIR spectra of CMC-*g*-PAM/MMT before **(a)** and after **(b)** Pb^{2+}, **(c)** Cd^{2+} adsorption.

that the q_m values of the macroporous monolith prepared in this study were much higher than those of the adsorbents reported previously. All the adsorption dates indicated that the as-prepared macroporous monolith materials were an efficient adsorbent for heavy metal ions and had potential application in purification of wastewater.

Adsorption Mechanism

FTIR and XPS of CMC-*g*-PAM before and after adsorption of Pb^{2+} and Cd^{2+} would provide powerful evidence to clarify the adsorption mechanism of metal ions onto the functional groups of the as-prepared adsorbent. As can be seen from the FTIR spectra in **Figure 13**, after adsorption of Pb^{2+} or Cd^{2+}, the strong absorption band at 3,434 cm^{-1} assigned to the O–H stretching vibration shifted to 3,411 cm^{-1}, indicating the electrostatic interaction and H-bonding between -OH and Pb^{2+} or Cd^{2+}. Besides, the band at 1,674 cm^{-1} ascribed to the vibration of C = O of carboxyl, and the asymmetric stretching vibration of $-COO^-$ at 1,562 cm^{-1} shifted to 1,663 and 1,535 cm^{-1} after adsorption, which proved that the combination of carboxyl and metal ions reduced electron cloud density of oxygen atoms on carboxyl. According to the above, it can be confirmed that the carboxyl group and the hydroxyl group are the main force of the adsorbent to adsorb metal ions.

The XPS spectra of CMC-*g*-PAM/MMT before and after adsorption were depicted in **Figure 14**, and the corresponding parameters were listed in **Table 3**. As the survey spectrum in

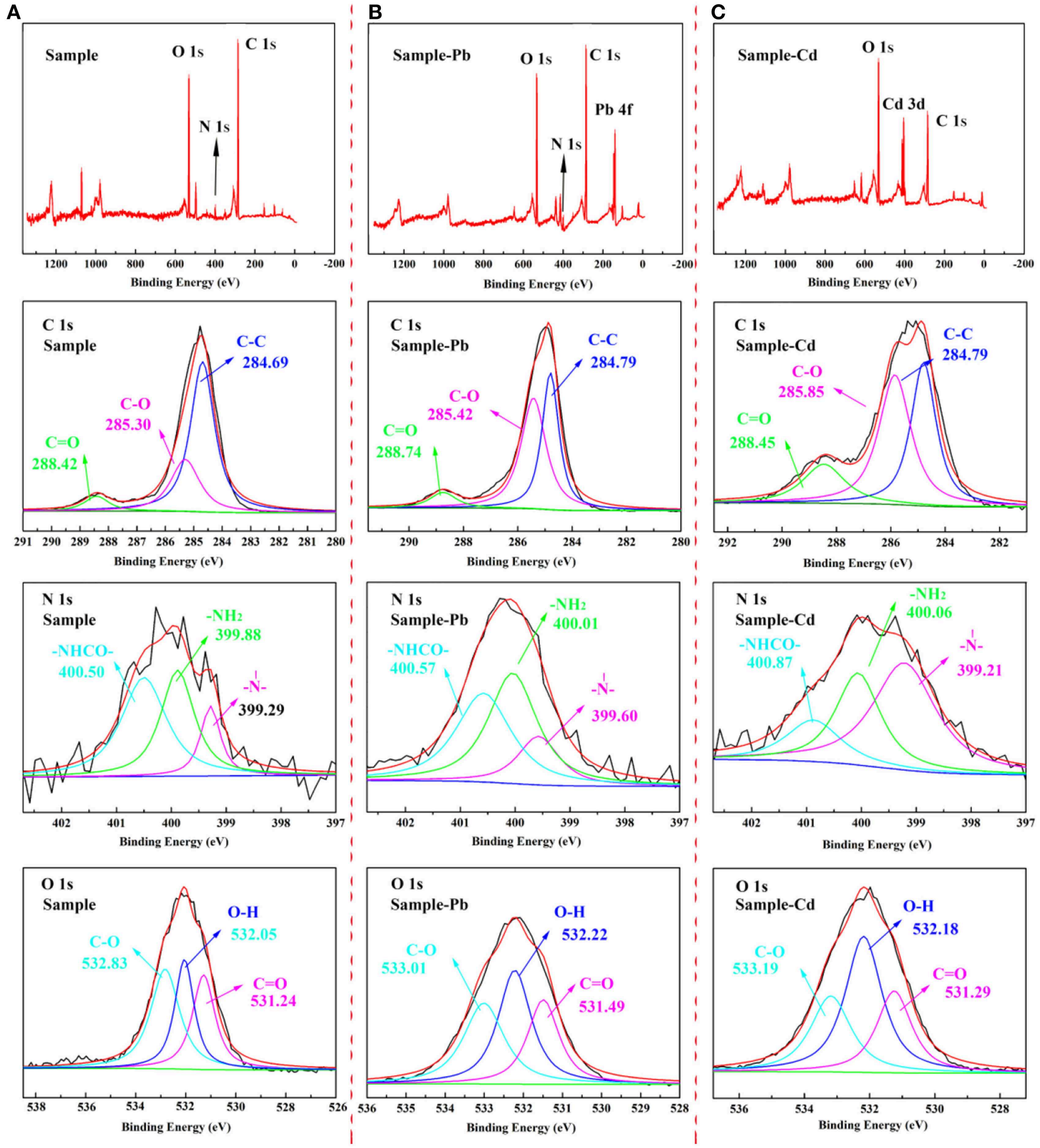

FIGURE 14 | The XPS spectra of CMC-*g*-PAM/MMT before **(A)** and after **(B)** Pb^{2+}, **(C)** Cd^{2+} adsorption.

TABLE 3 | Binding energy (eV) of CMC-*g*-PAM/MMT before and after adsorbed with Pb^{2+} and Cd^{2+}.

Element		Sample		Sample -Pb		Sample -Cd	
		BE(eV)	Percent (%)	BE (eV)	Percent (%)	BE (eV)	Percent (%)
C1S	C–C	284.69	65.99	284.79	42.14	284.79	38.54
	C–O	285.30	27.44	285.42	50.32	285.85	44.20
	C = O	288.42	6.57	288.74	7.54	288.46	17.25
N1S	$-\overset{|}{\mathrm{N}}-$	399.29	14.75	399.57	16.36	399.21	51.51
	-NH2	399.88	37.81	400.04	43.62	400.06	31.23
	-NHCO-	400.50	47.44	400.57	40.02	400.87	17.27
O1S	C = O	531.29	29.95	531.49	27.31	531.24	26.12
	O–H	532.05	29.69	532.22	38.80	532.18	45.92
	C–O	532.83	40.35	533.01	33.88	533.18	27.96

Figures 14B,C showed, the appearance of Pb 4f and Cd 3d at 139.48 and 412.38 eV after adsorption revealed that the Pb^{2+} and Cd^{2+} were specifically adsorbed onto the prepared porous adsorbent. In the high-resolution XPS spectra of C 1s, there were also obvious changes in integral area ratio and binding energy after adsorbing Pb^{2+} and Cd^{2+}. As listed in **Table 3**, the integral area ratios of C = O and C–O were both increased, while the integral area ratio of C–C decreased. The shift of binding energy can also be observed in the spectra, especially for the binding energy of C = O and C–O, which can be attributed to the decreased electron density of the adjacent O atoms, and thus the binding energy of the C atoms increased (Ma et al., 2019). The high-resolution O 1s spectra before adsorption presented three peaks at a binding energy of 532.83, 532.05, and 531.24 eV, which are assigned to the C–O, O–H, and C = O groups, respectively. After the adsorption of heavy metal ions, the binding energy increased; meanwhile, the integral area ratio of C = O and C–O decreased, and the integral area ratio of O–H increased. The shift of binding energy was attributed to the complexation between metal and -OH and -COO^{-}, in which O atoms donate electrons to metal ions and the electron density toward O atoms in these groups decrease, thus increasing the binding energy of O 1s peaks. The above results demonstrate that the -COO^{-} and -OH groups in porous adsorbent participate in the adsorption of heavy metal ions, but in different ways (Luo et al., 2014). Otherwise, the weak signal peak of N 1s in the XPS spectra showed that there was only a slight amount of acylamino existing in the materials after hydrolysis. As the high-resolution XPS spectra of N 1s shown, the binding energy of -NH$_2$ and -NHCO- increased slightly, while their integral area ratio decreased after the adsorption of heavy metal ions, demonstrating that the acylamino groups participated in the adsorption process. These results revealed the electrostatic attraction or coordination interaction between the functional groups and heavy metal ions, and the COO^{-} and -OH groups provide the main adsorption sites. The acylamino groups assisted in the adsorption process.

CONCLUSIONS

A series of novel macroporous monolithic adsorbents had been successfully prepared by polymerization of Pickering MIPEs with natural MMT and T-20 as the stabilizer and the non-toxic and eco-friendly flaxseed oil used in disperse phase. The structure of the macroporous monolith can be adjusted by changing the volume of oil phase and the content of MMT and T-20. The synergistic effects of MMT and T-20 were favorable to create the macroporous monolith materials with a closed-cell or highly interconnected macroporous structure. The prepared macroporous monoliths showed fast adsorption kinetics for Pb^{2+} and Cd^{2+}, and the adsorption equilibrium can be reached as fast as 30 min. Otherwise, the adsorption rate of the adsorbent can be improved by increasing the connectivity and porosity of the monolith. The adsorption capacities of the adsorbent for Pb^{2+} and Cd^{2+} were 456.05 and 278.11 mg/g, respectively. In addition, the macroporous monolith exhibited excellent reusability. After five adsorption–desorption cycles, the regenerated monolith still had good absorbability and maintained a well-porous structure. As a whole, we provided a new approach to fabricating macroporous monoliths that are highly efficient and recyclable using a type of eco-friendly Pickering MIPE. The prepared monoliths can be used as efficient adsorbent for the removal of heavy metals from wastewater.

DATA AVAILABILITY

The datasets generated for this study are available on request to the corresponding author.

AUTHOR CONTRIBUTIONS

FW and YZ contributed to the experiment process and data analysis, wrote the paper, and created all the figures. HX contributed to the design of the experiment, data analysis, and revision of the paper. AW contributed to the experiment design, data analysis, and revision of the paper.

FUNDING

The authors are grateful for the financial support from the National Natural Science Foundation of China (21706267), the

Major Projects of the National Natural Science Foundation of Gansu, China (18JR4RA001), the Funds for Creative Research Groups of Gansu, China (17JR5RA306), and the Scientific Research Project of Beibu Gulf University, China (17KYQD57).

SUPPLEMENTARY MATERIAL

The Supplementary Material for this article can be found online at: https://www.frontiersin.org/articles/10.3389/fchem.2019.00603/full#supplementary-material

REFERENCES

Ahmad, M., Manzoor, K., Chaudhuri, R. R., and Ikram, S. (2017). Thiocarbohydrazide cross-linked oxidized chitosan and poly(vinyl alcohol): a green framework as efficient Cu(II), Pb(II), and Hg(II) adsorbent. *J. Chem. Eng. Data* 62, 2044–2055. doi: 10.1021/acs.jced.7b00088

Alexandratos, S. D. (2008). Ion-exchange resins: a retrospective from industrial and engineering chemistry research. *Ind. Eng. Chem. Res.* 48, 388–398. doi: 10.1021/ie801242v

Binks, B. P., and Lumsdon, S. O. (1999). Stability of oil-in-water emulsions stabilised by silica particles. *Phys. Chem. Chem. Phys.* 1, 3007–3016. doi: 10.1039/a902209k

Busby, W., Cameron, N. R., and Jahoda, C. A. (2001). Emulsion-derived foams (PolyHIPEs) containing poly (ε-caprolactone) as matrixes for tissue engineering. *Biomacromolecules* 2, 154–164. doi: 10.1021/bm0000889

Chan-Thaw, C. E., Villa, A., Katekomol, P., Su, D., Thomas, A., and Prati, L. (2010). Covalent triazine framework as catalytic support for liquid phase reaction. *Nano Lett.* 10, 537–541. doi: 10.1021/nl904082k

Chingombe, P., Saha, B., and Wakeman, R. J. (2005). Surface modification and characterization of a coal-based activated carbon. *Carbon* 43, 3132–3143. doi: 10.1016/j.carbon.2005.06.021

Chu, L., Liu, C., and Zhou, G. (2015). A double network gel as low cost and easy recycle adsorbent: highly efficient removal of Cd(II) and Pb(II) pollutants from wastewater. *J. Hazard. Mater.* 300, 153–160. doi: 10.1016/j.jhazmat.2015.06.070

Copello, G. J., Diaz, L. E., and Orto, V. C. D. (2012). Adsorption of Cd(II) and Pb(II) onto a one step-synthesized polyampholyte: kinetics and equilibrium studies. *J. Hazard. Mater.* 217–218, 374–381. doi: 10.1016/j.jhazmat.2012.03.045

Dong, J., Worthen, A. J., Foster, L. M., Chen, Y., Cornell, K. A., Bryant, S. L., et al. (2014). Modified montmorillonite clay microparticles for stable oil-in-seawater emulsions. *ACS Appl. Mater. Interfaces* 6, 11502–11513. doi: 10.1021/am502187t

Efome, J. E., Rana, D., Matsuura, T., and Lan, C. Q. (2018). Insight studies on metal-organic framework nanofibrous membrane adsorption and activation for heavy metal ions removal from aqueous solution. *ACS Appl. Mater. Interfaces* 10, 18619–18629. doi: 10.1021/acsami.8b01454

El-Bahy, S. M. (2018). New iminodiacetate chelating resin-functionalized Fe_3O_4 nanoparticles: synthesis, characterization, and application for the removal of some noxious metal ions from wastewater. *J. Chem. Eng. Data* 63, 2299–2313. doi: 10.1021/acs.jced.8b00241

Gan, Q., Shi, W., Xing, Y., and Hou, Y. (2018). A polyoxoniobate/g-C3N4 nanoporous material with high adsorption capacity of methylene blue from aqueous solution. *Front. Chem.* 6:7. doi: 10.3389/fchem.2018.00007

Ghorai, S., Sarkar, A., Raoufi, M., Panda, A. B., Schönherr, H., and Pal, S. (2014). Enhanced removal of methylene blue and methyl violet dyes from aqueous solution using a nanocomposite of hydrolyzed polyacrylamide grafted xanthan gum and incorporated nanosilica. *ACS Appl. Mater. Interfaces* 6, 4766–4777. doi: 10.1021/am4055657

Horozov, T. S. (2008). Foams and foam films stabilised by solid particles. *Curr. Opin. Colloid Interface Sci.* 13, 134–140. doi: 10.1016/j.cocis.2007.11.009

Hu, Y., Gu, X., Yang, Y., Huang, J., Hu, M., Chen, W., et al. (2014). Facile fabrication of poly (l-lactic acid)-grafted hydroxyapatite/poly (lactic-co-glycolic acid) scaffolds by pickering high internal phase emulsion templates. *ACS Appl. Mater. Interfaces* 6, 17166–17175. doi: 10.1021/am504877h

Ikem, V. O., Menner, A., and Bismarck, A. (2010a). High-porosity macroporous polymers sythesized from titania-particle-stabilized medium and high internal phase emulsions. *Langmuir* 26, 8836–8841. doi: 10.1021/la9046066

Ikem, V. O., Menner, A., and Bismarck, A. (2011). Tailoring the mechanical performance of highly permeable macroporous polymers synthesized via Pickering emulsion templating. *Soft Matter* 7, 6571–6577. doi: 10.1039/c1sm05272a

Ikem, V. O., Menner, A., Horozov, T. S., and Bismarck, A. (2010b). Highly permeable macroporous polymers synthesized from pickering medium and high internal phase emulsion templates. *Adv. Mater.* 22, 3588–3592. doi: 10.1002/adma.201000729

Kou, Y., Xu, Y., Guo, Z., and Jiang, D. (2011). Supercapacitive energy storage and electric power supply using an aza-fused π-conjugated microporous framework. *Angew Chem.* 123, 8912–8916. doi: 10.1002/ange.201103493

Kovačič, S., AnŽlovar, A., Erjavec, B., Kapun, G., and Matsko, N. B., Žigon, M., et al. (2014). Macroporous ZnO foams by high internal phase emulsion technique: synthesis and catalytic activity. *ACS Appl. Mater. Interfaces* 6, 19075–19081. doi: 10.1021/am5050482

Li, M., Zhang, Z., Li, R., Wang, J. J., and Ali, A. (2016). Removal of Pb(II) and Cd(II) ions from aqueous solution by thiosemicarbazide modified chitosan. *Int. J. Biol. Macromol.* 86, 876–884. doi: 10.1016/j.ijbiomac.2016.02.027

Liang, J., Li, X., Yu, Z., Zeng, G., Luo, Y., Jiang, L., et al. (2017). Amorphous MnO_2 modified biochar derived from aerobically composted swine manure for adsorption of Pb (II) and Cd (II). *ACS Sustain. Chem. Eng.* 5, 5049–5058. doi: 10.1021/acssuschemeng.7b00434

Liu, R., Cho, S. I., and Lee, S. B. (2008). Poly (3, 4-ethylenedioxythiophene) nanotubes as electrode materials for a high-powered supercapacitor. *Nanotechnology* 19:215710. doi: 10.1088/0957-4484/19/21/215710

Luo, S., Li, X., Chen, L., Wan, Y., and Liu, C. (2014). Layer-by-layer strategy for adsorption capacity fattening of endophytic bacterial biomass for highly effective removal of heavy metals. *Chem. Eng. J.* 239, 312–321. doi: 10.1016/j.cej.2013.11.029

Ma, J., Li, T., Liu, Y., Cai, T., Wei, Y., Dong, W., et al. (2019). Rice husk derived double network hydrogel as efficient adsorbent for Pb(II), Cu(II) and Cd(II) removal in individual and multicomponent systems. *Bioresour. Technol.* 290:121793. doi: 10.1016/j.biortech.2019.121793

Madadrang, C. J., Kim, H. Y., Gao, G., Wang, N., Zhu, J., Feng, H., et al. (2012). Adsorption behavior of EDTA–graphene oxide for Pb(II) removal. *ACS Appl. Mater. Interfaces* 4, 1186–1193. doi: 10.1021/am201645g

Maity, J., and Ray, S. K. (2017). Competitive removal of Cu(II) and Cd(II) from water using a biocomposite hydrogel. *J. Phys. Chem. B* 121, 10988–11001. doi: 10.1021/acs.jpcb.7b08796

Özdemir, S., Kilinç, E., Poli, V., Okumuş, V., and Poli, A., Nicolaus, B., et al. (2016). Thermophilic *Geobacillus galactosidasius* sp. nov. loaded γ-Fe_2O_3 magnetic nanoparticle for the preconcentrations of Pb and Cd. *Bioresour. Technol.* 201, 269–275. doi: 10.1016/j.biortech.2015.11.052

Pierre, S. J., Thies, J. C., Dureault, A., Cameron, N. R., van Hest, J. C. M., Carette, N., et al. (2006). Covalent enzyme immobilization onto photopolymerized highly porous monoliths. *Adv. Mater.* 18, 1822–1826. doi: 10.1002/adma.200600293

Pulko, I., Wall, J., Krajnc, P., and Cameron, N. R. (2010). Ultra-high surface area functional porous polymers by emulsion templating and hypercrosslinking: efficient nucleophilic catalyst supports. *Chemistry* 16, 2350–2354. doi: 10.1002/chem.200903043

Schexnailder, P., and Schmidt, G. (2009). Nanocomposite polymer hydrogels. *Colloid Polym. Sci.* 287, 1–11. doi: 10.1007/s00396-008-1949-0

Shen, J., Cao, X., and James Lee, L. (2006). Synthesis and foaming of water expandable polystyrene–clay nanocomposites. *Polymer* 47, 6303–6310. doi: 10.1016/j.polymer.2006.06.068

Shibayama, M. (2012). Structure–mechanical property relationship of tough hydrogels. *Soft Matter* 8, 8030–8038. doi: 10.1039/c2sm25325a

Silverstein, M. S. (2014). PolyHIPEs: recent advances in emulsion-templated porous polymers. *Prog. Polym. Sci.* 39, 199–234. doi: 10.1016/j.progpolymsci.2013.07.003

Sitko, R., Musielak, M., Zawisza, B., Talik, E., and Gagor, A. (2016). Graphene oxide/cellulose membranes in adsorption of divalent metal ions. *RSC Adv.* 6, 96595–96605. doi: 10.1039/C6RA21432K

Venkateswarlu, S., and Yoon, M. (2015). Core–shell ferromagnetic nanorod based on amine polymer composite (Fe_3O_4@DAPF) for fast removal of Pb(II) from aqueous solutions. *ACS Appl. Mater. Interfaces* 7, 25362–25372. doi: 10.1021/acsami.5b07723

Vílchez, A., Rodríguez-Abreu, C., Esquena, J., Menner, A., and Bismarck, A. (2011). Macroporous polymers obtained in highly concentrated emulsions stabilized solely with magnetic nanoparticles. *Langmuir* 27, 13342–13352. doi: 10.1021/la2032576

Viswanathan, P., Johnson, D. W., Hurley, C., Cameron, N. R., and Battaglia, G. (2014). 3D surface functionalization of emulsion-templated polymeric foams. *Macromolecules* 47, 7091–7098. doi: 10.1021/ma500968q

Viswanathan, P., Ondeck, M. G., Chirasatitsin, S., Ngamkham, K., and Reilly, G. C. (2015). 3D surface topology guides stem cell adhesion and differentiation. *Biomaterials* 52, 140–147. doi: 10.1016/j.biomaterials.2015.01.034

Wang, C. P., Wu, J. Z., Sun, H. W., Wang, T., Liu, H. B., and Chang, Y. (2011). Adsorption of Pb(II) ion from aqueous solutions by tourmaline as a novel adsorbent. *Ind. Eng. Chem. Res.* 50, 8515–8523. doi: 10.1021/ie102520w

Wang, F., Zhu, Y., Wang, W., Zong, L., Lu, T., and Wang, A. (2017a). Fabrication of CMC-*g*-PAM superporous polymer monoliths via eco-friendly Pickering-MIPEs for superior adsorption of methyl violet and methylene blue. *Front. Chem.* 5:33. doi: 10.3389/fchem.2017.00033

Wang, J., Wei, L., Ma, Y., Li, K., Li, M., Yu, Y., et al. (2013). Collagen/cellulose hydrogel beads reconstituted from ionic liquid solution for Cu(II) adsorption. *Carbohydr. Polym.* 98, 736–743. doi: 10.1016/j.carbpol.2013.06.001

Wang, N., Ouyang, X. K., Yang, L. Y., and Omer, A. M. (2017b). Fabrication of a magnetic cellulose nanocrystal/metal-organic framework composite for removal of Pb(II) from water. *ACS Sustain. Chem. Eng.* 5, 10447–10458. doi: 10.1021/acssuschemeng.7b02472

Wang, Z. J., Ghasimi, S., Landfester, K., and Zhang, K. A. (2014). Highly porous conjugated polymers for selective oxidation of organic sulfides under visible light. *Chem. Commun.* 50, 8177–8180. doi: 10.1039/C4CC02861A

Wen, P., Xue, M., Ishikawa, Y., Itoh, H., and Feng, Q. (2012). Relationships between cell parameters of dye-sensitized solar cells and dye-adsorption parameters. *ACS Appl. Mater. Interfaces* 4, 1928–1934. doi: 10.1021/am3001693

Wong, L. L. C., Ikem, V. O., Menner, A., and Bismarck, A. (2011). Macroporous polymers with hierarchical pore structure from emulsion templates stabilised by both particles and surfactants. *Macromol. Rapid Commun.* 32, 1563–1568. doi: 10.1002/marc.201100382

Wu, D., Xu, F., Sun, B., Fu, R., He, H., and Matyjaszewski, K. (2012). Design and preparation of porous polymers. *Chem. Rev.* 112, 3959–4015. doi: 10.1021/cr200440z

Wu, Y., Ma, Y., Pan, J., Gu, R., and Luo, J. (2017). Porous and magnetic molecularly imprinted polymers via Pickering high internal phase emulsions polymerization for selective adsorption of λ-cyhalothrin. *Front. Chem.* 5:18. doi: 10.3389/fchem.2017.00018

Wu, Y., Tang, Y., Li, L., Liu, P., Li, X., Chen, W., et al. (2018). The correlation of adsorption behavior between ciprofloxacin hydrochloride and the active sites of Fe-doped MCM-41. *Front. Chem.* 6:17. doi: 10.3389/fchem.2018.00017

Xu, H., Zheng, X., Huang, Y., Wang, H., and Du, Q. (2015). Interconnected porous polymers with tunable pore throat size prepared via Pickering high internal phase emulsions. *Langmuir* 32, 38–45. doi: 10.1021/acs.langmuir.5b03037

Yang, J., Wu, J. X., Lü, Q. F., and Lin, T. T. (2014). Facile preparation of lignosulfonate–graphene oxide–polyaniline ternary nanocomposite as an effective adsorbent for Pb(II) ions. *ACS Sustain. Chem. Eng.* 2, 1203–1211. doi: 10.1021/sc500030v

Ye, S., Yu, H. Y., Wang, D., Zhu, J., and Gu, J. (2018). Green acid-free one-step hydrothermal ammonium persulfate oxidation of viscose fiber wastes to obtain carboxylated spherical cellulose nanocrystals for oil/water Pickering emulsion. *Cellulose* 25, 1–17. doi: 10.1007/s10570-018-1917-x

Yi, W., Wu, H., Wang, H., and Du, Q. (2016). Interconnectivity of macroporous hydrogels prepared via graphene oxide-stabilized pickering high internal phase emulsions. *Langmuir* 32, 982–990. doi: 10.1021/acs.langmuir.5b04477

Yu, S., Tan, H., Wang, J., Liu, X., and Zhou, K. (2015). High porosity supermacroporous polystyrene materials with excellent oil–water separation and gas permeability properties. *ACS Appl. Mater. Interfaces* 7, 6745–6753. doi: 10.1021/acsami.5b00196

Zhang, S., Chen, J., and Perchyonok, V. T. (2009). Stability of high internal phase emulsions with sole cationic surfactant and its tailoring morphology of porous polymers based on the emulsions. *Polymer* 50, 1723–1731. doi: 10.1016/j.polymer.2008.11.004

Zhang, S., Zhu, Y., Hua, Y., Jegat, C., Chen, J., and Taha, M. (2011). Stability of surfactant-free high internal phase emulsions and its tailoring morphology of porous polymers based on the emulsions. *Polymer* 52, 4881–4890. doi: 10.1016/j.polymer.2011.08.022

Zhang, Y., Wang, S., Eghtedari, M., Motamedi, M., and Kotov, N. A. (2005). Inverted-colloidal-crystal hydrogel matrices as three-dimensional cell scaffolds. *Adv. Funct. Mater.* 15, 725–731. doi: 10.1002/adfm.200400325

Zhang, Y., Zhao, L., Patra, P. K., and Ying, J. Y. (2008). Synthesis and catalytic applications of mesoporous polymer colloids in olefin hydrosilylation. *Adv. Synth. Catal.* 350, 662–666. doi: 10.1002/adsc.200700619

Zhao, C., Danish, E., Cameron, N. R., and Kataky, R. (2007). Emulsion-templated porous materials (PolyHIPEs) for selective ion and molecular recognition and transport: applications in electrochemical sensing. *J. Mater. Chem.* 17, 2446–2453. doi: 10.1039/b700929a

Zheng, X., Zhang, Y., Wang, H., and Du, Q. (2014). Interconnected macroporous polymers synthesized from silica particle stabilized high internal phase emulsions. *Macromolecules* 47, 6847–6855. doi: 10.1021/ma501253u

Zhou, Y., Fu, S., Zhang, L., Zhan, H., and Levit, M. V. (2014). Use of carboxylated cellulose nanofibrils-filled magnetic chitosan hydrogel beads as adsorbents for Pb(II). *Carbohydr. Polym.* 101, 75–82. doi: 10.1016/j.carbpol.2013.08.055

Zhu, Y., Wang, W., Zheng, Y., Wang, F., and Wang, A. (2016a). Rapid enrichment of rare-earth metals by carboxymethyl cellulose-based open-cellular hydrogel adsorbent from HIPEs template. *Carbohydr. Polym.* 140, 51–58. doi: 10.1016/j.carbpol.2015.12.003

Zhu, Y., Zhang, S., Hua, Y., Chen, J., and Hu, C. P. (2010). Hydrophilic porous polymers based on high internal phase emulsions solely stabilized by poly (urethane urea) nanoparticles. *Polymer* 51, 3612–3617. doi: 10.1016/j.polymer.2010.06.008

Zhu, Y., Zheng, Y., Wang, F., and Wang, A. (2016b). Fabrication of magnetic macroporous chitosan-*g*-poly (acrylic acid) hydrogel for removal of Cd^{2+} and Pb^{2+}. *Int. J. Biol. Macromol.* 93(Pt A), 483–492. doi: 10.1016/j.ijbiomac.2016.09.005

Zhu, Y., Zheng, Y., Wang, F., and Wang, A. (2016c). Monolithic supermacroporous hydrogel prepared from high internal phase emulsions (HIPEs) for fast removal of Cu^{2+} and Pb^{2+}. *Chem. Eng. J.* 284, 422–430. doi: 10.1016/j.cej.2015.08.157

Zou, S., Liu, H., Yang, Y., Wei, Z., and Wang, C. (2013a). Multihollow nanocomposite microspheres with tunable pore structures by templating Pickering double emulsions. *React. Funct. Polym.* 73, 1231–1241. doi: 10.1016/j.reactfunctpolym.2013.06.006

Zou, S., Yang, Y., Liu, H., and Wang, C. (2013b). Synergistic stabilization and tunable structures of Pickering high internal phase emulsions by nanoparticles and surfactants. *Colloids Surf. A Physicochem. Eng. Asp.* 436, 1–9. doi: 10.1016/j.colsurfa.2013.06.013

Conflict of Interest Statement: The authors declare that the research was conducted in the absence of any commercial or financial relationships that could be construed as a potential conflict of interest.

frontiers
in Environmental Science

ORIGINAL RESEARCH
published: 18 October 2019
doi: 10.3389/fenvs.2019.00156

Chemicals of Emerging Concern in Treated Wastewater Impact Microbial Growth

Nathan K. McLain and Emma W. Gachomo*

Department of Microbiology and Plant Pathology, University of California, Riverside, Riverside, CA, United States

Agriculture production in California is negatively impacted by soilborne fungi, such as *Verticillium dahliae*, and limited water availability for irrigation. Some regions have adapted the use of recycling wastewater, i.e., reclaimed water, to supplement the potable water supply. Wastewater purification is not fully efficient at removing all contaminants and small amounts of pharmaceutical products, known as chemicals of emerging concern (CECs), remain. Acetaminophen, trimethoprim, sulfamethoxazole and gemfibrozil are some of the most common CECs found in treated wastewater and were therefore used in this study. These CECs were evaluated for their potential to interact with microorganisms directly, or for their ability to alter the development of Verticillium wilt disease in eggplants. The microorganisms *Verticillium dahliae, Fusarium oxysporum* f. sp. *lycopersici*, *Piriformospora indica, Phytopthora capsici*, and *Bradyrhizobium japonicum* were used for *in vitro* growth assays in the presence of CECs. CECs induced varying responses in strains of the same fungi by promoting growth of one strain while inhibiting growth of the other. CECs influenced spore germination of *V. dahliae* and *F. oxysporum*. Greenhouse experiments in which *Solanum melongena* (eggplants) were inoculated with *V. dahliae* and irrigated with CECs were used to evaluate the impacts of these chemicals on disease development. Overall our results found that most of the organisms we tested were sensitive to the CECs. *P. capsici* was found to be the most sensitive microorganism, while *B. japonicum* growth was unaffected by the CECs at the concentrations used. The greenhouse assays results indicated that plant disease severity may be influenced by given CECs at certain stages of plant growth. Overall the results of this study indicate that the concentrations of CECs found in reclaimed water are occurring at biologically relevant concentrations.

Keywords: pharmaceuticals, reclaimed water, irrigation, soilborne, microorganisms

Edited by:
Rui C. Martins,
University of Coimbra, Portugal

Reviewed by:
Isaac Dennis Amoah,
Durban University of Technology,
South Africa
Konstantinos Plakas,
Centre for Research and Technology
Hellas, Greece
Joana Luísa Pereira,
University of Aveiro, Portugal

***Correspondence:**
Emma W. Gachomo
emma.gachomo@ucr.edu

Specialty section:
This article was submitted to
Water and Wastewater Management,
a section of the journal
Frontiers in Environmental Science

Received: *06 August 2019*
Accepted: *25 September 2019*
Published: *18 October 2019*

Citation:
McLain NK and Gachomo EW (2019)
Chemicals of Emerging Concern in
Treated Wastewater Impact Microbial
Growth. Front. Environ. Sci. 7:156.
doi: 10.3389/fenvs.2019.00156

INTRODUCTION

Extended periods of drought and the presence of soilborne plant pathogens jeopardize California's agricultural production, which contributes a significant portion to the United States food supply. Recent drought conditions and continued population growth in Southern California have place great demands on the region's limited potable water supply (AghaKouchak et al., 2015; Howitt et al., 2015). This valuable resource is consumed by the population directly or indirectly through irrigation of crops and landscape vegetation.

Since potable water is in such high demand, California has taken steps to conserve this limited resource. Recycling wastewater has been successfully employed to protect the supply of potable water to satiate the growing demands for clean water (Parsons et al., 2010; Schulte, 2011; Cooley and Phurisamban, 2016; Warsinger et al., 2018). Normally wastewater is treated to a limited capacity and allowed to exit the potable water supply and re-enter the natural water cycle. Alternatively, wastewater can be treated to a far greater extent, and used to supplement potable water supplies as reclaimed water (**Figure S1**; Warsinger et al., 2018). Reclaimed water can be used to recharge potable water supplies directly by injecting it into ground water reservoirs, or allowing it to mix with potable water aquifers (Warsinger et al., 2018). Reclaimed water can also be used to irrigate crops or landscape vegetation, thereby preserving potable water supplies for direct human consumption (Warsinger et al., 2018).

Chemicals of emerging concern (CECs) such as pharmaceuticals, personal care products, detergents, nanoparticles, etc. continue to be introduced in the environment, and have potential to impact human and aquatic life that would otherwise not be exposed to them (Kinney et al., 2006; Gros et al., 2010; EPA, 2019) Unfortunately, even after extensive treatment, CECs remain in the treated water (Kinney et al., 2006; Gros et al., 2010). The past consensus with these chemicals is that they do not pose much danger for human and environmental health since they occur in such low concentrations, and in the case of pharmaceuticals, well below therapeutic doses used for humans (Boxall et al., 2006; Wu et al., 2013; Zimmermann and Curtis, 2017). However, this notion has been eroded by the observations that sub-therapeutic concentrations of certain pharmaceuticals can impact microbial, plant, and insect life (Wang and Gunsch, 2011; Pennington et al., 2017, 2018). Additionally, some CECs have been observed to accumulate in soils upon repeated irrigation with reclaimed water containing the compounds (Wu et al., 2015). Therefore, the concentrations of CECs found in reclaimed water can be at biologically relevant concentrations or can be raised to that level with repeated irrigation or in the presence of chemicals that can increase their potency.

Given that CECs accumulate in plants (Wu et al., 2015), they may impact plant physiology, potentially altering a plants ability to interact with microorganisms (pathogenic or beneficial). Exacerbation of already prevalent soilborne fungi (or plant pathogens), and consequently plant diseases, found in agricultural soils is one potential outcome of chemical interference from the CECs that can impact plants, and/or the microbial community that is associated with plants. CECs may interact with soil microbes directly by stimulating or inhibiting their growth, thus impacting their ability to colonize or infect a host. CECs may alter microbial population equilibrium by promoting some, while inhibiting others and can thereby increase pathogen populations by reducing their competitors or antagonist in the soil (Mulligan et al., 1982; De Vries-Hospers et al., 1991; Azevedo et al., 2015).

Verticillium dahliae, the causative agent of Verticillium wilt, is a soilborne pathogen that may benefit from the anthropogenic inputs of CECs from reclaimed water. *V. dahliae* has a wide host range for many crops that are important to California's agriculture industry including bell peppers, eggplants, strawberries, tomatoes, and watermelon (Pegg, 1984; Aguiar et al., 1998; Bhat and Subbarao, 1999; Klosterman et al., 2009). California leads the nation in the production of the above mentioned crops (California Department of Food Agriculture, 2018) and major reductions in their yields could have devastating consequences to food supply and income. Plant diseases already reduce California's agriculture output and increase cost of production, and they may be exacerbated by anthropogenic input of CECs into agriculture soils.

Acetaminophen (APAP), trimethoprim (TMP), sulfamethoxazole (SMX), and gemfibrozil (GEM) are synthetic pharmaceutical products that are commonly found in recycled wastewater. APAP is an antipyretic pain killer that has been observed to have antimicrobial properties at concentrations above therapeutic use (Zimmermann and Curtis, 2017), and observed to have growth promoting effects on microorganism at therapeutic concentrations (Carvalho et al., 2010). TMP and SMX are antibiotics that are commonly taken in combination, but exhibit antimicrobial effects independently (Reeves and Wilkinson, 1979; Hida et al., 2005; Tunali et al., 2012). GEM is a medication used to treat high blood pressure, but has been observed to increase the antimicrobial potency of some pharmaceuticals (Rudin et al., 1992; Bulatova and Darwish, 2008) and to have direct impacts on plant growth (D'Abrosca et al., 2008; Pino et al., 2016). These four CECs are found consistently in wastewater treatment plant effluent such as reclaimed water, and in soils irrigated with recycled water in the ng/L and μg/L range (Kinney et al., 2006; Batt et al., 2007; Erickson et al., 2014; Wu et al., 2015).

Extended periods of drought conditions are common in arid regions such as Southern California, which makes water conservation efforts such as reclaimed water use a necessity (Brown et al., 2013). Despite the presence of chemicals remaining in the treated wastewater, reclaimed water has done much to alleviate water demands and California plans to increase its use (California State Water Resources Control Board, 2010). Therefore, it is critical for us to understand the direct impacts CECs have on plants and their associated soil microbiome to prevent elevation of plant losses from microorganisms. In our study we subject plants and microorganisms to concentrations similar to those found in treated wastewater effluent, or reclaimed water. A number of previous studies have found direct phytotoxic effects of various CECs, however these studies used concentrations that are higher than those found in typically treated wastewater effluent (D'Abrosca et al., 2008; Liu et al., 2009a; Pino et al., 2016; Madikizela et al., 2018). Some studies found phytotoxic effects to developing plants, but did not grow the plants in soil (D'Abrosca et al., 2008; Pino et al., 2016), which can impact plants uptake of chemicals through the roots (Pan and Chu, 2017). Use of higher concentrations of CECs and not growing the plants in soil means that the plants are exposed to unusually high concentrations of the compounds. This under states the potential severity of microbial community disturbances and phototoxic effects of *in situ* CEC concentrations found in recycled water. Therefore, the direct impacts of CECs on eggplants grown in soil were tested using concentrations within

TABLE 1 | Concentrations of CECs used for all assays in this study.

CEC	High concentration (H)	Low concentration (L)
Acetaminophen (APAP)	10 µg/L	5 µg/L
Trimethoprim (TMP)	2.5 µg/L	1 µg/L
Sulfamethoxazole (SMX)	2 µg/L	1 µg/L
Gemfibrozil (GEM)	10 µg/L	2 µg/L
No CEC control (No CECs)	0 ug/L	

the range of CECs detected in recycled water or wastewater treatment plant effluent. The impacts of CECs on the growth of microorganisms—fungi, oomycetes, and bacteria that are known to be beneficial or deleterious to plants were also tested using CECs concentrations that are relative to *in situ* concentrations. We hypothesized that the CECs will not impact microbial growth, since we are using relatively low concentrations of CECs that are well below therapeutic doses. We also hypothesized that CECs would not have any impact on disease development in eggplants inoculated with the plant pathogen *Verticillium dahliae.* Therefore, objective of this study was to determine the impact of CECs on microbial growth and disease development in eggplants.

MATERIALS AND METHODS

In total 4 CEC's -acetaminophen (APAP), trimethoprim (TMP), sulfamethoxazole (SMX), and gemfibrozil (GEM)—were evaluated to determine their impacts on the microbial growth and development of Verticillium wilt in eggplants. Each CEC was tested at a high concentration (H) and a low concentration (L) as specified in **Table 1** below. The concentrations used mimic the range of concentrations of the respective CECs that have been found in the final effluent of wastewater treatment plants or in soils irrigated with reclaimed water (Vanderford and Snyder, 2006; Batt et al., 2007; Stackelberg et al., 2007; Dia-Cruz and Barcelo, 2008; Fram and Belitz, 2011). These compounds at the concentrations listed in **Table 1** were used in all assays described below.

Media Preparation

Czapek-dox, buffered 10% V-8, potato dextrose agar (PDA), and Luria Bertani (LB) broth were used to cultivate the different microorganisms. Czapek-Dox agar was prepared as the "originally proposed" version described in Thom (1930) and Smith (1941). Briefly, 30.0 g of sucrose, 3.0 g of sodium nitrate, 1.0 g of dipotassium phosphate, 0.5 g of magnesium sulfate, 0.5 g of potassium chloride, and 0.01 g of ferrous sulfate per 1 L of sterile ddH$_2$O were used. The buffered 10% V-8 agar was made by adding 10% volume of V8 juice and 0.2 % (W/V) of calcium carbonate to sterile ddH$_2$O. The V8 calcium carbonate solution was clarified by centrifuging it at 3,000× g for 10 min, and the supernatant was added to the required amount of ddH$_2$O to make a final concentration of 10% V8. To make solid media for petri dishes, 10% agar (W/V) was added. LB broth and PDA were prepared based on the manufacturer's instructions. PDA amended with 0.833 µM of bromocresol purple sodium salt (BCP) for a growth assay described below (Masachis et al., 2016).

Cultivation of Organisms

The impacts of CECs on the growth of several microorganisms were tested. Organisms covering a wide range of classifications and common plant pathogens in regions where reclaimed water is used were also included in the study. Two *Verticillium dahliae* strains (0048 and 0049), two *Fusarium oxysporum lycopersici* strains (CS-3 and CS-5), *Phytophthora capsici, Piriformospora indica,* and *Bradyrhizobium japonicum* IRAT FA3 were tested. Two strains of *Verticillium* and *Fusarium* were used to assess the impacts of CECs on closely related organisms. *V. dahliae* strains were cultured on Czapek-Dox plates with 1% agar, *F. oxysporum* and *P. indica* were cultured on PDA and *B. japonicum* was cultured in LB broth. During growth rate assays, each organism was grown on their respective culturing media. The media was amended with the required volume of a given CEC working stock solution to reach the concentrations indicated in **Table 1**, after the base media was autoclaved and cooled, but before solidifying. An additional treatment containing no CECs was used as a control for each organism. Two strains of *V. dahliae* and *F. oxysporum* were tested to find out the response of closely related organism to the same CECs.

Verification of Organism Identity

DNA from *V. dahliae* and *F. oxysporum* f. sp. *lycopersici* strains were extracted using the DNeasy Plant Mini Kit (Qiagen) following the manufacture's protocol. Extracted DNA was used in PCR assays to confirm the identity of the fungal isolates used in this study. *V. dahliae* isolates were confirmed following the procedure and commonly used primers described in Inderbitzin et al. (2013). Briefly, each PCR reactions consisted of 12.5 µL of 2× Dream taq green master mix (Thermo Scientific), 1 µL of forward and reverse primer, 1 µL of extracted DNA (i.e., DNA template), and 9.5 µL of nuclease free water. All primers used in this assay were purchased from Integrated DNA Technologies. PCR reactions were carried out in a thermocycler with an initial denaturation step for 2 min (min) at 94°C. This was followed by 35 cycles of denaturation 94°C for 10 s (s), Annealing for 20 s, and elongation for 1 min at 72°C. Then, a final elongation step for 7 min at 72°C was used (**Figure S2**). Identification of *F. oxysporum* f. sp. *lycopersici* was confirmed in a similar fashion using a PCR approach described in Hirano and Arie (2006). The same PCR reaction mixture described above for identifying *V. dahliae.* To conduct the PCR, the mixtures went through 50 cycles of denaturation at 94°C for 1 min, Annealing at 62°C for 1 min, and elongation at 72 °C for 2 min. The *F. oxysporum* sample was screen using the Unif/r, Sp13f/r, Sp23f/r, and the sprlf/r primer sets described in Hirano and Arie (2006) to positively identify the *F. oxysporum* strains used in this study (**Figure S2**).

Growth Rate Assays

Every fungal and oomycete growth assay had 5 replicates for each treatment, while bacterial growth assays had 3 replicates. For fungal organisms, a 5 mm diameter plug taken from the edge

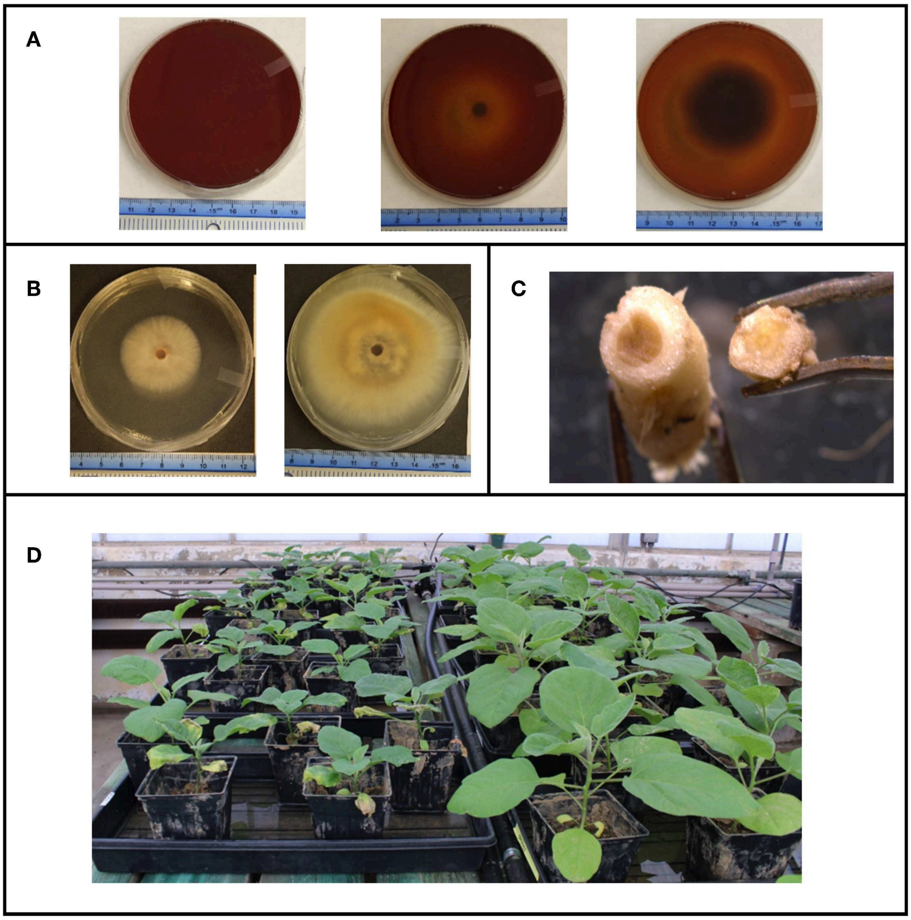

FIGURE 1 | (A) *Fusarium oxysporium* grown on media containing the pH indicator bromocresol purple to indicate how far beyond the visible mycelial tips, nutrients are being uptaken by the mycelia. **(B)** Typical growth of *Verticillium dahliae* on Czepeck dox agar. **(C)** Stem cross section of eggplants inoculated with *V. dahliae* (left) and an uninoculated (right). **(D)** Overall set up of eggplants in the green house with a side by side comparison of inoculated eggplants (left) to uninoculated eggplants (right).

of an actively growing colony was placed in the center of the agar plate. Growth of the organism was monitored by measuring the diameter across the colony. Two diameter measurements were taken from two different angles and averaged together per replicate *V. dahliae* strains were measured 3, 7, 14, and 21 days post inoculation (dpi). *F. oxysporum* strains were measured 3, 4, 5, 6, and 7 dpi, *P. indica* was measured 3, 7, 11, 12, 14 dpi, and *P. capsici* was measured 1, 2, 3, and 4 dpi (**Figures 1A–C**). A growth assay carried out on PDA plates amended with the pH indicator bromocresol purple was used to detect if nutrients were consumed beyond the growing mycelium tips in the solid media (**Figure 1A**).

A spectrophotometric assay was done to measure the growth rate of *B. japonicum* in LB broth. A culture of *B. japonicum* in exponential phase was used for the assay. The starting concentration was adjusted to OD_{600} 0.05. Using a spectrophotometer, readings (OD_{600}) were taken at 0, 4, 8, 12, 24, 36, 48, 60, and 72 h post inoculation (hpi). An additional specific plate count assay was done at the 18 h mark to verify spectrophotometer results. This was done by plating 10^{-6}, 10^{-7}, and 10^{-8} serial dilutions of the growing culture on to LB agar for each treatment. Colonies formed on the plate were counted as CFUs. All organisms were grown at their optimal temperatures for cultivation and for the growth rate assays. Growth on solid media was used to calculate the allelopathic index (RI) (i.e., relative index) described (Liu et al., 2009a).

Spore germination assays were conducted on *V. dahliae* 0049 and *F. oxysporum* CS-5 similarly as described by Williams et al. (2002) with a few exceptions. Organisms were grown on solid media until they covered the entire surface of a 15 mm × 100 mm petri dish. Spores were harvested from the plate using 0.17 M sterile sucrose solution. Spore suspensions containing CECs listed in **Table 1** were adjusted to 1.80×10^5 and 1.92×10^6 spores/ mL using a hemocytometer for *V. dahliae* 0049 and *F. oxysporum* CS-5 assays respectively. All final solutions contained 0.085 M of sucrose to make them have an osmotic potential of −2 bars or lower to ensure optimal spore germination as described in Ioannou et al. (1977). The spore solutions were allowed to germinate for 12 h. At this point, 0.2% Aniline blue in lactophenol blue (final concentration) was applied to solutions to prevent further germination (Williams et al., 2002). The number of spores germinated was enumerated using a compound microscope, each treatment had 3 replicates ($n = 3$).

Cultivation of Eggplants

The Patio Baby variety of eggplants from Johnny's seeds (Fairfiled, Maine, USA) was used for all eggplants in this study. A group of five eggplants ($n = 5$) were treated with a given CEC at a concentration specified in **Table 1**. An equivalent group of eggplants was treated in a similar fashion, except they were inoculated with *Verticillium dahliae* strain 0049 during transplanting (discussed below). The eggplant assay was carried out in two separate sets. Set one (set I) consisted of the acetaminophen, trimethoprim, and associated no CEC control treatments. The sulfamethoxazole, gemfibrozil, and associated no CEC control treatments were carried out on the second set of eggplants (set II).

Eggplant seeds were germinated in a growth room at 22°C. All plants were allowed to reach the 2–4 leaf stage before transplanting them into eggplant field soil obtained from farm lands in Bakersfield, California. This field is not irrigated with reclaimed water nor treated with fungicide because it is only used for organic farming. Eggplants were grown in this field, thus this soil was ideal for mimicking *in situ* agricultural soil conditions. During transplanting, the inoculated sets of eggplants were exposed to *V. dahliae* 0049 using the dipping method described by Bhat and Subbarao (1999). Plants were inoculated with 1.85 $\times$ 10^7 spores/ L. Tap water was used for the uninoculated controls. All seeds and plants were watered as needed using tap water for up to 1 week after transplanting to allow them to acclimatize. CEC treatments were applied to plants a week after transplanting. CEC were dissolved into the tap water to reach the final concentration listed in **Table 1**. The no CEC treatments were watered with tap water only. All treatments received 1L of the solution that contained the respective concentration of CEC per watering event. Watering was done 2–3 times a week as needed. All the plants for a given treatment ($n = 5$) were kept in the same tray. CEC solutions for the respective treatments were poured into the trays to ensure that all plants were receiving equal amounts of the solution (**Figure 1D**). This experiment was repeated 2 times.

Plant Measurements and Soil Collection

Stem height measurements of plants and disease assessments were taken weekly starting the week of transplantation. Disease assessments relied on observations of external symptoms to avoid destructive sampling. Disease severity assessments were based on a 0–5 scale (Liu et al., 2009b).Briefly: 0 represented no wilted leaves; 1 $\leq$ 25% wilted leaves; 2 = 25–50% wilted leaves; 3 = 50–75% wilted leaves; 4 = 75–100% wilted leaves; and 5 = dead plant. Upon the final sampling, eggplants were cut at the base of the stem and the fresh weight of shoots was determined for each plant. Disease index was calculated using the disease severity assessment values as described in Liu et al. (2009b).

Statistical Analyses

All parametric ANOVA and GLiM statistical analyses were done using SPSS software (ver. 24.0; SPSS; IBM, Somers, New York, USA). For the green house experiments repeated measures ANOVA was done to test for interactions between time and treatments. Repeated measures Friedman Ranks ANOVA were done using R software v. 3.5.3 (R Core Team, 2018) package npIntFactRep (Feys, 2015, 2016) when ANOVA assumptions could not be met. In both approaches, the Greenhouse-Geisser correction was applied when sphericity was not achieved. *Post-hoc* ANOVA were used when significant interactions with time were detected and the data satisfied all ANOVA assumptions. In cases were the assumptions could not be met, the best fitting generalized linear model (GLiM) was used as determined by the model with the lowest Akaike's information criterion (AIC). In all cases this model was found to be the normal model with identity link function. Tukey was used for all *post-hoc* pairwise analyses when ANOVA was valid. In the cases were GLiM analyses were done, the *post-hoc*, pairwise analyses were carried out using the GLiM model with sequential Bonferroni correction for multiple comparisons. All *post-hoc* pairwise comparisons considered to be significantly different when $P < 0.05$. The two eggplant sets were treated as two separate experiments, in which statistical comparisons were only made within the respective sets. Comparisons to the no CEC controls or uninoculated plants were used to assess the impacts of CECs, disease, or the combination of both. The non-repeated measures ANOVA and GLiM procedures were also used to evaluate treatment effects in microbial growth assays.

RESULTS

Identification of Microorganisms

The PCR assay generated results that positively identified the *V. dahliae* and *F. oxysporum* strains. In both cases, positive amplification of their template DNA occurred with primer pairs specific to their respective identities (**Figure S2**). Specifically, we saw positive amplification for *V. dahliae* with the Df/Dr primer pair only, and positive amplification with the Unif/Unir and Sp13f/Sp13r primer sets for *F. oxysporum* f. sp. *lycopersici* (Hirano and Arie, 2006; Inderbitzin et al., 2013).

Impact of CECS on Growth of Microorganisms

Overall, colony diameter measurements of organisms grown on solid media demonstrated that the fungi tested were sensitive to most of the CECs used in this study (**Figures S3A**, **S4**). This is greatly exemplified with the allelopathic index (RI) calculations that are based on colony growth. The RI calculations indicate that some of these chemicals promoted growth, hindered growth or had no effect on a given organism (**Figure 2** and **Figure S3B**). Positive RI values indicated that an organism's growth was promoted by the CECs, while a negative showed that its growth was inhibited. At 7 days post inoculation (dpi) *V. dahliae* strain 0049 grown with low concentrations of GEM (GEM-L) had a negative RI value that was significantly lower than the control (**Figure 3B**) (GLiM: $\chi^2_8 = 44.754$, $P < 0.001$). By 14 dpi the

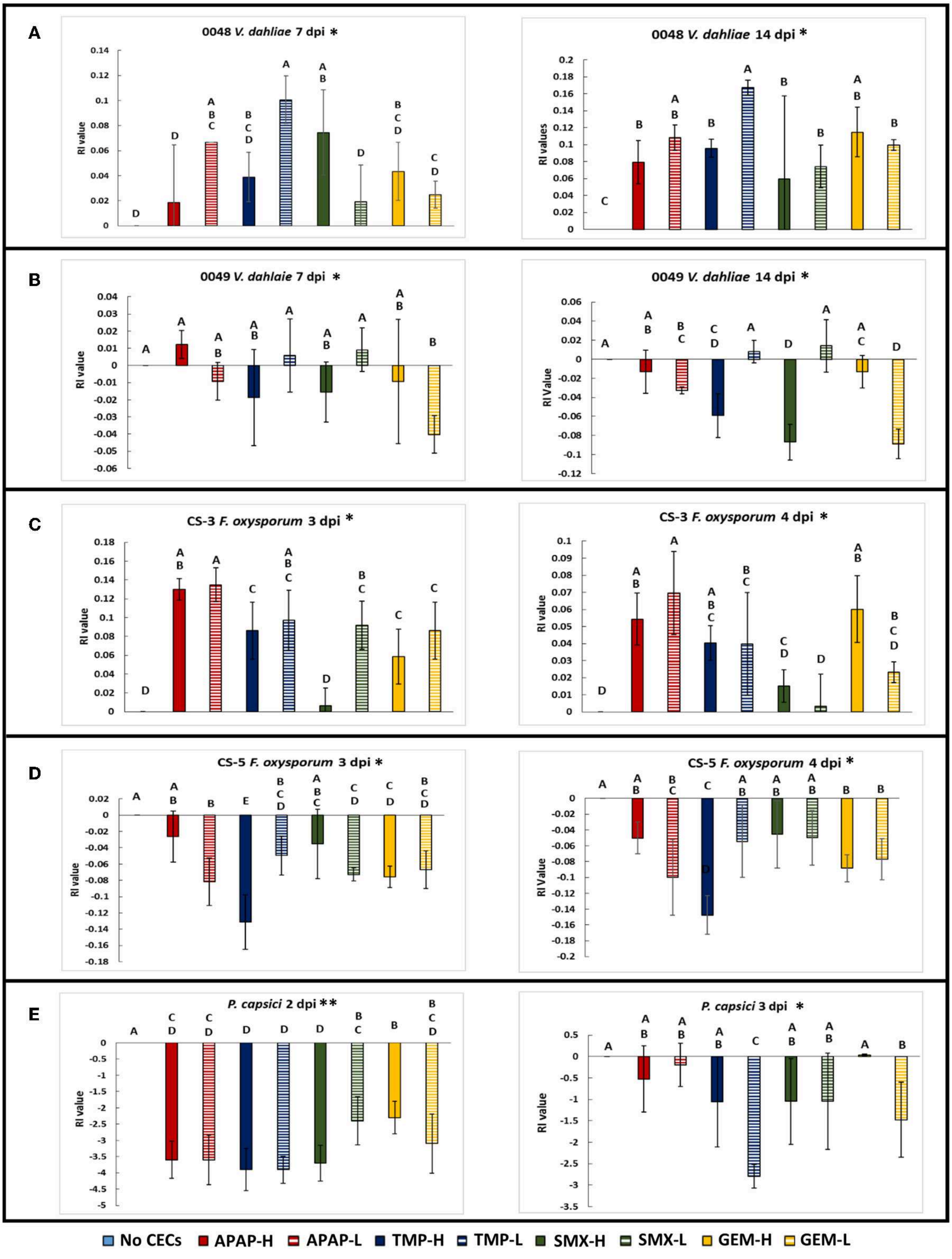

FIGURE 2 | Comparing the Allelopathic index values (RI) of the plant pathogens used in this study. **(A)** *Verticillium dahliae* strain 0048 measured at 7 and 14 dpi, **(B)** *Verticillium dahliae* strain 0049 measured at 7 and 14 dpi. **(C)** *Fusarium oxysporum f.sp lycopersici* strain CS-3 measured at 3 and 4 dpi. **(D)** *Fusarium oxysporum f.sp lycopersici* strain CS-5 measured at 3 and 4 dpi. **(E)** *Phytopthora capsici* measured at 2 and 3 dpi. *Samples compared statistically using GLiM with normal distribution and identity link function, pairwise analyses with sequential Bonferroni pairwise correction for multiple comparisons ($P < 0.05$). **ANOVA used for statistical analyses, *post-hoc* Tukey test used for pairwise analyses ($P < 0.05$).

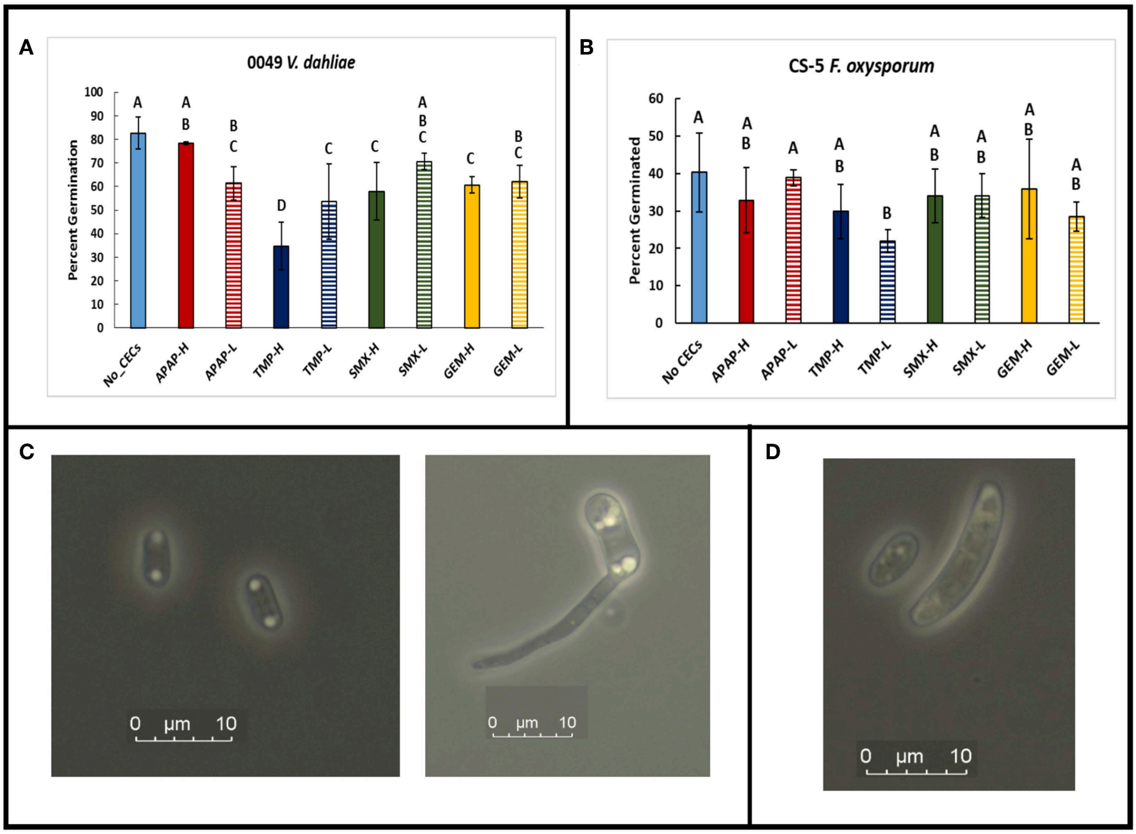

FIGURE 3 | Spore germination assays done in a mild sucrose solution. GLiM with normal distribution and identity link function used for all statistical comparisons. Samples that do not share the same letter are significantly different as determined by a *post-hoc*, pairwise GLiM analyses done with sequential Bonferroni correction for multiple comparisons (all *P*'s < 0.05). **(A)** Spore germination results for *Verticillium dahliae* after 12 h of incubation in a 0.085 M sucrose solution. **(B)** Spore germination results for *Fusarium oxysporum f.sp lycopersici* after 12 h of incubation in 0.085 M sucrose solution. **(C)** Photographs of *Verticillium dahliae* spores at 1,000× total magnification. Ungerminated spore (left), germinating spore (right) **(D)** Photograph of small and large *Fusarium oxysporum f.sp lycopersici* spores at 1,000× magnification.

inhibitory effects of CECs on *V. dahliae* 0049 growth were more apparent. Five treatments had significantly lower RI values than the control (**Figure 3B**) (GLiM: $\chi^2_8 = 247.137$, $P < 0.001$). GEM-L and high concentrations of SMX (SMX-H) treatments had the lowest RI values for 0049, which were significantly lower than all other treatments except for the high concentration of TMP (TMP-H) (GLiM: $\chi^2_8 = 247.137$, $P < 0.001$). Colony diameter growth of the other *V. dahliae* strain 0048 (**Figure S4A**), did not follow the same trends. CECs either benefited or had no effect on *V. dahliae* 0048 mycelial growth. By 7 dpi three treatments had significantly higher RI values than the control (TMP-L, SMX-H, and APAP-H) (GLiM: $\chi^2_8 = 83.749$, $P < 0.001$). By 14 dpi all treatments for *V. dahliae* 0048 had significantly higher RI values than the control (GLiM: $\chi^2_8 = 76.092$, $P < 0.001$) (**Figure 2A**).

The other plant pathogens examined, two *F oxysporum* strains, were also sensitive to the CECs tested. However, like *V. dahliae*, the CECs impacted the two *F. oxysporum* strains (CS-5 and CS-3) differently. The CECs appear to either have no impact, inhibit growth for one strain (CS-5), or enhance growth of the other strain (CS-3). By 3 dpi the RI values for all of the CEC treatments for *F. oxysporum* CS-5 were below the control, though, only 6 (APAP-L, TMP-H, TMP-L, SMX-L, GEM-H, and GEM–L) were significantly different (GLiM: $\chi^2_8 = 105.467$, $P < 0.001$) **(Figure 3D).** This trend continued into the following day at 4 dpi in which all treatments still had lower RI values than the control, though only 4 (APAP-L, TMP-H, GEM-H, and GEM-L) were significant (GLiM: $\chi^2_8 = 82.84$, $P < 0.001$). At this point the faster growing mycelia were approaching the edges of the agar plate. This most likely inhibited their growth, allowing slower growing mycelia to catch up and reduce differences found among treatments. Growth of *F. oxysporum* on PDA plates amended with BCP indicated that the fungal mycelia used up the nutrients in the media beyond the reach of the mycelia. This was shown by a color change in the media before the mycelia occupied it (**Figure 1A**). Treatment with high concentrations of TMP appeared to have the most dramatic impact on CS-5. At both time points TMP-H had the lowest RI value and at 4 dpi its RI value was significantly lower than all treatments (**Figure 2D**) (GLiM $\chi^2_8 = 82.84$, $P < 0.001$) except for APAP-L. Despite growth inhibiting effects seen for strain CS-5, growth promoting effects of CECs were observed on CS-3 (**Figure 2C** and **Figure S4B**). For instance, by 3 dpi the no CEC control had the smallest colony diameter (**Figure S4B**). The diameter was significantly smaller than all but two treatments, SMX-H and GEM-H (GLiM: $\chi^2_8 = 66.502$, $P < 0.01$) (**Figure S4B**). By the next day at 4 dpi growth approached the edges of the plate and no significant differences in colony sizes were observed among any of the treatments. Growth of the plant pathogen *P. capsici* was inhibited by all of the CECs used in this study. At 2 dpi all CEC treatments had smaller diameter than the control, while only two of these treatments, SMX-L and GEM-H, were not significantly lower (**Figure S4E**) (ANOVA: $F_8 = 7.496$, $P < 0.001$). The RI values for each treatment were negative and significantly lower than the control (**Figure 2E**) (ANOVA: $F_8 = 20.796$, $P < 0.001$). The RI values were also much smaller than any of the other organisms tested, indicating that this strain is particularly sensitive. By 3 dpi only TMP-L treatment had a significantly smaller diameter than the control (**Figure S4E**) (GLiM: $\chi^2_8 = 35.136$, $P < 0.001$). TMP-L and GEM-L treatments had significantly lower RI values than the control at this time point as well (**Figure 2E**) (GLiM: $\chi^2_8 = 69.872$, $P < 0.001$). Again, this is most likely due to declining growth rates as the colonies approach the edge of the plate allowing the slower growing organisms time to catch up in size.

Testing the impacts of CECs on the growth of the plant symbiont, *Piriformospora indica,* yielded mixed results. In this case there were CECs that either had no impact, inhibited, or enhanced the growth of this organism (**Figures S3A,B**). At 8 dpi, for example, only one treatment had significantly less growth than the no CEC control, SMX-L (GLiM: $\chi^2_8 = 52.329$, $P < 0.001$), while the rest of the treatments were not significantly different from the control. At 10 dpi only the TMP-H treatment was significantly larger than the no CEC control (GLiM: $\chi^2_8 = 48.169$ $P < 0.001$). Furthermore, the RI values calculated using colony diameter reinforce these trends (**Figure S3B**). At 8 dpi both the low and high concentrations of SMX had negative RI values that were below the no CEC control, but only the low concentration was significantly different (GLIM: $\chi^2_8 = 58.997$, $P < 0.001$). At 10 dpi the TMP-H treatment had a significantly higher RI value than the no CEC control, while none of the other treatments are significantly different (GLiM: $\chi^2_8 =. 52.512$, $P < 0.001$). Overall, only two treatments were significantly different than the control, suggesting that this organism was not very sensitive to the CECs being tested.

Another plant beneficial organism, *B. japonicum*, was found to be insensitive to the CECs tested. This plant growth promoting rhizobacteria (PGPR) did not exhibit any signs of sensitivity to the CECs during its growth rate assay carried out in liquid media. *B. japonicum* remained in the exponential growth phase from 0 to about 24 h post inoculation (hpi) (**Figures S3C–F**). During this time, no significant differences in optical density were detected among different treatments within a given sampling time point. Therefore, it appears that *B. japonicum* is not sensitive to the CECs at the concentrations tested. To confirm this result an additional specific plate count assay of cells at 18 hpi was carried out. There were no significant differences among cell counts from different treatments (ANOVA: $F_8 = 1.203$; $P = 0.36$) (data not shown).

Besides impacting mycelial growth of fungal organisms, CECs impacted spore germination of *V. dahliae* 0049 and *F. oxysporum* CS-5 (**Figure 3A**). At 12 hpi, the *V. dahliae* no CEC control had significantly greater spore germination than all but two treatments, APAP-H and SMX-L (GLIM: $\chi^2_8 = 95.648$, $P < 0.01$; *post-hoc* pairwise, $P < 0.05$). TMP-H treatment had the least number of germinated of spores compared to the other treatments (GLIM: $\chi^2_8 = 95.648$, $P < 0.001$). TMP also impacted spore germination of *F. oxysporum* CS-5. Both TMP treatments had lower spore germination than the control. TMP-L had the lowest spore germination out of all treatments and was significantly lower than the control and APAP-L (**Figure 3B**) (GLiM: $\chi^2_8 = 19.076$, $P = 0.014$).

Impact of CECS on Plant Growth and Development

A greenhouse assay was carried out to evaluate the direct impacts of CECs on plant growth, monitor for changes in Verticillium wilt disease progression and severity using eggplants and *V. dahliae* strain 0049. Overall, the greenhouse assay indicated that the CECs studied did not have major effects on the growth and development of plants. Repeated ANOVA analyses showed that there was a significant interaction between time and treatments for stem heights. (set I: $F_{25.137,111.721} = 3.901$, $P \leq 0.001$; set II: $F_{33.43,148.577} = 9.704$, $P \leq 0.001$). As expected though, inoculation with *V. dahliae* proved to have drastic effects on plant growth. Major differences in stem height and other plant metrics discussed below occurred between inoculated and uninoculated eggplants. No significant differences in stem height occurred among plants treated with different CECs, or a different concentration of the same CEC within the set of inoculated or uninoculated plants ($P > 0.05$ for all *post hoc* comparisons). However, all of the inoculated plants had significantly lower stem height than their uninoculated counter parts by week 6 and later (*P*'s < 0.05 for all *post hoc* tests) (**Figures 1D**, **4A–D**).

Not surprisingly, a similar trend is revealed when measuring the number of leaves retained by the eggplants during the growing season (**Figure 5A**). There was a significant interaction between time and treatment for leaves remaining on plants (repeated measures Friedman Ranks ANOVA: setI: $F_{32.856,146.027} = 2.207$, $P \leq 0.001$; set II: $F_{38.308,170.257} = 8.825$, $P \leq 0.001$). Inoculation with *V. dahliae* led to higher leaf loss than the uninoculated controls in all treatments (**Figures 1D**, **5A**). From the 6th week to the end of the experiment all of the inoculated plants retained significantly less leaves than their uninoculated counterparts (All *P*'s < 0.005). Some differences with leaf retention did occur between treatments and their respective controls, but only with inoculated plants. These differences occurred in weeks 4 (inoc APAP-H, inoc TMX-H, inoc SMX-L, and inoc GEM-L), 5 (inoc APAP-H and inoc SMX-L), 6 (inoc SMX-H), and 8 (inoc APAP-H) (*post hoc* comparisons all *P*'s < 0.05)

Shoot fresh weight followed the same trend as stem height and leaf loss discussed above except for 2 treatments. Among the uninoculated plants, both SMX-L and GEM-H had significantly higher shoot weight than their associated uninoculated no CEC

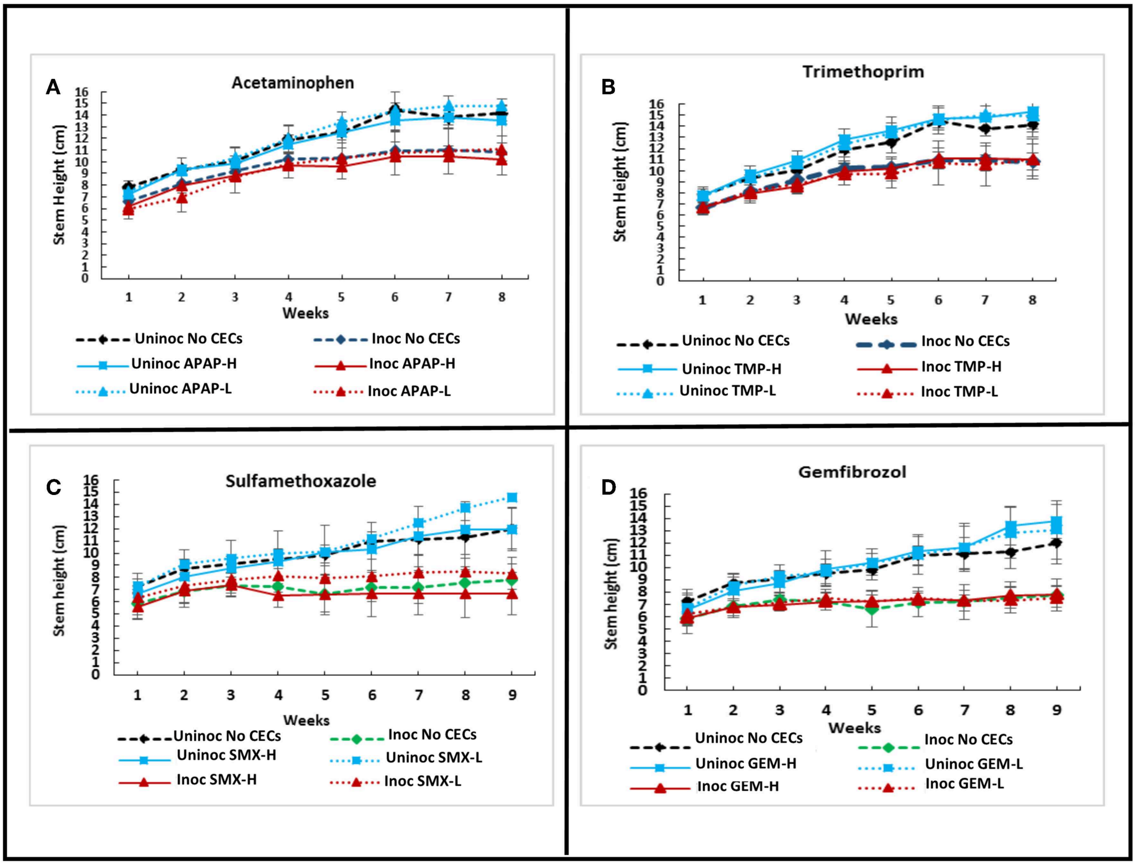

FIGURE 4 | Effects of chemicals of emerging concern (CECs) overtime on stem height of inoculated and uninoculated eggplants grown in the greenhouse. Error bars represent standard deviation. **(A)** Eggplants treated with acetaminophen (APAP) and a no CEC control. **(B)** Eggplants treated with trimethoprim (TMP) and the no CEC control. **(C)** Eggplants treated with sulfamethoxazole (SMX) and a no CEC control. **(D)** Eggplants treated with gemfibrozil (GEM) and a no CEC control. The same no CEC controls were used for **(A,B)**, while **(C,D)** have the same no CEC controls. For each CEC two concentrations were used high (H) and low (L).

control treatment (GLiM: χ^2_9 =186.179, $P < 0.001$). Major differences among inoculated and uninoculated samples were observed, with uninoculated samples having significantly higher shoot fresh weight than their inoculated counterparts (Set I plants: ANOVA: $F_9 = 20.281$, $P < 0.001$; Set II plants: GLiM: χ^2_9 =186.179, $P < 0.001$ (**Figure 5B**).

Impact of CECs on Disease Severity

Inoculation of eggplants with *V. dahliae* caused Verticillium wilt disease. Disease severity was calculated based on the disease scoring and disease severity index according to Liu et al. (2009b) (**Figure 6**). There was a significant interaction of disease severity between treatments and time (repeated measures Friedman Ranks ANOVA: set I: $F_{29.304,130.240} = 1.140$, $P \leq 0.001$; set II: $F_{30.609,136.038} = 25.0123$, $P \leq 0.001$). Disease severity varied with the type of CEC and the growth phase of the plants. Most treatments reached their disease index maximum by 5 weeks and had the fastest increase between week 3 and 5. Some of the plant treatments still increased in severity after week 5, while most remained steady. Plants treated with TMP had a higher, but not significant disease severity index earlier in the season (between week 2 and 5) compared to the other CECs and the no CECs control (**Figures 6A,B**). However, SMX and GEM had lower disease index than the control between week 2 and 5, but after that their disease index was above the control although it was not significant (**Figures 6C,D**). Both inoculated TMP-H and inoculated no CECs had steady increases in disease severity after 5 weeks (**Figures 6A,B**). APAP-L and TMP-L plateaued at low disease severity between week 5 and 7, but TMP-L plants sharply increased in severity near the end of the experiment. APAP-L, however, maintained relatively low levels of disease severity to the end of the experiment, week 8. Plants treated with TMP (high or low) increased in disease severity index between week 7 and 8, while the disease index of the control plants reduced in this time. APAP-L had significantly lower disease severity than the inoculated TMP-H and the inoculated no CEC treatment by week 8 (GLiM: $\chi^2_4 = 15.536$, $P = 0.004$) (**Figure 6A**). The disease severity of the eggplants was used to calculate the disease index. As expected, the disease index results paralleled the disease severity results (**Figures 6B,D**).

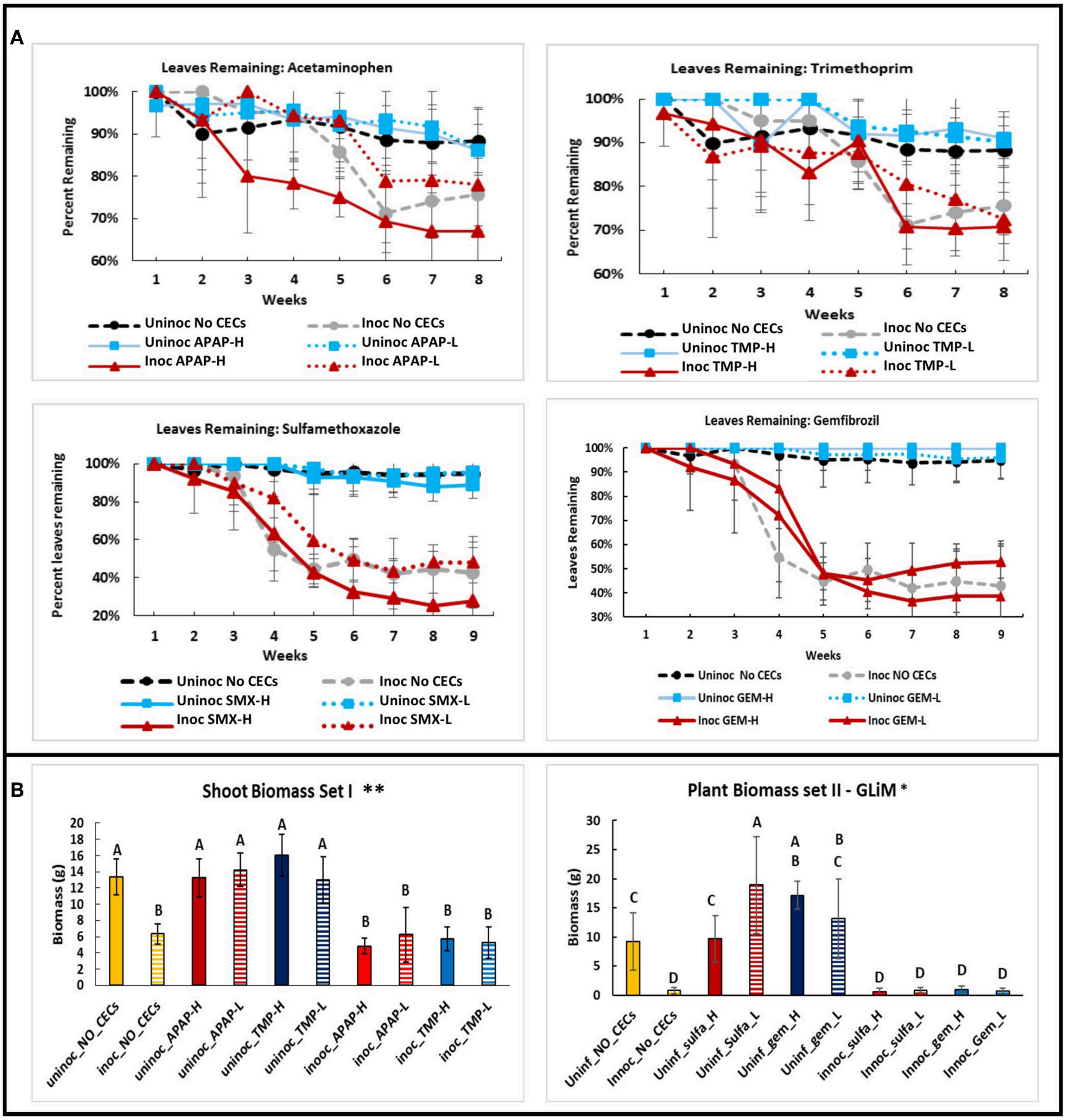

FIGURE 5 | Comparisons of plant health metrics of eggplants grown in the green house among different chemicals of emerging concern (CECs) treatments. **(A)** Line graphs of leaves remaining on plants over time for each CEC. **(B)** Above ground biomass of both sets of eggplants at the end of the experiment. The CECs used were acetaminophen (APAP), trimethoprim (TMP), sulfamethoxazole (SMX) and gemfibrozil (GEM). For each CEC two concentrations were used high (H) and low (L). *Samples compared statistically using GLiM with normal distribution and identity link function, pairwise analyses with sequential Bonferroni pairwise correction for multiple comparisons ($P < 0.05$). **ANOVA used for statistical analyses, *post-hoc* Tukey test used for pairwise analyses ($P < 0.05$).

DISCUSSION

In this study we investigated the impacts of CECs at concentrations found in reclaimed water on plant microbes and Verticillium wilt disease severity on eggplants. Microorganism growth assays done *in vitro* showed that the tested microorganisms were differentially affected by CECs. Even strains of the same fungus responded differently to the same CEC. In the greenhouse experiments, plant disease index varied with the stage of plant growth and the CEC that was applied. APAP and TMP had stronger impacts on disease development early in the season, while SMX and GEM appeared to have less impact on disease development early in the season. APAP and TMP had a stronger influence of disease development at higher concentrations than lower concentrations, but the concentrations of SMX and GEM used did not differently impact in disease development. Inoculation with the pathogen *V. dahliae* had the strongest impact on disease development than any CEC treatment.

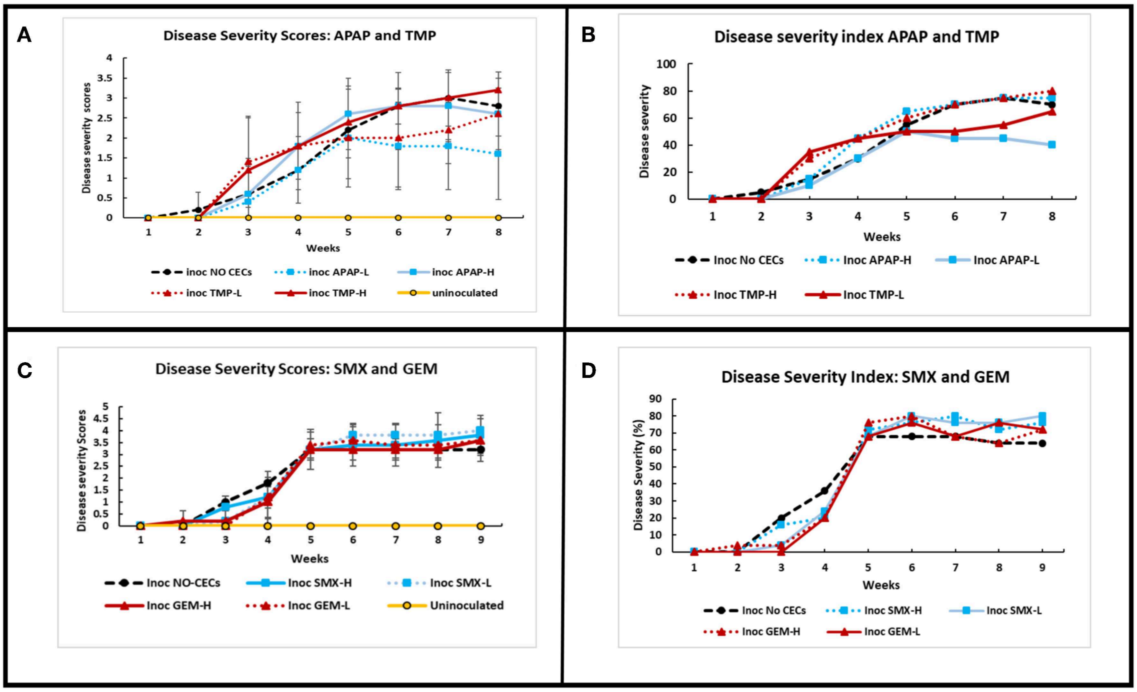

FIGURE 6 | Comparison of disease severity and disease severity index of greenhouse grown eggplants inoculated with *Verticillum dahliae* and watered with or without the addition of chemicals of emerging concern. Calculations to determine the disease severity index (DSI) are described in Liu et al. (2009b) and Chiang et al. (2017). All error bars shown represent standard deviation. **(A)** Disease severity of inoculated and uninoculated eggplants for acetaminophen (APAP) and trimethoprim (TMP), treatments. **(B)** Comparing DSI values for APAP and TMP treatments over time. **(C)** Disease severity of inoculated and uninoculated eggplants for sulfamethoxazole (SMX) and gemfibrozil (GEM)treatments over time. **(D)** Comparing DSI values for SMX and GEM treatments over time.

Impact of CECs on Microorganism Growth

In this study we investigated the impact of CECs on growth of microorganism *in vitro*. We used growth rates to calculate the allelopathic index, which is normally used to evaluate true allelopathy of chemicals excreted by organisms directly into the environment (Williamson and Richardson, 1988; Liu et al., 2009b). By applying this concept to extrinsically derived chemicals we can compare the impacts of anthropogenic CECs to naturally formed compounds used by the producing organism to influence other organisms. Originally the concept of allelopathy was used to refer to any chemical involved with positive or negative plant-plant interactions (Patrick, 1986). Over time this concept has evolved to include chemicals involved between plant-plant or plant-microbe interactions, but only in the negative, or inhibitory sense (Patrick, 1986). Lower, negative RI values have been associated with reduction of disease severity in plants in some experiments (Liu et al., 2009a; Zhou et al., 2011). Although, in the study by Liu et al. (2009b) significantly lower RI values of root exudates did not always associate with reduced disease severity or incidence. Suggesting that growth can only partially explain disease progression or infectivity. It is likely that there are many other factors involved in the interaction between hosts, CECs, and pathogenicity. Environmental factors such as pH (Zimmermann and Curtis, 2017) or carbon substrate availability (Hida et al., 2005) can influence potency of some CECs. Environmental factors can also influence a microorganism's ability to infect a given host (Jarosz and Burdon, 1988). The interactions of CECs with plants and microbes are multifaceted.

Our microbial growth assays showed that nearly all the microbes tested were sensitive to the CECs used in this study. However, the specific effects of the CECs varied, among the organisms. CECs have been observed to exhibit growth promoting effects on microbes (Carvalho et al., 2010; Zimmermann and Curtis, 2017), while growth inhibition by these chemicals typically occurs at higher concentrations (Koch and Burchall, 1971; Kabbash et al., 2004; Argyropoulou et al., 2009; Al-Janabi, 2010). For these reasons we predicted that the microorganisms would not be affected the presence of CECs. We observed increased growth in the presence of CECs with two fungi, *V. dahliae* 0048 and *F. oxysporum* CS-3. Both of these strains exhibited significantly more growth and higher RI values compared to their controls, suggesting that these CECs have growth promoting effects on these particular organisms. In contrast, other strains of the same fungi *V. dahliae* 0049 and *F. oxysporum* CS-5 had nearly an exact opposite trend in which the CECs either had no effect or were inhibitory to mycelial growth, suggesting that our hypothesis was partially correct. Their RI values correspond well to values found for root exudate of resistant tomato plant roots (−0.155 to −0.020) (Liu et al., 2009b). Having similar RI values to root exudates that exhibit antimicrobial effects also suggests that the *in situ* levels of CECs are at biologically relevant concentrations. Our results concurred with another study that showed that closely related fungi can respond differently to some CECs, in particular, sulfamethoxazole (Hida et al., 2005).

Not all the microorganisms evaluated were equally sensitive to all the CECs. *P. indica* was only affected by two CEC treatments in opposing ways at two separate time points, while the growth of the bacterium *B. japonicum* was not affected by any CEC. These CECs usually exhibit antimicrobial effects at equal or greater concentrations of those found in human blood plasma levels corresponding to therapeutic doses. Typical therapeutic plasma levels of these CECs fall within the ranges of 10,000–20,000 μg/L; 3,000–8,000 μg/L; 80,000–100,000 μg/L, and 19,000–45,000 μg/L for APAP, TMP, SMX, and GEM, respectively (Nolte and Buettner, 1974; Reeves and Wilkinson, 1979; Spence et al., 1995; Kyrklund et al., 2003; Niemi et al., 2003; Stuart et al., 2004; Clajus et al., 2013; Zimmermann and Curtis, 2017), which are about 10,000–100,000 times more than those used in our study (**Table 1**). However, these studies were conducted on human pathogens and not soilborne organisms. CECs have been shown to disrupt the functions of soilborne nitrogen cycling bacteria when tested at concentrations higher than therapeutic concentrations (Colloff et al., 2008) and at levels found in wastewater treatment plant effluent (Wang and Gunsch, 2011).

Taken together our results and those of others indicate that many more plant or soil associated organisms may be sensitive to CECs at the concentrations found in reclaimed water. Thus, additional studies on the impacts of CECs on free living and plant associated microorganisms are necessary to fully understand the impacts of these chemicals on disease severity especially in fields where reclaimed water has been used to irrigate plants for years. We observed that fungal strains were sensitive to CECs concentrations well below typical therapeutic doses. Our microbial growth rate assays demonstrated that these particular CECs are capable of impacting microbial growth at *in situ* concentrations and suggesting the potential to disrupt plant-pathogen dynamics.

Spore Germination of Microorganisms

The spore germination assays demonstrated that the CECs used in this study can affect fungal spore germination in addition to mycelial growth discussed above. In spore germination assays we used sucrose solutions to decrease the osmotic potential of the solution to optimal spore germination conditions as described for *V. dahliae* in Ioannou et al. (1977). We used the same sucrose solutions for the *F. oxysporum* CS-5 assay to optimize spore germination as well. When we used sterile water, the germination rate was only 5%. This is similar to results obtained by Steinkellner et al. (2005), who also obtained 5% germination rate of *F. oxysporum* in sterile water. The control (sucrose only solution) for our *V. dahliae* spore germination assay reached over 80%, which is comparable to the amount of spore germination in a previous study that uses similar methods (Ioannou et al., 1977). All of the CEC treatments had lower spore germination than the control, although two (APAP-H and SMX-L) were not significantly lower. TMP-H treatment had the greatest impact on *V. dahliae* 0049 spore germination and had significantly less germination than all treatments. This combined with the results of the mycelium growth assay, discussed above, suggest that this particular strain of *V. dahliae* is sensitive to TMP. Although spore germination did not get as high in the *F. oxysporum* CS-5 assay, the sucrose solution was successful with increasing spore germination rates. The average spore germination for the *F. oxysporum* assay reached above 40% for the controls, which is higher than the about 5% germination amounts generated in the water only (Steinkellner et al., 2005). Over all, spore germination of *F. oxysporum* CS-5 exhibited less sensitivity to the CECs, but TMP had an effect of decreasing spore germination. The effects of TMP in reducing spore germination and mycelial growth did not translate to reduced disease severity as discussed below. The combined results of our spore germination assay suggest that soilborne microbes may be altered by CECs found in reclaimed water, which may impact plant-microbe interactions and plant disease severity.

Impact of CECS on Plant Growth and Severity of Verticillium Wilt of Eggplants

Eggplants were grown in a greenhouse at the University of California, Riverside to evaluate the impacts of CECs on host-pathogen dynamics. Plants were watered with the range of concentrations of the respective CECs to simulate agriculture conditions in which plants are being irrigated with reclaimed water (**Table 1**) (Kinney et al., 2006; Vanderford and Snyder, 2006; Batt et al., 2007; Fram and Belitz, 2011). We predicted that disease severity would increase because the CECs would most likely enhance *V. dahliae* growth (Carvalho et al., 2010). Antibacterial compounds can displace microbes that are antagonistic toward plant pathogens, allowing them to increase in numbers and therefore have a higher chance to establish an infection (Mulligan et al., 1982; De Vries-Hospers et al., 1991; Azevedo et al., 2015). Previous studies have shown that certain pharmaceutical products can have detrimental impacts on plants (Liu et al., 2009a; Madikizela et al., 2018). The impacts of CECs on disease severity or disease severity index varied with the CEC: TMP-H had a higher severity index earlier in the season (week 2–4), while SMX at both concentrations had a greater impact later in the season (week 5–9). APAP-L and TMP-L had the least effects on disease index between week 5 and 7. However, these differences were not statistically significant from the associated controls. Our result indicated that APAP-L and TMP-L were beneficial to the eggplant in some capacity. However, the exact interaction or mechanism is not known and requires additional study.

Besides examining disease severity, plant growth metrics of stem height, leaf loss, and shoot fresh weight were used to assess if the CECs directly impacted plant growth, or if there were any interactions between plant growth, disease severity and CECs. As expected, both stem height and final shoot fresh weight were significantly lower in the *V. dahliae* inoculated plants than in the uninoculated ones. Inoculated plants also lost significantly more leaves. Uninoculated plants did not have any indications of Verticillium wilt. By the end of the experiment, there were no significant differences found for stem heights or percentage of leaf loss between the different CEC treatments for inoculated or uninoculated plants. Plant growth was not impacted in any visible way by the concentrations of the CECs we used. This fits well with other studies that indicate that larger, more complex organisms, such as developed plants, will not be impacted directly by CECs at low concentrations (Wu et al., 2013). Although, other studies indicate that plants take up these compounds and that these CECs can be found in tissues of plants that have been irrigated with water containing these CECs (Dodgen et al., 2013; Wu et al., 2013, 2015). Most of these studies have only been conducted within a single growing season. However, these chemicals can accumulate into tissues over time (Wu et al., 2010) thus longer studies are needed given that these compounds are impacting microbial and insect life at low concentrations (Pennington et al., 2018). Other studies have also found direct impacts to plants by anthropogenic compounds. The studies by D'Abrosca et al. (2008) and Pino et al. (2016) observed growth inhibition of plants when they were exposed to low levels of anthropogenic chemicals, including gemfibrozil. Inhibition of seed germination by CECs was also observed in the study D'Abrosca et al. (2008). Together these studies suggest that seeds and seedlings are more vulnerable to CECs, and the chemicals may have direct impacts on developed plants once they reach higher concentrations. In our study the plants used were at the 4th leaf stage and therefore had time to develop beyond the seedling stage before being exposed to CECs, which partially explains why there was not a great impact to their stem growth, or leaf production. In addition, some studies found that not all plants are impacted equally by a given CEC (D'Abrosca et al., 2008), and some plant tissues such as roots, maybe more sensitive to CECs than other parts of the plant (Pino et al., 2016).

By the end of the experiment we observe that two treatments had effects on shoot fresh weight. The uninoculated SMX-L treatment had significantly greater biomass than the associated uninoculated control. This result suggests that at low concentrations SMX may be beneficial for plant growth. Perhaps the plants are able to utilize the sulfur component of sulfamethoxazole. We also saw significant shoot fresh weight in plants treated with GEM-L than the associated uninocualted no CEC control. Other studies conducted on plants at the seed stage have indicated that even low concentrations of GEM can have deleterious impacts on growth (D'Abrosca et al., 2008; Pino et al., 2016). However, these studies were conducted on seeds. Developed plants appear to be more resistant to chemical interference. The study Wu et al. (2013) found no phytotoxic effects of the CECs they tested on mature plants at low concentrations. It has been observed that small amounts of harmful substances can actually stimulate plant growth in a concept known as hormesis (Pan and Chu, 2017). Hormesis may at least partially explain the increased shoot biomass observed in the SMX-L and GEM-L treatments (Pan and Chu, 2017). The two studies that found GEM to be harmful were also done in the absence of soil, while our plants were grown directly in soil. GEM was most likely broken down or partially absorbed by the soil, thus further reducing the amount of the chemical the eggplants were exposed to Pan and Chu (2017). A lower amount of GEM may not have phytotoxic effects and instead have stimulatory effects on a given plant due to hormesis. However, the concept of hormesis was not formally tested in this experiment and should be investigated further.

DATA AVAILABILITY STATEMENT

All datasets generated for this study are included in the manuscript/**Supplementary Files**.

AUTHOR CONTRIBUTIONS

EG conceived and planned the study. NM carried out the experimental work and data analyses. EG and NM interpreted the results and wrote the manuscript.

FUNDING

This work was supported by the University of California, Riverside Startup funds to EG.

ACKNOWLEDGMENTS

We would like to acknowledge the University of California, Riverside for start-up funds to EG. We would like to thank Dr. Alex Putman for donating the *Verticillium dahliae* strains, Dr. Soumaila Sanogo for donating *Phytophthora capsici*, and Dr. Ralf Oelmueller for donating the *Piriformospora indica* strain. We would also like to thank Rochelle Medel for her help with data collection.

SUPPLEMENTARY MATERIAL

The Supplementary Material for this article can be found online at: https://www.frontiersin.org/articles/10.3389/fenvs.2019.00156/full#supplementary-material

REFERENCES

AghaKouchak, A., Feldman, D., Hoerling, M., Huxman, T., and Lund, J. (2015). Water and climate: recognize anthropogenic drought. *Nature* 524, 409–411. doi: 10.1038/524409a

Aguiar, J., Molinar, R., and Valencia, J. (1998). *Eggplant Production in California*. doi: 10.3733/ucanr.7235

Al-Janabi, A. A. H. (2010). *In vitro* antibacterial activity of ibuprofen and acetaminophen. *J. Glob. Infect. Dis.* 2, 105–108. doi: 10.4103/0974-777X.62880

Argyropoulou, I., Geronikaki, A., Vicini, P., and Zani, F. (2009). Synthesis and biological evaluation of sulfonamide thiazole and benzothiazole derivatives as antimicrobial agents. *Arkivoc* 2009, 89–102. doi: 10.3998/ark.5550190.0010.611

Azevedo, M. M., Teixeira-Santos, R., Silva, A. P., Cruz, L., Ricardo, E., Pina-Vaz, C., et al. (2015). The effect of antibacterial and non-antibacterial compounds alone or associated with antifugals upon fungi. *Front. Microbiol.* 6:669. doi: 10.3389/fmicb.2015.00669

Batt, A. L., Kim, S., and Aga, D. S. (2007). Comparison of the occurrence of antibiotics in four full-scale wastewater treatment plants with varying designs and operations. *Chemosphere* 68, 428–435. doi: 10.1016/j.chemosphere.2007.01.008

Bhat, R. G., and Subbarao, K. V. (1999). Host range specificity in *Verticillium dahliae*. *Am. Phytopathol. Soc.* 89, 1218–1225. doi: 10.1094/PHYTO.1999.89.12.1218

Boxall, A. B. A., Johnson, P., Smith, E. J., Sinclair, C. J., Stutt, E., and Levy, L. S. (2006). Uptake of veterinary medicines from soils into plants. *J. Agric. Food Chem.* 54, 2288–2297. doi: 10.1021/jf053041t

Brown, E., Rodriquez, M., Marcus, F., Spivy-Webber, F., Doduc, T., and Moore, S. (2013). Policy for water quality control for recycled water (recycled water policy). *Calif. State Water Resour. Control Board* 1–14. Available online at: https://www.waterboards.ca.gov/water_issues/programs/water_recycling_policy/docs/recycledwaterpolicy_approved.pdf

Bulatova, N. R., and Darwish, R. M. (2008). Effect of chemosensitizers on minimum inhibitory concentrations of fluconazole in *Candida albicans*. *Med. Princ. Pract.* 17, 117–121. doi: 10.1159/000112964

California Department of Food and Agriculture (2018). *California Agricultural Statistics Review 2017-2018*. Sacromento, CA. Available online at: www.cdfa.ca.gov/statistics

California State Water Resources Control Board (2010). *Final Report (Draft for Public Comments) Monitoring Strategies for Chemicals of Emerging Recommendations of a Science Advisory Panel Panel Members*. Sacromento, CA. Available online at: http://www.santacruzwatersupply.com/sites/default/files/resource-files/CECMonitoringInCARecycledWater_FinalReport.pdf

Carvalho, A. P., Gursky, L. C., Rosa, R. T., Rymovicz, A. U. M., Campelo, P. M. S., Grégio, A. M. T., et al. (2010). Non-steroidal anti-inflammatory drugs may modulate the protease activity of *Candida albicans*. *Microb. Pathog.* 49, 315–322. doi: 10.1016/j.micpath.2010.07.007

Chiang, K. S., Liu, H. I., and Bock, C. H. (2017). A discussion on disease severity index values. Part I: warning on inherent errors and suggestions to maximise accuracy. *Ann. Appl. Biol.* 171, 139–154. doi: 10.1111/aab.12362

Clajus, C., Kuhn-Velten, W. N., Schmidt, J. J., Lorenzen, J. M., Pietsch, D., Beutel, G., et al. (2013). Cotrimoxazole plasma levels, dialyzer clearance and total removal by extended dialysis in a patient with acute kidney injury: risk of under-dosing using current dosing recommendations. *BMC Pharmacol. Toxicol.* 14:19. doi: 10.1186/2050-6511-14-19

Colloff, M. J., Wakelin, S. A., Gomez, D., and Rogers, S. L. (2008). Detection of nitrogen cycle genes in soils for measuring the effects of changes in land use and management. *Soil Biol. Biochem.* 40, 1637–1645. doi: 10.1016/j.soilbio.2008.01.019

Cooley, H., and Phurisamban, R. (2016). *The Cost of Alternative Water Supply and Efficiency Options in California*. Oakland, CA: Pacific Institute.

D'Abrosca, B., Fiorentino, A., Izzo, A., Cefarelli, G., Pascarella, M. T., Uzzo, P., et al. (2008). Phytotoxicity evaluation of five pharmaceutical pollutants detected in surface water on germination and growth of cultivated and spontaneous plants. *J. Environ. Sci. Heal. A* 43, 285–294. doi: 10.1080/10934520701792803

De Vries-Hospers, H. G., Tonk, R. H. J., and Van Der Waaij, D. (1991). Effect of intramuscular ceftriaxone on aerobic oral and faecal flora of 11 healthy volunteers. *Scand. J. Infect. Dis.* 23, 625–633. doi: 10.3109/00365549109105188

Dia-Cruz, M. S., and Barcelo, D. (2008). Trace organic chemicals contamination in ground water recharge. *Chemosphere* 72, 333–342. doi: 10.1016/j.chemosphere.2008.02.031

Dodgen, L. K., Li, J., Parker, D., and Gan, J. J. (2013). Uptake and accumulation of four PPCP/EDCs in two leafy vegetables. *Environ. Pollut.* 182, 150–156. doi: 10.1016/j.envpol.2013.06.038

EPA (2019). *Contaminants of Emerging Concern including Pharmaceuticals and Personal Care Products*. www.epa.gov. Available online at: https://www.epa.gov/wqc/contaminants-emerging-concern-including-pharmaceuticals-and-personal-care-products

Erickson, M. L., Langer, S. K., Roth, J. L., and Kroening, S. E. (2014). *Contaminants of Emerging Concern in Ambient Groundwater in Urbanized Areas of Minnesota, 2009–12 (ver. 1.2, September 2014): U.S. Geological Survey Scientific Investigations Report 2014–5096,* 38, with appendix. doi: 10.3133/sir20145096

Feys, J. (2015). *npIntFactRep: Nonparametric Interaction Tests for Factorial Designs With Repeated Measures*. Available online at: https://cran.r-project.org/web/packages/npIntFactRep/npIntFactRep.pdf

Feys, J. (2016). Nonparametric tests for the interaction in two-way factorial designs using R. *R J.* 8, 367–378. doi: 10.32614/RJ-2016-027

Fram, M. S., and Belitz, K. (2011). Occurrence and concentrations of pharmaceutical compounds in groundwater used for public drinking-water supply in California. *Sci. Total Environ.* 409, 3409–3417. doi: 10.1016/j.scitotenv.2011.05.053

Gros, M., Petrovi, M., Ginebreda, A., and Barceló, D. (2010). Removal of pharmaceuticals during wastewater treatment and environmental risk assessment using hazard indexes. *Environ. Int.* 36, 15–26. doi: 10.1016/j.envint.2009.09.002

Hida, S., Yoshida, M., Nakabayashi, I., Miura, N. N., Adachi, Y., and Ohno, N. (2005). Anti-fungal activity of sulfamethoxazole toward *Aspergillus* Species. *Biol. Pharm. Bull.* 28, 773–778. doi: 10.1248/bpb.28.773

Hirano, Y., and Arie, T. (2006). PCR-based differentiation of *Fusarium oxysporum* ff. sp. *lycopersici* and *radicis-lycopersici* and races of *F. oxysporum* f. sp. *lycopersici*. *J. Gen. Plant. Pathol.* 72, 273–283. doi: 10.1007/s10327-006-0287-7

Howitt, R., Macewan, D., Medellín-azuara, J., Lund, J. R., and Sumner, D. (2015). *Economic Analysis of the 2014 Drought for California Agriculture*. Davis, CA: Center for Watershed Sciences. University of California. Available online at: http://watershed.ucdavis.edu

Inderbitzin, P., Davis, R. M., Bostock, R. M., and Subbarao, K. V. (2013). Identification and differentiation of *Verticillium* species and *V. longisporum* lineages by simplex and multiplex PCR assays. *PLoS ONE* 8:e65990. doi: 10.1371/journal.pone.0065990

Ioannou, N., Schneider, R. W., Grogan, R. G., and Duniway, J. M. (1977). Effect of water potential and temperature on growth, sporulation, and production of microsclerotia by *Verticillium dahliae*. *Phytopathology* 67, 637–644. doi: 10.1094/Phyto-67-637

Jarosz, A. M., and Burdon, J. J. (1988). The effect of small-scale environmental changes on disease incidence and severity in a natural plant-pathogen interaction. *Oecologia* 75, 278–281. doi: 10.1007/BF00378609

Kabbash, C., Shuman, H. A., Silverstein, S. C., and Della-Latta, P. (2004). *Antimicrobial Activity of Gemfibrozil.* U.S. Patent No 6,713,043.

Kinney, C. A., Furlong, E. T., Werner, S. L., and Cahill, J. D. (2006). Presence and distribution of wastewater-derived pharmaceuticals in soil irrigated with reclaimed water. *Environ. Toxicol. Chem.* 25, 317–326. doi: 10.1897/05-187R.1

Klosterman, S. J., Atallah, Z. K., Vallad, G. E., and Subbarao, K. V. (2009). Diversity, pathogenicity, and management of verticillium species. *Annu. Rev. Phytopathol.* 47, 39–62. doi: 10.1146/annurev-phyto-080508-081748

Koch, A. E., and Burchall, J. J. (1971). Reversal of the antimicrobial activity of trimethoprim by thymidine in commercially prepared media. *Appl. Microbiol.* 22, 812–7. Available online at: https://aem.asm.org/content/22/5/812.short

Kyrklund, C., Backman, J. T., Neuvonen, M., and Neuvonen, P. J. (2003). Gemfibrozil increases plasma pravastatin concentrations and reduces pravastatin renal clearance. *Clin. Pharmacol. Ther.* 73, 538–544. doi: 10.1016/S0009-9236(03)00052-3

Liu, F., Ying, G. G., Tao, R., Zhao, J. L., Yang, J. F., and Zhao, L. F. (2009a). Effects of six selected antibiotics on plant growth and soil microbial and enzymatic activities. *Environ. Pollut.* 157, 1636–1642. doi: 10.1016/j.envpol.2008.12.021

Liu, N., Zhou, B., Zhao, X., Lu, B., Li, Y., and Hao, J. (2009b). Grafting eggplant onto tomato rootstock to suppress verticillium dahliae infection: the effect of root exudates. *HortScience* 44, 2058–2062. doi: 10.21273/HORTSCI.44.7.2058

Madikizela, L. M., Ncube, S., and Chimuka, L. (2018). Uptake of pharmaceuticals by plants grown under hydroponic conditions and natural occurring plant species: a review. *Sci. Total Environ.* 636, 477–486. doi: 10.1016/j.scitotenv.2018.04.297

Masachis, S., Segorbe, D., Turrà, D., Leon-ruiz, M., Fürst, U., Ghalid, M., et al. (2016). A fungal pathogen secretes plant alkalinizing peptides to increase infection. *Nat. Microbiol.* 1, 1–8. doi: 10.1038/nmicrobiol.2016.43

Mulligan, M., Citron, D. M., McNamara, B. T., and Finegold, S. M. (1982). Impact of cefoperazone therapy on fecal flora. *Antimicrob. Agents Chemother.* 22, 226–230. doi: 10.1128/AAC.22.2.226

Niemi, M., Backman, J. T., Granfors, M., Laitila, J., Neuvonen, M., and Neuvonen, P. J. (2003). Gemfibrozil considerably increases the plasma concentrations of rosiglitazone. *Diabetologia* 46, 1319–1323. doi: 10.1007/s00125-003-1181-x

Nolte, H., and Buettner, H. (1974). Investigations on plasma levels of sulfamethoxazole in man after single and chronic oral administration alone and in combination with trimethoprim. *Chemotherapy* 20, 321–330. doi: 10.1159/000221822

Pan, M., and Chu, L. M. (2017). Science of the total environment fate of antibiotics in soil and their uptake by edible crops. *Sci. Total Environ.* 600, 500–512. doi: 10.1016/j.scitotenv.2017.04.214

Parsons, L. R., Sheikh, B., Holden, R., and York, D. W. (2010). Reclaimed water as an alternative water source for crop irrigation. *HortScience* 45, 1626–1629. doi: 10.21273/HORTSCI.45.11.1626

Patrick, Z. A. (1986). Allelopathic mechanisms and their exploitation for biological control. *Can. J. Plant Pathol.* 8, 225–228. doi: 10.1080/07060668609501831

Pegg, G. F. (1984). The Impact of *Verticillium* diseases in agriculture. *Phytopathol. Mediterr.* 23, 176–192. Available online at: https://www.jstor.org/stable/pdf/42684709.pdf

Pennington, M. J., Rothman, J. A., Dudley, S. L., Jones, M. B., Mcfrederick, Q. S., and Gan, J. (2017). Contaminants of emerging concern affect Trichoplusia ni growth and development on artificial diets and a key host plant. *Proc. Natl. Acad. Sci. U.S.A.* 114, 1–9. doi: 10.1073/pnas.1713385114

Pennington, M. J., Rothman, J. A., Jones, M. B., Mcfrederick, Q. S., Gan, J., and Trumble, J. T. (2018). Effects of contaminants of emerging concern on *Myzus persicae* (Sulzer, Hemiptera : Aphididae) biology and on their host plant, *Capsicum annuum*. *Environ. Monit. Assess.* 190, 1–11. doi: 10.1007/s10661-018-6503-z

Pino, M. R., Muñiz, S., Val, J., and Navarro, E. (2016). Phytotoxicity of 15 common pharmaceuticals on the germination of *Lactuca sativa* and photosynthesis of *Chlamydomonas reinhardtii*. *Environ. Sci. Pollut. Res.* 23, 22530–22541. doi: 10.1007/s11356-016-7446-y

R Core Team (2018). *R: A Language and Environment for Statistical Computing*. R Foundation for Statistical Computing, Vienna.

Reeves, D. S., and Wilkinson, P. J. (1979). The pharmacokinetics of trimethoprim and trimethoprim/sulphonamide combinations, including penetration into body tissues. *Infection* 7, 330–341. doi: 10.1007/BF01639009

Rudin, D. E., Gao, P. X., Cao, C. X., Neu, H. C., and Silverstein, S. C. (1992). Gemfibrozil enhances the listeriacidal effects of fluoroquinolone antibiotics in J774 macrophages. *J. Exp. Med.* 176, 1439–1447. doi: 10.1084/jem.176.5.1439

Schulte, P. (2011). Using recycled water on agriculture : sea mist farms and Sonoma County. *Pacific Inst. Farm Water Success Stories Recycl. Water Agric.* 1–10. Available online at: https://pacinst.org/publication/california-farm-water-success-stories/

Smith, G. (1941). The effect of adding trace elements to czapek-dox medium. *Trans. Br. Mycol. Soc.* 32, 280–283. doi: 10.1016/S0007-1536(49)80018-0

Spence, J. D., Munoz, C. E., Hendricks, L., Latchinian, L., and Khouri, H. E. (1995). Pharmacokinetlcs of the combination of fluvastatln and gemflbrozll. *Am. J. Cardiol.* 76, 80–83. doi: 10.1016/S0002-9149(05)80024-4

Stackelberg, P. E., Gibs, J., Furlong, E. T., Meyer, M. T., Zaugg, S. D., and Lippincott, R. L. (2007). Efficiency of conventional drinking-water-treatment processes in removal of pharmaceuticals and other organic compounds. *Sci. Total Environ.* 377, 255–272. doi: 10.1016/j.scitotenv.2007.01.095

Steinkellner, S., Mammerler, R., and Vierheilig, H. (2005). Microconidia germination of the tomato pathogen *Fusarium oxysporum* in the presence of root exudates. *J. Plant Interact.* 1, 23–30. doi: 10.1080/17429140500134334

Stuart, R. K., Braine, H. G., Lietman, P. S., Saral, R., and Fuller, D. J. (2004). Carbenicillin-trimethoprim/sulfamethoxazole versus carbenicillin-gentamicin as empiric therapy of infection in granulocytopenic patients. *Am. J. Med.* 68, 876–885. doi: 10.1016/0002-9343(80)90217-X

Thom, C. (1930). *The Penicillia*. London: Bailiere, Tindall, and Cox.

Tunali, Y., Karaca, H., Işcan, G., Demirci, F., and Benkli, K. (2012). Antibacterial and antifungal activities of some trimethoprim salts. *Med. Chem. Res.* 21, 932–935. doi: 10.1007/s00044-011-9605-5

Vanderford, B. J., and Snyder, S. A. (2006). Analysis of pharmaceuticals in water by isotope dilution liquid chromatography/tandem mass spectrometry. *Environ. Sci. Technol.* 40, 7312–7320. doi: 10.1021/es0613198

Wang, S., and Gunsch, C. K. (2011). Effects of selected pharmaceutically active compounds on the ammonia oxidizing bacterium *Nitrosomonas europaea*. *Chemosphere* 82, 565–572. doi: 10.1016/j.chemosphere.2010.10.007

Warsinger, D. M., Chakraborty, S., Tow, E. W., Plumlee, M. H., Bellona, C., Loutatidou, S., et al. (2018). A review of polymeric membranes and processes for potable water reuse. *Prog. Polym. Sci.* 81, 209–237. doi: 10.1016/j.progpolymsci.2018.01.004

Williams, J. S., Hall, S. A., Hawkesford, M. J., Beale, M. H., and Cooper, R. M. (2002). Elemental sulfur and thiol accumulation in tomato and defense against a fungal vascular pathogen. *Plant Physiol.* 128, 150–159. doi: 10.1104/pp.010687

Williamson, B. G., and Richardson, D. (1988). Bioassays for allelopathy: measuring treatment responses with independent controls. *J. Chem. Ecol.* 14, 181–187. doi: 10.1007/BF01022540

Wu, C., Spongberg, A. L., Witter, J. D., Fang, M., and Czajkowski, K. P. (2010). Uptake of pharmaceutical and personal care products by soybean plants from soils applied with biosolids and irrigated with contaminated water. *Environ. Sci. Technol.* 44, 6157–6161. doi: 10.1021/es1011115

Wu, X., Dodgen, L. K., Conkle, J. L., and Gan, J. (2015). Plant uptake of pharmaceutical and personal care products from recycled water and biosolids: a review. *Sci. Total Environ.* 536, 655–666. doi: 10.1016/j.scitotenv.2015.07.129

Wu, X., Ernst, F., Conkle, J. L., and Gan, J. (2013). Comparative uptake and translocation of pharmaceutical and personal care products (PPCPs) by common vegetables. *Environ. Int.* 60, 15–22. doi: 10.1016/j.envint.2013.07.015

Zhou, B. L., Chen, Z. X., Du, L., Xie, Y. H., Zhang, Q., and Ye, X. L. (2011). Allelopathy of root exudates from different resistant eggplants to Verticillium dahliae and the identification of allelochemicals. *African J. Biotechnol.* 10, 8284–8290. doi: 10.5897/AJB10.2300

Zimmermann, P., and Curtis, N. (2017). Antimicrobial effects of antipyretics. *Antimicrob. Agents Chemother.* 61, 1–12. doi: 10.1128/AAC.02268-16

Conflict of Interest: The authors declare that the research was conducted in the absence of any commercial or financial relationships that could be construed as a potential conflict of interest.

frontiers in Chemistry

ORIGINAL RESEARCH
published: 19 November 2019
doi: 10.3389/fchem.2019.00796

A High-Efficiency CuO/CeO_2 Catalyst for Diclofenac Degradation in Fenton-Like System

Jia Zhu[1*†], *Guangming Zhang*[2†], *Guang Xian*[2,3†], *Nan Zhang*[2] *and Jinwei Li*[1]

[1] School of Construction and Environment Engineering, Shenzhen Polytechnic, Shenzhen, China, [2] School of Environment & Natural Resource, Renmin University of China, Beijing, China, [3] Department of Military Installations, Army Logistics University of PLA, Chongqing, China

An efficient Fenton-like catalyst CuO/CeO_2 was synthesized using ultrasonic impregnation and used to remove diclofenac from water. The catalyst was characterized by N_2 adsorption-desorption, SEM-EDS, XRD, HRTEM, Raman, and XPS analyses. Results showed that CuO/CeO_2 possessed large surface area, high porosity, and fine elements dispersion. Cu was loaded in CeO_2, which increased the oxygen vacancies. The exposed crystal face of CeO_2 (200) was beneficial to the catalytic activity. The diclofenac removal experiment showed that there was a synergistic effect between CuO and CeO_2, which might be caused by more oxygen vacancies generation and electronic interactions between Cu and Ce species. The experimental conditions were optimized, including pH, catalyst and H_2O_2 dosages, and 86.62% diclofenac removal was achieved. Diclofenac oxidation by ·OH and adsorbed oxygen species was the main mechanism for its removal in this Fenton-like system.

Keywords: CuO/CeO_2, ultrasonic impregnation, Fenton-like system, OH, oxygen vacancies

OPEN ACCESS

Edited by:
Renato Falcão Dantas,
Campinas State University, Brazil

Reviewed by:
Yanke Yu,
Xi'an Jiaotong University, China
Tomoo Mizugaki,
Osaka University, Japan

****Correspondence:***
Jia Zhu
7566874@qq.com

† These authors have contributed equally to this work and share first authorship

Specialty section:
This article was submitted to Catalysis and Photocatalysis, a section of the journal Frontiers in Chemistry

Received: *01 September 2019*
Accepted: *05 November 2019*
Published: *19 November 2019*

Citation:
Zhu J, Zhang G, Xian G, Zhang N and Li J (2019) A High-Efficiency CuO/CeO_2 Catalyst for Diclofenac Degradation in Fenton-Like System. Front. Chem. 7:796. doi: 10.3389/fchem.2019.00796

HIGHLIGHTS

- CuO/CeO_2 was prepared with ultrasound to remove diclofenac in Fenton-like system.
- Ultrasound made CuO/CeO_2 had large surface area, high porosity and fine elements dispersion.
- More oxygen vacancies caused by Cu doping were in favor of the catalytic reaction.
- 86.62% diclofenac removal was achieved under the optimal conditions.
- ·OH and adsorbed oxygen species were responsible for diclofenac degradation.

INTRODUCTION

Advanced oxidation processes (AOPs) for wastewater treatment have attracted extensive attention due to the quick and efficient pollutant removal by strong oxidizing free radicals, like hydroxyl radical (Silveira et al., 2015; Zhu et al., 2019). The most widely used AOP is Fenton reaction (Fe^{2+} activate H_2O_2), which is a homogeneous reaction that requires low pH (2.0–4.0) and forms large amount of iron sludge (Blanco et al., 2016). To overcome these disadvantages, heterogeneous catalysts have been adopted as the alternative (Lei et al., 2015), forming heterogeneous Fenton-like systems (Nidheesh, 2015).

The frequently used catalysts in heterogeneous Fenton-like systems are transition metal-based catalysts (Anipsitakis and Dionysiou, 2004; Bokare and Choi, 2014), due to the good catalytic activity, low cost, easily available materials, and abundant reserves. Among them, catalysts containing Cu^{2+} are in the limelight (Gu et al., 2019), because of the similar redox properties of Cu^{2+}/Cu^{+} to Fe^{3+}/Fe^{2+}, broad pH workable range, few sludge production and easily decomposition of Cu^{2+} complexes by ·OH (Bokare and Choi, 2014; Peng et al., 2019). As one of the most common and simplest copper compounds, CuO has successfully activated H_2O_2 to form ·OH to remove pollutants (Sehati and Entezari, 2017). However, CuO nanoparticles tend to agglomerate in water which is unfavorable for catalytic reaction. Besides, the leached Cu ions are poisonous. Loading CuO on support is an effective way to overcome the above problems.

Some metal oxides (such as CeO_2, Al_2O_3), clays, zeolites and carbon materials have been used as supports (Rao et al., 2018; Xu et al., 2018). The support increases the specific surface area of catalyst and reduces the leaching of metal ions (Du et al., 2016), which are beneficial to the adsorption property and stability of catalyst. Especially, CeO_2 can enhance the catalytic property of catalyst for its unique structure and redox property. CeO_2 has abundant oxygen vacancy defects and Ce^{4+}/Ce^{3+} redox couple (Chong et al., 2016), so it has high oxygen storage capacity, which is beneficial for catalytic reaction.

Doping transition metal ion into CeO_2 can create more oxygen vacancies due to the different ionic radii between Ce ion and transition metal ion, and the number of oxygen vacancies depends on the ionic radius and electrons of transition metal ions (Raj et al., 2017). Thus, the catalytic activity is improved by enhancing the oxygen storage and redox capacity (Parvas et al., 2014). The catalytic performance improvement by Cu doped into CeO_2 has been reported before (Wang et al., 2006; Yang et al., 2009; Lin et al., 2011).

The traditional impregnation method takes a long doping time and metal species agglomerate easily, due to the small mass transfer force between CeO_2 and the doping ions (Wang et al., 2006; Yang et al., 2009; Lin et al., 2011). Ultrasound has been used in the impregnation stage to overcome these disadvantages. Ultrasound waves induce the cavitation effect in water, which is related to the formation, growth, and rapid collapse of cavitation bubbles (Mirtamizdoust et al., 2017; Zhang et al., 2017). The ultrasonic cavitation can significantly accelerate the mass transfer velocity and provide thermal effects (Zhu and Zhang, 2008; Li et al., 2018). Therefore, ultrasound impregnation increases active components (transition metal ions) doped onto the surface of support (like CeO_2). Meanwhile, some active components may be introduced into the structure of support under the power of ultrasound, thus the catalyst prepared by ultrasound impregnation would have better catalytic performance (Chong et al., 2016). Moreover, ultrasound can significantly shorten the preparation time of catalyst by providing faster mass transfer rate.

In this paper, CuO was doped into CeO_2 by ultrasonic impregnation to form CuO/CeO_2, which was then applied as a catalyst in Fenton-like process. Diclofenac, a typical pharmaceutical and emerging contaminant, was used as the target pollutant to check the activity of the catalyst. The catalyst was characterized by N_2 adsorption-desorption, scanning electron microscope (SEM), X-ray powder diffraction (XRD), X-ray photoelectron spectra (XPS), high resolution transmission electron microscope (HRTEM), and Raman analyses. Influences of experimental parameters including pH, catalyst dosage, and H_2O_2 dosage on diclofenac removal were investigated. The potential reaction mechanism was proposed. The objective was to obtain a highly active Fenton-like catalyst with facial synthesis.

MATERIALS AND METHODS

Materials

All chemicals used were analytical grade. $Cu(NO_3)_2·4H_2O$ and $Ce(NO_3)_3·6H_2O$ were bought from Tianjin Guangfu Fine Chemical Co. (China). Thirty percent of H_2O_2 was obtained from Beijing Chemical (China). Diclofenac (98%) was bought from Tokyo Chemical (Japan). HPLC grade acetonitrile was purchased from Fisher Scientific (USA).

Synthesis of Catalysts

CuO was prepared by precipitation method (Ghasemi and Karimipour, 2018). One hundred and fifty milliliter NaOH solution (16.67 mol/L) was slowly injected into 150 mL of $Cu(NO_3)_2$ solution (0.67 mol/L). The mixture was stirred at ∼1,000 rpm at a constant temperature of 80°C for 3 h. The precipitate was separated by centrifugation, in which the solution was centrifuged for 20 min at 3,500 rpm. The precursor of CuO was dried for 3 h at 105°C and then calcined for 3 h at 700°C. The CuO powder was obtained after grinding.

CeO_2 was prepared by precipitation method (Zhao et al., 2014) and CuO/CeO_2 was prepared by ultrasonic impregnation method. As such, 2 g prepared CeO_2 powder was added to 20 mL 1 mol/L $Cu(NO_3)_2$ solution and impregnated for 30 min under 0.5 W/cm^3 ultrasound, and then the filtered solid particulars were calcined for 2 h at 450°C in muffle furnace to obtain CuO/CeO_2.

Characterization of CuO/CeO_2

The porosity and specific surface area of CuO/CeO_2 were characterized by N_2 adsorption-desorption test using 3H-2000PS2, BeiShiDe Instrument-S&T Company. CuO/CeO_2 morphology was recorded by SEM with energy dispersive spectroscopy (EDS) (Hitachi S 4700 SEM analyzer). The XRD patterns were carried out by Rigaku D/maxrc diffractometer. The HRTEM measurement was investigated by Thermo Scientific Dionex UltiMate 3000 instrument. The oxidation state of CuO/CeO_2 was characterized by XPS analysis (EScalab250Xi spectrometer), and the binding energies were calibrated by C 1s peak at 284.8 eV.

Diclofenac Removal Experiments

The operation processes of reactions were as follows: 50 mL diclofenac solution (20 mg/L) was added to a 150 mL beaker and adjusted to the desired pH using 1 mol/L NaOH and H_2SO_4 solutions. After that, certain dosages of CuO/CeO_2 and H_2O_2 were poured into the solution under continuous magnetic stirring. Finally, a small sample of the mixture was taken out by syringe at certain times and filtered by a 0.45 μm membrane filter. The filtered solution was measured by HPLC. The experiments were done in triplicate.

The diclofenac concentration in the experiment was analyzed by Thermo Scientific Dionex UltiMate 3000 liquid

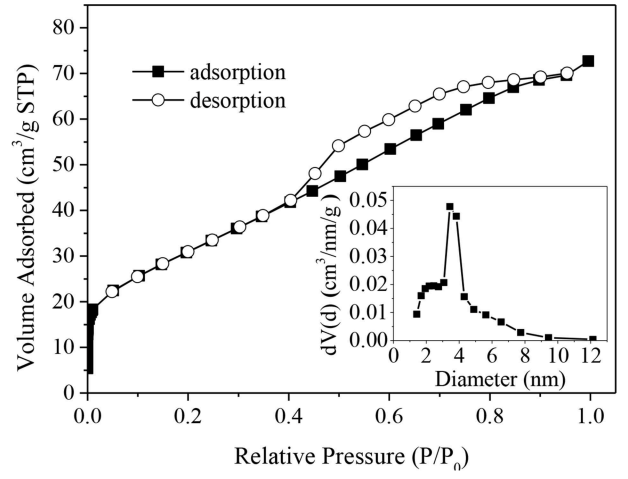

FIGURE 1 | N_2 adsorption-desorption isotherm and pore size distribution of CuO/CeO$_2$.

chromatographt with a C18 column. The operation parameters were as follows: the flowing phases were 70% acetonitrile and 30% acetic acid solution (volume fraction was 0.2%), the flow rate was 1 mL/min, the injection volume was 10 μL, and the detection wavelength was 275 nm. The leached metal ions were detected by inductively coupled plasma optical emission spectrometer (ICP-OES) (IRIS Intrepid II XSP, ThermoFisher).

RESULTS AND DISCUSSION

Catalyst Characterization

N_2 Adsorption-Desorption Analysis

Figure 1 shows the N_2 adsorption-desorption isotherm of CuO-CeO$_2$, which was typical type-IV isotherm with a H1-type hysteresis loop. This implied that mesoporous structure existed in the obtained CuO/CeO$_2$. The pore diameter distribution of CuO/CeO$_2$ was calculated from the adsorption branch and suggested the existence of mesopores at ∼10 nm with the average diameter 3.9 nm (the embedded diagram of **Figure 1**). **Table 1** summarized the basic structural parameters of CuO, CeO$_2$, and CuO/CeO$_2$. The specific surface area of CuO/CeO$_2$ reached 114.8 m^2/g which was higher than that of CuO and CeO$_2$, and was also much higher than that of other CuO-containing catalysts such as CuO/rGO (56.1 m^2/g) (Du et al., 2019) and CuO/Ti$_6$O$_{13}$ (6.93 m^2/g) (Sehati and Entezari, 2017). The high specific surface area allowed the rapid electron transfer (Prathap et al., 2012) and would benefit the catalytic performance of CuO/CeO$_2$. These results indicated that ultrasonic preparation might facilitate catalytic reaction by changing the surface structure of the catalyst. For one thing, the mechanical effect of ultrasound could cut CeO$_2$ into smaller particles increasing specific surface area. Furthermore, the ultrasonic cavitation effect made CuO more uniformly distributed on the surface of CeO$_2$. The decreases of pore volume and pore diameter after ultrasonic impregnation of CeO$_2$ (**Table 1**) exactly indicated that CuO was indeed loaded on CeO$_2$.

TABLE 1 | Basic structural parameters of CuO, CeO$_2$, and CuO/CeO$_2$.

Catalyst	Surface area (m^2/g)	Pore volume (cm^3/g)	Average pore diameter (nm)
CuO	0.5	1.9×10^{-3}	14.2
CeO$_2$	78.5	1.9×10^{-1}	9.4
CuO/CeO$_2$	114.8	1.1×10^{-1}	3.9

SEM Analysis

SEM was used to characterize the morphology of CuO/CeO$_2$, and the results were shown in **Figure 2**. **Figure 2A** shows an overview of CuO/CeO$_2$ in which the size of particles was uniform. CuO was finely loaded on CeO$_2$ (**Figure 2B**). Element mapping results of Cu, Ce, and O (**Figures 2D–F**) indicated that the three elements were all well-dispersed in the catalyst. To investigate how ultrasound affected the structure of catalyst, Mahdiani et al. (2018) prepared PbFe$_{12}$O$_{19}$ with and without ultrasound, and found that ultrasound could decompress the large structures and form fine and homogeneous structures. Thus, the fine dispersion of elements and uniform size of CuO/CeO$_2$ benefitted from the cavitation effect of ultrasound which created an intense environment in the reaction mixture (Shende et al., 2018). Moreover, Hočevar et al. (2000) showed that the high dispersion of Cu on CeO$_2$ had positive effect on the activity and selectivity of copper cerium oxide. The Cu, Ce, and O atomic percentages confirmed by EDS were 10.56, 18.07, and 71.37%, respectively. The lower content of Cu showed that the dispersion of Cu was relatively sparse.

XRD Analysis

XRD analysis was applied to identify the component and crystallography of the catalyst. The results were shown in **Figure 3**. The diffraction peaks at 28.46°, 32.9°, 47.44°, 56.24°, 76.260°, and 79.22° could be attributed to the cubic fluorite CeO$_2$ (JCPDS No. 48-1548), which are characteristics of the (111), (200), (220), (311), (400), and (331) crystal faces. There were also characteristic diffraction peaks owing to CuO crystal, and 35.46°, 38.66° were assigned to the (002) and (111) faces (JCPDS No. 04-0593). The characteristic diffraction peaks of CeO$_2$ in CuO/CeO$_2$ were slightly broadened compared with that in CeO$_2$. This might be associated with the incorporation of Cu^{2+} ions with a smaller ionic radius (0.73 Å) compared with Ce^{4+} (0.97 Å) (Cau et al., 2014). These phenomena indicated that lattice constriction occurred in CuO/CeO$_2$.

TEM and HRTEM Analyses

The TEM images of CuO/CeO$_2$ and CeO$_2$ were shown in **Figures 4A,C**. The particle size of CuO/CeO$_2$ was uniform, and was generally smaller than that of CeO$_2$, which was a favorable result of ultrasonic impregnation method and was good for catalytic reaction. The lattice fringes of CuO/CeO$_2$ were measured at 2.77 and 3.14 Å (**Figure 4B**), corresponding to (200) and (111) crystal faces. Compared with the two crystal faces of CeO$_2$ (**Figure 4D**), the lattice fringe spacing in CuO/CeO$_2$ had a slight increase. This phenomenon might be caused by some Cu atoms doped into CeO$_2$ structure. CuO/CeO$_2$ had lattice

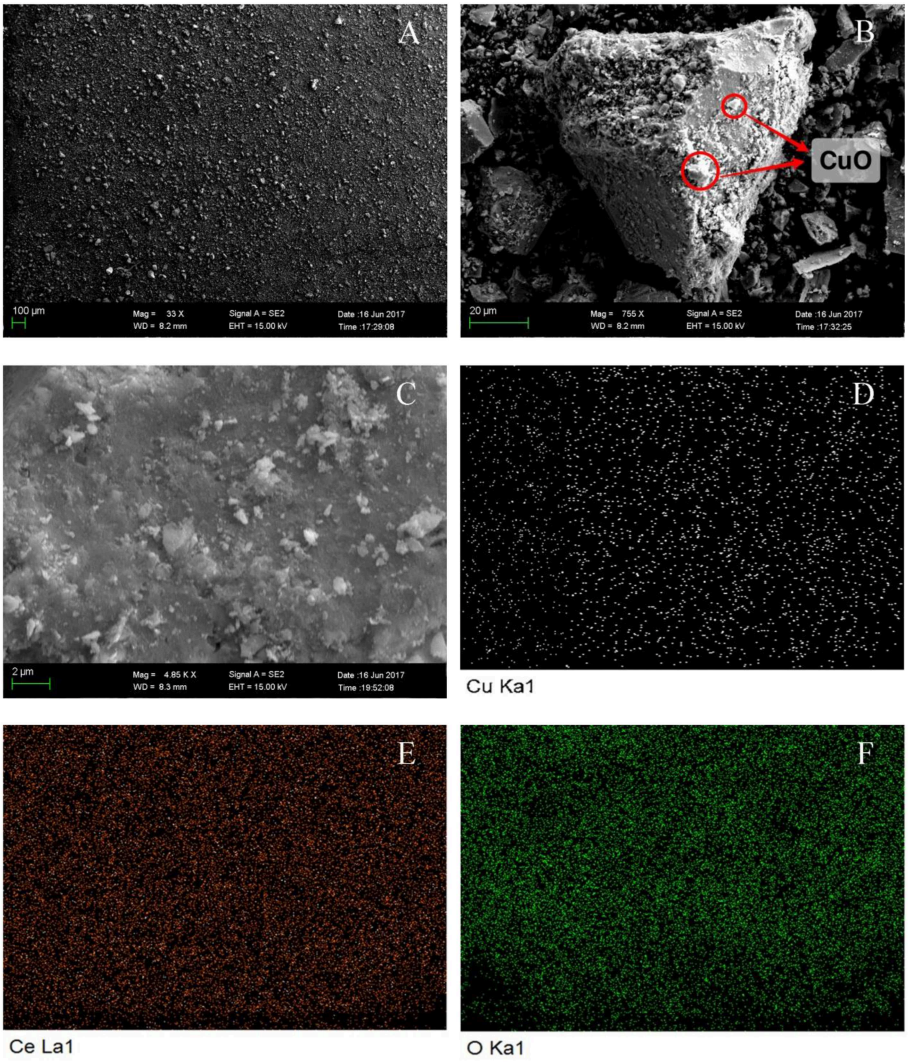

FIGURE 2 | SEM analysis of CuO/CeO_2: **(A)** general view, **(B)** detailed image, **(C)** mapping region, **(D)** Cu mapping image, **(E)** Ce mapping image, and **(F)** O mapping image.

constriction and generated a solid solution structure. The XRD analysis showed similar results.

The crystal face (111) of CeO_2 was the most stable crystal face in CeO_2 for its minimal surface energy. Thus, the stability of the catalyst would be enhanced with the increase of exposed crystal face (111). The catalytic activity could be improved by the crystal face (200) for its high surface energy. Moreover, oxygen vacancies were more favored to form on unstable face (200) than on (111). Thus, exposed (200) and (111) faces were beneficial to the catalytic performance and stability of CuO/CeO_2.

Raman Analysis

To investigate the effect of CuO doping on the quantities of oxygen vacancies over CuO/CeO_2, CuO/CeO_2, and CeO_2 were both characterized by Raman spectra. As shown in **Figure 5**, a strong peak at 462 cm^{-1} was observed, which was attributed to the vibration mode of the F2 g symmetry in cubic fluorite CeO_2 lattice. This peak of CuO/CeO_2 presented a red shift compared to pure CeO_2 because of the reduction in the lattice parameter as a result of shorter M-O bond length (Cau et al., 2014). The weak band at 1,172 cm^{-1} was assigned to the second-order phonon mode of fluorite structure. The band at 593 cm^{-1} was attributed to oxygen vacancies in CeO_2. With Cu doping into CeO_2, more oxygen vacancies were generated, which would promote the catalytic property of CuO/CeO_2.

XPS Analysis

The valence states of Cu, Ce, and O in CuO/CeO_2 were investigated by XPS analysis. **Figure 6A** shows the XPS spectrum of Cu 2p of CuO/CeO_2. The peak at 935.09 eV was the main peak of Cu $2p_{3/2}$, which was related to CuO (Jawad et al., 2018). CuO had a satellite peak accompanied by the main peak, which was approximately 9 eV higher binding energy than the main peak (Zeng et al., 2013). Thus, 944.27 eV was the satellite peak of CuO.

The XPS spectrum of Ce 3d is shown in **Figure 6B**. The four main $3d_{5/2}$ features appeared at 883.23, 885.2, 889.68, and 899.19 eV, while the $3d_{3/2}$ features appeared at 901.68, 903.38, 908.39, and 917.64 eV. Among them, the peaks at 883.23 and 901.68 eV were assigned to characteristic of Ce^{3+}, indicating that there were two valence states of Ce (+3 and +4) existed in CuO/CeO_2.

The O 1s XPS spectrum was shown in **Figure 6C**. O 1s existed in two groups, O^{2-} and OH^-, which were fitted with peaks at 529.89 and 532.12 eV, respectively. O^{2-} groups represented the lattice oxygen (O_{latt}) in metal oxides, generating from CuO and CeO_2. The peak at 532.12 eV was the characteristic of adsorbed oxygen species or surface OH species. The chemical adsorbed oxygen (O_{ads}) on the surface of CuO/CeO_2 might be transformed from O_{latt} through oxygen vacancies, which was a reactive oxygen specie to attack organics (Chong et al., 2017). This kind of conversion demonstrated that O_{latt} species participated in the degradation process of diclofenac, which was consistent with the study by Sedmak et al. (2003). Furthermore, XPS results indicated that CuO doped in CeO_2, which could improve the formation of O_{latt} in CuO/CeO_2 (Zou et al., 2011).

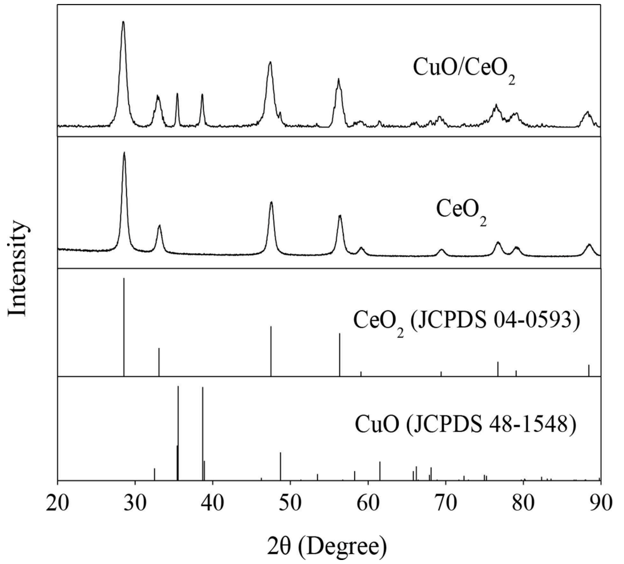

FIGURE 3 | XRD pattern of CuO/CeO_2.

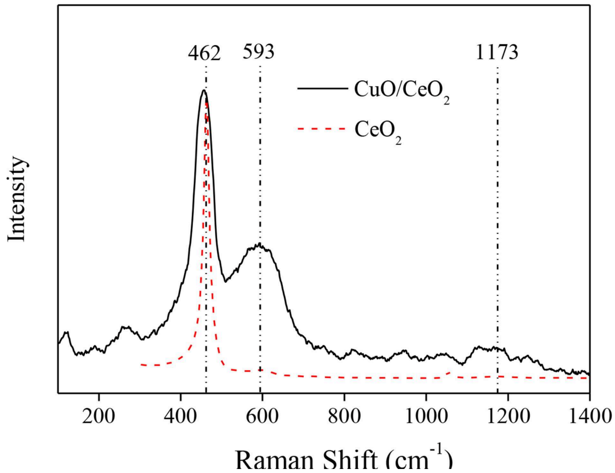

FIGURE 5 | Raman spectra of CuO/CeO_2 and CeO_2.

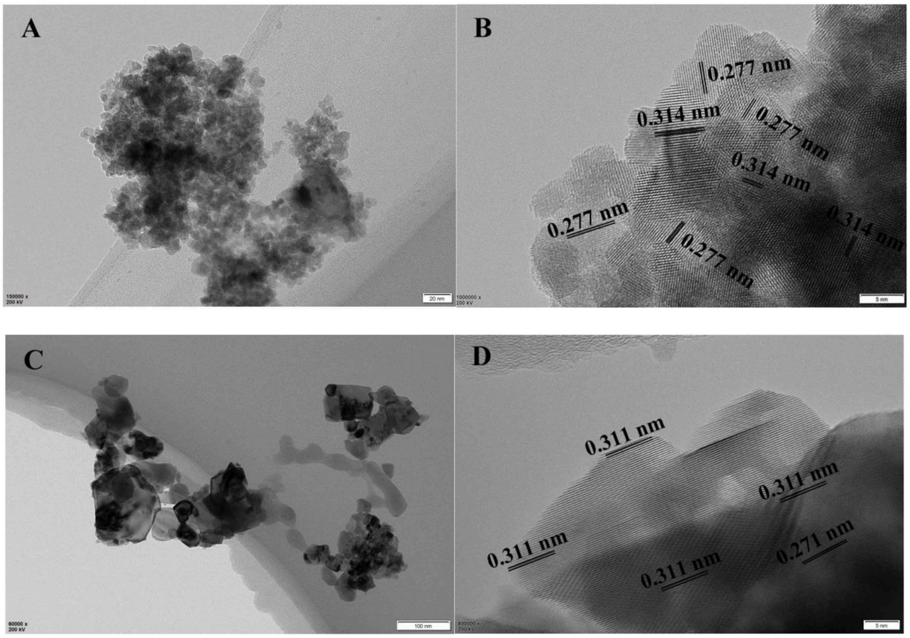

FIGURE 4 | (A) TEM and **(B)** HRTEM images of CuO/CeO_2, **(C)** TEM and **(D)** HRTEM images of CeO_2.

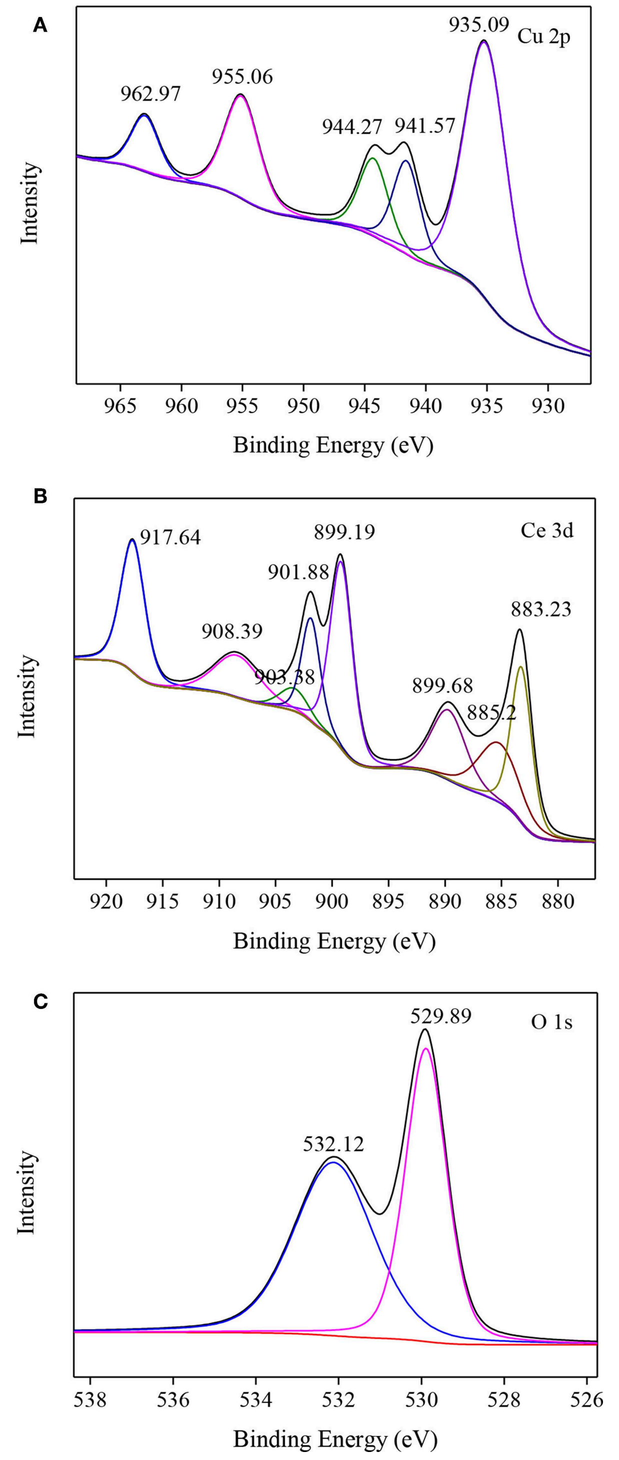

FIGURE 6 | XPS spectra of **(A)** Cu 2p, **(B)** Ce 3d, and **(C)** O 1s in CuO/CeO_2.

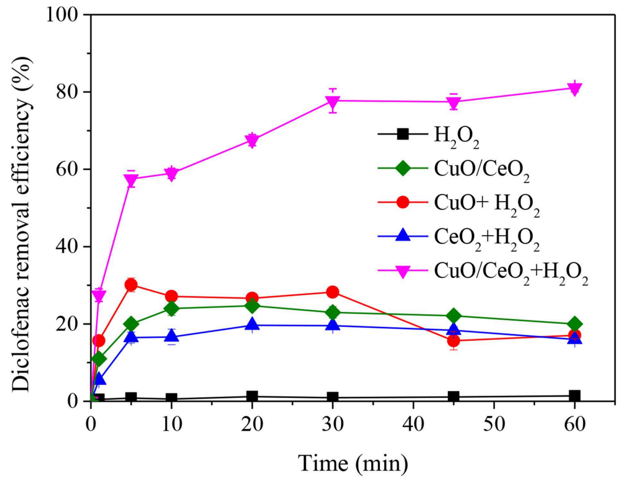

FIGURE 7 | Removal efficiency of diclofenac in different systems. Reaction conditions: pH = 5, H_2O_2 = 200 mg/L, catalyst = 1 g/L.

Diclofenac Removal in CuO/CeO_2-H_2O_2 Fenton-Like System

The comparison of diclofenac removal efficiency by H_2O_2, CuO/CeO_2, CuO-H_2O_2, CeO_2-H_2O_2, and CuO/CeO_2-H_2O_2 was shown in **Figure 7**. Single H_2O_2 and single CuO/CeO_2 could hardly remove diclofenac, the same for CuO-H_2O_2 and CeO_2-H_2O_2 system. However, CuO/CeO_2 could effectively catalyze H_2O_2 to remove diclofenac. The highest removal efficiency was 81.05, 30.01, and 19.67% for CuO/CeO_2-H_2O_2, CuO-H_2O_2 and CeO_2-H_2O_2 processes, respectively. Compared with CuO-H_2O_2 and CeO_2-H_2O_2 systems, diclofenac removal efficiency after 60 min in CuO/CeO_2-H_2O_2 system was increased by 63.99 and 65.05%, respectively.

Clearly, CuO/CeO_2-H_2O_2 system had higher diclofenac removal than the sum of CuO-H_2O_2 system and CeO_2-H_2O_2 system, showing a synergistic effect between CuO and CeO_2. The synergistic effect might be caused by two reasons. Firstly, more oxygen vacancies were formed for Cu doped in CeO_2, which was shown in the above characterization analyses. Lu et al. (2011) found that the formation energy of oxygen vacancy in Cu-doped ceria was lower than bare ceria, demonstrating that Cu dopant could serve as a seed for the formation of oxygen vacancies. Secondly, there were electronic interactions between metal and the support, i.e., the facilitation of redox interactions between Cu^{2+}/Cu^{+} and Ce^{4+}/Ce^{3+} redox couples, which would favor the CuO reduction (Konsolakis, 2016). Studies (Szabová et al., 2010, 2013) also reported that Cu doped on CeO_2 surface accompanied electron transfer process between Cu and neighboring Ce^{4+}, generating more Ce^{3+}.

Optimization of Operation Parameters for Diclofenac Removal

pH is an important parameter in AOPs. An advantage of Fenton-like process over Fenton reaction is avoiding of too acidic condition (pH < 3.5). As known, diclofenac was more likely to dissociate to ionic structure when the pH was higher than its pK_a (4.2), which was favorable to its adsorption and degradation. Thus, the effect of pH above 5 was investigated. As shown in **Figure 8A**, pH had a significant effect on diclofenac removal in CuO/CeO_2-H_2O_2 system, which decreased by 79.31% when the pH changed from 5 to 11. The result might attribute to two reasons: (1) the oxidation potential of ·OH decreased, and more H_2O_2 decomposed to O_2 and H_2O at high pH value; (2) deprotonation of the catalyst gradually increased, which was unfavorable to the electrostatic attraction between diclofenac and CuO/CeO_2 (Hassani et al., 2018).

Different dosages of CuO/CeO_2 were added to the Fenton-like system. **Figure 8B** shows that the diclofenac removal efficiency was improved from 25.21 to 86.62% when the catalyst dosage increased from 0.1 to 1.2 g/L. The active sites were mostly on the surface of the catalyst, so more catalyst meant that more active sites exposed. But when the active sites were adequate in CuO/CeO_2-H_2O_2 system, further addition of catalyst would bring little improvement. Thus, the optimum CuO/CeO_2 dosage was 1.2 g/L.

The effect of H_2O_2 on diclofenac removal was studied within the dosage of 25–500 mg/L. **Figure 8C** shows that with the continuous increase of H_2O_2 dosage, the removal efficiency of diclofenac reached 86.62% at 200 mg/L H_2O_2, then the reaction tended to stabilize. Excessive H_2O_2 reacted with ·OH, thus go against the diclofenac removal (Hassani et al., 2018). Taking into account the removal efficiency and cost, 200 mg/L was considered as the optimum dosage of H_2O_2.

Lee et al. (2014) found only about 24% diclofenac could be removed in 60 min by Cu(II)/H_2O_2 system. Xu et al. (2016) used Cu-doped α-FeOOH as Fenton-like catalyst to degrade diclofenac, <50% diclofenac was removed in 60 min. Zhou et al. (2018) found 80% diclofenac was removed in a magnetic field enhanced Fe^0/EDTA Fenton-like system. In comparsion, CuO/CeO_2 was a high-efficiency Fenton-like catalyst for diclofenac removal. Moreover, leaching test showed that there was almost no Ce leached (<0.05 mg/L) under the above optimal reaction conditions. The leached Cu concentration in the solution was 1.7 mg/L, which met the wastewater discharge standard of China ($Cu < 2\ mg\ L^{-1}$) (Wang et al., 2016) and was only 9‰ of the catalyst dosage. Besides, the removal of diclofenac still reached 70.12% in the third run of CuO/CeO_2-H_2O_2 system. These results showed a good stability and reusability of the CuO/CeO_2 catalyst.

Potential Mechanism of Diclofenac Degradation in CuO/CeO_2-H_2O_2 System

Potential mechanism of diclofenac degradation in CuO/CeO_2-H_2O_2 system was proposed in **Figure 9**. CuO could decompose H_2O_2 to form highly active ·OH (Drijvers et al., 1999), and the reaction was represented by Equations (1) and (2) (Yamaguchi et al., 2018). ·OH radical could also be produced by Ce^{3+} with H_2O_2, which was achieved by the division of O-O bond of H_2O_2, as shown in Equation (3) (Chong et al., 2017). Moreover, the synergistic copper and ceria interaction (Equation 4) facilitated the redox cycles of Cu^{2+}/Cu^{+} and further was conducive to ·OH generation (Konsolakis, 2016). Sehati and Entezari (2017) found that ·OH on the catalyst surface (·OH_{ads}) was the major reactive species, while ·OH in the solution had little effect on pollutant

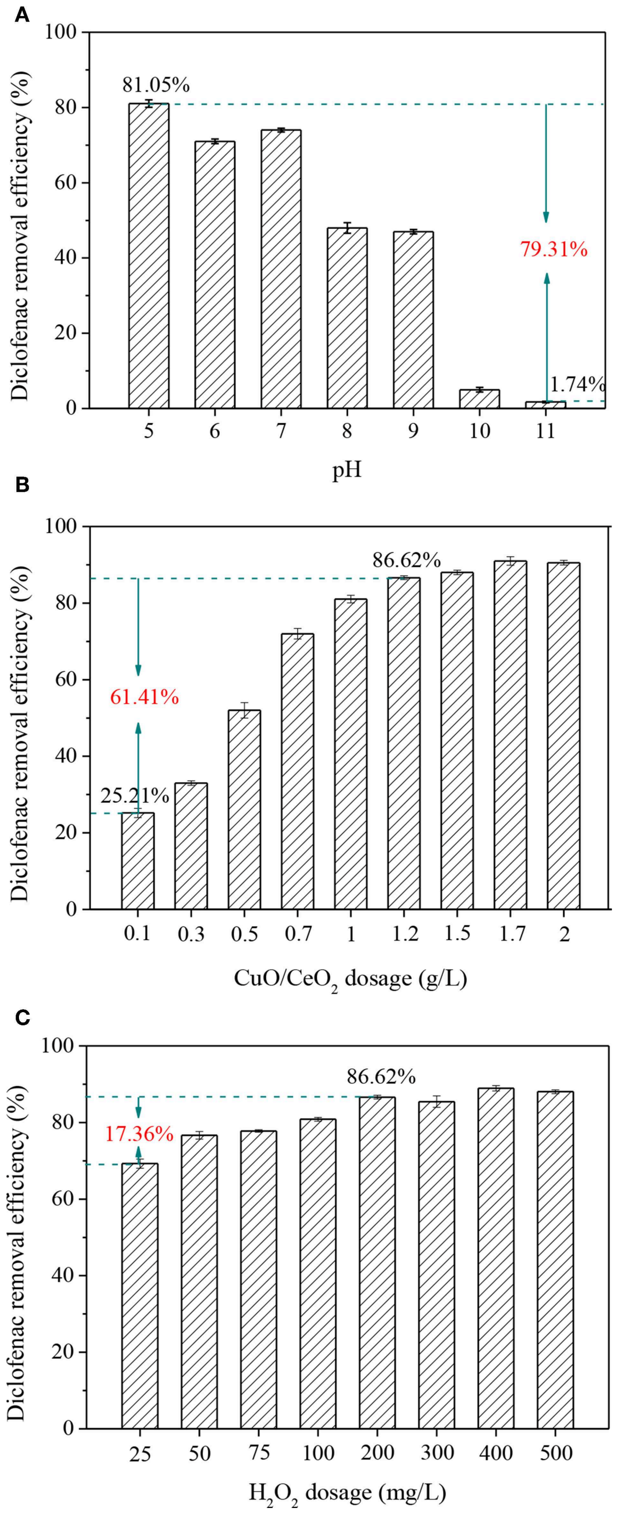

FIGURE 8 | Influencing factors of diclofenac removal in CuO/CeO_2-H_2O_2 system: **(A)** pH, **(B)** CuO/CeO_2 dosage, **(C)** H_2O_2 dosage. Reaction conditions: **(A)** H_2O_2 = 200 mg/L, catalyst = 1 g/L; **(B)** pH = 5, H_2O_2 = 200 mg/L; **(C)** pH = 5, catalyst = 1.2 g/L.

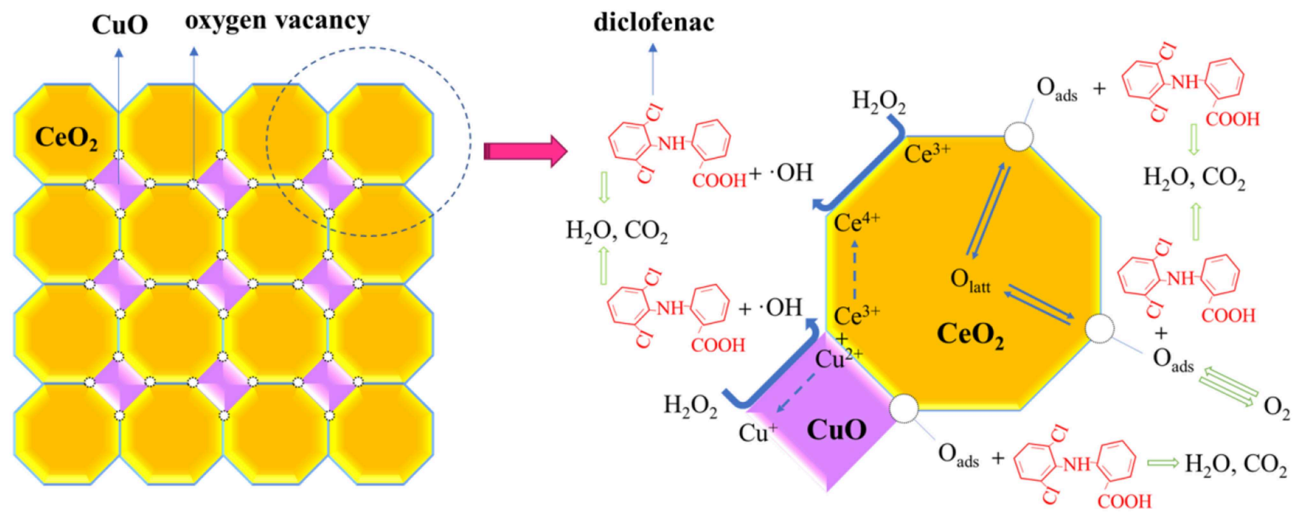

FIGURE 9 | Potential mechanisms of diclofenac degradation in CuO/CeO_2-H_2O_2 system.

removal in Fenton-like system. During diclofenac degradation, diclofenac molecules were adsorbed on the surface of the catalyst, meanwhile, H_2O_2 was decomposed to ·OH by Cu and Ce species on the catalyst surface. Then, the adsorbed diclofenac molecules reacted with $\cdot OH_{ads}$ and transformed into smaller molecules (intermediate products), H_2O or CO_2. The process continued until the complete decomposition of diclofenac was achieved (Ziylan et al., 2013).

$$Cu^{2+} + H_2O_2 \rightarrow Cu^{+} + \cdot OOH + H^{+} \tag{1}$$

$$Cu^{+} + H_2O_2 \rightarrow Cu^{2+} + \cdot OH + OH^{-} \tag{2}$$

$$Ce^{3+} + H_2O_2 + H^{+} \rightarrow Ce^{4+} + \cdot OH + H_2O \tag{3}$$

$$Cu^{2+} + Ce^{3+} \rightarrow Cu^{+} + Ce^{4+} \tag{4}$$

More oxygen vacancies were generated by Cu doped into CeO_2, which was proven by the Raman spectra (**Figure 5**). The oxygen storage capacity of a ceria-based catalyst benefited from oxygen vacancies (Soler et al., 2016). In the degradation process, the adsorbed O_2 on the surface of CuO/CeO_2 and bulk O_{latt} could replenish oxygen vacancies by diffusion from the surface and inner of the catalyst (Balcaen et al., 2010), then transformed to active oxygen (O_{ads}) accompanied by valence state transformation of CeO_2 and CuO (Ce^{3+}/Ce^{4+} and Cu^{+}/Cu^{2+}) (Dong et al., 2019). O_{ads} could also participate in the oxidation of diclofenac (Xian et al., 2019). Besides, large specific surface area and high porosity of ultrasonically prepared CuO/CeO_2 catalyst allowed rapid electron transfer, which improved the catalytic property (Prathap et al., 2012).

CONCLUSIONS

An efficient heterogeneous Fenton-like catalyst CuO/CeO_2 was synthesized by ultrasonic impregnation method and used to remove diclofenac from water. The prepared CuO/CeO_2 had large specific surface area, high porosity and fine elements dispersion. CuO and CeO_2 crystals coexisted in CuO/CeO_2 with a lattice constriction. HRTEM analysis demonstrated that the main exposed crystal faces of CeO_2 contained (200) face which readily formed oxygen vacancies and improved the catalytic property of CuO/CeO_2. Oxygen vacancies in CeO_2 were increased by Cu doping. The optimal operating conditions of CuO/CeO_2-H_2O_2 system were pH = 5, CuO/CeO_2 dosage = 1.2 g/L, and H_2O_2 dosage = 200 mg/L, with 86.62% diclofenac removal. The synergistic effect between CuO and CeO_2 on diclofenac removal might be caused by more oxygen vacancies generation and electronic interactions between Cu and Ce species in CuO/CeO_2. The degradation of diclofenac was mainly by ·OH and adsorbed oxygen species which were enhanced by oxygen vacancies.

DATA AVAILABILITY STATEMENT

All datasets generated for this study are included in the article/supplementary material.

AUTHOR CONTRIBUTIONS

GZ, GX, and JZ designed the experiments. GX, NZ, and JL performed the experiments. GZ and GX wrote the paper. GZ, GX, NZ, and JZ discussed the results and analyzed the data.

ACKNOWLEDGMENTS

The authors thank for the financial support from the National Natural Science Foundation of China (51778374) and National Water Pollution Control and Treatment Science and Technology Major Project of China (2018ZX07110003).

REFERENCES

Anipsitakis, G. P., and Dionysiou, D. D. (2004). Radical generation by the interaction of transition metals with common oxidants. *Environ. Sci. Technol.* 38, 3705–3712. doi: 10.1021/es035121o

Balcaen, V., Roelant, R., Poelman, H., Poelman, D., and Marin, G. B. (2010). TAP study on the active oxygen species in the total oxidation of propane over a CuO-CeO$_2$/γ-Al$_2$O$_3$ catalyst. *Catal. Today* 157, 49–54. doi: 10.1016/j.cattod.2010.02.048

Blanco, L., Hermosilla, D., Merayo, N., and Blanco, Á. (2016). Assessing the use of zero-valent iron microspheres to catalyze Fenton treatment processes. *J. Taiwan Inst. Chem. E* 69, 54–60. doi: 10.1016/j.jtice.2016.08.014

Bokare, A. D., and Choi, W. (2014). Review of iron-free Fenton-like systems for activating H$_2$O$_2$ in advanced oxidation processes. *J. Hazard. Mater.* 275, 121–135. doi: 10.1016/j.jhazmat.2014.04.054

Cau, C., Guari, Y., Chave, T., Larionova, J., and Nikitenko, S. I. (2014). Thermal and sonochemical synthesis of porous (Ce,Zr)O$_2$ mixed oxides from metal β-diketonate precursors and their catalytic activity in wet air oxidation process of formic acid. *Ultrason. Sonochem.* 21, 1366–1373. doi: 10.1016/j.ultsonch.2014.01.006

Chong, S., Zhang, G., Zhang, N., Liu, Y., Huang, T., and Chang, H. (2017). Diclofenac degradation in water by FeCeO$_x$ catalyzed H$_2$O$_2$: Influencing factors, mechanism and pathways. *J. Hazard. Mater.* 334, 150–159. doi: 10.1016/j.jhazmat.2017.04.008

Chong, S., Zhang, G., Zhang, N., Liu, Y., Zhu, J., Huang, T., et al. (2016). Preparation of FeCeO$_x$ by ultrasonic impregnation method for heterogeneous Fenton degradation of diclofenac. *Ultrason. Sonochem.* 32, 231–240. doi: 10.1016/j.ultsonch.2016.03.019

Dong, C.-D., Huang, C. P., Nguyen, T.-B., Hsiung, C.-F., Wu, C.-H., Lin, Y.-L., et al. (2019). The degradation of phthalate esters in marine sediments by persulfate over iron-cerium oxide catalyst. *Sci. Total Environ.* 696:133973. doi: 10.1016/j.scitotenv.2019.133973

Drijvers, D., Langenhove, H. V., and Beckers, M. (1999). Decomposition of phenol and trichloroethylene by the ultrasound/H$_2$O$_2$/CuO process. *Water Res.* 33, 1187–1194. doi: 10.1016/S0043-1354(98)00308-X

Du, X., Zhang, Y., Si, F., Yao, C., Du, M., Hussain, I., et al. (2019). Persulfate non-radical activation by nano-CuO for efficient removal of chlorinated organic compounds: reduced graphene oxide-assisted and CuO (001) facet-dependent. *Chem. Eng. J.* 356, 178–189. doi: 10.1016/j.cej.2018.08.216

Du, Y., Ma, W., Liu, P., Zou, B., and Ma, J. (2016). Magnetic CoFe$_2$O$_4$ nanoparticles supported on titanate nanotubes (CoFe$_2$O$_4$/TNTs) as a novel heterogeneous catalyst for peroxymonosulfate activation and degradation of organic pollutants. *J. Hazard. Mater.* 308, 58–66. doi: 10.1016/j.jhazmat.2016.01.035

Ghasemi, S., and Karimipour, A. (2018). Experimental investigation of the effects of temperature and mass fraction on the dynamic viscosity of CuO-paraffin nanofluid. *Appl. Therm. Eng.* 128, 189–197. doi: 10.1016/j.applthermaleng.2017.09.021

Gu, T., Dong, H., Lu, T., Han, L., and Zhan, Y. (2019). Fluoride ion accelerating degradation of organic pollutants by Cu(II)-catalyzed Fenton-like reaction at wide pH range. *J. Hazard. Mater.* 377, 365–370. doi: 10.1016/j.jhazmat.2019.05.073

Hassani, A., Celikdag, G., Eghbali, P., Sevim, M., Karaca, S., and Metin, O. (2018). Heterogeneous sono-Fenton-like process using magnetic cobalt ferrite-reduced graphene oxide (CoFe$_2$O$_4$-rGO) nanocomposite for the removal of organic dyes from aqueous solution. *Ultrason. Sonochem.* 40, 841–852. doi: 10.1016/j.ultsonch.2017.08.026

Hočevar, S., Krašovec, U. O., Orel, B., Arićo, A. S., and Kim, H. (2000). CWO of phenol on two differently prepared CuO-CeO$_2$ catalysts. *Appl. Catal. B Environ.* 28, 113–125. doi: 10.1016/S0926-3373(00)00167-3

Jawad, A., Lang, J., Liao, Z., Khan, A., Ifthikar, J., Lv, Z., et al. (2018). Activation of persulfate by CuO$_x$@Co-LDH: A novel heterogeneous system for contaminant degradation with broad pH window and controlled leaching. *Chem. Eng. J.* 335, 548–559. doi: 10.1016/j.cej.2017.10.097

Konsolakis, M. (2016). The role of Copper-Ceria interactions in catalysis science: Recent theoretical and experimental advances. *Appl. Catal. B Environ.* 198, 49–66. doi: 10.1016/j.apcatb.2016.05.037

Lee, H.-J., Lee, H., and Lee, C. (2014). Degradation of diclofenac and carbamazepine by the copper(II)-catalyzed dark and photo-assisted Fenton-like systems. *Chem. Eng. J.* 245, 258–264. doi: 10.1016/j.cej.2014.02.037

Lei, Y., Chen, C. S., Tu, Y. J., Huang, Y. H., and Zhang, H. (2015). Heterogeneous degradation of organic pollutants by persulfate activated by CuO-Fe$_3$O$_4$: mechanism, stability, and effects of pH and bicarbonate ions. *Environ. Sci. Technol.* 49, 6838–6845. doi: 10.1021/acs.est.5b00623

Li, J. X., Qin, Z. B., Li, Y. H., and Cui, G. H. (2018). Sonochemical synthesis and properties of two new nanostructured silver(I) coordination polymers. *Ultrason. Sonochem.* 48, 127–135. doi: 10.1016/j.ultsonch.2018.05.016

Lin, K.-S., Chowdhury, S., Yeh, H.-P., Hong, W.-T., and Yeh, C.-T. (2011). Preparation and characterization of CuO/ZnO–Al$_2$O$_3$ catalyst washcoats with CeO$_2$ sols for autothermal reforming of methanol in a microreactor. *Catal. Today* 164, 251–256. doi: 10.1016/j.cattod.2010.11.038

Lu, Z., Yang, Z., He, B., Castleton, C., and Hermansson, K. (2011). Cu-doped ceria: oxygen vacancy formation made easy. *Chem. Phys. Lett.* 510, 60–66. doi: 10.1016/j.cplett.2011.03.091

Mahdiani, M., Soofivand, F., and Salavati-Niasari, M. (2018). Investigation of experimental and instrumental parameters on properties of PbFe$_{12}$O$_{19}$ nanostructures prepared by sonochemical method. *Ultrason. Sonochem.* 40, 271–281. doi: 10.1016/j.ultsonch.2017.06.023

Mirtamizdoust, B., Travnicek, Z., Hanifehpour, Y., Talemi, P., Hammud, H., and Joo, S. W. (2017). Synthesis and characterization of nano-peanuts of lead(II) coordination polymer [Pb(qcnh)(NO$_3$)$_2$]$_n$ with ultrasonic assistance: a new precursor for the preparation of pure-phase nano-sized PbO. *Ultrason. Sonochem.* 34, 255–261. doi: 10.1016/j.ultsonch.2016.05.041

Nidheesh, P. V. (2015). Heterogeneous Fenton catalysts for the abatement of organic pollutants from aqueous solution: a review. *RSC Adv.* 5, 40552–40577. doi: 10.1039/C5RA02023A

Parvas, M., Haghighi, M., and Allahyari, S. (2014). Degradation of phenol via wet-air oxidation over CuO/CeO$_2$-ZrO$_2$ nanocatalyst synthesized employing ultrasound energy: physicochemical characterization and catalytic performance. *Environ. Technol.* 35, 1140–1149. doi: 10.1080/09593330.2013.863952

Peng, J., Zhang, C., Zhang, Y., Miao, D., Zhang, Y., Liu, H., et al. (2019). Enhanced Cu(II)-mediated fenton-like oxidation of antimicrobials in bicarbonate aqueous solution: kinetics, mechanism and toxicity evaluation. *Environ. Pollut.* 252, 1933–1941. doi: 10.1016/j.envpol.2019.05.148

Prathap, M. U., Kaur, B., and Srivastava, R. (2012). Hydrothermal synthesis of CuO micro-/nanostructures and their applications in the oxidative degradation of methylene blue and non-enzymatic sensing of glucose/H$_2$O$_2$. *J. Colloid Interf. Sci.* 370, 144–154. doi: 10.1016/j.jcis.2011.12.074

Raj, A. K. V., Prabhakar Rao, P., Sreena, T. S., and Aju Thara, T. R. (2017). Influence of local structure on photoluminescence properties of Eu$^{(3+)}$ doped CeO$_2$ red phosphors through induced oxygen vacancies by contrasting rare earth substitutions. *Phys. Chem. Chem. Phys.* 19, 20110–20120. doi: 10.1039/C7CP02741A

Rao, W., Lv, G., Wang, D., and Liao, L. (2018). Enhanced degradation of Rh 6G by zero valent iron loaded on two typical clay minerals with different structures under microwave irradiation. *Front. Chem.* 6:463. doi: 10.3389/fchem.2018.00463

Sedmak, G., Hočevar, S., and Levec, J. (2003). Kinetics of selective CO oxidation in excess of H$_2$ over the nanostructured Cu$_{0.1}$Ce$_{0.9}$O$_2$-y catalyst. *J. Catal.* 213, 135–150. doi: 10.1016/S0021-9517(02)00019-2

Sehati, S., and Entezari, M. H. (2017). Sono-incorporation of CuO nanoparticles on the surface and into the mesoporous hexatitanate layers: enhanced Fenton-like activity in degradation of orange-G at its neutral pH. *Appl. Surf. Sci.* 399, 732–741. doi: 10.1016/j.apsusc.2016.12.079

Shende, T. P., Bhanvase, B. A., Rathod, A. P., Pinjari, D. V., and Sonawane, S. H. (2018). Sonochemical synthesis of Graphene-Ce-TiO$_2$ and Graphene-Fe-TiO$_2$ ternary hybrid photocatalyst nanocomposite and its application in degradation of crystal violet dye. *Ultrason. Sonochem.* 41, 582–589. doi: 10.1016/j.ultsonch.2017.10.024

Silveira, J. E., Zazo, J. A., Pliego, G., Bidóia, E. D., and Moraes, P. B. (2015). Electrochemical oxidation of landfill leachate in a flow reactor: optimization using response surface methodology. *Environ. Sci. Pollut. Res.* 22, 5831–5841. doi: 10.1007/s11356-014-3738-2

Soler, L., Casanovas, A., Escudero, C., Perez-Dieste, V., Aneggi, E., Trovarelli, A., et al. (2016). Ambient pressure photoemission spectroscopy reveals the mechanism of carbon soot oxidation in ceria-based catalysts. *ChemCatChem* 8, 2748–2751. doi: 10.1002/cctc.201600615

Szabová, L., Camellone, M. F., Huang, M., Matolin, V., and Fabris, S. (2010). Thermodynamic, electronic and structural properties of Cu/CeO_2 surfaces and interfaces from first-principles DFT+U calculations. *J. Chem. Phys.* 133:234705. doi: 10.1063/1.3515424

Szabová, L., Skála, T., Matolínová, I., Fabris, S., Farnesi Camellone, M., and Matolín, V. (2013). Copper-ceria interaction: a combined photoemission and DFT study. *Appl. Surf. Sci.* 267, 12–16. doi: 10.1016/j.apsusc.2012.04.098

Wang, C., Wan, J., Ma, Y., and Wang, Y. (2016). Insights into the synergy of zero-valent iron and copper oxide in persulfate oxidation of Orange G solutions. *Res. Chem. Intermed.* 42, 481–497. doi: 10.1007/s11164-015-2035-0

Wang, X., Rodriguez, J. A., Hanson, J. C., Gamarra, D., Martínez-Arias, A., and Fernández-García, M. (2006). *In situ* studies of the active sites for the water gas shift reaction over Cu-CeO_2 catalysts: complex interaction between metallic copper and oxygen vacancies of ceria. *J. Phys. Chem. B* 110, 428–434. doi: 10.1021/jp055467g

Xian, G., Zhang, G., Chang, H., Zhang, Y., Zou, Z., and Li, X. (2019). Heterogeneous activation of persulfate by Co_3O_4-CeO_2 catalyst for diclofenac removal. *J. Environ. Manage.* 234, 265–272. doi: 10.1016/j.jenvman.2019.01.013

Xu, D., Lv, H., and Liu, B. (2018). Encapsulation of metal nanoparticle catalysts within mesoporous zeolites and their enhanced catalytic performances: a review. *Front. Chem.* 6:550. doi: 10.3389/fchem.2018.00550

Xu, J., Li, Y., Yuan, B., Shen, C., Fu, M., Cui, H., et al. (2016). Large scale preparation of Cu-doped α-FeOOH nanoflowers and their photo-Fenton-like catalytic degradation of diclofenac sodium. *Chem. Eng. J.* 291, 174–183. doi: 10.1016/j.cej.2016.01.059

Yamaguchi, R., Kurosu, S., Suzuki, M., and Kawase, Y. (2018). Hydroxyl radical generation by zero-valent iron/Cu (ZVI/Cu) bimetallic catalyst in wastewater treatment: heterogeneous Fenton/Fenton-like reactions by Fenton reagents formed in-situ under oxic conditions. *Chem. Eng. J.* 334, 1537–1549. doi: 10.1016/j.cej.2017.10.154

Yang, W., Li, D., Xu, D., and Wang, X. (2009). Effect of CeO_2 preparation method and Cu loading on CuO/CeO_2 catalysts for methane combustion. *J. Nat. Gas Chem.* 18, 458–466. doi: 10.1016/S1003-9953(08)60141-3

Zeng, S., Zhang, W., Śliwa, M., and Su, H. (2013). Comparative study of CeO_2/CuO and CuO/CeO_2 catalysts on catalytic performance for preferential CO oxidation. *Int. J. Hydrogen Energ.* 38, 3597–3605. doi: 10.1016/j.ijhydene.2013.01.030

Zhang, N., Zhao, H., Zhang, G., Chong, S., Liu, Y., Sun, L., et al. (2017). Preparation of a magnetic N-Fe/AC catalyst for aqueous pharmaceutical treatment in heterogeneous sonication system. *J. Environ. Manage.* 187, 201–211. doi: 10.1016/j.jenvman.2016.11.043

Zhao, H., Zhang, G., and Zhang, Q. (2014). MnO_2/CeO_2 for catalytic ultrasonic degradation of methyl orange. *Ultrason. Sonochem.* 21, 991–996. doi: 10.1016/j.ultsonch.2013.12.002

Zhou, T., Feng, K., Xiang, W., Lv, Y., Wu, X., Mao, J., et al. (2018). Rapid decomposition of diclofenac in a magnetic field enhanced zero-valent iron/EDTA Fenton-like system. *Chemosphere* 193, 968–977. doi: 10.1016/j.chemosphere.2017.11.090

Zhu, L., and Zhang, H. (2008). A novel method for the modification of zinc powder by ultrasonic impregnation in cerium nitrate solution. *Ultrason. Sonochem.* 15, 393–401. doi: 10.1016/j.ultsonch.2007.09.016

Zhu, Y., Zhu, R., Xi, Y., Zhu, J., Zhu, G., and He, H. (2019). Strategies for enhancing the heterogeneous Fenton catalytic reactivity: a review. *Appl. Catal. B Environ.* 255, 117739. doi: 10.1016/j.apcatb.2019.05.041

Ziylan, A., Koltypin, Y., Gedanken, A., and Ince, N. H. (2013). More on sonolytic and sonocatalytic decomposition of Diclofenac using zero-valent iron. *Ultrason. Sonochem.* 20, 580–586. doi: 10.1016/j.ultsonch.2012.05.005

Zou, H., Chen, S., Liu, Z., and Lin, W. (2011). Selective CO oxidation over CuO-CeO_2 catalysts doped with transition metal oxides. *Powder Technol.* 207, 238–244. doi: 10.1016/j.powtec.2010.11.005

Conflict of Interest: The authors declare that the research was conducted in the absence of any commercial or financial relationships that could be construed as a potential conflict of interest.

frontiers in Chemistry

ORIGINAL RESEARCH
published: 15 January 2020
doi: 10.3389/fchem.2019.00913

Enhanced As(III) and As(V) Adsorption From Aqueous Solution by a Clay Based Hybrid Sorbent

Rabelani Mudzielwana[1]*, *Mugera Wilson Gitari*[1] *and Patrick Ndungu*[2]

[1] Environmental Remediation and Nano Science, Department of Ecology and Resource Management, University of Venda, Thohoyandou, South Africa, [2] Department of Applied Chemistry, University of Johannesburg, Johannesburg, South Africa

In this study, a hybrid arsenic adsorbent was synthesized through intercalation inorganic and organic surfactant cations onto kaolin clay interlayers. The synthesized adsorbent was characterized X-ray fluorescence (XRF), Fourier Transform Infrared spectroscopy (FTIR), Scanning electron microscopy (SEM), and Brunauer-Emmett-Teller (BET). Batch studies were conducted to determine As(III) and As(V) removal capacity of hybrid sorbent synthesized. It is found that As(III) removal is optimum at pH range of 4-6 while As(V) removal is optimum at pH range 4-8. The data for adsorption kinetics fitted to pseudo second order model implying that adsorption of As(III) and As(V) is chemisorption. The isotherm studies showed a better fit to Langmuir isotherm model indicating that adsorption of both As(III) and As(V) occurred on a mono-layered surface. The maximum adsorption As(III) and As(V) capacity at room temperature as determined by Langmuir model were found to be 7.99 and 7.32 mg/g, respectively. Thermodynamic parameters, ΔG° and ΔH° were found to be negative indicating that adsorption process occurred spontaneously and exothermic. Inorgano-organo modified kaolin clay was successfully regenerated for up 7 adsorption-regeneration cycles using 0.01 M HCl as regenerant. This study concluded that hybrid sorbent synthesized in this study is suitable for arsenic removal from groundwater.

Keywords: arsenic removal, clay based hybrid sorbent, adsorption kinetics, adsorption isotherms, thermodynamics

OPEN ACCESS

Edited by:
Maria Graca Rasteiro,
University of Coimbra, Portugal

Reviewed by:
Nito Angelo Debacher,
Federal University of Santa Catarina, Brazil
Licínio Manuel Gando-Ferreira,
University of Coimbra, Portugal

****Correspondence:***
Rabelani Mudzielwana
mudzrabe@gmail.com

Specialty section:
This article was submitted to Green and Sustainable Chemistry, a section of the journal Frontiers in Chemistry

Received: *13 August 2019*
Accepted: *16 December 2019*
Published: *15 January 2020*

Citation:
Mudzielwana R, Gitari MW and Ndungu P (2020) Enhanced As(III) and As(V) Adsorption From Aqueous Solution by a Clay Based Hybrid Sorbent. Front. Chem. 7:913. doi: 10.3389/fchem.2019.00913

INTRODUCTION

Arsenic is a toxic element that is widely distributed in different matrixes within the natural environment. In groundwater, arsenic is mainly introduced through weathering of arsenic bearing rock minerals such as; arsenopyrite (FeAsS), realgar (AsS), cobaltite (CoAsS), and scorodite ($FeAsO_4.2H_2O$) (Smedley and Kinniburgh, 2002). Other anthropogenic activities such as; mining, burning of fossil fuel and agriculture also result in groundwater contamination by arsenic (Zhang et al., 2017). Arsenic occurs in both organic and inorganic form. The inorganic form of arsenic is dominantly found in water and it exist as arsenite [As(III)) and arsenate (As(V)] depending on oxidation state. The arsenate is found in oxidizing conditions while the arsenite is found under reducing conditions (Duker et al., 2005). Arsenite is highly toxic and mobile compared to arsenate (Qi et al., 2015).

Long term exposure to arsenic through drinking water is linked to arsenicosis disease which is manifested by different types of cancer, hypertension, neurological complications and cardiovascular disease (Bhowmick et al., 2018). More than 200 million cases of these diseases has been reported in countries like India, Bangladesh, Argentina, Taiwan, Mexico, and China where elevated concentration of arsenic has been reported (Bardach et al., 2015; Ghosh et al., 2019). The World Health Organization (WHO) has set the provisional guideline for arsenic in drinking water at 10 μg/L (WHO, 2017). Technologies such as precipitation and coagulation, oxidation, reverse osmosis, ion-exchange, and adsorption are generally used for removal of arsenic to acceptable levels (Ghosh et al., 2019). Amongst these technologies, adsorption is widely preferred due to its cost effectiveness, ease of operation and higher efficiency (Qi et al., 2015). Materials such as activated alumina, activated carbon, graphene oxides, clay soils, bone char, and granular ferric hydroxides have been evaluated for their efficiency toward arsenic removal. Although these materials have shown good potential for use in arsenic removal, not all of them can be regenerated effectively and some operate at a narrow pH level which limit their application.

Clay and their minerals are used in removal of arsenic and other contaminants from water because of their properties such as chemical and mechanical stability, higher cation/anion capacity, and higher surface area (Bhattacharyya and Gupta, 2008). Furthermore, their sorption efficiency may be enhanced through modification by high density inorganic polycations and organic surfactants (Gitari and Mudzielwana, 2018). Mishra and Mahato (2016) reported enhanced arsenic adsorption efficiency of bentonite clay modified using iron and manganese oxides while octadecyl benzyl dimethyl ammonium modified bentonite prepared by Su et al. (2011) also showed better As(III) and As(V) adsorption capacity as compared to bare bentonite. Inorgano-organo modified clay mineral has received greater attention from researchers due to their important features such as, possession of two sorption sites which in turn enhances the sorption capacity and also good settling property (Tiwari and Lee, 2012). However, most of the inorgano-organo modified clay adsorbent have shown better sorption efficiency toward As(V) as compared to As(III) which is highly mobile and toxic. Manganese and iron are closely related elements in terms of their chemical properties and occurs concurrently in nature. Manganese oxides are known for their ability to adsorb and oxidize As(III) to As(V) while Fe oxides have greater potential to adsorb As(V) species (Zhang et al., 2012). Therefore, the present investigation aims at developing a novel clay based hybrid adsorbent for As(III) and As(V) removal by modifying kaolin clay mineral with Fe-Mn oxides and HDTMA-Br cationic surfactant.

MATERIALS AND METHODS

Materials

Natural kaolin clay was collected from Limpopo, South Africa. $FeCl_3$, $MnCl_2.4H_2O$, NaOH, $AsNaO_2$, and $HAsNa_2O_4$ were purchased from Rochelle Chemicals & Lab Equipment CC, South Africa Ltd. Hexadecyltriammonium bromide (HDTMA-Br) was purchased from Merck chemicals, South Africa. All chemicals were of analytical grade and they were used without further purification. Milli-Q water (18.2 MΩ/cm) produced from Millipore system was used for rinsing and preparation of solutions.

Synthesis of Clay Based Hybrid Sorbent

Inorgano-organo hybrid clay based sorbent was synthesized as follows: 0.25 M $FeCl_3$ and 0.25 M $MnCl_2.4H_2O$ were prepared by dissolving a known amounts of $FeCl_3$ and $MnCl_2.4H_2O$ into 250 mL volumetric flasks. Extracts of the respective solutions were mixed at a volume ratio of 3:1 in 250 mL plastic bottle and 1 g of raw kaolin clay (RK) was added and soaked for 10 min. Thereafter, pH of the solution was adjusted to 8.5 by adding 10 mL of 2 M NaOH drop wise into each of the bottles to precipitate Fe^{3+} and Mn^{2+} into their respective oxides. Thereafter, 100 mL of 5 mM HDTMA-Br was added to the mixture and agitated for 60 min at 250 rpm and then aged for 62 h. After aging, the mixture was centrifuged at 3,000 rpm. Residues were washed with Milli-Q water to remove excess supernatants then oven dried for 12 h at 60°C. The modified clay was then milled to pass through 250 μm sieve and then stored in a zip lock plastic bag. The hybrid sorbent was then designated IOK.

Characterization

Handheld x-ray fluorescence (XRF, S1 titan 600, Bruker, Berlin, Germany) was used to determine the elemental composition, surface chemistry of the adsorbent was determined using Fourier Transform Infra-red spectrum-attenuation total reflectance (FTIR-ATR) (Bruker, Germany) at wavelength range 450 to 4,500 cm^{-1}. The pore size distribution, pore volume and surface area were determined using Barrett Joyner Halenda (BJH) (micrometrics ASAP 2020, Norcross, GA, USA) and Brunauer Emmett Teller (BET) (micrometrics Gemini 2375, Norcross, GA, USA) models, respectively. The morphology was determined using scanning electron microscopy (SEM) (Leo1450 SEM, Voltage 10 kV, working distance 14 mm, Ramsey, NJ, USA).

Batch Experiments

Stock solutions containing 1,000 mg/L As(III) and As(V) were prepared by dissolving an appropriate amounts of $AsNaO_2$ and $HAsNa_2O_4$ in Milli-Q water (18.2 MΩ/cm). Solutions were preserved through the addition of few drops of 3 M HNO_3. Appropriate dilutions were made from the stock solution to prepare working solutions. The adsorption kinetics were evaluated by varying time from 10 to 120 min. Adsorbent dosage of 0.1 g/100 mL and adsorbate concentration of 0.5 mg/L were used. To evaluate the adsorption isotherms, the initial concentration of As(III)/As(V) was varied from 0.5 to 30 mg/L and the adsorbent dosage of 0.1 g/100 mL and contact time of 60 min were maintained. The experiment was carried out at a temperature of 298, 323, and 343 K. The obtained data was used to evaluate the adsorption thermodynamics. The effect of initial pH was evaluated by varying solution pH from 2 to 12 using 0.01 M NaOH and 0.01 M HCl to adjust the pH. The initial adsorbate concentration of 0.5 mg/L, contact time of 60 min and adsorbent dosage of 0.1 g/100 mL were used. The influence of co-existing ions (F^-, Cl^-, NO_3^-, CO_3^{2-}, SO_4^{2-}, Mg^{2+}, and Ca^{2+}) was evaluated by spiking 5 mg/L of each co-existing ions in a solution containing 0.5 mg/L of As(III)/As(V). The adsorbent dosage of

TABLE 1 | Elemental composition of RK and IOK.

Oxides	RK (%w/w)	IOK (%w/w)
SiO_2	57.1	32.29
Al_2O_3	22.05	8.74
Fe_2O_3	3.88	9.31
MgO	0.57	0.74
MnO	0.02	1.23
CaO	0.95	0.21
K_2O	0.16	0.08
TiO_2	1.76	0.82
P_2O_5	0.02	0.012

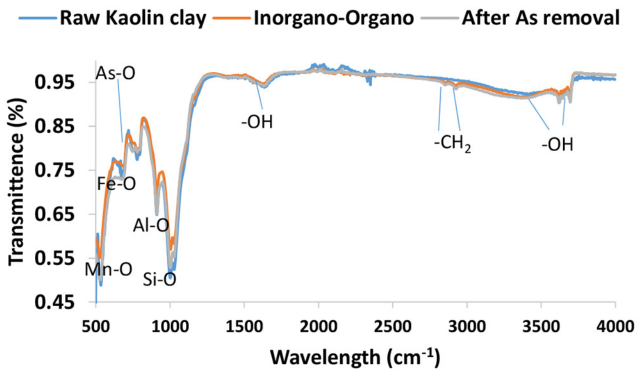

FIGURE 1 | FTIR spectrum of RK, IOK before and after arsenic adsorption.

0.1 g/100 mL and 60 min contact time were used. All experiments were conducted in triplicate and the mean values were reported. Unless otherwise stated, experiments were conducted at room temperature and initial pH of 6 ± 0.5.

Adsorbent Regeneration-Reuse Cycles

To evaluate the regeneration and reuse potential of the adsorbent, As(III)/As(V) removal experiment was conducted by treating solution containing 0.5 mg/L As(III)/As(V) with 1.0 g of IOK at initial pH of 6 for 60 min. After agitation, mixtures were filtered through 0.45 μm filter membranes and the residuals of As(III) and As(V) were analyzed. Residues were washed with Milli-Q water and oven dried for 12 h at 60°C and then regenerated using 100 mL of 0.01 M HCl by agitating the mixture for 60 min. The obtained residues were rinsed with excess of Milli-Q water and oven dried for 12 h at 60°C. Thereafter, they were pulverized with a mortar and pestle to pass through 250 μm sieve. After regeneration, As(III)/As(V) removal experiment was conducted as in other experiments. The regeneration-reuse cycle were continued up to 7th cycle.

Analysis of Residual Arsenic

The residual As(III)/As(V) concentration was measured using ScTRACE Gold electrode attached to 884 professional VA Polarography (Metrohm, SA). A composite solution containing 1 mol/L sulfamic acid, 0.5 mol/L citric acid and 0.45 mol/L KCl was used an electrolyte. For total As concentration, $KMnO_4$ was added as an oxidizing agent.

RESULTS AND DISCUSSION

Physicochemical Characterization

Elemental Composition

Table 1 present a comparison of the elemental composition between the RK and IOK. It is observed that SiO_2 and Al_2O_3 are major oxides the kaolin clay mineral. After modification their contents of reduced from 57.1 and 22.05% to 32.29 and 8.75%, respectively. Conversely, Fe_2O_3 and MnO increased from 3.88 and 0.02% to 9.31 and 1.23%, respectively.

FTIR Analysis

Figure 1 presents the FTIR spectrum of RK, IOK before and after arsenic removal. The bands at 3,453 and 1,645 cm^{-1} are ascribed to the vibration and stretching of hydroxyl groups and water molecules within the clay interlayers. The prominent IR peaks at wavelength region of 1,030 cm^{-1} could be due to the vibration of Si-O bonds. The bands at 906, 790, and 540 cm^{-1} could be due to the vibration of Al-O, Mn-O, and Fe-O, respectively. After modification by new bands were observed at 2,930 and 2,846 cm^{-1} indicating the presence of $–CH_2$ bonds which confirm the introduction of HDTMA-Br within the clay interlayers (Thanhmingliana and Tiwari, 2015). Furthermore, the intensity of bands at 1030, 906, 790, and 540 cm^{-1} increased. This could be attributed to increased concentration of Fe_2O_3 and MnO contents as confirmed by XRF analysis. After arsenic removal a new band was observed at 778 cm^{-1} which could be ascribed to As-O bond. The intensity of bands at other wavelength ranges decreased after arsenic removal. This confirms the ion exchange between the hydroxyl groups in the clay interlayers and arsenic species and surface complexation between arsenic and Fe, Mn, Al, and other metals in the surface of the clay minerals.

Morphological Analysis

Figure 2 presents the SEM micrographs of RK and IOK. No significant difference observed in the raw and modified kaolin clay mineral. The raw kaolin clay mineral has spongy like rough and porous surface with some irregular shapes. After modification, micrographs shows larger pores. This could be attributed to swelling and expansion of the clay interlayers during modification. The SEM-EDS spectrums of RK shows the presence of Fe, Al, Si, Mg, Ti, K Ca, and C. The spectrum of IOK showed a new peak showing Mn was observed.

Surface Area Analysis

The surface area and pore analysis are summarized in **Table 2**. It is noted that the total BET surface area of kaolin clay increased from 19.02 to 87.51 m^2/g after modification with Fe^{3+} and Mn^{2+} polycations and HDTMA surfactant. Furthermore, the pore volume increased from 0.04 to 0.09 cm^3/g after modification. The increase in surface area and pore volume could provide more active sites for sorption of ions leading to higher sorption capacity. The average pore size decreased from 9.54 to 4.68 nm after modification. The pore

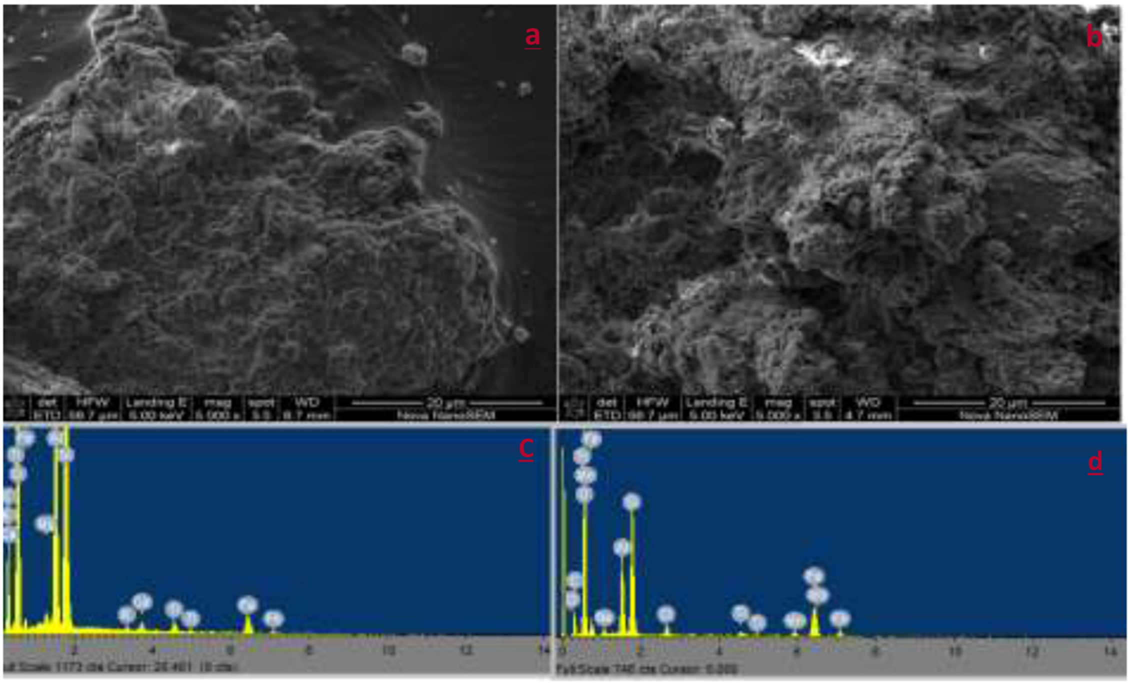

FIGURE 2 | SEM micrographs and SEM-EDS spectrum of RK **(a,c)** and IOK **(b,d)**.

TABLE 2 | Surface area and pore analysis.

	Surface area (m^2/g)	Pore volume (cm^3/g)	Pore diameter (nm)
RK	19.02	0.04	9.54
IOK	87.51	0.09	4.68

diameter within 2 and 50 nm indicates mesopore nature of the material.

Batch Experiments

Effect of pH

The effect of pH in As(III) and As(V) removal is presented in **Figure 3A**. The percentage As(V) removal was optimum at pH between 4 and 8 while adsorption of As(III) was optimum at pH range 4 to 6. Arsenic species exist in different forms under various pH levels and its adsorption is influences by the net surface charges. Therefore, to further elucidate the behavior of As(III) and As(V) at various pH levels the pH point of zero charge (pHpzc) of the material was determined using titration method. The results showed that the hybrid material prepared in this study has pHpzc of 8 ± 0.5 (**Figure 3B**). The material carries net positive charges at pH below pHpzc and net negative charges at pH above pHpzc. **Table 3** depicts different speciation of arsenic determined using Visual MINTEQ Version 3.0 at different equilibrium pH levels. Therefore, the decrease in percentage arsenic removal at strong alkaline pH where the surface is negatively charged, could be attributed to electrostatic repulsion since both As(III) and As(V) exist as negatively charged species such as $HAsO_4^{2-}$, AsO_4^{3-}, $H_2AsO_3^-$, and $HAsO_3^{2-}$. The decrease as the pH goes to 2 could be attributed to the fact that these species exist as neutrally charged H_3AsO_4 and H_3AsO_3 making it difficult to remove via electrostatic attraction to positively charged surface (Lee et al., 2015). Equation 1 to 5 hypothesizes the adsorption of As(III) and As(V).

$$\equiv MOH + H_3As_3 \leftrightarrow \equiv MH_2As_3 + H_2O \tag{1}$$

$$\equiv MOH + H_2As_3^- \leftrightarrow \equiv MHAs_3^- + H_2O \tag{2}$$

$$\equiv MOH + H_3AsO_4 \leftrightarrow \equiv MH_2AsO_4 + H_2O \tag{3}$$

$$\equiv MOH + H_2AsO_4^- \leftrightarrow \equiv MHAsO_4^- + H_2O \tag{4}$$

$$\equiv MOH + HAs_4^{2-} \leftrightarrow \equiv MAs_4^{2-} + H_2O \tag{5}$$

Adsorption Kinetics

Adsorption kinetics studies were performed in order to predict the rate of adsorption and to give insight in the rate limiting factor and the adsorption mechanism. **Figures 4A,B** presents the variation of As(III) and As(V) adsorption capacity with time. The adsorption capacity increased rapidly within the first 40 min and then proceed at slow rate up to 120 min suggesting that the system has reached equilibrium. The same trend was observed for arsenic species.

The pseudo first and second order of reaction kinetics models were used to predict the rate and the mechanism of As(III) and As(V) adsorption onto Inorgano-organo modified kaolin clay mineral. The mathematical representation of the models are depicted in equation 1 and 2, respectively (Qi et al., 2015; Munagapati and Kim, 2017).

$$q_t = q_e(1 - e^{-k_1 t}) \quad (1)$$

$$q_t = \frac{q_e^2 k_2 t}{1 + k_2 q_e t} \quad (2)$$

Where q_e and q_t are the adsorption capacities (mg/g) of the sorbent at equilibrium and at any given time, t (min), respectively; K_1 (min^{-1}) and K_2 (g/mg.min) are the pseudo first order and second order rate constants for adsorption processes, respectively. The initial adsorption rate, h (mg/g.min^{-1}) was determined based on the value of qe^2 (mg/g) and K_2 (g/mg.min) from the pseudo second order model. The non-linear plots for As(III) and As(V) are presented in **Figures 4A,B**, respectively, while the constants parameters are presented in **Table 4**.

The R^2-values for pseudo second order for As(III) and As(V) were found to be 0.94 and 0.98, respectively higher than those pseudo first order (0.70 and 0.80). The values for theoretical adsorption capacity of pseudo second order were found to be higher compared to those from pseudo first order (**Table 4**). This implies that the adsorption data fitted better to pseudo second order of reaction kinetics. Better fitting to pseudo second order suggests the dominance of chemisorption during the adsorption of As(III) and As(V) onto the hybrid adsorbent.

To further elucidate the rate limiting steps, the adsorption kinetics data was fitted to intra-particle diffusion model of Weber Morris (Weber and Morris, 1963). Equation (3) presents the linearized form of intra-particle diffusion model.

$$q_t = k_i t^{0.5} + C \quad (3)$$

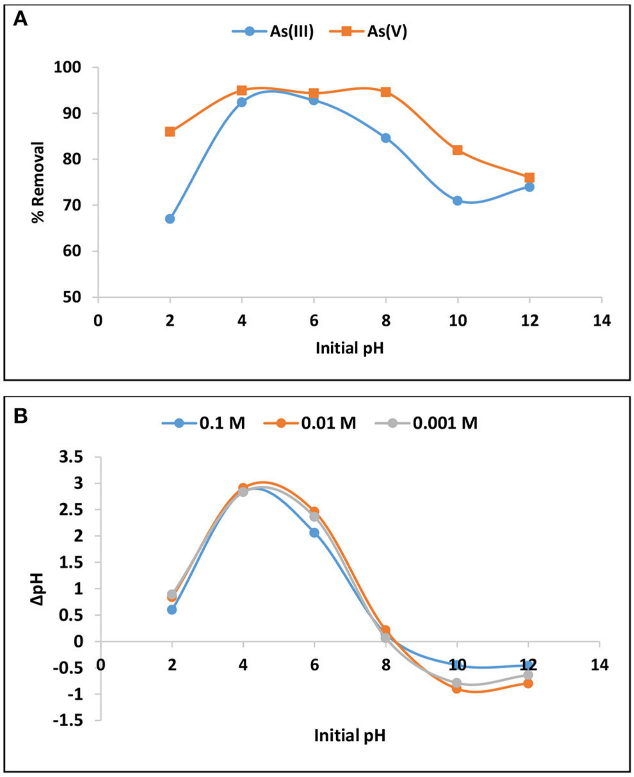

FIGURE 3 | **(A)** Variation of As(III) and As(V) percentage removal with initial pH and **(B)** point of zero charge (pHpzc).

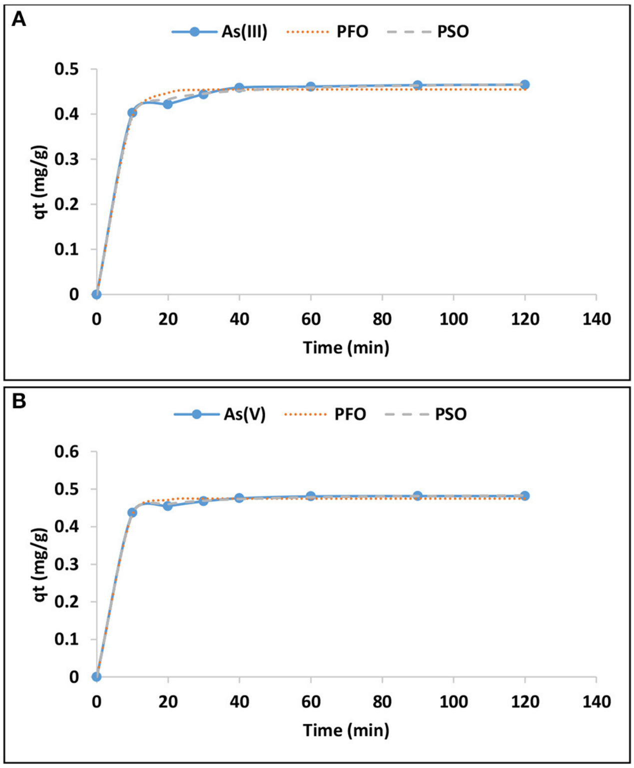

FIGURE 4 | Variation of adsorption capacity of As(III) **(A)** and As(V) **(B)** with time and adsorption kinetics (0.1 g/100 mL adsorption dosage, 0.5 mg/L adsorbate concentration, pH 6.5 ± 0.2).

TABLE 3 | Arsenic species at different equilibrium pH levels.

Eq. pH	H_3AsO_4	$H_2AsO_4^-$	$HAsO_4^{2-}$	AsO_4^{3-}	H_3AsO_3	$H_2AsO_3^-$	$HAsO_3^{2-}$
3.62	4.50	95.44	0.042	–	100.00	–	–
6.41	–	78.92	21.07	–	99.82	0.174	–
6.96	–	51.25	48.78	–	99.38	0.61	–
7.02	–	47.78	52.21	–	99.29	0.76	–
9.46	–	0.32	99.17	0.47	33.67	66.31	–
11.53	–	–	59.38	40.61	0.41	99.27	0.30

TABLE 4 | Parameters for pseudo first and second order reactions.

	Pseudo first order			Pseudo second order			
	q_e (mg/g)	K_1 (min^{-1})	R^2	q_e (mg/g)	K_2 (g/mg.min)	h (mg/g.min^{-1})	R^2
As(III)	0.45	0.20	0.70	0.47	1.12	0.26	0.94
As(V)	0.47	0.24	0.80	0.48	1.67	0.38	0.98

TABLE 5 | Constant parameters for Weber-Morris intra-particle model.

	Phase 1			Phase 2		
	K_1	C_1	R^2	K_2	C_2	R^2
As(III)	0.013	0.39	0.99	0.0012	0.47	0.97
As(V)	0.017	0.34	0.97	0.0014	0.44	0.70

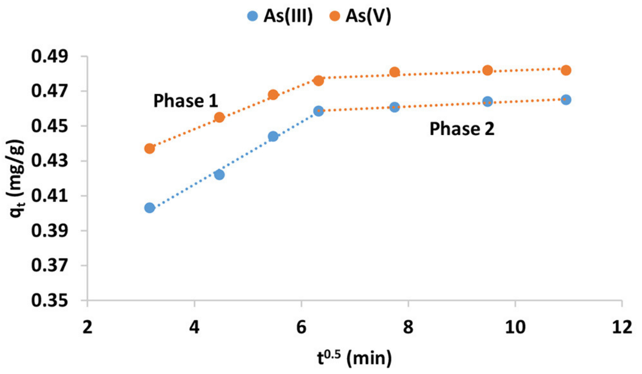

FIGURE 5 | Weber-Morris intra-particle plot for As(III) and As(V) adsorption onto IOK.

Where q_t (mg/g) is the adsorption capacity at a given time, t (min); K_i is the rate of intra-particle diffusion model C (mg/g) is the constant associated with the thickness of the boundary layer. If the plot of q_t against $t^{0.5}$ is linear or passes through origin, the adsorption is solely governed by intra-particle diffusion. However, if the plot yields two or more linear plots, then adsorption is governed by both surface and intra-particle diffusion. The intra-particle plot and the constant parameters for adsorption of As(III) and As(V) is presented in **Figure 5** and **Table 5**, respectively.

The plot (**Figure 5**) for both species yielded bilinear plots indicating that adsorption of As(III) and As(V) by synthesized adsorbent is a complex process involving both physical and chemical interactions between the adsorbate and the adsorbent. Ryu et al. (2017) observed the same trend during adsorption of As(III) and As(V) onto Fe-Mn modified activated carbon. Phase 1 the film diffusion leading to physiosorption wherein As(III) and As(V) ions are attracted to the boundary layer of the adsorbent through electrostatic attraction forces. Phase 2 reflects the intra-particle diffusion wherein As(III) and As(V) ions diffuse into the pores of the adsorbent leading to chemisorption. This phase involves ion exchange between the hydroxyl ions and arsenic species and weak hydrogen bonding. The rate constant for surface adsorption at phase 1 was found to be higher than the adsorption rate at phase 2 (**Table 5**). This suggest that intra-particle diffusion is a slower process compared to surface adsorption. This results suggest that adsorption of As(III) and As(V) is a complex process involving both surface and intra-particle diffusion.

Adsorption Isotherms

The adsorption isotherms were evaluated by varying the initial adsorbate concentration from 0.5 to 30 mg/L. The experiment was conducted at 298, 323, and 343 K. The results are presented in **Figures 6A,B** in terms of equilibrium concentrations against adsorption capacity. As expected, the adsorption capacity increases with increasing equilibrium As(III) and As(V) concentration. Furthermore, the adsorption capacity increased with increasing temperature. Equations (4) and (5) of Langmuir and Freundlich adsorption isotherms, respectively, were used to explain the relationship between the adsorbent and the adsorbate (Tran et al., 2016).

$$q_e = \frac{q_{\max} b C_e}{1 + bC_e} \tag{4}$$

$$q_e = K_f C_e^{1/n} \tag{5}$$

Where q_e (mg/g) is the adsorption capacity, C_e (mg/L) is the As(III) and As(V) concentration at equilibrium, b (L/mg) and q_{max} (mg/g) are Langmuir constants related to equilibrium adsorption constant and maximum monolayer adsorption capacity. K_f (mg/g) and 1/n are Freundlich constant values related to adsorption capacity and adsorption intensity, respectively. The nonlinear plots of Langmuir and Freundlich isotherms are presented in **Figures 6A,B** for As(III) and As(V), respectively while the models constant parameters are presented in **Table 6**.

The adsorption isotherm data for As(III) and As(V) adsorption onto IOK was described by Langmuir isotherm model rather than Freundlich isotherm model. This suggest that the adsorption of As(III) and As(V) occurred on a mono-layered surface. The maximum theoretical adsorption capacities for As(III) were found to be 7.99, 9.88, and 12.15 mg/g at 298, 323, and 343 K, respectively while for As(V) adsorption capacities were found to be 7.32, 8.36, and 9.45 mg/g at these temperature ranges (**Table 6**). Conversely, the experimental adsorption capacities for As(III) at 298 and 323 K were found to be lower than those reported at the same temperature ranges for As(V).

Adsorption Thermodynamics

To further elucidate the adsorption mechanisms, thermodynamics parameters such as Gibbs energy change (ΔG°), the enthalpy change (ΔH°), and the entropy (ΔS°) were determined from Equations (6) and (7) (Singh et al., 2016).

$$\Delta G^{\circ} = -RT \ln K_c \tag{6}$$

$$\ln K_L = -\frac{\Delta H^{\circ}}{\Delta RT^{\circ}} + \frac{S}{R} \tag{7}$$

Where R is the molar gas constant, 8.314 J.mol^{-1}K^{-1}, T is the absolute temperature in Kelvin, ΔG° (KJ/mol) is the Gibbs free energy change. ΔH° (J/mol) is enthalpy change, ΔS° (J/mol) is the change in entropy and K_c is the dimensionless parameter derived from the Langmuir adsorption constant, b (L/mg) by multiplying b by the molecular weight of the adsorbate (Mw; g/mol), by 1,000 and then by 55.5 (number of moles of pure water per liter) (Tran et al., 2017). Values ΔH° and ΔS° of are determined from the slope and intercept of a plot of lnK_c against 1/T (**Figure 7**). The thermodynamic parameters are shown in **Table 7**.

The value of enthalpy of change (ΔG°) for the adsorption of As(III) and As(V) onto Inorgano-organo modified kaolin clay mineral was found to be negative at both initial temperatures. This suggest that adsorption of As(III) and As(V) occurred spontaneously. The ΔH° value was found to be negative which indicating exothermic nature of the adsorption process. Exothermic reactions involves both physiosorption and chemisorption processes (Tran et al., 2016). The positive value of

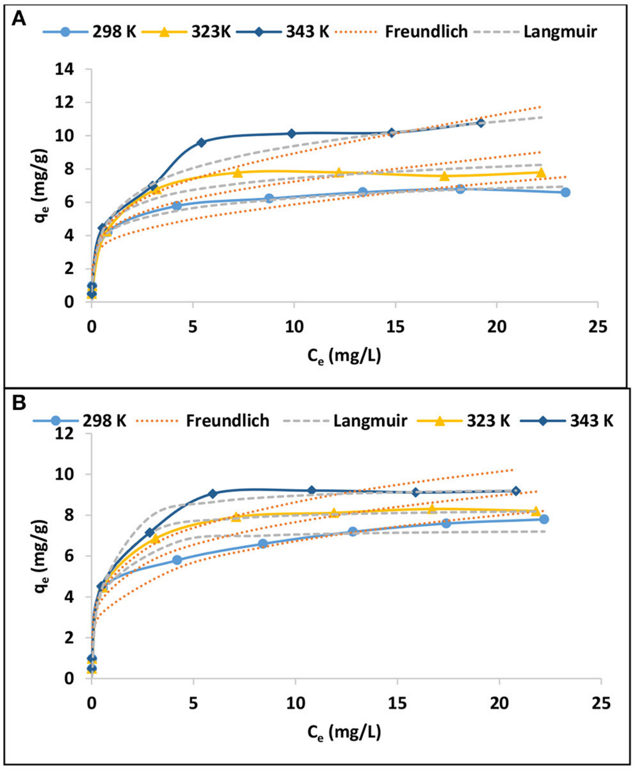

FIGURE 6 | Adsorption isotherms for **(A)** As(III) and **(B)** As(V) (0.1 g/100 mL adsorbent dosage, 0.5–30 mg/L initial concentration, 60 min contact time, pH 6.5 ± 0.2).

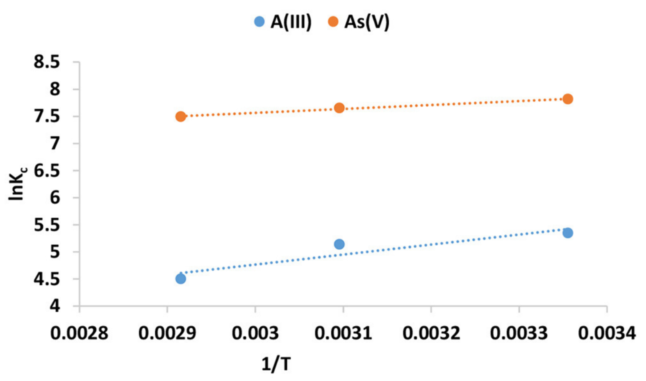

FIGURE 7 | lnK_c as a function of reciprocal of adsorption temperature.

TABLE 7 | Thermodynamics parameters for As(III) and As(V) adsorption by IOK.

	ΔG° (KJ/mol)	ΔH° (KJ/mol)	ΔS° (J/mol)
As(III)	298 K = −13.27 323 K= −13.79 343 K= −12.83	−15.35	6.4
As(V)	298 K= −19.36 323 K= −20.54 343 K= −21.35	−6.09	44.57

TABLE 6 | Langmuir and Freundlich adsorption isotherm parameters.

			Langmuir			Freundlich		
		$q_{e\ exp}$ (mg/g)	q_m (mg/g)	b (L/mg)	R^2	K_f (mg/g)	1/n	R^2
As(III)	298 K	6.79	7.99	0.21	0.98	1.88	0.4	0.90
	323 K	7.79	9.8	0.17	0.97	2.15	0.42	0.89
	343 K	10.77	12.15	0.09	0.99	1.96	0.52	0.95
As(V)	298 K	7.79	7.32	2.48	0.96	3.76	0.25	0.93
	323 K	8.2	8.36	2.10	0.99	4.52	0.22	0.93
	343 K	9.18	9.45	1.78	0.98	5.07	0.23	0.93

ΔS° suggest that As(III) and As(V) were randomly distributed on the surface of the adsorbent.

Effect of Co-existing Ions

Figure 8 depicts the influence co-existing anions in adsorption of As(III) and As(V) by IOK. It is observed that the presence of Ca^{2+} and Mg^{2+} slightly increases the adsorption As(III) and As(V). This could be an indication that the presence of Ca^{2+} and Mg^{2+} makes the surface of the adsorbent to be more positively charged which consequently facilitate the attraction of As(III) and As(V) onto the created sorption sites (Qi et al., 2015). The presence of co-existing anions slightly inhabited the sorption As(III) and As(V). The adsorption of As(III) decreased significantly in the presence of carbonates while the adsorption of As(V) decreased significantly in the presence of sulfate. The decrease in percentage removal in the presence of anions could be attributed to competition for adsorption sites between the co-existing anions and arsenic species.

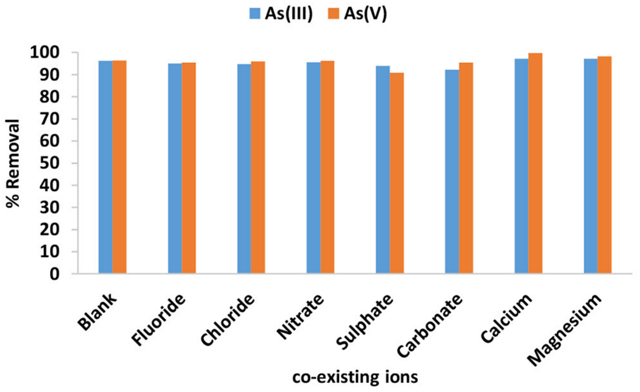

FIGURE 8 | Effect of co-existing ions in the adsorption of As(III) and As(V) from the solution.

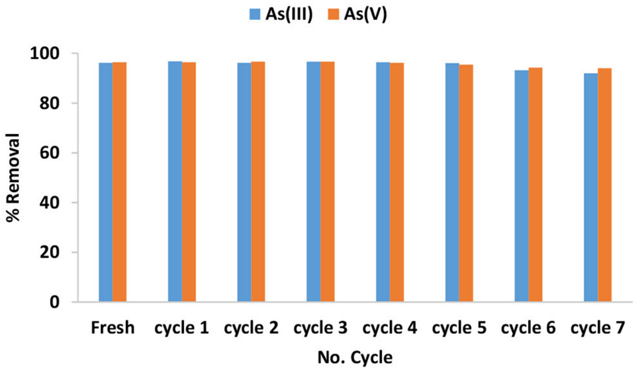

FIGURE 9 | Variation of As(III) and As(V) removal as a function of regeneration-reuse cycles.

Regeneration Study

The regeneration and reuse of adsorbent was studied using 0.01 M HCl as a regenerating agent and the results for 7 successive cycles are presented in **Figure 9**. The percentage As(III) and As(V) removal achieved from the regeneration cycle 1 to cycle 5 was found to be >95% which is relatively equal to the percentage removal achieved from the virgin material. This could be an indication that treatment of the adsorbent with HCl increases the positive sites on the surface of the material. Slight decrease as the reuse-regeneration cycles continues to 7th cycle. The decrease could be due to inadequate regeneration of the sorption sites. This results suggests that IOK is a good material for use in arsenic removal from groundwater as it can be regenerated. The concentration of Fe and Mn were detected at trace concentrations below 0.1 mg/L in the filtrate after 7th cycle. Indicating that the adsorbent is stable.

Comparison With Other Adsorbents

Table 8 present the comparison for As(III) and As(V) adsorption capacities of different adsorbents reported in the literature with the maximum adsorption capacity obtained from the present study. From the table it can be noted that the maximum adsorption capacity obtained from the present study is quite higher as compared to those reported in the literature.

TABLE 8 | Comparison of adsorption capacities.

Adsorbent	Experimental conditions	q_e As(III) (mg/g)	q_e As(V) (mg/g)	References
HDTMA-Al-bentonite	Initial concentration:2–18 mg/; Adsorbent dosage: 2 g/L; pH: 4.5	2.24	8.93	Lee et al., 2015
Iron impregnated charred GAP	Initial concentration: 0.05–200 mg/L; Adsorbent dosage: 0.5 g/100 mL; pH:7	3.25	5.09	Yin et al., 2017
Aluminum pillared HDTMA sericite	Initial concentration: 1 to 20 mg/L; adsorbent dosage: 0.2 g/100 mL; pH 4.5.	0.40	0.46	Tiwari and Lee, 2012
CTMAB-Fe-Montmorillonite	Initial concentration: 1–60 mg/L; adsorbent dosage: 0.1 g/25 mL; pH 6.5	11.36	8.85	Ren et al., 2014
Fe/Mn-HDTMA kaolin	Initial concentration: 0.5–30 mg/L; adsorbent dosage; 0.1 g/100 mL; pH:6.5 ± 0.5, Temp: 298 K	7.99	7.32	This study

CONCLUSION

A clay based hybrid adsorbent for As(III) and As(V) was successfully synthesized through intercalation of Fe-Mn oxides and HDTMA-Br. Batch experiments showed that As(III) removal was optimum at pH range of 4-6 while the As(V) removal was optimum at pH range 4-8. The adsorption data for both species of arsenic fitted better to pseudo second order of reaction kinetics which suggest that the dominant adsorption mechanism was chemisorption. The isotherm studies showed that the data fitted better to Langmuir isotherm model as compared to Freundlich model indicating that adsorption of both As(III) and As(V) occurred on a monolayered surface. The maximum adsorption As(III) and As(V) capacity at room temperature as determined by Langmuir model were found to be 7.99 and 7.32 mg/g, respectively. The thermodynamic studies for sorption of As(III) and As(V) showed that values of ΔG° and ΔH° were negative indicating that adsorption process occurred spontaneously and is exothermic in nature. The regeneration study showed that the inorgano-organo modified kaolin clay mineral can be reused for up 7 adsorption-regeneration cycles using 0.01 M HCl as a regenerant. This findings showed that IOK developed in this study is suitable for use in removal of arsenic from groundwater.

DATA AVAILABILITY STATEMENT

All datasets generated for this study are included in the article/supplementary material.

AUTHOR CONTRIBUTIONS

RM designed and conducted the experiments, and also wrote the draft manuscript. MG made conceptual contribution, supervised the work, and edited the draft manuscript. PN made the conceptual contribution, made suggestions on the manuscript and supervised the work.

ACKNOWLEDGMENTS

Authors would like to acknowledge financial support from NRF, Saif, and University of Venda RPC grant Number: SES/17/ERM/03, TESPESKOM grant.

REFERENCES

Bardach, A. E., Ciapponi, A., Soto, N., Chaparro, M. R., Calderon, M., Briatore, A., et al. (2015). Epidemiology of chronic disease related to arsenic in Argentina: a systematic review. *Sci. Total Environ*. 538, 802–816. doi: 10.1016/j.scitotenv.2015.08.070

Bhattacharyya, K. G., and Gupta, S. S. (2008). Adsorption of a few heavy metals on natural and modified kaolinite and montmorillonite: a review. *Adv. Coll. Interf. Sci.* 140, 114–131. doi: 10.1016/j.cis.2007.12.008

Bhowmick, S., Pramanik, S., Singh, P., Mondal, P., Chatterjee, D., and Nriagu, J. (2018). Arsenic in groundwater ofWest Bengal, India: a review of human health risks and assessment of possible intervention options. *Sci. Total Environ*. 612, 148–169. doi: 10.1016/j.scitotenv.2017.08.216

Duker, A. A., Carranza, E. J. M., and Hale, M. (2005). Arsenic geochemistry and health. *Environ. Int*. 31, 631–641. doi: 10.1016/j.envint.2004.10.020

Ghosh, S., Debsarkar, A., and Dutta, A. (2019). Technology alternatives for decontamination of arsenic rich groundwater—a critical review. *Environ. Technol. Innovat.* 13, 277–303. doi: 10.1016/j.eti.2018.12.003

Gitari, W., and Mudzielwana, R. (2018). *Mineralogical and Chemical Characteristics of Raw and Modified Clays and Their Application in Arsenic and Fluoride Removal: Review, Current T* Zoveidavianpoor *opics in the Utilization of Clay in Industrial and Medical Applications, Mansoor Zoveidavianpoor.* IntechOpen. doi: 10.5772/intechopen.74474

Lee, S. M., Lalhmunsiama, Thanhmingliana, and Tiwari, D. (2015). Porous hybrid materials in the remediation of water contaminated with As(III) and As(V). *Chem. Eng. J.* 270, 496–507 doi: 10.1016/j.cej.2015.02.053

Mishra, T., and Mahato, D. K. (2016). A comparative study on enhanced arsenic(V) and arsenic(III) removal by iron oxide and manganese oxide pillared clays from ground water. *J. Environ. Chem. Eng*. 4, 1224–1230. doi: 10.1016/j.jece.2016.01.022

Munagapati, V. S., and Kim, D. S. (2017). Equilibrium isotherms, kinetics, and thermodynamics studies for congo red adsorption using calcium alginate beads impregnated with nano-goethite. *Ecotoxicol. Environ. Safety* 141, 226–234. doi: 10.1016/j.ecoenv.2017.03.036

Qi, J., Zhang, G., and Li, H. (2015). Efficient removal of arsenic from water using a granular adsorbent: Fe–Mn binary oxide impregnated chitosan bead. *Bioresour Technol*. 193, 243–249. doi: 10.1016/j.biortech.2015.06.102

Ren, X., Zhang, Z., Luo, H., Hu, B., Dang, Z., Yang, C., et al. (2014). Adsorption of arsenic on modified montmorillonite. *Appl. Clay Sci*. 97–98, 17–23. doi: 10.1016/j.clay.2014.05.028

Ryu, S. R., Jeom, E. K., Yang, J. S., and Baek, K. (2017). Adsorption of As(III) and As(V) in groundwater by Fe–Mn binary oxide-impregnated granular activated carbon (IMIGAC). *J. Taiwan Inst. Chem. Eng.* 72, 62–69. doi: 10.1016/j.jtice.2017.01.004

Singh, M., Dosanjhm, H. S., and Singh, H. (2016). Surface modified spinel cobalt ferrite nanoparticles for cationic dye removal: kinetics and thermodynamics studies. *J. Water Process Eng*. 11, 152–161. doi: 10.1016/j.jwpe.2016.05.006

Smedley, P. L., and Kinniburgh, D. G. (2002). A review of the source, behaviour and distribution of arsenic in natural waters. *Appl. Geochem.* 17, 517–568. doi: 10.1016/S0883-2927(02)00018-5

Su, J., Huang, H. G., Jin, X. Y., Lu, X. Q., and Chen, Z. L. (2011). Synthesis, characterization and kinetic of a surfactant-modified bentonite used to remove As(III) and As(V) from aqueous solution. *J. Hazard. Mater.* 185, 63–70. doi: 10.1016/j.jhazmat.2010.08.122

Thanhmingliana and Tiwari, D. (2015). Efficient use of hybrid materials in the remediation of aquatic environment contaminated with micro-pollutant diclofenac sodium. *Chem. Eng. J.* 263, 364–373. doi: 10.1016/j.cej.2014.10.102

Tiwari, D., and Lee, S. M. (2012). Novel hybrid materials in the remediation of ground waters contaminated with As(III) and As(V). *Chem. Eng. J.* 204–206, 23–31. doi: 10.1016/j.cej.2012.07.086

Tran, H. N., You, S. J., and Chao, H. P. (2016). Thermodynamic parameters of cadmium adsorption onto orange peel calculated from various methods: a comparison study. *J. Environ. Chem. Eng.* 4, 2671–2682. doi: 10.1016/j.jece.2016.05.009

Tran, H. N., You, S. J., Hosseini-Bandegharaei, A., and Chao, H. P. (2017). Mistakes and inconsistencies regarding adsorption of contaminants from aqueous solutions: a critical review. *Water Res.* 120, 88–116. doi: 10.1016/j.watres.2017.04.014

Weber, W. J., and Morris, J. C. (1963). Kinetics of adsorption on carbon from solution. *J. Sanit. Eng. Div*. 89, 31–60.

WHO (2017). World Health Organization. *Guidelines for Drinking-Water Quality: Fourth Edition Incorporating the First Addendum*. Geneva: Licence: CC BY-NC-SA 3.0 IGO.

Yin, H., Kong, M., Gu, X., and Chen, H. (2017). Removal of arsenic from water by porous charred granulated attapulgite-supported hydrated iron oxide in bath and column modes. *J. Clean. Product.* 166, 88–97. doi: 10.1016/j.jclepro.2017.08.026

Zhang, G., Liu, H., Qu, J., and Jefferson, W. (2012). Arsenate uptake and arsenite simultaneous sorption and oxidation by Fe–Mn binary oxides: Influence of Mn/Fe ratio, pH, Ca^{2+}, and humic acid. *J. Colloid Interf. Sci.* 366, 141–146. doi: 10.1016/j.jcis.2011.09.058

Zhang, L., Qin, X., Tang, J., Liu, W., and Yang, H. (2017). Review of arsenic geochemical characteristics and its significance on arsenic pollution studies in karst groundwater, Southwest China. *Appl. Geochem.* 77, 80–88. doi: 10.1016/j.apgeochem.2016.05.014

Conflict of Interest: The authors declare that the research was conducted in the absence of any commercial or financial relationships that could be construed as a potential conflict of interest.

frontiers in Chemistry

ORIGINAL RESEARCH
published: 30 January 2020
doi: 10.3389/fchem.2020.00005

Evaluation of Anionic and Cationic Pulp-Based Flocculants With Diverse Lignin Contents for Application in Effluent Treatment From the Textile Industry: Flocculation Monitoring

*Kinga Grenda [1,2], José A. F. Gamelas [1], Julien Arnold [2], Olivier J. Cayre [3] and Maria G. Rasteiro [1]**

[1] Department of Chemical Engineering, CIEPQPF—Chemical Process Engineering and Forest Products Research Centre University of Coimbra, Coimbra, Portugal, [2] AQUA+TECH Specialities, Chemin du Chalet-du-Bac 4, Geneva, Switzerland, [3] School of Chemical and Process Engineering, University of Leeds, Leeds, United Kingdom

Edited by:
Florent Allais,
AgroParisTech Institut des Sciences et Industries du Vivant et de L'environnement, France

Reviewed by:
Mathieu Lapointe,
McGill University, Canada
Koenraad Muylaert,
KU Leuven, Belgium

***Correspondence:**
Maria G. Rasteiro
mgr@eq.uc.pt

Specialty section:
This article was submitted to Green and Sustainable Chemistry, a section of the journal Frontiers in Chemistry

Received: *10 November 2019*
Accepted: *06 January 2020*
Published: *30 January 2020*

Citation:
Grenda K, Gamelas JAF, Arnold J, Cayre OJ and Rasteiro MG (2020) Evaluation of Anionic and Cationic Pulp-Based Flocculants With Diverse Lignin Contents for Application in Effluent Treatment From the Textile Industry: Flocculation Monitoring. Front. Chem. 8:5. doi: 10.3389/fchem.2020.00005

In wastewater treatment, flocculation is a widely used solid/liquid separation technique, which typically employs a charged polymer, a polyelectrolyte (PEL). Polyelectrolytes features, such as charge type, charge density and molecular weight, are essential parameters affecting the mechanism of flocculation and subsequent floc sedimentation. The effectiveness of the process is also influenced by the characteristics of the system (e.g., type, size, and available surface area of suspended particles, pH of the medium, charge of suspended particles). Thus, a good understanding of the flocculation kinetics, involved mechanisms and flocs structure is essential in identifying the most adequate treatment conditions, having also into consideration possible subsequent treatments. In this study, *Eucalyptus* bleached pulp and a cellulosic pulp with high lignin content (∼4.5 wt%) obtained from *Eucalyptus* wood waste were used for bio-PELs production. Firstly, a pre-treatment with sodium periodate increased the pulps reactivity. To produce cationic cellulose the oxidation step was followed by the introduction of cationic groups in the cellulose chains, through reaction with Girard's reagent T. Applying different molar ratios (0.975 and 3.9) of Girard's reagent T to aldehyde groups led to cationic PELs with diverse charge density. On the other hand, to obtain anionic cellulose a sulfonation reaction with sodium metabisulfite was applied to the intermediate dialdehyde cellulose-based products, during 24 or 72 h, and anionic-PELs with diverse features were obtained. The developed water soluble, anionic and cationic bio-PELs were characterized and tested as flocculation agents for a textile industry effluent treatment. Initially, jar-tests were used to tune the most effective flocculation procedure (pH, flocculant dosage, etc.). Flocculation using these conditions was then monitored continuously, over time, using laser diffraction spectroscopy (LDS). Due to the small size of the dyes molecules, a dual system with an inorganic complexation agent (bentonite) was essential for effective decolouration of the effluent. Performance in the treatment was monitored first by turbidity removal evaluation (75–88% with cationic-PELs, 75–81% with anionic-PELs) and COD reduction evaluation (79–81% with cationic-PELs, 63–77% with anionic-PELs) in the jar tests. Additionally, the evolution of flocs characteristics (structure and size) during their growth and the flocculation kinetics, were studied using the LDS technique, applying the different PELs produced and for a range of PEL concentration. The results obtained through this monitoring procedure allowed to discuss the possible flocculation mechanisms involved in the process. The results obtained with the bio-PELs were compared with those obtained using synthetic PELs, commonly applied in effluents treatment, polyacrylamides. The developed bio-PELs can be competitive, eco-friendly flocculation agents for effluents treatment from several industries, when compared to traditional synthetic flocculants with a significant environmental footprint. Moreover, LDS proved to be a feasible technique to monitor flocculation processes, even when a real industrial effluent is being tested.

Keywords: anionic cellulose, cationic cellulose, bio-polyelectrolytes, flocculation, textile wastewater, decolouration, wood wastes valorization, laser diffraction spectroscopy

INTRODUCTION

Dye-containing wastewaters present several difficulties related to their treatment, due to their high chemical complexity, diverse dye structures usually with low molecular weight. Several industries, among which textile, paper or pharmaceutical are nowadays the most significant producers of this type of effluents. The struggle with removing dye contaminants from aqueous streams is real, since the direct discharge of dye wastes into natural water reservoirs forbidden by strict regulations, can significantly affect the environment (reduction of the dissolved oxygen, a change of pH, as well as blocking sunlight). Also, in effluents containing dyes it is common to find metals, salts, surfactants, sulfides or formaldehyde (Carliell et al., 1998), which are known for their high toxicity. Furthermore, discharged dyes without proper treatment are stable and remain in the environment for long periods of time (Hao et al., 2000). Bearing in mind the variation of the properties of dye containing effluents, due to the industrial process itself and dyes composition, as well as the presence of inorganic/organic-based additives used in the process (dos Santos et al., 2007), effective, economical and environmentally friendly treatments are required and in high demand.

Although very interesting approaches have been proposed for effective color removal, it is difficult to find a solution that works for the wide range of existing dyes (Hao et al., 2000). In fact, several factors (constraints) must be taken into account such as the type and concentration of dyes present, the eventual presence of other interfering substances, pH and the temperature of operation etc. In most wastewater treatment plants, coagulation and flocculation are widely used separation processes. These typically employ an oligomer or polymer of charged nature (polyelectrolyte). Polyelectrolytes features, such as charge type, density and molecular weight, are essential parameters affecting the conformation of a polymer chain in solution, which then influence the mechanism of flocculation and subsequent sedimentation/separation. The effectiveness of the process is also influenced by the characteristics of the system (e.g., type, size and available surface area of suspended particles, pH of the medium, charge of suspended particles). Due to the small size of the dyes molecules and high stability in the aqueous medium, additives to stimulate the destabilization of the colloidal mixtures and promote the agglomeration of sub-millimeter particles are required, which leads to the formation of flocs that can settle over a period of seconds to hours. Thus, a good understanding of flocculation kinetics, involved mechanisms and flocs structure is critical in identifying the most adequate treatment conditions for a given system.

In flocculation studies often, the floc settling behavior is measured in terms of the supernatant formation kinetics using a liquid dispersion optical characterization instrument (Turbiscan). The underlying principle of the technique is to measure and analyze the changes in the light transmission and backscattering by the sample in a cylindrical cell, as a function of particle movements (aggregation, creaming and/or sedimentation) (Kaombe et al., 2013). During the flocculation process particles aggregate, forming flocs, and become larger in size, strongly bounded and heavier than as individual particles. Increasing the combined mass enhances the sedimentation of the particles aggregates. By performing the measurement with Turbiscan the formation of the sediment layer is monitored over time. This methodology, however, is not suitable to evaluate flocculation mechanisms or to determine the floc features (structure or size) over time, as well as floc breakage.

Evolution with time of floc size and their structure can also be monitored by image analysis, which is considered as one of the easiest and the most direct measuring technique including image capture using a digital camera coupled to a microscope and its processing (Costa et al., 2013). However, this methodology requires preparation and manual selection/evaluation of a large number of samples (particles) over time in order to obtain data regarding flocculation kinetics. It is important to note that, the statistical representativeness of the sample must always be considered, and, to assure this, the technique is usually very time consuming.

An alternative technique to monitor flocculation processes is the focused beam reflectance microscopy (FBRM) (Blanco et al., 2002; Antunes et al., 2015), broadly used in real-time flocculation monitoring of large scale processes, as well as to screen the changes in particle population during the process (Liang et al., 2015). FBRM is a technique based on light scattering that does not involve sampling procedures. FBRM uses a highly focused laser beam, at a high movement speed, measuring the backward scattering light of a sample with suspended particles. The described technique can produce good quality data for particle size in relatively concentrated suspensions, but only for the large aggregates sizes. However, in the initial stages of the flocculation process where the particles size is relatively small, FBRM shows difficulties in detecting and recording good quality data, due to limited resolution, which is the main disadvantage of this technique.

Alternatively, the evolution of flocs characteristics (structure and size) during their growth, as well as the flocculation kinetics, can be studied using laser diffraction spectroscopy (LDS) (Rasteiro et al., 2007, 2008). Typically, with no particles in the system, the laser beam passes through the sample without changing its direction. The opposite happens when there are particles on the laser path. This event results in the scattering of light and alteration of the laser beam. In LDS, the angle between the scattered light and the incident beam (scattering angle) is related with the particle size. Moreover, the intensity of the scattered light is related to the number of particles in each size class. From this acquisition it is then possible to generate the scattering matrix, based on data (intensity of scattered light) for the different scattering angles, and, afterwards, particle size and size distribution can be obtained by applying an adequate model (Liang et al., 2015).

When studying the flocculation kinetics, it is very important to take into account the events of floc breakage during the process (this is not possible to observe in a typical/classical jar-test), as well as the size distribution of particles and aggregates (Rasteiro et al., 2007). Several reports refer the use of LDS in flocculation processes monitoring, in general model particle systems (Rasteiro et al., 2008). The LDS was also applied in flocculation monitoring in papermaking processes, using a standard paper filler, precipitated calcium carbonate (Rasteiro et al., 2008). Another study refers the possibility to evaluate the flocculation mechanisms involved, while working with several different synthetic flocculation agents applied in the treatment of an industrial potato crisps manufacturing effluent (Lourenço et al., 2018). The use of laser diffraction spectroscopy allowed to extract data on floc size distribution, average floc size and aggregates structure, described by the fractal dimension (dF- to characterize the primary aggregates compactness) and scattering exponent (SE- to characterize the secondary aggregates structure), in a continuous flocculation process (Rasteiro et al., 2011). The density (compactness) of the flocs can be estimated based on the fractal dimension, since it is related to the number of primary particles that fill the space in the nominal volume of an aggregate (Chakraborti et al., 2003). Furthermore, for the secondary aggregates, resulting from aggregation of the primary ones, the scattering exponent provides information for the larger length scales of the floc and their structure, as for these larger aggregates the fractal approximation is not valid (Rasteiro et al., 2011). Additionally, when using LDS it is possible to control the hydrodynamic conditions in the system (mechanical stirring rate and flow rate) so that flocculation can be conducted in controlled hydrodynamic conditions which can easily be reproduced in industrial flocculation processes (Antunes et al., 2015).

Typically, colored wastewaters from textile industries, due to their complex composition, may affect the performance of polyelectrolytes. Moreover, traditional colored water treatments, using metal-based coagulants or synthetic polyelectrolytes generate large amounts of sludge. The transport of this sludge for disposal, is the main cost and environmental burden. Therefore, the minimization of sludge production is important. A biodegradable coagulant or flocculant could reduce the volume of sludge generated. In this perspective the development and the application of novel cationic and anionic natural-based polyelectrolytes as flocculants to treat industrial effluents is of high interest (Lee et al., 2014).

The high biodegradability, and low or non-toxicity, as well as wide availability make cellulose-based PELs a more environmentally friendly option. Moreover, valorization of cellulosic wastes itself to provide end products with higher added value is also an important aspect (Grenda et al., 2019). Due to the low water solubility of cellulose it is essential to introduce charged groups, either cationic or anionic, in the cellulose backbone, and modification possibilities are limited. Pre-modification to dialdehyde cellulose, due to its efficiency (Ramírez et al., 2006) is typically applied. This reaction provides a significant modification degree, since two highly reactive aldehyde groups are introduced per anhydroglucose unit (AGU) at C-2 and C-3 positions, by opening the AGU unit at C2-C3 linkage, which allows to obtain highly modified end products—the dialdehyde cellulose (DAC). Usually selective oxidation with periodate has been applied as the first step, in which the cellulose crystalline structure is partially destroyed, associated with a decrease of the polymerization degree (Kim et al., 2000; Liu et al., 2012). Several reaction parameters may influence the properties of obtained DAC, as was reported previously (Nikolic et al., 2010; Sirviö et al., 2011a; Liu et al., 2012), which may affect further steps of the modification. Cellulose-based PELs, can be produced by introduction of positively charged groups through the cationization reaction of DAC with Girard's reagent T (Liimatainen et al., 2011; Sirviö et al., 2011b). In this procedure, more than one cationic quaternary ammonium group per AGU unit is introduced into the cellulose backbone by the formation of an imine bond. This treatment allows the end material to be highly charged (high degree of substitution) making it easy to solubilize in water at room temperature. Sirviö et al. (2011b) and Liimatainen et al. (2011) reported the modification of bleached pulp from birch wood, using the aforementioned procedure, and Grenda et al. (2019, 2020) reported the modification of bleached and unbleached *Eucalyptus globulus* pulp using the same strategy.

Typically, cellulose functionalization through anionization occurs by the introduction of sulfonate groups (-SO_3-) in the cellulosic chain. This modification can follow the direct sulfonation of cellulose in N,N-dimethylformamide (Zhu et al., 2014) or can be based in the anionization of DAC with e.g., sodium metabisulfite in aqueous medium. The latter procedure can provide anionic cellulose-based PELs with higher ionic character, due to the substitution of more than one anionic sulfonate group per AGU unit, which significantly increases the degree of substitution and provides water solubility at room temperature. The characteristics of the anionic derivatives of dialdehyde cellulose, as the sulfonate groups content, affect their solubility (Rajalaxmi et al., 2010) what is also driven by the aldehyde content of the previously produced dialdehyde cellulose. Similar paths were described in different studies developed by Liimatainen et al. (2012) (using bleached birch (*Betula verrucosa*) chemical pulp), Hou et al. (2007) (using bleached softwood kraft pulp) or Rajalaxmi et al. (2010) (using bleached hardwood kraft pulp).

In the present study, both cationic and anionic cellulosic polyelectrolytes were produced. The reaction conditions were adjusted to obtain bio-PELs with different charges (degree of substitution). Jar-test was used to adjust the most efficient flocculation procedures, while LDS was used to evaluate continuously the flocculation process of a real industrial colored wastewater from textile industry. In all trials performed, dual systems with bentonite and cellulose-based PELs were evaluated. Bentonite promotes adsorption of the dye and the PELs act as flocculation agent of the bentonite particles with adsorbed dye. The industrial colored effluent was treated with two cationic and two anionic polyelectrolytes obtained from *Eucalyptus* bleached fibers, and with two cationic and two anionic polyelectrolytes obtained from a pulp with high lignin content (kappa number of 26.7). The size and structure of the flocs produced were monitored and analyzed, and the possible flocculation mechanisms are discussed, for each polyelectrolyte, separately. The effect on the performance during flocculation, of the chemical heterogeneity of the raw material used in the production of the bio-PELs, as well as of the degree of substitution and zeta potential of the bio-PELs, was evaluated at different pH values and flocculant concentrations. Overall, results of the assessment of cellulose-based PELs as flocculants for the treatment of a real dye-containing effluent and the tracking of the corresponding flocculation performance through LDS are presented here for the first time.

MATERIALS AND METHODS

Raw Materials

Eucalyptus globulus industrial bleached kraft pulp (C_p) (supplied by *The Navigator* Company, Portugal) was used as a reference cellulose sample of very low lignin content. The chemical composition of this pulp is summarized in **Table S1**.

Eucalyptus globulus industrial wood chips wastes, with a high size heterogeneity, supplied by *The Navigator Company* (Portugal), were used as lignocellulosic raw material. These were further processed by mild kraft pulping, in a rotary digester equipped with 4 independent 1.5 L vessels supplied by Apineq. The cooking was carried out using an active alkali charge of 14% (aqueous liquor of sodium hydroxide, sodium sulfide and sodium carbonate) and a liquor-to-wood ratio of 3.5. The reactor maximum temperature was 160 °C and the time at maximum temperature was 60 min. At the end of cooking, the produced pulp was thoroughly washed with a large amount of water and then dried. Kappa number of the final pulp was measured according to TAPPI Standard T236 om-99. The kraft pulp from wood chips wastes (C_w) was also analyzed for sugars and lignin content. Klason and acid-soluble lignin were determined using the TAPPI Standards T 222 om-98 and T UM 250, respectively, while the sugars content was determined in the hydrolysates using high-performance liquid chromatography—HPLC. The HPLC analysis was run in an equipment from Knauer (Berlin, Germany), equipped with a Smartline pump 1000, Smartline RI Detector S2300 and an Agilent Hi-Plex Ca, 300 x 7.7 mm column from Agilent Technologies. The results of the chemical analysis of C_w pulp are presented in **Table S1**.

Modification of Pulps and Characterization of the Obtained Materials

Pulp Oxidation Pre-treatment by Reaction With Sodium Periodate

The periodate oxidation of *Eucalyptus globulus*-based pulps (C_p and C_w) followed the procedure described elsewhere (Grenda et al., 2017). In general, prior to the process, 4 g (dry basis) of pulp (C_p or C_w) were disintegrated/swelled overnight in distilled water at 4% consistency. The suspension was then treated with a mixture of 300 mL of distilled water, 7.2 g of LiCl and 8.2 g of $NaIO_4$. A highly oxidized material was produced after 3 h of oxidation at 75°C, which was filtered and washed with distilled water. The non-dried cellulose-based dialdehyde (DAC_p or DAC_w) product was stored in the fridge and used later for further modifications (cationization and anionization). Moreover, DAC samples oven-dried at 60°C were used for FTIR-ATR measurements. The aldehyde content of DAC was determined based on the oxime reaction between aldehyde groups and $NH_2OH{\cdot}HCl$, as described in the literature (Grenda et al., 2017), having been obtained the values of 10.96 mmol aldehyde/g for DAC_p and 10.19 mmol aldehyde/g for DAC_w.

Preparation of Water-Soluble Cationic Cellulose-Based Polyelectrolytes

Cationization of non-dried DAC_p or DAC_w was performed through reaction with Girard's reagent T (GT) at two different GT/aldehyde molar ratios, 0.975 and 3.9, at pH 4.5 in 80 mL of distilled water. The reaction mixture was stirred for 1 h at 70°C for cationization to occur. After cooling, isopropanol was added to precipitate the soluble product (CDAC—cationic dialdehyde cellulose-based polyelectrolyte). The mixture was centrifuged for 30 min at 4,500 rpm, after which, the supernatant was removed. The solid product was washed several times with a water/isopropanol solution (1/9, v/v), until the supernatant showed no GT. Removal of the residual GT was monitored by adding a small amount of $AgNO_3$ to the supernatant (absence of AgCl precipitate indicated washing was complete). Applying two different GT/aldehyde molar ratios allowed to obtain cationic cellulose-based polyelectrolytes with diverse characteristics. The final cationic products were oven-dried at 60°C and then stored in a desiccator for further characterizations and evaluation as flocculation agents.

Preparation of Water-Soluble Anionic Cellulose-Based Polyelectrolytes

The anionization of non-dried DACs, either DAC_p or DAC_w was performed through reaction of 14 mmol of sodium metabisulfite/g DAC in 60 mL of deionized water. The reaction mixture was stirred with a magnetic stirrer for 24 or 72 h at room temperature (25°C). The flask was well sealed during the reaction to avoid any changes of concentration. After reaction, the transparent solution was also mixed with isopropanol to precipitate the soluble product, and then the mixture was centrifuged at 4,500 rpm for 45 min. The separated solid was then washed with a water/isopropanol solution (1/9, v/v). The anionic DAC (ADAC) product was oven-dried at 60°C and stored in a desiccator. Through application of different anionization times (24 and 72 h), anionic cellulose-based products with varied degrees of anionization were obtained. The final anionic celluloses were characterized by several techniques and further used as flocculation agents.

Characterization of Water-Soluble Cationic and Anionic Cellulose-Based Polyelectrolytes

The obtained cationic and anionic cellulose-based PELs were characterized by FTIR spectroscopy to confirm the presence of the new functional groups introduced in the polysaccharide's backbone (Grenda et al., 2019) and by elemental analysis in order to determine the cationicity or anionicity index of the products. The nitrogen content assessed by elemental analysis was used to obtain the degree of cationization while the sulfur content was used to determine the degree of anionization of cellulose in the ADAC samples. The results obtained (N% or S%, w/w) were an average of at least 3 measurements.

Hydrodynamic diameter and zeta potential measurements of the PELs were also performed, by dynamic light scattering (DLS) and electrophoretic light scattering (ELS), respectively, in a Zetasizer NanoZS, ZEN3600, from Malvern Instruments, with temperature set up to 25°C. For the hydrodynamic diameter, backscatter detection at 173° angle was employed. Using automatic measurements mode, with at least 5 repetitions of the measurement, the average hydrodynamic diameter (nm) (z-average diameter) and the PDI (polydispersity index) of the hydrodynamic diameter distribution were obtained. Similarly, zeta potential values were taken as an average of 5 repeated measurements. Details of the sample's preparations can be found elsewhere (Grenda et al., 2019).

Evaluation of Performance in Textile Wastewater Treatment

Industrial Effluent Characterization

In the present study, a colored industrial effluent was supplied by *Rosarios4*, Portugal. The textile wastewater was collected from a single dyeing session, and contained only one shade of Turquoise Blue dye. The effluent characterization in terms of COD, pH, turbidity and zeta potential, is summarized in **Table S2**.

The zeta potential of the initial industrial colored effluent as well as the changes in zeta potential as a function of pH were measured using Electrophoretic Light Scattering (ELS) in a Malvern Zetasizer Nano ZS, model ZEN3600 (Malvern Instruments Ltd, UK). At desired pH 1 mL of sample was injected directly into the disposable plastic capillary cell and the measurements were conducted at 25°C, using the automatic measurement mode, with at least 5 repetitions of the measurement.

Flocculation Experiments

Jar-tests were applied in order to pre-evaluate the flocculation performance of the water-soluble cationic ($CDAC_p$ and $CDAC_w$) and anionic ($ADAC_p$ and $ADAC_w$) cellulose-based polyelectrolytes with diverse chemical complexity (lignin contents) that possessed two different degrees of substitution of charged groups (either cationic or anionic). The cellulose-based polyelectrolyte solutions used in the flocculation tests were prepared by dissolving the CDAC or ADAC, at 0.1 wt% concentration, in distilled water, and stirring at 500 rpm for 30 min.

For the flocculation experiment (jar-test), a volume of 100 mL of pre-agitated colored effluent, at room temperature, was adjusted to the required pH using hydrochloric acid (HCl) aqueous solution, with a pH meter SCAN3BW (Scansci). Three different pH values (1.5, 3.0, and 7.0) were considered to assess the influence of pH on the flocculation performance. A suitable dosage of flocculant was then added dropwise to the effluent, while mixing slowly during 20 s. For most of the experiments, bentonite purchased from Vermeer Portugal under the commercial name Cebo Premium (which possessed ζ-potential of −43 ± 1 mV, d(0.5) - median of the particle size distribution of 2.3 μm and D[3.2] - surface weighted mean of the particle size distribution of 2.1 μm) was also added before the flocculant addition. Supernatant samples of approximately 5 mL were collected at about 75% height from the center of the beaker, for evaluation of the effluent clarification over time (1 min, 30 min, 1 h, and 24 h). The color removal (clarification) was calculated based on Equation 1, by measuring the initial turbidity of the effluent and the turbidity of the supernatant after a certain settling time.

$$\mathit{Color\ removal}\ (\%) = \frac{T_0 - T_f}{T_0} \cdot 100 \tag{1}$$

where T_0 is the turbidity of the initial wastewater at time zero, and T_f is the turbidity of the supernatant of the treated sample at a given time. In some cases, values of turbidity removal lower than zero were obtained. This is because just after addition of bentonite turbidity usually increases, and, if the settling of the particles is poor, even after further addition of flocculant, for non-optimal conditions turbidity can still be higher than that of the original effluent, providing thus negative values of color removal.

At least three repetitions of the turbidity measurements of each sample, using a Photometer MD600 (Lovibond, UK), were performed. The variation between replica of turbidity measurements for each sample was always below 1%. Comparison of the efficiency of the new bio-PELs on color removal, was made with commercial cationic (cPAM- SnowFlake E2 with 45 wt% charge) and anionic (aPAM- SnowFlake X0 with 30 wt% charge) polyacrylamides of similar charge, supplied by aquaTECH, Geneva.

The chemical oxygen demand (COD) of the treated supernatant was measured for selected trials (polymers and procedures) after 24 h of settling. COD tests were performed with 2 mL of supernatant, added directly to the COD test tube (COD Kit, Lovibond, UK) and allowed to remain at 150°C for 2 h in the thermo-reactor (VELP Scientifica). After reaching room temperature, and resting for 12 h in dark conditions, the COD value was measured in the Photometer MD600 (Lovibond, UK).

Additionally, laser diffraction spectroscopy (LDS), Malvern Mastersizer 2000 (Malvern Instruments), was used to monitor the flocculation process in low mixing conditions, following the procedure developed previously by the authors (Lourenço et al., 2018). LDS was used to evaluate the flocculation performance of modified cellulose from bleached pulp both cationized ($CDAC_pA$, B) and after introducing anionic groups ($ADAC_pA$, B), as well as modified cellulose obtained from a pulp with a kappa number of 26.7, either with cationic ($CDAC_wA$, B) or anionic ($ADAC_wA$, B) groups. To conduct the LDS tests a 50% dilution with distilled water, of the initial industrial effluent used in the jar-tests, was required, to ensure an acceptable level of obscuration in the equipment, after addition of the appropriate amount of the complexation agent (bentonite). This is the main limitation when using LDS to monitor flocculation processes, even if in most cases results obtained follow the same trends obtained in the jar-tests. The concentrations of the used treatment agents were recalculated considering the dilution factor, to reproduce the procedures evaluated in the jar-tests. Initial turbidity of the effluent with bentonite, before dilution, was 212 NTU (177 NTU effluent initial turbidity), while after dilution it was reduced till 100 NTU. A volume of 23 mL of bentonite suspension (at 5 wt%) was added to 750 mL of the effluent in the equipment dispersion unit, which corresponded to an average bentonite concentration of 0.15 wt%. The initial industrial effluent, at pH 3.0, was stirred at a speed of 2,000 rpm to guarantee homogenization, and the size distribution of the particles in the effluent was acquired. Bentonite was then added at 1,200 rpm, followed by the addition of the cellulose-based PELs, using the same stirring speed. The overall concentrations of PEL in the system tested were: 1.3, 2.6 mg/l (corresponding to procedure A and D in the jar-tests), 4.0 and 5.3 mg/L (corresponding to procedure B and C in the jar-tests). During the monitoring of the flocculation process the tests were carried out at the optimized stirring speed of 350 rpm (shear rate $20s^{-1}$ based on CFD modeling of the sampling vessel) in the flocculation vessel of the Malvern Mastersizer 2000, to guarantee an effective floc circulation in the sampling system, ensuring that floc sedimentation was not occurring and avoiding also floc breakage. The size of the flocs was measured every 36 s for a total period of 20 min (i.e., until the floc size stabilized).

The scattering matrix obtained by LDS was treated off-line to calculate the scattering exponent (SE) of the flocs (Rasteiro et al., 2011). The SE parameter provides information about floc structure. From the scattering matrix obtained by LDS it is possible to plot, in logarithmic scale, the scattering intensity vs. q (see Equation 2), and the slope of the first region of this plot is related to SE (Rasteiro et al., 2011). The scattering matrix, acquired during each measurement, can be exported through the equipment software and then processed, offline, for each acquisition, in order to obtain the scattering exponents, including their evolution over time.

$$q = \frac{4\pi n_0}{\lambda_0} \sin(\theta/2) \tag{2}$$

Where n_0 is the refractive index of the dispersing medium, θ is the scattering angle and λ_0 corresponds to the incident light wavelength.

RESULTS AND DISCUSSION

Synthesis and Characterization of Cationic and Anionic Cellulose-Based Polyelectrolytes

Derivatization of different *Eucalyptus*-based cellulosic materials (see **Table S1**), in order to obtain cationic or anionic PELs, was carried out following the route described in **Figure 1**. Initially, DAC was produced by periodate oxidation of the cellulose-rich material. The resultant DAC was reacted with Girard's reagent T yielding the cationic derivative (CDAC), or with sodium metabisulfite producing the anionic derivative (ADAC).

The periodate oxidation as well as the quaternary ammonium cationization procedure with Girard's reagent T developed for *Eucalyptus* bleached fibers, described by Grenda et al. (2020), was implemented in the same way for a pulp with high lignin content (4.4%, kappa number of 26.7) obtained from Eucalyptus wood wastes. It is expected that different composition of the raw materials, namely the cellulose, hemicellulose (xylan) and lignin content can influence not only the characteristics of the final polyelectrolytes but also their potential application as flocculants. Applying different GT/aldehyde molar ratios allows to obtain different degrees of substitution by the cationic unit (see **Table 1**). There is a trend of decrease of zeta potential of the final product, with the increase of complexity of the raw material used in the periodate oxidation, and the lowest value was observed while performing cationization of the wood pulp with a high kappa number of 26.7 at low GT/aldehyde molar ratio. Higher complexity of the raw material, namely larger lignin and xylan content, led to obtain cationic cellulose-based PELs with lower zeta potential that varied from 40 ± 3 mV ($CDAC_wB$; obtained using 0.975 of GT/aldehyde molar ratio) to 46 ± 1 mV ($CDAC_wA$; using 3.9 GT/aldehyde molar ratio). While applying the same conditions to the pulp with higher chemical homogeneity (bleached pulp, negligible lignin content) the obtained polyelectrolytes were characterized by a higher positive charge (zeta potential of 52–54 mV). However, the obtained $CDAC_p$ products presented significantly reduced hydrodynamic diameter when compared to the $CDAC_w$ products, probably due to a reduction of the cellulose chain length during bleaching.

The synthesis of anionic cellulose-based polyelectrolytes (ADAC) followed the reaction described in **Figure 1**. **Table 2** shows the reaction conditions used to produce the ADAC samples and the characterization results. Again, different initial materials were considered (*Eucalyptus* bleached pulp and a pulp with high lignin content). The reaction time was varied from

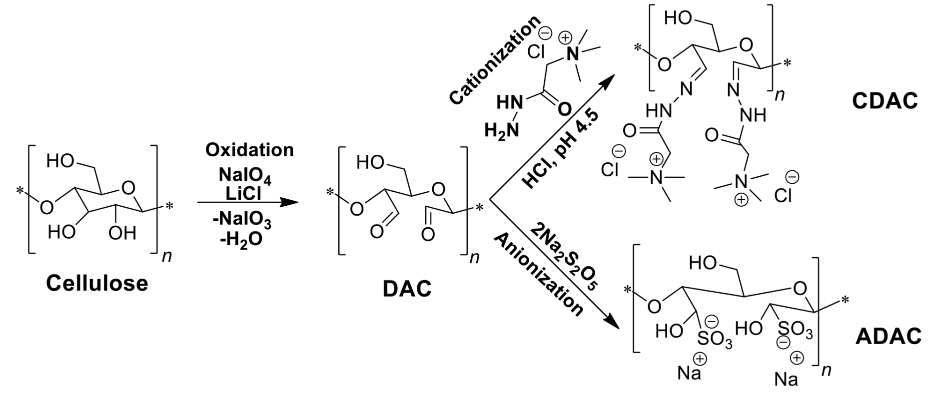

FIGURE 1 | Production of positively and negatively charged cellulose-based PELs, by periodate oxidation (DAC) followed by cationization of DAC with Girard's reagent T (CDAC) or anionization with sodium metabisulfite (ADAC).

TABLE 1 | Cationization reaction conditions used for synthesis of cationic bio-PELs and characterization of final products.

Name	Time (h)	Temp (°C)	GT/aldehyde (molar ratio)	Cationicity index (mmol/g)	ζ-potential (mV)	Z-Average diameter (nm)	PDI
CDAC$_{p}$A	1	70	3.9	3.74	52 ± 2	124 ± 2	0.34 ± 0.03
CDAC$_{p}$B	1	70	0.975	3.08	54 ± 1	176 ± 4	0.5 ± 0.01
CDAC$_{w}$A	1	70	3.9	3.56	46 ± 1	247 ± 8	0.43 ± 0.02
CDAC$_{w}$B	1	70	0.975	2.84	40 ± 3	292 ± 10	0.45 ± 0.02

Cationicity determined as the amount of alkylammonium groups (mmol) per g (dry weight) of cationic cellulosic sample; PDI- polydispersity index of the hydrodynamic diameter distribution; cationic cellulose-based polyelectrolytes from bleached pulp or from wood wastes pulp with kappa number 26.7, respectively, CDAC$_{p}$ and CDAC$_{w}$.

TABLE 2 | Anionization reaction conditions used for synthesis of anionic bio-PELs and characterization of final products.

Name	Time (h)	Temp (°C)	Anionicity index (mmol/g))	ζ-potential (mV)	Z-Average diameter (nm)	PDI
ADAC$_{p}$A	24	25	4.23	−44 ± 2	157 ± 10	0.59 ± 0.08
ADAC$_{p}$B	72	25	4.17	−50 ± 1	127 ± 6	0.52 ± 0.02
ADAC$_{w}$A	24	25	4.47	−45 ± 1	137 ± 8	0.47 ± 0.02
ADAC$_{w}$B	72	25	4.90	−36 ± 2	116 ± 7	0.46 ± 0.03

Anionicity determined as the amount of sulfonate groups (mmol) per g (dry weight) of anionic cellulosic sample; PDI- polydispersity index of the hydrodynamic diameter distribution; anionic cellulose-based polyelectrolytes from bleached pulp or from wood wastes pulp with kappa number 26.7, respectively, ADAC$_{p}$ and ADAC$_{w}$.

24 to 72 h, while keeping constant the reaction temperature (room temperature, 25°C) and the molar ratio of sodium metabisulfite to the aldehyde groups' content of DAC. Once more, it is expected that different composition of initial raw materials used in the production of DAC precursors for anionization, namely a lower content of cellulose and the presence of other constituents as lignin, should have some influence not only on the reaction kinetics but also on the characteristics of the obtained ADACs. The influence of the different reaction times (24–72 h) on the characteristics of the final products (anionic groups content, zeta potential, hydrodynamic diameter and PDI) is summarized in **Table 2**. Again, when using a more heterogeneous starting material, the zeta potential of the modified cellulose-based PELs is lower. It was also observed that with the increase of reaction time there is a slight decrease in the hydrodynamic diameter of the obtained anionized products, independently of the raw material used. Regarding the degree of substitution by anionic groups there is a clear trend of the effect of reaction time in the case of the ADAC$_{w}$ products.

The solubility of CDACs and ADACs was confirmed by the total transparency of the reaction solution at the end of the modifications. The overall results showed that highly charged, cellulose-based cationic and anionic polyelectrolytes can be prepared by a two-step modification: periodate oxidation/cationization or periodate oxidation/anionization sequence, using various GT/aldehyde molar ratios (in the case of cationization) or different reaction times (while performing anionization). As a result, a range of PELs with different charge densities were prepared that apparently exhibit adequate features to be applied as flocculation agents in industrial wastewater treatment. The final evaluation of the products produced (cellulosic PELs) is going to be conducted by jar-test as well as by LDS.

Evaluation of Performance of Cellulosic Pels in Textile Wastewater Treatment

The performance of obtained cationic ($CDAC_pA$, B and $CDAC_wA$, B) and anionic ($ADAC_pA$, B and $ADAC_wA$, B) cellulose-based polyelectrolytes (with diverse characteristics) in the decolouration of an effluent from textile industry will be presented here and discussed individually, for each type of cellulosic polyelectrolyte (cationic or anionic). Also, the influence of the source of the raw material used in the production of tested bio-PELs, as well as their substitution degree, is going to be evaluated, based on the jar-tests and on LDS studies. In all performed jar-tests the cellulosic PELs were compared with a synthetic reference, either cationic, or anionic PAM (Grenda, 2018).

When applying flocculation or coagulation strategies in the water treatment, it is very important to understand the charge characteristics of the tested system. The stability of dye effluents can significantly influence the success of used procedure. Determination of the particles charge is then crucial and the stability of the system can be tuned by changing the pH of the system, due to ionization of certain groups in the dye structures. The zeta potential of the industrial effluent, after adjustment for the pH's to be used in the performance jar-tests, was measured, and the obtained values are presented in **Figure S1**. For the tested effluent, the particles surface is mainly negatively charged. With the increase of alkalinity, a significant increase in negative charge was also observed. The highly negatively charged suspended dye molecules of the system tested promotes the stabilization of the effluent, due to the repulsion effect, making it more difficult to treat the effluent at alkaline pH. It is then expected that pH changes will impact clarification performance of tested effluent and better color removals are going to be obtain at acidic conditions where the effluent presents lower charges. At neutral pH, pH 7, the zeta potential of the colored effluent tested was clearly in the stable zone (-49 mV).

Jar-Test Flocculation Study

Cationic cellulose-based flocculants, hold positively charged groups, which are fundamental for the neutralization of negatively charged suspended dye molecules. Also, due to the relatively long chains of the polymers with medium charge densities, bridging between the particles will be a complementary mechanism. The adsorbed polymer chain can extend from the particle surface and interact with other particles or polymer chains.

The influence of pH and dosage of inorganic complexation agent (bentonite), as well as the dosage of cellulose-based flocculants obtained from *Eucalyptus*-based raw materials of different chemical complexity (cellulose and lignin contents), on the turbidity reduction and on color removal are summarized in **Figures 2–5**. **Figure 2** presents the results obtained using a single system, only the polyelectrolyte, either synthetic, or natural-based (either anionic or cationic).

In this study, the values of the supernatant water turbidity were used to evaluate the PELs performance in the treatment of this industrial effluent. **Figure 2** shows the color removal results at two different pH's (1.5 and 7.0) for 5.34 mg/L $CDAC_pA$ or synthetic cPAM, in single system (left insert) or when using 5.34 mg/L $ADAC_pA$ or synthetic aPAM, also in single system (right insert). The decolouration results were always better for acidic conditions for both cellulose-based and synthetic flocculation agents. At pH 1.5, $CDAC_pA$ was more effective in this effluent treatment: in the first hour of treatment it allowed to remove 36% of color (after 30 min) and 41% (after 1h), while cPAM removed 26 and 32%, respectively after 30 min and 1 h of treatment. For a long period of treatment, after 24 h of settling, both polymers showed similar color reduction. Moreover, at neutral pH (7.0) cPAM showed a slightly superior performance over $CDAC_pA$, removing 36% of turbidity after 24 h, while the cellulose-based flocculant removed 27%. The better results obtained with both flocculants for acidic pH are due to the effluent lower stability (**Figure S1**) for this pH; the lower repulsion effect between the particles, makes it easier to treat the effluent at low pH, when compared to more alkaline pH levels. As mentioned before, also with the anionic polyelectrolytes, the best results (19% turbidity reduction after 24 h) were obtained when pH was adjusted to 1.5, due to the lower effluent stability. When comparing the performance of the synthetic aPAM to that of the natural-based $ADAC_pA$, lower turbidity reductions were always obtained for the latter one, for the same pH levels, possibly due to a slightly lower charge density and molecular weight of the anionic natural-based PEL, compared to the synthetic one. As expected, considering the average negative charge of the effluent for the different pHs, the cationic PELs performed better than the anionic ones.

Considering that removal with single flocculation system was still not adequate (maximum around 50% for the cationic PELs at pH 1.5), the industrial effluent was also treated using a dual system with bentonite (an inorganic material). **Figures 3–5** show results obtained at pH 1.5, 3.0, and 7.0 (the initial effluent pH was 12.0) while using two different concentrations of flocculation agent (either natural-based or synthetic) 2.67 mg/L (procedures A and D) or 5.34 mg/L (procedures B and C), and two different amounts of bentonite 0.3 wt% (procedures A and C) or 0.6 wt% (procedures B and D). Additionally, all procedures A - D at all tested pH levels were compared with the treatment performed only with bentonite (mono system, see **Figure 6**). In all the presented cases A - D and tested pH levels, better color removal was always obtained after 24 h of treatment, while using dual system (bentonite followed by addition of flocculant), when compared to procedures using only bentonite (**Figure 6**), or single system with flocculant (**Figure 2**), at the same pH.

As can be seen, in **Figure 3**, at pH 1.5, due to the highest instability of the treated effluent, higher turbidity removals were obtained in general, when compared to the other pHs (3.0 and 7.0) (see **Figures 4**, **5**). Also, at high acidic pH bentonite tends to have the most positively charged surface (Kim, 2003) compared to pH 3.0 or 7.0. Thus, complexation of the dye with the particles is enhanced, allowing PELs to interact with those complexes, and then flocculate through the bridging mechanism. Moreover, with the increase of bentonite or flocculant dosage, performance did not improve significantly regarding final removal (24 h), even if when using procedure B settling was faster. Thus, at pH 1.5 both procedures A and B showed to be the most effective. Interactions

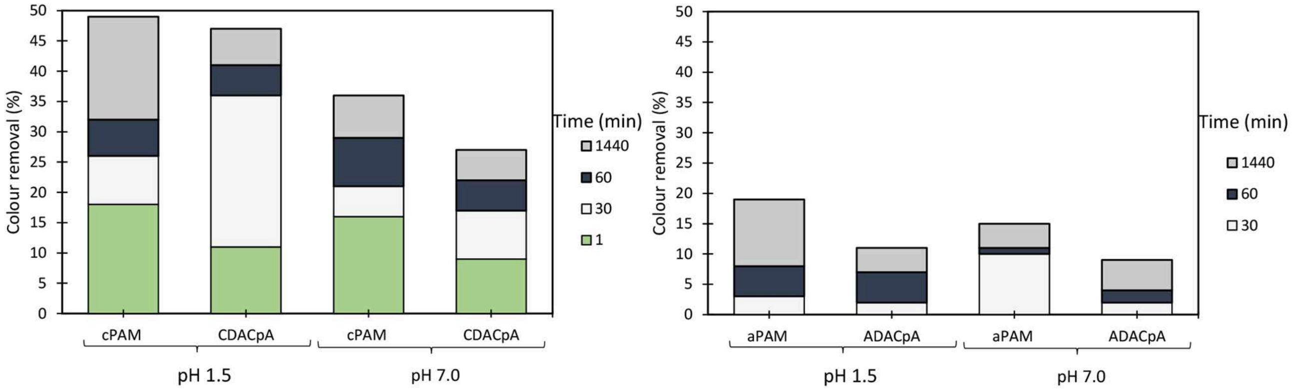

FIGURE 2 | Industrial colored effluent treatment (based on turbidity reduction) using only a single flocculation agent [5.34 mg/L of synthetic (cPAM or aPAM) or cellulose-based ($CDAC_pA$ or $ADAC_pA$)] at two different pH levels, 1.5 and 7.0.

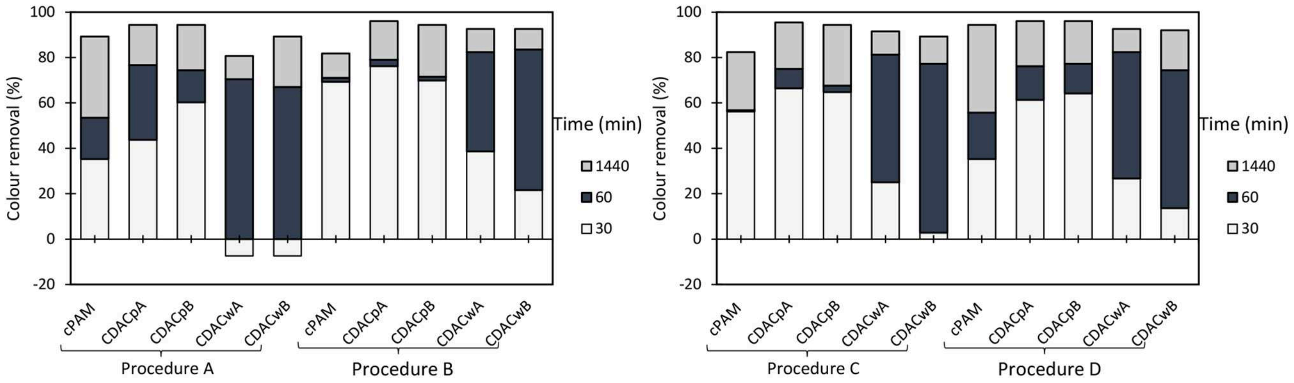

FIGURE 3 | Turbidity removal of industrial effluent as a function of time of settling, using cationic cellulose-based flocculation agents from bleached pulp ($CDAC_p$ A and B) and from wood chips ($CDAC_w$ A and B), in a dual system with bentonite, at pH 1.5. Procedure A: 0.3 wt% bentonite followed by 2.67 mg/L of flocculant. Procedure B: 0.6 wt% bentonite and 5.34 mg/L of flocculant. Procedure C: 0.3 wt% bentonite and 5.34 mg/L of flocculant. Procedure D: 0.6 wt% bentonite and 2.67 mg/L of flocculant. A cationic synthetic cPAM (in dual system with the same concentrations described in procedures A-D), was used as reference.

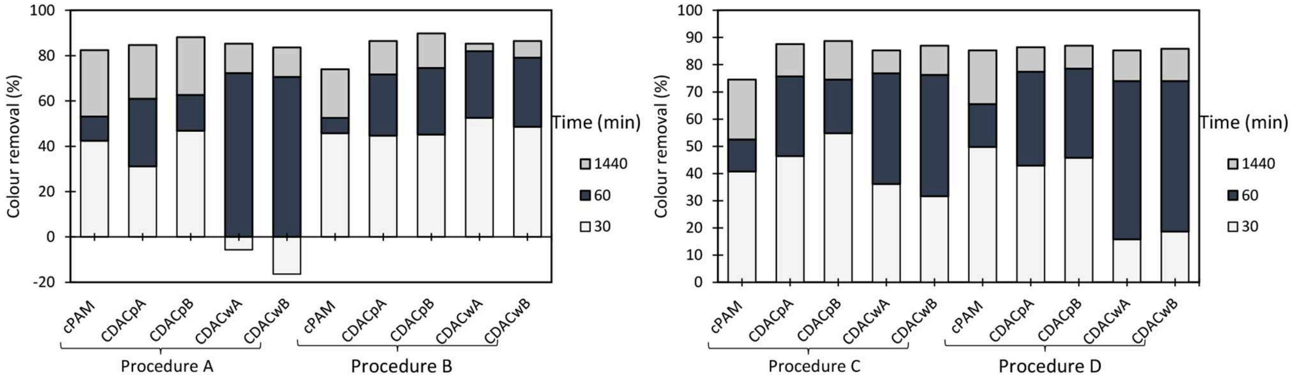

FIGURE 4 | Turbidity removal of industrial effluent as a function of time of settling, using cationic cellulose-based flocculation agents from bleached pulp ($CDAC_p$ A and B) and from wood chips ($CDAC_w$ A and B), in a dual system with bentonite, at pH 3.0. Procedure A: 0.3 wt% bentonite followed by 2.67 mg/L of flocculant. Procedure B: 0.6 wt% bentonite and 5.34 mg/L of flocculant. Procedure C: 0.3 wt% bentonite and 5.34 mg/L of flocculant. Procedure D: 0.6 wt% bentonite and 2.67 mg/L of flocculant. A cationic synthetic cPAM (in dual system with the same concentrations described in procedures A-D), was used as reference.

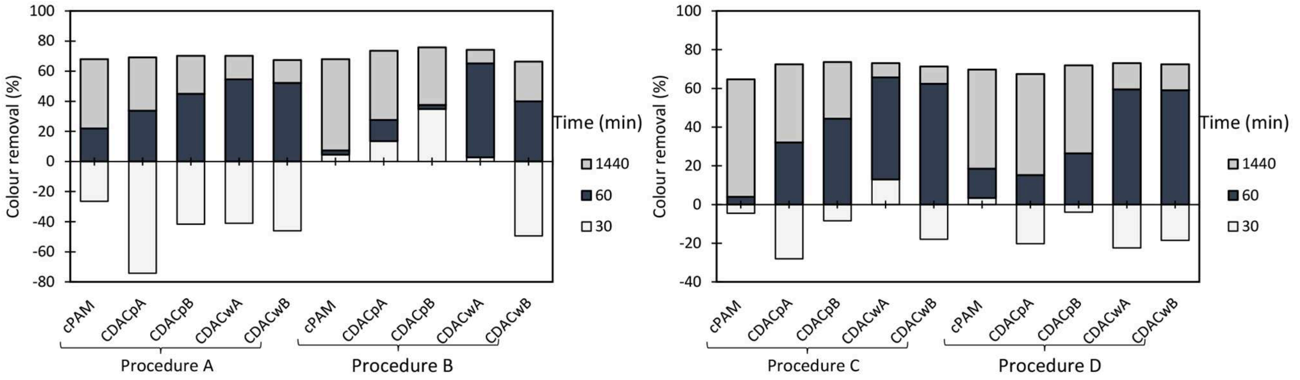

FIGURE 5 | Turbidity removal of industrial effluent as a function of time of settling, using cationic cellulose-based flocculation agents from bleached pulp (CDAC$_p$ A and B) and from wood chips (CDAC$_w$ A and B), in a dual system with bentonite, at pH 7.0. Procedure A: 0.3 wt% bentonite followed by 2.67 mg/L of flocculant. Procedure B: 0.6 wt% bentonite and 5.34 mg/L of flocculant. Procedure C: 0.3 wt% bentonite and 5.34 mg/L of flocculant. Procedure D: 0.6 wt% bentonite and 2.67 mg/L of flocculant. A cationic synthetic cPAM (in dual system with the same concentrations described in procedures A–D), was used as reference.

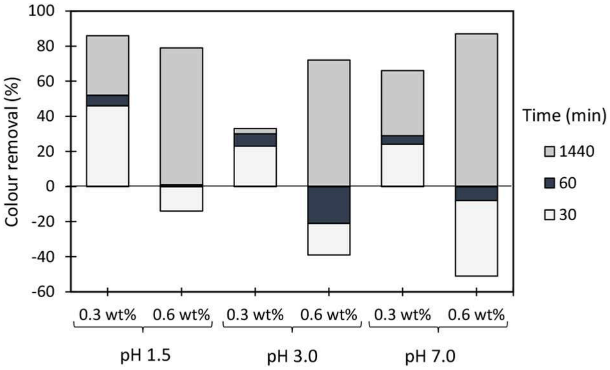

FIGURE 6 | Industrial colored effluent treatment (based on turbidity reduction) when using only bentonite at two different dosages (0.3 and 0.6 wt%) and three different pH levels, 1.5, 3.0, and 7.0.

should be mainly electrostatic between alkylammonium groups of cationic cellulosic PEL (**Figure 1**) and sulfonate groups of negatively charged dyes. Hydrogen bonding through hydroxyl groups of the cellulosic backbone and amine functions of the dye may also be effective, as well as van der Waals interactions (Lapointe and Barbeau, 2020). Initially, the interactions of the dye with bentonite should be mainly electrostatic. Bridging must then be the main flocculation mechanism of the bentonite particles after addition of the cellulose PELs. The molecular weight of the cellulose-based PELs was not determined. Notwithstanding, considering a typical polymerization degree of the initial kraft pulps used in the present work near 3000 (corresponding to a molecular weight of around 486 kDa) (Lourenço et al., 2019), and even considering that some depolymerization of cellulose has occurred during the PEL production, namely in the step of periodate oxidation, it is reasonable to expect a final PEL still with a medium molecular weight, for which bridging mechanisms are possible (Bolto and Gregory, 2007).

Additionally, for the best treatment conditions, CDAC$_p$A and CDAC$_p$B presented superior efficiency in the reduction of turbidity 44% (30 min), 77% (1 h), and 94% (24 h) for CDAC$_p$A and 60% (30 min), 74% (1 h), and 94% (24 h) for CDAC$_p$B due to their high cationicity index and substitution degree, when compared with the CDAC$_w$ samples. CDAC$_p$ are natural-based polyelectrolytes obtained from relatively more homogenous raw material (bleached fibers) compared to the other tested cellulose-based PELs. This trend appeared for all the pHs and conditions tested. It is worth stressing that the not so good performance of CDAC$_w$ (A and B) is more obvious when referring to the rate of turbidity removal (settling is lower) than when we compare the final turbidity removal results. Comparing **Figures 3**, **4**, it is also clear that good, but slightly lower turbidity reductions, were obtained at pH 3.0, compared to performance at pH 1.5. The worst results, especially for low settling times, even if still reasonable, were obtained for pH 7 (**Figure 5**). This indicates a higher stability of the effluent at this pH, which resulted in an increase of turbidity in the first moments after addition of bentonite.

Furthermore, in dual system, results obtained with the natural-based flocculants are very similar or slightly higher than the ones obtained with the synthetic reference cPAM.

For the cationic natural-based PELs from modified bleached pulp, with high (CDAC$_p$A), and lower (CDAC$_p$B) substitution degree, as for the cationic PELs from wood wastes, obtained from pulp with significant lignin content (kappa number 26.7), CDAC$_w$A (higher cationicity index) and CDAC$_w$B (lower cationicity index), and for the reference polymer cPAM (Snow Flake E2), COD reduction was measured, after 24 h of treatment, at pH 3.0, for two conditions: with minimum dosages of bentonite and flocculant, which corresponds to procedure A (0.3 wt% bentonite followed by 2.67 mg/L of flocculation agent) and with maximum dosage of the two components, procedure B (0.6 wt% bentonite followed by 5.34 mg/L of flocculation agent). The results of COD reduction together with the turbidity removal after 24 hours obtained using these procedures are plotted in **Figure 7**. The COD reduction is closely related with the turbidity removal, and with the increase of effluent clarification higher COD reduction was observed. For the procedure with

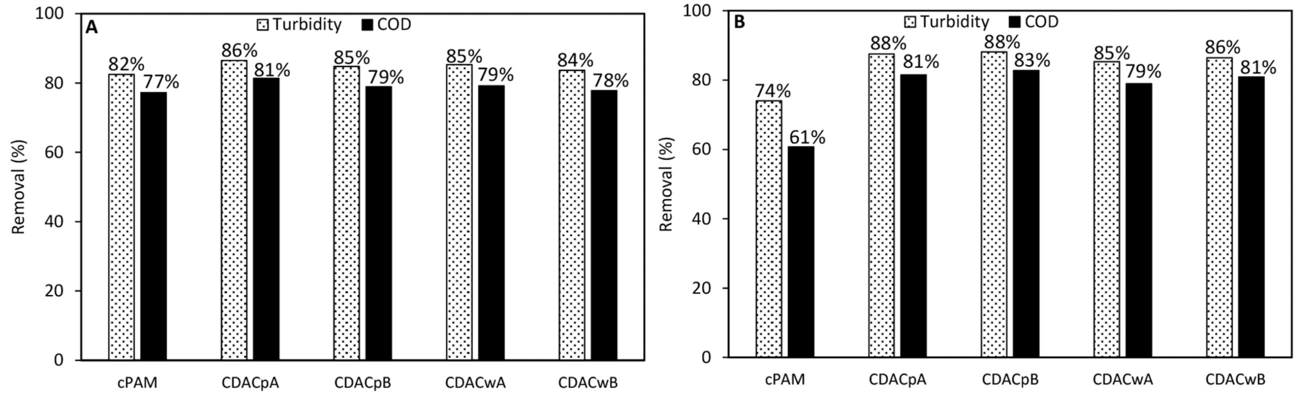

FIGURE 7 | COD reduction and turbidity removal during the industrial effluent treatment with CDAC$_p$A, B and CDAC$_w$ A, B and reference Snow Flake E2 (cPAM), at pH 3.0, after 24 h of treatment, in two conditions: **(A)** 0.3 wt% bentonite followed by 2.67 mg/L of flocculation agent and **(B)** 0.6 wt% bentonite followed by 5.34 mg/L of flocculation agent.

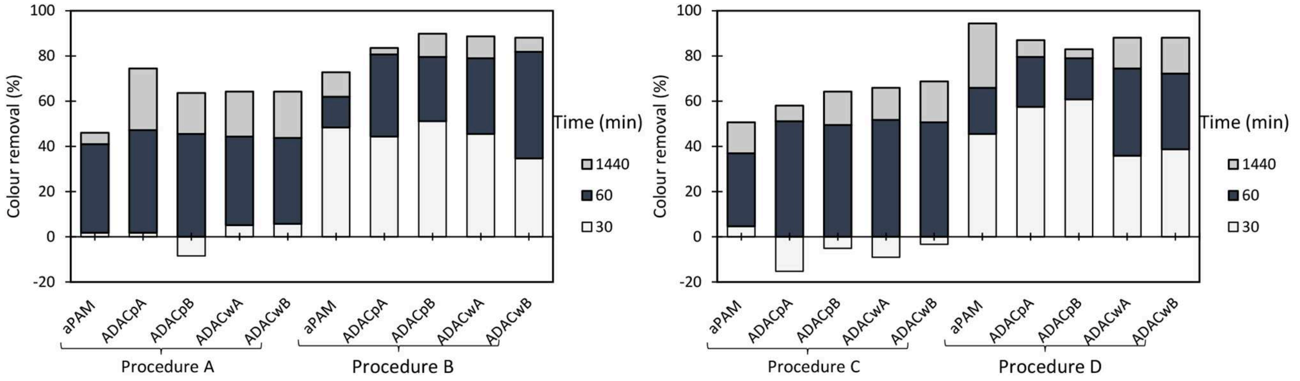

FIGURE 8 | Turbidity removal of industrial effluent as a function of time of settling, using anionic cellulose-based flocculation agents from bleached pulp (ADAC$_p$ A and B) and from wood chips (ADAC$_w$ A and B), in a dual system with bentonite, at pH 1.5. Procedure A: 0.3 wt% bentonite followed by 2.67 mg/L of flocculant. Procedure B: 0.6 wt% bentonite and 5.34 mg/L of flocculant. Procedure C: 0.3 wt% bentonite and 5.34 mg/L of flocculant. Procedure D: 0.6 wt% bentonite and 2.67 mg/L of flocculant. An anionic synthetic aPAM (in a dual system with the same concentrations described in procedures A-D), was used as reference.

addition of lower amounts of treatment agents (procedure A), the COD reduction obtained was in the range of 78–81%, for the new natural-based flocculation agents, while for the synthetic reference was 77%. Moreover, procedure B, with double amounts of added components, when compared to procedure A, presents only slightly higher turbidity removals and COD reductions. In this case, the COD reduction obtained was in the range of 79–83%, for the new natural-based flocculation agents, while for the synthetic reference only 61% of COD reduction was achieved. Considering the overall results, the natural-based flocculation agent CDAC$_p$A, seems to be the cellulose-based flocculant that has the best performance in the treatment of the industrial colored effluent (higher turbidity reduction, with low dosage, and high COD reduction) among the tested cationic flocculation agents, leading also to faster decolouration (faster settling) (see also **Figures 3–5**).

On the other hand, the cationic cellulose-based flocculation agents, namely CDAC$_p$A, showed superior performance in turbidity removal and COD reduction, over the synthetic cPAM reference. It is worth stressing that the use of procedure A, with low addition of bentonite (0.3 wt%), followed by a low dosage of CDAC (2.67 mg/L) showed good results, similar to the ones with increased dosages of used components, which is a positive aspect, since using lower dosage of bentonite and flocculant can significantly reduce the costs associated to the treatment process.

Anionic cellulose-based flocculation agents hold negatively charged groups, which are able to establish strong interactions with oppositely charged particles which can also be dispersed in the effluent. The developed anionic cellulose-based flocculants (ADAC$_p$ and ADAC$_w$ series) were tested in turbidity reduction of the industrial colored effluent. The variation of supernatant water turbidity, over time (30 min, 1 h, and 24 h), was used to evaluate the PELs performance in the treatment of this industrial effluent. The single system (only the anionic flocculant as described previously, see **Figure 2**), as well as a dual system with inorganic complexation agent (bentonite), were tested. The summary of the results while applying the dual systems are presented in **Figures 8–10**, for different pHs (1.5, 3.0, and 7.0).

Considering the poor results obtained only with the negatively charged flocculants, as it was expected since the effluent is,

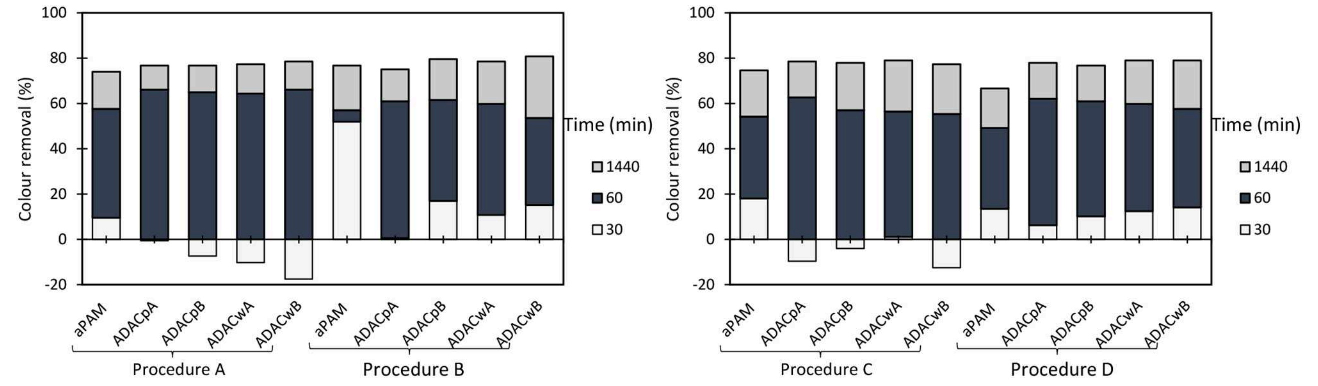

FIGURE 9 | Turbidity removal of industrial effluent as a function of time of settling, using anionic cellulose-based flocculation agents from bleached pulp (ADAC$_p$ A and B) and from wood chips (ADAC$_w$ A and B), in a dual system with bentonite, at pH 3.0. Procedure A: 0.3 wt% bentonite followed by 2.67 mg/L of flocculant. Procedure B: 0.6 wt% bentonite and 5.34 mg/L of flocculant. Procedure C: 0.3 wt% bentonite and 5.34 mg/L of flocculant. Procedure D: 0.6 wt% bentonite and 2.67 mg/L of flocculant. An anionic synthetic aPAM (in a dual system with the same concentrations described in procedures A-D), was used as reference.

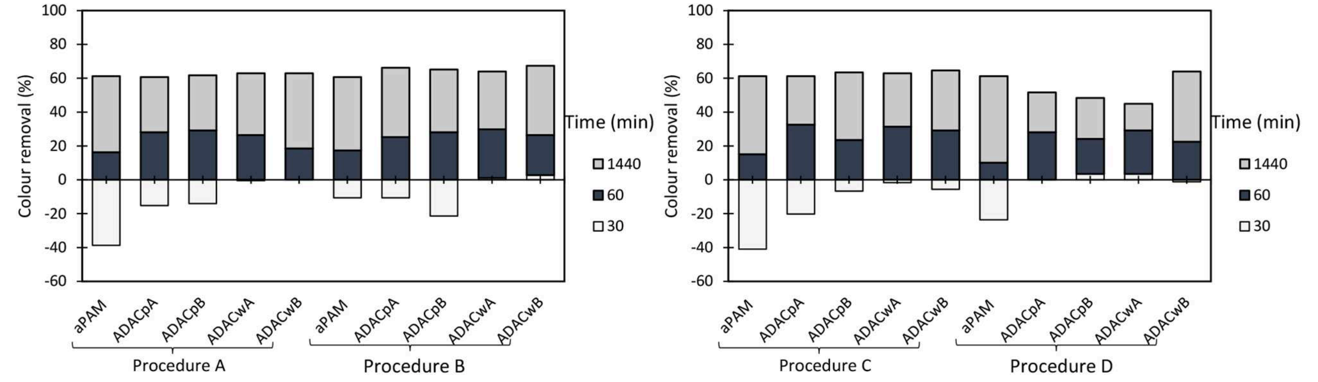

FIGURE 10 | Turbidity removal of industrial effluent as a function of time of settling, using anionic cellulose-based flocculation agents from bleached pulp (ADAC$_p$ A and B) and from wood chips (ADAC$_w$ A and B), in a dual system with bentonite, at pH 7.0. Procedure A: 0.3 wt% bentonite followed by 2.67 mg/L of flocculant. Procedure B: 0.6 wt% bentonite and 5.34 mg/L of flocculant. Procedure C: 0.3 wt% bentonite and 5.34 mg/L of flocculant. Procedure D: 0.6 wt% bentonite and 2.67 mg/L of flocculant. An anionic synthetic aPAM (in a dual system with the same concentrations described in procedures A-D), was used as reference.

on average, negatively charged, the decision was to introduce a second component, a complexation agent (bentonite), with the objective to improve the flocculation kinetics. **Figures 8–10** show the results obtained at pH 1.5, 3.0, and 7.0 (the initial effluent pH was 12.0) while using two different concentrations of flocculation agent (either anionic natural-based ADAC or synthetic aPAM), 2.67 mg/L (procedures A and D) or 5.34 mg/L (procedures B and C) and two different amounts of bentonite 0.3 wt% (procedures A and C) or 0.6 wt% (procedures B and D). For all the conditions tested, A-D, and tried pH levels (1.5, 3.0, and 7.0), better color removals were obtained after 24 h of treatment, when using the dual system bentonite-anionic PEL, compared to the single system, only with polyelectrolyte (**Figure 2**), at the same pH. As mentioned before for the cationic polyelectrolytes, also with anionic polyelectrolytes, the best results, after 24 h, were obtained when the pH was adjusted to 1.5, due to the lower effluent stability. In addition, bentonite positive charge increases with the increase of acidity level (Kim, 2003), which can significantly influence the interactions with the negatively charged effluent. Furthermore, in a dual system with bentonite, results obtained with the natural-based anionic flocculants are always better when compared to the results obtained with the synthetic aPAM reference. After adding bentonite, the effluent is destabilized and, in some cases, this can lead, initially, to some increase in turbidity of the system.

In general, the slightly positively charged bentonite surface (for acidic conditions) interacts with the negatively charged system (effluent), and further addition of the polymer allows faster and more effective flocculation, due to the charge neutralization and bridging mechanisms, resulting in rapid settling. In all tested procedures, at different pH levels, the same flocculation mechanisms must have been involved. However, with the increase of alkalinity, bentonite surface becomes less and less positively charged (Kim, 2003), the system becomes more stable, and less turbidity removal was obtained. Interactions between anionic cellulosic PEL and bentonite-dye complex should be mainly through the sulfonate groups (electrostatic) or hydroxyl groups (hydrogen bonding) of the cellulosic structure (**Figure 1**), although no favorable electrostatic interaction is anticipated directly between the anionic PEL and the negatively charged dye. Additionally, as can be seen, in **Figures 8–10**, considering the relatively high negative charge of the system, better clarification results were obtained at higher dosages of bentonite (procedures B and D).

Additionally, at the best treatment conditions (pH and dosages of bentonite and flocculant) ADAC$_w$A and ADAC$_w$B presented superior efficiency in the reduction of turbidity, especially for low contact times.

Comparing the performance of the treatments using ADACs with the treatments using cationic polymers (CDACs), combined, in both cases, with bentonite, the second ones performed always better (see **Figure S2**). This agrees with the average negative charge of the effluent, even if positive bentonite is added to the system. This is evident not only when we look at the final color removal after 24 h, but also analyzing the settling rate of the effluent particles, which is faster when using the cationic polymers.

For the anionic natural-based PELs obtained from modified bleached pulp, ADAC$_p$A, obtained after 24 h of sulfonation, and ADAC$_p$B, obtained after 72 h of reaction, for the anionic PELs derived from the pulp with the high lignin content, ADAC$_w$A (24 h reaction) and ADAC$_w$B (72 h reaction), and for the reference polymer aPAM, COD reduction efficiency was evaluated at pH 3.0, for two conditions: with lower dosages of bentonite and flocculant, which corresponds to procedure A (0.3 wt% bentonite followed by 2.67 mg/L of flocculation agent), and with maximum dosages of the two components, procedure B (0.6 wt% bentonite followed by 5.34 mg/L of flocculation agent). In **Figure 11** we have plotted both the COD reduction after 24 h of treatment and the corresponding turbidity reduction. Once again, as it was observed for the cationic PELs (**Figure 7**), the COD reduction was closely related with the turbidity removal after 24 h. With the increase of effluent clarification higher COD reduction was observed. For the procedure with low addition of bentonite and flocculant components (procedure A), the COD reduction obtained was in the range of 65–69% for the new anionic natural-based flocculation agents produced (for CDACs it was 78–81%), while for the synthetic aPAM reference it was 61%. ADACs show lower performance in turbidity reduction, as already described, and also in COD reduction. Moreover, procedure B, with double levels of added components when compared to procedure A, presents slightly higher turbidity reductions, which results also in higher values of COD reduction, in the range of 69–77%, while for the synthetic reference 66% of COD reduction was achieved. Considering the overall results, natural-based flocculation agent ADAC$_w$B, produced from the more heterogeneous fibers, Cw, seems to be the anionic cellulose-based flocculant that has the best performance in the treatment of the tested effluent, higher turbidity removal, with low dosage, and high COD reduction, for the described operation conditions at pH 3.

In general, a superior performance in turbidity reduction and water clarification was exhibited by the dual system with bentonite and cationic cellulose-based flocculation agents, compared to the dual system bentonite/anionic polyelectrolyte, due to the effluent nature, and repulsion interactions when using polyelectrolytes of similar charge to the average charge of the wastewater. Additionally, bentonite successfully destabilized the system, through the interaction with effluent impurities (especially dye molecules) allowing to create larger particles/larger complexes, heavier and easier to flocculate and settle.

Furthermore, natural-based PELs presented, in general, better turbidity and COD reductions, compared to the synthetic references. It is worth noticing that the use of procedure A with low dosages of bentonite (0.3 wt%) and natural-based PEL (2.67 mg/L), at pH 3.0, showed quite good turbidity reduction. Acidic conditions proved to be required to achieve adequate color removal.

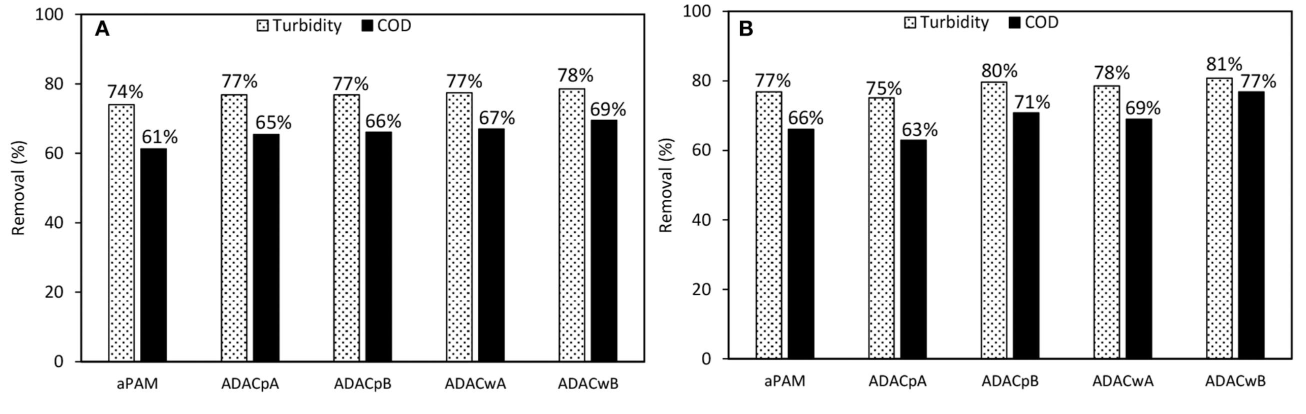

FIGURE 11 | COD reduction and turbidity removal during the industrial effluent treatment with ADAC$_p$A, B and ADAC$_w$ A, B and reference aPAM, at pH 3.0, after 24 h of treatment, in two conditions: **(A)** 0.3 wt% bentonite followed by 2.67 mg/L of flocculation agent and **(B)** 0.6 wt% bentonite followed by 5.34 mg/L of flocculation agent.

Flocculation Monitoring by LDS

LDS was recently, successfully used in the flocculation monitoring of a real oily effluent (Lourenço et al., 2018) using especially designed synthetic flocculants, and following previous studies where only model particles were tested. Here, cationic natural-based PELs, $CDAC_pA$, B, and $CDAC_wA$, B, and anionic cellulose-based PELs, $ADAC_pA$, B, and $ADAC_wA$, B, with different features, were applied in the flocculation of an industrial colored effluent in dual system with bentonite and flocculation was monitored by LDS. Due to the different features of the tested cationic (CDACs) and anionic (ADACs) flocculants, differences in the flocculation process are expected to be observed. The conditions used in the LDS trials of the industrial colored effluent were based on the jar-tests experiments developed and described previously.

An example of the particle size distribution of the initial industrial colored effluent, at pH 3.0, after addition of the bentonite and at the end of the flocculation process (20 min of treatment), is shown in **Figure S3**, for the process carried out using cellulose-based flocculants, either the cationic $CDAC_pA$ or anionic $ADAC_pA$. In both cases, the particle size distribution evolves from a bimodal distribution in the low particle size range to monomodal distributions which are displaced, with time, toward higher particle sizes, as expected. Moreover, $ADAC_pA$ showed slightly larger aggregates than $CDAC_pA$. The median size of the particles in the initial industrial effluent, measured by LDS, was 0.106 μm, while after the addition of bentonite it was 3.88 μm, corresponding to the formation of effluent-bentonite complexes. The addition of flocculant, either cationic or anionic (4.0 mg/L), increased drastically the median size of the particles at the end of the process, monitored over 20 min. Adding $CDAC_pA$, increased the median particle size to a value of 94 μm, while adding $ADAC_pA$ increased the median particle size to a value of 193 μm.

Figure 12A and **Figure S4** show the evolution of aggregate size over time, obtained by LDS, for four tested PEL concentrations (1.3, 2.6, 4.0, and 5.3 mg/L), for the cationic cellulose-based polyelectrolytes tested (obtained from bleached pulp, with high substitution degree, $CDAC_pA$ and lower substitution degree, $CDAC_pB$, and obtained from pulp with kappa number of 26.7, with higher substitution degree, $CDAC_wA$ and lower substitution degree, $CDAC_wB$). In these figures both the evolution of the median of the floc size distribution d(0.5) (**Figure 12A**), and the 90% undersize percentile diameter d(0.9) (**Figure S4**), are plotted. The trends in these curves are, in general, similar for all the cases tested if PELs produced from the same type of raw material are compared ($CDAC_pA$ with $CDAC_pB$ and $CDAC_wA$ with $CDAC_wB$). Furthermore, the floc size reaches its maximum within 60 s after addition of flocculant to the effluent/bentonite system and then stabilizes. **Figure 12A** and **Figure S4** demonstrate that the characteristics of used bio-PELs influence both aggregate size and the flocculation kinetics. Following the flocs size evolution with time, it is possible to conclude that in first minutes of the flocculation, aggregation predominates, allowing to obtain large floc size. After reaching the maximum value of floc size, breakage of the large flocs, even in low turbulent environment can happen (Rasteiro et al., 2008, 2011), and aggregates size stabilizes only when the balance between breakage and reaggregation occurs. Similar trends can be observed when analyzing both the evolution of the d(0.5) and d(0.9) with time.

The rearrangement of aggregates appears in all the tests while working at high polyelectrolyte concentrations (4.0 and 5.3 mg/L), especially when using PELs with lower charge density, $CDAC_pB$ and $CDAC_wB$, which do also present higher molecular weight (considering the hydrodynamic diameter). This tendency is more obvious when looking at the d(0.9) plots, which correspond to the larger aggregates in the system. Additionally, with the increase of cationic-PEL dosage used in the effluent-bentonite system an increase in the floc size was observed. For all tested cellulose-based flocculants from bleached pulp, the influence of concentration is significant and is more pronounced for PEL with lower substitution degrees ($CDAC_pB$). For the PELs produced from the pulp with a high kappa number of 26.7 ($CDAC_wA$ and $CDAC_wB$) the influence of concentration is not so evident. This can be attributed to the expected wider distribution of molecular weight of these PELs, considering their higher heterogeneity (presence of other polymers besides cellulose). Additionally, the high charge and substitution degree of $CDAC_pA$ led to superior results regarding the flocs growth, over the slightly lower charged $CDAC_pB$, which led to smaller aggregates, especially while working at lower polymer concentrations of 1.3 and 2.6 mg/L. This can be attributed to insufficient bridging of the particles while working with a lower charged polymer and lower concentrations. The predominant flocculation mechanism for the $CDAC_p$ must be bridging, which explains why working at significantly low polymer concentrations results in small flocs, since only few particles will be bridged together in this case. It is also important to note, that the results obtained in the jar-test are in agreement to those obtained by LDS.

The SE profiles, calculated from the scattering matrix obtained via LDS, for the four cationic cellulose-based PELs, with four concentrations, were plotted in **Figure 12B**. For all the tests, independently of used cationic natural-PEL and concentration, the scattering exponent increases rapidly at the beginning of the flocculation process, when a rapid growth of the flocs size also occurs. The higher is the value of SE the more compact aggregates were obtained. Due to the very low particles size of the initial model effluent, it was not possible to obtain their SE value. The initial SE values in **Figure 12B** correspond to the effluent-bentonite system, and the continuous growth of SE indicates the continuous increase of floc compactness through the flocculation process. Comparing with literature (Lourenço et al., 2018), where an industrial oily-based effluent was flocculated with synthetic anionic polyelectrolytes, also under low turbulent conditions, SE values below 1.7 were reached for that case, while for the present industrial colored effluent-bentonite system, under similar stirring conditions, higher SE values were obtained in several trials, corresponding to more compact flocs. The floc structure results based on SE (**Figure 12B**) indicate that the flocculation process takes place by the bridging mechanism; supported by the fast flocculation rate and the relatively open aggregates (maximum

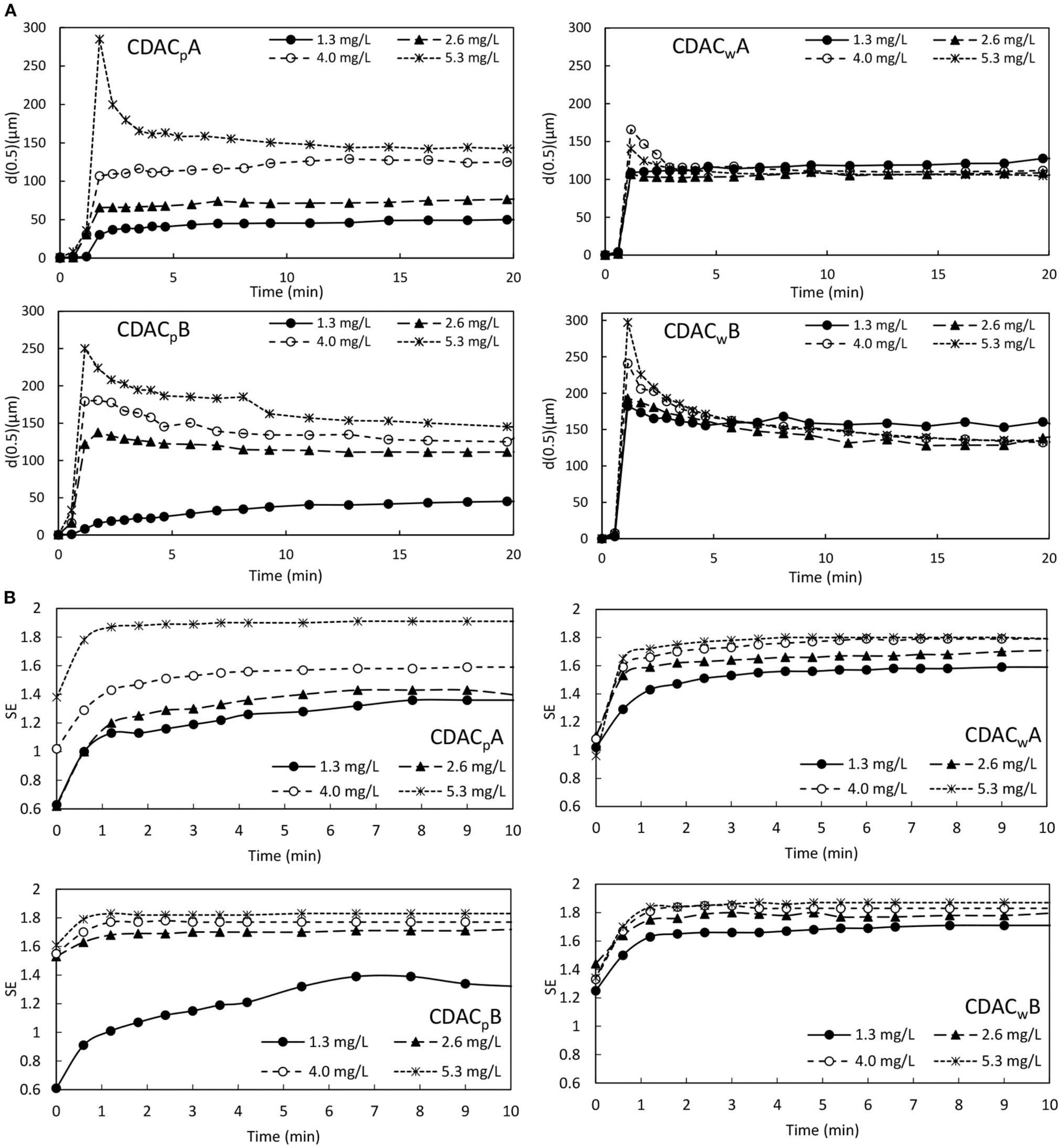

FIGURE 12 | Industrial effluent treatment - evolution of **(A)** median particle size (d(0.5)) and **(B)** floc structure (SE) over time, obtained *via* LDS, for four different flocculant dosages of cationic cellulose-based polyelectrolytes obtained from bleached pulp, CDAC$_p$A, B and obtained from pulp with kappa number of 26.7, CDAC$_w$A, B, combined with bentonite.

SE around 1.9). Higher PEL concentration leads to more compact flocs, which correspond to higher values of SE, due to inclusion of more particles in the aggregate. In general, cationic flocculants from pulp with high lignin content (CDAC$_w$A and CDAC$_w$B) exhibit a lower influence of PEL concentration on floc compactness, agreeing with the trends observed when analyzing the influence of PEL concentration on floc size. Also, the flocs obtained with these two PELs are, in general, more compact than the ones obtained with CDAC$_p$, when comparing results for the lower concentrations used. This may, again, be related to the wider distribution of molecular weights of these bio-PELs.

With the increase in charge density the less extended conformation of the polymer chain on the particles surface leads to more compact flocs, as it was also reported in the literature (Biggs et al., 2000). Comparing all the cationic polymers, the more compact flocs correspond to the situations where larger flocs were obtained, which is related to a more efficient flocculation process resulting in aggregation of more particles.

As it was observed while performing the jar-tests, with the increase of acidity the industrial effluent color removal obtained with ADACs increased, due to the lower stability of the system. However, using LDS has some limitations regarding the pH levels that can be used, due to which the tests with the effluent treated with ADACs were performed at pH 3.0. For this pH the effluent showed to be negatively charged, and thus, applying slightly positively charged bentonite followed by the addition of the negatively charged cellulose based PEL, led to effective flocculation results. **Figure 13A** and **Figure S5** show the evolution of aggregates size over time, monitored by LDS, for four tested PEL concentrations (1.3, 2.6, 4.0, and 5.3 mg/L), for the anionic cellulose-based polyelectrolytes tested (obtained from bleached pulp, after 24 h of sulfonation procedure, $\text{ADAC}_\text{P}\text{A}$ and after 72 h of sulfonation, $\text{ADAC}_\text{P}\text{B}$, and obtained from pulp with kappa number of 26.7, after 24 h of sulfonation, $\text{ADAC}_\text{W}\text{A}$ and after 72 h of sulfonation, $\text{ADAC}_\text{W}\text{B}$). In these figures both the evolution of the median of the floc size distribution d(0.5), and the 90% undersize percentile diameter d(0.9) of the aggregates size distribution, are plotted.

From **Figure 13A** and **Figure S5** it is clear that the features of tested PELs affect either floc size or the flocculation kinetics. The floc size reaches its maximum within few seconds after addition of flocculant to the effluent-bentonite system and then stabilizes. The only exception is when using $\text{ADAC}_\text{P}\text{A}$, significantly longer time having been required to achieve the stabilization stage for the concentration of 5.3 mg/L, especially for the largest aggregates size, d(0.9). This can be attributed to the fact that much larger flocs are obtained for this case, which requires a longer period to reach equilibrium between aggregation and breakage. This is the bio-PEL from the ADACs that must have the largest molecular weight, considering the values of the hydrodynamic diameters measured (see **Table 2**). Considering the floc size evolution with time, it is possible to conclude that in the first minutes of the flocculation process aggregation predominates, allowing to obtain large aggregates. After reaching the maximum floc size, floc breakage of the large flocs, even in low turbulent conditions can occur, as it was also observed in flocculation of this colored effluent with cationic PELs, previously described, and, after that, eventually, equilibrium between breakage and reaggregation is achieved, and the floc size stabilizes. The rearrangement of flocs is not significant when working with the anionic cellulose-based polyelectrolytes, in most tested conditions, except for the highest concentration of $\text{ADAC}_\text{P}\text{A}$, which led to the largest flocs. Comparing the results using CDACs (**Figure 12A** and **Figure S4**) and ADACs (**Figure 13A** and **Figure S5**), due to the low flocs rearrangement in the tests with ADACs, the final floc size obtained with these polymers was in general larger, when compared to the CDACs. In general, with the increase of anionic PEL dosage used in the effluent-bentonite system, an increase in the floc size was observed. For all tested anionic natural-based flocculants the influence of concentration is significant and is more pronounced for PELs obtained from the pulp with higher heterogeneity (high lignin content). Moreover, the predominant flocculation mechanism for anionic-PELs must also be bridging, which explains why working at significantly low polymer concentrations results in smaller flocs, since fewer particles will be bridged together in this case. Besides, anionic PELs led to obtain stronger aggregates with lower tendency to rearrange, when compared with the flocs obtained with the cationic bio-PELs.

Analyzing now the calculated SE profiles, obtained via LDS, for the four anionic bio-PELs, for the four concentrations tested, **Figure 13B**, the SE values are, in general, smaller than the ones obtained with the cationic bio-PELs (maximum value around 1.7). Thus, it is obvious that the anionic bio-PELs resulted in less compact flocs, when compared to the cationic cellulose-based PELs. Also, SE values vary less with time, when working with ADACs, what agrees with the lower rearrangement of the aggregates, as discussed when analyzing the flocculation kinetics.

The higher porosity of the flocs obtained with the ADACs can explain the lower turbidity reductions obtained in the jar-tests, with these polymers, since more porous flocs will take longer to settle.

The ADACs obtained from the pulp with high lignin content and higher heterogeneity resulted in slightly lower floc porosity (at the end of the flocculation process), especially for low concentrations, when compared with the PELs obtained from bleached pulp, for the same concentration. This must be the result of a higher affinity of the lignin, in the modified cellulose, to the effluent particles, especially at low concentrations, as was already described for jar-tests results.

In general, the success of the flocculation process and its kinetics is strongly dependent on the tested polyelectrolyte features and concentration, which conditions the flocculation mechanisms involved (Rasteiro et al., 2008). In the flocculation of the industrial effluent-bentonite system with both anionic and cationic, cellulose-based PELs, bridging is likely to be the predominant flocculation mechanism. Furthermore, in this effluent, the anionic cellulose-based flocculants, in general, tend to produce slightly larger aggregates with a lower tendency to reconform, but slightly less compact, when compared to cationic PELs. By using LDS, it was possible, for this effluent, to obtain information not only about the flocculation kinetics but also about the aggregates size distribution and their structure, as time evolved. One can conclude that LDS is a very useful technique to evaluate and differentiate polyelectrolytes for a desired application, not only in model effluents but also in industrial wastewaters.

CONCLUSIONS

Cationic and anionic cellulose-based polyelectrolytes (PELs), varying in charge density, raw material used in the modification and chemical heterogeneity, were tested in terms of performance in the flocculation of an industrial colored effluent from a textile industry, revealing to be a very promising alternative to

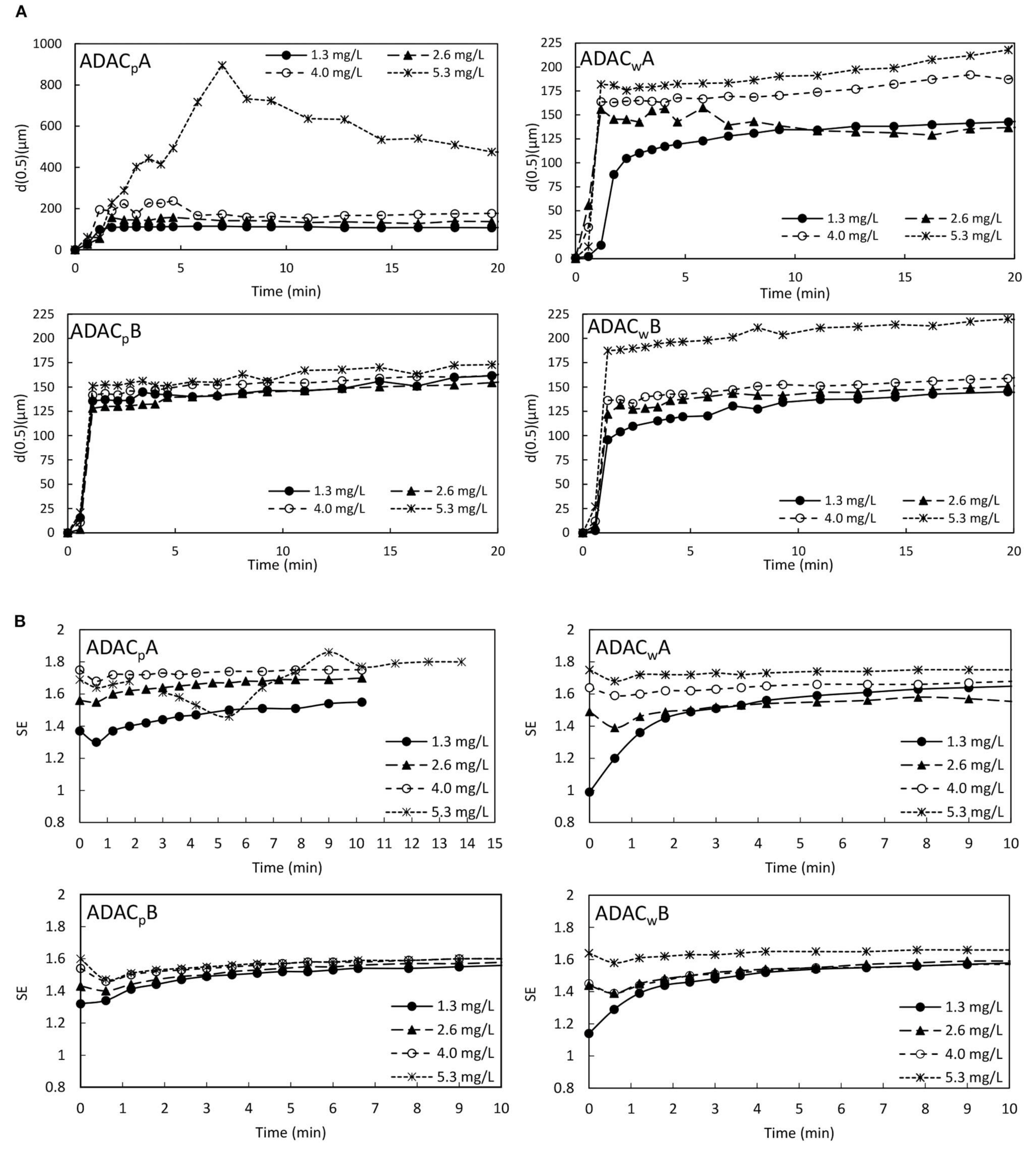

FIGURE 13 | (A) Industrial effluent treatment - evolution of **(A)** median particle size (d(0.5)) and **(B)** floc structure (SE) over time, obtained *via* LDS, for four different flocculant dosages of anionic cellulose-based polyelectrolytes obtained from bleached pulp, ADAC$_p$A, B and obtained from pulp with kappa number of 26.7, ADAC$_w$A, B, combined with bentonite.

the conventional synthetic PELs, for the evaluated application. The experimental technique used, laser diffraction spectroscopy (LDS), which was tested in the present work for the first time in the monitoring of the treatment of an industrial colored effluent of very low particle size (effluent from textile industry), allowed obtaining data about the influence of the polyelectrolyte's characteristics and concentration on the flocculation process. Flocculation monitoring using LDS was complemented with traditional jar-tests, both techniques revealing the same trends, regarding the influence of the different parameters evaluated (flocculant type and concentration) on the flocculation process. Due to the very low particle size in the initial colored effluent, all flocculation tests were performed while applying a dual system with an inorganic complexation agent (bentonite).

Typically, polyelectrolyte bridging was involved in all tested flocculation systems either using cationic or anionic PELs. As expected, the results showed that with the increase of flocculant concentration, in general, the floc size increases and less porous aggregates are obtained, which is an indication of aggregation of a larger number of particles, agreeing with the trends observed previously in the jar-tests. Also, working with cationic PELs at higher concentrations favors the flocs rearrangement. Moreover, the effect of PEL concentration in the tested flocculation systems was more pronounced when using PELs from bleached pulp, probably due to their higher charge, and homogeneity, regarding molecular weight, when compared to the samples produced from the pulp with high kappa number (high lignin content, higher heterogeneity). In general, performance in flocculation was better when working in acidic conditions, for both the cationic and anionic bio-PELs. This is typical of flocculation processes applied to dye containing waste waters (Zemaitaitiene et al., 2003; Gao et al., 2007).

The use of LDS to monitor the flocculation processes allowed to determine some important flocs characteristics in a mild turbulent environment. It was possible to obtain information not only about the flocculation kinetics but also about the aggregates size distribution and their structure. Consequently, LDS proved to be a very useful technique to evaluate and differentiate polyelectrolytes for a desired application, in wastewater treatment, where important aspects are the knowledge of floc size and structure (large or small, open or compact) and flocculation kinetics, having in mind the final separation process to be used in the treatment (filtration, sedimentation, etc.).

Comparing the results obtained with the bio-PELs (color removal and COD reduction) with the ones obtained using standard polyacrylamides, better results were always obtained with the bio-PELs.

In conclusion, the results obtained show that the LDS technique can significantly improve the selection/optimization process of the adequate flocculant for a certain effluent treatment, before pilot-plant trials, after a primary, less extensive evaluation of performance in jar-tests, since it provides information about important characteristics of the flocs not available through the standard techniques.

DATA AVAILABILITY STATEMENT

The datasets generated for this study are available on request to the corresponding author.

AUTHOR CONTRIBUTIONS

KG performed the experiments and wrote the manuscript. KG and MR analyzed and interpreted the data. JG, JA, and OC contributed to the manuscript by commenting on the research findings and on the manuscript. All authors contributed to manuscript preparation, revision, read and approved the submitted version.

FUNDING

Marie Curie Initial Training Networks (ITN)—European Industrial Doctorate (EID)—Grant agreement FP7-PEOPLE-2013-ITN-604825; Portuguese Science and Technology Foundation (Pest/C/EQB/UI0102/2013); European Regional Development Fund (ERDF), COMPETE (POFC).

ACKNOWLEDGMENTS

The authors would like to thank financial support from Marie Curie Initial Training Networks (ITN)—European Industrial Doctorate (EID), through Grant agreement FP7-PEOPLE-2013-ITN-604825 which allowed the development of the Ph.D. thesis of KG, on which this manuscript is based. Acknowledgment is also given to the Portuguese Science and Technology Foundation (Pest/C/EQB/UI0102/2013), co-financed by the European Regional Development Fund (ERDF) through the program COMPETE (POFC).

SUPPLEMENTARY MATERIAL

The Supplementary Material for this article can be found online at: https://www.frontiersin.org/articles/10.3389/fchem.2020.00005/full#supplementary-material

REFERENCES

Antunes, E., Garcia, F. A. P., Blanco, A., Negro, C., and Rasteiro, M. G. (2015). Evaluation of the flocculation and reflocculation performance of a system with calcium carbonate, cationic acrylamide co-polymers, and bentonite microparticles. *Ind. Eng. Chem. Res.* 54, 198–206. doi: 10.1021/ie503342d

Biggs, S., Habgood, M., Jameson, G. J., and Yan, Y. (2000). Aggregate structures formed via a bridging flocculation mechanism. *Chem. Eng. J.* 80, 13–22. doi: 10.1016/S1383-5866(00)00072-1

Blanco, A., Fuente, E., Negro, C., and Tijero, J. (2002). Flocculation monitoring: focused beam reflectance measurement as a measurement tool. *Can. J. Chem. Eng.* 80, 1–7. doi: 10.1002/cjce.54508004

Bolto, B., and Gregory, J. (2007). Organic polyelectrolytes in water treatment. *Water Res.* 41, 2301–2324. doi: 10.1016/j.watres.2007.03.012

Carliell, C. M., Barclay, S. J., Shaw, C., Wheatley, A. D., and Buckley, C. A. (1998). The effect of salts used in textile dyeing on microbial decolourisation of a reactive azo dye. *Environ. Technol.* 19, 1133–1137. doi: 10.1080/09593331908616772

Chakraborti, R. K., Gardner, K. H., Atkinson, J. F., and Van Benschoten, J. E. (2003). Changes in fractal dimension during aggregation. *Water Res.* 37, 873–883. doi: 10.1016/S0043-1354(02)00379-2

Costa, J. C., Mesquita, D. P., Amaral, A. L., Alves, M. M., and Ferreira, E. C. (2013). Quantitative image analysis for the characterization of microbial aggregates in biological wastewater treatment: a review. *Environ. Sci. Pollut. Res.* 20, 5887–5912. doi: 10.1007/s11356-013-1824-5

dos Santos, A. B., Cervantes, F. J., and van Lier, J. B. (2007). Review paper on current technologies for decolourisation of textile wastewaters: perspectives for anaerobic biotechnology. *Bioresour. Technol.* 98, 2369–2385. doi: 10.1016/j.biortech.2006.11.013

Gao, B. Y., Wang, Y., Yue, Q. Y., Wei, J. C., and Li, Q. (2007). Color removal from simulated dye water and actual textile waste water using a composite coagulant prepared by polyferric chloride and polydimethyldiallylammonium chloride. *Separation Purif. Tech.* 54, 157–163. doi: 10.1016/j.seppur.2006.08.026

Grenda, K. (2018). *Modification of Natural Polymers and Natural by-Products for Coagulation and Flocculation Purposes* (Ph.D. thesis). University of Coimbra, Coimbra, Portugal.

Grenda, K., Arnold, J., Gamelas, J. A. F., Cayre, O. J., and Rasteiro, M. G. (2020). Flocculation of silica nanoparticles by natural, wood-based polyelectrolytes. *Separation Purif. Technol.* 231:115888. doi: 10.1016/j.seppur.2019.115888

Grenda, K., Arnold, J., Gamelas, J. A. F., and Rasteiro, M. G. (2017). Environmentally friendly cellulose-based polyelectrolytes in wastewater treatment. *Water Sci. Technol.* 76, 1490–1499. doi: 10.2166/wst.2017.299

Grenda, K., Gamelas, J. A. F., Arnold, J., Cayre, O. J., and Rasteiro, M. G. (2019). Cationization of Eucalyptus wood waste pulps with diverse lignin contents for potential application in colored wastewaters treatment. *RSC Adv.* 9, 34814–34826. doi: 10.1039/C9RA05757A

Hao, O. J., Kim, H., and Chiang, P. (2000). Decolorization of wastewater. *Critic. Rev. Environ. Sci. Technol.* 30, 449–505. doi: 10.1080/10643380091184237

Hou, Q. X., Liu, W., Liu, Z. H., and Bai, L. L. (2007). Characteristics of wood cellulose fibers treated with periodate and bisulfite. *Ind. Eng. Chem. Res.* 46, 7830–7837. doi: 10.1021/ie0704750

Kaombe, D. D., Lenes, M., Toven, K., and Glomm, W. R. (2013). Turbiscan as a tool for studying the phase separation tendency of pyrolysis oil. *Energy Fuels.* 27, 1446–1452. doi: 10.1021/ef302121r

Kim, D.-S. (2003). Measurement of point zero charge of bentonite by solubilization technique and its dependence of surface potential on pH. *Environ. Eng. Res.* 8, 222–227. doi: 10.4491/eer.2003.8.4.222

Kim, U., Kuga, S., Wada, M., Okano, T., and Kondo, T. (2000). Periodate oxidation of crystalline cellulose. *Biomacromolecules* 1, 488–492. doi: 10.1021/bm0000337

Lapointe, M., and Barbeau, B. (2020). Understanding the roles and characterizing the intrinsic properties of synthetic vs. natural polymers to improve clarification through interparticle bridging: a review. *Separation Purif. Technol.* 231:115893. doi: 10.1016/j.seppur.2019.115893

Lee, C. S., Robinson, J., and Chong, M. F. A. (2014). Review on application of flocculants in wastewater treatment. *Process Saf. Environ. Prot.* 92, 489–508. doi: 10.1016/j.psep.2014.04.010

Liang, L., Peng, Y., Tan, J., and Xie, G. (2015). A review of the modern characterization techniques for flocs in mineral processing. *Miner. Eng.* 84, 130–144. doi: 10.1016/j.mineng.2015.10.011

Liimatainen, H., Sirvi,ö, J., Sundman, O., Visanko, M., Hormi, O., and Niinimäki, J. (2011). Flocculation performance of a cationic biopolymer derived from a cellulosic source in mild aqueous solution. *Bioresour. Technol.* 102, 9626–9632. doi: 10.1016/j.biortech.2011.07.099

Liimatainen, H., Sirviö, J., Sundman, O., Hormi, O., and Niinimäki, J. (2012). Use of nanoparticular and soluble anionic celluloses in coagulation-flocculation treatment of kaolin suspension. *Water Res.* 46, 2159–2166. doi: 10.1016/j.watres.2012.01.035

Liu, X., Wang, L., Song, X., Song, H., Zhao, J. R., and Wang, S. (2012). A kinetic model for oxidative degradation of bagasse pulp fiber by sodium periodate. *Carbohydrate Polymers* 90, 218–223. doi: 10.1016/j.carbpol.2012.05.027

Lourenço, A., Arnold, J., Cayre, O. J., and Rasteiro, M. G. (2018). Flocculation treatment of an industrial effluent: performance assessment by laser diffraction spectroscopy. *Ind. Eng. Chem. Res.* 57, 2628–2637. doi: 10.1021/acs.iecr.7b04521

Lourenço, A. F., Godinho, D., Gamelas, J. A. F., Sarmento, P., and Ferreira, P. J. T. (2019). Carboxymethylated cellulose nanofibrils in papermaking: influence on filler retention and paper properties. *Cellulose* 26, 3489–3502. doi: 10.1007/s10570-019-02303-5

Nikolic, T., Kostic, M., Praskalo, J., Pejic, B., Petronijevic, Z., and Skundric, P. (2010). Sodium periodate oxidized cotton yarn as carrier for immobilization of trypsin. *Carbohydrate Polymers* 82, 976–981. doi: 10.1016/j.carbpol.2010.06.028

Rajalaxmi, D., Jiang, N., Leslie, G., and Ragauskas, A. J. (2010). Synthesis of novel water-soluble sulfonated cellulose. *Carbohydrate Res.* 345, 284–290. doi: 10.1016/j.carres.2009.09.037

Ramírez, H. L., Cao, R., Fragoso, A., Torres-Labandeira, J. J., Dominguez, A., Schacht, E. H., et al. (2006). Improved anti-inflammatory properties for naproxen with cyclodextrin-grafted polysaccharides. *Macromol. Biosci.* 6, 555–561. doi: 10.1002/mabi.200600023

Rasteiro, M. G., Garcia, F. A. P., and del Mar Pérez, M. (2007). Applying LDS to monitor flocculation in papermaking. *Particul. Sci. Technol.* 25, 303–308. doi: 10.1080/02726350701375956

Rasteiro, M. G., Garcia, F. A. P., Ferreira, P., Blanco, A., Negro, C., and Antunes, E. (2008). The use of LDS as a tool to evaluate flocculation mechanisms. *Chem. Eng. Process.* 47, 1323–1332. doi: 10.1016/j.cep.2007.04.009

Rasteiro, M. G., Pinheiro, I., Garcia, F. A. P., Ferreira, P. J., and Hunkeler, D. (2011). Using light scattering to screen polyelectrolytes (PEL) Performance in Flocculation. *Polymers* 3, 915–927. doi: 10.3390/polym3020915

Sirviö, J., Honka, A., Liimatainen, H., Niinimäki, J., and Hormi, O. (2011b). Synthesis of highly cationic water-soluble cellulose derivative and its potential as novel biopolymeric flocculation agent. *Carbohydrate Polymers* 86, 266–270. doi: 10.1016/j.carbpol.2011.04.046

Sirviö, J., Hyvakko, U., Liimatainen, H., Niinimäki, J., and Hormi, O. (2011a). Periodate oxidation of cellulose at elevated temperatures using metal salts as cellulose activators. *Carbohydrate Polymers* 83, 1293–1297. doi: 10.1016/j.carbpol.2010.09.036

Zemaitaitiene, R. J., Zliobaite, E., Klimaviciute, R., and Zemaitaitis, A. (2003). The role of anionic substances in removal of textile dyes from solutions using cationic flocculant. *Colloids Surf A.* 214, 37–47. doi: 10.1016/S0927-7757(02)00406-5

Zhu, L., Qin, J., Yin, X., Ji, L., Lin, Q., and Qin, Z. (2014). Direct sulfation of bacterial cellulose with a ClSO3H/DMF complex and structure characterization of the sulfates. *Polymers Adv. Technol.* 25, 168–172. doi: 10.1002/pat.3218

Conflict of Interest: JA was employed by company AQUA+Tech.

The remaining authors declare that the research was conducted in the absence of any commercial or financial relationships that could be construed as a potential conflict of interest.

frontiers in Chemistry

ORIGINAL RESEARCH
published: 07 February 2020
doi: 10.3389/fchem.2020.00027

Understanding the Efficiency of Aluminum Coagulants Used in Dissolved Air Flotation (DAF)

*Ruben Miranda, Isabel Latour and Angeles Blanco**

Department of Chemical and Materials Engineering, Faculty of Chemistry, Complutense University of Madrid, Madrid, Spain

This paper reports on the efficiency of five aluminum coagulants for the treatment of a paper mill wastewater by dissolved air flotation (DAF). The coagulants studied were: alum, a polyaluminum chloride coagulant of high aluminum content and intermediate basicity (PAC-MB), another with intermediate aluminum content and high basicity (PAC-HB), a polyaluminum nitrate sulfate of intermediate aluminum content and basicity (PANS) and one hybrid coagulant formed by the combination of PANS and a mixture of polyamines (PANS-PA). The influence of Al speciation on contaminants removal and the main flocculation mechanisms involved have been analyzed. High removal of suspended solids together with significant removal of dissolved and colloidal material (COD and silica) were obtained, which is required for extended reuse of this process water. PAC-HB was the best product for removing suspended solids (85%) and soluble silica (50%) with a rather limited COD removal (5%), while PANS-PA obtained high turbidity (90%) and silica removal (45%) together with a significant soluble COD removal (15%). Monomeric Al (Al_a, Al_m) was more efficient in removing suspended solids and soluble COD than polymeric or colloidal Al (Al_c, Al_u), but the latter was more efficient in removing soluble silica. Results demonstrated that the main flocculation mechanism varies with the aluminum dosage, being predominantly charge neutralization at low dosages and sweep flocculation at high dosages. The floc strength factor however, was very high and similar for all the coagulants and dosages tested (85–90%), as it was mainly determined by the behavior of the pre-flocculated suspended solids present in wastewater. The reflocculation factor varied from 45 to 75% at the lowest dosages to almost zero at the highest dosages, confirming the transition from charge neutralization to sweep flocculation. The flocs formed by PANS-PA had lower strength than the others and it decreased with the dosage while its reflocculation factor was almost zero, even at low dosages. Due to the polyamines present in this coagulant, its flocculation mechanism is through both charge neutralization and patch formation, especially at low dosages, and sweep flocculation and interparticle bridge formation at high dosages.

Keywords: flocculation mechanisms, aluminum coagulants, dissolved air flotation (DAF), hybrid coagulants, focused beam reflectance measurement (FBRM), water reuse

Edited by:
Maria Graca Rasteiro,
University of Coimbra, Portugal

Reviewed by:
Priyanka Sharma,
Stony Brook University, United States
Mansoor Ahammed,
Sardar Vallabhbhai National Institute
of Technology Surat, India

***Correspondence:**
Angeles Blanco
ablanco@ucm.es

Specialty section:
This article was submitted to
Green and Sustainable Chemistry,
a section of the journal
Frontiers in Chemistry

Received: *13 November 2019*
Accepted: *09 January 2020*
Published: *07 February 2020*

Citation:
Miranda R, Latour I and Blanco A
(2020) Understanding the Efficiency of
Aluminum Coagulants Used in
Dissolved Air Flotation (DAF).
Front. Chem. 8:27.
doi: 10.3389/fchem.2020.00027

INTRODUCTION

Dissolved air flotation (DAF) is a very efficient treatment technology for the removal of suspended matter, either oil and grease or solids (Edzwald and Haarhoff, 2011; Bolto and Xie, 2019). Internal water reuse after DAF is the most common alternative used in paper mills to reduce fresh water consumption (Hubbe et al., 2016). In recycled newsprint mills, there are up to three or four DAF units in each production line (one within each water loop). In these systems, suspended solids are efficiently removed but the dissolved and colloidal material (DCM) is almost completely recirculated into the process, accumulating in the water circuits, and thus limiting their closure (Miranda et al., 2009a; Hubbe et al., 2016; Ordaz-Díaz et al., 2017). However, by extending the limits of coagulation/flocculation by an improved understanding of the destabilization mechanisms it is possible to develop improved chemicals which are able to remove also finely dispersed and colloidal particles (>0.1–$0.2\ \mu m$) by DAF. In these conditions, DAF units can remove 80–99% of suspended solids, together with, in the best cases, up to 10–30% of soluble chemical oxygen demand (COD) (Miranda et al., 2008, 2009b,c, 2013).

A variety of coagulants have been used in DAF systems including alum, ferric chloride, polyaluminum chloride (PAC), polyamine (PA), polydiallyldimethylammonium chloride (PDADMAC), chitosan, etc. (Ordaz-Díaz et al., 2017; Bolto and Xie, 2019). Aluminum based coagulants are generally the most versatile and widely used. In addition to alum, many types of polyaluminum coagulants are commercially available for water treatment such as aluminum chlorohydrate, PAC, and polyaluminum sulfates. These products differ in their basicity and strength, and can contain small amounts of other compounds such as sulfate, nitrate, silica, and calcium (Pernitsky and Edzwald, 2006; Edzwald and Haarhoff, 2011). Furthermore, polyaluminum coagulants can be used in composite coagulants in combination with PA, PDADMAC, polyacrylamides, bioflocculants, and even other inorganic coagulants, e.g., polymeric aluminum ferric silicates, to improve their performance (Lee et al., 2012; Chen et al., 2015; Huang et al., 2015; Tang et al., 2015; Latour et al., 2016; Sun et al., 2017; Wang X. et al., 2017). The distribution of aluminum species in polymeric aluminum coagulants influences their coagulation performance, however, the relationship is not well-established yet and depends on the exact wastewater and contaminants considered.

Understanding the flocculation mechanism is also of great importance as both the size and the structure of the formed aggregates affect the removal efficiency of contaminants (Lin et al., 2008). There are several possible flocculation mechanisms described in the literature including charge neutralization, sweep flocculation (flocculation by enmeshment), interparticle bridging and patch formation (Bache and Gregory, 2007; Bratby, 2016). The predominant flocculation mechanisms for alum and polyaluminum coagulants are charge neutralization and sweep flocculation (Edzwald and Haarhoff, 2011). Neutral conditions are considered favorable for aluminum-based coagulants due to the presence of positively charged Al species and to the fact that most of the Al is precipitated, forming floc particles [conditions of minimum solubility of $Al(OH)_3$] (Pernitsky and Edzwald, 2006; Edzwald and Haarhoff, 2011). At these conditions, charge neutralization is the predominant mechanism at low aluminum dosages, while the precipitation of $Al(OH)_3$ and the subsequent enmeshment of colloids in the precipitate predominates at high dosages. However, it is important to notice that the DCM destabilization cannot be exclusively attributed to a particular mechanism, especially when complex industrial waters are treated (Bratby, 2016). Apart from the nature and dosage of the coagulant used, there are also other factors determining the flocculation mechanisms such as the nature and the surface charge of the particles, the pH, the amount of colloidal and suspended solids, the ionic strength, etc.

There are many studies analyzing flocculation with aluminum salts, some of them analyzing floc strength under different shear forces (deflocculation studies) and the reversibility of the flocculation after breakage (reflocculation studies). However, these studies usually focus on model suspensions of kaolin (Cheng et al., 2011; Wang et al., 2011), humic acids (Wang et al., 2009), or a combination of both (Yu et al., 2009; Zhao et al., 2010; Yao et al., 2014; Nan et al., 2016; Wang Z. et al., 2017) and only in some cases with drinking waters (Yao et al., 2015; Jiao et al., 2016). However, the study of flocculation mechanisms in industrial wastewaters are very limited. Furthermore, there are only limited references regarding the flocculation mechanisms of hybrid or composite coagulants, most of them with iron-based hybrids (Wei et al., 2010; Zhang et al., 2015; Wang B. et al., 2017), and only a few recent studies with aluminum-based hybrid coagulants (Latour et al., 2016; Kangama et al., 2018; Shen et al., 2020).

The main objective of this paper is to analyse how to extend the removal of contaminants by DAF using different aluminum coagulants by understanding the influence of their speciation and flocculation mechanisms. The study is aimed specifically at treating process waters from the paper industry.

MATERIALS AND METHODS

Materials

Water Samples

They were taken from the inlet of a DAF unit from a 100% recycled newsprint mill located in Madrid (Spain). The main characteristics of these waters are shown in **Table 1**.

Coagulants

Table 2 summarizes the properties of the tested aluminum-based coagulants. Alum [$Al_2(SO_4)_3 \cdot 18H_2O$], reagent grade, was supplied by Panreac. PAC-MB is a conventional polyaluminum chloride with high aluminum content and intermediate basicity, and PAC-HB is a high-basicity polyaluminum chloride with intermediate aluminum content and a small amount of silica in its composition. On the other hand, PANS is a polyaluminum nitrate sulfate with an intermediate aluminum content and basicity, and PANS-PA is a hybrid coagulant obtained by the addition of a small amount of high charge quaternary polyamines of different molecular weights to PANS. PAC-MB, PANS, and

PANS-PA were supplied by Sachtleben Wasserchemie GmbH while PAC-HB was supplied by Kemira Ibérica, S.A.

Furthermore, the aluminum species distribution of the used coagulants were measured by the ferron test and ^{27}Al NMR spectroscopy (**Table 3**). Ferron test was carried out in duplicate according to the method described in Wang et al. (2004), with a total concentration of aluminum of 10^{-5} M and maintaining the ferron/Al_T molar ratio >10. In this method, Al_a denotes aluminum species that reacted with ferron instantaneously (within 1 min). Al_b denotes species that reacted within 120 min and finally, Al_c denotes species that did not react. These species are assumed to be monomeric, polymeric and colloidal aluminum species, respectively. A Varian Cary 50 UV-Visible spectrophotometer was used for the absorbance measurements at 366 nm in 1-cm quartz cells. ^{27}Al NMR spectra of the coagulants were obtained in Bruker Avance 500 spectrometer at a frequency 130.318 MHz. A 3 mm internal diameter capillary tube was inserted into a 5 mm internal diameter sample tube. This capillary tube containing a 0.1 M solution of $NaAlO_2$ in D_2O was used as inner standard of deuterium lock and for Al quantification. In all the samples, the number of scans was fixed to 64, the pulse width to 7.0 µs and the temperature to 298 K. The resonance corresponding to the monomeric aluminum such as Al^{3+}, $Al(OH)^{2+}$, and $Al(OH)^{3+}$, was assigned a chemical shift of 0 mg/L (Al_m). The signal at 62.5 mg/L denotes $Al_{13}O_4(OH)_{24}^{7+}$ (Al_{13} in short). Finally, the signal at 80.0 mg/L indicates the formation of $Al(OH)_4^-$ from $NaAlO_2$ used standard. Based on the integral areas of these three peaks, the aluminum concentration of the background and the sample, and the ratio of the cross-sectional areas of capillary to the sample tube, Al_m and Al_{13} were calculated. The undetectable aluminum (Al_u) was obtained from the remaining Al_T. Details for the calculations can be found in Gao et al. (2002). Previous studies have demonstrated that Al_a, Al_b, and Al_c species can be regarded approximately as Al_m, Al_{13}, and Al_u, both methods obtaining similar Al species distribution (Hu et al., 2012).

TABLE 1 | Characteristics of the DAF inlet waters and DAF blank.

	DAF Inlet	DAF blank
Raw waters		
pH	6.9 ± 0.2	6.8 ± 0.2
Conductivity (25°C) (mS/cm)	2.62 ± 0.18	2.12 ± 0.16
Total solids (mg/L)	5520 ± 185	3395 ± 165
COD (mg/L)	3665 ± 150	2332 ± 105
Total suspended solids (mg/L)	1620 ± 80	183 ± 20
Turbidity (NTU)	680 ± 45	268 ± 20
Cationic demand (meq/L)	1.16 ± 0.08	0.99 ± 0.07
Total alkalinity (mg/L $CaCO_3$)	860 ± 60	645 ± 45
After centrifugation		
Total solids (mg/L)	3900 ± 160	3210 ± 140
Silica (mg/L SiO_2)	273 ± 15	225 ± 12
COD (mg/L)	2600 ± 90	2050 ± 60
Turbidity (NTU)	21.8 ± 1.5	18.0 ± 1.4

Average values and 95% confidence intervals were obtained from three replicates.

The species distribution of PACl depends on preparing conditions such as basicity, total concentration of Al, rate of base addition, temperature, and so on. In general, Al_b and Al_{13} percentage in PACl increases with increasing basicity. The inclusion of sulfate in PACl did not largely influence aluminum species (Kimura et al., 2013). On the other hand, the presence of silica, for a constant basicity, usually imply lower shares of Al_m (Al_a) and Al_{13} (Al_b) but higher shares of Al_u (Al_c) (Gao et al., 2002), which could justify why the Al_{13} (Al_b) content of the highest basicity product is not the highest. Monomeric aluminum (Al_m or Al_a) in alum (basicity = 0%) is usually 100%. In the present study, this content was slightly lower (around 85%) due to the formation of $Al(H_2O)_5(SO_4)^+$, evidenced by the presence of the resonance peak at −3.3 mg/L.

Coagulants in DAF tests were used in combination with an anionic polyacrylamide of high molecular weight and medium charge, supplied by SERTEC-20 S.L. (Spain). Dosages of the coagulants were selected according to preliminary tests with these waters, varying from 25 to 250 mg/L Al_2O_3, while the flocculant dosage was fixed to 10 mg/L in all cases.

TABLE 3 | Distribution of coagulants aluminum species by ferron test and ^{27}Al NMR for $Al_T = 10^{-5}$ M.

	Ferron test			^{27}Al NMR		
Coagulant	Al_a	Al_b	Al_c	Al_m	Al_{13}	Al_u
Alum	83.9	4.1	12.0	86.4	0	13.6
PAC-MB	54.5	44.3	1.3	36.9	50.0	13.1
PAC-HB	12.8	14.8	72.4	19.8	25.7	54.5
PANS	26.9	23.7	49.4	29.4	18.5	52.1
PANS-PA	23.2	24.4	52.4	25.1	20.7	54.2

TABLE 2 | Characteristics of the coagulants used in this study.

Coagulant	Al_2O_3 (%)	Basicity (%)	Charge density (meq/g)	Density (g/cm^3)	pH	Dry content (%)
Alum	15.3	0	–	–	–	–
PAC-MB	16.8	37	1.77	1.37	<1	34.1
PAC-HB	9.7	85	1.67	1.22	2.7	29.5
PANS	10.2	46	1.22	1.27	2.6	21.7
PANS-PA	6.05	–	2.57	1.23	3.0	20.4

Methodology

DAF Tests

DAF tests were carried out in a laboratory-scale unit (Flottatest FTH3) supplied by Orchidis Laboratoires (France) using a sample volume of 1 L. For an easier comparison between the performance and flocculation mechanism of the coagulants, they were tested at the same equivalent Al_2O_3 dosage, from 25 to 250 mg/L Al_2O_3 (Chuang et al., 2007; Zhang et al., 2010), First, the coagulant was added from a 10% wt./vol. solution and mixed at high speed (180 rpm) for 2.5 min, and then the flocculant was added from a 0.10% wt./vol. solution and mixed at slow speed (40 rpm) for 10 min. Next, the flocculated waters were flotated adding a 20% tap water (200 mL) saturated with air at 7 bar. After 10 min flotation time, samples were collected from the bottom of the jars. A number of blanks were performed without adding any chemical before flotation, to consider both the dilution of the samples due to the addition of air-saturated tap water during flotation (20%) and also the physical efficiency of DAF to remove contaminants, even without chemical aids. The characteristics of these blanks, referred as 0 mg/L dosage, are included in **Table 1**. All experiments were carried out at room temperature (20–25°C) by duplicate, and the average error between replicates was ~5%. To avoid the possible water degradation, all tests and analyses were carried out within 5 days after sampling and the waters were always kept at 4°C before testing.

Clarified waters were characterized by pH, conductivity, turbidity, total solids, COD, cationic/anionic demand, and alkalinity. Furthermore, the dissolved fraction (obtained by centrifugation of clarified waters at 2,000 g for 15 min), was characterized by turbidity, total solids, silica, and sulfates. Total solids and turbidity were measured according to Standard Methods 2540B and 2130B, respectively, using a Hanna LP-2100 turbidimeter for turbidity. COD was measured by the Nanocolor® COD 1500 method from Macherey-Nagel GmbH, using an Aquamate Vis spectrophotometer (Thermo Scientific Inc.), according to ISO 15705:2003. Cationic/anionic demand was measured by colloidal titration using a Charge Analyzing System (CAS) supplied by AFG Analytic GmbH and polydiallyldimethylammonium chloride (PDADMAC) (0.001 N) and polyethylene sulfonic acid sodium salt (PES-Na) (0.001 N) as titrants. Dissolved silica was measured using the silico-molybddate method using flow injection analysis (FIA) according to ISO 16264:2002. Total alkalinity was measured by titration of the sample to $pH = 4.5$ with H_2SO_4 0.1 N according to EPA 310.1 method. Sulfates were measured by the Nanocolor® Sulfate 200 or 1000 methods from Macherey-Nagel GmbH, using an Aquamate Vis spectrophotometer (Thermo Scientific Inc.). Finally, the pH and conductivity of the samples were analyzed using a GLP-22 pH-meter and a GLP-32 conductivity meter (both supplied by Crison Instruments, S.A.).

Flocculation Monitoring

Flocculation monitoring was carried out using a focused beam reflectance measurement (FBRM) system M500L, supplied by Mettler Toledo (USA), which measures in real time the chord length distribution of particles in suspension from 1 to 1,000 μm. From these data, total number of counts (TNC), mean chord size (MCS), counts in specific size intervals, and other statistical parameters can be easily calculated (Blanco et al., 2002a,b; Dunham et al., 2002), allowing the monitoring of flocculation, deflocculation, and reflocculation processes and thus, the characterization of the flocs properties and flocculation mechanisms. FBRM is able to study the flocculation process without the limitations of traditional methods such as charge titration, which are not valid when bridging or patching mechanisms dominate the system (Rasteiro et al., 2008). FBRM has been specifically used for the chemical optimization of DAF units treating thermomechanical pulp and deinked pulp waters (Saarimaa et al., 2006a,b; Miranda et al., 2008, 2013).

Two different flocculation studies were carried out: the flocculation tests by successive coagulant additions and the flocculation-deflocculation-reflocculation tests. In both cases, a sample of 250 mL was used. The flocculation by successive coagulant additions was carried out adding 25 mg/L Al_2O_3 of coagulant each 30 s using a 10% wt./vol. coagulant solution until a total dosage of 500 mg/L Al_2O_3 using 200 rpm stirring rate. In the flocculation-deflocculation-reflocculation tests, single dosages of coagulant, from 25 to 250 mg/L Al_2O_3, were used. First, the sample was stirred at 200 rpm during 30 s for stabilization and then the coagulant dosage was added from a 10% wt./vol. solution and the system was allowed to evolve for 2.5 min. After this time, the stirring rate was increased to 500 rpm and maintained during 2 min to break the formed flocs. Finally, the mixing speed was reduced to 200 rpm again and the system was monitored for other 5 min to analyse the reversibility of the flocculation. Mixing intensities used for flocculation and the breakage of the flocs stages were selected according to preliminary tests carried out with these waters.

The strength or breakage factor (SF) and recovery or reflocculation factor (RF) were calculated using Equations (1) and (2), where: MCS_1 is the maximum MCS value before the flocs breakage, MCS_2 is the MCS value when the flocs were broken after intensive stirring and MCS_3 is the maximum MCS value for the flocs re-growth after the intensive stirring.

$$\mathrm{SF} = \frac{\mathrm{MCS}_2}{\mathrm{MCS}_1} \tag{1}$$

$$\mathrm{RF} = \frac{\mathrm{MCS}_3 - \mathrm{MCS}_2}{\mathrm{MCS}_1 - \mathrm{MCS}_2} \tag{2}$$

RESULTS AND DISCUSSION

Removal of Contaminants by DAF

Turbidity

The initial size of the suspended solids is large enough to be partly removed by DAF. The mean chord size of the suspended solids was 41.7 μm while the distribution of particles among the different chord size intervals was: 34.6% (1–20 μm), 30.3% (20–50 μm), 26.3% (50–100 μm), and 8.9% (>100 μm) (FBRM measurements). Without chemicals, DAF reduced the turbidity from 680 NTU to 268 NTU (blank), which allows for the 20% decrease due to the dilution of raw waters with water saturated in air. The addition of a small amount of flocculant (10 mg/L) further reduced the turbidity to 196 NTU (27% removal referred

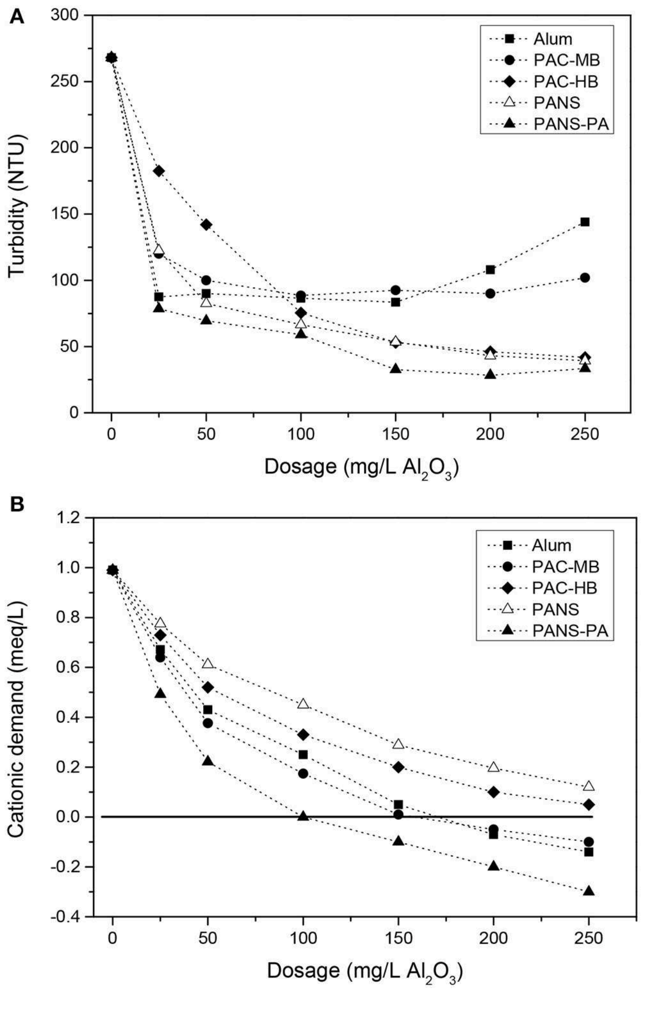

FIGURE 1 | **(A)** Turbidity and **(B)** cationic demand of clarified waters vs. dosage of coagulants.

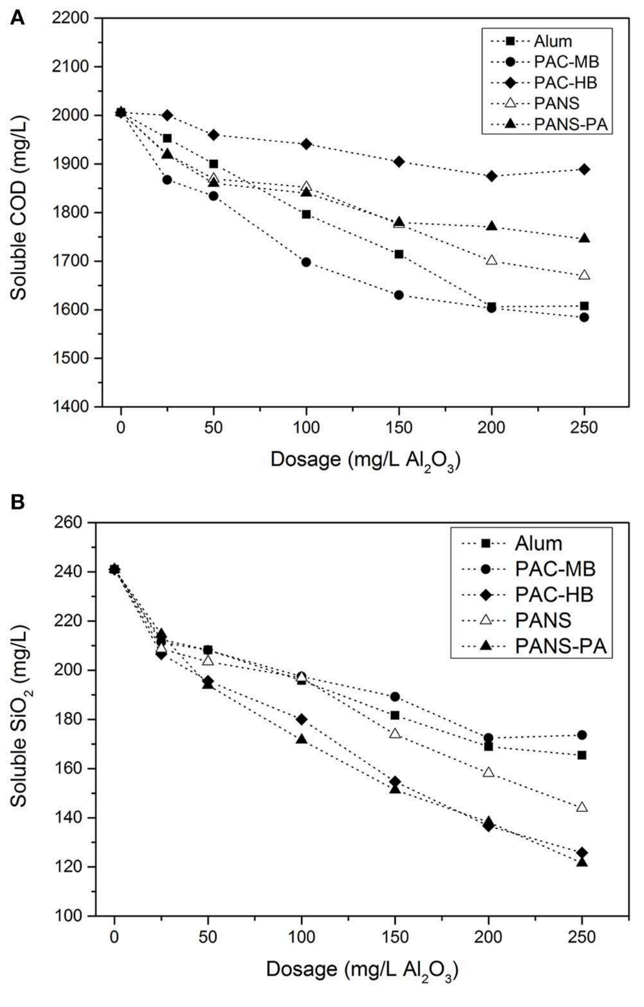

FIGURE 2 | **(A)** Soluble COD and **(B)** soluble silica of clarified waters vs. dosage of coagulants.

to blank). However, coagulant addition was necessary to increase the efficiency. Turbidity removal increased greatly with coagulant addition but reached almost a constant value at dosages higher than 100–150 mg/L (**Figure 1A**). PANS, PANS-PA, and PAC-HB decreased the turbidity to a greater extent (30–40 NTU residual turbidity, 85–90% removal referred to blank) than alum and PAC-MB (80–90 NTU, 65–70% removal).

At the highest dosages of alum and PAC-MB (200–250 mg/L), charge reversal and restabilization was observed (see **Figure 1B**), producing an increase of the turbidity of the clarified waters. Although PANS-PA (the highest charged coagulant) reached charge reversal at lower dosages (100–150 mg/L), restabilization did not occur and turbidity removal did not decrease, which indicates a different flocculation mechanism for the hybrid coagulant. Charge reversal did not occur neither for PAC-HB nor PANS, the maximum reduction of cationic demand was 75% (final cationic demand of 0.25 meq/L).

The least efficient products were those having the highest monomeric Al content (Al_a or Al_m) and the lowest basicities, thus producing the largest pH decreases after the treatment. Final pHs with these coagulants were lower than pH of minimum solubility of $Al(OH)_3$, which is the most efficient pH to produce the largest amount of $Al(OH)_3$ precipitates and the lower residual Al concentration in the clarified waters. Final pHs with alum and PAC-MB were around 0.5 pH units lower than the pH of minimum solubility, which is around 6.0 for alum and 6.2–6.4 for PACs, although the exact value depends on the wastewater composition (Pernitsky and Edzwald, 2003).

Soluble COD

For all the coagulation treatments, the higher the dosage the higher the soluble COD removal, however, at the highest dosages (200–250 mg/L Al_2O_3) only marginal COD removals were obtained (**Figure 2A**). The most efficient products were PAC-MB, alum, and PANS (20% removal). PANS-PA showed an intermediate efficiency (15% removal) and PAC-HB was the least efficient product (5% removal).

The soluble COD removal can be reasonably predicted by the species distribution of the coagulants. The best products in removing silica were those having the highest amount of monomeric Al (Al_a or Al_m) except PANS, and the least efficient product (PAC-MB) was the one with the lowest monomeric Al. This means sweep flocculation, enhanced by high contents of monomeric Al, is more efficient than high contents of Al_b or Al_{13} for COD removal, which usually are more efficient for removing contaminants by charge neutralization and interparticles bridging mechanisms (Li et al., 2006).

Soluble Silica

Other parameter of interest in these process waters is soluble silica concentration. High levels of silica produce deposits in the process, impairing both the operational performance and the quality of the final product. Most important, the technical and economic feasibility of effluent reuse schemes by reverse osmosis treatments is limited by severe silica scale on membranes (Ordóñez et al., 2010). Thus, it would be very interesting to use the existing DAF units to partly remove the silica content in process water and thus in the effluent, especially taking into account that it has been previously demonstrated that silica removal by coagulation can be enhanced by the presence of suspended solids (Miranda et al., 2015a).

Silica removal increased with the coagulant dosage (**Figure 2B**). PAC-HB and PANS-PA were the most efficient products, with a 45–50% silica removal (125–130 mg/L residual silica), while PANS, PAC-MB, and alum, obtained a 30–35% removal (155–175 mg/L residual silica). The soluble silica removal can be related to the content of colloidal aluminum (Al_c or Al_u) in the coagulants. Most efficient products (PAC-HB and PANS-PA) were those with the highest contents while the least efficiency products (alum and PAC-MB) are those with the lowest ones. This is in agreement with a previous work studying the effect of aluminum speciation on silica removal during the coagulation of heavy-oil wastewater using polyaluminum chlorides (Zhao et al., 2016). These authors demonstrated that Al_a and Al_c promoted the removal of Si_c (polymeric) and Si_a (monomer and dimers), while they did not find a clear trend for Al_b. In the present study, most silica species are monomers and dimers of silicilic acid (Si_a) as demonstrated by the fact that the silica concentration measured by silico-molybdate method was around the same than the total silica measured by ICP-OES: 273 mg/L vs. 277 mg/L SiO_2. Thus, present study corroborates Al_c is the most important Al species for the removal of soluble silica consisting in monomer and dimers.

Previous studies have demonstrated that the coagulants with the highest efficiency in removing COD were usually those with the lowest efficiency in silica removal, and vice versa (Hermosilla et al., 2012; Latour et al., 2013; Miranda et al., 2015b). However, the reason for this was not established. According to the results obtained in this study, the explanation seems to be related to Al speciation: coagulants with high Al_a (Al_m) content are more efficient in removing soluble COD while coagulants with high Al_c (Al_u) content are more efficient in removing soluble silica. This is very important as the coagulant type and dosage used in industrial DAFs is usually optimized in terms of suspended solids (turbidity). However, the removal of soluble contaminants is required to further closing the water circuits.

pH and Conductivity

These parameters are also important when reusing process waters. When added to water, aluminum ions hydrolyse to form soluble monomeric and polymeric species and solid precipitates, which causes an alkalinity consumption and a parallel pH decrease, the extent of this decrease depends on the aluminum dosage and the basicity of the coagulants (Pernitsky and Edzwald, 2006). As the same aluminum dosages have been tested for all the coagulants, the highest pH decrease was observed for the products with the lowest basicity. Alum and PAC-MB decreased the pH of clarified waters to pH 5.4 and 6.0, respectively, at the highest dosage tested. On the opposite, PAC-HB and PANS-PA decreased less the pH of the treated waters, this decrease being always lower than 0.5 pH units (final pH 6.5–6.8 at the highest dosage). The pH decrease with PANS was intermediate. As commented before, the pH of minimum solubility of $Al(OH)_3$, which produces the larger amount of $Al(OH)_3$ and the lower residual aluminum concentration, is around 6.0 for alum and 6.2–6.4 for PACs (Pernitsky and Edzwald, 2003). For this reason, the lowest pH at which aluminum salts can be used is usually limited to around 5.5–5.8, depending on the temperature and the presence of other species in the waters, i.e., sulfates, phosphates, etc. (Kvech and Edwards, 2002). Accordingly, for the treatments based on alum or PAC-MB, especially if high dosages are used, it would be recommended to add alkalinity to the waters.

Similarly to pH, PAC-HB, and PANS-PA were the products that induced a lower increase of conductivity, from 2.1 mS/cm (blank) to 2.4–2.5 mS/cm. The other coagulants increased the conductivity of the treated waters to 2.8 mS/cm (PANS and PAC-MB) or 2.9 mS/cm (alum); all these values were obtained at the highest dosages tested.

It is also important to notice that the distribution of aluminum species depends primarily of the coagulation pH. When added to water, aluminum ions hydrolyse to form soluble monomeric and polymeric species and solid precipitates, the main ones being Al^{3+}, $Al(OH)^{2+}$, $Al(OH)_2^+$, $Al(OH)_3$ (s), $Al(OH)_4^-$, $Al_2OH)_2^{4+}$, $Al_3(OH)_4^{5+}$, $Al_{13}O_4(OH)_{24}^{7+}$, and $Al(OH)_3$ (s). Under normal water treatment conditions, alum chemistry can be described by the presence of three species: $Al(H_2O)_6^{3+}$ (usually shortened to Al^{3+}), $Al(OH)^{2+}$, and $Al(OH)^{4-}$ in equilibrium with an amorphous $Al(OH)_3$ solid phase. Below the pH of minimum solubility, the highly charged Al^{3+} and $Al(OH)^{2+}$ species are the most prevalent species, while at greater pHs, become predominant $Al(OH)_4^-$ (Pernitsky and Edzwald, 2006; Edzwald and Haarhoff, 2011). The solid phase formed upon precipitation, $Al(OH)_3$ (s), has amphoteric hydroxyl groups that can charge positively or negatively depending on the pH. The chemistry of PACs is very similar to that of alum but PACs contain highly charged polymeric aluminum species in addition of the monomers described for alum, the most predominant being Al_{13}^{7+}, which is more stable in a wide range of pHs than other polymerized Al_{13}^{7+} is more stable in a wider range of pH. The basicity of PACs affects the alkalinity consumption of the coagulant but also the relative prevalence of polymeric and monomeric species. In general, the higher basicity, the greater Al_{13}^{7+} fraction, up to ~70% basicity (Pernitsky and Edzwald, 2006). As a rule of thumb, the best efficiency is obtained by coagulation near the pH of minimum solubility (pH from 6 to 7) where the amount of aluminum hydroxide precipitated is the largest, while keeping the Al residual levels in water at minimum. If coagulation pH is low or pH suppression has been important, e.g., coagulation at pHs 5.5 or less, then the positively charged Al species become predominant. This fact together with the higher Al dissolved levels make the primary mechanism for the removal of contaminants complexation and direct precipitation (Edzwald and Haarhoff, 2011).

Comparison Among the Treatments

Comparing the obtained results for turbidity, COD, and silica removal, PANS-PA and PAC-HB, those which also produced the lowest pH decrease and conductivity increase, were the most efficient treatments. PAC-HB will be the recommended treatment if the most important objective of the treatment is suspended solids and soluble silica removal, while PANS-PA would be better option for obtaining high suspended and soluble silica removal together with an intermediate COD removal. An interesting fact to notice is that different aluminum compounds can be selected depending on the exact needs of the plant, i.e., tailor-made solutions.

Dissolved air flotation is a very efficient technique for the removal of suspended solids. However, the combination of DAF with a suitable coagulation chemistry has demonstrated it is also possible to important removals of dissolved contaminants such as COD and silica, even when most of the initial suspended solids were lower than 50 μm.

The comparison of the results obtained with data from the literature is challenging as the removal efficiencies in these treatments depend largely of the exact water treated as well as the coagulation chemicals and conditions tested (pH, dosages, etc.). It has been previously demonstrated that even in the same paper mill, using the same chemicals, important efficiency differences are found depending on the process water quality (Miranda et al., 2015a). **Table 4** shows the most relevant studies found in the literature using similar chemicals and treating similar waters. It is observed that the chemicals tested in the present study were similar in the removal of turbidity and soluble COD, to other products however, they also allowed a high removal of soluble silica, which was one of the main objectives of this study. This is an important achievement because an inverse relationship between soluble COD and silica removal is usually found (Latour et al., 2013).

Flocculation Studies

Flocculation by Successive Coagulant Additions

As the coagulant dosage increased, the total number of counts (TNC) decreased and the mean chord size (MCS) increased, indicating an increased aggregation of the particles. This behavior

TABLE 4 | Comparison of the results obtained for the removal of contaminants by coagulation with relevant literature.

Water type	Removal of contaminants obtained	References
Process waters from recycled paper production	PANS-PA: 90% turbidity, 45% soluble silica, and 15% soluble COD. PAC-HB: 85% turbidity, 50% soluble silica, and 5% soluble COD. Alum, PAC-MB, and PANS: 65–80% turbidity, 30–35% soluble silica, and 20% soluble COD.	Present study
Process waters from recycled paper production	DAF1 waters: PANS-PA, PAC-HB, and PANS removed 80–85% turbidity, 25–35% soluble silica, and 5–20% soluble COD. Alum and PAC-MB removed 65–70% turbidity, 20% soluble silica, and 20% soluble COD. DAF2 waters: PANS-PA, PAC-MB, and alum removed 95% turbidity, 20–35% soluble silica, and 20–25% soluble COD. PANS and PAC-HB removed 65–80% turbidity, 20–25% soluble silica, and 10–20% soluble COD.	Miranda et al., 2015a
Effluent from recycled paper production	Newly developed hybrid coagulants combining PANS and three polyamines of different molecular weights and similar charge densities. Without pH adjustment (pH 8.4), the following removals were obtained: >75% turbidity, 40–50% soluble silica, and up to 40% soluble COD.	Latour et al., 2016
Process waters from recycled paper production	Different coagulation treatments, including bentonite + anionic polyacrylamide, PDADMAC, or PAC. The following contaminants removal were obtained: 60–90% turbidity, 5–50% COD, 0% silica.	Sarja et al., 2004
Process waters from recycled paper production	Different polyaluminum based coagulants (including hybrid coagulants) obtained 90% removal of turbidity and 15% of soluble COD.	Miranda et al., 2009a
Process waters from recycled paper production	Dual treatment (chitosans + anionic bentonite microparticles): 80–90% turbidity, 5–10% soluble silica, and 20% soluble COD.	Miranda et al., 2013
The secondary treatment effluent from a high-tech industrial park	PAC/alum coagulation in combination with waste flocs and polyacrylic acid flocculant achieved the following removals at optimal conditions: 95% removal of turbidity, 45–50% colloidal and soluble silica, and 60% soluble COD.	Chuang et al., 2007

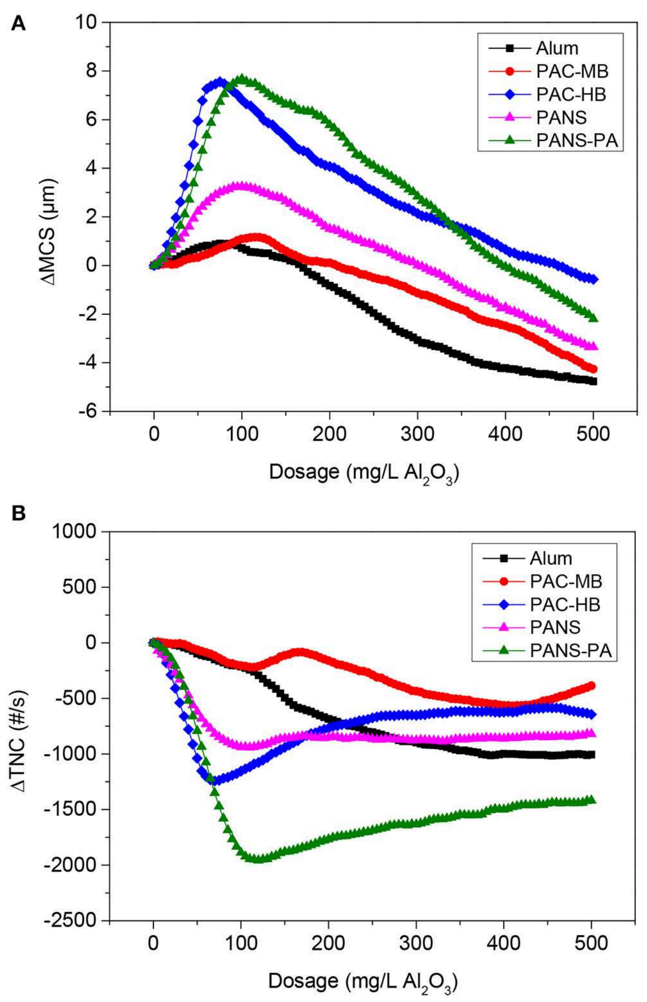

FIGURE 3 | (A) ΔMCS and (B) ΔTNC vs. dosage of coagulants without flocculant addition ($MCS_o = 41.7\ \mu m$, $TNC_o = 2{,}860$ #/s).

was observed until reached an optimal dosage and no more aggregation took place after: TNC stopped decreasing and started to increase, while MCS stopped increasing and started to decrease due to steric stabilization or electrostatic repulsion (**Figure 3**).

Two products stood out from the rest, PANS-PA and PAC-HB. At their optimal dosages, they reduced notably the initial TNC (70% reduction for PANS-PA and 45% for PAC-HB) while increased around 8 μm the MCS of the particles. PANS shown an intermediate efficiency both in terms of MCS increase (3 μm) and TNC reduction (35%). Finally, PAC-MB and alum were the coagulants increasing less the MCS (around 1 μm); PAC-MB was the coagulant producing also the lowest TNC decrease (20%), while alum obtained an intermediate TNC reduction (35%).

The important decrease of the initial TNC is in agreement with the high efficiency in the removal of contaminants in DAF tests. For example, turbidity removals varied from 65 to 70% with the least efficient products to 85–90% with the most efficient products. Despite an extensive flocculation was observed during these flocculation tests, the observed MCS increases obtained by FBRM could be considered small. However, this is explained by the following two facts. First, floc larger than 1,000 μm, visually observed during the flocculation, are not detected by the FBRM probe (measurement range from 1 to 1,000 μm). Second, the important destabilization of DCM (as demonstrated by the high removals of soluble COD and silica) forms new small flocs, previously not detected by FBRM, which decreases the MCS of the present particles.

The dosage at which the maximum MCS or the minimum TNC was observed can be used as rough estimation of the optimal coagulant dosage. In this case, the optimal dosages ranged between 75 and 125 mg/L Al_2O_3 for all the coagulants tested. These preliminary optimal dosages are in agreement with those observed for turbidity removal in DAF tests (**Figure 1A**), as the flocculation of suspended solids is the main contributor of turbidity. However, as commented before, the maximum removal of soluble COD or silica was only achieved at the highest dosages tested. As soluble COD and silica are not associated with suspended solids, a poor relation between ΔMCS and ΔTNC and COD and silica removal was observed.

Flocculation-Deflocculation-Reflocculation Studies

Growth, breakage and regrowth of the flocs formed by coagulation with different dosages of the aluminum compounds were studied. As the observed behavior showed a continuous transition from the lowest (25 mg/L) to the highest (250 mg/L) dosages tested, the flocculation-deflocculation-reflocculation curves only for these two dosages are shown in **Figures 4**, **5**.

Flocculation stage

At low dosages (25–50 mg/L) neither the MCS increased nor the TNC decreased significantly except for PAC-HB. However, at higher dosages ($\geq$100 mg/L), a significant increase in the MCS and a significant decrease in TNC were observed for all the coagulants, indicating an important agglomeration of the particles. The extent of this agglomeration increased with the dosage for all the coagulants except for PAC-HB. At the lowest dosage tested (25 mg/L), PAC-HB was the coagulant increasing in a larger extent the MCS (around 10 μm compared to 1.0–1.5 μm for the other coagulants) and decreasing the TNC (850 #/s compared to 100–250 #/s for the other coagulants). However, at the highest dosage tested (250 mg/L), PANS-PA produced the highest increase in the MCS (around 12 μm compared to <4 μm for the other coagulants) and the highest decrease in TNC (1,400 #/s compared to 500–1,000 #/s).

According to these results, PANS-PA seems to be the most efficient product, especially at intermediate and high dosages, while PAC-HB would be the most efficient at low dosages. However, PAC-HB was one of the most efficient coagulants in DAF tests (especially in turbidity and soluble silica removal) and its efficiency always increased with the dosage, with no apparent restabilization or charge reversal according to turbidity and cationic demand measurements. The reason for this apparent controversy is related to the shape of the flocs formed by PAC-HB. A previous study of the authors demonstrated this coagulant can induce the linear aggregation of the particles, especially at high dosages, generating cylindrical

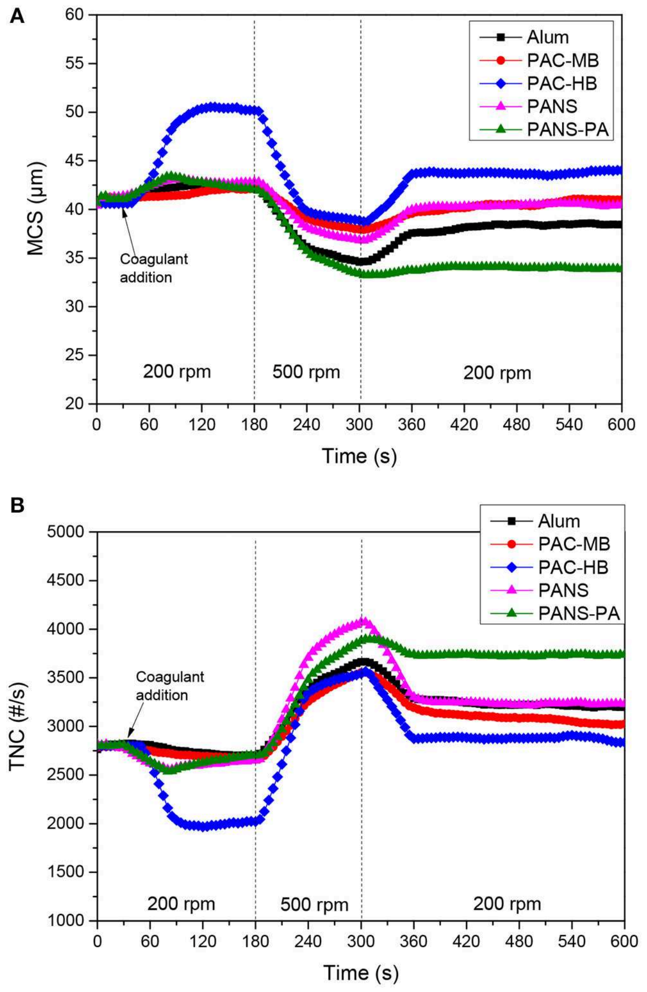

FIGURE 4 | (A) MCS and **(B)** TNC at 25 mg/L Al_2O_3 coagulant vs. time in flocculation-deflocculation-reflocculation studies.

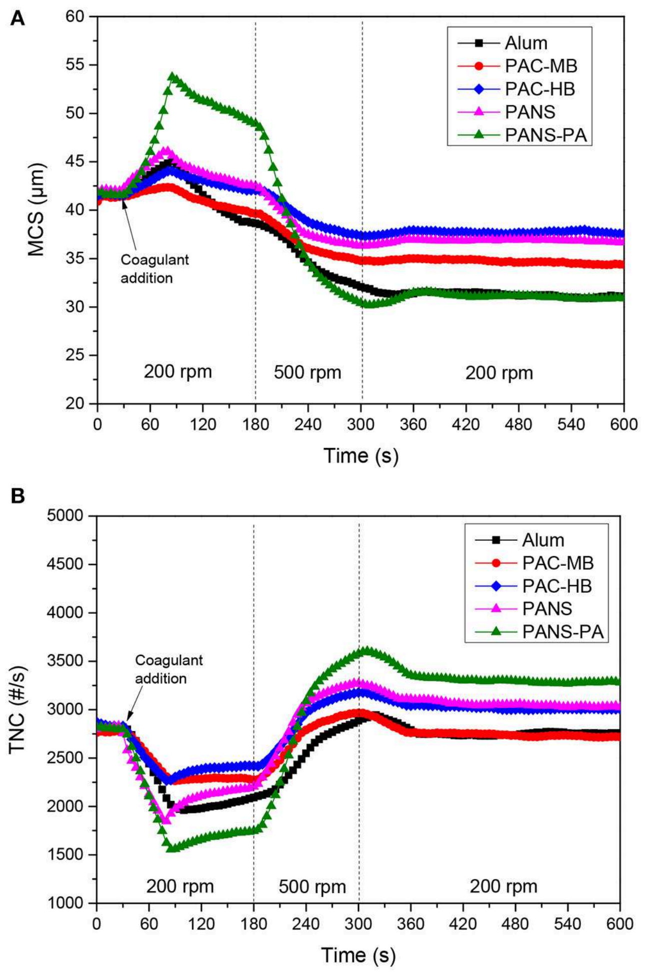

FIGURE 5 | (A) MCS and **(B)** TNC at 250 mg/L Al_2O_3 coagulant vs. time in flocculation-deflocculation-reflocculation studies.

coagula (Hermosilla et al., 2012). These coagula are much longer than the original particles but with similar diameter. As the probability of the laser beam of FBRM to intercept the particle at the longer side is much lower than at the shorter side, this aggregation was not directly observed by FBRM.

The other three coagulants gave similar results from flocculation monitoring tests, the efficiency of PANS being slightly higher than that of alum and PAC-MB, which is also in agreement with the observed removal of contaminants in DAF tests.

Deflocculation stage and strength factor

The observed behavior was very similar for all the coagulants but PANS-PA. During the deflocculation of flocs formed by pure aluminum coagulants, the MCS decreased 4–8 µm while the TNC increased 750–1,500 #/s. The MCS decrease and TNC increase of the flocs formed by PANS-PA was higher and varying largely with the dosage: the MCS decrease varied from 8 µm at 25 mg/L to 18 µm at 250 mg/L, while the TNC increase varied from 1,800 #/s at 25 mg/L to 2,500 #/s at 250 mg/L. The differences in the strength of the formed flocs was further analyzed by the strength factor (**Figure 6**). The strength factor for pure aluminum coagulants was high (most of them between 70 and 75%), indicating the flocs formed were very resistant to shear forces, and only small differences with the coagulant type and dosage was observed. The strength factor of PANS-PA was, however, lower than those obtained by pure aluminum coagulants and decreased significantly with the dosage, from around 80 to 65%.

However, flocs formed by charge neutralization or sweep flocculation, which are the two main flocculation mechanisms associated to aluminum based coagulants, are weak and prone to breakage (Bache and Gregory, 2007; Ghernaout and Ghernaout, 2012; Bratby, 2016). Although the strength factor is dependent on the breakage shear rate and the mixer characteristics (Jarvis et al., 2005), a review of the literature indicates that regular strength factors for charge neutralization and sweep flocculation mechanisms are much lower than those obtained in the present

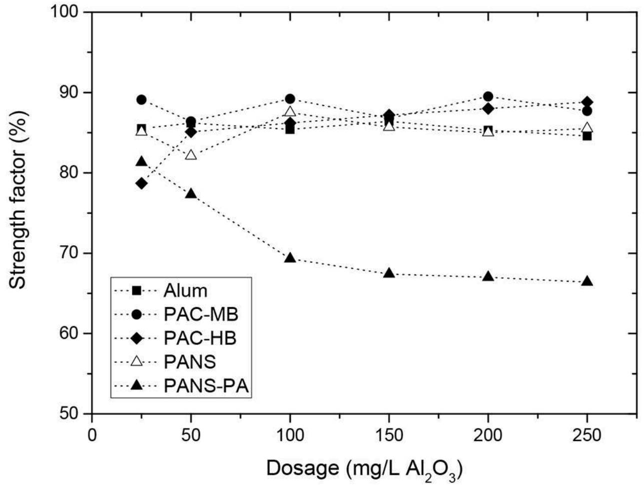

FIGURE 6 | Strength factor for the different coagulants and used dosages.

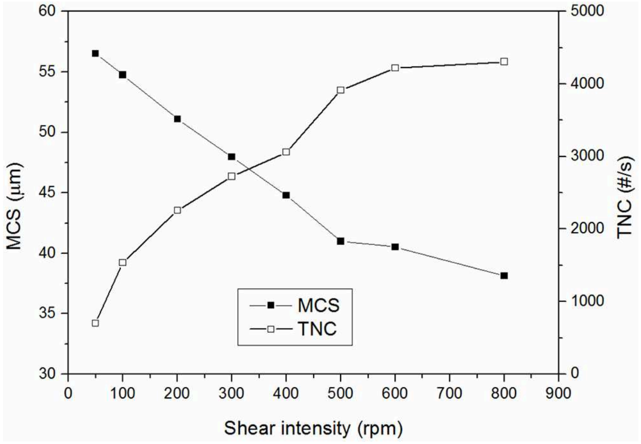

FIGURE 7 | Effect of shear intensity on MCS and TNC of the initial water.

study. Xu and Gao (2012), for example, obtained strength factors around 50–65% for different aluminum coagulants at low shear intensities (breakage at 100 rpm during 5 min) and values from 10 to 25% at high shear intensities (breakage at 400 rpm during 5 min).

The high strength factors obtained in this study are similar to those obtained by other flocculation mechanisms such as interparticles bridges formation. This apparent controversy can be explained taking into count the effect of shear forces on the initially present suspended solids in wastewater. The wastewater tested is the filtrate from a gravity table used to thicken the sludge rejects from different process stages. To improve the sludge dewatering, the sludge was flocculated before the gravity table, thus the suspended solids initially present in the wastewater are partially flocculated.

Figure 7 shows the effect of shear forces on the MCS and TNC of the wastewater without adding any coagulant. As it can be observed, the shear forces had a large impact on the TNC and MCS of the initially present suspended solids. Additionally, deflocculation-reflocculation tests were also carried out at the same experimental conditions and the MCS of the initial solids decreased 14.3 ± 1.7 µm and the TNC increased 230 ± 20 #/s, giving a strength factor of around 80 ± 2% (three replicates). This high strength factor is in agreement with interparticles bridges formation mechanism, which typically occurs when high molecular weight and low charge polyelectrolytes are used, which is exactly the characteristics of the cationic polyacrylamide used as flocculant in the gravity table. This justifies the high strength factors obtained in the present study as the observed flocs strength was mainly determined by the strength of the pre-flocculated suspended solids which were initially present in the wastewater. The flocs formed by aluminum coagulants only reduced the strength of the flocs from around 80% to 70–75%, in agreement with the expected lower strength of the flocs formed by either charge neutralization or sweep flocculation mechanisms.

From the obtained results it is difficult to distinguish if the main flocculation mechanism for aluminum coagulants was charge neutralization or sweep flocculation. First, the strength factors were very similar for all the treatments tested and second, it is not clear from the literature which flocs are more resistant to shear forces. In these sense, some authors have obtained a higher strength for the flocs formed by charge neutralization than those formed by sweep flocculation (Li et al., 2006; Wang et al., 2009), while others have obtained the opposite result (Gregory and Duan, 2001). This is probably because the flocs produced by precipitation are of widely varying strength and density (Bratby, 2016). In general, charge neutralization typically occurs at low pHs ($pH < 6.5$) and low ionic strength waters. Sweep coagulation, in contrast, occurs principally at near neutral pH and at coagulant dosages >0.05 mmol Al/L (2.5 mg/L Al_2O_3) (Jiang and Graham, 1998). The experimental conditions at which the coagulants were tested are the optimal for sweep flocculation (pH near neutral and high conductivity and soluble organics), especially at high coagulant dosages. However, charge neutralization may be also taking place at the lowest dosages tested, especially for the pre-polymerized coagulants, as it will be demonstrated clearer with the analysis of the reversibility of the flocs breakage.

It is also difficult to distinguish different behavior from different aluminum coagulants. In general, PACl products give slightly stronger flocs than alum at equivalent aluminum dosages (Jarvis et al., 2005). However, in the present study, the strength of alum flocs was similar than for PACls. PAC-HB was the only coagulant showing a slightly different behavior than the rest of PACls. In this case, the strength factor was around 10–15 points lower at 25 mg/L than those of the other coagulants. This coagulant was the one with the lowest Al_a (Al_m) content and thus producing the lowest amount of $Al(OH)_3$. Previous studies have demonstrated that monomeric aluminum produced strongest flocs than the flocs formed by PACl with lower amount of Al_m and higher contents of Al_{13} and Al_c in the flocculation of humic acids (Wang et al., 2009), thus this could be the explanation. Furthermore, PAC-HB was the coagulant achieving the highest increase in the MCS at 25 mg/L (10 μm increase vs. 1.5–2.5 μm for other coagulants) and the floc strength increases with decreasing flocs size (McCurdy et al., 2004). For these two facts, it is reasonable PAC-HB had a slightly lower floc strength than the other coagulants, especially at low dosages.

Flocs formed by PANS-PA were weaker than those formed by pure aluminum compounds, which could be explained by the different flocculation mechanism but also taking into account that the formed flocs by PANS-PA were the largest before the deflocculation stage, especially at high dosages, and larger flocs are usually the weakest (Bache and Gregory, 2007). It was observed a negative correlation between the strength factor and size of the flocs after coagulation. The highest strength factors were observed at the lowest dosages, when the lowest MCS increases after coagulation were observed (7–9 μm), and then decreased and maintained constant at the dosages at which the highest MCS were observed (17–18 μm). PANS-PA flocculation mechanism is a combination of the main flocculation mechanism of PANS and that of the polyamines used in its formulation. Depending on its molecular weight and charge density, the flocculation mechanism of polyamines is usually explained by patches formation or interparticles bridging formation. The flocs formed by patches are generally soft, small and rigid, while the flocs formed by bridges are big, hard, and flexible. If the main flocculation mechanism would be bridges formation, the strength factor should be higher than those for pure aluminum coagulants, while if patches formation is predominant, the strength factors should be very similar to that for pure aluminum coagulants. PANS-PA had strength factors similar to that of pure aluminum coagulants at 25 mg/L but much lower at higher dosages. High charge and low molecular weight polyamines as those used in the PANS-PA formulation usually works by patches formation, which could explain the similar strength factor of PANS-PA to those of the other coagulants at 25 mg/L. The weaker flocs obtained at high dosages can be explained by the impaired formation of patches at these conditions, which is in agreement with the high cationic demand removals obtained with this product and the charge reversal obtained at dosages ≥100 mg/L. Furthermore, the flocs obtained were larger and were associated to higher removal efficiencies of contaminants at high dosages. Therefore, flocculation mechanism is a combination of sweep flocculation by PANS and the formation of large and loose organic flocs induced by polyamines.

Reflocculation stage and reflocculation factor

For all the coagulants and dosages tested, the reflocculation was very limited, especially for PANS-PA. In general, the higher dosage the lower MCS increase after the shear forces stopped and thus, the reversibility of the flocs. For pure aluminum coagulants, the MCS increase after reflocculation was 3–5 μm at low dosages (25–50 mg/L) and then decreased to 0–1 μm at the highest dosages. With PANS-PA, the reflocculation was almost negligible, even at the lowest dosage tested. Similarly to strength factors, reflocculation factors were calculated (**Figure 8**). Recovery factors decreased largely with the dosage for the pure aluminum-based coagulants, the main differences found at the lowest dosage tested. At 25 mg/L, the recovery factors varied in the following order: PAC-MB (73.2%) > PANS (60.5%) > alum (50.5%) > PAC-HB (45.6%) > PANS-PA (6%), while at the highest dosage (250 mg/L), recovery factors only varied between −8% (PAC-MB) and 5% (PANS).

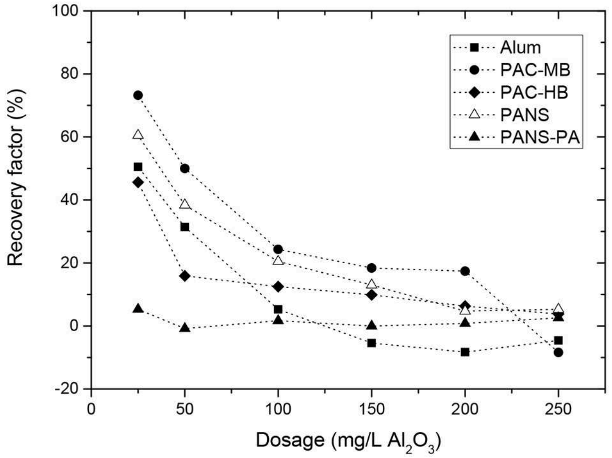

FIGURE 8 | Reflocculation factors for the different coagulants and used dosages.

At this point it is also interesting to take into account the reflocculation factor obtained without adding any coagulant, which shows the behavior of the initially present suspended solids: this value is 25.7 ± 1.5% (three replicates). This agrees well with the fact that initially suspended solids are partially flocculated by interparticles bridges (flocs of high strength but very limited recovery). Consequently, the recovery factors of the flocs formed by all coagulants but PANS-PA were greater than those from the initially present suspended solids. If charge neutralization would be the predominant flocculation mechanism, the reflocculation should be almost total after the shear forces ends (Blanco et al., 2002a,b). However, if sweep flocculation is predominant, the flocs will likely have a reduced recovery compared to charge neutralization (Gregory and Duan, 2001). The continuous decrease of the reflocculation factors with the dosage, from 45–75 to 0%, can be explained by the continuous transition from charge neutralization to sweep flocculation mechanism. At the lowest dosages, the contribution of charge neutralization mechanism is still important and high recovery factors are observed. As the dosage of the coagulant increases, sweep flocculation (irreversible flocs) became predominant, and a parallel decrease in the reflocculation factor of the formed flocs was observed. At the highest dosages (100–250 mg/L), the reflocculation factor was even lower than this obtained for the initially present suspended solids, thus indicating sweep flocculation became predominant.

The reflocculation factor was always close to zero for PANS-PA, independently of the dosage. The polyamines in its formulation could induce a partial patching mechanism, which would generate flocs that are partially reversible. These flocs are less reversible than charge neutralization but still more reversible than sweep flocculation. However, at the highest dosages, when charge reversal occurred, it is expected a transition from patches formation (reversible flocs) to interparticles bridges formation (irreversible flocs), which agrees well both with the larger flocs obtained by PANS-PA during flocculation and the null reversibility of the flocs, typical situation for interparticles bridge formation flocculation mechanism. Furthermore, the higher concentration of suspended solids after deflocculation favors interparticles bridging formation instead of patches (Tripathy and De, 2006; Zhou and Franks, 2006; Lee et al., 2014). This behavior would be explained by an increase in the contribution of interparticles bridges formation at the reflocculation conditions, where the high concentration of small solids promote interparticles bridges instead of patches formation.

CONCLUSIONS

Aluminum coagulants were very efficient in removing contaminants by DAF, not only suspended solids but also soluble COD and silica. Large differences were found depending on coagulant composition and flocculation mechanism, which depends on the used dosage. Alum and PAC-MB were the least efficient coagulants, PANS had an intermediate efficiency, and PAC-HB and PANS-PA were the most efficient. The optimum coagulation treatment depends on the target contaminant, which depends on the particular needs of the industry. PAC-HB will be the recommended treatment when the most important objective of the treatment is suspended solids and silica removal, while PANS-PA is the recommended treatment for obtaining high silica removals together with high turbidity and COD removals. High Al_a (Al_m) content of the coagulants is translated into high soluble COD removals but low or intermediate silica removals. On the other side, high Al_c content in the coagulants produced high silica removal but low or intermediate soluble COD removals.

Regarding flocculation mechanisms by pure aluminum coagulants, there is a continuous transition between charge neutralization and sweep flocculation. At the lowest dosages tested (25–50 mg/L), charge neutralization is the main flocculation mechanism while sweep flocculation is the main flocculation mechanism at the higher dosages (≥100–150 mg/L). The hybrid coagulant showed a rather different behavior result of the combination of the aluminum and the polyamines present, these polyamines acting by patches formation at low dosages (with a reduced shear resistance) and interparticles bridges formation at high dosages (confirmed by the large flocs observed and the limited reflocculation ability after flocs breakage). Strength and recovery factors were clearly affected by the behavior of the initially present suspended solids, which were flocculated in a previous stage (sludge thickening) by a high molecular weight and low charge flocculant in a process stage before sampling. These pre-existing flocs formed by interparticles bridging mechanism, characterized by high strength and null reversibility, modified the resulting flocs by aluminum coagulants which shown high strength and low reversibility after breakage, even at the lowest dosage when charge neutralization mechanism is predominant. As it was observed, the flocculation mechanisms taking place treating industrial waters is rather complex due to the large number of variables affecting the coagulation, including the presence of pre-flocculated suspended solids. However, these studies are necessary to get a deeper understanding of the flocculating mechanisms in such real systems.

The obtained results have demonstrated the different role of Al species of polyaluminum chlorides for the removal of suspended solids and soluble contaminants (COD and silica). This is an interesting starting point to develop tailor-made coagulants for target contaminants in other industrial applications. In the papermaking sector, it has been specifically demonstrated that the selection of an adequate chemistry allows existing DAF units to be optimized for removing specific contaminants even simultaneously if hybrid coagulants are used.

DATA AVAILABILITY STATEMENT

The datasets generated for this study are available on request to the corresponding author.

AUTHOR CONTRIBUTIONS

RM and IL made the experimental tests and the analysis of the results. RM wrote the first draft of the manuscript. All authors contributed to the conception and design of the study, manuscript revision, read and approved the submitted version.

FUNDING

This work was funded by the Spanish Ministry of Economy, Industry and Competitiveness through the project CTM2016-77948-R and the Community of Madrid through the programme RETOPROSOST-2-CM (P2018/EMT-4459).

ACKNOWLEDGMENTS

Authors acknowledge the collaboration of Sachtleben Wasserchemie GmbH, Kemira Ibérica S.A., and Sertec-20 S.L. for supplying the chemicals used in the study and Holmen Paper Madrid for providing the process waters.

REFERENCES

Bache, D. H., and Gregory, R. (2007). *Flocs in Water Treatment*. London: IWA Publishing.

Blanco, A., Fuente, E., Negro, C., Monte, M. C., and Tijero, J. (2002b). Focused beam reflectance measurement as a tool to measure flocculation. *Tappi J.* 1, 14–20.

Blanco, A., Fuente, E., Negro, C., and Tijero, J. (2002a). Flocculation monitoring: focused beam reflectance measurement as a measurement tool. *Can. J. Chem. Eng*. 80, 1–7. doi: 10.1002/cjce.5450800403

Bolto, B., and Xie, Z. (2019). The use of polymers in the flotation treatment of wastewater. *Processes* 7:374. doi: 10.3390/pr7060374

Bratby, J. (2016). *Coagulation and Flocculation in Water and Wastewater Treatment, 3rd Edn*. London: IWA publishing.

Chen, W., Zheng, H., Zhai, J., Wang, Y., Xue, W., Tang, X., et al. (2015). Characterization and coagulation–flocculation performance of a composite coagulant: poly-ferric-aluminum-silicate-sulfate. *Desalin. Wat. Treat*. 56, 1776–1786. doi: 10.1080/19443994.2014.958109

Cheng, W. P., Chen, P. H., Yu, R. F., Hsieh, Y. J., and Huang, Y. W. (2011). Comparing floc strength using a turbidimeter. *Int. J. Miner. Process.* 100, 142–148. doi: 10.1016/j.minpro.2011.05.010

Chuang, S. H., Chang, T. C., Ouyang, C. F., and Leu, J. M. (2007). Colloidal silica removal in coagulation processes for wastewater reuse in a high-tech industrial park. *Water Sci. Technol.* 55, 187–195. doi: 10.2166/wst.2007.054

Dunham, A. J., Sherman, L. M., and Alfano, J. C. (2002). Effect of dissolved and colloidal substances on drainage properties of mechanical suspensions. *J. Pulp Pap. Sci*. 28, 298–304.

Edzwald, J., and Haarhoff, J. (2011). *Dissolved Air Flotation for Water Clarification.* New York, NY: McGraw Hill Professional.

Gao, B., Yue, Q., and Wang, B. (2002). The chemical species distribution and transformation of polyaluminum silicate chloride coagulant. *Chemosphere* 46, 809–813. doi: 10.1016/S0045-6535(01)00180-1

Ghernaout, D., and Ghernaout, B. (2012). Sweep flocculation as a second form of charge neutralization – a review. *Desalin. Water Treat*. 44, 15–28. doi: 10.1080/19443994.2012.691699

Gregory, J., and Duan, J. (2001). Hydrolyzing metal salts as coagulants. *Pure Appl. Chem*. 73, 2017–2026. doi: 10.1351/pac200173122017

Hermosilla, D., Ordóñez, R., Blanco, L., de la Fuente, E., and Blanco, A. (2012). pH and particle structure effects on silica removal by coagulation. *Chem. Eng. Technol*. 35, 1632–1640. doi: 10.1002/ceat.201100527

Hu, C., Liu, H., Chen, G., and Qu, J. (2012). Effect of aluminum speciation on arsenic removal during coagulation process. *Sep. Purif. Technol.* 86, 35–40. doi: 10.1016/j.seppur.2011.10.017

Huang, X., Sun, S., Gao, B., Yue, Q., Wang, Y., and Li, Q. (2015). Coagulation behavior and floc properties of compound bioflocculant–polyaluminum chloride dual-coagulants and polymeric aluminum in low temperature surface water treatment. *J. Environ. Sci*. 30, 215–222. doi: 10.1016/j.jes.2014.07.033

Hubbe, M. A., Metts, J. R., Hermosilla, D., Blanco, M. A., Yerushalmi, L., Haghighat, F., et al. (2016). Wastewater treatment and reclamation: a review of pulp and paper industry practices and opportunities. *BioResources* 11, 7953–8091. doi: 10.15376/biores.11.3.Hubbe

Jarvis, P., Jefferson, B., Gregory, J., and Parsons, S. A. (2005). A review of floc strength and breakage. *Water Res*. 39, 3121–3137. doi: 10.1016/j.watres.2005.05.022

Jiang, J. Q., and Graham, N. J. D. (1998). Pre-polymerised inorganic coagulants and phosphorous removal by coagulation – A review. *Water SA* 24, 237–244.

Jiao, R., Fabris, R., Chow, C. W., Drikas, M., van Leeuwen, J., and Wang, D. (2016). Roles of coagulant species and mechanisms on floc characteristics and filterability. *Chemosphere* 150, 211–218. doi: 10.1016/j.chemosphere.2016.02.030

Kangama, A., Zeng, D., Tian, X., and Fang, J. (2018). Application of chitosan composite flocculant in tap water treatment. *J. Chem.* 2018:2768474. doi: 10.1155/2018/2768474

Kimura, M., Matsui, Y., Kondo, K., Tairyo, B., Ishikawa, T. M., and Shirasaki, N. (2013). Minimizing residual aluminum concentration in treated water by tailoring properties of polyaluminum coagulants. *Water Res*. 47, 2075–2084. doi: 10.1016/j.watres.2013.01.037

Kvech, S., and Edwards, M. (2002). Solubility controls on aluminum in drinking water at relatively low and high pH. *Water Res*. 36, 4356–4368. doi: 10.1016/S0043-1354(02)00137-9

Latour, I., Miranda, R., and Blanco, A. (2013). Silica removal from newsprint mill effluents with aluminum salts. *Chem. Eng. J.* 230, 522–531. doi: 10.1016/j.cej.2013.06.039

Latour, I., Miranda, R., Carceller, R., and Blanco, A. (2016). Efficiency of polyaluminum nitrate sulfate–polyamine hybrid coagulants for silica removal. *Desalin. Water Treat*. 57, 17973–17984. doi: 10.1080/19443994.2015.1091992

Lee, C. S., Robinson, J., and Chong, M. F. (2014). A review on application of flocculants in wastewater treatment. *Process Saf. Environ. Prot.* 92, 489–508. doi: 10.1016/j.psep.2014.04.010

Lee, K. E., Morad, N., Teng, T. T., and Poh, B. T. (2012). Development, characterization and the application of hybrid materials in coagulation/flocculation of wastewater: a review. *Chem. Eng. J*. 203, 370–386. doi: 10.1016/j.cej.2012.06.109

Li, T., Zhu, Z., Wang, D., Yao, C., and Tang, H. (2006). Characterization of flocs size, strength and structure under various coagulation mechanisms. *Powder Technol*. 168, 104–110. doi: 10.1016/j.powtec.2006.07.003

Lin, J.-L., Huang, C.-J., Chin, M., and Pan, J. R. (2008). Coagulation dynamics of fractal flocs induced by enmeshment and electrostatic patch mechanisms. *Water Res*. 42, 4457–4466. doi: 10.1016/j.watres.2008.07.043

McCurdy, K., Carlson, K., and Gregory, D. (2004). Floc morphology and cycling shearing recovery: comparison of alum and polyaluminum chloride coagulants. *Water Res*. 38, 486–494. doi: 10.1016/j.watres.2003.10.005

Miranda, R., Blanco, A., de la Fuente, E., and Negro, C. (2008). Separation of contaminants from deinking process water by dissolved air flotation: effect of flocculant charge density. *Sep. Sci. Technol*. 43, 3732–3754. doi: 10.1080/01496390802286587

Miranda, R., Blanco, A., and Negro, C. (2009a). Accumulation of dissolved and colloidal material in papermaking – Application to simulation. *Chem. Eng. J.* 148, 385–393. doi: 10.1016/j.cej.2008.09.014

Miranda, R., Latour, I., and Blanco, A. (2015a). Influence of suspended solids on silica removal by coagulation with aluminum salts. *Cell. Chem. Technol.* 49, 497–510.

Miranda, R., Latour, I., Hörsken, A., Jarabo, R., and Blanco, A. (2015b). Enhanced silica removal by polyamine-and polyacrylamide-polyaluminum hybrid coagulants. *Chem. Eng. Technol*. 38, 2045–2053. doi: 10.1002/ceat.201400604

Miranda, R., Negro, C., and Blanco, A. (2009b). Internal treatment of process waters in paper production by dissolved air flotation with newly developed chemicals. 1. Laboratory tests. *Ind. Eng. Chem. Res*. 48, 2199–2205. doi: 10.1021/ie801047h

Miranda, R., Negro, C., and Blanco, A. (2009c). Internal treatment of process waters in paper production by dissolved air flotation with newly developed chemicals. 2. Field trials. *Ind. Eng. Chem. Res.* 48, 3672–3677. doi: 10.1021/ie801826m

Miranda, R., Nicu, R., Latour, I., Lupei, M., Bobu, E., and Blanco, A. (2013). Efficiency of chitosans for the treatment of papermaking process water by dissolved air flotation. *Chem. Eng. J.* 231, 304–313. doi: 10.1016/j.cej.2013.07.033

Nan, J., Yao, M., Chen, T., Wang, Z., Li, Q., and Zhan, D. (2016). Experimental and numerical characterization of floc morphology: role of changing hydraulic retention time under flocculation mechanisms. *Environ. Sci. Pollut. Res*. 23, 3596–3608. doi: 10.1007/s11356-015-5539-7

Ordaz-Díaz, L. A., Valle-Cervantes, S., Rodríguez-Rosales, J., Bailón-Salas, A. M., Madrid-Del Palacio, M., Torres-Fraga, K., et al. (2017). Zeta potential as a tool to evaluate the optimum performance of a oagulation-flocculation process for wastewater internal treatment for recirculation in the pulp and paper Process. *BioResources* 12, 5953–5969. doi: 10.15376/biores.12.3.5953-5969

Ordóñez, R., Hermosilla, D., San Pío, I., and Blanco, A. (2010). Replacement of fresh water use by final effluent recovery in a highly optimized 100% recovered paper mill. *Water Sci. Technol*. 62, 1694–1703. doi: 10.2166/wst.2010.933

Pernitsky, D. J., and Edzwald, J. K. (2003). Solubility of polyaluminum coagulants. *J. Water Suppl.* 52, 395–406. doi: 10.2166/aqua.2003.0036

Pernitsky, D. J., and Edzwald, J. K. (2006). Selection of alum and polyaluminum coagulants: principles and applications. *J. Water Suppl.* 55, 121–141. doi: 10.2166/aqua.2006.062

Rasteiro, M. G., García, F. A. P., Ferreira, P., Blanco, A., Negro, C., and Antunes, E. (2008). The use of LDS as a tool to evaluate flocculation mechanisms. *Chem. Eng. Process*. 47, 1323–1332. doi: 10.1016/j.cep.2007.04.009

Saarimaa, V., Sundberg, A., Holmbom, B., Blanco, A., Fuente, E., and Negro, C. (2006b). Monitoring of dissolved air flotation by focused beam reflectance measurement. *Ind. Eng. Chem. Res*. 45, 7256–7263. doi: 10.1021/ie060250+

Saarimaa, V., Sundberg, A., Holmbom, B. H., Blanco, A., Negro, C., and Fuente, E. (2006a). Purification of peroxide-bleached TMP water by dissolved air flotation. *Tappi J*. 5, 15–21.

Sarja, T., Zabihian, M., Kourunen, P., and Niinimäki, J. (2004). New method for measuring potential secondary stickies in deinked pulp filtrates. *Water Sci. Technol*. 50, 207–215. doi: 10.2166/wst.2004.0197

Shen, X., Gao, B., Guo, K., and Yue, Q. (2020). Characterization and influence of floc under different coagulation systems on ultrafiltration membrane fouling. *Chemosphere* 238:124659. doi: 10.1016/j.chemosphere.2019.124659

Sun, Y., Zhu, C., Zheng, H., Sun, W., Xu, Y., Xiao, X., et al. (2017). Characterization and coagulation behavior of polymeric aluminum ferric silicate for high-concentration oily wastewater treatment. *Chem. Eng. Res. Des*. 119, 23–32. doi: 10.1016/j.cherd.2017.01.009

Tang, H., Xiao, F., and Wang, D. (2015). Speciation, stability, and coagulation mechanisms of hydroxyl aluminum clusters formed by PACl and alum: a critical review. *Adv. Colloid Interface Sci.* 226, 78–85. doi: 10.1016/j.cis.2015.09.002

Tripathy, T., and De, B. R. (2006). Flocculation: a new way to treat the waste water. *J. Phys. Sci*. 10, 93–127.

Wang, B., Shui, Y., He, M., and Liu, P. (2017). Comparison of flocs characteristics using before and after composite coagulants under different coagulation mechanisms. *Biochem. Eng. J*. 121, 107–117. doi: 10.1016/j.bej.2017.01.020

Wang, D., Sun, W., Xu, Y., Tang, H., and Gregory, J. (2004). Speciation stability of inorganic polymer flocculant–PACl. *Colloids Surf. A* 243, 1–10. doi: 10.1016/j.colsurfa.2004.04.073

Wang, D., Wu, R., and Yiang, C. W. K. (2011). Characterization of floc structure and strength: role of changing shear rates under various coagulation mechanisms. *Colloids Surf. A* 379, 36–42. doi: 10.1016/j.colsurfa.2010.11.048

Wang, X., Tang, X., Feng, P., Li, X., Zhao, C., Chen, W., et al. (2017). A novel preparation method of polyaluminum chloride/polyacrylamide composite coagulant: composition and characteristic. *J. Appl. Polym. Sci*. 134:44500. doi: 10.1002/app.44500

Wang, Y., Gao, B.-Y., Xu, X.-M., Xu, W.-Y., and Xu, G.-Y. (2009). Characterization of floc size, strength and structure in various aluminum coagulants treatments. *J. Colloid Interface Sci*. 332, 354–359. doi: 10.1016/j.jcis.2009.01.002

Wang, Z., Nan, J., Yao, M., and Yang, Y. (2017). Effect of additional polyaluminum chloride and polyacrylamide on the evolution of floc characteristics during floc breakage and re-growth process. *Sep. Purif. Technol*. 173, 144–150. doi: 10.1016/j.seppur.2016.09.020

Wei, J. C., Gao, B. Y., Yue, Q. Y., and Wang, Y. (2010). Strength and regrowth properties of polyferric-polymer dual-coagulant flocs in surface water treatment. *J. Hazard. Mater*. 175, 949–954. doi: 10.1016/j.jhazmat.2009.10.101

Xu, W., and Gao, B. (2012). Effect of shear conditions on floc properties and membrane fouling in coagulation/ultrafiltration hybrid process – The significance of Al_b species. *J. Membr. Sci*. 415–416, 153–160. doi: 10.1016/j.memsci.2012.04.046

Yao, M., Nan, J., and Chen, T. (2014). Effect of particle size distribution on turbidity under various water quality levels during flocculation processes. *Desalination* 354, 116–124. doi: 10.1016/j.desal.2014.09.029

Yao, M., Nan, J., Chen, T., Zhan, D., Li, Q., Wang, Z., et al. (2015). Influence of flocs breakage process on membrane fouling in coagulation/ultrafiltration process—effect of additional coagulant of poly-aluminum chloride and polyacrylamide. *J. Membr. Sci*. 491, 63–72. doi: 10.1016/j.memsci.2015.05.018

Yu, W., Li, G., Xu, Y., and Yang, X. (2009). Breakage and re-growth of flocs formed by alum and PACl. *Powder Technol*. 189, 439–443. doi: 10.1016/j.powtec.2008.07.008

Zhang, Y., Li, S., Wang, X., and Li, X. (2015). Coagulation performance and mechanism of polyaluminum ferric chloride (PAFC) coagulant synthesized using blast furnace dust. *Sep. Purif. Technol*. 154, 345–350. doi: 10.1016/j.seppur.2015.09.075

Zhang, Y. J., Zhao, X. L., Li, X. X., Liu, C., and Zhu, L. L. (2010). Performance of PAC/PDM composite coagulants for removal of algae from Lake Taihu waters in summer. *Water Sci. Technol*. 62, 330–339. doi: 10.2166/wst.2010.292

Zhao, B., Wang, D., Li, T., Chow, C. W. K., and Huang, C. (2010). Influence of floc structure on coagulation-microfiltration performance: effect of Al speciation characteristics of PACls. *Sep. Purif. Technol*. 72, 22–27. doi: 10.1016/j.seppur.2009.12.023

Zhao, X., Yang, T., Liu, L., Zhang, X., Fan, L., and Huang, Y. (2016). Effect of aluminum speciation on silica removal during coagulation of heavy-oil wastewater using polyaluminum chloride. *Des. Water Treat.* 57, 11789–11799. doi: 10.1080/19443994.2015.1044917

Zhou, Y., and Franks, G. V. (2006). Flocculation mechanism induced by cationic polymers investigated by light scattering. *Langmuir* 22, 6775–6786. doi: 10.1021/la060281+

Conflict of Interest: The authors declare that the research was conducted in the absence of any commercial or financial relationships that could be construed as a potential conflict of interest.

ORIGINAL RESEARCH
published: 12 February 2020
doi: 10.3389/fchem.2020.00080

Catalytic Ozonation of Nitrobenzene by Manganese-Based Y Zeolites

Jingze Hu*[1], *Yiming Li*[1], *Shaoshuai Nan*[1], *Brandon A. Yoza*[2], *Yifan Li*[1], *Yali Zhan*[1], *Qinghong Wang*[1], *Qing X. Li*[3], *Shaohui Guo*[1] and *Chunmao Chen*[1]

[1] State Key Laboratory of Petroleum Pollution Control, China University of Petroleum-Beijing, Beijing, China, [2] Hawaii Natural Energy Institute, University of Hawaii at Manoa, Honolulu, HI, United States, [3] Department of Molecular Biosciences and Bioengineering, University of Hawaii at Manoa, Honolulu, HI, United States

Catalytic ozonation process (COP) is considered as a cost-efficient technology for the treatment of refractory chemical wastewaters. The catalyst performance plays an important role for the treatment efficiency. The present study investigated efficiencies and mechanisms of manganese (Mn)-based Y zeolites in COPs for removing nitrobenzene from water. The catalysts of Mn/NaY and Mn/USY were prepared by incipient wetness impregnation, while Mn-USY was obtained by hydrothermal synthesis. Mn-USY contained a greater ratio of Mn^{2+} than Mn/NaY, and Mn/USY. Mn oxides loaded on Y zeolites promoted the COP efficiencies. Mn/NaY increased total organic carbon removal in COP by 7.3% compared to NaY, while Mn/USY and Mn-USY increased 11.5 and 15.8%, respectively, relative to USY in COP. Multivalent Mn oxides (Mn^{2+}, Mn^{3+}, and Mn^{4+}) were highly dispersed on the surface of NaY or USY, and function as catalytic active sites, increasing mineralization. Mn-USY showed the highest total organic carbon removal (44.3%) in COP among the three catalysts, because Mn-USY had a higher ratio of Mn^{2+} to the total Mn oxides on the surface than Mn/NaY and Mn/USY and the catalytic effects from intercorrelations between Mn oxides and mesoporous surface structures. The hydroxyl radicals and superoxide radicals governed oxidations in COP using Mn-USY. Nitrobenzene was oxidized to polyhydroxy phenol, polyhydroxy nitrophenol, and p-benzoquinone. The intermediates were then oxidized to small organic acids and ultimately carbon dioxide and water. This study demonstrates the potential of Y zeolites used in COP for the treatment of refractory chemical wastewaters.

Keywords: ozonation, catalytic ozonation, Y zeolites, Mn oxides, wastewater treatment

OPEN ACCESS

Edited by:
Renato Falcão Dantas,
Campinas State University, Brazil

Reviewed by:
Zhihua Xu,
Jianghan University, China
Aihua Xu,
Wuhan Textile University, China

****Correspondence:***
Chunmao Chen
c.chen@cup.edu.cn;
chunmaochan@163.com

Specialty section:
This article was submitted to
Catalysis and Photocatalysis,
a section of the journal
Frontiers in Chemistry

Received: *14 October 2019*
Accepted: *24 January 2020*
Published: *12 February 2020*

Citation:
Hu J, Li Y, Nan S, Yoza BA, Li Y,
Zhan Y, Wang Q, Li QX, Guo S and
Chen C (2020) Catalytic Ozonation of
Nitrobenzene by Manganese-Based Y
Zeolites. Front. Chem. 8:80.
doi: 10.3389/fchem.2020.00080

INTRODUCTION

Nitrobenzene is an electrophilic and refractory environmental contaminant that contains a nitro group and a benzene ring. Nitrobenzene is listed as a potential carcinogen by the National Institute of Environmental Health Sciences (Wang and Ma, 2018). Nitrobenzene is removed from water by adsorption (Dasgupta et al., 2018), reduction (Li Y. et al., 2018), and oxidation (El Metwally et al., 2019). The catalytic ozonation process (COP) is widely studied for its application toward the removal of refractory organic chemicals (ROCs) from water. This process is easy to manage, highly efficient, and safe (Chen et al., 2018). The use of catalysts facilitates the decomposition of ozone into highly active species of oxygen, including hydroxyl radicals (·OHs), superoxide radicals ($O_2^{\cdot-}$) and singlet oxygen radicals ($^1O_2$) (Zhao et al., 2009; Wang et al., 2019). Many catalysts have been previously studied to treat refractory environmental contaminants. Those include natural minerals (Chen et al., 2015), Al_2O_3 and ZSM-5 loaded with metal oxides (Chen et al., 2017, 2018; Xu et al., 2019), and waste sludge biochar (Chen et al., 2019). The use of zeolites catalysts (Nawrocki and Kasprzyk-Hordern, 2010), including those that contain active metallic components (Rosal et al., 2010), have been investigated. However, the catalytic mechanisms that are involved with the degradation of organic chemicals in water remain unclear. ZSM-5 zeolites adsorb ozone and organic molecules onto its surface, promoting proximal reactions (Ikhlaq et al., 2013). For example, Fe-SBA-15 was found to adsorb oxalic acid, which is then oxidized by radical species (Yan et al., 2016). Acid-treatment of natural zeolite has been determined to promote the removal of methylene blue mainly via ·OHs mediated oxidation (Valdes et al., 2012).

Dealuminated Y zeolite (USY) was initially recognized as an effective catalyst for use with the COP treatment of phenol (Dong et al., 2008). USY facilitates ozone decomposition and ·OHs generation (Dong et al., 2008). The Y zeolites possessing a large specific surface area can effectively disperse metal oxides (Vu et al., 2018). While the utilization of Y zeolites for the treatment of volatile organic compounds in gases has been well-documented, little attention has been given to the COP treatment of ROCs in water (Kwong et al., 2008; Einaga et al., 2011). The USY zeolite is produced by the application of an ammonium ion exchange and dealumination by NaY (Sato et al., 1999; Santikunaporn et al., 2004). NaY and USY are differentiated by its textures, structures, and the molar ratio of Si to Al. These differences influence catalytic performance (Sato et al., 2001). To further improve catalytic performance, the surface loading of metallic oxides (Jeirani and Soltan, 2017) such as manganese (Mn) is widely used (Sui et al., 2011; Sun et al., 2014).

In the present study, loadings of Mn oxides on NaY and USY were studied for the catalytic ozonation efficiencies. In addition, Mn loaded Y zeolites (Mn/NaY, Mn/USY, and Mn-USY) were compared with NaY and USY to understand the catalytic mechanisms of the Mn loaded Y zeolites for the reduction of nitrobenzene in water.

EXPERIMENTAL

Materials

The NaY zeolite was purchased from Nanjing Xianfeng Nanomaterials Technology Co., Ltd., China. Sodium bicarbonate ($NaHCO_3$; 99.5 wt.%), ammonium chloride (NH_4Cl; 99.5 wt.%), manganese nitrate solution ($Mn(NO_3)_2$; 50 wt.%) and potassium hydroxide (KOH; 99.5 wt.%) were all obtained from Beijing Chemical Reagents Co., Ltd., Beijing, China. Methanol (CH_3OH; 99.9 wt.%), p-benzoquinone ($C_6H_4O_2$; 99.5 wt.%) and methylene chloride (CH_2Cl_2; 99.9 wt.%) were purchased from Fisher Scientific. Inc. 5,5-Dimethyl-1-pyrroline (DMPO) was purchased from Sigma-Aldrich. Inc. Ultrapure water (18.2 mΩ/cm) was produced by a Direct-Pure UP ultrapure water system (Rephile Shanghai Bioscience Co., Ltd., Shanghai, China).

Preparation of Catalysts

One hundred grams of NaY was washed by 500 mL of ultrapure water three times and then dried prior to use. Forty grams of NaY was exchanged using 1 mol/L NH_4Cl solution in a mass ratio of 1:10 (solid-liquid ratio) at an initial pH value at 3–3.5. After stirring at 90°C for 90 min and filtering, the obtained solid sample was dried at 90°C for 4 h and calcined at 550°C for 4 h. After a repeated operation, the USY catalyst was obtained. Mn/NaY and Mn/USY were prepared according to the incipient wetness impregnation method. Briefly, an aliquot of 1.3 mL of 50 wt.% $Mn(NO_3)_2$ solution was added to 8.0 g water followed by impregnation of 10 g NaY or USY, then dried at 90°C for 4 h and calcined at 550°C for 4 h. Mn-USY was obtained by hydrothermal synthesis. $Mn(NO_3)_2$ and $CO(NH_2)_2$ were blended in a molar ratio of 1:4 in 20 mL deionized water. This mixture was further blended with 10 g of USY and stirred at 80°C for 90 min and then the sample was placed in a crystallization kettle and heated to 100°C for 4 h under slow rotation. Afterwards, the sample was filtered, washed, dried, and calcined at 550°C for 4 h. Mn oxides (MnO_x) were synthesized according to the same procedure, but without USY. The contents of Mn on Mn-based Y zeolites were detected by ICP-AES. 0.1 g of catalyst was dissolved in a mixture of 5 mL HNO_3 and 1 mL HF, and saturated H_3BO_3 solution was added to eliminate the interference of F^-. The three zeolites (Mn/NaY, Mn/USY, and Mn-USY) contained a similar content (3.0 wt.%) of Mn.

Characterization of Catalysts

X-ray powder diffraction (XRD) was recorded on XRD-6000 powder diffraction instrument (Shimadzu, Kyoto, Japan) with a 40.0 kV working voltage and 40.0-mA electric current. Crystallinities of the Y samples were calculated from the eight defined peak areas ($2\ \theta = 15.6, 18.6, 20.3, 23.6, 27.0, 30.7, 31.3$, and 34°) with the NaY standard sample as a reference according to the ASTM standards (D3906-03). The pore structures were determined with an ASAP 2000 accelerated surface area and porosimetry system (Micromeritics, Norcross, GA, USA). An Inductively Coupled Plasma-Atomic Emission Spectrometer (ICP-AES) (Perkin Elmer DV7000, Waltham, MA, USA) was used for determining the actual Mn content in Mn-based Y zeolites. X-ray photoelectron spectroscopy (XPS) results were obtained on a PHI Quantera SXM photoelectron spectrometer (ULVAC-PHI, Chanhassen, MN, USA) using Al Ka radiation ($h\nu = 1486.6$ eV). The binding energy (BE) values were referred to the C1s line at 284.8 eV. Atomic ratios in the XPS sampling region were evaluated by peak area integration. The surface morphology and element compositions were examined on a Quanta 200 F scanning electron microscope (SEM) and a Tecnai G2 F20 transmission electron microscope (TEM) (FEI, Hillsboro, OR, USA) with an energy-dispersive X-ray (EDX) spectroscope (FEI, Hillsboro, OR, USA). H_2-temperature-programmed reduction (H_2-TPR) was performed on an AutoChem II 2920 (Micromeritics, USA) with 10 vol.% H_2 in Ar. A Magna-IR 560 ESP FT-IR spectrometer (Nicolet, Madison, WI, USA) was used for identifying the functional groups on the surface. The diffuse reflectance spectra were recorded on a U-4100 UV-Vis spectrophotometer (Hitachi, Japan) with an integrated sphere diffuse reflectance attachment. The powder samples were loaded in a transparent quartz cell and UV-Vis absorbance values were measured in the region of 200–800 nm at room temperature. The reflectance of the standard support was used as the baseline for the relative catalyst measurement.

Ozonation of Refractory Organic Chemicals

Nitrobenzene is one of typical ROCs in chemically contaminated wastewaters. In the present study, nitrobenzene at a concentration of 100 $mg{\cdot}L^{-1}$ in ultrapure water was used to determine catalytic activity. The initial total organic carbon (TOC) and pH value of nitrobenzene solution were 55 $mg{\cdot}L^{-1}$ and 5.89, respectively.

The COP experiments were performed with a system (**Figure S1**) that consists of a 40 L of oxygen tank (Beijing Jinggao Gas Co., Ltd., Beijing, China), a COM-AD-02 ozone generator (Anseros Asvanced Oxidation Technologies Co., Ltd., Tübingen-Hirschau, Germany), two GM-6000-OEM ozone gas analyzers (Anseros Asvanced Oxidation Technologies Co., Ltd., Tübingen-Hirschau, Germany), a D07-7 mass flow controller coupled with a D08-1F flow readout box (Beijing Sevenstar Flow Co., Ltd., Beijing, China), a 800 mL quartz column reactor and an exhaust gas collector. The reactor was placed on a ZNCL-BS intelligent magnetic stirrer (Shanghai Kankun Instrument Equipment Co., Ltd., Shanghai, China) at 700 $rpm{\cdot}min^{-1}$ to promote mass transfer among nitrobenzene, ozone and catalysts. During COP experiments, an aliquot of 500 mL of nitrobenzene solution and 0.5 g of catalyst was added in the reactor at 25°C. The gaseous ozone was then introduced through a porous diffuser at the bottom of the reactor having a flow rate of 7.5 $mg{\cdot}min^{-1}$. After treatment, nitrogen gas was sparged into the nitrobenzene solution at a rate of 3.0 $L{\cdot}min^{-1}$ to quench the reaction. Fifteen milliliter of treated solution was extracted into a 40 mL of syringe when sampling. The solution in the syringe was then filtered through a 0.45 μm end filter (Tianjin Jinteng Experimental Equipment Co., Ltd., Tianjin, China) to remove catalyst particles before further analysis. The filtered catalyst was dried and recycled for repetitive experiments. The lost amount of the catalyst was supplemented to 0.5 g by addition of the fresh catalyst ($\sim$ 5% in average) prior to the next use. After reaction, the concentration of Mn ion in solution was detected by ICP-AES at 259.37 nm for the quantification of Mn. Single adsorption process and single ozonation process (SOP) experiments were performed with the same experimental system as COP. Controls did not have ozone or a catalyst. All adsorption, SOP, and COP experiments were performed in triplicate.

The radicals quenching experiments were performed for identification of the oxidation mechanism. The ·OHs scavenger $NaHCO_3$ (0.5 and 1.0 $g{\cdot}L^{-1}$), methanol (5 $mg{\cdot}L^{-1}$) and the $O_2^{\cdot-}$ scavenger p-benzoquinone (5 $mg{\cdot}L^{-1}$) were added into nitrobenzene solution prior to experiments.

Electron spin resonance (ESR) experiments were performed on a Bruker ElexSys E500 spectrometer to directly identify radical species. The test was performed under −183°C (90 K), the operating conditions were centerfield: 3,520 G; sweep width: 200 G; microwave frequency: 9.057 GHz; modulation frequency: 100 GHz; power: 10.00 mW. For radical analysis, 5,5-dimethyl-1-pyrroline (DMPO) was employed as the spin-trapping agents. DMPO was used for capture ·OHs alone, and DMPO with methyl alcohol was used for capture $O_2^{\cdot-}$.

Nitrobenzene and degradation intermediates were identified by a Gas Chromatograph-Mass Spectrometer (GC-MS, 7890 B/MS, Agilent Technologies), a High Performance Liquid Chromatograph (HPLC, Ultimate 3,000, Thermo Scientific) and an Ion Chromatograph (IC, Dionex IC2100, Thermo Scientific). When GC-MS was used for analysis, CH_2Cl_2 was the extraction solvent. A DB-35 capillary column (30 m × 0.25 mm × 0.25 μm) was used. The initial temperature was 30°C, held for 2 min, increased to 45°C at a rate of 10°C/min and kept for 5 min. It was then heated up to 150°C at a rate of 2°C/min, and kept at 150°C for 5 min, then heated up to 225°C at 2°C/min, and kept at 225°C for 5 min. HPLC was equipped with a Hypersil ODS-C18 column (150 × 4.6 mm × 5 μm), and using a mixture of methanol and ultra-pure water (volume ratio was 4:6) as the mobile phase. The flow rate was 0.8 mL/min. The temperature was maintained at 35°C. The concentration of nitrobenzene and intermediates were detected at 254 and 280 nm, respectively (Zhang and Ma, 2008). Ion chromatographic separation of small organic acids was accomplished on an AG11-HC column (4 × 250 mm). The mobile phase was KOH solution (30 mmol/L). The injection volume was 25 μL. The flow rate was 1.0 mL/min.

RESULTS AND DISCUSSION

Characteristics of Catalysts

The XRD peak patterns for both the Y zeolites and Mn-based Y zeolites (**Figure 1A**) were similar, and have the typical characteristic peaks associated with the FAU type Y zeolite (Li R. et al., 2018). The relative crystallinities were as follows: Mn/NaY (90%), Mn/USY (73%) and Mn-USY (77%), NaY (100%), and USY (81%). Significant crystallinity differences were observed between NaY and USY. Dealumination of the NaY (Si/Al molar ratio at 3.19) results in a partial destruction of the resultant USY (Si/Al, 5.16) skeleton structures, reducing its crystallinity. Introduction of Mn oxides into Y zeolites also results in a slight decrease of relative crystallinity. XRD diffraction peaks from Mn oxides were not observed for the Mn-based Y zeolites, due to surface dispersion, low concentration and/or small size. Negligible but observed changes in the FT-IR spectra of the Y zeolites were noted after loading Mn oxides. A typical peak at about 1,040 cm^{-1} (**Figure 1B**) is attributed to the asymmetrical stretching of Si–O–Si and Al–O–Si bending vibrations in the Y zeolites (Lutz et al., 2010; Asadi et al., 2018). The peak at 451 cm^{-1} is related to the Si–O and/or Al–O vibrational bending of the internal tetrahedral aluminosilicate framework (Zhao et al., 2016; Li et al., 2019). The typical absorption peak at 510 cm^{-1} due to Mn–O stretching (Naidja et al., 2002) was not observed, due to its masking from the stronger signals produced by the Al–O–Si.

According to IUPAC classification, the adsorption-desorption isotherms of NaY and Mn/NaY exhibited a typical micropore structure (**Figure 1C**). The isotherms for USY, Mn/USY, and Mn-USY zeolites suggest mixed micropore-mesopore structures due to the partial dealumination of Y zeolites (Denayer and Baron, 1997). The USY, Mn/USY, and Mn-USY had an additional

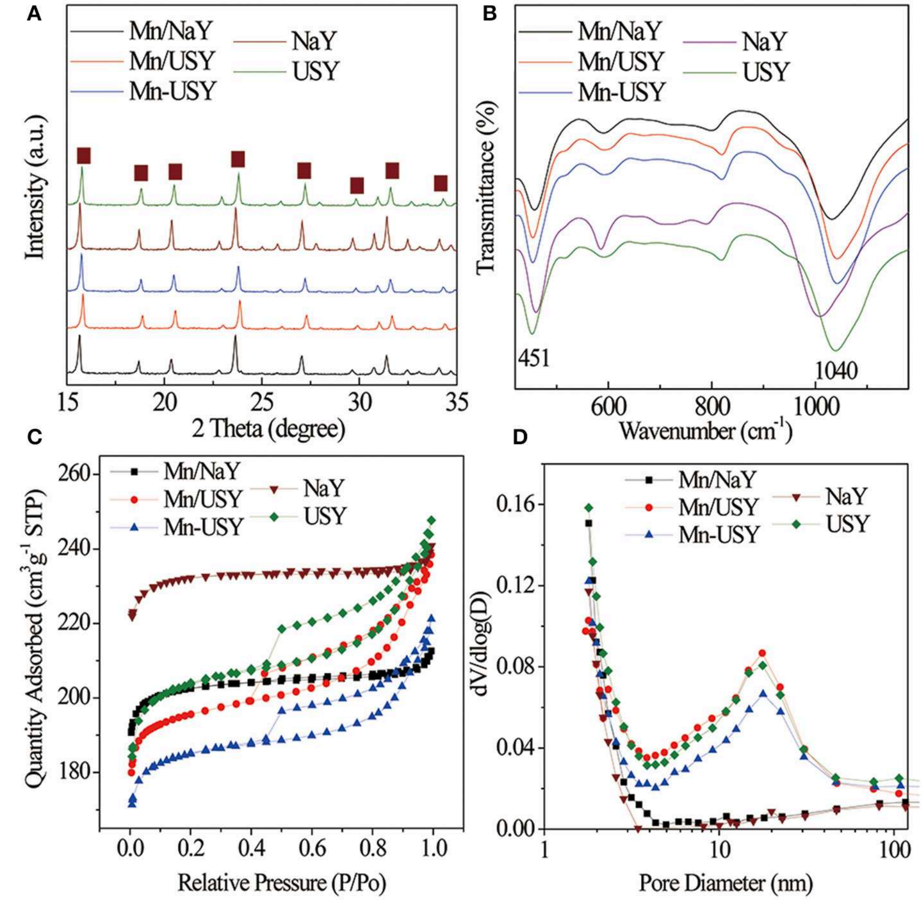

FIGURE 1 | XRD spectra **(A)**, FT-IR **(B)** spectra, adsorption-desorption isotherms **(C)**, and pore distributions **(D)** of Mn-based Y zeolites.

peak at 20 nm in pore distribution in comparison with NaY and Mn/NaY (**Figure 1D**). High mesopore areas and pore volumes were observed in USY zeolites relative to NaY zeolites (**Table 1**). The surface area and pore volume of Y zeolites decrease after loading the Mn oxides because the formed Mn oxides occupy the surface and block the micropores of the Y zeolites (Yang et al., 2019). The differences in surface area and pore volume for the Mn/USY (624 m^2/g and 0.37 cm^3/g) and Mn-USY (588 m^2/g and 0.34 cm^3/g) are related to the Mn oxides morphology as surface dispersion.

Cubic particles about 400–600 nm were observed on the Y zeolites surface (**Figure 2** and **Figure S2**), which are typical for FAU types of zeolite (Zhang et al., 2019). A microanalysis performed using EDS confirmed the presence of the Mn oxides. Interestingly, the Mn/NaY (**Figure 2A**), Mn/USY (**Figure 2B**), and Mn-USY (**Figure 2C**) varied visually and were dark brown, light brown and blue gray, respectively. The NaY (**Figure S2A**) and USY (**Figure S2B**) were white.

The weighted Mn percentages, defined by EDX were: Mn/NaY (5.05%), Mn/USY (3.11%), and Mn-USY (2.75%). The darker colored Mn/NaY is related to the high surface content of the distributed Mn, and the valency of the oxides. The Mn oxides that were deposited on the surfaces of the Y zeolites formed irregularly shaped micro-agglomerates. The surface Mn oxides were clearly observed according to TEM images of Mn/NaY (**Figure 3a**) and Mn/USY (**Figure 3b**) compared to NaY (**Figure S3A**) and USY (**Figure S3B**). The Mn oxides on the Mn-USY are unclear in the TEM image (**Figure 3c**). The USY catalysts exhibit clear mesoporous surface structures by TEM.

The peaks reduced between 200 and 500°C were observed by H_2-TPR profiles for Mn/NaY, Mn/USY, and Mn-USY (**Figure 4A**). The Mn/NaY display two well-developed peaks at 200–350 and 350–500°C, while the Mn/USY has a broad undefined peak in 200–500°C. The Mn-USY has a weak peak at 200–350°C and a broad peak at 350–500°C. During the process of hydrogen reduction, the Mn oxides are reduced in two steps: MnO_2 or $Mn_2O_3 \rightarrow Mn_3O_4$ and $Mn_3O_4 \rightarrow MnO$ (Li et al., 2013; Wu et al., 2015). The different multivalent states of Mn oxides coexist with the catalysts. Additionally, the relative peak area at 200–350°C was higher than that at 350–500°C for Mn/NaY, while the opposite trend was observed for Mn-USY. The peak areas for Mn/USY fell between the other two catalysts. Mn having higher valency exists in the Mn/NaY. The reduced peak temperature for the Mn/NaY suggests a weaker interaction between the support and Mn oxides.

TABLE 1 | Zeolites pore structures determined by N_2 adsorption-desorption and surface element contents by XPS.

Zeolites	NaY	USY	Mn/NaY	Mn/USY	Mn-USY
Pore structures by N_2 adsorption-desorption (surface area: $m^2 \cdot g^{-1}$; pore volume: $cm^3 \cdot g^{-1}$)					
Total surface areas	739	652	646	624	588
Micropore surface areas	706	585	604	565	538
Mesopore surface areas	33	67	42	59	50
Total pore volumes	0.37	0.38	0.33	0.37	0.34
Micropore volumes	0.34	0.28	0.30	0.27	0.26
Mesopore volumes	0.03	0.10	0.03	0.10	0.08
Surface element contents by XPS					
Mn2p weight %			5.03	2.02	1.81
$Mn^{2+}/Mn^{3+}/Mn^{4+}$			0.20/0.39/0.41	0.33/0.32/0.35	0.43/0.36/0.21

UV-Vis spectra for Mn/NaY, Mn/USY, and Mn-USY were generated between the range of 200–800 nm (**Figure 4B**). The Mn/USY had an absorption at 200–330 (L1) nm and another broad adsorption (L2) between 350 and 650 nm. The absorption profile is associated with a charge transfer (CT) that from $O^{2-} \rightarrow Mn^{2+}$ and $O^{2-} \rightarrow Mn^{4+}$ and Mn^{3+}, respectively (Lamaita et al., 2005; Stamati et al., 2007). The Mn/NaY displayed a weaker L1 and an enhanced L2, while Mn-USY exhibited an enhanced L1 and a weakened L2. This observation suggests a greater Mn^{2+} ratio in Mn-USY than that in Mn/NaY and Mn/USY.

XPS was used to further determine Mn distribution and valency. The XPS spectra for Mn/USY and Mn-USY indicate lower content of Na (binding energy at about 1,070 eV) relative to Mn/NaY. This is likely resulted from the removal of Na^+ during NH_4^+ exchange (initial pH value at 3–3.5) for USY preparation (**Figure 5A**). The weight of Na for the Mn/NaY, Mn/USY, and Mn-USY was 7.36, 0.32, and 0.27%, respectively. A strong elemental Mn peak (binding energy at about 640 eV) was observed in Mn/NaY relative to the Mn/USY and Mn-USY, suggesting high surface distribution of Mn oxides. The Mn2p weight was 5.03% for Mn/NaY, 2.02% for Mn/USY, and 1.81% for Mn-USY. The binding energies of Si2p (**Figure 5B**) and Al2p (**Figure 5C**) were at ∼101–102 and 72–74 eV, attributable to Si^{4+} (Plymale et al., 2015) and Al^{3+} (Hadnadjev et al., 2008), respectively. Broad peaks are associated with Al2p XPS for Mn/USY and Mn-USY. The four-coordinate Al framework is partially transformed to five-coordinate Al and non-framework Al during preparation of USY from NaY (Wang et al., 2014). Mn/NaY have low intensity XPS Si2p peaks compared to Mn/USY and Mn-USY, and identical XPS Al2p observed among the catalysts. The surface molar ratio of Si to Al (Si/Al) was 2.7, 4.3, and 3.6 for Mn/NaY, Mn/USY, and Mn-USY, respectively. The observable peak shifts of XPS Si2p and Al2p are related to slight differences in the chemical coordination environment. The XPS spectra from Mn2p are centered between 640–643 and 650–653 eV, and are from the $Mn2p_{3/2}$ and $Mn2p_{1/2}$ (Zhang et al., 2015; **Figure 5D**). According to $Mn2p_{3/2}$ peaks fitting results, multivalent Mn oxides (Mn^{2+}, Mn^{3+}, and Mn^{4+}) are formed in all the catalysts (Dai et al., 2012). The multivalent Mn in Mn/NaY has the highest Mn^{4+} (0.41) content when compared to Mn/USY (0.35) and Mn-USY (0.21). The multivalent Mn in Mn-USY has the highest Mn^{2+} (0.43) contents relative to Mn/NaY (0.20) and Mn/USY (0.33). Black or brown coloration is observed for the MnO, MnO_2, MnOOH, Mn_2O_3, and $MnO(OH)_2$, a light color is seen with $Mn(OH)_2$ (white). The valence state (**Figure 5**) and visual color difference (**Figure 2**) suggest that more $Mn(OH)_2$ (white) is distributed in the Mn-USY catalyst (**Figure 2C**). The different properties for the catalysts observed are resulted from the differences in support material and the methods used to load Mn oxides.

Catalytic Efficiencies

The adsorption of nitrobenzene in solution quickly reached saturation (4–6%) for all Y zeolites (**Figure 6A**). The Y zeolites exhibited weak adsorption toward nitrobenzene, and slight adsorption capacity differences were observed for the NaY, USY and their Mn-based catalysts. In the previous report using ZSM-5 as catalysts during COP, NaZSM-5 (high Na^+) had weaker adsorption toward nitrobenzene in solution when compared with HZSM-5 (low Na^+) (Chen et al., 2018). These results that were influenced by the Na^+ content were not observed with the Y zeolites. The COPs using NaY, USY, Mn/NaY, Mn/USY, and Mn-USY, degraded 31.0, 32.7, 38.8, 44.2, and 49.9% of the nitrobenzene, respectively, 10 min after treatment. In contrary, the SOP degraded 29.5% of the nitrobenzene (**Figure 6B**). Due to catalytic activity of Mn-based Y zeolites, the nitrobenzene degraded after 10 min by COPs was higher than the total sums of SOP and adsorption. Increased activity related with catalysis was however not observed with NaY and USY. The catalytic efficacy between the COPs and SOP gradually decreased with time. After a 60 min treatment, the COPs and SOP degraded identical amounts of nitrobenzene (92–96%).

As determined by TOC, 25.7% of the nitrobenzene was removed after a 60 min treatment using SOP (**Figure 6C**). Including NaY and USY in the COPs reduced TOC by 27.8 and 28.5% of TOC after 60 min treatment. The NaY and USY promote a small increase in TOC that is attributable to the weak adsorption. Using the Mn/NaY, Mn/USY, and Mn-USY as catalysts during COP increases the TOC removal. After a 60 min of treatment, the TOC was reduced by 35.1, 40.0, and 44.3%, respectively. The greater difference in TOC removals cannot be attributed to adsorption (2–4%) (**Figure S4**) and is therefore a realized catalytic influence. The TOC removed by COPs using Mn-based Y zeolites is consistently greater than SOP. The oxidized nitrobenzene produces oxalic acid intermediates (Zhao et al., 2008b) that are further mineralized during COPs with Mn-based Y zeolites, but not with SOP or when NaY and USY are used.

Within 10 min, the pH values of nitrobenzene solution rapidly decreased after the initiation of SOP or COPs, followed by a slow decrease over the treatment time (**Figure 6D**). Higher pH values were observed with the COPs using Mn-based Y zeolites when

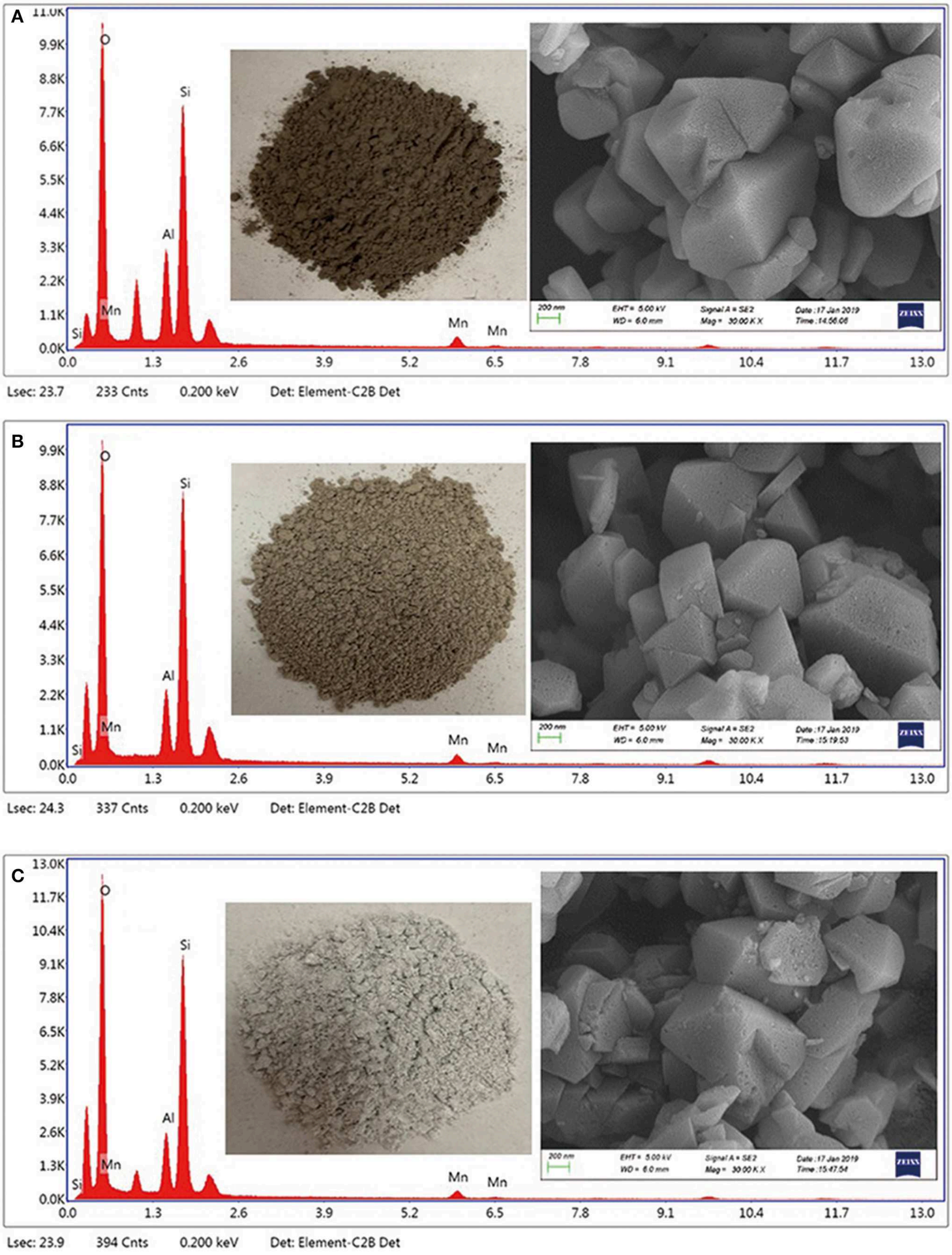

FIGURE 2 | SEM images-EDX spectra of Mn/NaY **(A)**, Mn/USY **(B)**, and Mn-USY **(C)**.

compared with COPs containing NaY or USY, and also compared with SOP. Adsorption has little to no influence on pH values. The COPs and SOP generate acidic intermediates that decrease solution pH values (Zhao et al., 2008a). The Mn-based Y zeolites used during COP further mineralize acidic intermediates, which reduces acidity.

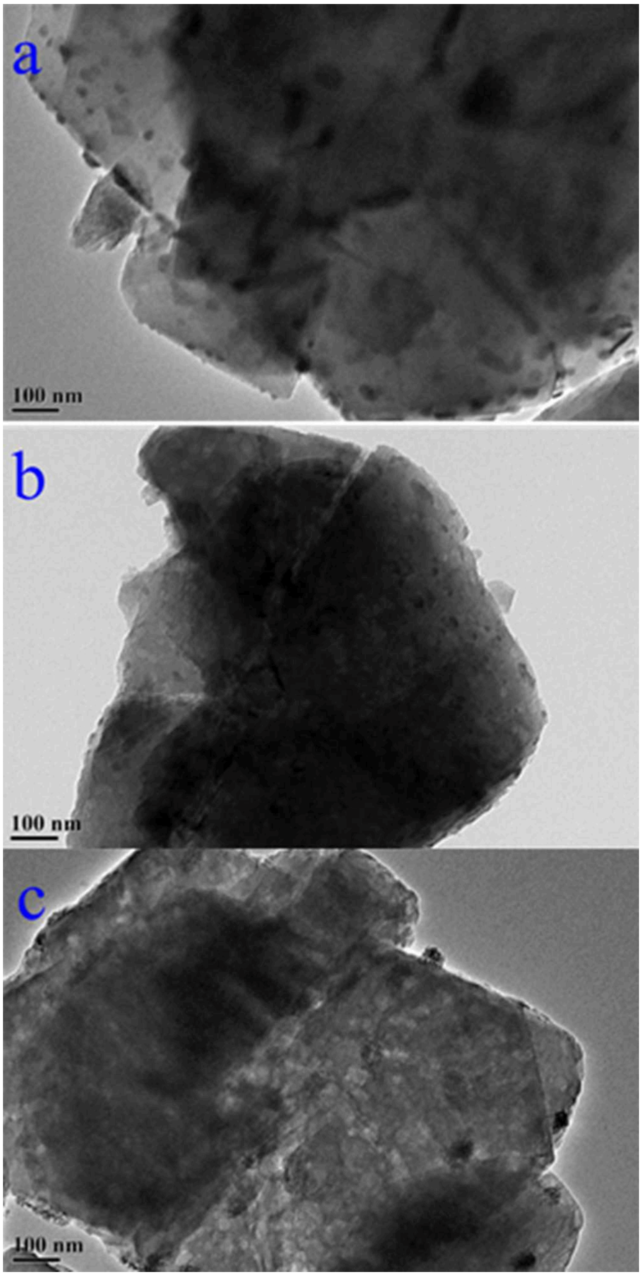

FIGURE 3 | TEM images of Mn/NaY**(a)**, Mn/USY**(b)** and Mn-USY**(c)**.

Catalytic activity with the NaY and USY was not observed. The catalytic activities of 4A and ZSM-5 during COP were previously determined (Chen et al., 2018; Ikhlaq et al., 2018). The types of zeolites and the specific ROCs have an influence on catalytic performances during COPs. The Mn-based Y zeolites are catalytically active, which may be attributed to the multivalent Mn oxides (Mn^{2+}, Mn^{3+}, and Mn^{4+}) (Sun et al., 2014; Huang et al., 2017) or the Mn irons in solution (Gracia et al., 1998; Andreozzi et al., 2001). The leaching of Mn irons from catalysts during ozonation was determined by ICP-AES and the concentrations of Mn irons were 4.25, 3.38, and 1.75 $mg \cdot L^{-1}$ in 60 min of COP with Mn/NaY, Mn/USY and Mn-USY, respectively, after first run. In order to verify the role of Mn ions and Mn oxides in the COP of nitrobenzene, 0.015 g of MnO_x and 11 μL of $Mn(NO_3)_2$ solution were added into the ozonation system, respectively. The TOC removal in ozonation of nitrobenzene with Mn^{2+} was 28.88% (**Figure 6C**), slightly higher than single ozonation (25.67%). When NaY and USY were mixed with solid MnOx, both "MnO_x + NaY" and "MnO_x + USY" showed approximately 32% of TOC removal in ozonation of nitrobenzene (**Figure 6C**), which was slightly lower than the COP with Mn/NaY (33.2%). The experimental results suggest that MnO_x is the main factor promoting catalytic ozonation of nitrobenzene with Mn-based Y zeolites. The Mn/NaY has relatively low catalytic activity when compared with Mn/USY and Mn-USY. The Mn/NaY did not have high activity during COP, although it had a high concentration of surface distributed Mn. Overly concentrated Mn oxides on the surface can result in aggregation decreasing available active sites (Qi et al., 2012; Chen et al., 2017). It has been previously demonstrated that mesoporous supports can improve the interactions between metallic oxides and facilitate the adsorption of ozone during COPs (Zhuang et al., 2014; Ryu et al., 2019). The mesoporous USY facilitates proximal reactions with the Mn oxides and ozone relative to the microporous NaY. Different methods used for the loading the metal oxides can result in different catalytic performances (Bing et al., 2012). This may plausibly explain why the Mn/USY catalyst exhibits lower catalytic activity in comparison with the Mn-USY catalyst. Additionally, a lower oxide state of Mn facilitates ozone decomposition (Ryu et al., 2019). The highest activity observed for Mn-USY may be also attributed to its high ratio of Mn^{2+}.

The leaching of Mn ions (5.83%) from Mn-USY after 60 min reaction was detected by ICP-AES. The reusability of Mn-USY after repeated uses during COP treatment was examined. TOC removal of COP with Mn-USY decreased gradually with the increase of repeated times due to the leaching of Mn from the catalyst. When the number of runs increased from 3 to 4, TOC removals of COP with Mn-USY decreased to <35%, and gradually approaching to the TOC removal in SOP after 5 runs. The results showed Mn-based Y zeolites had a weak-moderate stability in COPs of pollutants, which warrants further investigations to improve the stability of Mn oxides on Y zeolites.

Mechanisms

The introduction of $NaHCO_3$ was performed to conifirm whether the generation of ·OHs promoted the removal of TOC during COP with Mn-USY (Ma and Graham, 2000). Methanol and p-benzoquinone were used to study the roles of the oxygen species in COP with Mn-USY (Khataee et al., 2017; Asgari and Salari, 2019). $NaHCO_3$ (0.5 $g \cdot L^{-1}$) significantly reduced the TOC removal during COP with Mn-USY (**Figure 7A**), which suggests that ·OH mediates oxidation to remove TOC. When a higher concentration of $NaHCO_3$ (1.0 $g \cdot L^{-1}$) was used, changes in TOC removal were not observed, suggesting that the ·OH generated was mostly consumed. The TOC removal with 1.0 $g \cdot L^{-1}$ of $NaHCO_3$ in the COP using the Mn-USY was higher than by SOP. The other active oxygen species (other than ·OHs) coexist during

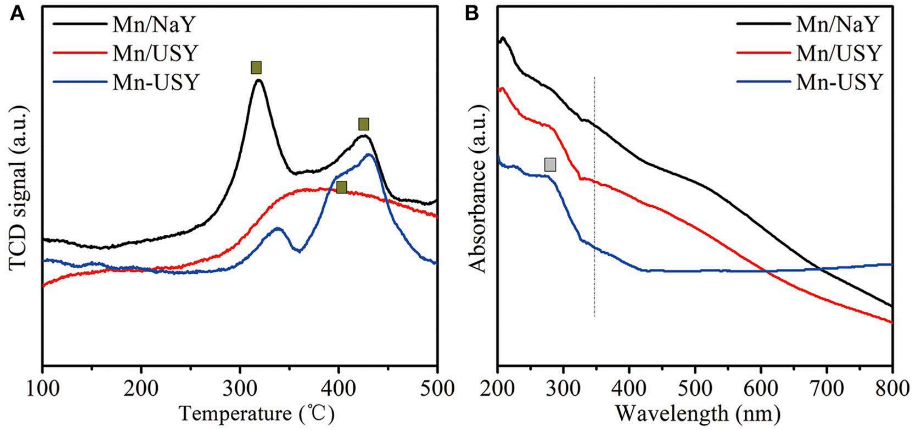

FIGURE 4 | H_2-TPR **(A)** and UV-vis **(B)** spectra of Mn/NaY, Mn/USY, and Mn-USY.

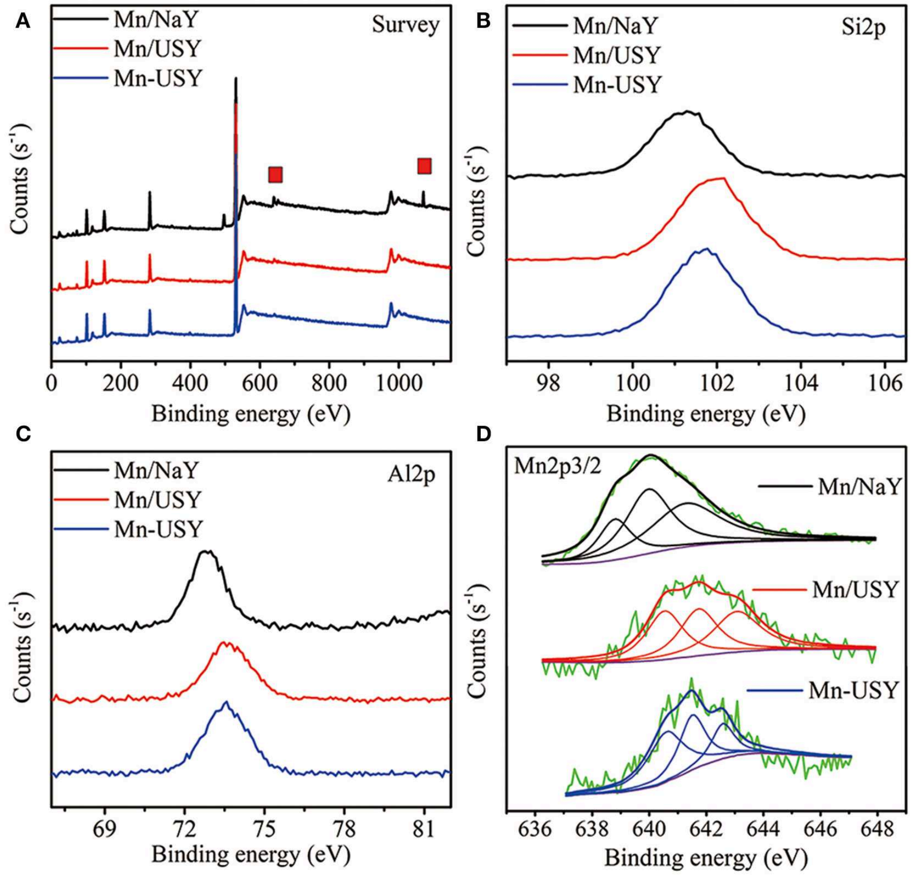

FIGURE 5 | Survey **(A)**, Si2p **(B)**, Al2p **(C)** and Mn2p **(D)** XPS spectra of Mn/NaY, Mn/USY and Mn-USY.

COP. This contributes toward the mineralization of nitrobenzene in solution. The degradation of nitrobenzene significantly decreased to 77.5% upon addition of methanol ($5\,mg{\cdot}L^{-1}$) (**Figure 7B**). After addition of both methanol ($5\,mg{\cdot}L^{-1}$) and p-benzoquinone ($5\,mg{\cdot}L^{-1}$), the degradation of nitrobenzene dropped to 72.4% at 30 min. The experimental results showed that ·OHs and $O_2^{\cdot -}$ promote the degradation of nitrobenzene. ESR was performed to directly detect the radicals and it does prove this. The DMPO-·OH peak (**Figure 7C**) has an intensity ratio of 1:2:2:1 (Fang et al., 2009) and DMPO- $O_2^{\cdot -}$ (**Figure 7D**)

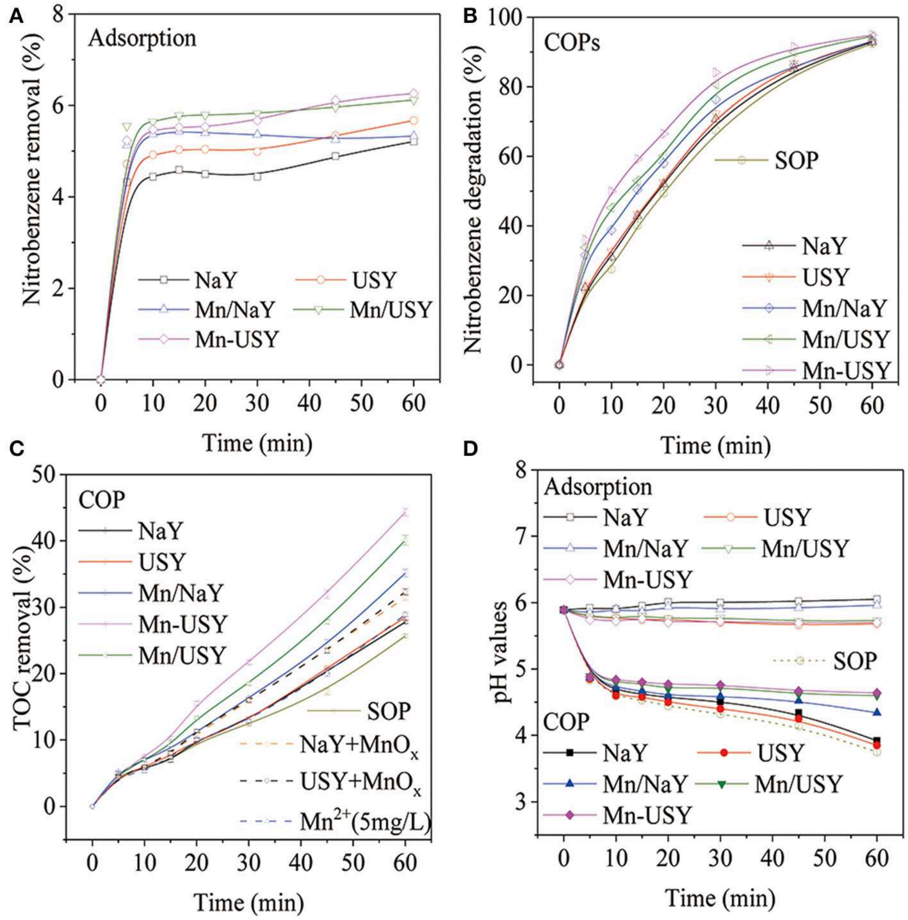

FIGURE 6 | Nitrobenzene removal by adsorption **(A)**, nitrobenzene degradation after COPs **(B)**, TOC removal after COPs **(C)**, and pH changes **(D)** with catalysts (0.5 g catalyst, ozone 7.5 mg·min^{-1}, initial solution pH 5.89, reaction temperature 25°C and 60 min treatment).

is peaked at 1:1:1:1 (Zhao et al., 2018), further confirming the production of ·OH and $O_2^{\cdot -}$ during COP with Mn-USY. The multivalent Mn oxides (Mn^{2+}, Mn^{3+}, and Mn^{4+}) in Mn-USY promotes the generation of ·OHs and $O_2^{\cdot -}$ by the transferring electrons between the metallic oxides and ozone molecules.

Proposed Pathways for Nitrobenzene Degradation

In order to better understand the pathways of nitrobenzene degradation during COP, the intermediates formed during the degradation of nitrobenzene by COP using Mn-USY were determined by GC-MS, HPLC, and IC. **Figure 8** shows that p-nitrophenol, m-nitrophenol, o-nitrophenol, phenol, resorcinol, hydroquinone, catechol, p-benzoquinone, 4-nitrocatechol, 1, 3, 4-trihydroxy-6-nitrobenzene, nitrate, carbonate, oxalic acid, formic acid, acetic acid, succinic acid, maleic acid, and fumaric acid were generated during COP. The production of phenol indicated the occurrence of denitration. The nitro group can be removed from nitrobenzene by a nucleophilic substitution reaction with ozone and $O_2^{\cdot -}$, and the unstable intermediates were then further oxidized to phenol (Wang et al., 2015; Yang et al., 2018). Alternatively, the ·OHs can transfer electron forming phenyl radicals that can be in turn transformed into phenol (Zhao et al., 2008a). The phenolic hydroxyl group belongs to the electron-donating group, ozone molecules and ·OHs tend to react with the ortho- and para-positions of hydroxyl to form catechol and hydroquinone. With further oxidation, p-benzoquinone and 1, 2, 4-trihydroxybenzene are formed prior to ring opening. The accumulation of p-benzoquinone concentration increases to its maximum after 20 min, confirming this.

Moreover, ·OHs could easily react with the α-, β-, or/and γ-carbons of nitrobenzene by electrophilic addition to form o-nitrophenol, m-nitrophenol, and p-nitrophenol, respectively (Bhatkhande et al., 2003). During the COP, the concentration of p-nitrophenol, m-nitrophenol and o-nitrophenol is low, indicating that the electrophilic radicals may continue to attack p-nitrophenol, m-nitrophenol and o-nitrophenol. Similarly, the reaction can occur preferentially in the ortho- and para- positions of phenolic hydroxyl groups (Goi et al., 2004). The ·OHs attack the carbon atoms attached to the nitro group and nitrate ions are released by the radical addition. The ·OHs electrophilic addition occurs continuously to form resorcinol, hydroquinone, catechol, 4-nitrocatechol and 1,3,4-trihydroxy-6-nitrobenzene.

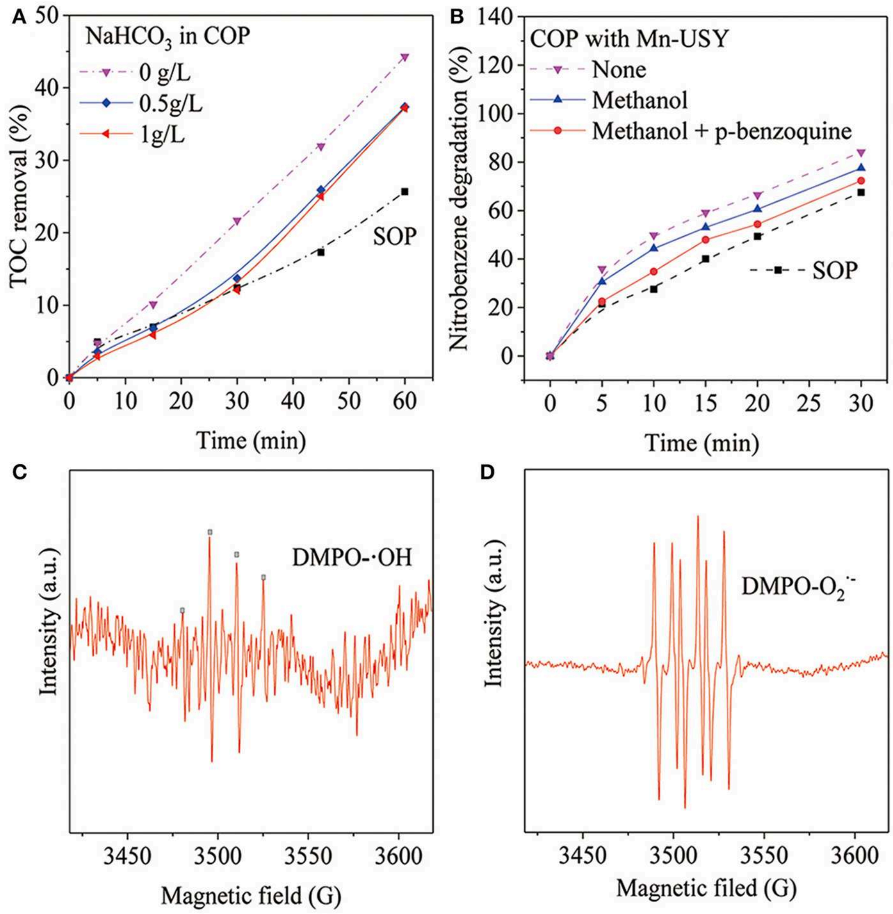

FIGURE 7 | TOC reduction after COP treatment (60 min) using Mn-USY with the addition of NaHCO$_3$ **(A)**, methanol (5 mg·L^{-1}) and p-benzoquinone (5 mg·L^{-1}) **(B)**, liquid-phase ESR spectra of ·OHs **(C)** and O$_2^{\cdot-}$ **(D)** with DMPO spin trapping.

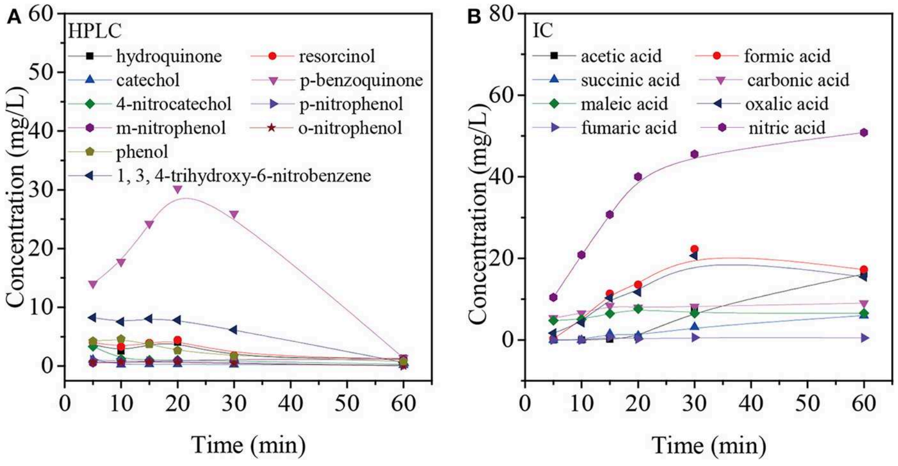

FIGURE 8 | Intermediate products based on HPLC **(A)** and IC **(B)** from the degradation of nitrobenzene using COP with Mn-USY.

The above-mentioned intermediates will further react with ·OHs forming carboxylic acid such as formic acid, acetic acid and oxalic acid. These small molecules are finally mineralized to CO_2 and H_2O. In addition, the accumulation of nitrate indicates that the COP has been accompanied by the reaction of denitration (**Figure 9**).

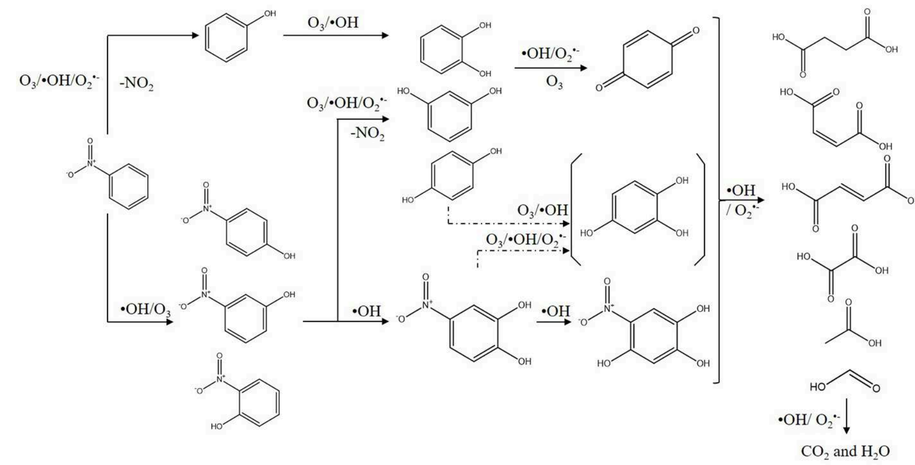

FIGURE 9 | Proposed degradation pathways of nitrobenzene using COP with Mn-USY (All compounds were detected, except the one in the parenthesis).

CONCLUSIONS

The catalysts of Mn-based Y zeolites were investigated for catalytic ozonation efficiencies and mechanisms during the COP treatment of nitrobenzene in water. The multivalent Mn oxides (Mn^{2+}, Mn^{3+}, and Mn^{4+}) are highly dispersed on the surface of NaY or USY, and function as catalytically active sites that increase mineralization. The Mn-USY removed the most TOC during COP which is related to its high surface ratio of Mn^{2+}, and coordinated interaction between the Mn oxides and mesoporous structures. The oxidation is mediated by ·OHs and $O_2^{\cdot -}$, contributing to the TOC removal. These catalytic mechanistic results are broadly applicable to catalyst design for use with the COP treatment of ROCs in water.

DATA AVAILABILITY STATEMENT

The datasets generated for this study are available on request to the corresponding author.

AUTHOR CONTRIBUTIONS

JH and CC conceived and designed the experiments. JH, SN, and YimL performed the experiments. JH, YZ, QW, BY, and SG interpreted and analyzed the data. YifL and SN contributed reagents, materials, analysis tools. BY, QL, CC, and JH. wrote the manuscript.

FUNDING

This study was supported in part by the National Natural Science Foundation of China (No. 21776307) and the Independent Project Program of State Key Laboratory of Petroleum Pollution Control (Grant No. PPCIP2017004), CNPC Research Institute of Safety and Environmental Technology.

SUPPLEMENTARY MATERIAL

The Supplementary Material for this article can be found online at: https://www.frontiersin.org/articles/10.3389/fchem.2020.00080/full#supplementary-material

Figure S1 | Schematic representation of the experimental setup.

Figure S2 | SEM images and EDX spectra of NaY **(a)** and USY **(b)**.

Figure S3 | TEM images of NaY **(a)** and USY **(b)**.

Figure S4 | TOC removal in adsorption process with Y zeolites.

REFERENCES

Andreozzi, R., Caprio, V., Marotta, R., and Tufano, V. (2001). Kinetic modeling of pyruvic acid ozonation in aqueous solutions catalyzed by Mn(II) and Mn(IV) ions. *Water Res.* 35, 109–120. doi: 10.1016/S0043-1354(00)00237-2

Asadi, A. A., Alavi, S. M., Royaee, S. J., and Bazmi, B. (2018). Dependency of acidic and surficial characteristics of steamed Y zeolite on potentially effective synthesis parameters: screening, prioritizing and model development. *Micropor. Mesopor. Mat.* 259, 142–154. doi: 10.1016/j.micromeso.2017.09.028

Asgari, G., and Salari, M. (2019). Optimized synthesis of carbon-doped nano-MgO and its performance study in catalyzed ozonation of humic acid in aqueous solutions: modeling based on response surface methodology. *J. Environ. Manage.* 239, 198–210. doi: 10.1016/j.jenvman.2019.03.055

Bhatkhande, D. S., Pangarkar, V. G., and Beenackers, A. A. C. M. (2003). Photocatalytic degradation of nitrobenzene using titanium dioxide and concentrated solar radiation: chemical effects and scaleup. *Water Res.* 37, 1223–121230. doi: 10.1016/S0043-1354(02)00490-6

Bing, J., Li, L., Lan, B., Liao, G., Zeng, J., Zhang, Q., et al. (2012). Synthesis of cerium-doped MCM-41 for ozonation of p-chlorobenzoic acid in aqueous solution. *Appl Catal B Environ.* 115–6, 16–24. doi: 10.1016/j.apcatb.2011.12.017

Chen, C., Ma, W., Guo, S., Wang, Q., and Li, Q. X. (2017). Mn-Fe-Mg-Ce loaded Al2O3 catalyzed ozonation for mineralization of refractory organic chemicals in petroleum refinery wastewater. *Sep. Purif. Technol.* 183, 1–10. doi: 10.1016/j.seppur.2017.03.054

Chen, C., Yan, X., Xu, Y., Yoza, B. A., Wang, X., Kou, Y., et al. (2019). Activated petroleum waste sludge biochar for efficient catalytic ozonation of refinery wastewater. *Sci. Total Environ.* 651, 2631–2640. doi: 10.1016/j.scitotenv.2018.10.131

Chen, C., Yan, X., Yoza, B. A., Zhou, T., Li, Y., Zhan, Y., et al. (2018). Efficiencies and mechanisms of ZSM-5 zeolites loaded with cerium, iron, or manganese oxides for catalytic ozonation of nitrobenzene in water. *Sci. Total Environ.* 612, 1424–1432. doi: 10.1016/j.scitotenv.2017.09.019

Chen, C., Yoza, B. A., Chen, H., and Li, Q. X. (2015). Manganese sand ore is an economical and effective catalyst for ozonation of organic contaminants in petrochemical wastewater. *Water Air Soil Pollut.* 226:182. doi: 10.1007/s11270-015-2446-y

Dai, Y., Wang, X., Dai, Q., and Li, D. (2012). Effect of Ce and La on the structure and activity of MnOx catalyst in catalytic combustion of chlorobenzene. *Appl. Catal. B Environ.* 111–112, 141–149. doi: 10.1016/j.apcatb.2011.09.028

Dasgupta, A., Matos, J., Muramatsu, H., Ono, Y., Gonzalez, V., Liu, H., et al. (2018). Nanostructured carbon materials for enhanced nitrobenzene adsorption: physical vs. chemical surface properties. *Carbon* 139, 833–844. doi: 10.1016/j.carbon.2018.07.045

Denayer, J., and Baron, G. (1997). Adsorption of normal and branched paraffins in faujasite zeolites NaY, HY, Pt/Nay and USY. *Adsorption* 3, 251–265. doi: 10.1007/BF01653628

Dong, Y., Yang, H., He, K., Wu, X., and Zhang, A. (2008). Catalytic activity and stability of y zeolite for phenol degradation in the presence of ozone. *Appl. Catal. B Environ.* 82, 163–168. doi: 10.1016/j.apcatb.2008.01.023

Einaga, H., Teraoka, Y., and Ogat, A. (2011). Benzene oxidation with ozone over manganese oxide supported on zeolite catalysts. *Catal. Today* 164, 571–574. doi: 10.1016/j.cattod.2010.10.067

El Metwally, A. E., Eshaq, G., Al-Sabagh, A. M., Yehia, F. Z., Philip, C. A., Moussa, N. A., et al. (2019). Insight into heterogeneous fenton-sonophotocatalytic degradation of nitrobenzene using metal oxychlorides. *Sep. Purif. Technol.* 210, 452–462. doi: 10.1016/j.seppur.2018.08.029

Fang, Y., Deng, A., and Huang, Y. (2009). Determination of hydroxyl radical in fenton system. *Chin. Chem. Lett.* 20, 1235–121240. doi: 10.1016/j.cclet.2009.05.004

Goi, A., Trapido, M., and Tuhkanen, T. (2004). A study of toxicity, biodegradability, and some by-products of ozonised nitrophenols. *Adv. Environ. Res.* 8, 303–3311. doi: 10.1016/S1093-0191(02)00102-8

Gracia, R., Aragues, J. L., and Ovelleiro, J. L. (1998). Mn(II)-catalyzed ozonation of raw ebro river water and tis ozonation by products. *Water Res.* 32, 57–62. doi: 10.1016/S0043-1354(97)00188-7

Hadnadjev, M., Vulic, T., and Marinkovic-Neducin, R. (2008). The iron oxidation state in Mg-Al-Fe mixed oxides derived from layered double hydroxides: an XPS study. *Appl. Surf. Sci.* 254, 4297–4302. doi: 10.1016/j.apsusc.2008.01.063

Huang, Y., Sun, Y., Xu, Z., Luo, M., Zhu, C., and Li, L. (2017). Removal of aqueous oxalic acid by heterogeneous catalytic ozonation with MnOx/sewage sludge-derived activated carbon as catalysts. *Sci. Total Environ.* 575, 50–57. doi: 10.1016/j.scitotenv.2016.10.026

Ikhlaq, A., Brown, D. R., and Kasprzyk-Hordern, B. (2013). Mechanisms of catalytic ozonation: an investigation into superoxide ion radical and hydrogen peroxide formation during catalytic ozonation on alumina and zeolites in water. *Appl. Catal. B Environ.* 129, 437–449. doi: 10.1016/j.apcatb.2012.09.038

Ikhlaq, A., Waheed, S., Joya, K. S., and Kazmi, M. (2018). Catalytic ozonation of paracetamol on zeolite a: non-radical mechanism. *Catal. Commun.* 12, 15–20. doi: 10.1016/j.catcom.2018.01.010

Jeirani, Z., and Soltan, J. (2017). Improved formulation of Fe-MCM-41 for catalytic ozonation of aqueous oxalic acid. *Chem. Eng. J.* 307, 756–765. doi: 10.1016/j.cej.2016.08.141

Khataee, A., Rad, T. S., and Fathinia, M. (2017). The role of clinoptilolite nanosheets in catalytic ozonation process: insights into the degradation mechanism, kinetics and the toxicity. *J. Taiwan Inst. Chem. Eng.* 77, 205–2215. doi: 10.1016/j.jtice.2017.05.004

Kwong, C., Chao, C. Y. H., Hui, K. S., and Wan, M. P. (2008). Catalytic ozonation of toluene using zeolite and MCM-41 materials. *Environ. Sci. Technol.* 42, 8504–8509. doi: 10.1021/es801087f

Lamaita, L., Peluso, M. A., Sambeth, J. E., and Thomas, H. J. (2005). Synthesis and characterization of manganese oxides employed in VOCs abatement. *Appl. Catal. B Environ.* 61, 114–119. doi: 10.1016/j.apcatb.2005.03.014

Li, J., Li, L., Wu, F., Zhang, L., and Liu, X. (2013). Dispersion-precipitation synthesis of nanorod Mn3O4 with high reducibility and the catalytic complete oxidation of air pollutants. *Catal. Commun.* 31, 52–56. doi: 10.1016/j.catcom.2012.11.013

Li, R., Chong, S., Altaf, N., Gao, Y., Louis, B., and Wang, Q. (2019). Synthesis of ZSM-5/siliceous zeolite composites for improvement of hydrophobic adsorption of volatile organic compounds. *Front. Chem.* 7:505. doi: 10.3389/fchem.2019.00505

Li, R., Xue, T., Bingre, R., Gao, Y., Louis, B., and Wang, Q. (2018). Microporous zeolite@vertically aligned Mg-Al layered double hydroxide core@shell structures with improved hydrophobicity and toluene adsorption capacity under wet conditions. *ACS Appl. Mater. Interf.* 10, 34834–34839. doi: 10.1021/acsami.8b15118

Li, Y., Wei, G., He, H., Liang, X., Chu, W., Huang, D., et al. (2018). Improvement of zinc substitution in the reactivity of magnetite coupled with aqueous Fe(II) towards nitrobenzene reduction. *Colloid Interface Sci.* 517, 104–112. doi: 10.1016/j.jcis.2018.01.103

Lutz, W., Kurzhals, R., Kryukova, G., Enke, D., Weber, M., and Heidemann, D. (2010). Formation of mesopores in USY zeolites: a case revisited. *Z. Anorg. Allg. Chem.* 636, 1497–1505. doi: 10.1002/zaac.201000025

Ma, J., and Graham, N. J. D. (2000). Degradation of atrazine by manganese-catalysed ozonation—influence of radical scavengers. *Water Res.* 34, 3822–3823828. doi: 10.1016/S0043-1354(00)00130-5

Naidja, A., Liu, C., and Huang, P. M. (2002). Formation of protein-birnessite complex: XRD, FTIR, and AFM analysis. *J. Colloid Interf. Sci.* 251, 46–56. doi: 10.1006/jcis.2002.8349

Nawrocki, J., and Kasprzyk-Hordern, B. (2010). The efficiency and mechanisms of catalytic ozonation. *Appl. Catal. B Environ.* 99, 27–42. doi: 10.1016/j.apcatb.2010.06.033

Plymale, N. T., Kim, Y. G., Soriaga, M. P., and Brunschwig, B. S. (2015). Synthesis, characterization, and reactivity of ethynyl- and propynyl-terminated Si (111) surfaces. *J. Phys. Chem. C* 119, 19847–19862. doi: 10.1021/acs.jpcc.5b05028

Qi, F., Xu, B., Zhao, L., Chen, Z., Zhang, L., Sun, D., et al. (2012). Comparison of the efficiency and mechanism of catalytic ozonation of 2, 4, 6-trichloroanisole by iron and manganese modified bauxite. *Appl. Catal. B Environ.* 121–2, 171–81. doi: 10.1016/j.apcatb.2012.04.003

Rosal, R., Gonzalo, M., Rodríguez, A., Perdigón-Melón, J., and García-Calvo, E. (2010). Catalytic ozonation of atrazine and linuron on MnOx/Al2O3 and MnOx /SBA-15 in a fixed bed reactor. *Chem. Eng. J.* 165, 806–812. doi: 10.1016/j.cej.2010.10.020

Ryu, H. W., Song, Y., Park, J. S., Kim, J. M., Jung, S. C., Song, J., et al. (2019). Removal of toluene using ozone at room temperature over mesoporous Mn/Al2O3 catalysts. *Environ. Res.* 172, 649–657. doi: 10.1016/j.envres.2019.03.016

Santikunaporn, M., Herrera, J. E., Jongpatiwut, S., Resasco, D. E., Alvarez, W. E., and Sughrue, E. L. (2004). Ring opening of decalin and tetralin on HY and Pt/HY zeolite catalysts. *J. Catal.* 228, 100–113. doi: 10.1016/j.jcat.2004.08.030

Sato, K., Iwata, Y., Miki, Y., and Shimada, H. (1999). Hydrocracking of tetralin over NiW/USY zeolite catalysts: for the improvement of heavy-oil upgrading catalysts. *J. Catal.* 186, 45–56. doi: 10.1006/jcat.1999.2546

Sato, K., Nishimura, Y., Honna, K., Matsubayashi, N., and Shimada, H. (2001). Role of HY zeolite mesopores in hydrocracking of heavy oils. *J. Catal.* 200, 288–297. doi: 10.1006/jcat.2001.3184

Stamati, N., Goundani, K., Vakros, J., Bourikas, K., and Kordulis, C. (2007). Influence of composition and preparation method on the activity of MnOx/Al2O3 catalysts for the reduction of benzaldehyde with ethanol. *Appl. Catal. A Gen.* 325, 322–327. doi: 10.1016/j.apcata.2007.02.044

Sui, M., Liu, J., and Li, S. (2011). Mesoporous material supported manganese oxides (MnOx/MCM-41) catalytic ozonation of nitrobenzene in water. *Appl. Catal. B Environ.* 106, 195–203. doi: 10.1016/j.apcatb.2011.05.025

Sun, Q., Li, L., Yan, H., Hong, X., Hui, K. S., and Pan, Z. (2014). Influence of the surface hydroxyl groups of MnOx/SBA-15 on heterogeneous catalytic ozonation of oxalic acid. *Chem. Eng. J.* 242, 348–356. doi: 10.1016/j.cej.2013.12.097

Valdes, H., Tardon, R. F., and Zaror, C. A. (2012). Role of surface hydroxyl groups of acid-treated natural zeolite on the heterogeneous catalytic ozonation of methylene blue contaminated waters. *Chem. Eng. J.* 211–2, 388–95. doi: 10.1016/j.cej.2012.09.069

Vu, H., Harth, F. M., and Wilde, N. (2018). Silylated zeolites with enhanced hydrothermal stability for the aqueous-phase hydrogenation of levulinic acid to gamma-valerolactone. *Front. Chem.* 6:143. doi: 10.3389/fchem.2018.00143

Wang, F., and Ma, Y. (2018). MPC-973: a low-cost and effective adsorbent for the removal of nitrobenzene from aqueous solutions. *Mater. Chem. Phys*. 208, 157–162. doi: 10.1016/j.matchemphys.2018.01.049

Wang, X., Deng, X., Bai, Z., Zhang, X., Feng, X., and Huang, W. (2014). The synthesis of super-hydrophilic and acid-proof Ge-ZSM-5 membranes by simultaneous incorporation of Ge and Al into a silicalite-1 framework. *J. Membr. Sci.* 468, 202–208. doi: 10.1016/j.memsci.2014.06.007

Wang, Y., Cao, H., Chen, C., Xie, Y., Sun, H., Duan, X., et al. (2019). Metal-free catalytic ozonation on surface-engineered graphene: microwave reduction and heteroatom doping. *Chem. Eng. J.* 355, 118–129. doi: 10.1016/j.cej.2018.08.134

Wang, Y., Xie, Y., Sun, H., Xiao, J., Cao, H., and Wang, S. (2015). Hierarchically shape-controlled mixed-valence calcium manganites for catalytic ozonation of aqueous phenolic compounds. *Catal. Sci. Technol.* 6, 2918–2929. doi: 10.1039/C5CY01967B

Wu, G., Gao, Y., Ma, F., Zheng, B., Liu, L., Sun, H., et al. (2015). Catalytic oxidation of benzyl alcohol over manganese oxide supported on MCM-41 zeolite. *Chem. Eng. J.* 271, 14–22. doi: 10.1016/j.cej.2015.01.119

Xu, Y., Wang, Q., Yoza, B. A., Li, Q. X., Kou, Y., Tang, Y., et al. (2019). Catalytic ozonation of recalcitrant organic chemicals in water using vanadium oxides loaded ZSM-5 zeolites. *Front. Chem*. 7:384. doi: 10.3389/fchem.2019.00384

Yan, H., Chen, W., Liao, G., Li, X., Ma, S., and Li, L. (2016). Activity assessment of direct synthesized Fe-SBA-15 for catalytic ozonation of oxalic acid. *Sep. Purif. Technol*. 159, 1–6. doi: 10.1016/j.seppur.2015.12.055

Yang, P., Luo, S., Liu, Y., and Jiao, W. (2018). Degradation of nitrobenzene wastewater in an acidic environment by Ti(IV)/H2O2/O3 in a rotating packed bed. *Environ. Sci. Pollut. Res*. 25, 25060–25070. doi: 10.1007/s11356-018-2551-8

Yang, X., Cheng, X., Elzatahry, A. A., Chen, J., Alghamdi, A., and Deng, Y. (2019). Recyclable fenton-like catalyst based on zeolite Y supported ultrafine, highly-dispersed Fe2O3 nanoparticles for removal of organics under mild conditions. *Chin. Chem. Lett*. 30, 324–330. doi: 10.1016/j.cclet.2018.06.026

Zhang, R., Xu, S., Raja, D., Khusni, N. B., Liu, J., Zhang, J., et al. (2019). On the effect of mesoporosity of FAU Y zeolites in the liquid-phase catalysis. *Micr. Meso. Mater.* 278, 297–306. doi: 10.1016/j.micromeso.2018.12.003

Zhang, T., and Ma, J. (2008). Catalytic ozonation of trace nitrobenzene in water with synthetic goethite. *J. Mol. Catal. A Chem.* 279, 82–89. doi: 10.1016/j.molcata.2007.09.030

Zhang, Z., Liu, B., Wang, F., and Zheng, S. (2015). High-temperature desulfurization of hot coal gas on Mo modified Mn/KIT-1 sorbents. *Chem. Eng. J.* 272, 69–78. doi: 10.1016/j.cej.2015.02.091

Zhao, J., Yin, Y., Li, Y., Chen, W., and Liu, B. (2016). Synthesis and characterization of mesoporous zeolite y by using block copolymers as templates. *Chem. Eng. J.* 284, 405–411. doi: 10.1016/j.cej.2015.08.143

Zhao, J., Zhao, Z., Li, N., Nan, J., Yu, R., and Du, J. (2018). Visible-light-driven photocatalytic degradation of ciprofloxacin by a ternary Mn2O3/Mn3O4/MnO2 valence state heterojunction. *Chem. Eng. J.* 353, 805–8813. doi: 10.1016/j.cej.2018.07.163

Zhao, L., Ma, J., and Sun, Z. (2008a). Oxidation products and pathway of ceramic honeycomb-catalyzed ozonation for the degradation of nitrobenzene in aqueous solution. *Appl. Catal. B Environ*. 79, 244–253. doi: 10.1016/j.apcatb.2007.10.026

Zhao, L., Ma, J., Sun, Z., and Zhai, X. (2008b). Catalytic ozonation for the degradation of nitrobenzene in aqueous solution by ceramic honeycomb-supported manganese. *Appl. Catal. B Environ*. 83, 256–264. doi: 10.1016/j.apcatb.2008.02.009

Zhao, L., Sun, Z., Ma, J., and Liu, H. (2009). Enhancement mechanism of heterogeneous catalytic ozonation by cordierite-supported copper for the degradation of nitrobenzene in aqueous solution. *Environ. Sci. Technol.* 43, 2047–2053. doi: 10.1021/es803125h

Zhuang, H., Han, H., Hou, B., Jia, S., and Zhao, Q. (2014). Heterogeneous catalytic ozonation of biologically pretreated Lurgi coal gasification wastewater using sewage sludge based activated carbon supported manganese and ferric oxides as catalysts. *Biores. Technol*. 166, 178–1186. doi: 10.1016/j.biortech.2014.05.056

Conflict of Interest: The authors declare that the research was conducted in the absence of any commercial or financial relationships that could be construed as a potential conflict of interest.

frontiers in Chemistry

ORIGINAL RESEARCH
published: 24 March 2020
doi: 10.3389/fchem.2020.00177

Synthesis of Spinel Ferrite MFe_2O_4 (M = Co, Cu, Mn, and Zn) for Persulfate Activation to Remove Aqueous Organics: Effects of M-Site Metal and Synthetic Method

Guang Xian[1,2†], Shengyan Kong[1†], Qiangang Li[1], Guangming Zhang[1,3*], Ningyu Zhou[2*], Hongbiao Du[1] and Lijun Niu[1]

[1] School of Environment & Natural Resource, Renmin University of China, Beijing, China, [2] Department of Military Installations, Army Logistics University of PLA, Chongqing, China, [3] School of Energy & Environmental Engineering, Hebei University of Technology, Tianjin, China

OPEN ACCESS

Edited by:
Renato Falcão Dantas,
Campinas State University, Brazil

Reviewed by:
Fernando Fresno,
IMDEA Energy Institute, Spain
Yang Liu,
Dalian University of Technology, China

****Correspondence:***
Guangming Zhang
zgm@ruc.edu.cn
Ningyu Zhou
a86909304@163.com

†These authors have contributed equally to this work and share first authorship

Specialty section:
This article was submitted to Catalysis and Photocatalysis, a section of the journal Frontiers in Chemistry

Received: *30 December 2019*
Accepted: *26 February 2020*
Published: *24 March 2020*

Citation:
Xian G, Kong S, Li Q, Zhang G, Zhou N, Du H and Niu L (2020) Synthesis of Spinel Ferrite MFe_2O_4 (M = Co, Cu, Mn, and Zn) for Persulfate Activation to Remove Aqueous Organics: Effects of M-Site Metal and Synthetic Method. Front. Chem. 8:177. doi: 10.3389/fchem.2020.00177

Metal species and synthetic method determine the characteristics of spinel ferrite MFe_2O_4. Herein, a series of MFe_2O_4 (M = Co, Cu, Mn, Zn) were synthesized to investigate the effect of M-site metal on persulfate activation for the removal of organics from aqueous solution. Results showed that M-site metal of MFe_2O_4 significantly influenced the catalytic persulfate oxidation of organics. The efficiency of the removal of organics using different MFe_2O_4 + persulfate systems followed the order of $CuFe_2O_4 > CoFe_2O_4 > MnFe_2O_4 > ZnFe_2O_4$. Temperature-programmed oxidation and cyclic voltammetry analyses indicated that M-site metal affected the catalyst reducibility, reversibility of M^{2+}/M^{3+} redox couple, and electron transfer, and the strengths of these capacities were consistent with the catalytic performance. Besides, it was found that surface hydroxyl group was not the main factor affecting the reactivity of MFe_2O_4 in persulfate solution. Moreover, synthetic methods (sol–gel, solvothermal, and coprecipitation) for MFe_2O_4 were further compared. Characterization showed that sol–gel induced good purity, porous structure, large surface area, and favorable element chemical states for ferrite. Consequently, the as-synthesized $CuFe_2O_4$ showed better catalytic performance in the removal of organics (96.8% for acid orange 7 and 62.7% for diclofenac) along with good reusability compared with those obtained by solvothermal and coprecipitation routes. This work provides a deeper understanding of spinel ferrite MFe_2O_4 synthesis and persulfate activation.

Keywords: ferrite, M-site metal, synthesis, persulfate, organics

HIGHLIGHTS

- Effects of M-site metal and synthetic method on ferrite were investigated.
- Suitable ferrite and its synthetic method for PS activation were screened out.
- Catalytic PS performance was $CuFe_2O_4 > CoFe_2O_4 > MnFe_2O_4 > ZnFe_2O_4$.
- M-site metal affected MFe_2O_4 reducibility, M^{2+}/M^{3+} reversibility, and electron transfer.
- Sol–gel method was ideal to synthesize ferrite to activate PS for organics removal.

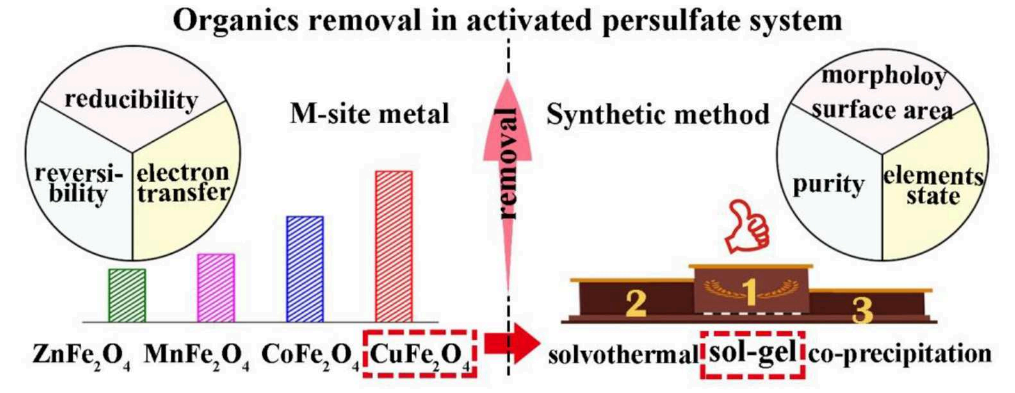

GRAPHICAL ABSTRACT | Effects of M-site metal and synthetic method of spinel ferrite on persulfate activation for organics removal.

INTRODUCTION

Advanced oxidation processes (AOPs) that involve highly reactive radicals are powerful treatment techniques for the removal of organics in water, especially for removing highly toxic, persistent, and nonbiodegradable organics (Wang and Wang, 2018; Malvestiti et al., 2019). Among AOPs, activated persulfate (PS) process has received extensive attention. Compared with hydroxyl radical generated in conventional AOPs (Fenton or Fenton-like), sulfate radical ($SO_4^{\bullet-}$) generated from PS has comparable oxidizing power ($E^0 = 2.5$-3.1 V), higher selectivity (for benzene ring and unsaturated bond), longer half-life (30-40 μs), and greater stability, and is less influenced by natural organic materials (Oh et al., 2016; Alexopoulou et al., 2019). Moreover, PS offers some advantages over other AOP oxidants [e.g., H_2O_2 and peroxymonosulfate (PMS)], such as the ease of storage, high stability, high redox potential, good solubility, and relatively low cost (Xu and Li, 2010; Wacławek et al., 2017). Therefore, activated PS process is expected to be promising for treating organics.

Heterogeneous catalysis is the most studied method for PS activation, not only because of the energy conservation and ease of operation (vs. thermolysis, photolysis, radiolysis, etc.) (Oh et al., 2016; Zhu et al., 2019) but also owing to the mild reaction conditions, retrievability, and little metal dissolution (vs. homogeneous catalysis) (Wang and Wang, 2018). Available and efficient catalytic material is the priority in heterogeneous catalysis. Over the past decades, iron oxides have been generally used as heterogeneous catalysts because of their low price, abundant reserves, and nontoxicity (Li et al., 2017; Silveira et al., 2018). However, their weak catalytic activity limits the efficiency of pollutant removal (Lei et al., 2015). Hitherto, multimetallic iron-based materials can relieve this problem and render catalytic processes more efficient toward long-term application (Deng et al., 2017; Wacławek et al., 2017). With ongoing explorations, a typical bimetallic iron-based oxide, spinel ferrite with the general formula of MFe_2O_4 (M is a divalent 3d transition metal such as Co, Cu, Mn, and Zn), has attracted much attention (Lassoued et al., 2017). The excellent activity and desirable magnetic recovery property render it useful in several applications (Garcia-Muñoz et al., 2020). For example, $CoFe_2O_4$ was effective for activating PMS to degrade atrazine (Li et al., 2018). $CuFe_2O_4$ and $MnFe_2O_4$ could be applied as catalysts of PS for acetaminophen and phenol removal (Stoia et al., 2017; Zhang et al., 2019). Further, in combination with PS, $ZnFe_2O_4$ exhibited good photocatalytic performance in the degradation of Orange II (Cai et al., 2016).

As mentioned, although certain ferrites have been applied to activate PS, the differences in the effectiveness of various ferrites in organics treatment have not been studied well. For example, metal species in a catalyst can critically impact the catalytic performance. Anipsitakis and Dionysiou (2004) reported that Fe^{2+} was the most efficient metal ion to activate H_2O_2, while Co^{2+} was the best for PMS activation and Ag^{+} showed the best results toward PS activation. The metal in M-site of MFe_2O_4 was known to be the main catalytic center for PS activation (Equation 1) (Li et al., 2017). However, the effect of different M-site metals in ferrite on PS activation to remove organics is not yet clear. Moreover, synthetic method is important for catalyst, which usually results in distinction on morphology, particle size, surface property, magnetism, etc., and thereby influences the catalytic performance (Kennaz et al., 2017; Zhang et al., 2018). Gupta and Garg (2017) found that compared with those prepared by coprecipitation and sol–gel methods, CuO/CeO_2 synthesized by solution combustion method led to the maximum oxidation of organics and showed the minimum metal leaching in catalytic H_2O_2 system. Priyanka et al. (2019) found that modified TiO_2 with lower band gap energy synthesized by sol–gel method had better mineralization of gray water in photocatalysis vs. those synthesized by ultrasonication and microwave methods. Ferrite can be also prepared by various methods including sol–gel, solvothermal, coprecipitation, and high-energy milling (Zhang et al., 2018). Hence, it is necessary to explore the effect of synthetic method of ferrite on organics removal in PS system.

$$M(II) + S_2O_8^{2-} \rightarrow M(III) + SO_4^{\bullet-} + SO_4^{2-} \qquad (1)$$

In this work, the differences and causes in the catalytic performance of a series of MFe_2O_4 (M = Co, Cu, Mn, and Zn) were explored. Then, the characteristics and catalytic performances of ferrites synthesized by different methods, i.e., sol–gel, solvothermal, and coprecipitation, for activated PS process were investigated with $CuFe_2O_4$ as the representative. The efficacy of the catalyst was evaluated by applying it in the removal of two model refractory organics, a traditional dye pollutant [acid orange 7 (AO7)] and an emerging pharmaceutical pollutant (diclofenac). The main objectives were to (i) scrutinize the high-efficiency PS activator out and reveal the effect of M-site metal on the reactivity of ferrite and (ii) determine the effect of synthetic method on the performance of ferrite and find an ideal ferrite synthetic method for PS activation in organics treatment. The results can contribute to better understanding of the synthesis and application of ferrite and promote decontamination with activated PS process.

MATERIALS AND METHODS

Materials

All chemicals used were of analytical grade. $Ni(NO_3)_2{\cdot}6H_2O$, $Fe(NO_3)_3{\cdot}9H_2O$, $Zn(NO_3)_2{\cdot}6H_2O$, NaOH, H_2SO_4 (95-98%), HCl (36-38%), $C_2H_6O_2$ (ethylene glycol), and C_2H_5OH (ethanol) were purchased from Beijing Chemical Works, China. $Cu(NO_3)_2{\cdot}3H_2O$ and $Na_2S_2O_8$ were obtained from Tianjin Fuchen Chemical Reagents Factory, China. $Co(NO_3)_2{\cdot}6H_2O$ and diclofenac sodium were purchased from Shanghai Macklin Biochemical Co. Ltd., China. $Mn(NO_3)_2$ (50% solution), $C_6H_8O_7{\cdot}H_2O$ (citric acid), $C_2H_3NaO_2{\cdot}3H_2O$ (NaAc), and Na_2SO_4 were obtained from Sinopharm Chemical Reagent Co. Ltd., China. AO7 was purchased from Tianjin Guangfu Fine Chemical Research Institute, China.

Synthesis of Ferrite

A series of spinel ferrite MFe_2O_4 (M = Co, Cu, Mn, and Zn) were prepared by sol–gel method (Li et al., 2017) to investigate the effect of M-site metal on PS activation. Then, the three most common methods, sol–gel, solvothermal (Ueda Yamaguchi et al., 2016), and coprecipitation (Jaafarzadeh et al., 2017), were used to study the effect of synthetic method on the properties of ferrite obtained for PS activation, with $CuFe_2O_4$ as a representative. $CuFe_2O_4$ synthesized by sol–gel, solvothermal, and coprecipitation methods were denoted as $CuFe_2O_4$-SG, $CuFe_2O_4$-ST, and $CuFe_2O_4$-CP, respectively. The detailed synthetic procedures were described in the **Supplementary Information**.

Characterization of Ferrite

X-ray powder diffraction (XRD) of ferrite was carried out on a Rigaku D/max-rc diffractometer using Cu K_α radiation. The morphology of ferrite was observed on a Hitachi S 4700 scanning electron microscope (SEM). N_2 adsorption–desorption analysis was performed on a QuadraSorb Station 4 instrument. X-ray photoelectron spectra (XPS) were measured on a Thermo Fisher Scientific EscaLab 250Xi system with a monochromatic Al K_α source.

Catalytic PS Oxidation Experiment

The typical experimental steps were as follows: known amounts of ferrite and PS solution were added simultaneously into a 20 mg/L organics solution (AO7 or diclofenac) under magnetic stirring. At known intervals, 3 ml solution was taken using a syringe and filtered through a 0.22 µm filter head. The concentration of the organics in the filtrate was analyzed to evaluate the efficacy of ferrite. The used ferrite was collected using a magnet, washed several times with ethanol and deionized water, and dried for the next run to investigate its reusability. The experiments were done in triplicate.

Analytical Methods

The concentration of AO7 was determined by TU-1900 UV-visible spectrophotometer (Beijing Persee General Instrument Co., Ltd.) at a maximum absorbance wavelength of 484 nm. The concentration of diclofenac was determined by Ultimate 3000 high performance liquid chromatography (Thermo Fisher Scientific Inc.). The UV detection wavelength was 275 nm, and the mobile phase consisted of acetonitrile and 0.2% acetic acid solution at a volume ratio of 7:3.

The redox property of ferrite was evaluated by oxygen temperature-programmed oxidation (O_2-TPO) and cyclic voltammetry (CV). O_2-TPO was performed from 200 to 500°C at a rate of 10°C/min on a ChemBET Pulsar TPR/TPD instrument (Quantachrome Instruments Inc.) equipped with a thermal conductivity detector (TCD) to measure the change of gas composition. A 5% O_2/He (vol.) gas mixture with a flow rate of 100 ml/min was used in the analysis. CV was conducted on a CHI 760E electrochemical workstation (Shanghai Chenhua instrument Co. Ltd.) with a foamed nickel working electrode, a platinum sheet counter electrode, and a saturated Ag/AgCl reference electrode. Before use, the foamed nickel electrode was dipped in the suspension of ferrite for 10 min to load the catalyst and then air-dried. A mixture of 0.1 mol/L Na_2SO_4 and 0.4 mmol/L PS was used as the electrolyte.

The surface hydroxyl group of ferrite was quantified by the saturated deprotonation method (Ren et al., 2015). In this method, 20 ml of a 0.05 mol/L NaOH solution dispersed with 0.12 g of ferrite was shaken for more than 4 h at 25°C. After separating the solid by filtration, the solution was titrated with a diluted HCl solution.

RESULTS AND DISCUSSION

Catalytic Performance of Ferrites With Different M-Site Metals

To investigate the effect of M-site metal on the catalytic performance of spinel ferrite, a series of MFe_2O_4 (M = Co, Cu, Mn, and Zn) were synthesized by sol–gel method. XRD patterns presented in **Supplementary Figure 1** confirmed the successful synthesis of the ferrite samples.

Figure 1 clearly shows that the removal efficiencies of organics in different MFe_2O_4 + PS systems were different, but all were higher than that of PS oxidation and MFe_2O_4 adsorption (**Supplementary Figure 2**). For both AO7 and diclofenac removal (**Figures 1A,C**), the catalytic performance of

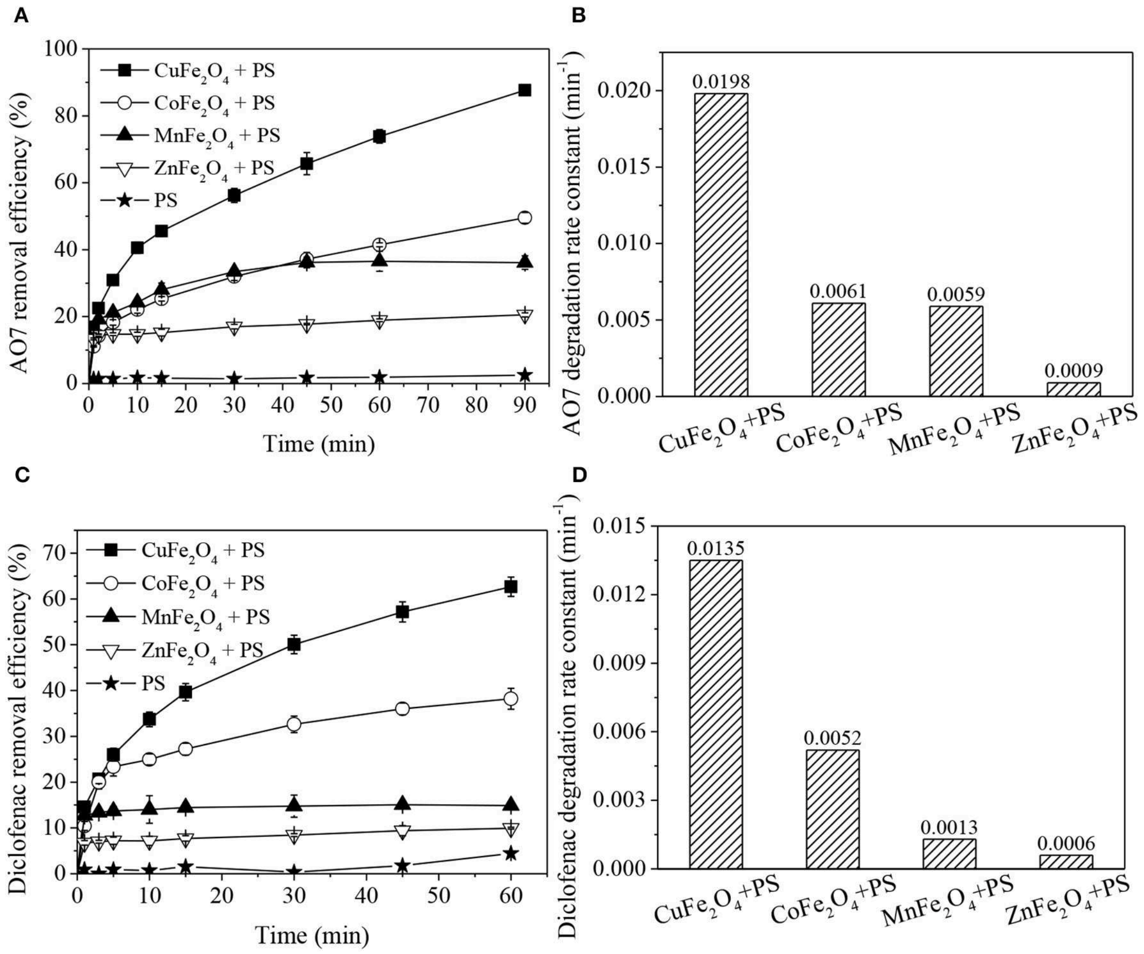

FIGURE 1 | Organics removal and degradation rate constants in PS systems activated by ferrites with different M-site metals: **(A,B)** AO7 removal; **(C,D)** diclofenac removal. Conditions: [organics] = 20 mg/L, **(A,B)** catalyst dosage = 0.2 g/L, [PS] = 0.8 g/L, unadjusted pH = 6.5; **(C,D)** catalyst dosage = 0.6 g/L, [PS] = 0.1 g/L, pH = 5.

ferrite ranked as follows: $CuFe_2O_4$ > $CoFe_2O_4$ > $MnFe_2O_4$ > $ZnFe_2O_4$. The organics removal processes involved two stages: rapid adsorption-dominated stage (0-1 min) and catalytic degradation stage (> 1 min), which could be fitted by pseudo-first order reaction. The degradation rate constant (**Figures 1B,D**) was also significantly affected by M-site metal, and the trend was basically consistent with the aforementioned catalytic performance order of MFe_2O_4. In detail, $CuFe_2O_4$ presented the best and fastest catalytic performance in organics removal. Almost 87.6% AO7 was removed in PS solution coupled with $CuFe_2O_4$. In comparison, Yue et al. (2016) found that only 53.5% AO7 removal was obtained in Fe_3O_4 + PS system. Moreover, the diclofenac degradation rate constant of $CuFe_2O_4$ + PS system was about 3.5 times of that of thermally activated PS system at 60°C (Chen et al., 2016). The high removal of AO7 and diclofenac (which have different molecular structures: AO7 is an azo dye and diclofenac is a secondary aromatic amine drug) indicated that $CuFe_2O_4$ + PS could effectively remove multiple organic pollutants.

These results demonstrated that M-site metal indeed affected the catalytic performance of ferrite. Among the ferrites, $CuFe_2O_4$ was found to be the best activator of PS for organics removal.

Redox Properties of Ferrites With Different M-Site Metals

According to above degradation experiments, it has been identified that ferrites with different M-site metals exhibit different catalytic performances. As is known, for PS activation by transition metal, the basic mechanism is chemical reduction of PS through electron transfer (Wacławek et al., 2017). Thus, the reducibility of catalyst is probably the vital factor affecting the effectiveness of PS activation system (Wang and Wang, 2018). Therefore, O_2-TPO and CV were carried out to investigate the redox properties of ferrites with different M-site metals.

Figure 2 shows the O_2-TPO profiles of various MFe_2O_4. The temperature of O_2 consumption surge is an important parameter for evaluating the ease of oxidation-state change of M-site metal ion. As shown, the four ferrites exhibited distinct peaks with temperature increasing from 200 to 500°C, implying the oxidation reaction occurrence of M^{n+} to $M^{(n+1)+}$. The peak temperatures of $CuFe_2O_4$, $CoFe_2O_4$, $MnFe_2O_4$, and $ZnFe_2O_4$ gradually increased, at 330.8, 353.8, 384.6, and 401.9°C, respectively, which were similar to some other studies. For example, Wang et al. (2011) found that the initial oxidation of $CoFe_2O_4$ occurred at 350°C resulting from the oxidation of Co. Cihlar et al. (2017) reported that Mn^{2+} in binary oxide was mostly oxidized in the 350–500°C region. The lower oxidation temperature of MFe_2O_4, that was, the easier transition of the oxidation state of M-site metal ion accounted for its better performance in the activation of PS (Su et al., 2017).

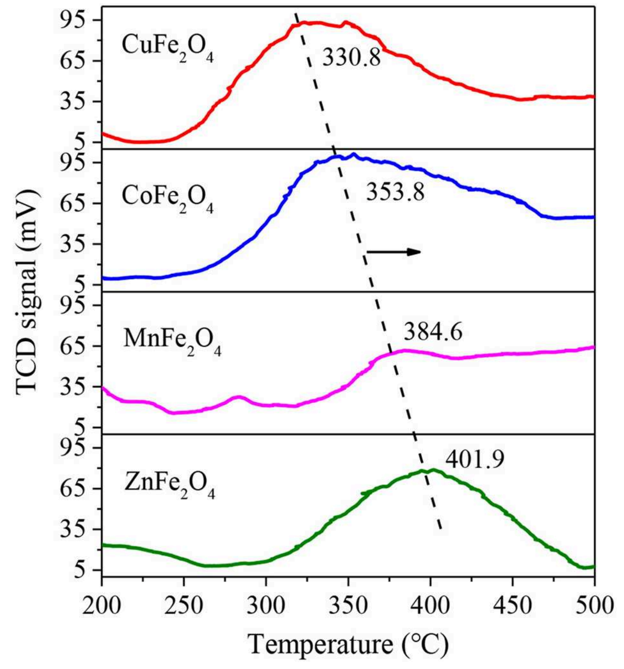

FIGURE 2 | O_2-TPO profiles of ferrites with different M-site metals.

To further reveal the redox properties of ferrites, CV curves of different MFe_2O_4 on electrodes were recorded (**Figure 3**). Except for the couple of redox peaks, the curves of all samples were identical in shape to the control curve, indicating that there was no interference of impossible peak in the solution. $CuFe_2O_4$ electrode exhibited a well-defined oxidation peak at 0.268 V, which was attributed to the Cu(II)/Cu(III) redox cycle. Likewise, the peaks at 0.350 and 0.401 V were assigned to the oxidation of Co(II) and Mn(II), respectively. $ZnFe_2O_4$ electrode gave an indistinct oxidation peak at 0.410 V. The lower potential of oxidation peak meant that it was easier for the catalyst to donate electrons, which was favorable for PS activation (Duan et al., 2018). Thus, the reducibility of the ferrites could be ranked as $CuFe_2O_4 > CoFe_2O_4 > MnFe_2O_4 > ZnFe_2O_4$. Moreover, there was no certain rule about the reduction peak positions of MFe_2O_4 electrodes. However, interestingly, for these ferrite electrodes, the trend of potential separation of redox peaks (ΔE_p)

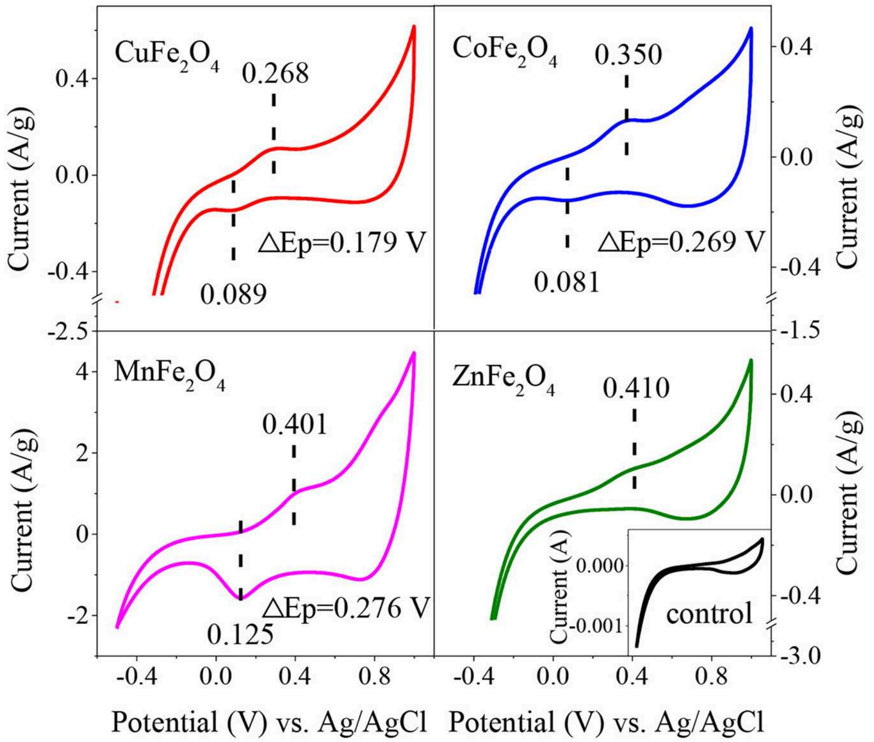

FIGURE 3 | Cyclic voltammograms obtained on electrodes of ferrites with different M-site metals after 4th cycle. Scan rate = 50 mV/s, Scan range = −0.5-1 V.

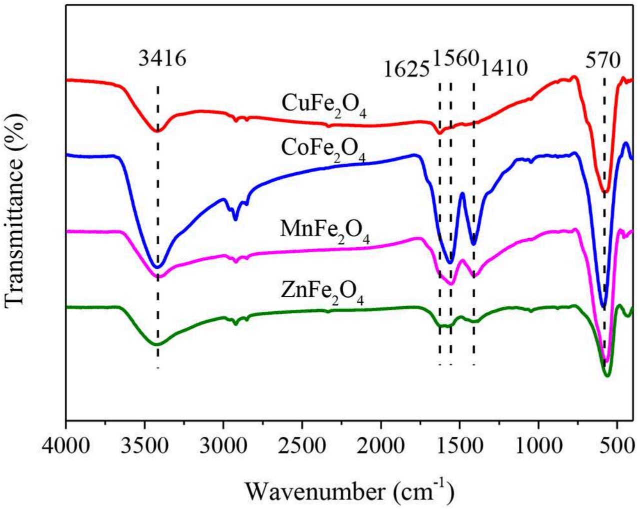

FIGURE 4 | FTIR spectra of ferrites with different M-site metals.

TABLE 1 | Surface hydroxyl quantities of ferrites with different M-site metals.

Ferrite	Surface hydroxyl quantity (mmol/g)
$CuFe_2O_4$	0.75
$CoFe_2O_4$	3.13
$MnFe_2O_4$	2.58
$ZnFe_2O_4$	1.17

was similar to the trend of oxidation peak potential. $CuFe_2O_4$ electrode displayed the lowest ΔE_p of 0.179 V. Meanwhile, the ΔE_p values of $CoFe_2O_4$ and $MnFe_2O_4$ electrodes were higher at 0.269 and 0.276 V, respectively. In the case of $ZnFe_2O_4$, it might need much more negative potential than that in the CV curve to make it accept electrons to generate reduction peak. The lower ΔE_p of an electrode indicated the stronger reversibility and more electron transfer of M^{2+}/M^{3+} redox reaction (Bard et al., 1980), which were good for the catalytic reaction.

Therefore, from the above results, it can be concluded that M-site metal would affect the catalytic performance of MFe_2O_4 by affecting the reducibility, reversibility of M^{2+}/M^{3+} redox couple, and electron transfer on the catalyst surface.

Surface Oxygen Functional Groups of Ferrites With Different M-Site Metals

The surface oxygen functional groups of a catalyst might participate in the activation of PS, and thereby affect the catalytic performance of the catalyst (Xiao et al., 2018). Therefore, ferrites with different M-site metals were characterized by FTIR spectra (**Figure 4**). The broad bands at about 3,416 cm^{-1} of all samples indicated the obvious presence of hydroxyl group (-OH) (Zhang et al., 2019). The peak at 1,625 cm^{-1} was due to the deformation vibration of water molecules in the interlayer (Parvas et al., 2014). The two adsorption bands at 1,560 and 1,410 cm^{-1} (COO-stretching) implied the residual of some citrates in the pores of ferrite. The peak at around 570 cm^{-1} was associated with the metal–oxygen bond (Zhao et al., 2018).

Among the observed functional groups, -OH should be of particular concern. It was reported that phenol removal was related to the surface hydroxyl concentration of TiO_2 during catalytic ozonation (Song et al., 2010). Hydroxyl group on $CuFe_2O_4$ surface was found to be critical for radical generation in PMS activation (Guan et al., 2013). Therefore, surface -OH quantities of ferrites with different M-site metals were measured. As shown in **Table 1**, different M-site metals led to different -OH quantities. Unexpectedly, ferrite with good catalytic performance (e.g., $CuFe_2O_4$) did not have many surface -OH. This phenomenon was different from the finding of Ren et al. (2015) that MFe_2O_4 containing more surface -OH showed better catalytic performance for PMS. Ren et al. proposed that surface -OH was the main binding site for PMS (surface -OH of ferrite formed hydrogen bond with side -O-OH of PMS), and then PMS accepted electron from metal ion and its O-OH bond was broken to generate $SO_4^{\bullet-}$. The results of this study showed that surface -OH was not crucial for the catalytic performance of MFe_2O_4 in PS system. The reason might be that PS activation involved a different process; $SO_4^{\bullet-}$ in MFe_2O_4 + PS system was mainly generated from the fission of middle O-O bond of PS (Wang and Wang, 2018).

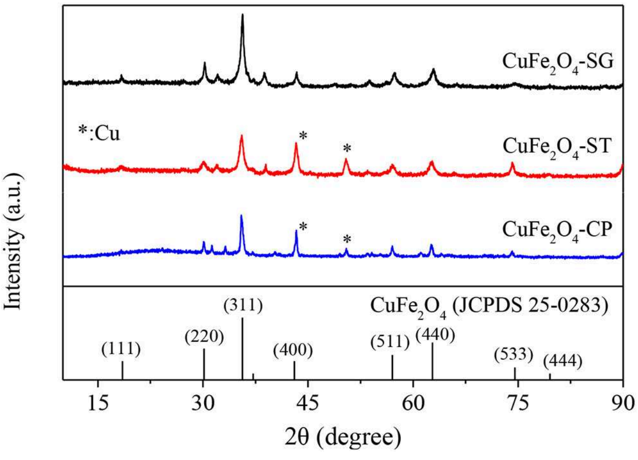

FIGURE 5 | XRD patterns of $CuFe_2O_4$ synthesized by different methods.

Characterization of $CuFe_2O_4$ Synthesized by Different Methods

According to the above results, $CuFe_2O_4$ was selected as the representative ferrite to further explore the effect of synthetic method on the physicochemical property and catalytic performance of ferrite for PS activation.

XRD Analysis

The XRD patterns of $CuFe_2O_4$ synthesized by sol–gel, solvothermal, and coprecipitation methods ($CuFe_2O_4$-SG, $CuFe_2O_4$-ST, and $CuFe_2O_4$-CP) were shown in **Figure 5**. The major crystal phase of the samples was in agreement with typical

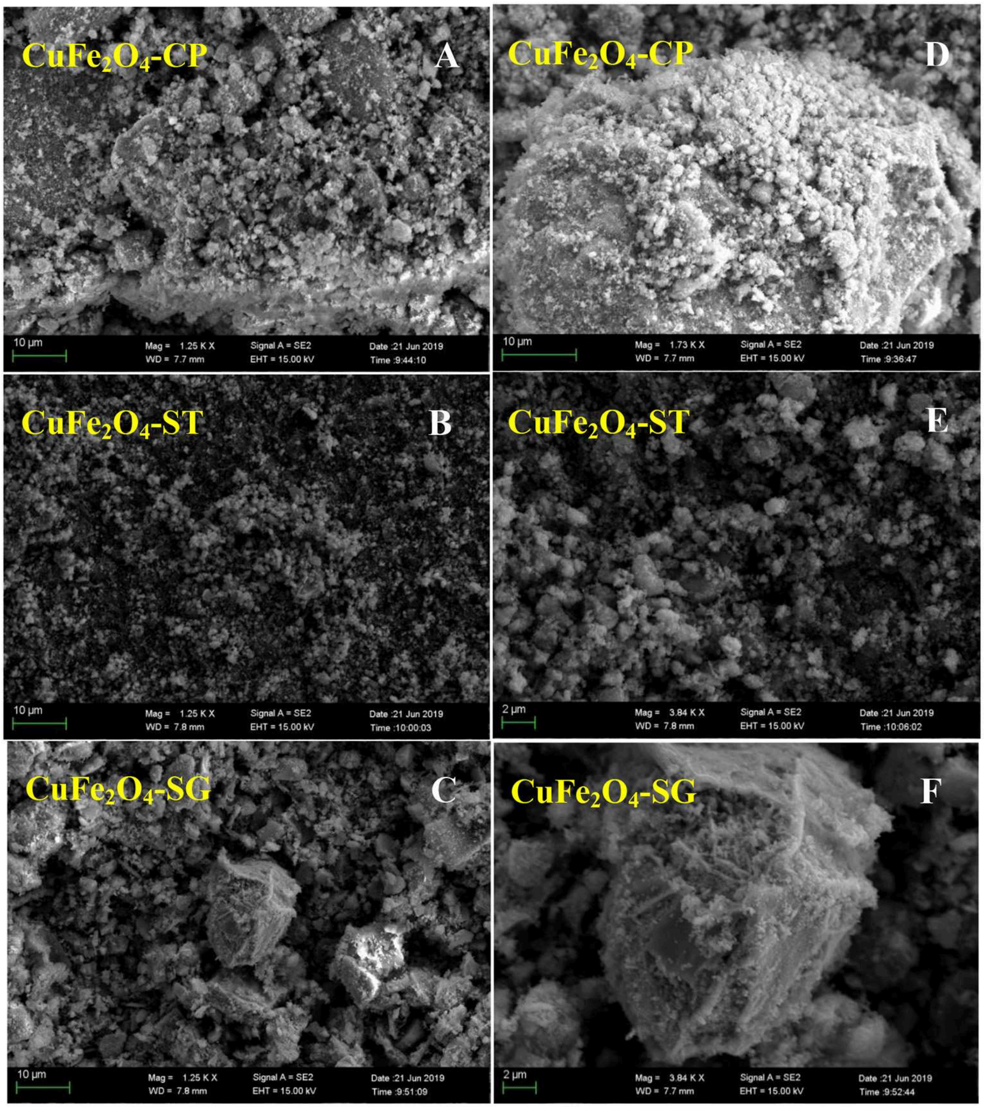

FIGURE 6 | SEM images of $CuFe_2O_4$ synthesized by different methods: **(A–C)** 1250 times magnification; **(D)** 1730 times magnification; **(E,F)** 3840 times magnification.

spinel $CuFe_2O_4$ (JCPDS 25-0283), indicating that $CuFe_2O_4$ was indeed formed by all three methods. Moreover, no obvious impurity peak was found in the XRD pattern of $CuFe_2O_4$-SG, while two weak Cu (JCPDS 89-2838) diffraction peaks were observed in $CuFe_2O_4$-ST and $CuFe_2O_4$-CP. Meanwhile, the XRD peaks of $CuFe_2O_4$-SG were stronger and sharper. These results showed that ferrite prepared by sol–gel method was purer with better crystallinity than the samples prepared by the other two methods.

SEM Analysis

The SEM images in **Figure 6** show that the morphological structure of ferrite strongly depended on synthetic method. $CuFe_2O_4$-CP particles agglomerated into large and compact bulk forms, which might be caused by particle sintering that occurred during the calcination of coprecipitation precursor. This tended to reduce the contact area between the catalyst and other reactants, which was not conducive to pollutant removal (Xue et al., 2007). $CuFe_2O_4$-ST had a typical morphology of a solvothermal catalyst (Ueda Yamaguchi et al., 2016; Chen et al., 2017) with high dispersion, relatively uniform spherical-like shape, and minimum particle size, which could increase the external surface area. $CuFe_2O_4$-SG particles were found to be of moderate size and irregular shape. By the observation of enlarged SEM images of the three samples (**Figures 6D–F**), it is noteworthy that $CuFe_2O_4$-SG showed a spongy structure. Owing to the volatilization of citric acid, $CuFe_2O_4$-SG did not sinter as $CuFe_2O_4$-CP did, but had many discernible tiny pores. This porous structure was significantly advantageous in catalytic reaction because it could afford a large amount of reactive sites and enhance the reactant diffusion (Hou et al., 2018).

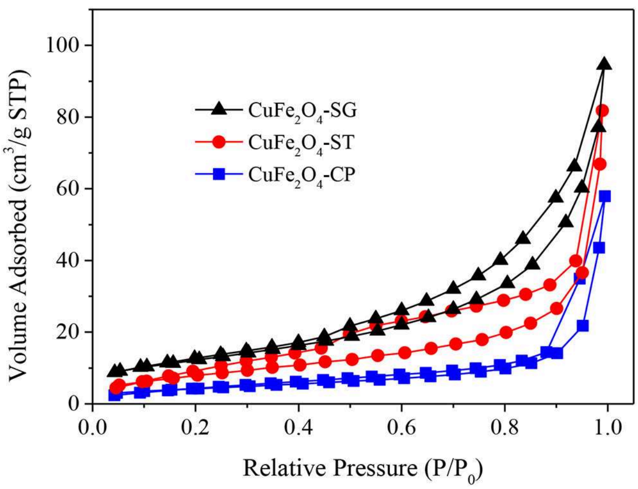

FIGURE 7 | N_2 adsorption-desorption isotherms of $CuFe_2O_4$ synthesized by different methods.

TABLE 2 | Basic structural parameters of $CuFe_2O_4$ synthesized by different methods.

Catalyst	Surface area (m^2/g)	Pore volume (cm^3/g)	Pore size (nm)
$CuFe_2O_4$-SG	44	0.146	2.744
$CuFe_2O_4$-ST	30	0.130	1.964
$CuFe_2O_4$-CP	15	0.090	2.775

N_2 Adsorption–Desorption Analysis

The N_2 adsorption–desorption isotherms of the three $CuFe_2O_4$ were presented in **Figure 7**. The isotherms all belonged to Type IV curve with H3 hysteresis loop, which pointed to the disordered, lamellar mesoporous structure of the catalysts. Obviously, the adsorption capacity of $CuFe_2O_4$ ranked as follows: $CuFe_2O_4$-SG > $CuFe_2O_4$-ST > $CuFe_2O_4$-CP. **Table 2** summarizes the basic structural parameters of the various as-synthesized $CuFe_2O_4$ samples. $CuFe_2O_4$-SG had the largest surface area and pore volume, followed by $CuFe_2O_4$-ST, and the values of $CuFe_2O_4$-CP were much lower than those of the former two, which was consistent with the SEM observation. Interestingly, the sequences of surface area and pore volume were completely consistent with the adsorption capacity of the prepared sample, but the mesopore size and particle size (observed in SEM images) did not follow this rule. These results indicated that sol–gel method endowed ferrite with a large surface area and pore volume, which played a pivotal role in the material's adsorption capacity, while the pore size and particle size were not the key factors affecting the adsorption capacity. When the adsorption capacity of ferrite was stronger, the amounts of pollutant and PS gathered were greater, and when the surface area was larger, the amount of active component exposed was greater, which were conducive to promoting the catalytic degradation of organics.

XPS Analysis

Figure 8 presents the surface elements chemical state of $CuFe_2O_4$ synthesized by different methods. As shown in **Figure 8A**, all samples yielded Cu(II) $2p_{3/2}$ peak at around 933.4 eV along with two satellite peaks at 941.3 and 943.8 eV (Lei et al., 2015). However, the surface of $CuFe_2O_4$-SG consisted uniquely of Cu(II); the surfaces of $CuFe_2O_4$-ST and $CuFe_2O_4$-CP also contained a small proportion of Cu(0) (the peak at 932.2 eV) (Li et al., 2019). The calculation of peak area showed that $CuFe_2O_4$-ST contained more surface Cu(0) than $CuFe_2O_4$-CP contained, which was in agreement with the diffraction peak intensities in the XRD patterns.

Figure 8B shows that Fe(III) ($2p_{3/2}$ 712.2 eV, $2p_{1/2}$ 725.9 eV) and Fe(II) ($2p_{3/2}$ 710.4 eV, $2p_{1/2}$ 723.8 eV) coexisted on the surface of the three $CuFe_2O_4$ samples (Li et al., 2019; Zhang et al., 2019). Obviously, the proportion of Fe(II) in $CuFe_2O_4$-SG and $CuFe_2O_4$-CP was much higher than that in $CuFe_2O_4$-ST. These results were favorable for organics removal because Fe was also an electron donor for PS activation (Zhang et al., 2019).

The O 1s spectra of $CuFe_2O_4$ synthesized by the three methods were shown in **Figure 8C**. All three samples showed peaks of lattice oxygen (O_{latt}, 529.9 eV) and OH adsorbed on the surface (531.3 eV) (Li et al., 2017). The highest proportion of O_{latt} in $CuFe_2O_4$-SG suggested the good crystal structure obtained by sol–gel method. The spectra of $CuFe_2O_4$-ST and $CuFe_2O_4$-CP contained another peak at 532.6 eV ascribed to adsorbed H_2O (Zeng et al., 2017). The high proportion of adsorbed OH and H_2O on the surface indicated the strong hydroxylation of $CuFe_2O_4$ during coprecipitation and solvothermal processes (Wang et al., 2019).

Catalytic Performance of $CuFe_2O_4$ Synthesized by Different Methods

Figure 9 displays AO7 and diclofenac removal in different $CuFe_2O_4$ + PS systems. As seen, the effectiveness and reusability of the catalyst were significantly influenced by synthetic method.

Figure 9A shows that $CuFe_2O_4$-SG had the best PS catalytic performance. AO7 removal efficiency in $CuFe_2O_4$-SG + PS, $CuFe_2O_4$-ST + PS, and $CuFe_2O_4$-CP + PS systems were 96.8, 90.1, and 45.3%, respectively. In contrast, only 46.5, 53.4, and 36.3% of AO7 were adsorbed by the corresponding catalyst alone. In the early stage of reaction, the relatively large external surface area of the catalyst enabled $CuFe_2O_4$-ST to activate PS to remove more AO7. However, as the reaction proceeded, PS and AO7 gradually diffused into the pores of $CuFe_2O_4$-SG and reacted on the abundant active sites, ultimately leading to a better removal of AO7. Meanwhile, the corrosion and dissolution of the metallic Cu impurity observed on $CuFe_2O_4$-ST reduced the content of active metal and led to a gradual loss of activation ability of $CuFe_2O_4$-ST (Li et al., 2019). As for $CuFe_2O_4$-CP, its adsorption and catalytic capacity were greatly hindered owing to the serious sintering. Moreover, the reusability of $CuFe_2O_4$ synthesized by different methods was also found to be different (**Figure 9B**). After three runs, the decrease of AO7 removal in $CuFe_2O_4$-SG + PS system (19.9%) was lower than that in $CuFe_2O_4$-ST + PS system (22.0%). AO7 removal efficiency in

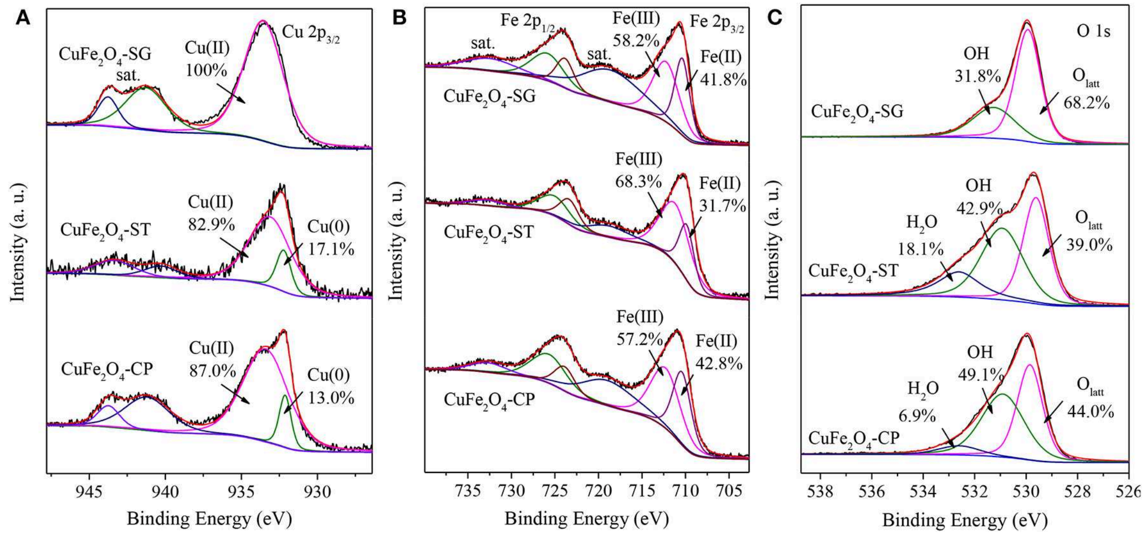

FIGURE 8 | XPS spectra of $CuFe_2O_4$ synthesized by different methods: **(A)** Cu 2p, **(B)** Fe 2p, and **(C)** O 1s.

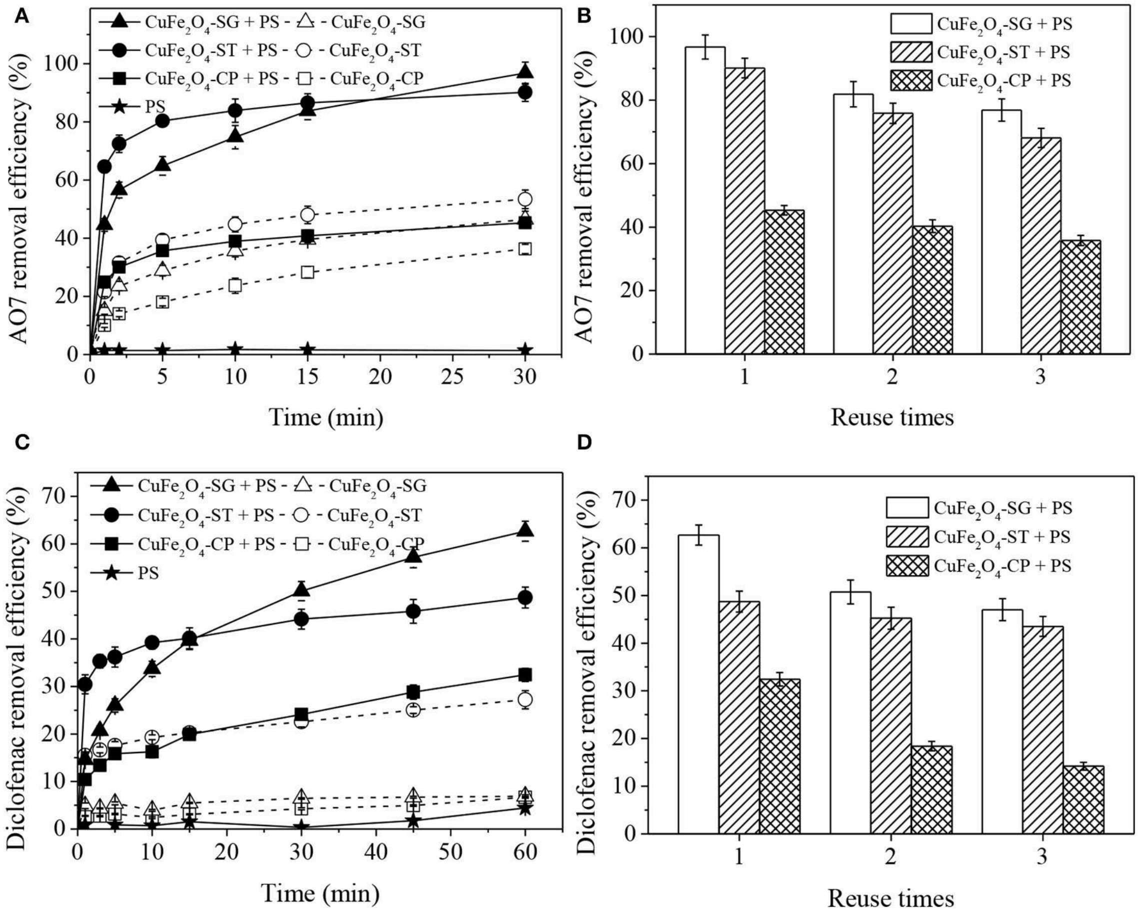

FIGURE 9 | Organics removal in different $CuFe_2O_4$ activated PS systems and reusability of $CuFe_2O_4$ synthesized by different methods: **(A,B)** AO7 removal; **(C,D)** diclofenac removal. Conditions: [organics] = 20 mg/L, [catalyst] = 0.6 g/L, **(A,B)** [PS] = 0.8 g/L, unadjusted pH = 6.5; **(C,D)** [PS] = 0.1 g/L, pH = 5.

$CuFe_2O_4$-SG + PS, $CuFe_2O_4$-ST + PS and $CuFe_2O_4$-CP + PS systems became 76.9, 68.1, and 35.8%, respectively. The lower decreasing trend of activity and higher pollutant removal efficiency after repeated uses suggested that $CuFe_2O_4$-SG had a good reusability. The removal of diclofenac in different $CuFe_2O_4$ + PS systems (**Figures 9C,D**) was similar to that of AO7. Once again, $CuFe_2O_4$-SG showed the best performance, followed by $CuFe_2O_4$-ST and then $CuFe_2O_4$-CP.

These results demonstrated that synthetic method would influence the catalytic performance of ferrite from morphological structure, surface area, and element chemical state. Sol–gel method was the ideal one to synthesize ferrite applicable in activated PS process.

CONCLUSIONS

M-site metal and synthetic method significantly influenced the catalytic performance and physicochemical property of spinel ferrite. The sequence of the effectiveness of ferrite-activated PS system for organics removal was $CuFe_2O_4 > CoFe_2O_4 > MnFe_2O_4 > ZnFe_2O_4$. The high catalytic performance of MFe_2O_4 resulted from its good reducibility, strong reversibility of M^{2+}/M^{3+} redox couple, and active electron transfer on the surface, which were affected by M-site metal. Surface -OH was not crucial for the catalytic performance of MFe_2O_4 in PS system. Moreover, sol–gel method was found to be the ideal one to synthesize ferrite to effectively activate PS for organics removal. The as-prepared ferrite had good purity, porous structure, large surface area, and favorable element chemical states, leading to superior catalytic performance and reusability compared with those prepared by solvothermal and coprecipitation methods. The results served as a reference for screening ferrite and promoting PS activation.

DATA AVAILABILITY STATEMENT

All datasets generated for this study are included in the article/**Supplementary Material**.

AUTHOR CONTRIBUTIONS

GX, SK, GZ, and NZ designed the experiments. GX, SK, QL, and HD performed the experiments. GX, SK, and GZ wrote the paper. GX, SK, QL, GZ, NZ, HD, and LN discussed the results and analyzed the data.

ACKNOWLEDGMENTS

The authors thank for financial support by the National Water Pollution Control and Treatment Science and Technology Major Project of China (2018ZX07110003).

SUPPLEMENTARY MATERIAL

The Supplementary Material for this article can be found online at: https://www.frontiersin.org/articles/10.3389/fchem.2020.00177/full#supplementary-material

REFERENCES

Alexopoulou, C., Petala, A., Frontistis, Z., Drivas, C., Kennou, S., Kondarides, D. I., et al. (2019). Copper phosphide and persulfate salt: a novel catalytic system for the degradation of aqueous phase micro-contaminants. *Appl. Catal. B Environ.* 244, 178–187. doi: 10.1016/j.apcatb.2018.11.058

Anipsitakis, G. P., and Dionysiou, D. D. (2004). Radical generation by the interaction of transition metals with common oxidants. *Environ. Sci. Technol.* 38, 3705–3712. doi: 10.1021/es035121o

Bard, A. J., Faulkner, L. R., Leddy, J., and Zoski, C. G. (1980). *Electrochemical Methods: Fundamentals and Applications*. New York, NY: Wiley.

Cai, C., Liu, J., Zhang, Z., Zheng, Y., and Zhang, H. (2016). Visible light enhanced heterogeneous photo-degradation of Orange II by zinc ferrite ($ZnFe_2O_4$) catalyst with the assistance of persulfate. *Sep. Purif. Technol.* 165, 42–52. doi: 10.1016/j.seppur.2016.03.026

Chen, C.-B., Zhang, F., Li, C.-X., Lu, J.-Y., Cui, S., Liu, H.-Q., et al. (2017). A magnetic $CoFe_2O_4$-CNS nanocomposite as an efficient, recyclable catalyst for peroxymonosulfate activation and pollutant degradation. *RSC Adv.* 7, 55020–55025. doi: 10.1039/C7RA09665H

Chen, J., Qian, Y., Liu, H., and Huang, T. (2016). Oxidative degradation of diclofenac by thermally activated persulfate: implication for ISCO. *Environ. Sci. Pollut. Res.* 23, 3824–3833. doi: 10.1007/s11356-015-5630-0

Cihlar, J., Vrba, R., Castkova, K., and Cihlar, J. (2017). Effect of transition metal on stability and activity of La-Ca-M-(Al)-O (M = Co, Cr, Fe and Mn) perovskite oxides during partial oxidation of methane. *Int. J. Hydrogen Energ.* 42, 19920–19934. doi: 10.1016/j.ijhydene.2017.06.075

Deng, J., Chen, Y.-J., Lu, Y.-A., Ma, X.-Y., Feng, S.-F., Gao, N., et al. (2017). Synthesis of magnetic $CoFe_2O_4$/ordered mesoporous carbon nanocomposites and application in fenton-like oxidation of rhodamine B. *Environ. Sci. Pollut. Res.* 24, 14396–14408. doi: 10.1007/s11356-017-8941-5

Duan, X., Su, C., Miao, J., Zhong, Y., Shao, Z., Wang, S., et al. (2018). Insights into perovskite-catalyzed peroxymonosulfate activation: maneuverable cobalt sites for promoted evolution of sulfate radicals. *Appl. Catal. B Environ.* 220, 626–634. doi: 10.1016/j.apcatb.2017.08.088

Garcia-Muñoz, P., Fresno, F., de la Peña O'Shea, V. A., and Keller, N. (2020). Ferrite materials for photoassisted environmental and solar fuels applications. *Top. Curr. Chem.* 378:6. doi: 10.1007/s41061-019-0270-3

Guan, Y. H., Ma, J., Ren, Y. M., Liu, Y. L., Xiao, J. Y., Lin, L. Q., et al. (2013). Efficient degradation of atrazine by magnetic porous copper ferrite catalyzed peroxymonosulfate oxidation via the formation of hydroxyl and sulfate radicals. *Water Res.* 47, 5431–5438. doi: 10.1016/j.watres.2013.06.023

Gupta, D., and Garg, A. (2017). Effect of the preparation method on the catalytic activity of the heterogeneous catalyst CuO/CeO_2 for the oxidative degradation of sulfide and phenolic compounds. *React. Kinet. Mech. Cat.* 124, 101–121. doi: 10.1007/s11144-017-1318-4

Hou, J., Yang, S., Wan, H., Fu, H., Qu, X., Xu, Z., et al. (2018). Highly effective catalytic peroxymonosulfate activation on N-doped mesoporous carbon for o-phenylphenol degradation. *Chemosphere* 197, 485–493. doi: 10.1016/j.chemosphere.2018.01.031

Jaafarzadeh, N., Ghanbari, F., and Ahmadi, M. (2017). Efficient degradation of 2,4-dichlorophenoxyacetic acid by peroxymonosulfate/magnetic copper ferrite nanoparticles/ozone: a novel combination of advanced oxidation processes. *Chem. Eng. J.* 320, 436–447. doi: 10.1016/j.cej.2017.03.036

Kennaz, H., Harat, A., Guellati, O., Momodu, D. Y., Barzegar, F., Dangbegnon, J. K., et al. (2017). Synthesis and electrochemical investigation of spinel cobalt ferrite magnetic nanoparticles for supercapacitor application. *J. Solid State Electrochem.* 22, 835–847. doi: 10.1007/s10008-017-3813-y

Lassoued, A., Ben hassine, M., Karolak, F., Dkhil, B., Ammar, S., and Gadri, A. (2017). Synthesis and magnetic characterization of Spinel ferrites MFe_2O_4 (M

= Ni, Co, Zn and Cu) via chemical co-precipitation method. *J. Mater. Sci. Mater. Electron.* 28, 18857–18864. doi: 10.1007/s10854-017-7837-y

Lei, Y., Chen, C. S., Tu, Y. J., Huang, Y. H., and Zhang, H. (2015). Heterogeneous degradation of organic pollutants by persulfate activated by CuO-Fe_3O_4: mechanism, stability, and effects of pH and bicarbonate ions. *Environ. Sci. Technol.* 49, 6838–6845. doi: 10.1021/acs.est.5b00623

Li, J., Ren, Y., Ji, F., and Lai, B. (2017). Heterogeneous catalytic oxidation for the degradation of *p*-nitrophenol in aqueous solution by persulfate activated with $CuFe_2O_4$ magnetic nano-particles. *Chem. Eng. J.* 324, 63–73. doi: 10.1016/j.cej.2017.04.104

Li, J., Xu, M., Yao, G., and Lai, B. (2018). Enhancement of the degradation of atrazine through $CoFe_2O_4$ activated peroxymonosulfate (PMS) process: kinetic, degradation intermediates, and toxicity evaluation. *Chem. Eng. J.* 348, 1012–1024. doi: 10.1016/j.cej.2018.05.032

Li, Z., Guo, C., Lyu, J., Hu, Z., and Ge, M. (2019). Tetracycline degradation by persulfate activated with magnetic Cu/$CuFe_2O_4$ composite: efficiency, stability, mechanism and degradation pathway. *J. Hazard. Mater.* 373, 85–96. doi: 10.1016/j.jhazmat.2019.03.075

Malvestiti, J. A., Fagnani, E., Simao, D., and Dantas, R. F. (2019). Optimization of UV/H_2O_2 and ozone wastewater treatment by the experimental design methodology. *Environ. Technol.* 40, 1910–1922. doi: 10.1080/09593330.2018.1432698

Oh, W.-D., Dong, Z., and Lim, T.-T. (2016). Generation of sulfate radical through heterogeneous catalysis for organic contaminants removal: current development, challenges and prospects. *Appl. Catal. B Environ.* 194, 169–201. doi: 10.1016/j.apcatb.2016.04.003

Parvas, M., Haghighi, M., and Allahyari, S. (2014). Degradation of phenol via wet-air oxidation over CuO/CeO_2-ZrO_2 nanocatalyst synthesized employing ultrasound energy: physicochemical characterization and catalytic performance. *Environ. Technol.* 35, 1140–1149. doi: 10.1080/09593330.2013.863952

Priyanka, K., Remya, N., and Behera, M. (2019). Comparison of titanium dioxide based catalysts preparation methods in the mineralization and nutrients removal from greywater by solar photocatalysis. *J. Clean. Prod.* 235, 1–10. doi: 10.1016/j.jclepro.2019.06.314

Ren, Y., Lin, L., Ma, J., Yang, J., Feng, J., and Fan, Z. (2015). Sulfate radicals induced from peroxymonosulfate by magnetic ferrospinel MFe_2O_4 (M = Co, Cu, Mn, and Zn) as heterogeneous catalysts in the water. *Appl. Catal. B Environ.* 165, 572–578. doi: 10.1016/j.apcatb.2014.10.051

Silveira, J. E., Claro, E. M. T., Paz, W. S., Oliveira, A. S., Zazo, J. A., and Casas, J. A. (2018). Optimization of disperse Blue 3 mineralization by UV-LED/$FeTiO_3$ activated persulfate using response surface methodology. *J. Taiwan Inst. Chem. Eng.* 85, 66–73. doi: 10.1016/j.jtice.2017.12.015

Song, S., Liu, Z., He, Z., Zhang, A., Chen, J., Yang, Y., et al. (2010). Impacts of morphology and crystallite phases of titanium oxide on the catalytic ozonation of phenol. *Environ. Sci. Technol.* 44, 3913–3918. doi: 10.1021/es100456n

Stoia, M., Muntean, C., and Militaru, B. (2017). $MnFe_2O_4$ nanoparticles as new catalyst for oxidative degradation of phenol by peroxydisulfate. *J. Environ. Sci.* 53, 269–277. doi: 10.1016/j.jes.2015.10.035

Su, C., Duan, X., Miao, J., Zhong, Y., Zhou, W., Wang, S., et al. (2017). Mixed conducting perovskite materials as superior catalysts for fast aqueous-phase advanced oxidation: a mechanistic study. *ACS Catal.* 7, 388–397. doi: 10.1021/acscatal.6b02303

Ueda Yamaguchi, N., Bergamasco, R., and Hamoudi, S. (2016). Magnetic $MnFe_2O_4$-graphene hybrid composite for efficient removal of glyphosate from water. *Chem. Eng. J.* 295, 391–402. doi: 10.1016/j.cej.2016.03.051

Wacławek, S., Lutze, H. V., Grübel, K., Padil, V. V. T., Cerník, M., and Dionysiou, D. D. (2017). Chemistry of persulfates in water and wastewater treatment: a review. *Chem. Eng. J.* 330, 44–62. doi: 10.1016/j.cej.2017.07.132

Wang, B. W., Gao, C. C., Zhao, H. B., and Zheng, C. G. (2011). Preparation of $CoFe_2O_4$ nanocrystallite by sol-gel combustion synthesis and evaluation of its reaction performance. *Adv. Mater. Res.* 341–342, 63–67. doi: 10.4028/www.scientific.net/AMR.341-342.63

Wang, J., and Wang, S. (2018). Activation of persulfate (PS) and peroxymonosulfate (PMS) and application for the degradation of emerging contaminants. *Chem. Eng. J.* 334, 1502–1517. doi: 10.1016/j.cej.2017.11.059

Wang, Z., Zhang, X., Zhang, H., Zhu, G., Gao, Y., Cheng, Q., et al. (2019). Synthesis of magnetic nickel ferrite/carbon sphere composite for levofloxacin elimination by activation of persulfate. *Sep. Purif. Technol.* 215, 528–539. doi: 10.1016/j.seppur.2019.01.063

Xiao, R., Luo, Z., Wei, Z., Luo, S., Spinney, R., Yang, W., et al. (2018). Activation of peroxymonosulfate/persulfate by nanomaterials for sulfate radical-based advanced oxidation technologies. *Curr. Opin. Chem. Eng.* 19, 51–58. doi: 10.1016/j.coche.2017.12.005

Xu, X.-R., and Li, X.-Z. (2010). Degradation of azo dye Orange G in aqueous solutions by persulfate with ferrous ion. *Sep. Purif. Technol.* 72, 105–111. doi: 10.1016/j.seppur.2010.01.012

Xue, L., Zhang, C., He, H., and Teraoka, Y. (2007). Catalytic decomposition of N_2O over CeO_2 promoted Co_3O_4 spinel catalyst. *Appl. Catal. B Environ.* 75, 167–174. doi: 10.1016/j.apcatb.2007.04.013

Yue, X., Guo, W., Li, X., Zhou, H., and Wang, R. (2016). Core-shell Fe_3O_4@MIL-101(Fe) composites as heterogeneous catalysts of persulfate activation for the removal of Acid Orange 7. *Environ. Sci. Pollut. Res. Int.* 23, 15218–15226. doi: 10.1007/s11356-016-6702-5

Zeng, T., Yu, M., Zhang, H., He, Z., Zhang, X., Chen, J., et al. (2017). *In situ* synthesis of cobalt ferrites-embedded hollow N-doped carbon as an outstanding catalyst for elimination of organic pollutants. *Sci. Total Environ.* 593-594, 286–296. doi: 10.1016/j.scitotenv.2017.03.180

Zhang, Y., Rimal, G., Tang, J., and Dai, Q. (2018). Synthesis of $NiFe_2O_4$ nanoparticles for energy and environment applications. *Mater. Res. Express* 5:025023. doi: 10.1088/2053-1591/aaacde

Zhang, Y., Zhang, Q., Dong, Z., Wu, L., and Hong, J. (2019). Structurally modified $CuFe_2O_4$/persulfate process for acetaminophen scavenging: high efficiency with low catalyst addition. *J. Chem. Technol. Biot.* 94, 785–794. doi: 10.1002/jctb.5824

Zhao, X., Niu, C., Zhang, L., Guo, H., Wen, X., Liang, C., et al. (2018). Co-Mn layered double hydroxide as an effective heterogeneous catalyst for degradation of organic dyes by activation of peroxymonosulfate. *Chemosphere* 204, 11–21. doi: 10.1016/j.chemosphere.2018.04.023

Zhu, K., Wang, X., Chen, D., Ren, W., Lin, H., and Zhang, H. (2019). Wood-based biochar as an excellent activator of peroxydisulfate for Acid Orange 7 decolorization. *Chemosphere* 231, 32–40. doi: 10.1016/j.chemosphere.2019.05.087

Conflict of Interest: The authors declare that the research was conducted in the absence of any commercial or financial relationships that could be construed as a potential conflict of interest.

frontiers in Chemistry

ORIGINAL RESEARCH
published: 25 May 2020
doi: 10.3389/fchem.2020.00398

Preparation of Carboxymethyl Cellulose-*g*-Poly(acrylamide)/Attapulgite Porous Monolith With an Eco-Friendly Pickering-MIPE Template for Ce(III) and Gd(III) Adsorption

Feng Wang [1,2], Yongfeng Zhu [1] and Aiqin Wang [1]*

[1] Key Laboratory of Clay Mineral Applied Research of Gansu Province, Center of Eco-material and Green Chemistry, Lanzhou Institute of Chemical Physics, Chinese Academy of Sciences, Lanzhou, China, [2] Qinzhou Key Laboratory of Biowaste Resources for Selenium-Enriched Functional Utilization, College of Petroleum and Chemical Engineering, Beibu Gulf University, Qinzhou, China

Due to their high specific surface and metal-binding functional groups in their crosslinked polymeric networks, monolithic materials incorporating a porous structure have been considered one of the most efficient kinds of adsorbents for rare earth element recovery. Herein, a facile and novel monolithic multi-porous carboxymethyl cellulose-*g*-poly(acrylamide)/attapulgite was synthesized by free radical polymerization via green vegetable oil-in-water Pickering medium internal phase emulsion (O/W Pickering-MIPEs), which was synergically stabilized by attapulgite and tween-20. The homogenizer rotation speed and time were investigated to form stable Pickering-MIPEs. The effects of different types of oil phase on the formation of Pickering-MIPEs were investigated with stability tests and rheological characterization. The structure and composition of the porous material when prepared with eight kinds of vegetable oil were characterized by FTIR and SEM. The results indicate that the obtained materials, which have abundant interconnected porosity, are comparable to those fabricated with Pickering-HIPE templates. The adsorption experiment demonstrated that the prepared materials have a fast capture rate and high adsorption capacities for Ce(III) and Gd(III), respectively. The saturation adsorption capacities for Ce(III) and Gd(III) are 205.48 and 216.73 mg/g, respectively, which can be reached within 30 min. Moreover, the monolithic materials exhibit excellent regeneration ability and reusability. This work provides a feasible and eco-friendly pathway for the construction of a multi-porous adsorbent for adsorption and separation applications.

Keywords: porous materials, pickering emulsions, attapulgite, adsorption, rare earth elements

Edited by:
Maria Graca Rasteiro,
University of Coimbra, Portugal

Reviewed by:
Vinod Kumar Gupta,
Indian Institute of Technology Roorkee, India
Priyanka Sharma,
Stony Brook University, United States

****Correspondence:***
Aiqin Wang
aqwang@licp.cas.cn

Specialty section:
This article was submitted to Green and Sustainable Chemistry, a section of the journal Frontiers in Chemistry

Received: *02 January 2020*
Accepted: *15 April 2020*
Published: *25 May 2020*

Citation:
Wang F, Zhu Y and Wang A (2020) Preparation of Carboxymethyl Cellulose-g-Poly(acrylamide)/Attapulgite Porous Monolith With an Eco-Friendly Pickering-MIPE Template for Ce(III) and Gd(III) Adsorption. Front. Chem. 8:398. doi: 10.3389/fchem.2020.00398

INTRODUCTION

Rare earth elements (REE) are critical components in special functional materials for industrial applications as well as in cutting-edge technology fields, such as biomedical engineering, information storage, communications, wind turbines, spaceflight, nuclear energy, and military applications (Saravanan et al., 2013; Ogata et al., 2015; Anastopoulos et al., 2016; Rajendran et al., 2016; Zhao et al., 2016, 2019; Wang et al., 2017a). China possesses more than 90% of the global

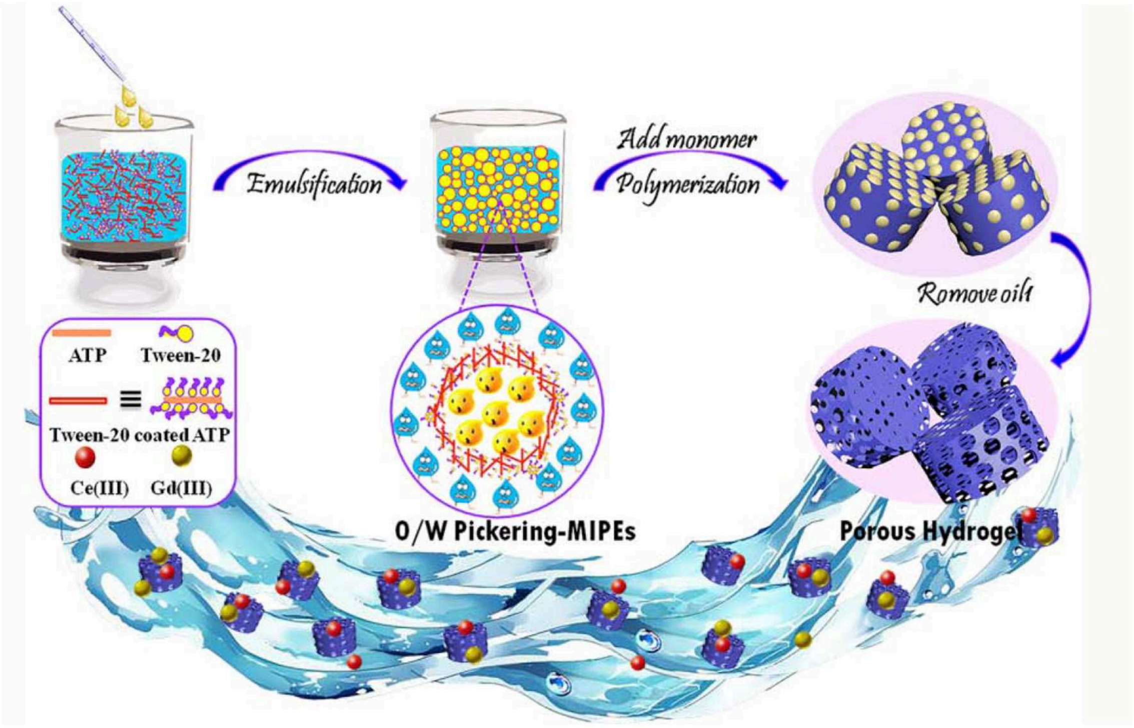

GRAPHICAL ABSTRACT | The preparation of porous monolith with Pickering-MIPE template and it's application for Ce(III) and Gd(III) adsorption.

potential reserves (Survey, 2014; Ogata et al., 2015). Recently, the adsorption and recovery of REEs from aqueous solutions has become a significant issue owing to their significance (Voßenkaul et al., 2015; Alshameri et al., 2019), and many technologies are being developed to enrich REEs, including solvent extraction (Hou et al., 2013; Schirhagl, 2014), adsorption (Maranescu et al., 2019; Mondal et al., 2019; Yang et al., 2019), ion-exchange (Moldoveanu and Papangelakis, 2012; Page et al., 2019), and co-precipitation (Chatterjee et al., 2009). Among them, adsorption is considered one of the most promising methods for the removal of REEs due to its simple operation, easy separation, high efficiency, and reusability (Ogata et al., 2015; Wang et al., 2017a).

At present, various adsorbent materials have been employed to adsorb REEs from aqueous solutions including red clay (Gładysz-Płaska et al., 2014), hydrogel porous materials (Zhu et al., 2016a), carbon materials (Babu et al., 2018), silica gels (Ogata et al., 2015), marine sediments (Liatsou et al., 2015), and biopolymer microcapsules (Delrish et al., 2014). Among various adsorbents used, hydrogel porous materials are one of the most efficient types of adsorbents due to their superhydrophilic features and the metal-binding functional groups of the cross-linked polymeric networks (Ren et al., 2016). Moreover, hydrogel porous materials can be designed and tailored by various functional groups to provide them with specific properties, and the resulting functional materials are favorable for a stable adsorption process. Furthermore, the adsorption properties of adsorbents depend on their functional groups and specific surface area. A high specific surface favors the exposure of the functional groups, improving the probability of reaction between adsorbates and adsorbents. Thus, incorporating a porous structure into adsorbents can provide a high specific surface area for adsorbents to effectively remove REE, and the porous structure also has the benefits that it reduces transmission resistance and enhances the adsorption activity of adsorbents to adsorbates (Zhu et al., 2016b). Therefore, it is indispensable to develop functional hydrogel materials with a porous structure.

The soft template method is a common method of constructing materials with ordered and disordered porous matrices (Jiaxi et al., 2015). In this method, oil-in-water Pickering high internal phase emulsions (O/W Pickering HIPEs) containing more than 74% internal phase is considered the most effective pathway for the preparation of hydrogels with well-defined porosity (Zhu et al., 2016a,b). This technology involves the polymerization of monomers in the continuous phase and the removal of the dispersed phase, which could create a solid foam material (polyHIPE) with an interconnected porous structure (Ma et al., 2014; Oh et al., 2014). Interestingly, the interconnectivity and pore structure of polyHIPEs can be easily tailored by varying the parameters of O/W Pickering HIPEs (Ikem et al., 2010a; Ye et al., 2013). Therefore, large numbers of adsorbents with interconnected structures have been successfully prepared by using O/W Pickering HIPEs (Yi et al., 2016), and the as-prepared adsorbents exhibited enhanced adsorption capacity to model pollutants due to abundant porosity and high permeability (Zhang et al., 2016).

However, the O/W Pickering HIPEs have some obvious drawbacks. For example, this method often requires more than 74% of an organic solvent (such as liquid paraffin, toluene, *p*-xylene, or *n*-hexane) as the dispersion phase, and needing a large amount of these organic solvents greatly increases the preparation cost; in addition, these are harmful to the environment and human health. It is thus desirable to decrease the oil phase fraction and substitute poisonous organic solvent with an eco-friendly oil phase. Compared with Pickering-HIPEs, the formation of Pickering-medium internal phase emulsions (Pickering-MIPEs) requires less of the dispersion phase. Therefore, in this research, porous materials with medium internal phase emulsions have been fabricated by using cheap vegetable oil as the dispersion phase. In addition, particles with appropriate wettability are a necessary condition for preparing a stable O/W Pickering emulsion. In order to achieve the necessary wettability, solid particles [such as inorganic particles (Gudarzi and Sharif, 2011), polymer micelles (Yang et al., 2016), colloidal particles (Gautier et al., 2007), and carbon materials (Sullivan and Kilpatrick, 2002)] usually need to be modified by chemical and physical processes, but it is inevitable that this will result in waste energy and an increase of production cost. For these reasons, natural particles that require no further modification are considered excellent stabilizers for the construction of interconnected porous materials. Due to their plentiful hydroxyl groups and negative charge, clay minerals are highly hydrophilic and present the potential for use in the formation of an O/W emulsion as stable particles without any further modification.

In this study, natural attapulgite (ATP) was employed as the stable particle, tween-20 (T-20) served as the co-stabilizer, and vegetable oil was selected as the disperse phase to form eco-friendly O/W Pickering-MIPEs for the construction of porous materials. In order to form stable Pickering-MIPEs, the effects of the type of oil phase, the homogenizer rotation speed, and time on the formation of Pickering-MIPEs were investigated. Sodium carboxymethyl cellulose (CMC) has two different end groups: one has a chemically reducing functionality (a hemiacetal unit), and the other has a pendant hydroxyl group that can be used to react with other monomers (Klemm et al., 2005). Moreover, the groups on CMC were found to be effective for the removal of metal ions from water (Sharma et al., 2017; Klemm et al., 2018). Thus, in this research, CMC was employed as the grafting backbone onto which to graft acrylamide (AM), which was used as the functional monomer due to its ability to combine with metals and its reactivity. The adsorption properties of the obtained porous cellulose-*g*- poly(acrylamide)/attapulgite materials for Ce(III) and Gd(III) from aqueous solution was also studied.

EXPERIMENTAL SECTION

Materials

CMC (CP, viscosity: 300-800 mpa·s) and AM (CP) were purchased from Shanpu Chemical Factory (Shanghai, China) and used without further treatment. Ammonium persulfate (APS, AR), *N,N,N'N'*-tetramethyl ethylenediamine (TMEDA, AR), Methyl violet (MV), and Methylene blue (MB) were provided by Sinopharm Chemical Reagent Co., Ltd. (Shanghai, China). ATP was obtained from Huangnishan Mine in Xuyi county, Jiangsu province, China, and then ground and passed through a 200-mesh sieve. *N,N'*-methylenebisacrylamide (MBA, CP) was received from Yuanfan Vegetable Additives (Shanghai, China). T-20 (AR) was received from BASF Corporation. 3A molecular sieve 103 was obtained from Molsion Molecular Sieve Co., Ltd. (Shanghai, China). Linseed oil was purchased from Yongfan Trading Co. (Lanzhou, China). Colza oil and soybean oil were purchased from Yihaijiali Arawana Edible Oil Co., China. Peanut oil, sunflower oil, olive oil, and sesame oil were obtained from Shandong Luhua Group Co., Ltd. China. Corn oil was purchased from Cofco Food Marketing Co., Ltd. China. Other reagents were all of analytical grade, and all solutions were prepared with deionized water.

Preparation of Pickering-MIPEs

T-20 (0.2 g) and ATP (0.5 g) were dissolved into 10 mL deionized water under 3,000 rpm stirring for 1 min, and then various vegetable oils (10 mL) were added into the mixed suspension separately and emulsified with a GJD-B12K homogenizer at certain rpm values for a designed time to form Pickering MIPEs. The type of emulsion was detected by the pendant-drop method with deionized water and *p*-xylene. The emulsion droplet could disperse into deionized water but remained round in *p*-xylene, indicating that the as-prepared Pickering-MIPEs were O/W emulsions. The feed composition of reactants, the codes of the emulsions, and the corresponding droplet diameters are listed in **Table 1**.

Preparation of Porous CMC-g-PAM Monolith

The stable Pickering-MIPEs containing 0.1 g CMC, 0.31 g MBA, 2% T-20, and 5% ATP were prepared by first dissolving CMC and MBA in the continuous phase. After the emulsion was obtained, 1.42 g (2 mmol) AM, 91 mg APS, and 0.1 mL of TMEDA were added into it with rapid stirring for 1 min, and then the prepared mixture was transferred into test tubes, sealed, and immersed in a 65°C water bath for 12 h to complete the polymerization reaction. After that, the porous polymers were sectioned and washed with acetone via Soxhlet extraction for 10 h. In order to activate the porous polymers, they were immersed in 0.5 M NaOH aqueous alcohol solution (V/V, 3/7) for 24 h to transform amide groups into carboxyl groups. The redundant NaOH and undesirable residues were washed away with a water/ethanol ($V_{\text{water}}/V_{\text{alcohol}} = 3/7$) solvent, repeatedly, and then the monolithic hydrogels were dehydrated with 3A molecular sieve in absolute ethanol and then dried at 60°C in a vacuum for 8 h. The feed composition of the reactants, the codes of the porous monoliths, and the corresponding pore diameters are also summarized in **Table 1**. Photographs of the materials are shown in **Figure 4**.

Characterization

FTIR spectra were obtained by a Nicolet NEXUS FTIR spectrometer (U.S.A.) in the 4,000–400 cm^{-1} wavenumber region after the samples had been prepared as KBr pellets. The morphologies of the porous monoliths were characterized using

TABLE 1 | Feed composition of Pickering MIPE formulations and porous CMC-*g*-PAM/ATP monoliths and their corresponding average droplet and pore sizes.

Emulsion	Speed (rpm)	Time (min)	Emulsion	Speed (rpm)	Time (min)	Oil
ES-4000	4,000	10	ES-12000	12,000	10	Linseed oil
ES-6000	6,000	10	ET-1	10,000	1	Linseed oil
ES-8000	8,000	10	ET-3	10,000	3	Linseed oil
ES-4000	4,000	10	ET-5	10,000	5	Linseed oil
ES-10000	10,000	10	ET-7	10,000	7	Linseed oil
ES-11000	11,000	10	ET-9	10,000	9	Linseed oil
Emulsion	**D_E (μm)[a]**	**Materials**	**D_M (μm)[b]**	**Speed (rpm)**	**Time (min)**	**Oil**
E1	2.54	S1	2.35	10,000	7	Linseed oil
E2	2.48	S2	2.29	10,000	7	Colza oil
E3	2.57	S3	2.39	10,000	7	Peanut oil
E4	2.49	S4	2.32	10,000	7	Sunflower oil
E5	2.52	S5	2.27	10,000	7	Soybean oil
E6	2.58	S6	2.31	10,000	7	Corn oil
E7	2.55	S7	2.28	10,000	7	Olive oil
E8	2.43	S8	2.24	10,000	7	Sesame oil

[a] *Average diameter of emulsion droplets.*
[b] *Average pore diameter of materials.*

a field emission scanning electron microscope (SEM, JSM-6701F, JEOL, Japan) after being coated with gold film. The average pore diameter was obtained by measuring 100 pores using Image-Pro Plus 6.0 software. A Leica DM1000 digital biological microscope equipped with a built-in camera was used to record optical microscopy images of the Pickering-MIPEs.

Evaluation of Adsorption Performance

Working solutions containing different concentrations of Ce(III) and Gd(III) were prepared by diluting the stock solution of $Ce(NO_3)_3$ or $Gd(NO_3)_3$ using deionized water. The monolithic adsorbents were ground into granular particles with a particle size in the range of 12–40 mesh to conduct the adsorption experiments.

The adsorption process was performed by immersing 20 mg of adsorbent in 25 mL Ce(III) and Gd(III) solutions and shaking with a thermostatic shaker (THZ-98A) at 120 rpm and 30°C for a given time to reach adsorption equilibrium. After that, the monolith was separated from the solution, and the absorbance of solutions was measured by a UV-visible spectrophotometer (UV-3010, HITACHI, Japan) to measure the concentrations of Ce(III) and Gd(III) in the solution. The complexing agents used in this case are chlorophosphonazo and azo arsine for Ce(III) and Cd(III), respectively. The maximum absorbance wavelengths are 666 nm for Ce(III) and 656 nm for Gd(III). The adsorption capacities of the porous monolith for Ce(III) and Gd(III) were calculated according to Equation (1):

$$q_e = (C_0 - C_e) \times 0.025/m \tag{1}$$

where, q_e (mg/g) is the amount of Ce(III) or Gd(III) adsorbed by per unit mass of adsorbent and C_0 and C_e (mg/L) are the concentrations of Ce(III) or Gd(III) before and after adsorption, respectively, 0.025 (L) is the volume of Ce(III) or Gd(III) solution used for adsorption, and m (mg) is the mass of adsorbent.

During the experiment, the pH of the solution was adjusted to the required value with 0.1 mol/L HCl or NaOH solutions. The influence of pH value on the adsorption capacities of the porous monolith (S2) was evaluated in rare earth metal solutions with an initial concentration of 200 mg/L and pH values from 1 to 7. The effect of initial concentration on the adsorption capacities of the porous monolith was investigated by adding adsorbent (S2) into solutions with concentrations in the range of 100–400 mg/L for 1 h at the original pH of the solution. The adsorption kinetics was determined by ranging the adsorption duration from 5 to 120 min at the original pH of the solution and with a solution concentration of 200 mg/L. All adsorption experiments were repeated thrice to obtain the average value.

Desorption experiments were conducted to show the recyclability of the prepared porous hydrogel. Typically, 20 mg of the adsorbent (S2) was fully contacted with 25 mL 200 mg/L at 120 rpm and 30°C for 1 h to attain saturation adsorption. The metal-loaded adsorbent was then soaked in 30 mL HCl (0.5 mol/L) solution for 2 h to desorb, and then soaked with 0.5 mol/L NaOH solution and fully washed to neutral with deionized water to activate, after which the adsorbent was used for another adsorption process. The adsorption-desorption cycle was repeated five times to evaluate the reusability of the monolith.

RESULTS AND DISCUSSION

Preparation of Pickering-MIPEs Stabilized by ATP and T-20

The eco-friendly O/W Pickering MIPEs were formed by using vegetable oil as the dispersion phase and ATP and T-20 as the stabilizer after vigorous stirring for the designed time. During the stirring progress, T-20 first coated the surface of the ATP and then coated ATP nanorods synergistically with other free surfactants at the oil–water interface, acting as a barrier to prevent the coalescence of oil droplets and to generate a stable emulsion, as shown in **Scheme 1**.

The Effects of Emulsification Speed and Time

The homogenizer rotation speed and time are important factors for obtaining a homogenous emulsion (Colla et al., 2006), and thus the effects of the stirring velocity and time were investigated in this case. The experiment details are listed in **Table 1**; all the emulsions were stabilized by 5% ATP and 2% T-20. After preparation, the emulsion was kept for a month to observe its stability. As shown in **Figure 1**, the homogenizer rotation speed had a greater effect on the stability of emulsions compared with emulsification duration (**Figure 1A**). As the emulsification velocity and shear stress increased, the energy of the emulsion systems also increased to reduce the system energy, and the droplet size of emulsions largely reduced. The increase in the emulsification velocity expanded the contact area of the aqueous and oil phases, allowing more efficient dispersal and breakup of oil droplets in the emulsion and thus greatly enhancing the stability of emulsions. It is worth noting that an excessive emulsification speed introduced a large amount of bubbles into the emulsion. According to **Figure 1**, the volume of emulsion remained the same after the velocity reached 10,000 rpm, and thus 10,000 rpm was selected for the evaluation of the effect of emulsification duration.

At the same emulsification speed, an increase in the emulsification duration also helped to form a stabilized emulsion. Sufficient emulsification time could enhance the dispersion of the emulsion, decrease the diameter and wall thickness of droplets, and also increase the amount of droplets. However, collisions between droplets due to the mechanical agitation led to their aggregation and the formation of foam at the critical time, and

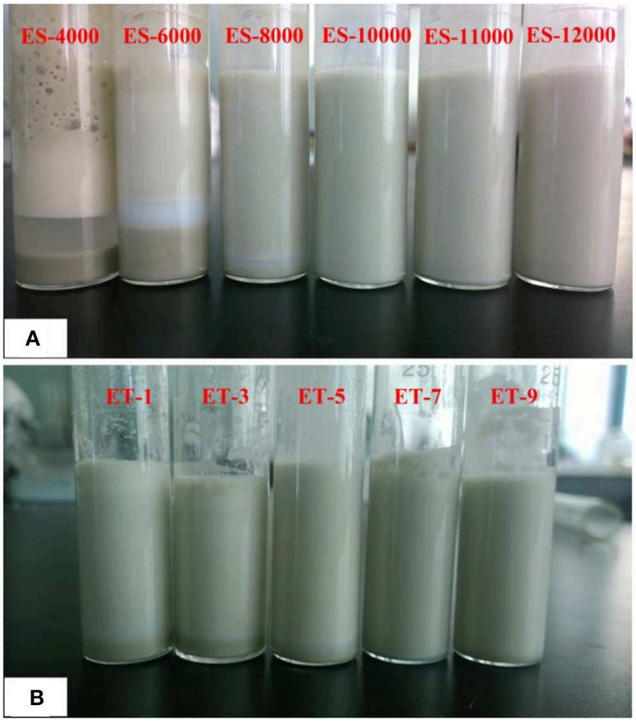

FIGURE 1 | Effects of **(A)** the homogenizer rotation speed and **(B)** time on the formation of Pickering-MIPEs. All of the emulsions were stabilized by 5% ATP and 2% T-20.

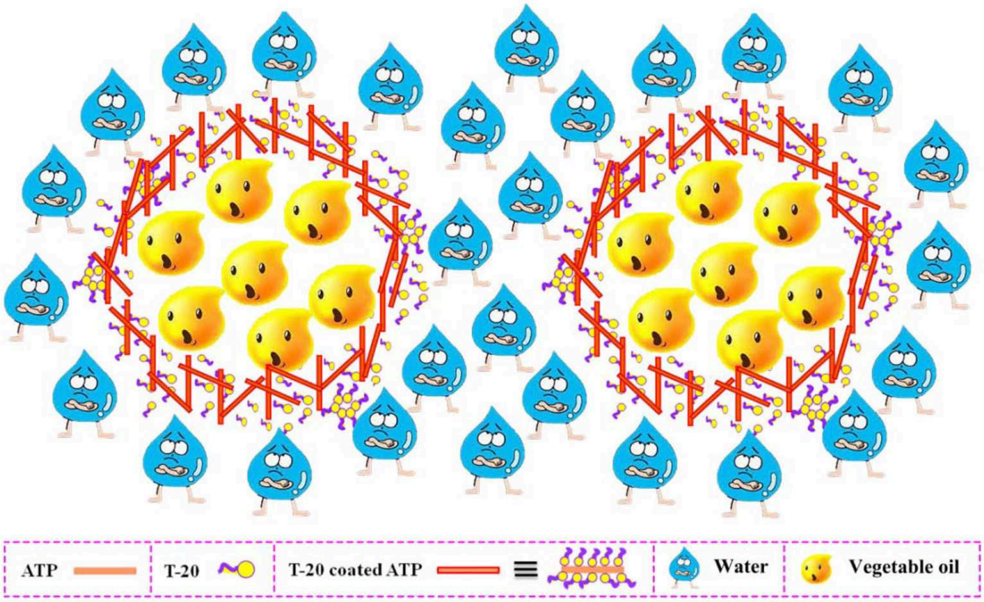

SCHEME 1 | Formation of O/W Pickering-MIPEs stabilized by ATP and T-20.

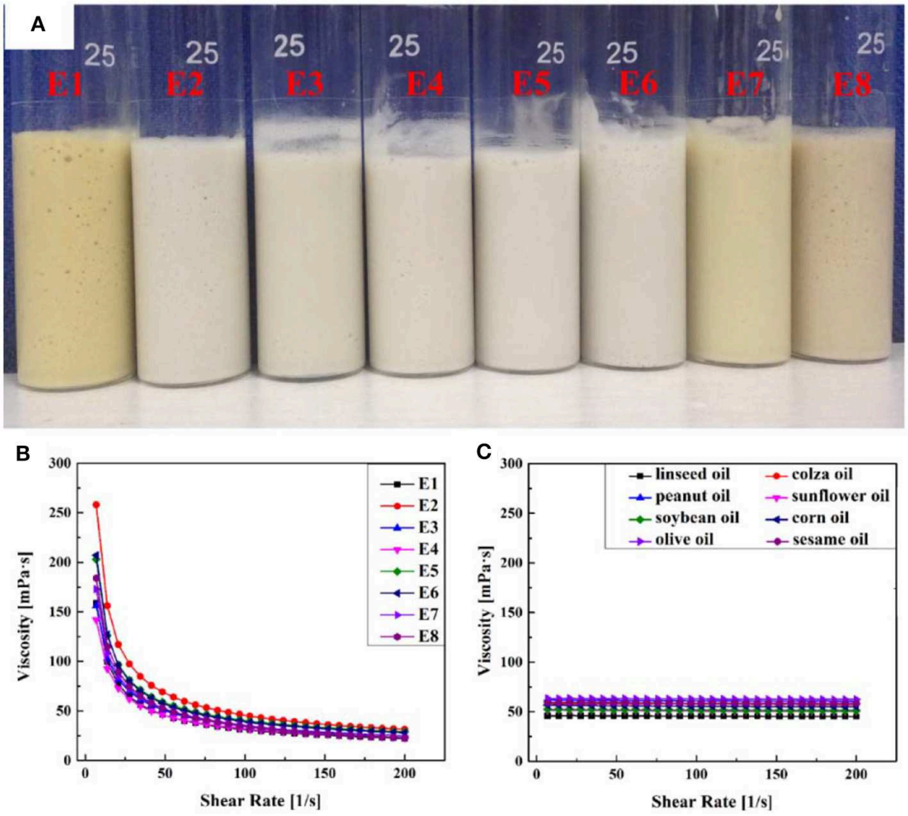

FIGURE 2 | (A) Digital photographs of Pickering emulsions prepared with various vegetable oils. Rheological characterization of **(B)** the corresponding Pickering emulsions and **(C)** the different vegetable oils.

thus it was essential to find the appropriate duration for an emulsion process. As shown in **Figure 1B**, stabilized emulsions were obtained after being stirred for 7 min, and thus the optimal duration of the emulsion process was 7 min.

The Effect of the Oil Phase

The effect of eight types of vegetable oil on the emulsions was also studied. Digital photographs and rheological characterization of Pickering emulsions with various vegetable oils are shown in **Figure 2**. As depicted in **Figure 2A**, the emulsions prepared with eight kinds of vegetable oils maintained good stability for at least 1 month after being agitated at 10,000 rpm for 7 min, and no oil–water separation was observed. The different colors of the eight emulsions might be attributable to the different original colors of the oil phases. A sliding test indicated that the emulsions could stay on a vertical glass tube without any flow, which suggested that the emulsions formed were typical gel emulsions and that the oil drops were closely packed, which was also verified from their optical micrographs (**Figure 3**). It was also confirmed that the increase in the viscosity of emulsions could inhibit the coalescence of emulsion droplets and improve the stability of emulsion (Ikem et al., 2008). Therefore, a stress-controlled rheometer was used to evaluate the viscosity of the prepared Pickering emulsions. The rheological characterization reveals that there was no significant difference in the viscosity of the eight emulsions (**Figure 2B**) and the viscosity of the corresponding vegetable oils (**Figure 2C**).

The optical microscope images of the obtained emulsions are shown in **Figure 3**. It was found that the droplets of all eight emulsions accumulated together compactly and that the average droplet diameters of the eight emulsion droplets were almost the same (**Table 1**). The lack of visible difference between the emulsion diameters might be another important reason for the similar viscosity of the emulsions. The above experimental results proved that type of oil did not have a significant influence on the emulsion, and thus all vegetable oils used in this research were suitable for preparing a stable O/W Pickering emulsion.

Formation of CMC-g-PAM/ATP

The porous monoliths were obtained by free radical polymerization of the reactants in the continuous phase using APS as the initiator. The decomposition of APS at 65°C induced the CMC to generate macro-radicals, and the monomer of AM was grafted onto CMC. The three-dimensional net structure polymer was then formed in the presence of the crosslinker MBA. After the reaction was finished, the products were Soxhlet extracted with acetone immediately for 10 h to remove the oil phase, and monoliths with porous morphology were observed (**Figure 4**). This suggested that the incorporation of appropriate ATP and a low dosage of T-20 as a Pickering stabilizer was

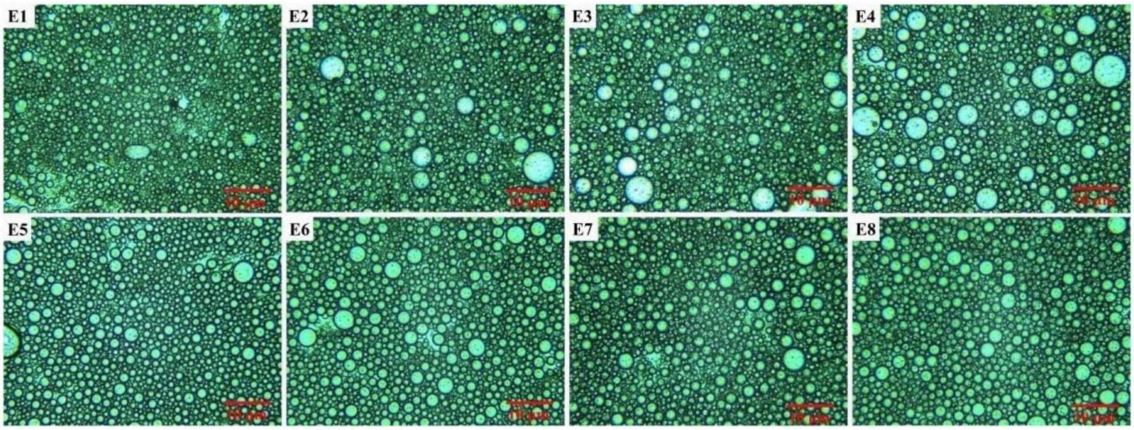

FIGURE 3 | Optical microscope images of Pickering emulsions prepared with different oil phases.

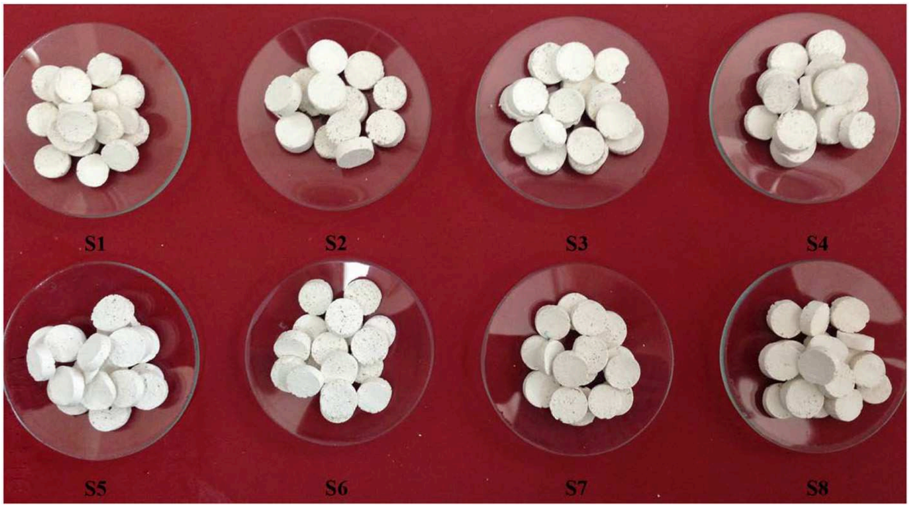

FIGURE 4 | Digital photographs of the porous CMC-*g*-PAM/ATP hydrogels prepared through the use of Pickering-MIPEs with various vegetable oils.

successful in forming a porous structure inside hydrogels during the polymerization and post-treatment. The elution of the oil phase contributed to the formation of macropores, while the thinner monomer layer between neighboring droplets resulted in open pore throats between neighboring macropores (Xu et al., 2016; Wang et al., 2017b).

FTIR spectra of AM, CMC, and CMC-*g*-PAM/ATP before and after hydrolysis are compared in **Figure 5** to confirm the formation of the target porous adsorbent. The absorption band of CMC at 3,434 cm^{-1} (the OH stretching vibration of CMC) overlapped with the O-H stretching vibrations of the (Fe, Mg) O-H and (Al, Mg) O-H of ATP (Wang et al., 2015) after the reaction and appeared at 3,401 cm^{-1} in the spectrum in **Figure 5C**. The band of AM at 1,673 cm^{-1} assigned to C=O stretching vibration and the band of CMC at 1,603 cm^{-1} attributed to asymmetric stretching vibration of carboxylate overlapped and appeared at 1,663 cm^{-1} in the spectrum of CMC-*g*-PAM/ATP (**Figure 5C**), indicating successful grafting of the AM monomer onto the CMC (Xiao et al., 2015). The absorption band at 1,036 cm^{-1} (**Figure 5C**) was assigned to the Si-O-Si asymmetric stretching vibration, indicating the existence of ATP in the porous monolith. After hydrolysis, the characteristic absorption at 3,196 cm^{-1} (**Figure 5C**) ascribed to -NH_2 groups disappeared, and the O-H stretching vibration presented an obvious blue shift and appeared at 3,433 cm^{-1}. Furthermore, the characteristic absorption band of the C=O in amide at 1,663 cm^{-1} weakened, and the absorption peaks at 1,562 and 1,405 cm^{-1}, which were assigned to asymmetric and symmetric stretching vibration of -COO^- groups, appeared after hydrolysis, indicating that the amide groups were successfully converted into carboxyl groups (Ghorai et al., 2014). Moreover, the absorption band of Si-O-Si asymmetric stretching vibration of ATP persisted after hydrolysis.

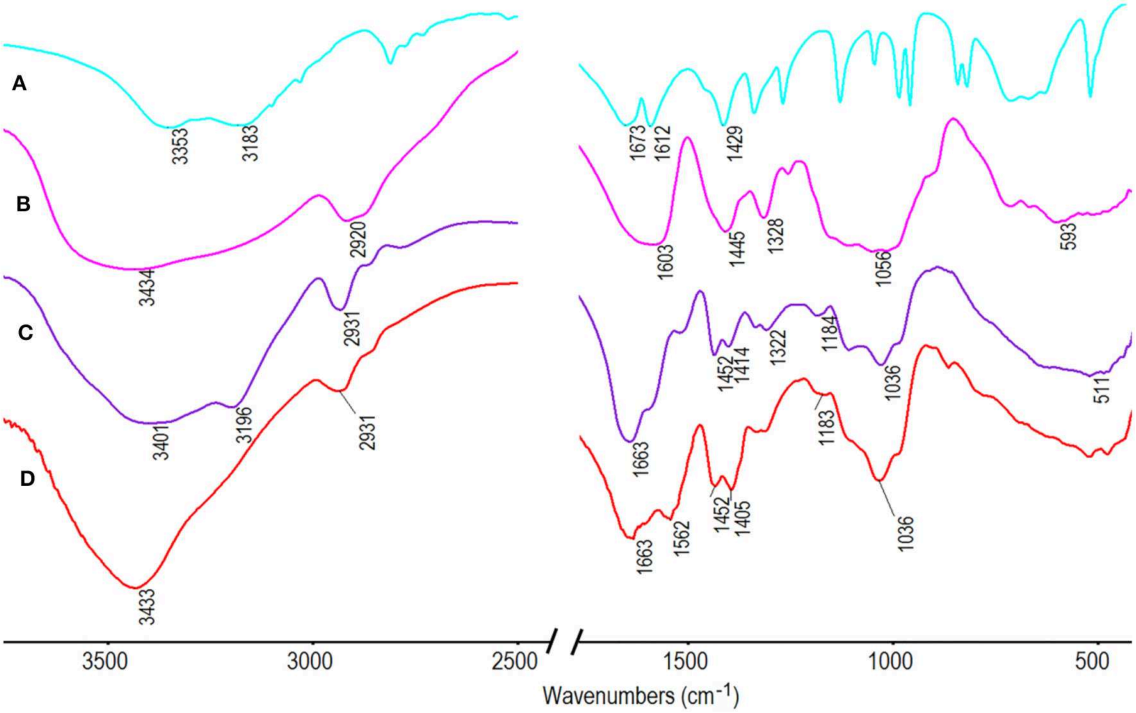

FIGURE 5 | FTIR spectra of **(A)** AM; **(B)** CMC and CMC-*g*-PAM/ATP **(C)** before and **(D)** after hydrolysis.

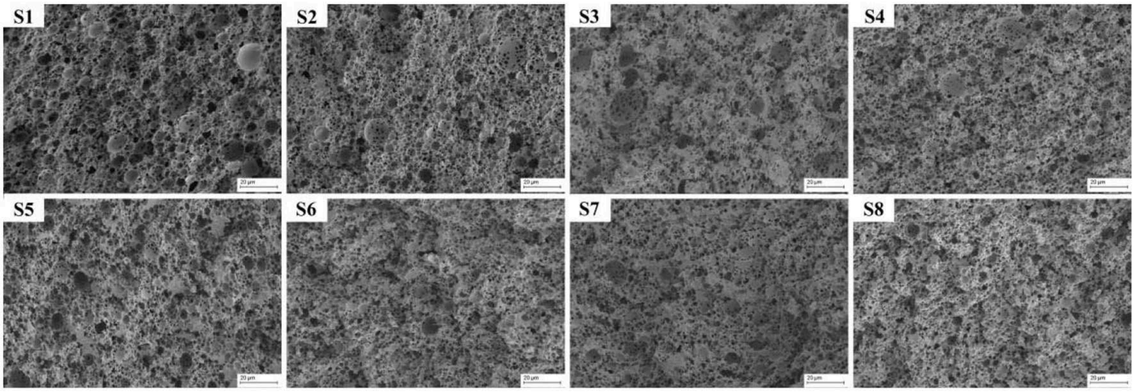

FIGURE 6 | SEM images of porous CMC-*g*-PAM/ATP prepared with different oils.

The surface morphologies of the porous materials prepared by Pickering MIPEs with different vegetable oils are exhibited in **Figure 6**. The SEM images of eight porous materials presented similar surface morphologies, which indicated that the effect of the type of vegetable oil on the pore structure was almost negligible. All of the materials exhibit interconnected and distinct hierarchical porous structures, with both macropores and pore throats clearly visible in their SEM images. The statistical data in **Table 1** indicated that the average macropore sizes of the eight materials were relatively uniform about 2.3 μm, which was consistent with the droplet size of the corresponding emulsions, indicating that there was no structural shrinkage during the polymerization and post-treatment process. In general, the macropore size of materials prepared by the high internal phase emulsion template method is about 100–700 μm (Ikem et al., 2010b). By contrast, the macropore diameter of materials prepared in this paper was greatly reduced, which could effectively improve the specific surface area of the materials.

Adsorption Properties of CMC-g-PAM/ATP for Ce(III) and Gd(III)

The adsorption properties of CMC-*g*-PAM/ATP for Ce(III) and Gd(III) were next evaluated. As shown in **Figure 7A**, all adsorbents exhibited almost the same adsorption efficiency, with

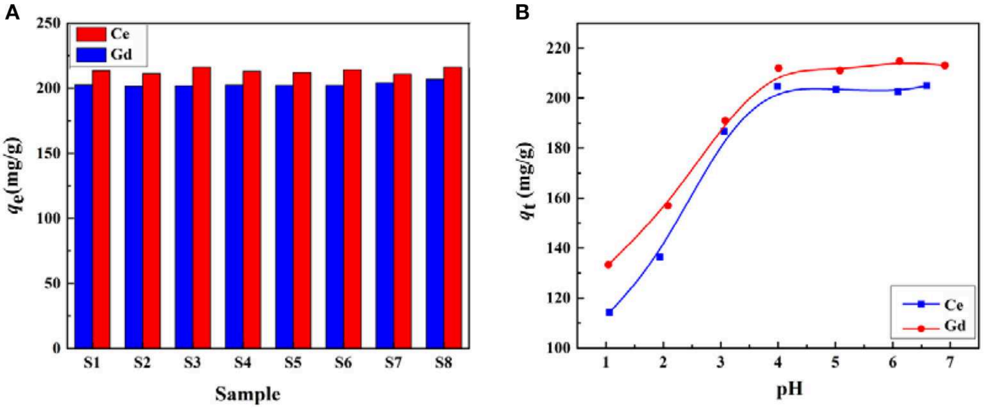

FIGURE 7 | (A) Effect of oil phase on the adsorption capacity of the porous CMC-*g*-PAM/ATP materials for Ce(III) and Gd(III). **(B)** Effect of pH on the adsorption capacity of CMC-*g*-PAM/ATP S2 for Ce(III) and Gd(III).

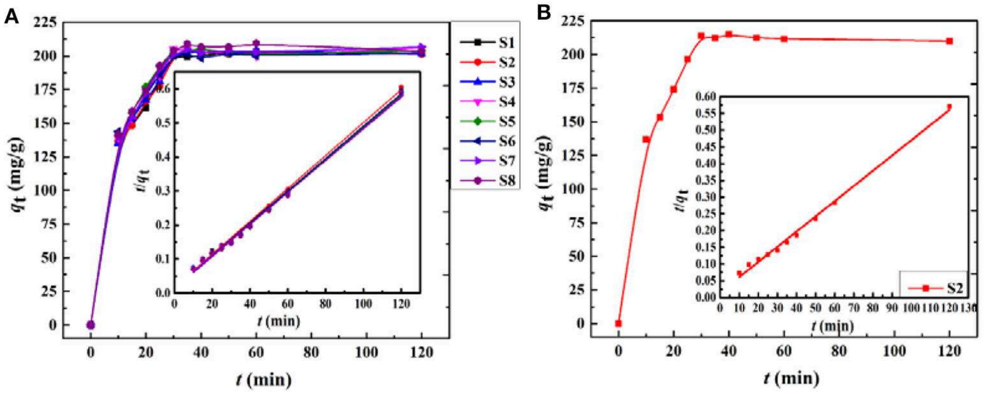

FIGURE 8 | Adsorption kinetics curves of the porous CMC-*g*-PAM/ATP materials for **(A)** Ce(III) and **(B)** Gd(III) (inset plot of t/q_t vs. t for the pseudo-second-order equation).

adsorption capacities for Ce(III) and Gd(III) of around 205 and 216 mg/g, respectively. The similar adsorption properties for Ce(III) and Gd(III) might be due to the similar chemical compositions and porous structures of the as-prepared porous monoliths. The results indicate that the Pickering MIPEs prepared in this study exhibit wide applicability and can be prepared from various kinds of vegetable oils.

Effect of pH on Adsorption of Ce(III) and Gd(III)

To determine the effects of pH on adsorption of Ce(III) and Gd(III), the adsorption experiments were carried out at different pH values; the results are shown in **Figure 7B**. When the pH value was higher than 7.0, the metal ions involved were hydrolyzed, so pH values from 1 to 7 were selected for the tests. The adsorption properties of monoliths were highly pH-dependent, and the adsorption capacity was mainly governed by the number of charged functional groups on the backbone. It was clear that the adsorption capacity of the CMC-*g*-PAM/ATP to Ce(III) and Gd(III) presented a remarkable increase with an increase in pH up to 4.0, above which the adsorption capacity became stable. This phenomenon might be attributable to the protonation of –COO$^-$ under the strongly acidic conditions (Wang W. et al., 2013). The protonation would reduce the complexation ability of the adsorbent with metal ions (Ijagbemi et al., 2010). With the increase in pH value, a part of the –COOH groups transformed into –COO$^-$ groups, which had stronger complexing ability with metal ions than –COOH, so the higher pH value facilitated the adsorption capacity of the adsorbents. As the initial pH increased from 4.0 to 7.0, all the carboxylic groups of the adsorbent had been dissociated and charged, and thus a constant adsorption capacity was observed.

Effect of Contact Time on Adsorption of Ce(III) and Gd(III)

The adsorption kinetics of the adsorbent is a significant parameter for practical application. The kinetic adsorption curves of the porous monoliths with different oil phases are shown in **Figure 8**. The figure demonstrates that the adsorption rate of the porous monoliths for the metal ions increased remarkably in the first 30 min and that the degree of adsorption

TABLE 2 | Adsorption kinetic parameters for adsorption of Ce(III) and Gd(III) onto CMC-*g*-PAM/ATP.

	Pseudo-first-order equation			Pseudo-second-order equation				
Sample	$q_{e,cal}$ (mg/g)	$K_1 \times 10^{-2}$ (min^{-1})	R^2	$q_{e,cal}$ (mg/g)	$K_2 \times 10^{-3}$ (g/mg min)	R^2	$q_{e,exp}$ (mg/g)	Metal
S1	45.99	04.34	0.4823	212.28	1.19	0.9959	203.58	Ce(III)
S2	36.84	3.29	0.2594	207.12	1.30	0.9973	205.61	Ce(III)
S3	37.91	3.73	0.3651	211.15	1.35	0.9971	204.37	Ce(III)
S3	91.89	7.39	0.4706	214.61	1.22	0.9975	206.17	Ce(III)
S5	33.72	3.64	0.3197	211.40	1.57	0.9977	205.73	Ce(III)
S6	46.79	3.14	0.5010	210.46	1.42	0.9977	202.56	Ce(III)
S7	123.97	8.35	0.7361	215.43	1.23	0.9975	206.65	Ce(III)
S8	23.99	2.85	0.0633	211.93	1.78	0.9958	208.94	Ce(III)
S2	38.93	3.02	0.2651	220.26	1.33	0.9943	215.15	Gd(III)

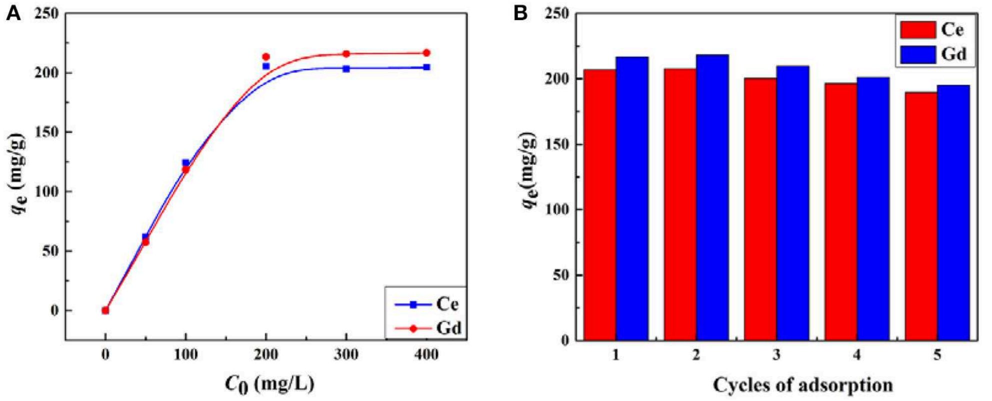

FIGURE 9 | (A) Effect of the initial Ce(III) and Gd(III) concentrations on the adsorption capacity of porous material S2 and **(B)** the amount adsorbed for Ce(III) and Gd(III) as a function of the adsorption-desorption cycle.

reached a steady state after 30 min. The adsorption curves also showed that the adsorption rates of the eight materials for Ce(III) were basically consistent, and thus only S2 was selected as a representative to evaluate the adsorption rate for Gd(III). The adsorption tendency for Gd(III) showed that S2 also had a fast adsorption rate for Gd(III) and reached adsorption equilibrium by 30 min, which was similar to the adsorption behavior for Ce(III). The fast adsorption rate profited from the interconnected pores of the materials, which efficiently reduced the mass transfer resistance and exposed more binding sites for metal ions, thus improving the accessibility of metal ions to the adsorbent (Gupta et al., 2014).

In order to examine the potential rate-controlling steps during the adsorption process, pseudo-first-order (Equation 2) and pseudo-second-order (Equation 3) models (Ghaedi et al., 2015) were tested to fit the experimental data. The equations of the kinetic models are expressed as follows:

$$\mathrm{Log}(qe - qt) = \log qe - (k1/2.303)t \tag{2}$$

$$t/qt = 1/(k2 \times qe2) + t/qe \tag{3}$$

where q_t is the adsorption capacity for Ce(III) or Gd(III) at time *t,* and q_e is the equilibrium adsorption capacity. k_1 (min^{-1}) and k_2 [g/(mg min)] are the adsorption rate constants of the pseudo-first-order and pseudo-second-order models, respectively. As shown in **Table 2**, the adsorption of Ce(III) and Gd(III) onto the porous monolith adsorbents followed the pseudo-second-order model rather than pseudo-first-order model by comparison with their linear correlation coefficients (R^2). In addition, the calculated q_e values ($q_{e,cal}$) with the pseudo-second-order kinetic model were much closer to the experimental values ($q_{e,exp}$). This suggested that the adsorptions of the porous monoliths for Ce(III) and Gd(III) were probably controlled by a chemical adsorption process (Zhou S. et al., 2014; Zhou Y. et al., 2014).

Effect of Initial Concentration on Adsorption of Ce(III) and Gd(III)

The influence of the initial concentrations of metal ions on the adsorption capacity of the materials was investigated in the range of 50–400 mg/L. As shown in **Figure 9A**, the saturation adsorptions of the porous monolith (S2) for Ce(III) and Gd(III) were reached when the initial concentration increased to 200 mg/L, and then the increasing trend flattened. The maximum

TABLE 3 | Adsorption isotherm constants of Ce(III) and Gd(III) onto CMC-*g*-PAM/ATP.

Metal	Langmuir model				Freundlich model		
	$q_{e,\,exp}$ (mg/g)	q_m (mg/g)	*b* (L/mg)	R^2	K	*n*	R^2
Ce^{3+}	205.48	205.56	0.7734	0.9999	86.68	5.57	0.6563
Gd^{3+}	216.73	224.52	0.1489	0.9973	56.73	3.58	0.6148

TABLE 4 | Comparison of adsorption capacities (q_m, mg/g) and rates (T, min) of various adsorbents for Ce(III) and Gd(III).

Adsorbent	Ce(III)		Gd(III)		References
	q_m (mg/g)	T (min)	q_m (mg/g)	T (min)	
Zn/Al LDH-intercalated cellulose	96.25	10	–	–	Iftekhar et al., 2017
Corn style	180.20	240	–	–	Jaya et al., 2014
Prawn carapace	218.30	360	–	–	Jaya et al., 2014
Mesoporous conjugate adsorbent	192.31	25	–	–	Awual et al., 2013
Loofah fiber-*g*-acrylic acid (LF-AA)	527.5	120	–	–	Liu et al., 2017
Wheat straw	298.60	100	–	–	Zhou et al., 2016
Poly(allylamine)/silica composite	111.8	60	–	–	Zhou S. et al., 2014
Colloidal graphene oxide	–	–	286.86	30	Chen et al., 2014
1,2-HOPO-SAMMS	–	–	80	30	Yantasee et al., 2010
Cross-linked polyvinyl amidoxime fiber	–	–	14.83	150	Yang et al., 2018
By-pass cement	–	–	100		Ali et al., 2011
Polyethyleneglycol (phosphomolybdate and tungstate)	–	–	57	–	Zhang et al., 2009
CTS-*g*-(AA-*co*-SS)/ISC hydrogel	174.05	20	223.79	20	Wang et al., 2017a
Kenaf cellulose-based poly(hydroxamic acid)	245	–	220	–	Rahman et al., 2017
CMC-*g*-PAM/ATP	205.48	30	216.73	30	This study

adsorption capacities for Ce(III) and Gd(III) were 205.48 and 216.73 mg/g, respectively. As the concentrations of Ce(III) and Gd(III) increased, the inside and outside concentration gradient of the material increased, thus strengthening the adsorption driving force, which was beneficial for Ce(III) and Gd(III) to overcome the transfer resistance and spread to the interior of the 3D network. Once all the adsorption sites of the adsorbent were completely occupied by metals ions, adsorption equilibrium was reached.

The adsorption process was simulated by the Langmuir (Equation 4) and Freundlich (Equation 5) isotherm models (Mittal et al., 2010; Chen et al., 2019). The respective equations are as follows.

$$\frac{C_e}{q_e} = \frac{1}{q_m b} + \frac{C_e}{q_m} \tag{4}$$

$$\log q_e = \log K + (1/n) \log C_e \tag{5}$$

where C_e (mg/L) represents the equilibrium concentration of metal ions, and q_e and q_m are the adsorption capacity (mg/g) of adsorbent at any time and in equilibrium state (mg/g), respectively. b (L/mg) is the Langmuir constant related to the affinity of binding sites (mg), which can be calculated by the slope ($1/\ q_m$) and intercept ($1/\ q_m \times$ b) of plot ($C_e/\ q_e$) vs. C_e. *K* is a Freundlich constant related to adsorption capacity, and *n* is a dimensionless constant representing an index of adsorption intensity or surface heterogeneity. *K* and *n* can also be calculated by the slope ($1/n$) and intercept ($\log K$) of plot ($\log q_e$) vs. $\log C_e$.

The related isotherm parameters and correlation coefficients (R^2) were calculated and are summarized in **Table 3**. The fitting results proved that the relevant parameters of the Langmuir isothermal model (Ce(III): 0.9999, Gd(III): 0.9973) were much higher than those of the Freundlich isothermal model (Ce(III): 0.6563, Gd(III): 0.6148). The maximum adsorption capacities for Ce(III) and Gd(III) calculated by the Langmuir model were 205.56 and 224.52 mg/g, respectively, which were very close to the experimental values of 205.48 and 216.73 mg/g, respectively. The above analysis indicates that the Langmuir model was suitable for fitting the adsorption process of rare earth metals onto the adsorbent, suggesting that the binding sites were evenly distributed on the adsorbent surface, as these binding sites exhibited the same affinity for adsorption as a single molecular layer (Wang J. et al., 2013). Moreover, it can also be seen from **Table 4** that the saturated adsorption capacities of the macroporous monolith prepared in this study were much higher than those of the adsorbents reported previously, and so was the adsorption rate.

Reusability of CMC-g-PAM/ATP for Ce(III) and Gd(III)

Reusability is an important parameter for evaluating the properties of an adsorbent. In this section, S2 was selected to investigate the regeneration performance. Given that the prepared porous adsorbent contains a large number of carboxyl groups, which are sensitive to H^+, hydrochloric acid (0.5 mol/L) was selected as the eluent for desorption of Ce(III) and Gd(III) from CMC-*g*-PAM/ATP after adsorption. After the desorption experiment, the material was activated with 0.1 mol/L NaOH and used for the next adsorption process. As shown in **Figure 9B**, the adsorption capacities of the adsorbent in the second cycle were a little higher than the initial capacities, suggesting that some adsorption sites can be created during the regeneration process; a similar phenomenon was also found in earlier studies (Zhu et al., 2015). After the second cycle, there was only a subtle decrease in the adsorption capacities for Ce(III) and Gd(III). Furthermore, the prepared porous material maintained relatively high adsorption capacities to Ce(III) and Gd(III) during the whole consecutive adsorption-desorption processes, indicating that the as-prepared hydrogel CMC-*g*-PAM/ATP exhibited excellent reusability.

CONCLUSION

A convenient, economical, and environmentally friendly strategy was developed for the preparation of interconnected porous adsorbent of CMC-*g*-PAM/ATP with vegetable oil-in-water Pickering-MIPE templates that was stabilized by raw ATP and a trace amount of T-20. The stability of the emulsion could be facilely modulated by the emulsification rate and duration. The type of vegetable oil has no significant influence on either the properties of the emulsion or the porous structure of the material. SEM images indicated that all materials derived via the Pickering-MIPE template method exhibited an excellent interconnected hierarchical porous structure that was not inferior to that prepared with HIPE. Due to the highly permeable porous structure and abundant functional groups, the materials prepared presented promising potential as excellent adsorbents for the rapid extraction of Ce(III) and Gd(III) from aqueous solution. Furthermore, the materials still exhibited excellent reusability after five consecutive adsorption-desorption processes. This work can be taken as a new contribution to efforts to develop a new pathway to construct porous adsorbents for the adsorption and enrichment of REEs.

DATA AVAILABILITY STATEMENT

All datasets generated for this study are included in the article/supplementary material.

AUTHOR CONTRIBUTIONS

FW contributed to the experimental process and data analysis, wrote the paper, and drew all the figures. YZ contributes to the data analysis and revision of the paper. AW contributed to the experimental design and revision of the paper.

FUNDING

The authors are grateful for financial support from the National Natural Science Foundation of China (21706267), the Major Projects of the National Natural Science Foundation of Gansu, China (18JR4RA001), a Scientific Research Project of Beibu Gulf University, China (17KYQD57), a College Scientific Research Project of the Education department of Guangxi, China (18KY0610), and the Natural Science Fund for Distinguished Young Scholars of Guangxi Province (2017GXNSFFA198007).

REFERENCES

Ali, O., Osman, H., Sayed, S., and Shalabi, M. (2011). The removal of some rare earth elements from their aqueous solutions on by-pass cement dust (BCD). *J. Hazard. Mater.* 195, 62–67. doi: 10.1016/j.jhazmat.2011.08.014

Alshameri, A., He, H., Xin, C., Zhu, J., Xinghu, W., Zhu, R., et al. (2019). Understanding the role of natural clay minerals as effective adsorbents and alternative source of rare earth elements: adsorption operative parameters. *Hydrometallurgy* 185, 149–161. doi: 10.1016/j.hydromet.2019.02.016

Anastopoulos, I., Bhatnagar, A., and Lima, E. C. (2016). Adsorption of rare earth metals: A review of recent literature. *J. Mol. Liq.* 221, 954–962. doi: 10.1016/j.molliq.2016.06.076

Awual, M. R., Yaita, T., and Shiwaku, H. (2013). Design a novel optical adsorbent for simultaneous ultra-trace cerium(III) detection, sorption and recovery. *Chem. Eng. J.* 228, 327–335. doi: 10.1016/j.cej.2013.05.010

Babu, C. M., Binnemans, K., and Roosen, J. (2018). EDTA-functionalized activated carbon for the adsorption of rare earths from aqueous solutions. *Ind. Eng. Chem. Res.* 57, 1487–1497. doi: 10.1021/acs.iecr.7b04274

Chatterjee, S., Lee, M. W., and Woo, S. H. (2009). Influence of impregnation of chitosan beads with cetyl trimethyl ammonium bromide on their structure and adsorption of congo red from aqueous solutions. *Chem. Eng. J.* 155, 254–259. doi: 10.1016/j.cej.2009.07.051

Chen, H., Sharma, S. K., Sharma, P. R., Yeh, H., Johnson, K., and Hsiao, B. S. (2019). Arsenic(III) removal by nanostructured dialdehyde cellulose-cysteine microscale and nanoscale Fibers. *ACS Omega*. 4, 22008–22020. doi: 10.1021/acsomega.9b03078

Chen, W., Wang, L., Zhuo, M., Liu, Y., Wang, Y., and Li, Y. (2014). Facile and highly efficient removal of trace Gd(III) by adsorption of colloidal graphene oxide suspensions sealed in dialysis bag. *J. Hazard. Mater.* 279, 546–553. doi: 10.1016/j.jhazmat.2014.06.075

Colla, E., do Amaral Sobral, P. J., and Menegalli, F. C. (2006). Amaranthus cruentus flour edible films: influence of stearic acid addition, plasticizer concentration, and emulsion stirring speed on water vapor permeability and mechanical properties. *J. Agr. Food Chem.* 54, 6645–6653. doi: 10.1021/jf0611217

Delrish, E., Khanchi, A., Outokesh, M., Tayyebi, A., and Tahvildari, K. (2014). Study on the adsorption of samarium and gadolinium ions by a biopolymer microcapsules containing DEHPA/ TOPO extract. *J. Appl. Chem. Res.* 220, 448–455. doi: 10.1016/j.snb.2015.05.101

Gautier, F., Destribats, M., Perrier-Cornet, R., Dechézelles, J.-F., Giermanska, J., Héroguez, V., et al. (2007). Pickering emulsions with stimulable particles: from highly-to weakly-covered interfaces. *Phys. Chem. Chem. Phys.* 9, 6455–6462. doi: 10.1039/b710226g

Ghaedi, M., Hajjati, S., Mahmudi, Z., Tyagi, I., Agarwal, S., Maity, A., et al. (2015). Modeling of competitive ultrasonic assisted removal of the dyes-Methylene blue and Safranin-O using Fe_3O_4 nanoparticles. *Chem. Eng. J*, 268, 28–37. doi: 10.1016/j.cej.2014.12.090

Ghorai, S., Sarkar, A., Raoufi, M., Panda, A. B., Schönherr, H., and Pal, S. (2014). Enhanced removal of methylene blue and methyl violet dyes from aqueous solution using a nanocomposite of hydrolyzed polyacrylamide grafted xanthan gum and incorporated nanosilica. *ACS Appl. Mater. Inter.* 6, 4766–4777. doi: 10.1021/am4055657

Gładysz-Płaska, A., Majdan, M., and Grabias, E. (2014). Adsorption of La, Eu and Lu on raw and modified red clay. *J. Radioanal. Nucl. Chem.* 301, 33–40. doi: 10.1007/s10967-014-3111-4

Gudarzi, M. M., and Sharif, F. (2011). Self assembly of graphene oxide at the liquid–liquid interface: a new route to the fabrication of graphene based composites. *Soft Matter.* 7, 3432–3440. doi: 10.1039/c0sm01311k

Gupta, V. K., Nayak, A., Agarwal, S., and Tyagi, I. (2014). Potential of activated carbon from waste rubber tire for the adsorption of phenolics: effect of pre-treatment conditions. *J. Colloid. Interface. Sci*, 417, 420–430. doi: 10.1016/j.jcis.2013.11.067

Hou, H., Wang, Y., Xu, J., and Chen, J. (2013). Solvent extraction of La(III) with 2-ethylhexyl phosphoric acid-2-ethylhexyl ester (EHEHPA) by membrane dispersion micro-extractor. *J. Rare Earth.* 31, 1114–1118. doi: 10.1016/S1002-0721(12)60413-X

Iftekhar, S., Srivastava, V., and Sillanpää, M. (2017). Synthesis and application of LDH intercalated cellulose nanocomposite for separation of rare earth elements (REEs). *Chem. Eng. J.* 309, 130–139. doi: 10.1016/j.cej.2016.10.028

Ijagbemi, C. O., Baek, M. H., and Kim, D. S. (2010). Adsorptive performance of un-calcined sodium exchanged and acid modified montmorillonite for Ni^{2+} removal: equilibrium, kinetics, thermodynamics and regeneration studies. *J. Hazard. Mater.* 174, 746–755. doi: 10.1016/j.jhazmat.2009.09.115

Ikem, V. O., Angelika, M., Horozov, T. S., and Alexander, B. (2010a). Highly permeable macroporous polymers synthesized from pickering medium and high internal phase emulsion templates. *Adv. Mater.* 22, 3588–3592. doi: 10.1002/adma.201000729

Ikem, V. O., Menner, A., and Bismarck, A. (2008). High Internal Phase Emulsions Stabilized Solely by Functionalized Silica Particles. *Angew. Chem. Int. Ed.* 47, 8277–8279. doi: 10.1002/anie.200802244

Ikem, V. O., Menner, A., and Bismarck, A. (2010b). High-porosity macroporous polymers sythesized from titania-particle-stabilized medium and high internal phase emulsions. *Langmuir* 26, 8836–8841. doi: 10.1021/la9046066

Jaya, S. V. C., Das, D., and Das, N. (2014). Optimization of parameters for cerium(III) biosorption onto biowaste materials of animal and plant origin using 5-level Box-Behnken design:Equilibrium, kinetic, thermodynamic and regeneration studies. *J. Rare Earth.* 32, 745–757. doi: 10.1016/S1002-0721(14)60136-8

Jiaxi, H., Kaijun, X., Zhongjie, D., Wei, Z., and Chen, Z. (2015). β-Cyclodextrin functionalized polystyrene porous monoliths for separating phenol from wastewater. *Carbohyd. Polym.* 120, 85–91. doi: 10.1016/j.carbpol.2014.12.011

Klemm, D., Cranston, E. D., Fischer, D., Gama, M., Kedzior, S. A., Kralisch, D., et al. (2018). Nanocellulose as a natural source for groundbreaking applications in materials science: today's state. *Mater. Today* 21, 720–748. doi: 10.1016/j.mattod.2018.02.001

Klemm, D., Heublein, B., Fink, H. P., and Bohn, A. (2005). Cellulose: fascinating biopolymer and sustainable raw material. *Angew. Chem. Int. Ed*. 44, 3358–3393. doi: 10.1002/anie.200460587

Liatsou, I., Efstathiou, M., and Pashalidis, I. (2015). Adsorption of trivalent lanthanides by marine sediments. *J. Radioanal. Nucl. Chem.* 304, 41–45. doi: 10.1007/s10967-014-3448-8

Liu, C., Yan, C., Zhou, S., and Ge, W. (2017). Fabrication of sponge biomass adsorbent through UV-induced surface-initiated polymerization for the adsorption of Ce(III) from wastewater. *Water Sci. Technol.* 75:2755. doi: 10.2166/wst.2017.144

Ma, L., Luo, X., Ning, C., Xue, Y., Zhu, S., Zhen, F., et al. (2014). Facile fabrication of hierarchical porous resins via high internal phase emulsion and polymeric porogen. *Appl. Surf. Sci.* 305, 186–193. doi: 10.1016/j.apsusc.2014.03.036

Maranescu, B., Lupa, L., and Visa, A. (2019). Synthesis, characterization and rare earth elements adsorption properties of phosphonate metal organic frameworks. *Appl. Surf. Sci.* 481, 83–91. doi: 10.1016/j.apsusc.2019.03.067

Mittal, A., Mittal, J., Malviya, A., and Gupta, V. K. (2010). Removal and recovery of Chrysoidine Y from aqueous solutions by waste materials. *J. Colloid Interf. Sci.* 344, 497–507. doi: 10.1016/j.jcis.2010.01.007

Moldoveanu, G. A., and Papangelakis, V. G. (2012). Recovery of rare earth elements adsorbed on clay minerals: I. Desorption mechanism. *Hydrometallurgy* 117-118, 71-78. doi: 10.1016/j.hydromet.2012.02.007

Mondal, S., Ghar, A., Satpati, A. K., Sinharoy, P., Singh, D. K., Sharma, J. N., et al. (2019). Recovery of rare earth elements from coal fly ash using TEHDGA impregnated resin. *Hydrometallurgy* 185, 93-101. doi: 10.1016/j.hydromet.2019.02.005

Ogata, T., Narita, H., and Tanaka, M. (2015). Adsorption behavior of rare earth elements on silica gel modified with diglycol amic acid. *Hydrometallurgy* 152, 178–182. doi: 10.1016/j.hydromet.2015.01.005

Oh, B. H. L., Alexander, B., and Chan-Park, M. B. (2014). High internal phase emulsion templating with self-emulsifying and thermoresponsive chitosan-graft-PNIPAM-graft-oligoproline. *Biomacromolecules* 15, 1777–1787. doi: 10.1021/bm500172u

Page, M. J., Quinn, J. E., and Soldenhoff, K. H. (2019). The impact of sulfate ions on the ion exchange of rare earth elements. *Hydrometallurgy* 186, 12–20. doi: 10.1016/j.hydromet.2019.03.003

Rahman, M. L., Biswas, T. K., Sarkar, S. M., Yusoff, M. M., Sarjadi, M. S., Arshad, S. E., et al. (2017). Adsorption of rare earth metals from water using a kenaf cellulose-based poly(hydroxamic acid) ligand. *J. Mol. Liq.* 243, 616–623. doi: 10.1016/j.molliq.2017.08.096

Rajendran, S., Khan, M. M., Gracia, F., Qin, J., Gupta, V. K., and Arumainathan, S. (2016). Ce^{3+}-ion-induced visible-light photocatalytic degradation and electrochemical activity of ZnO/CeO_2 nanocomposite. *Sci Rep*. 6:31641. doi: 10.1038/srep31641

Ren, H., Gao, Z., Wu, D., Jiang, J., Sun, Y., and Luo, C. (2016). Efficient Pb(II) removal using sodium alginate-carboxymethyl cellulose gel beads: preparation, characterization, and adsorption mechanism. *Carbohyd. Polym.* 137, 402–409. doi: 10.1016/j.carbpol.2015.11.002

Saravanan, R., Joicy, S., Gupta, V. K., Narayanan, V., and Stephen, A. (2013). Visible light induced degradation of methylene blue using CeO_2/V_2O_5 and CeO_2/CuO catalysts. *Mater. Sci. Eng. C* 33, 4725–4731. doi: 10.1016/j.msec.2013.07.034

Schirhagl, R. (2014). Bioapplications for molecularly imprinted polymers. *Anal. Chem.* 86, 250–261. doi: 10.1021/ac401251j

Sharma, P. R., Joshi, R., Sharma, S. K., and Hsiao, B. S. (2017). A simple approach to prepare carboxycellulose nanofibers from untreated biomass. *Biomacromolecules*. 18, 2333–2342. doi: 10.1021/acs.biomac.7b00544

Sullivan, A. P., and Kilpatrick, P. K. (2002). The effects of inorganic solid particles on water and crude oil emulsion stability. *Ind. Eng. Chem. Res.* 41, 3389–3404. doi: 10.1021/ie010927n

Survey, U. S. G. (2014). *Rare Earths, Mineral Commodity Summaries*, 128–129.

Voßenkaul, D., Stoltz, N., Meyer, F. M., and Friedrich, B. (2015). "Extraction of rare earth elements from non- chinese ion adsorption clays," in *European Metallurgical Conference* (Düsseldorf).

Wang, F., Wang, W., Zhu, Y., and Wang, A. (2017a). Evaluation of Ce(III) and Gd(III) adsorption from aqueous solution using CTS-g-(AA-*co*-SS)/ISC hybrid hydrogel adsorbent. *J. Rare Earth.* 35, 697–708. doi: 10.1016/S1002-0721(17)60966-9

Wang, F., Zhu, Y., Wang, W., Zong, L., Lu, T., and Wang, A. (2017b). Fabrication of CMC-*g*-PAM superporous polymer monoliths via eco-friendly pickering-MIPEs for superior adsorption of methyl violet and methylene blue. *Front. Chem.* 5:33. doi: 10.3389/fchem.2017.00033

Wang, J., Wei, L., Ma, Y., Li, K., Li, M., Yu, Y., et al. (2013). Collagen/cellulose hydrogel beads reconstituted from ionic liquid solution for Cu(II) adsorption. *Carbohyd. Polym.* 98, 736–743. doi: 10.1016/j.carbpol.2013.06.001

Wang, W., Kang, Y., and Wang, A. (2013). One-step fabrication in aqueous solution of a granular alginate-based hydrogel for fast and efficient removal of heavy metal ions. *J. Polym. Res.* 20, 1–10. doi: 10.1007/s10965-013-0101-0

Wang, W., Wang, F., Kang, Y., and Wang, A. (2015). Enhanced adsorptive removal of methylene blue from aqueous solution by alkali-activated palygorskite. *Water Air Soil Poll.* 226, 1–13. doi: 10.1007/s11270-015-2355-0

Xiao, J., Lu, Z., and Li, Y. (2015). Carboxymethylcellulose-supported palladium nanoparticles generated in situ from palladium (II) carboxymethylcellulose: an efficient and reusable catalyst for Suzuki-Miyaura and Mizoroki-Heck reactions. *Ind. Eng. Chem. Res.* 54, 790–797. doi: 10.1021/ie503075d

Xu, H., Zheng, X., Huang, Y., Wang, H., and Du, Q. (2016). Interconnected porous polymers with tunable pore throat size prepared via pickering high internal phase emulsions. *Langmuir* 32, 38–45. doi: 10.1021/acs.langmuir.5b03037

Yang, L., Li, C., Wang, D., Li, F., Liu, Y., Zhou, X., et al. (2019). Leaching ion adsorption rare earth by aluminum sulfate for increasing efficiency and lowering the environmental impact. *J. Rare Earth.* 37, 429–436. doi: 10.1016/j.jre.2018.08.012

Yang, P., Mykhaylyk, O. O., Jones, E. R., and Armes, S. P. (2016). RAFT dispersion alternating copolymerization of styrene with n-phenylmaleimide: morphology control and application as an aqueous foam stabilizer. *Macromolecules.* 49, 6731–6742. doi: 10.1021/acs.macromol.6b01563

Yang, T., Wang, L., Mei, L., Yang, C., and Zou, H. (2018). Cross-linked polyvinyl amidoxime fiber: a highly selective and recyclable adsorbent of gallium from Bayer liquor. *Iran. Polym. J.* 27, 1–9. doi: 10.1007/s13726-018-0635-4

Yantasee, W., Fryxell, G. E., Porter, G. A., Pattamakomsan, K., Sukwarotwat, V., Chouyyok, W., et al. (2010). Novel sorbents for removal of gadolinium-based contrast agents in sorbent dialysis and hemoperfusion: preventive approaches to nephrogenic systemic fibrosis. *Nanomed-Nanotechno.* 6, 1–8. doi: 10.1016/j.nano.2009.05.002

Ye, H., Zhang, S., Yun, Z., Chu, Y., and Chen, J. (2013). Hydrophilic polymer foams with well-defined open-cell structure prepared from pickering high internal phase emulsions. *J. Polym. Sci. Pol. Chem.*, 51, 2181–2187. doi: 10.1002/pola.26588

Yi, W., Wu, H., Wang, H., and Du, Q. (2016). Interconnectivity of macroporous hydrogels prepared via graphene oxide-stabilized pickering high internal phase emulsions. *Langmuir* 32, 982–990. doi: 10.1021/acs.langmuir.5b04477

Zhang, L., Ding, S.-D., Yang, T., Zheng, G.-C. (2009). Adsorption behavior of rare earth elements using polyethyleneglycol (phosphomolybdate and tungstate) heteropolyacid sorbents in nitric solution. *Hydrometallurgy* 99, 109–114. doi: 10.1016/j.hydromet.2009.07.002

Zhang, Y., Pan, J., Chen, Y., Shi, W., Yan, Y., and Yu, L. (2016). HIPEs template: Towards the synthesis of polymeric catalysts with adjustable porous structure, acid–base strength and wettability for biomass energy conversation. *Chem. Eng. J.* 283, 956–970. doi: 10.1016/j.cej.2015.08.090

Zhao, F., Repo, E., Meng, Y., Wang, X., Yin, D., and Sillanpää, M. (2016). An EDTA-β-cyclodextrin material for the adsorption of rare earth elements and its application in preconcentration of rare earth elements in seawater. *J. Colloid Interf. Sci.* 465, 215-224. doi: 10.1016/j.jcis.2015.11.069

Zhao, H., Xia, J., Yin, D., Luo, M., Yan, C., and Du, Y. (2019). Rare earth incorporated electrode materials for advanced energy storage. *Coordin. Chem. Rev.* 390, 32-49. doi: 10.1016/j.ccr.2019.03.011

Zhou, Q., Yan, C., and Luo, W. (2016). Preparation of a novel carboxylate-rich wheat straw through surface graft modification for efficient separation of Ce(III) from wastewater. *Mater. Design* 97, 195–203. doi: 10.1016/j.matdes.2016.02.081

Zhou, S., Li, X., Shi, Y., Alshameri, A., and Yan, C. (2014). Preparation, characterization, and Ce(III) adsorption performance of poly(allylamine)/silica composite. *Desalin. Water Treat.* 56,1–14. doi: 10.1080/19443994.2014.979239

Zhou, Y., Fu, S., Zhang, L., Zhan, H., and Levit, M. V. (2014). Use of carboxylated cellulose nanofibrils-filled magnetic chitosan hydrogel beads as adsorbents for Pb(II). *Carbohyd. Polym.* 101, 75–82. doi: 10.1016/j.carbpol.2013.08.055

Zhu, Y., Wang, W., Zheng, Y., Wang, F., and Wang, A. (2016a). Rapid enrichment of rare-earth metals by carboxymethyl cellulose-based open-cellular hydrogel adsorbent from HIPEs template. *Carbohyd. Polym.* 140, 51–58. doi: 10.1016/j.carbpol.2015.12.003

Zhu, Y., Zheng, Y., and Wang, A. (2015). Preparation of granular hydrogel composite by the redox couple for efficient and fast adsorption of La(III) and Ce(III). *J. Environ. Chem. Eng.* 3, 1416–1425. doi: 10.1016/j.jece.2014.11.028

Zhu, Y., Zheng, Y., Wang, F., and Wang, A. (2016b). Monolithic supermacroporous hydrogel prepared from high internal phase emulsions (HIPEs) for fast removal of Cu^{2+} and Pb^{2+}. *Chem. Eng. J.* 284, 422–430. doi: 10.1016/j.cej.2015.08.157

Conflict of Interest: The authors declare that the research was conducted in the absence of any commercial or financial relationships that could be construed as a potential conflict of interest.

frontiers
in Environmental Science

ORIGINAL RESEARCH
published: 08 July 2020
doi: 10.3389/fenvs.2020.00056

Functionalized Sawdust-Derived Cellulose Nanocrystalline Adsorbent for Efficient Removal of Vanadium From Aqueous Solution

Bongiwe Zulu[1], *Opeyemi A. Oyewo*[1*], *Bruce Sithole*[2], *Taile Y. Leswifi*[3] and *Maurice S. Onyango*[1*]

[1] *Department of Chemical, Metallurgical and Materials Engineering, Tshwane University of Technology, Pretoria, South Africa,* [2] *Council for Scientific and Industrial Research, University of KwaZulu-Natal, Durban, South Africa,* [3] *Department of Chemical and Civil Engineering, University of South Africa, Florida Campus, Pretoria, South Africa*

Edited by:
Maria Graca Rasteiro,
University of Coimbra, Portugal

Reviewed by:
Tiziana Tosco,
Politecnico di Torino, Italy
Sajjad Khezrianjoo,
Malayer University, Iran

***Correspondence:**
Opeyemi A. Oyewo
atiba.opeyemi@gmail.com
Maurice S. Onyango
Onyangoms@tut.ac.za

Specialty section:
This article was submitted to Water and Wastewater Management, a section of the journal Frontiers in Environmental Science

Received: *10 January 2020*
Accepted: *27 April 2020*
Published: *08 July 2020*

Citation:
Zulu B, Oyewo OA, Sithole B, Leswifi TY and Onyango MS (2020) Functionalized Sawdust-Derived Cellulose Nanocrystalline Adsorbent for Efficient Removal of Vanadium From Aqueous Solution. Front. Environ. Sci. 8:56. doi: 10.3389/fenvs.2020.00056

Water quality degradation due to noxious heavy metals has become a serious concern because of its impact on human health and the ecosystem. In this study, cellulose nanocrystal (CNC) derived from sawdust as a green renewable and sustainable resource was functionalized and used as adsorption media to remove pentavalent vanadium (V) from aqueous solution. The physicochemical properties of the adsorbent were studied using various characterization techniques such as Fourier transform infrared (FTIR) spectroscopy, scanning electron microscopy (SEM), and X-ray diffraction (XRD). The performance of the functionalized CNC adsorbent was explored as a function of solution pH, temperature, adsorbent mass, time, and initial concentration in batch adsorption. XRD results confirmed the crystalline nature of the CNC, which was more pronounced upon modification. The SEM micrograph revealed rough surface and high porosity, which suggested that the CNC possessed prerequisite properties of a good adsorbent. From the FTIR spectra results, the interaction between anionic vanadium species and functionalized CNC was confirmed by the reduction in wavelength of carboxylic groups (–COOH) of the CNC. Meanwhile, from the adsorption results, V removal efficiency was found to be affected by solution pH, temperature, adsorbent mass, and initial concentration. The Langmuir maximum adsorption capacity was 37.9–47.2 mg/g in the temperature range studied. In evaluating the reusability of the CNC through adsorption–desorption studies, results confirmed that the functionalized CNC could be used more than once with about 20% reduction in adsorption of V in each adsorption–desorption cycle. So far, there are indications that modified CNC may be an alternative adsorption media for V.

Keywords: adsorption, cellulose nanocrystals, functionalization, sawdust, vanadium

INTRODUCTION

Mining and metallurgical industries are the largest contributors to South Africa's economy but are at the same time the major contributors to water pollution crisis (Roy et al., 2019). These industries release large quantities of untreated (waste) water containing high level of heavy metal pollutants. In particular, toxic metals such as mercury, chromium, copper, zinc, lead, and vanadium have been found in waste streams (Parmar and Thakur, 2013). Among these metals, vanadium has been recognized as one of the most dangerous pollutants in the same class with mercury, lead, and arsenic (Hegazi, 2013). Prolonged exposure to high levels of vanadium is known to cause damage to the human respiratory organ and can also increase the risk of cancer related to lungs (Li et al., 2019). Vanadium is not biodegradable (Carolin et al., 2017); therefore, contaminated effluents need to be treated using robust techniques that ensure either its complete removal or reduction to acceptable levels that comply with environmental regulatory laws.

Various treatment techniques have been explored in vanadium (V) removal from contaminated effluents. These include chemical precipitation, ion exchange, chemical oxidation, reverse osmosis, ultrafiltration, electrodialysis, and adsorption (Montaña et al., 2013; Mulas et al., 2017). These techniques have inherent negative features such as high operation cost, the requirement of highly skilled personnel to operate, slow kinetics, incomplete removal of the metal ions and creation of hazardous metal-containing sludge which are difficult to treat (Quesada et al., 2019). These challenges hinder their wide application, especially in less developed countries. Proponents of adsorption technology in water treatment argue that the technology is robust, low cost if appropriate adsorbents are used, and associated with low environmental footprint when the adsorbents are reused multiple times before disposal. Consequently, several studies have reported the use of adsorption technology in V removal (Burakov et al., 2018). In the algorithm of adsorption process development, one of the starting points is the selection of an appropriate adsorbent. In this regard, a good adsorbent should have several features such as high affinity for the target pollutant, availability (abundance), fast kinetics, high selectivity, low cost per unit of polluted water treated, and renewable (Al-ghouti and Da'ana, 2020). In respect to these properties, various researchers have studied the performance of activated carbons, zeolites, clays silica gel, metal oxides, and biosorbent in vanadium removal (Barakat, 2011; Ince and Ince, 2017). Most of these materials do not provide high capacity for vanadium uptake and therefore would require large fixed beds.

The forestry, timber, pulp, and paper (FTPP) industries produce a lot of cellulosic waste materials that pose disposal problems. The use of these wastes as adsorbents can significantly contribute to environmental protection and reduce the cost of water treatment (Putro et al., 2017). Recently, nanoscale solid materials derived from these wastes have dramatically received tremendous attention because of their attractive advantages including eco-friendliness, cost-effectiveness, high efficiency, reusability, and possibility of metal recovery (Mahfoudhi and Boufi, 2017). Out of the variants of nanoscale cellulosic materials, cellulose nanocrystals (CNC) have large specific surface area with hydroxyl and anionic sulfate ester groups, which make the CNC a perfect substrate for preparing composites for adsorption of heavy metals from water and wastewater (Abdullah et al., 2013; Kumar et al., 2017).

Vanadium exists in an aqueous environment as an oxyanion, which is negatively charged. The charge on the CNC structure is also negative (Jiang et al., 2020). Consequently, CNC in its pristine form cannot be efficient for vanadium removal. The CNC matrix must, therefore, be re-engineered to make it suitable for adsorption of vanadium. Cationic surfactants are considered to be the most prominent materials for the enhancement of the adsorption capacity of adsorbents via functionalization (Hokkanen et al., 2016). So far, hexadecyltrimethylammonium bromide (HDTMA-Br) has been the most utilized surfactant for surface modification of CNC due to its ability to enhance the surface affinity of the CNC (Kaboorani and Riedl, 2015; Lizundia et al., 2016). To date, there is limited information available on the application of functionalized CNC derived from sawdust as an adsorbent for the removal of vanadium ions from water. Therefore, it is worthwhile to design a simple modification route to synthesize functionalized CNC adsorbent with tailored properties, while preserving their original morphology and maintaining the integrity and strength of the crystal.

This study presents the development of a simple route for cationic surfactant functionalization of CNC as an adsorbent for remediation of V pollutant from water. Upon functionalization, the adsorption media was characterized to obtain important features of the adsorption media and insights into V adsorption mechanism. Thereafter, batch adsorption studies were conducted to determine the adsorption capacity and kinetics characteristics of V. The effects of solution pH, sorbent mass, contact time, initial ion concentration, and temperature were systematically investigated. The equilibrium and kinetics data were interpreted using appropriate models.

MATERIALS AND METHODS

CNC suspension derived from sawdust was supplied by CSIR-Durban (South Africa) and was used as raw material for the preparation of sorption media. HDTMA-Br, ammonium metavanadate (NH_4VO_3), sodium hydroxide pellets (NaOH), and hydrochloric acid (HCl, 32% concentration) were purchased from Sigma-Aldrich (Germany). De-ionized water produced with the Purite water system (Model Select Analyst HP40, UK) was used to prepare relevant solution concentrations throughout this study. All chemicals used were of analytical grade.

Functionalization of CNC Adsorbent

The procedure for CNC involved a one-pot synthesis route using deionized (DI) water and sulfuric acid, which were subsequently ultra-sonicated to afford CNC suspension (Gibril et al., 2018; Sithole, 2019). The HDTMA-Br solution was prepared separately by mixing 0.73 g of HDTMA-Br powder with 48 ml of DI water and heated at 45°C under magnetic stirring. The modification reaction was initiated by introducing 35.09 g of 2.0% consistency CNC suspension into a 300-ml triple neck round bottom flask.

Trials confirmed that about 17 ml of the prepared HDTMA-Br solution was suitable for the modification of the amount of CNC used in synthesis procedure and was added slowly under continuous stirring for 2 h. Thereafter, the suspension was washed with DI water and then centrifuged for 45 min at 40,000 rpm to remove any possible excess of quaternary ammonium salt that could have aggregated on the CNC surface. The functionalized CNC sample was then removed from the centrifuge, filtered, and air-dried for 5 days at room temperature. Finally, the obtained dry cake was crushed into a fine powder and is hereafter referred to as HDTMA-Br functionalized CNC (HDTMA-Br/CNC) adsorbent.

Preparation of Vanadium Synthetic Water

A 1,000 mg/L stock solution of V was prepared by dissolving 2.2960 g of NH_4VO_3 powder in DI water using a 1-L volumetric flask while heating at ∼200°C. The working solution concentrations for batch equilibrium and kinetic experiments were obtained by diluting stock solution to appropriate concentrations.

Characterization of Adsorbent

Fourier transform infrared (FTIR) spectroscopy, X-ray diffraction (XRD), and scanning electron microscopy (SEM) were used to study different physical and chemical features of the HDTMA-Br/CNC adsorbent. The FTIR spectrometer (Perkin–Elmer Spectrum 100 spectrometer) equipped with an FTIR microscopy accessory, on the attenuated total reflection (ATR) diamond crystal was used to determine the functional groups present on the surface of the adsorbent. All spectra were recorded in the frequency range of 500–4,000 cm^{-1} with a spectra resolution of 4 cm^{-1}. To ascertain surface morphology of functionalized CNC adsorbent before and after adsorption process, SEM analysis was performed using a JEOL JSM-7500F FE-SEM equipped with an SEM-EDS analyzer running at a 2-kV accelerating voltage. The X-ray powder diffraction pattern was obtained using a Panalytical X'Pert Pro MPD-Ray diffractometer equipped with an X'celerator detector and operated with Ni-filtered Cu Kα radiation ($\lambda = 0.15406$ nm) generated at a voltage of 45 kV and a current of 40 mA.

Batch Adsorption Studies

Batch adsorption equilibrium experiments were carried out to determine the efficiency of the developed adsorbent on V removal as a function of variables such as adsorbent mass, initial solution pH, and temperature. Known amounts of the adsorbent were placed in contact with V solutions of known initial concentrations in 100 ml of polyethene (PE) plastic sample bottles. The contact between V solution and the adsorbent was facilitated by agitation in a temperature-controlled thermostatic shaker operated at 160 rpm for 24 h. The solution pH was varied from pH 2 to 8, temperature from 298 to 318 K, and adsorbent mass from 0.025 g to 0.2 g. At the end of each experiment, the samples were centrifuged for 45 min at 40,000 rpm and then filtered using a 0.45-µm syringe filter and were analyzed for residual metal ion concentration using an inductively coupled plasma atomic emission spectrometer (ICP-AES, 9000, Shimadzu, Japan). To determine the adsorption efficiency and uptake of V onto HDTMA-Br/CNC adsorbent, Equations 1 and 2 were used, respectively:

$$R_t = \frac{C_o - C_e}{C_o}.100 \qquad (1)$$

$$q_e = \frac{C_o - C_e}{m}.V \qquad (2)$$

where q_e is the adsorption capacity (mg/g) C_o and C_e are the initial and equilibrium concentrations (mg/L) of polluting ion, respectively. V is the volume (L) of the solution and (m) is the weight (g) of the adsorbent.

The kinetic experiments were conducted using a 1-L batch reactor stirred at a speed of 220 rpm. The effect of initial concentration was explored by varying the V initial concentration from 25 to 75 mg/L. The pH and adsorbent mass were fixed in the kinetic experiments. At various time intervals, a known amount of sample was taken and immediately filtered using a syringe filter of 0.45 µm pore size. Thereafter, the filtered samples were analyzed for residual V using an inductively coupled plasma atomic emission spectrometer (ICP-AES, 9000, Shimadzu, Japan). The amount of V adsorbed onto modified-CNC at the time (t) was evaluated using Equation 3:

$$q_t = \frac{C_o - C_t}{m}.V \qquad (3)$$

where q_t is the time-dependent amount of V adsorbed per unit mass of adsorbent and C_t is the concentration of V at any time t.

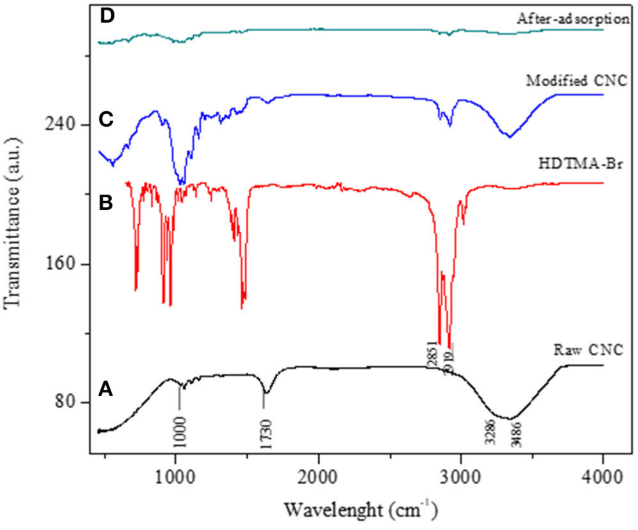

FIGURE 1 | FTIR spectra of **(A)** raw CNC (unmodified), **(B)** HDTMA-Br, **(C)** HDTMA-Br/modified CNC, and **(D)** HDTMA-Br/modified CNC after-V adsorption.

All the adsorption experiments were conducted in duplicate and the average values are reported.

Adsorption–Desorption Studies

The reusability of the adsorbent is an important factor in determining the economic viability of an adsorption process. In this regard, the adsorption–desorption study was conducted to assess the number of cycles the HDTMA-Br/CNC adsorbent would be used before replacement. The adsorption part of the cycle was done as described in adsorption experimental section while desorption of V from the surface of spent adsorbent was investigated using deionized water, NaCl and HCl eluents. As such, the spent adsorbent was dried and dispersed in the different eluents and then the mixtures were placed in a thermostatic bath shaker operated at 160 rpm and 298 K for 24 h. Thereafter, the desorbed solution was analyzed using ICP-AES to determine the amount of V desorbed. The adsorption–desorption procedure was repeated three times, and for each cycle, the percentage desorption efficiency was determined using the following equation:

$$\% \, Desorption \; efficiency = \frac{released \; V concentration}{initial \; adsorbed \; V} \tag{4}$$

RESULTS AND DISCUSSION

FTIR Spectroscopy

FTIR spectroscopy is an important tool for studying the functional groups incorporated onto the surface of an adsorbent and also to confirm the changes after surface modification. The FTIR spectra of raw CNC (unmodified), pure HDTMA-Br, and HDTMA-Br-modified CNC and the material after adsorption of V are shown in **Figures 1a–d**, respectively. The bands around 2,919 and 2,851 cm^{-1} in both pure HDTMA-Br and modified CNC are due to the characteristic symmetric and

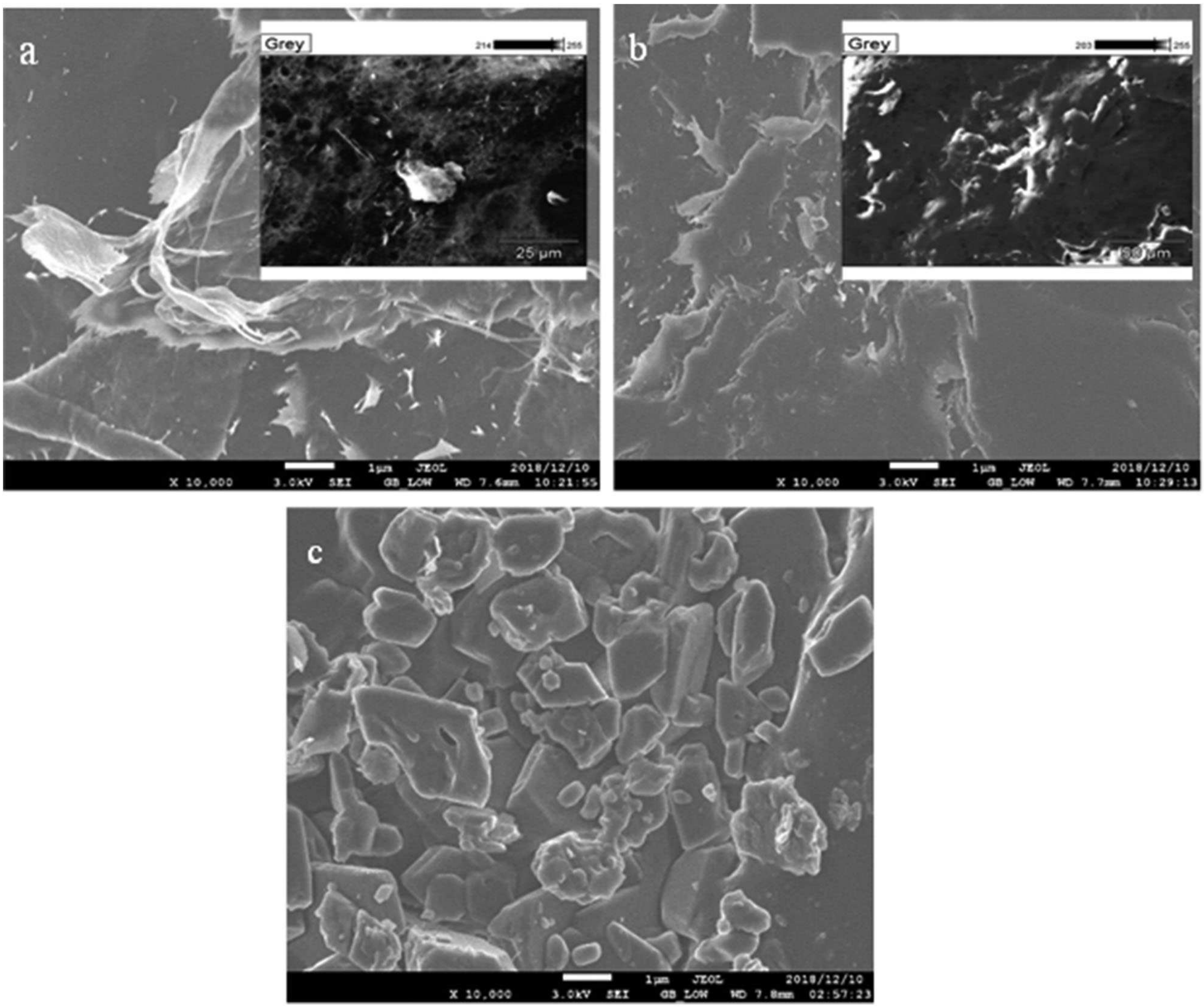

FIGURE 2 | SEM images of **(a)** raw CNC (unmodified) and **(b)** HDTMA-Br/modified CNC **(c)** HDTMA-Br/modified CNC after-V adsorption.

asymmetric C–H stretching vibrations of methyl and methylene groups (Kaboorani and Riedl, 2015). In the spectrum of raw CNC, the peak at 3,850 cm^{-1} could be ascribed to the O–H stretching vibrations on the surface of CNC. The peak at 1,730 cm^{-1} is the CO of a carbonyl group and could be attributed to the presence of carboxylic groups responsible for the coordination of metal ions during the adsorption process due to its disappearance in the spectrum of spent adsorbent (**Figure 1a**). The vibrational frequency at 1,250 cm^{-1} is due to the asymmetrical S=O vibration, which confirms the presence of a sulfate group present on the surface of pristine CNC. This functional group was formed during acid hydrolysis of CNC by sulfuric acid (Singh et al., 2015). A reduction in the intensity of the O–H band is noticeable upon functionalization (**Figure 1c**), and this phenomenon could be due to a reduction in the degree of the hydrogen bonding associated with –OH vibrations (Bezerra et al., 2017). A shift in the position of certain peaks after the adsorption of V is also observed, and this could be attributed to the interaction of the CNC with vanadium during the adsorption process.

Scanning Electron Microscopy

SEM analysis was used to explore the surface or external morphology of CNC adsorbent. **Figure 2** shows the SEM images of (a) raw CNC, (b) HDTMA-Br-modified CNC, and (c) HDTMA-Br/CNC after vanadium adsorption, respectively. **Figure 2a** shows that the raw CNC possessed a high porous surface and also indicates that CNC has high cellulose content with the average particle size between 6 and 36 nm (Nkalane et al., 2019). **Figure 2c** demonstrates a noticeable coverage of pores by the adsorbed vanadium ions after the adsorption process. Also, EDS analysis (**Table 1**) reveals a high percentage of carbon, oxygen and other elements corresponding to their binding energies as expected in all nanocellulose materials. As such the pristine CNC possesses mostly carbon (62.91%) and oxygen (33.15%). However, the presence of vanadium confirms the adsorption of V on the surface of modified CNC due to chemical interaction between V ion and modified CNC during the adsorption process.

X-Ray Diffraction

The crystallinity analysis of CNC adsorbents (unmodified, modified, and spent modified CNC) is presented in **Figure 3**. The XRD patterns in these cellulose samples show two major peaks at 15.51° and 22.4° corresponding to the 101 and 002 crystalline planes, respectively, ($C_{60}H_{88}O_8$ and $C_2H_{192}N_{64}O_{16}$), which are assigned to the cellulose 1α and 1β phases (Schwanningerab, 2004). However, this intensity is more pronounced upon modification and after adsorption of V, suggesting an increase in very strong interactions between the HDTMA-Br and cellulose structure. The appearance of other additional phases at 30° is also noticed after modification of CNC, which is further ascribed to the presence of modifiers used in the synthesis of modified CNC (Yin et al., 2018). Overall, the phases identified on CNC used in this study are similar to the reported characteristics of pure cellulose reported in our previous studies (Nkalane et al., 2019).

TABLE 1 | EDS analysis of raw CNC modified CNC before and after adsorption.

Element wt.%	Raw CNC	Modified CNC	After V adsorption
C	62.91	57.88	76.92
O	33.15	37.51	14.27
Na	0.25	-	-
Mg	0.04	0.03	-
Al	0.09	1.72	0.75
Si	0.06	0.03	0.05
S	3.30	1.28	-
Ti	-	0.18	-
Cl	0.11	-	-
V	-	-	7.92
Cu	-	-	0.09
K	0.03	-	-
Ca	0.04	-	-
Br	-	1.37	-
Cr	0.03	-	-
Total	100	100	100

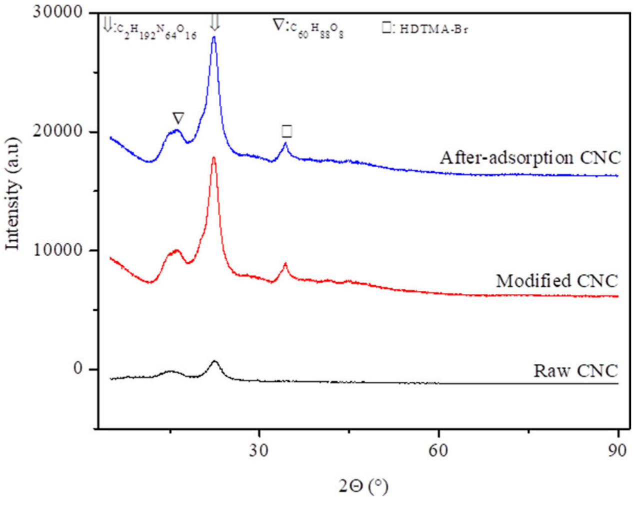

FIGURE 3 | X-ray diffraction patterns of unmodified, modified, and after V adsorption formed of cellulose nanocrystals.

Effect of Initial Solution pH

The pH of the metal ion solution is a very important variable that affects the degree of ionization and hence the adsorption process (Salehi and Anbia, 2019). Therefore, the effect of the initial solution pH on V uptake onto the surface of the surfactant-modified CNC was investigated in the pH 2–8 range. The results, summarized in **Figure 4**, show that highest V uptake is achieved at pH 3.0–4.0. This is because of the change in the chemistry of vanadium ion in aqueous solution with a change in pH. Vanadium has been reported to oxidize to its pentavalent anion (VO_3^-) at $3 < pH > 5$ in aqueous solution. This narrow pH range is the most conductive region for the adsorption of V ion

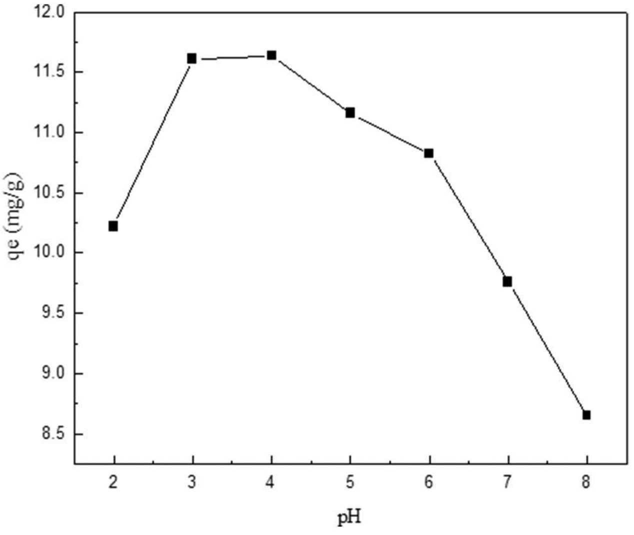

FIGURE 4 | Effect of initial pH on V adsorption onto modified CNC adsorbent (initial concentration, 25 mg/L; temperature, 298 K; adsorbent dose, 0.1 g).

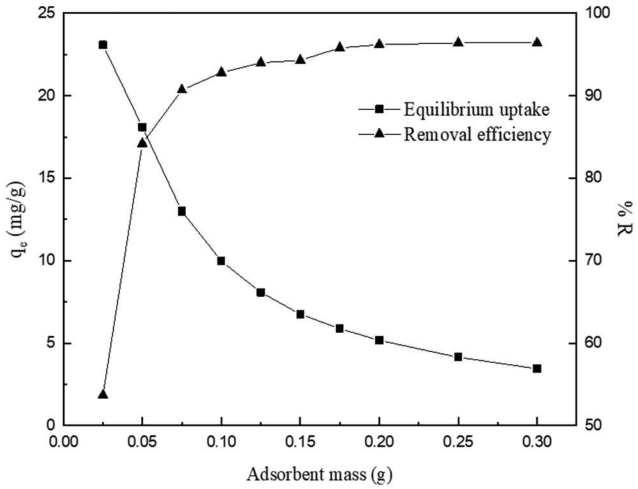

FIGURE 5 | Effect of adsorbent dosage on the removal of V onto modified CNC (initial concentration, 25 mg/L; pH 4.01; temperature, 298 K).

on the positively charged adsorbent surface. Meanwhile, below or above the optimum pH range, lower adsorption values are observed. In a study by Mthombeni et al. (2016) to investigate the effect of solution pH on the adsorption of V, a similar trend was observed, which can be ascribed to the decrease in the removal efficiency at pH 3.0 to the existence of VO_2^+ ions, which promoted the electrostatic repulsion of the protonated amino groups of the adsorbent. Besides, the decrease in adsorption uptake at increased initial pH might be attributed to the increased OH^- concentration on the surface of the adsorbent at high solution pH, which enhanced competitive adsorption with vanadium oxyanions.

Effect of Adsorbent Mass

The effect of modified CNC mass on the V uptake efficiency shows that the percentage of V removed increased with an increase in the adsorbent dosage (**Figure 5**). This is because at high adsorbent mass, the active sites for V uptake form solution increases (Mojiri et al., 2017). However, metal ion uptake decreases from 23.08 to 3.46 mg/g, with an increase in the dose from 0.025 to 0.3 g. Similar results were reported on the adsorption of V using adsorbent derived from agricultural waste (Kajjumba et al., 2018). Also, the results reveal that at higher sorbent dosage beyond 0.1 g, a slight increase in adsorption efficiency was attained. This is attributed to possible aggregation of particles of the adsorbent at higher dose, causing overlap and overcrowding during the process, and hence resulting in a decrease in accessibility of the available adsorption sites. Hence, in this study, 0.1 g was used for subsequent experiments.

Adsorption Isotherms

The temperature dependence of V adsorption onto modified CNC from simulated water was explored by varying the temperature from 298 to 318 K. The relationship between the amounts of adsorbed ions per unit mass of the CNC adsorbent (q_e) and the equilibrium concentration (C_e) of V solution is shown in **Figure 6A**. It is observed that the adsorption capacity of V increased with an increase in metal ion concentration and temperature of the system, suggesting that the adsorption of V onto modified CNC is endothermic in nature. The enhanced adsorption at higher temperature might be due to the increase in the diffusion rate of metal ions across the external boundary layer and into the internal pores of the adsorbent particles (Ahmad et al., 2015). The data obtained from adsorption equilibrium are used to describe the interaction between adsorbate and adsorbent for effective design of an adsorption process. Subsequently, the experimental data were analyzed using Langmuir, Freundlich, and Temkin models (**Table 2**). The linear form of the Langmuir, Freundlich, and Temkin adsorption isotherm equations (Onyango et al., 2004; Mthombeni et al., 2016) are given in Equations 5–7, respectively:

$$\frac{C_e}{q_e} = \frac{C_e}{q_m} + \frac{1}{k_L q_m} \tag{5}$$

$$\ln q_e = \ln k_f + \frac{1}{n} \ln C_e \tag{6}$$

$$q_e = \frac{RT}{b} \ln A + \frac{RT}{b} \ln C_e \tag{7}$$

where C_e is the equilibrium concentration of the polluting ion (mg/L), q_e is the amount of vanadium ions adsorbed on the adsorbent at the equilibrium (mg/g), q_m is the maximum adsorption capacity that describes a complete monolayer adsorption (mg/g), k_L is the Langmuir isotherm constant (L/mg) related to the free energy of adsorption, k_f and N are the Freundlich constants, R is a gas constant 8,314 J/mol·K, and T is the adsorption process temperature in K; A_T is the Temkin isotherm equilibrium

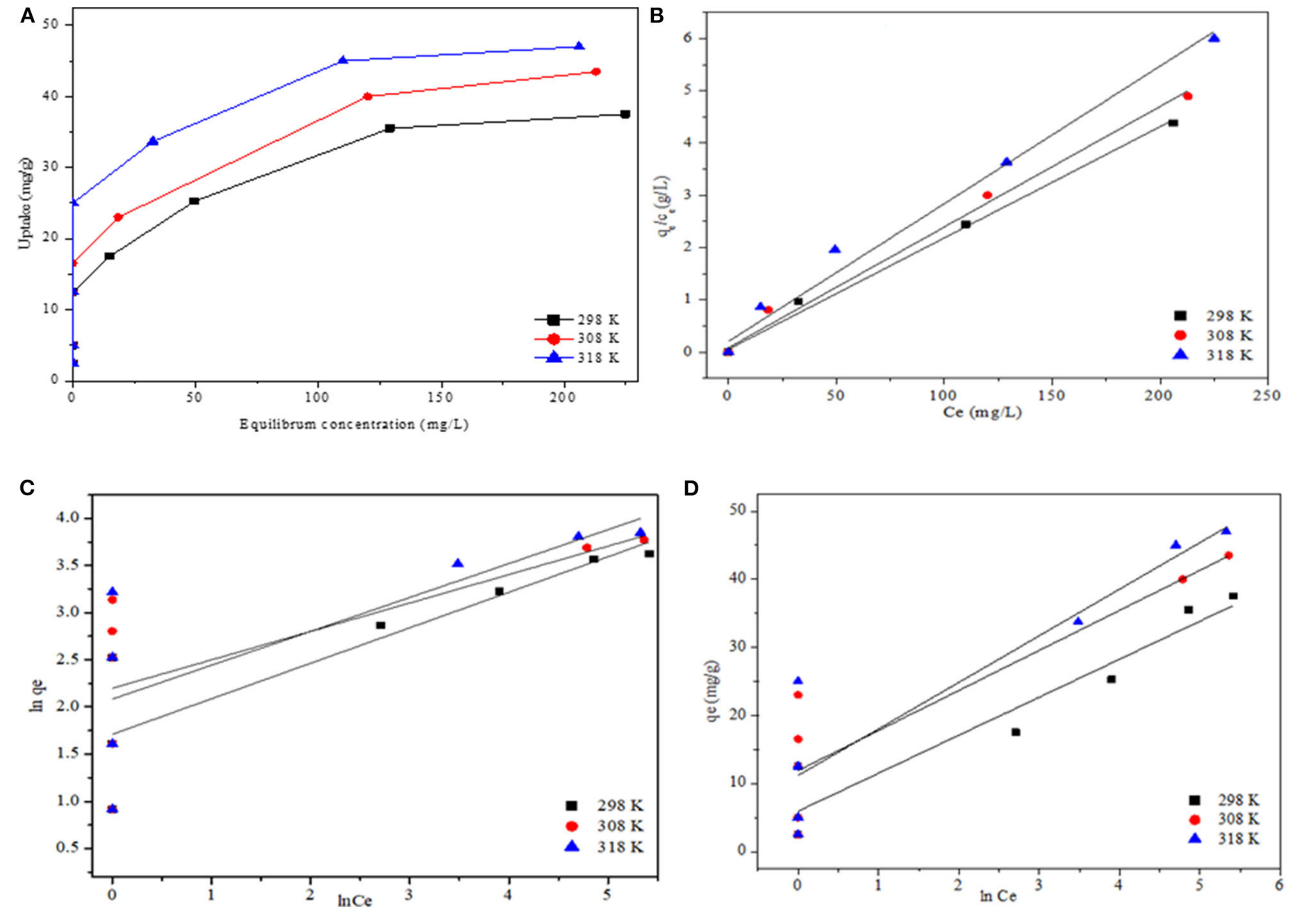

FIGURE 6 | Effect of temperature on V adsorption onto modified CNC **(A)**. Adsorption isotherm **(B)** and equilibrium data fit to Langmuir isotherm model, **(C)** Freundlich isotherm model, and **(D)** Temkin isotherm model.

TABLE 2 | Summary of equilibrium isotherms parameters of V sorption onto modified CNC.

Temperature °K		Langmuir		Freundlich			Temkin			
	q_m (mg g^{-1})	B (L mg^{-1})	R_L	R^2	K_F (L g^{-1})	n	R^2	b_T	A_T	R^2
298	37.9	0.13	0.221	0.987	5.536	2.66	0.786	417.73	2.48	0.929
308	43.3	0.28	0.939	0.994	9.017	3.32	0.501	215.20	2.54	0.820
318	47.2	0.41	0.704	0.996	8.039	2.78	0.601	236.35	2.27	0.846

binding constant (L/g) and b_T is constant related to heat of sorption.

The equilibrium isotherm parameters were extracted from the linear plots presented in **Figures 6B–D** and are summarized in **Table 2**. Based on the correlation coefficients, only the Langmuir isotherm describes the adsorption process sufficiently well. This may be an indication of adsorption on homogeneous surfaces. The results further show an increase in the Langmuir maximum adsorption capacity (q_m) and $k_L$from 37.9 to 47.2 mg/g and 0.130 to 0.410 (L/mg), respectively, with an increase in temperature. Compared with other biomaterials summarized in **Table 2**, the adsorption capacity obtained in this study is quite competitive. In exploring the favorability of the adsorption process using the separation factor (R_L), results reveal that the values are within $0 < R_L > 1$ range, indicating that the adsorption of V onto modified CNC was favorable. Overall, the adsorption capacity obtained in this study is highly competitive compared to the performances of some adsorbents reported in the literature with the same operating condition (see **Table 3**).

Adsorption Kinetics

Adsorption kinetics is useful in determining the rate of adsorption and the mechanism involved in the removal of any contaminant from water. In the present study, the effect of the initial concentration in the range 25–75 mg/L was investigated as a function of contact time (0–280 min), and the results are summarized in **Figure 7**. The graph presents a two-step process: an initial stage characterized by rapid adsorption as a result of the availability of sufficient binding sites and a second stage in which the rate gradually decreases as equilibrium stage is approached. The later slow adsorption rate is attributed to the electrostatic hindrance caused by already adsorbed vanadium species and the slow pore diffusion of the ions (Mekonnen et al., 2015). The results were interpreted using adsorption kinetic models that give insights into the possible rate-controlling steps and from which preliminary design parameters may be obtained. The kinetic models considered are pseudo-first-order (Equation 7), pseudo-second-order (Equation 8), and Elovich models (Equation 9).

$$\log\left(q_e - q_t\right) = \log q_e - \frac{k_1}{2.303}t \tag{8}$$

$$\frac{t}{q_t} = \frac{1}{k_2 q_e} + \frac{1}{q_e}t \tag{9}$$

$$q_t = \frac{1}{\beta}\ln \alpha\beta + \frac{1}{\beta}\ln t \tag{10}$$

where q_e and q_t are the adsorption capacity (mg/g) of solute at equilibrium and at a time t (min), respectively, k_1 (min^{-1}) and k_2 (g/mg·min) are the rate constants of the pseudo-first-order and pseudo-second-order adsorption, respectively. α is the initial adsorption rate (mg/g·min) and β is the desorption constant (g/mg) related to the extent of surface coverage and activation energy for chemisorption.

The kinetic model parameters and the linear regression values are presented in **Table 4**. The linear regression values obtained from the pseudo-second-order model are higher compared to the other two models, suggesting that the interaction between the adsorbent and V followed the pseudo-second-order mechanism and that this interaction was chemical in nature, further supporting the FTIR characterization results presented in earlier sections. Also revealed in **Table 4** is the increase

TABLE 3 | Comparison of capacity values between modified CNC and different waste-derived adsorbents in V removal.

Adsorbent	Sorption capacity q_m (mg/g)	References
Cassava waste biomass	20.0	Simate et al., 2015
Nano-sized banana peels	27.94	Oyewo et al., 2018
Brown seaweed (Biomass)	43.3	
Metal sludge	24.8	
Posidonia oceanica biomass	18.0	Pennesi et al., 2013
HDTMA-Br/CNC	47.2	Present study

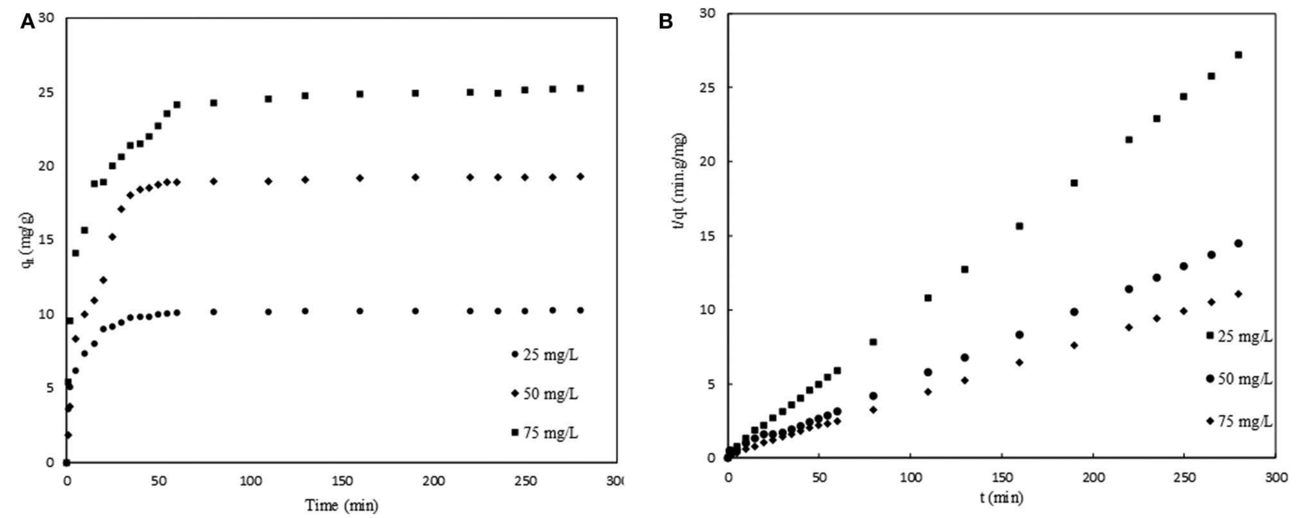

FIGURE 7 | (A) Adsorption kinetics for adsorption of V (V) onto modified CNC (HDTMA-Br/CNC) at different concentrations. **(B)** Pseudo-second-order kinetics model.

TABLE 4 | Kinetics parameters of V adsorption onto surfactant modified CNC.

Initial conc. (mg/L)		Pseudo-first order			Pseudo-second order			Elovich		
	q_e (mg g^{-1})	$q_{e,cal}$ (mg g^{-1})	k_1	R^2	$q_{e,cal}$ (mg g^{-1})	k_2	R^2	α	β	R^2
25	10.3	1.303	0.018	0.798	10.4	0.041	0.999	1.359	12.1	0.808
50	19.3	2.129	0.024	0.863	19.8	0.009	0.999	3.359	0.72	0.888
75	25.3	2.559	0.0.17	0.904	25.6	0.007	0.998	3.740	1.54	0.906

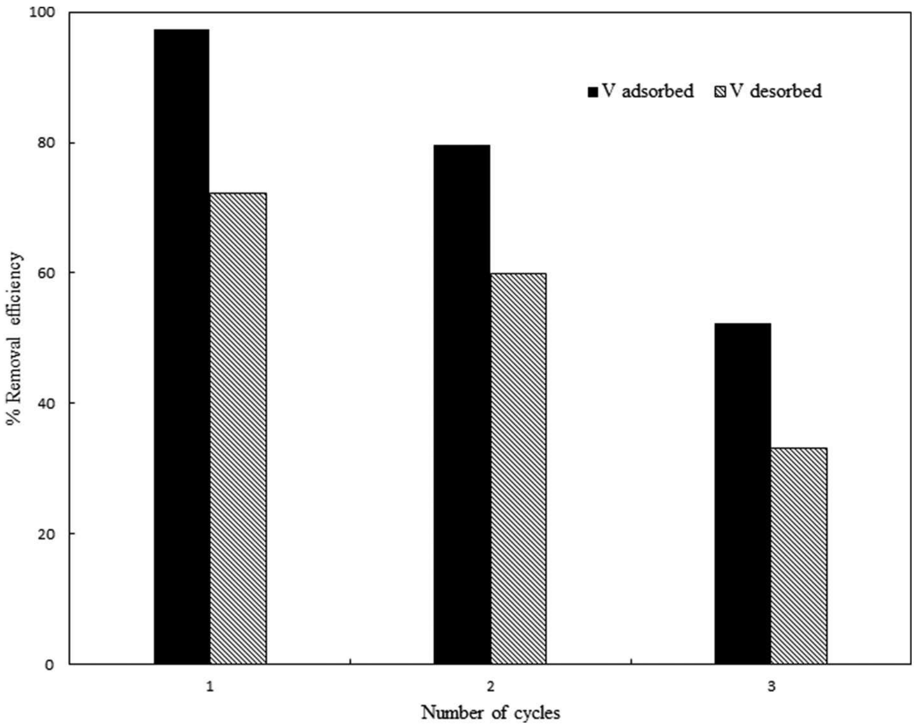

FIGURE 8 | Adsorption–desorption efficiency of vanadium using 2.0 M NaCl eluents.

in experimental adsorption capacity, q_e, with an increase in initial concentration. This is due to the higher driving force usually occurring at higher initial concentration of solute that overcomes the resistance of the mass transfer between bulk solution and the solid–liquid interface (Mthombeni et al., 2018). The experimental equilibrium capacities are very close to those determined using the pseudo-second-order model, which further point to the fact that indeed the process followed the pseudo-second-order mechanism.

Desorption Studies

The cyclic adsorption–desorption experiments were performed to evaluate the reusability of modified CNC to assess the economic viability of the adsorption process. Furthermore, reusability is also key to saving the environment from secondary pollution as a result of the disposal of the metal-loaded adsorbent. Three different eluents were investigated during the preliminary studies but only one (NaCl) was found to perform and was therefore chosen for subsequent desorption process. The adsorption–desorption results are presented in **Figure 8**. Two features are observed. First, both the adsorption and desorption efficiencies decrease in each operation cycle. For example, about 20% reduction in adsorption percentage was observed after the first cycle. Second, in each cycle, the adsorption efficiency is higher than that of desorption. Several reasons could explain the observations. The decrease in adsorption efficiency in each cycle is because not all active sites are released during the desorption step, rendering the adsorbent to lose its activity. Also, the decrease in desorption efficiency in each cycle is a manifestation of the strong bonds formed between the adsorbing vanadium ions and active sites. Moreover, the observations could also be ascribed to the dissolution of CNC and subsequent loss in mass of the adsorbent, which might have affected the mechanisms of interaction between V and the modified CNC active sites (Han et al., 2006). Overall, the adsorption–desorption results suggest that the modified-CNC could be reused more than once. Similar results were reported for the adsorption of cadmium and the reusability of brown seaweed derived cellulosic biosorbent using NaCl as an efficient eluent (Stirk and Staden, 2002).

CONCLUSION

CNC was successfully modified using HDTMA-Br, and its performance in V removal from water is explored. Characterization results of modified CNC showed dramatic improvement in the surface properties, which resulted in the enhancement of its adsorption capacity. The Langmuir adsorption isotherm model described the experimental data satisfactorily well-compared to other isotherm models. Meanwhile a rapid adsorption rate was observed as a result of availability of sufficient high-affinity binding sites at the initial stages of adsorption. In interpreting the kinetics of adsorbent–adsorbate interaction, a number of kinetic models were tested and results reveal that the pseudo-second-order model gives the best description of the data.

Indeed, therefore, the characterization and adsorption results point to the chemisorption nature of V interaction with modified CNC. In performing adsorption–desorption experiments to explore reusability of the adsorbent, it was observed that the media is reusable; however, the activity of the media decreased in each cycle. In general, the study demonstrated that modified CNC could be used as a promising adsorbent for removal of V from water. Further studies are ongoing to explore the applicability of this media in different water matrices.

DATA AVAILABILITY STATEMENT

All datasets generated for this study are included in the article/supplementary material.

AUTHOR CONTRIBUTIONS

All authors conceptualized the idea and experimental aspect. BZ and OO wrote the draft. BS and MO coordinated and corrected the final draft of the paper. TL coordinated and corrected the revised version of the manuscript.

ACKNOWLEDGMENTS

The authors would like to acknowledge the Tshwane University of Technology, Department of Science and Technology–Republic of South Africa for financial support of the Biorefineries Consortium and the Council for Scientific and Industrial Research (CSIR) for providing raw CNC and allowing access to analytical facilities.

REFERENCES

Abdullah, R., Abustan, I., and Ibrahim, A. N. M. (2013). Wastewater treatment using bentonite, the combinations of bentonite-zeolite, bentonite-alum, and bentonite-limestone as adsorbent and coagulant. *Int. J. Environ. Sci.* 4, 379–391. doi: 10.6088/ijes.2013040300014

Ahmad, M. A., Ahmad, N., and Bello, O. S. (2015). Removal of remazol brilliant blue reactive dye from aqueous solutions using watermelon rinds as adsorbent. *J. Dispersion Sci. Technol.* 36, 845–858. doi: 10.1080/01932691.2014.925400

Al-ghouti, M. A., and Da'ana, D. A. (2020). Guidelines for the use and interpretation of adsorption isotherm models: a review. *J. Hazard. Mater.* 393:122383. doi: 10.1016/j.jhazmat.2020.122383

Barakat, M. (2011). New trends in removing heavy metals from industrial wastewater. *Arabian J. chem.* 4, 361–377. doi: 10.1016/j.arabjc.2010.07.019

Bezerra, R. C., Leal, R. S., Da silva, M. I. S., Morais, A., Marques, T. A., Osajima, J. B., et al. (2017). Direct modification of microcrystalline cellulose with ethylenediamine for use as adsorbent for removal amitriptyline drug from environment. *Molecules* 22:E2039. doi: 10.3390/molecules22112039

Burakov, A. E., Galunin, E. V., Burakova, I. V., Kucherova, A. E., Agarwal, S., Tkachev, A. G., et al. (2018). Adsorption of heavy metals on conventional and nanostructured materials for wastewater treatment purposes: a review. *Ecotoxicol. Environ. Saf.* 148, 702–712. doi: 10.1016/j.ecoenv.2017.11.034

Carolin, F., Ponnusamy, S. K., Anbalangan, S., Joshiba, J., Naushad, M. (2017). Efficient Techniques for the Removal of Toxic Heavy Metals from Aquatic Environment: A Review. *J. Environ. Chem. Eng.* 5:3. doi: 10.1016/j.jece.2017.05.029

Gibril, M., Tesfaye, T., Sithole, B., Lekha, P. and Ramjugernath, D. (2018). Optimisation and enhancement of crystalline nanocellulose production by ultrasonic pretreatment of dissolving wood pulp fibres. *Cellulose Chem. Technol.* 52, 9–10. doi: 10.3390/molecules22112039

Han, R., Zhang, J., Zou, W., Shi, J., Xiao, H., and Liu, H. M. (2006). Biosorption of copper(II) and lead(II) from aqueous solution by chaff in a fixed bed column. *J. Hazard. Mater.* 133, 262–268. doi: 10.1016/j.jhazmat.2005.10.019

Hegazi, H. A. (2013). Removal of heavy metals from wastewater using agricultural and industrial wastes as adsorbents. *HBRC J.* 9, 276–282. doi: 10.1016/j.hbrcj.2013.08.004

Hokkanen, S., Bhatnagar, A., and Sillanpä, M. (2016). A review on modification methods to cellulose-based adsorbents to improve adsorption capacity. *Water Res.* 91,156–173. doi: 10.1016/j.watres.2016.01.008

Ince, M., and Ince, O. K. (2017). An Overview of adsorption technique for heavy metal removal from water/wastewater: a critical review. *Int. J. Pure Appl. Sci.* 3,10–19. doi: 10.29132/ijpas.358199

Jiang, Q., Xing, X., Jing, Y., and Han, Y. (2020). Preparation of cellulose nanocrystals based on waste paper via different systems. *Int. J. Biol. Macromol.* 149, 1318–1322. doi: 10.1016/j.ijbiomac.2020.02.110

Kaboorani, A., and Riedl, B. (2015). Surface modification of cellulose nanocrystals (CNC) by a cationic surfactant. *Ind. Crops Prod.* 65,45–55. doi: 10.1016/j.indcrop.2014.11.027

Kajjumba, G. W., Aydin, S., and Güneysu, S. (2018). Adsorption isotherms and kinetics of vanadium by shale and coal waste. *Adsorpt. Sci. Technol*. 36, 936–952. doi: 10.1177/0263617417733586

Kumar, R., Sharma, R. K., and Singh, A. P. (2017). Cellulose based grafted biosorbents - Journey from lignocellulose biomass to toxic metal ions sorption applications - a review. *J. Mol. Liq.* 232, 62–93. doi: 10.1016/j.molliq.2017.02.050

Li, J., Xiao, F., Zhang, L., and Amirkhanian, S. N. (2019). Life cycle assessment and life cycle cost analysis of recycled solid waste materials in highway pavement: A review. *J. Clean. Prod.* 233, 1182–1206. doi: 10.1016/j.jclepro.2019.06.061

Lizundia, E., Meaurio, E., and Vilas, J. (2016). "Grafting of cellulose nanocrystals," in *Multifunctional Polymeric Nanocomposites Based on Cellulosic Reinforcements*, eds P. Debora, E. Fortunati, J. M. Kenny (Elsevier), 61–113. doi: 10.1016/B978-0-323-44248-0.00003-1

Mahfoudhi, N., and Boufi, S. (2017). Nanocellulose: a challenging nanomaterial towards environment remediation. *Cell. Reinfor. Nanofibre Composites* 2017, 277–304. doi: 10.1016/B978-0-08-100957-4.00012-7

Mekonnen, E., Yitbarek, M., and Soreta, T. R. (2015). Kinetic and thermodynamic studies of the adsorption of Cr (VI) onto some selected local adsorbents. *South Afr. J. Chem.* 68, 45–52. doi: 10.17159/0379-4350/2015/v68a7

Mojiri, A., Hui, W., Arshad, A. K., Ridzuan, A. R. M., Hamid, N., Farraji, H., et al. (2017). Vanadium(V) removal from aqueous solutions using a new composite adsorbent (BAZLSC): Optimization by response surface methodology. *Adv. Environ. Res*, 6, 173–187. doi: 10.12989/aer.2017.6.3.173

Montaña, M., Camacho, A., Serrano, I., Devesa, R., Matia, L., and Vallés, I. (2013). Removal of radionuclides in drinking water by membrane treatment using ultrafiltration, reverse osmosis and electrodialysis reversal. *J. Environ. Radioact.* 125, 86–92. doi: 10.1016/j.jenvrad.2013.01.010

Mthombeni, N. H., Mbakop, S., Ochieng, A., and Onyango, M. S. (2016). Vanadium(V) adsorption isotherms and kinetics using polypyrrole coated magnetized natural zeolite. *J. Taiwan Inst. Chem. Eng.* 66, 172–180. doi: 10.1016/j.jtice.2016.06.016

Mthombeni, N. H., Mbakop, S., Ochieng, A., and Onyango, M. S. (2018). Adsorptive removal of V (V) ions using clinoptilolite modified with polypyrrole and iron oxide nanoparticles in column studies. *MRS Adv.* 3, 2119–2127. doi: 10.1557/adv.2018.229

Mulas, D., camacho, A., Serrano, I., Montes, S., Devesa, R., and Duch, M.A. (2017). Natural and artificial radionuclides in sludge, sand, granular activated carbon and reverse osmosis brine from a metropolitan drinking water treatment plant. *J. Environ. Radioact.* 177, 233–240. doi: 10.1016/j.jenvrad.2017.07.001

Nkalane, A., Oyewo, O. A., Leswifi, T., and Onyango, M. S.(2019). Application of coagulant obtained through charge reversal of sawdust-derived cellulose nanocrystals in the enhancement of water turbidity removal. *Mat. Res. Exp.* 6:105060. doi: 10.1088/2053-1591/ab3b49

Onyango, M. S., Kojima, Y., Aoyi, O., Bernardo, E. C., and Matsuda, H. (2004). Adsorption equilibrium modeling and solution chemistry dependence of fluoride removal from water by trivalent-cation-exchanged zeolite F-9. *J. Colloid Interf. Sci.* 279, 341–350. doi: 10.1016/j.jcis.2004.06.038

Oyewo, O. A., Wolkersdorfer, C., Onyango, M. S., and Adeniyi, A. (2018). "The performance of nano-sized Banana Peels in the removal of vanadium from mine water" in *11th ICARD | IMWA | MWD Conference – "Risk to Opportunity"*. South Africa.

Parmar, M., and Thakur, L. S. (2013). Heavy metal Cu, Ni and Zn: toxicity, health hazards and their removal techniques by low cost adsorbents: a short overview. *Int. J. Plant Anim. Environ. Sci*. 3, 2231–4490. Available online at: www.ijpaes.com.

Pennesi, C., Totti, C., and Beolchini, F. (2013). Removal of vanadium (III) and molybdenum (V) from wastewater using *Posidonia oceanica* (Tracheophyta) biomass. *PLoS ONE* 8:e76870. doi: 10.1371/journal.pone.0076870

Putro, J. N., Kurniawan, A., Ismadji, S., and Ju, Y.-H. (2017). Nanocellulose based biosorbents for wastewater treatment: study of isotherm, kinetic, thermodynamic and reusability. *Environ. Nanotechnol. Monit. Manage.* 8, 134–149. doi: 10.1016/j.enmm.2017.07.002

Quesada, H. B., Baptista, A. T. A., Cusioli, L. F., Seibert, D., De oliveira, B. C., and Bergamasco, R. (2019). Surface water pollution by pharmaceuticals and an alternative of removal by low-cost adsorbents: a review. *Chemosphere* 222, 766–780. doi: 10.1016/j.chemosphere.2019.02.009

Roy, S., Tang, M., and Edwards, M. A. (2019). Lead release to potable water during the Flint, Michigan water crisis as revealed by routine biosolids monitoring data. *Water Res.* 160, 475–483. doi: 10.1016/j.watres.2019.05.091

Salehi, S., and Anbia, M. (2019). Performance comparison of chitosan–clinoptilolite nanocomposites as adsorbents for vanadium in aqueous media. *Cellulose* 26, 1–25. doi: 10.1007/s10570-019-02450-9

Schwanningerab, M. (2004). Effects of short-time vibratory ball milling on the shape of FT-IR spectra of wood and cellulose. *Vibrat. Spectrosc.* 36, 23–40. doi: 10.1016/j.vibspec.2004.02.003

Simate, G. S., Ndlovu, S., and Seepe, L. (2015). Removal of heavy metals using cassava peels waste biomass in a multi-stage countercurrent batch operation. *J. S. Afr. Inst. Min. Metall.* 115, 1137–1141. doi: 10.17159/2411-9717/2015/v115n12a1

Singh, K., Sinha, T. J. M., and Srivastava, S. (2015). Functionalized nanocrystalline cellulose: smart biosorbent for decontamination of arsenic. *Int. J. Mineral Process.* 139, 51–63. doi: 10.1016/j.minpro.2015.04.014

Sithole, B. (2019). *Beneficiation of Pulp and Paper Mill Sludge*. Clean Technologies and Environmental Policy. doi: 10.1016/B978-0-323-44248-0.00003-1

Stirk, W., and Staden, V. (2002). desorption of cadmium and the reuse of brown seaweed derived products as biosorbents. *Bot. Marina* 45, 9–16. doi: 10.1515/BOT.2002.002

Yin, X., Meng, X., Zhang, Y., Zhang, W., Sun, H., Lessl, J. T., et al. (2018). Removal of V (V) and Pb (II) by nanosized TiO2 and ZnO from aqueous solution. *Ecotoxicol. Environ. Saf.* 164, 510–519. doi: 10.1016/j.ecoenv.2018.08.066

Conflict of Interest: The authors declare that the research was conducted in the absence of any commercial or financial relationships that could be construed as a potential conflict of interest.

Advantages of publishing in Frontiers

OPEN ACCESS
Articles are free to read
for greatest visibility
and readership

FAST PUBLICATION
Around 90 days
from submission
to decision

HIGH QUALITY PEER-REVIEW
Rigorous, collaborative,
and constructive
peer-review

TRANSPARENT PEER-REVIEW
Editors and reviewers
acknowledged by name
on published articles

Frontiers
Avenue du Tribunal-Fédéral 34
1005 Lausanne | Switzerland

Visit us: www.frontiersin.org
Contact us: info@frontiersin.org | +41 21 510 17 00

REPRODUCIBILITY OF RESEARCH
Support open data
and methods to enhance
research reproducibility

DIGITAL PUBLISHING
Articles designed
for optimal readership
across devices

FOLLOW US
@frontiersin

IMPACT METRICS
Advanced article metrics
track visibility across
digital media

EXTENSIVE PROMOTION
Marketing
and promotion
of impactful research

LOOP RESEARCH NETWORK
Our network
increases your
article's readership